

FINAL TECHNICAL REPORT

for

NASA GRANT NAG 5-501

GODDARD
GRANT
IN-90-CR
332 295
P297

SIMULTANEOUS SOLAR MAXIMUM MISSION (SMM)
AND VERY LARGE ARRAY (VLA) OBSERVATIONS OF SOLAR ACTIVE
REGIONS

A NASA SMM GUEST INVESTIGATOR GRANT

for the period

01 February 1985 to 31 January 1991

Date of submission: 28 February, 1991

Robert F. Willson

Robert F. Willson
Principal Investigator
NASA Grant NAG 5-501
Research Associate Professor of Astronomy
Department of Physics and Astronomy
Robinson Hall
Tufts University
Medford, MA 02155

INTRODUCTION

Research support under NASA Grant 5-501 with the SMM Guest Investigator Program from 01 February, 1985 to 31 January, 1991 has resulted in a total of 25 publications in refereed journals of the highest quality. The main body of this Final Technical Report consists of an index and reprints of these papers.

But first we can highlight the important new results that are given in these papers: Very Large Array (VLA) observations at 20 cm wavelength can detect the hot coronal plasma previously observed at soft X-ray wavelengths. Thermal cyclotron line emission has been detected at the apex of coronal loops where the magnetic field strength is relatively constant. Detailed comparisons of simultaneous Solar Maximum Mission (SMM) Satellite and VLA data indicate that physical parameters such as electron temperature, electron density and magnetic field strength can be obtained, but that some coronal loops remain invisible in either spectral domain. These early collaborative studies led to the Coronal Magnetic Structures Observing Campaign (COMSTOC), involving simultaneous SMM, VLA and other ground-based observations; the combined data have been used to infer emission mechanisms and plasma parameters for quiescent coronal loops above active regions.

Collaborative SMM, VLA and Nancay Radioheliograph observations have also provided new perspectives about the spatial and temporal evolution of intense solar flares. The unprecedented spatial resolution of the VLA at 20 cm wavelength has shown that the precursor, impulsive and post-flare components of solar bursts originate in nearby, but separate loops or systems of loops. In some cases preburst heating and magnetic changes are observed from loops tens of minutes prior to the impulsive phase. Comparisons with soft X-ray images and spectra and with hard X-ray data specify the

magnetic field strength and emission mechanism of flaring coronal loops.

At the longer 91 cm wavelength, the VLA has detected extensive emission interpreted as a hot 10^5 K interface between cool, dense $H\alpha$ filaments and the surrounding hotter, rarefied corona. Observations at 91 cm also provide evidence for time-correlated bursts in active regions on opposite sides of the solar equator; they are attributed to flare triggering by relativistic particles that move along large-scale, otherwise-invisible, magnetic conduits that link active regions in opposite hemispheres of the Sun.

PUBLISHED PAPERS

Page

A. "VLA OBSERVATIONS OF SOLAR ACTIVE REGIONS AT CLOSELY SPACED FREQUENCIES: EVIDENCE FOR THERMAL CYCLOTRON LINE EMISSION": Robert F. Willson, *Astrophysical Journal*, **298**, 911-917.....8

B. HIGH-RESOLUTION MICROWAVE OBSERVATIONS OF THE SUN AND NEARBY STARS", Kenneth R. Lang, *Solar Maximum Analysis*, (eds. V.E. Stepanov and V.N. Obridko, VNU Science Press, 1986) 69-89.15

C. "SOLAR BURST PRECURSORS AND ENERGY BUILDUP AT MICROWAVE WAVELENGTHS", Kenneth R. Lang and Robert Willson, *Advances in Space Research*, **6**, no. 6 97-100 (1986),.....36

D. "VLA OBSERVATIONS OF COMPACT, VARIABLE SOURCES ON THE SUN", Robert F. Willson and Kenneth R. Lang, *Astrophysical Journal*, **308**, 443-447 (1986).....40

E. "CORONAL PLASMAS ON THE SUN AND NEARBY STARS", Kenneth R. Lang, *Coronal and Prominence Plasmas*, (NASA Conference Pub. 2442, 186) 309-317.....46

F. "CORONAL DIAGNOSTICS", Kenneth R. Lang, *Coronal and Prominence Plasmas*, (NASA Conference pub. 2442, U.S. Govt Printing, 1986) 279-289.55

G. COMPACT, VARIABLE SOURCES ON THE SUN AT 2 CENTIMETER WAVELENGTH", Robert F. Willson and Kenneth R. Lang, *Solar Physics*, **114**, 93-104 (1987).....67

H. "VLA OBSERVATIONS OF SOLAR NOISE STORMS", Kenneth R. Lang and Robert F. Willson, *Astrophysical Journal*, **319**, 514-519 (1987).79

I. "SIMULTANEOUS SMM FLAT CRYSTAL SPECTROMETER AND VERY LARGE ARRAY OBSERVATIONS OF SOLAR ACTIVE REGIONS", Kenneth R. Lang, Robert F. Willson, Kermit L. Smith, and Keith T. Strong, <i>Astrophysical Journal</i> , 322 , 1035-1043 (1987).	85
J. "SOLAR ACTIVE REGION PHYSICAL PARAMETERS INFERRED FROM A THERMAL CYCLOTRON LINE AND SOFT X-RAY SPECTRAL LINES", Kenneth R. Lang, Robert F. Willson, Kermit L. Smith, and Keith T. Strong, <i>Astrophysical Journal</i> , 322 , 1044-1051 (1987).	94
K. "HIGH RESOLUTION VLA MAPS OF THE QUIESCENT CORONA AT 90 CM WAVELENGTH", Kenneth R. Lang, Robert F. Willson and Gerard Trottet, <i>Astrophysical Journal</i> , 199 , 325-328 (1988).	102
L. "MICROWAVE OBSERVATIONS OF SOLAR AND STELLAR CORONAE", Robert F. Willson, in <i>Solar and Stellar Coronal Structure and Dynamics</i> , (ed. Richard C. Altrock, National Solar Observatory, 1988) 54-65.	106
M. "SIMULTANEOUS VLA-SATELLITE OBSERVATIONS OF THE SUN", Kenneth R. Lang. <i>Advances in Space Research, Proceedings of the XXVII Committee on Space Research (COSPSR) Meeting</i> (Pergamon Press, 1988):	119
N. "HIGH-RESOLUTION VLA-NANCAY OBSERVATIONS OF THE SUN", Alain Kerdraon, Gerard Trottet, Kenneth R. Lang and Robert F. Willson, <i>Advances in Space Research; Proceedings of the XXVII Committee on Space Research (COSPAR) Meeting</i> (Pergamon Press, 1988).	128

O. "TIME-CORRELATED BURSTS FROM WIDELY-SEPARATED SOLAR ACTIVE REGIONS", Kenneth R. Lang and Robert F. Willson, <i>Astrophysical Journal (Letters)</i> , 344 , L77-L80 (1989).....	136
P. "RADIO EMISSION FROM QUIESCENT SOLAR FILAMENTS AT 91.6 CM WAVELENGTH", Kenneth R. Lang and Robert F. Willson, <i>Astrophysical Journal (Letters)</i> , 344 , L73-L75 (1989).	141
Q. "IMPULSIVE MICROWAVE BURST AND SOLAR NOISE STORM EMISSION RESOLVED WITH THE VLA", Robert F. Willson, Kenneth R. Lang and Margaret Liggett, <i>Astrophysical Journal</i> , 350 , 856-867 (1990).....	145
R. "RADIO EMISSION FROM QUIESCENT FILAMENTS", Kenneth R. Lang, <i>Proceedings of IAU Colloquium No. 177, Dynamics of Prominences</i> , Hvar Observatory Bulletin B , 93-111 (1989).	157
S. "FLARE STARS AT RADIO WAVELENGTHS", Kenneth R. Lang, <i>Proceedings of IAU Symposium No. 98, Flare Stars in Star Clusters, Associations and the Solar Vicinity</i> , (eds. V. Mirzoyan et al.) The Netherlands: STU Publishers, 1990.	175
T. "VLA OBSERVATIONS OF THE CORONAL PLASMA", Kenneth R. Lang, <i>Proceedings of IAU SYMPOSIUM No. 142. Basic Plasma Processes on the Sun</i> (eds. E.R. Priest and V. Krishan) Boston:Kluwer Academic Press, 1990).....	189

U. "VLA-PHOENIX OBSERVATIONS OF A NARROW BAND DECIMETRIC BURST", Robert F. Willson and Arnold A. Benz, <i>Proceedings of IAU Symposium No. 142. Basic Plasma Processes on the Sun</i> (eds. E.R. Priest and V. Krishan) Boston: Kluwer Academic Press, 1990).....	195
V. "MULTI-WAVELENGTH OBSERVATIONS OF ENERGY RELEASE DURING A SOLAR FLARE", Robert F. Willson, Karl-Ludwig Klein, Alain Kerdraon, Kenneth R. Lang and Gerard Trottet, <i>Astrophysical Journal</i> , 357, 662-671 (1990).	197
W. "VLA STUDIES OF LARGE-SCALE CORONAL LOOPS", Robert F. Willson, to appear in the <i>Proceedings of the Flares 22 Workshop, Chantilly, France</i> (eds. E.R. Priest and B. Schmieder, 1991).....	208
X. "MULTI-WAVEBAND SMM-VLA OBSERVATIONS OF AN M2 FLARE AND ASSOCIATED CORONAL MASS EJECTION", Robert F. Willson, Joan T. Schmelz, Raymond D. Gonzalez, Kenneth R. Lang and Kermit L. Smith, (to appear in the <i>Astrophysical Journal</i> , 1991).....	210
Y. "COMSTOC IV: MULTIBAND OBSERVATIONS OF SUNSPOT AND PLAGE ASSOCIATED CORONAL EMISSION", Jeffrey Brosius, Robert F. Willson, Gordon Holman and Joan T. Schmelz, submitted to the <i>Astrophysical Journal</i> , 1991.	256

A. VLA OBSERVATIONS OF SOLAR ACTIVE REGIONS AT CLOSELY SPACED FREQUENCIES: EVIDENCE FOR THERMAL CYCLOTRON LINE EMISSION

ROBERT F. WILLSON

Department of Physics, Tufts University

Received 1984 August 10; accepted 1985 May 20

ABSTRACT

VLA observations of a solar active region at 10 closely spaced frequencies between 1440 and 1720 MHz are presented. The synthesis maps show, on two successive days, significant changes in the brightness temperature within this narrow frequency range. We show that these changes cannot be due to either thermal bremsstrahlung or gyroresonance emission from a coronal loop in which the temperature, density, or magnetic field varies monotonically with height. Instead, we attribute the brightness spectrum to cyclotron line emission from a narrow layer where the temperature is elevated above the surrounding part of the loop.

Subject headings: interferometry — radiation mechanisms — Sun: radio radiation

I. INTRODUCTION

Very Large Array (VLA)¹ observations of solar active regions near 20 cm wavelength delineate looplike structures that appear to connect lower lying areas of opposite magnetic polarity (Lang, Willson, and Rayrole 1982; Dulk and Gary 1983; Lang, Willson, and Gaizauskas 1983; McConnell and Kundu 1983). These sources have peak brightness temperatures of between 1.5×10^6 and 4.0×10^6 K, suggesting that they are the radio wavelength counterparts of coronal loops seen at soft X-ray wavelengths.

The radiation mechanism responsible for this emission is, however, the subject of some controversy. Lang, Willson, and Rayrole (1983) and Dulk and Gary (1983) have, for example, attributed 20 cm emission to optically thick thermal bremsstrahlung of a hot plasma trapped within magnetic arches connecting underlying sunspots. There is no detectable polarization near the magnetic neutral lines, and this has been attributed to optically thick emission or to magnetic fields that are transverse to the line of sight. A few 20 cm loops exhibit small circular polarization ($\rho_c \leq 20\%$) near their legs, and this has been attributed to the effects of bremsstrahlung propagating in longitudinal magnetic fields of strength $H_l \approx 20\text{--}70$ G (Dulk and Gary 1983).

Other VLA observations suggest that low-harmonic gyroresonance absorption may provide the bulk of the opacity in 20 cm loops. McConnell and Kundu (1983) have, for example, found that the brightness of one loop could be best explained by gyroemission near the loop top and thermal bremsstrahlung near the feet. Velusamy and Kundu (1981) also compared radio and X-ray observations of systems of postflare loops, and found that gyroresonance emission was the most likely mechanism in these sources.

Both competing processes of bremsstrahlung and gyroresonance emission predict a smoothly varying continuum spectrum that decreases slowly with increasing frequency. The theory of cyclotron absorption, for example, indicates that observations at a given frequency, ν , refer to a narrow layer in the solar atmosphere at which $\nu = s\nu_H$, where $s = 2, 3, 4$ is the harmonic number and ν_H is the gyrofrequency. If the magnetic field in a

coronal loop decreases uniformly with height, then it was thought that the individual cyclotron lines would merge to form a smooth continuum. Theoretical work has shown however, that individual cyclotron lines might also be detected as narrow-band enhancements in the radio-frequency spectra of solar active regions if the radiation were emitted from relatively thin layers in the corona where the magnetic field is relatively constant (Syrovatskii and Kuznetsov 1980; Kuznetsov and Syrovatskii 1981). The presence of neutral current sheets, in which the temperature and density are higher than in the surrounding parts of the loop, might also lead to abrupt changes in the brightness temperature over a small frequency range (Syrovatskii 1977; Syrovatskii and Kuznetsov 1980). Recently, Willson (1983) mapped several active regions at three closely spaced frequencies near 1446 MHz and found that two of the sources showed striking changes in brightness within these narrow frequency ranges. These changes could not be explained by either thermal bremsstrahlung or gyroresonance emission from a loop in which the temperature, density, or magnetic field varied uniformly with height. They could, however, be explained by individual cyclotron lines emitted in small regions ($10''\text{--}30''$) where the magnetic field was relatively constant with $H \approx 125\text{--}180$ G.

Observations of cyclotron line emission are potentially important because they provide a means of specifying the physical conditions within coronal loops and current sheets. We have now tried to confirm the presence of cyclotron lines on the Sun by using the VLA to map an active region on two successive days at 10 different frequencies between 1440 and 1720 MHz. In this paper we present these observations and compare them with theoretical spectra of cyclotron line emission from coronal loops.

II. OBSERVATIONS

The VLA (B-configuration) was used to observe the active region AR 4398 on 1984 January 28 and 29. The position of AR 4398 at 1300 UT on January 28 and 29 was $14^\circ\text{N } 11^\circ\text{W}$ and $14^\circ\text{N } 24^\circ\text{W}$, respectively. The active region was observed at 10 different frequencies between 1440 MHz (21.8 cm) and 1720 MHz (17.4 cm) with bandwidths of 12.5 MHz during a 10 hr period between 1300 UT and 2300 UT on each day. At these frequencies the half-power beamwidth of the individual antennas ranges between 26.0 and 31.2 and the synthesized

¹ The VLA is a facility of the National Radio Astronomy Observatory, which is operated by Associated Universities, Inc., under contract with the National Science Foundation.

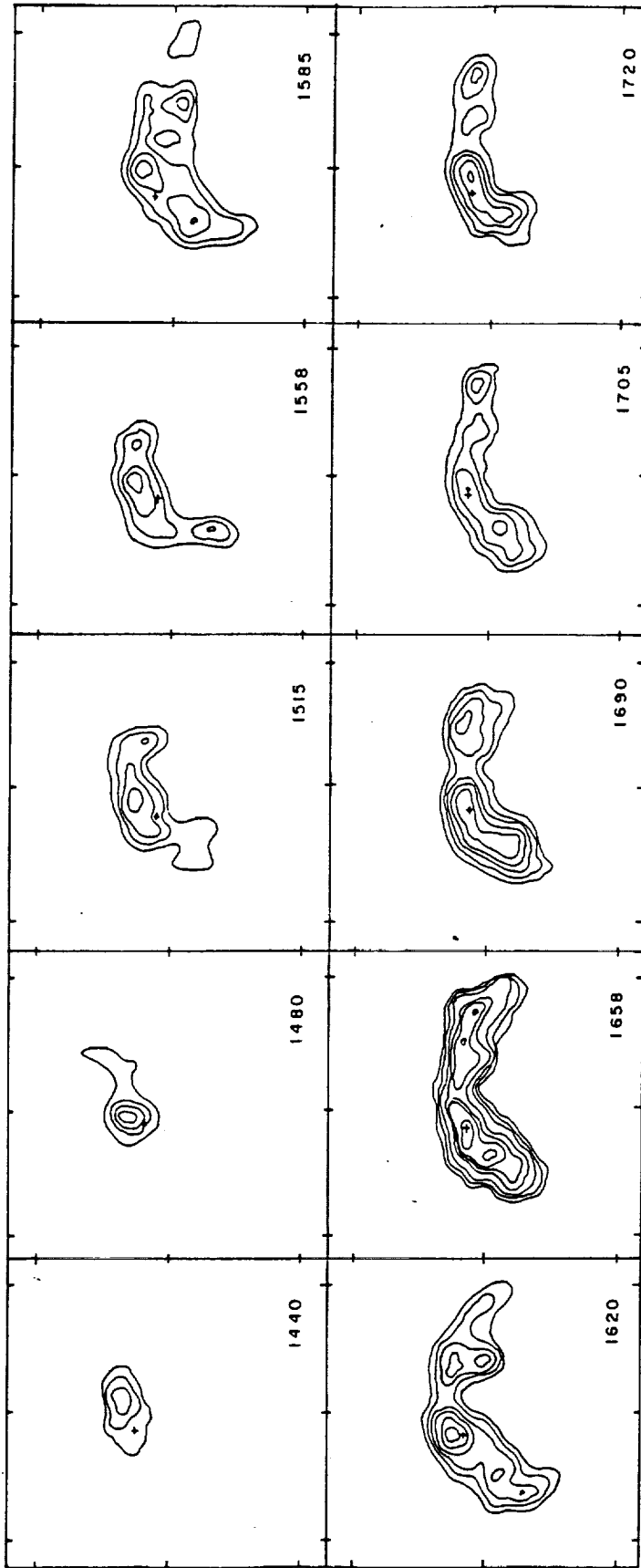


FIG. 1.—VLA synthesis maps of total intensity, I , of AR 4398 at 10 closely spaced frequencies during a 10 hr period on 1984 January 28. Synthesized beamwidth is $\theta \approx 3'' \times 4''$. Contours of the maps mark levels of equal brightness temperature. Outermost contour and contour interval are equal to 1.1×10^6 and 4.0×10^5 K, respectively. Angular scale can be determined from the $60''$ spacing between fiducial marks on the area.

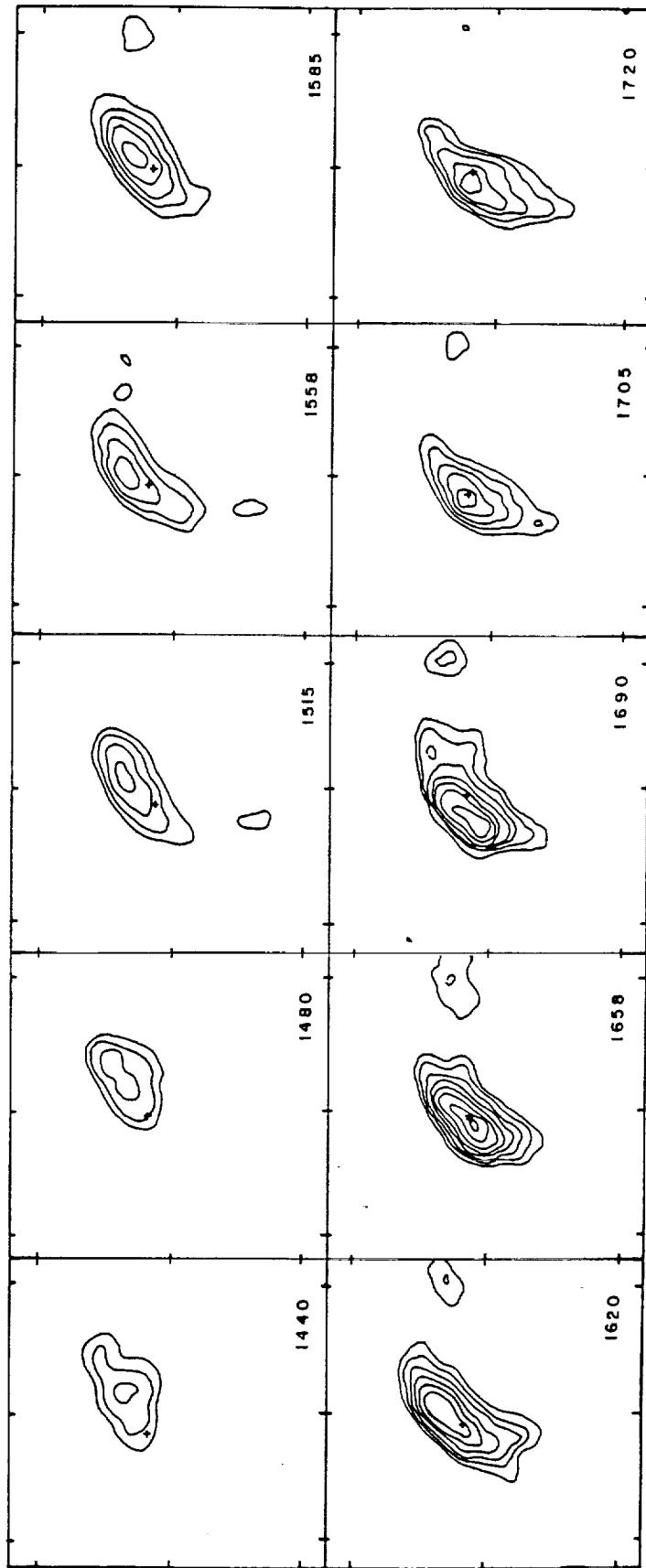


FIG. 2.—VLA synthesis maps of total intensity, I , of AR 4398 at 10 closely spaced frequencies using data obtained during a 10 hr interval on 1984 January 29. Contour levels and angular scale are same as in Fig. 1.

beamwidth varies between $3''0 \times 3''5$ and $3''6 \times 4''2$. The four independent intermediate frequency channels now available at the VLA made it possible to record the left and right circularly polarized signals of two different frequencies at once. The active region was observed at successive pairs of frequencies for a period of 5 minutes, so that all 10 frequencies could be observed in 25 minutes. This sequence of observations was followed by successive 2 minute observations of the calibrator source 3C 48. The data were calibrated using 3C 48 together with a correction for the difference in the signals from high-temperature noise sources located on four of the antennas. The temperatures of these sources were measured at each frequency and polarization prior to the solar observations and are believed to be accurate to $\leq 5\%$. The flux of 3C 48 at each frequency was determined from its flux of 15.37 Jy at 1465 MHz and its spectral index of $\alpha = -0.81$. Since some of the observations were made outside of the nominal protected radio band near 1421 MHz, the total power signal from two of the antennas was monitored for the presence of interference. No interference was detected during these observations, however. We also examined the data for the presence of solar bursts which could have corrupted the maps at one or more frequencies. Only one burst was detected, between 1820 and 1950 UT on January 29, and these data were edited before maps were made. The calibrated data were edited and used together with the standard CLEAN procedure to make synthesis maps of both total intensity, I , and circular polarization, V .

The maps of total intensity are shown in Figures 1 and 2. There was no detectable circular polarization ($V/I \leq 15\%$) on either day, suggesting that the regions were optically thick to both the ordinary and extraordinary modes of wave propagation. On both days the region shows a looplike structure of 1:0 to 1:5 in length, whose peak brightness temperature first increases systematically from $\sim 1.5 \times 10^6$ K at 1440 MHz to $\sim 4.0 \times 10^6$ K at 1658 MHz, and then begins to decrease at the highest frequencies. In Table 1 we give the brightness temperatures at a point denoted by a cross on the peak intensity at 1658 MHz, and in Figure 3 we plot these temperatures as a function of frequency. The error bars in Figure 3 represent 3σ uncertainties determined from the residual noise left on the CLEANed maps.

As a check on the integrity of the solar calibration procedure, we have also plotted the brightness temperatures observed in a loop within the active region AR 4399, located ~ 6.5 to the east of AR 4398. This was the only other major active region on the Sun during these 2 days. In contrast to AR 4398, the brightness spectrum of AR 4399 is nearly constant on both days, with an average brightness temperature of $T_b \approx 1.5 \times 10^6$ K. This result seems to indicate that the changes in brightness temperature observed from AR 4398 are not common to all sources, and therefore not due to an artifact of the calibration or CLEANing procedure.

In Figure 4 we compare the radio maps at the peak frequency of 1658 MHz with Kitt Peak magnetograms taken on

the same day. The radio emission appears to connect regions of opposite magnetic polarity, suggesting that the sources are dipolar loops which join the underlying sunspots. Observations made at Mount Wilson Observatory (R. Howard, private communication) indicate that the two dominant spots have magnetic field strengths of $|H| \approx 2000$ G, and that the morphology and surface fields of these spots did not change appreciably from one day to the next. As we will argue in the next section, this may explain why the spectrum and morphology of the radio loops were also similar on the two days.

III. DISCUSSION

In this section we will show that the observed changes in brightness temperature of about a factor of 2.5 over a frequency range of ~ 300 MHz are difficult to explain by either thermal bremsstrahlung or gyroresonance emission from a loop in which the temperature, density, and magnetic field vary uniformly with height. These radio results, then, appear to conflict with the results of numerical models of quasi-static coronal loops which predict smooth gradients in both temperature and density along the loop (e.g., Rosner, Tucker, and Vaiana 1978; Veseky, Antiochos, and Underwood 1979). On the other hand, these sharp changes in brightness temperature are consistent with the existence of neutral current sheets or thin inhomogeneous layers in the coronal loop where the temperature or density are thought to be higher than in their surroundings (Syrovatskii 1977).

As a starting point in our analysis, we assume that the magnetic field strength $B(Z)$ in the loop can be represented by a dipole function, $B(Z) = B_0 R_D^3 / (Z + R_D)^3$, where Z is the height above the photosphere, B_0 (~ 2000 G) is the magnetic field at the solar surface, and R_D is the depth of the dipole below the loop base. If R_D is taken to be equal to one-half the distance, D , between the two footpoints, then Mount Wilson sunspot observations indicate $D \approx 8.0 \times 10^9$ cm and $R_D \approx 4 \times 10^9$ cm. We next divide the loop into thin layers of thickness 1.0×10^8 cm and compute the optical depth due to thermal bremsstrahlung and gyroresonance emission with assumed values of temperature and density at each height, Z , in the loop. In the simplest models, we assume that the loop has a constant temperature and density between $Z = 2 \times 10^9$ cm and 5×10^9 cm, the approximate height of 20 burst centimeter loop emission (Willson and Lang 1984). The equation of transfer for the emergent brightness temperature and circular polarization as a function of frequency was then solved for temperatures between 1.5×10^6 and 4.0×10^6 K, and densities between 1.0×10^9 and 5.0×10^9 cm $^{-3}$, using the equations for the thermal bremsstrahlung and gyroresonance optical depth given by Willson (1983). Models were also computed for different values of the parameter θ ($20^\circ < \theta < 90^\circ$), the angle between the magnetic field and the line of sight.

The results of these calculations indicate that for this range of temperatures and densities, and for $\theta > 60^\circ$, gyroresonance absorption would render the loop optically thick with a nearly

TABLE 1
MAXIMUM BRIGHTNESS TEMPERATURES, $T_b(\text{max})$, WITHIN AR 4398 AT DIFFERENT FREQUENCIES

Date	1440 ^a	1480	1515	1558	1585	1620	1658	1690	1705	1724
1984 Jan 28	1.4×10^6	1.4×10^6	1.6×10^6	1.8×10^6	2.2×10^6	3.0×10^6	3.7×10^6	3.2×10^6	2.5×10^6	2.6×10^6
1984 Jan 29	1.3×10^6	1.7×10^6	1.8×10^6	2.0×10^6	2.2×10^6	3.2×10^6	4.0×10^6	2.8×10^6	2.7×10^6	2.3×10^6

^a All frequencies are in megahertz, all temperatures are in kelvins.

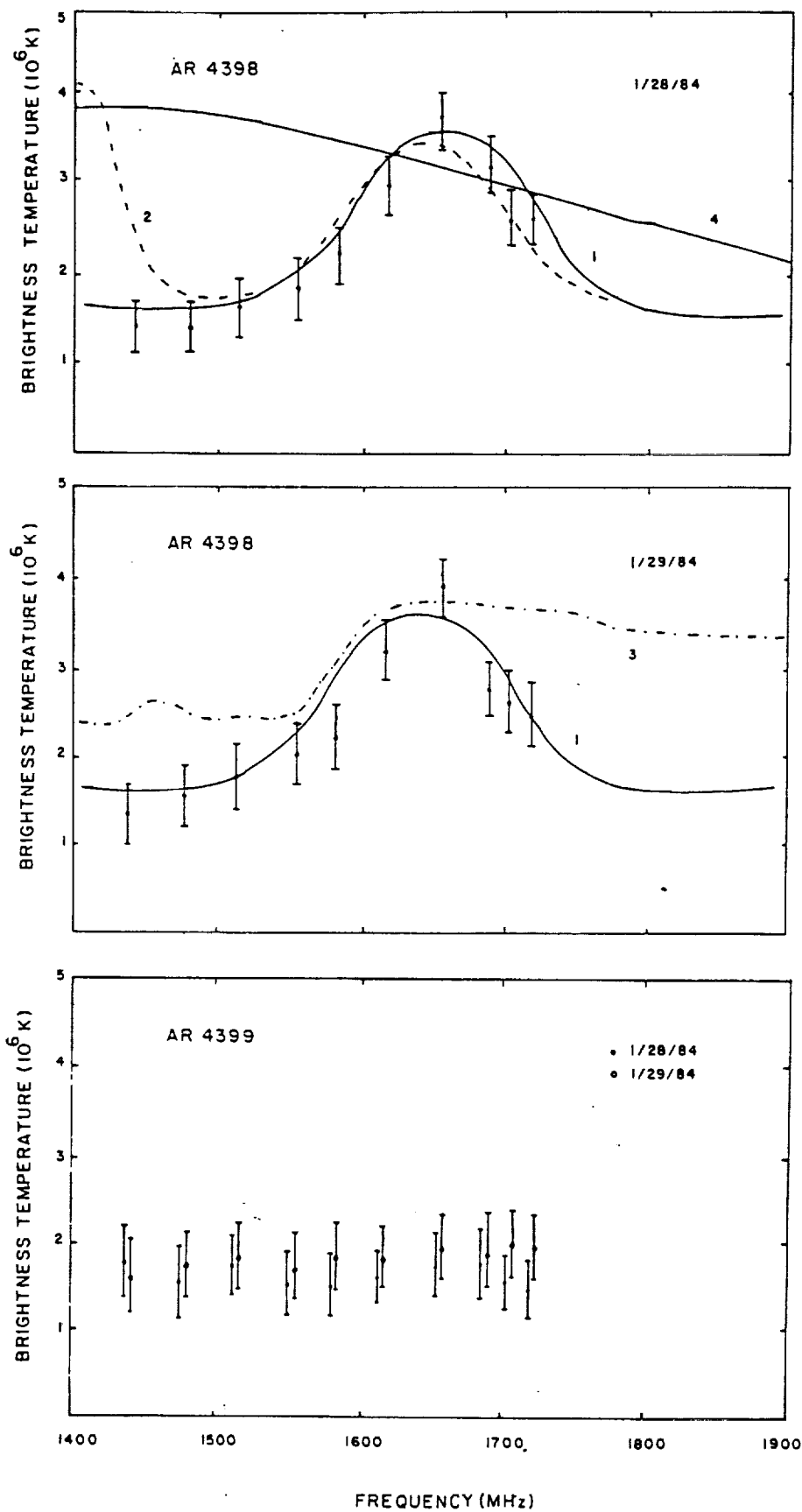


FIG. 3.—Theoretical plots of brightness temperature for different values of temperature density, and magnetic field strength in a coronal loop (*top, middle*). Maximum brightness temperatures of the loops in AR 4398 (*top, middle*) and AR 4399 (*bottom*) are also plotted with error bars corresponding to peak-to-peak fluctuations in background temperature of the synthesis maps. Curves 1 and 2 correspond to a coronal loop model that contains a thin ($\Delta L = 1.0 \times 10^8$ cm) layer where the magnetic field is $H = 145$ and 119 G, respectively, and where the temperature and density at $T_e = 3.8 \times 10^6$ K and $N_e = 1.0 \times 10^9$ cm^{-3} . The temperature and density in the rest of the loop are taken to be equal to $T_e = 1.5 \times 10^6$ K and $N_e = 1.0 \times 10^9$ cm^{-3} . Curve 3 corresponds to the same parameters as model 1, except that $N_e = 2.0 \times 10^{10}$ cm^{-3} . Curve 4 corresponds to a loop in which electron temperature increases monotonically from $T_e = 1.5 \times 10^6$ at $z = 5 \times 10^9$ cm to $T_e = 3.8 \times 10^6$ K at $z = 6 \times 10^9$ cm. In all cases, the angle θ between magnetic field and line of sight was taken to be equal to $\theta = 70^\circ$.

Brightness temperature of active region AR 4399, located ~ 6.5 east of AR 4398, together with typical error bars, is plotted on bottom panel of figure.

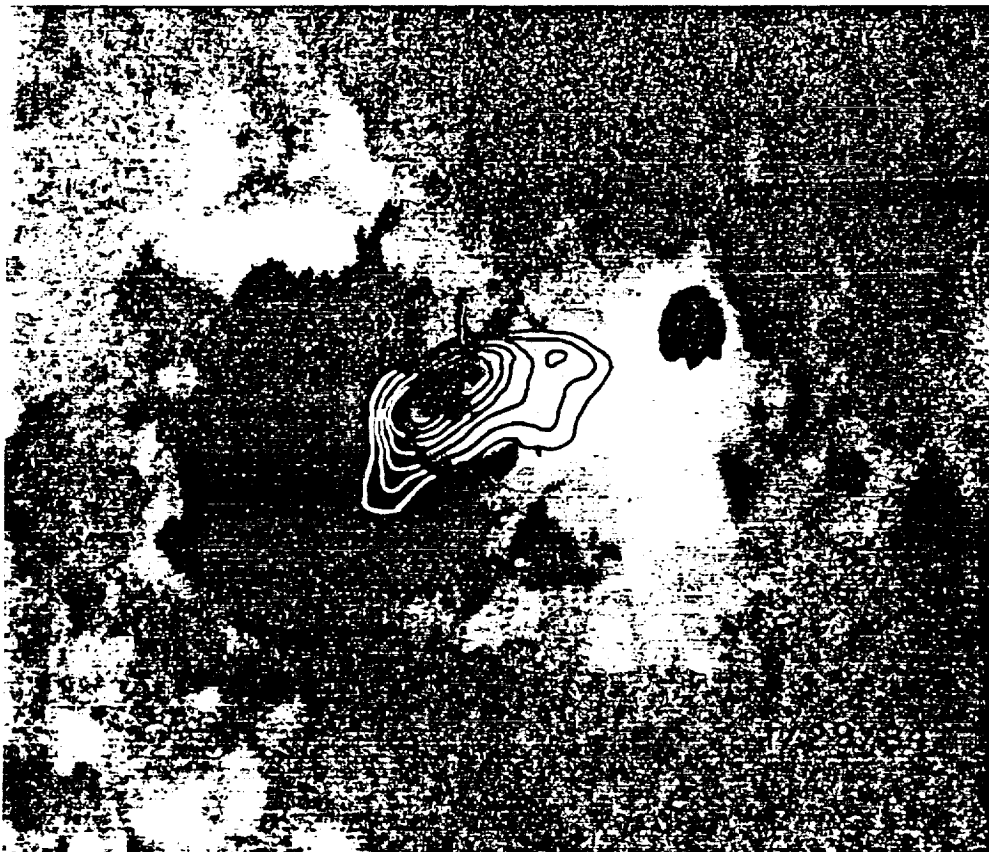
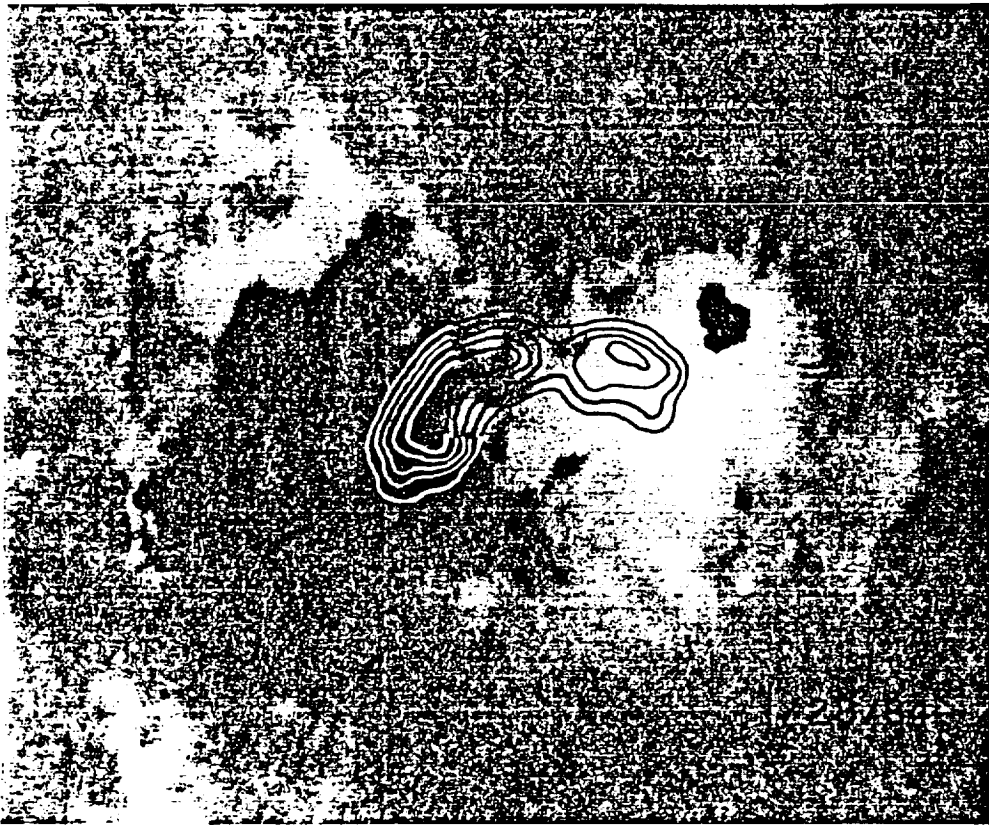


FIG. 4.—VLA synthesis maps of total intensity at 1658 MHz on 1984 January 28 (*top*) and 29 January (*bottom*), superposed on Kitt Peak magnetograms taken on the same day. Note that radio emission appears to connect areas of opposite magnetic polarity, and that peak brightness temperature occurs nearly along magnetic neutral line.

constant brightness temperature between 1.5×10^6 and 4×10^6 K, and a low degree of circular polarization ($\rho_c < 20\%$) throughout the range of frequencies observed. This is because the individual cyclotron lines at different harmonics that are emitted from a layer with constant temperature would merge to form a continuum. These results are in agreement with those of McConnell and Kundu (1983) who found that 20 cm coronal loops would be optically thick to gyroresonance emission at the third harmonic of the gyrofrequency for magnetic fields $H \approx 130\text{--}170$ G, temperatures $T \approx 1.5 \times 10^6$ K, and densities of $N_e \approx 5 \times 10^8 \text{ cm}^{-3}$. We also found that these results are unchanged if the temperature and density are allowed to vary monotonically with height. In Figure 3 we show one such model in which the temperature varied from $T_e = 1.5 \times 10^6$ K at $Z = 5 \times 10^9$ cm to $T_e = 3.8 \times 10^6$ K at $Z = 6 \times 10^9$ cm.

Instead, we find that the peak in brightness temperature can be produced if the temperature, say T_e , in one of the layers with constant magnetic field is assumed to be higher than in the other layers. In this case, the individual cyclotron line with peak brightness temperature T_e will appear above the continuum spectrum produced by the other layers in the loop. The results of these model calculations are shown in Figure 3 for different values of the magnetic field strength, temperature, and density for which the peak at ~ 1658 MHz is a harmonic of the gyrofrequency. We find that the spectrum can be satisfactorily fit if the loop contains a thin layer in which $T_e = 3.5\text{--}4.0 \times 10^6$ K, where the magnetic field is $H \approx 145$ G ($n = 4$), or possibly $H = 119$ G ($n = 5$). For $n = 3$ ($H = 197$ G), the line profile is too wide and flat-topped, while for $n > 6$ ($H > 100$ G) the lines are optically thin. That is, one explanation of these brightness temperature variations is the existence of a thin layer in which the temperature is ~ 3 times higher than in the rest of the loop where $T_e \approx 1.5 \times 10^6$ K. For an electron density of $N_e = 10^9 \text{ cm}^{-3}$, we obtain good fits for $1 \times 10^7 \text{ cm} < \Delta L < 1 \times 10^8 \text{ cm}$. For narrower layers, the lines become optically thin and do not give a good fit to the data. The data also constrain the angle θ to $\theta \approx 65^\circ\text{--}80^\circ$, since smaller values would yield unacceptably high circular polarization ($\rho_c > 30\%$), and higher values would result in cyclotron line profiles that are too wide and flat-topped. We also find

that these results are relatively insensitive to the assumed density in the heated layer, up to $N_e \approx 2 \times 10^{10} \text{ cm}^{-3}$. For higher densities, thermal bremsstrahlung becomes dominant in the layer, resulting in a sharp step in brightness temperature above ~ 1600 MHz (Fig. 3).

The fact that the brightness spectrum is nearly identical on both days suggests that the physical conditions in the loop were similar on these days. As noted earlier, the magnetic fields of underlying sunspots were relatively constant, so that one might also expect the coronal extension of these photospheric fields to be also relatively unchanged. The frequency of the cyclotron line emission would, under these conditions be relatively unaffected, and this might explain the similarity of the microwave spectrum from one day to the next.

The physical mechanism that gives rise to a thin, apparently stable, hot layer in the corona is uncertain. We note, however, that EUV observations of coronal loops have revealed the presence of temperature inhomogeneities in a number of sources (Foukal 1975, 1976; Raymond and Foukal 1982; Pye *et al.* 1978). These inhomogeneities cannot be explained by quasi-static loop models in which the pressure is assumed to be uniform (e.g., Rosner, Tucker, and Vaiana 1978), but they may be accommodated in more sophisticated models in which the pressure and heat deposition are allowed to vary with height and distance in the loop (Serio *et al.* 1981). Whether these structures represent current sheets or regions where the heating rate is higher than in the surrounding parts of the loop is also an open question at this time. Future observations with the VLA and other multifrequency radio interferometers, together with observations at ultraviolet and X-ray wavelength with the repaired SMM, may provide a more complete description of the magnetic field temperature and density stratification of active region coronal loops.

The author wishes to thank Kenneth R. Lang for useful discussions and an anonymous referee for helpful suggestions. Solar radio interferometric studies at Tufts University are supported under grant AFSOR-83-0019 with the Air Force Office of Scientific Research. Comparisons of VLA and *Solar Maximum Mission* satellite data are supported under NASA Guest Investigator grant NAG 5-501.

REFERENCES

- Dulk, G. A., and Gary, D. E. 1983, *Astr. Ap.*, **124**, 103.
 Foukal, P. 1975, *Solar Phys.*, **43**, 327.
 ———. 1976, *Ap. J.*, **210**, 575.
 Kuznetsov, V. D., and Syrovatskii, S. I. 1981, *Solar Phys.*, **69**, 361.
 Lang, K. R., Willson, R. F., and Gaizauskas, V. 1983, *Ap. J.*, **267**, 455.
 Lang, K. R., Willson, R. F., and Rayrole, J. 1982, *Ap. J.*, **258**, 384.
 McConnell, D., and Kundu, M. R. 1983, *Ap. J.*, **269**, 698.
 Pye, J. P., Evans, K. D., Hutcheon, R. J., Gerassimenko, M., Davis, J. M., Krieger, A. S., and Vesecky, J. F. 1978, *Astr. Ap.*, **65**, 123.
 Raymond, J. C., and Foukal, P. 1982, *Ap. J.*, **253**, 323.
 Rosner, R., Tucker, W. H., and Vaiana, G. S. 1978, *Ap. J.*, **220**, 643.
 Serio, S., Peres, G., Vaiana, G. S., Golub, L., and Rosner, R. 1981, *Ap. J.*, **243**, 288.
 Syrovatskii, S. I., and Kuznetsov, V. D. 1980, in *IAU Symposium 86, Radio Physics of the Sun*, ed. M. R. Kundu and T. E. Gergeley (Dordrecht: Reidel), p. 109.
 Syrovatskii, V. D. 1977, *Astr. Zh. (Letters)*, **3**, 133.
 Velusamy, T., and Kundu, M. R. 1981, *Ap. J. (Letters)*, **243**, L103.
 Vesecky, J. F., Antiochos, S. K., and Underwood, J. H. 1979, *Ap. J.*, **233**, 987.
 Willson, R. F. 1983, *Solar Phys.*, **89**, 103.
 Willson, R. F., and Lang, K. R. 1984, *Ap. J.*, **279**, 427.

ROBERT F. WILLSON: Department of Physics, Tufts University, Medford, MA 02155

B. HIGH-RESOLUTION MICROWAVE OBSERVATIONS OF THE SUN AND NEARBY STARS

Kenneth R. Lang
Department of Physics and Astronomy
Robinson Hall
Tufts University
Medford, MA 02155
U.S.A.

ABSTRACT

Multiple-wavelength VLA observations uniquely specify the three-dimensional structure of the magnetic field and the plasma in the coronal atmosphere above solar active regions. Synthesis maps at 20 cm wavelength specify the density, temperature, and magnetic fields of the ubiquitous coronal loops that are the dominant structural element of the low solar corona; the 6 cm maps delineate the magnetic structure of the legs of coronal loops that radiate at the second or third harmonic of the gyrofrequency. Individual cyclotron lines have been detected at 20 cm wavelength at the apex of a coronal loop where the magnetic field strength is relatively constant and neutral current sheets may lead to enhanced emission from a relatively thin coronal layer. Although thermal bremsstrahlung and/or thermal gyroresonance emission dominate the quiescent microwave emission from solar active regions, some plage-associated microwave sources require nonthermal emission mechanisms in the presence of weak magnetic fields. Intense filament-associated sources might be attributed to the nonthermal gyrosynchrotron emission of subrelativistic electrons.

Snapshot synthesis maps for time intervals as short as ten seconds have led to a new understanding of the excitation and eruption of solar bursts. The impulsive phase of 20 cm bursts is released near the apex of coronal loops located at a height of about 40,000 km above the solar photosphere. Solar bursts are triggered by preburst heating and/or magnetic changes that precede the bursts on time scales of 10 minutes to an hour. The preburst changes can occur within single coronal loops or arcades of coronal loops. Magnetic triggering can also be caused by current sheets that develop during the emergence of coronal loops or the interaction of preexisting coronal loops. Successive bursts can be excited in adjacent coronal loops. Observations of microwave bursts at closely spaced wavelengths provide evidence for narrow-band, highly circularly polarized bursts that may be attributed to gyrosynchrotron masers or electron-cyclotron masers.

Observations of nearby stars with high time resolution provide stringent limits to the size of the stellar bursting sources; highly circularly polarized emitters with very high brightness temperatures suggest coherent emission mechanisms. The slowly varying emission from one nearby flare star also exhibits narrow-band microwave emission characteristic of a coherent mechanism.

I. QUIESCENT (NONFLARING) MICROWAVE EMISSION FROM SOLAR ACTIVE REGIONS

Because the microwave emission from quiescent (non-flaring) active regions varies slowly over time scales of several hours, one may investigate its detailed structure by using the Earth-rotation aperture synthesis technique. When the Very Large Array is used in this way, the rotation of the Earth changes the relative orientation of the array and the radio source; Fourier inversion methods are then used to determine the angular power distribution of the radio source from the array response (visibility functions). Angular resolutions of better than one second of arc are achieved for fields of view that can be as large as the entire solar disk. These angular resolutions exceed those of optical telescopes or existing spacecraft telescopes at X-ray or ultraviolet wavelengths.

Synthesis maps of total intensity, I , describe the two-dimensional distribution of source brightness, whereas synthesis maps of circular polarization, or Stokes parameter V , describe the two-dimensional structure of the magnetic field. The observed radiation from quiescent active regions is circularly polarized in the extraordinary mode of wave propagation, with right-handed circular polarization corresponding to a positive magnetic field directed toward the observer.

The microwave synthesis maps of circular polarization uniquely provide direct measurements of the strength and structure of the magnetic fields in the low corona and the transition region (between the photosphere and the corona). This is not possible with any other technique. When thermal bremsstrahlung is the dominant radiation mechanism, the circular polarization is due to propagation effects in the presence of a magnetic field; the longitudinal magnetic field strength is then inferred from the polarization and the optical depth. When gyroresonant radiation of thermal electrons dominates, the circularly polarized radiation is emitted at the second or third harmonic of the gyrofrequency. One is then able to infer the longitudinal magnetic field strength from the observed frequency.

Single wavelength V.L.A. synthesis maps of quiescent active regions at 20 cm wavelength have been used as coronal magnetograms that specify the strength and structure of the magnetic field in the low solar corona, while also specifying the temperature distribution

along the coronal loops that are the dominant structural element in the low corona. [Lang et al. (1982); McConnell and Kundu (1984); Lang et al. (1983); Lang and Willson (1983); Shevgoankar and Kundu (1984, 1985); Kundu and Lang (1985)]

Our recent Very Large Array observations have revealed three powerful new approaches to the study of these ubiquitous coronal loops. They include multiple wavelength observations that establish the three-dimensional structure of active regions and specify the physical parameters and radiation mechanisms at different levels in the solar atmosphere (following Section I A), observations of cyclotron line emission from individual loops (following Section B), and observations of nonthermal emission in regions of relatively weak magnetic fields (following Section I C).

I A. Quiescent Microwave Emission at Widely Spaced Wavelengths

The quiescent, or nonflaring, radio emission at longer wavelengths originates at higher levels in the atmosphere. This is because the local electron density, N_e , decreases with height, and emission at a given frequency, ν , can arise only from regions where the electron plasma frequency, $\nu_p = 8.9 \times 10^3 N_e^{1/2}$ Hz is equal to or lower than ν .

Radiation at longer microwave wavelengths, λ , also originates at higher hotter levels in the solar atmosphere. The brightness temperatures, T_B , are comparable to the local electron temperature, T_e . They range from $T_B \sim 6.5 \times 10^3$ K at $\lambda = 2$ mm in the low chromosphere through 10^5 K at $\lambda = 2$ cm in the chromosphere-corona transition region to 10^6 K at $\lambda = 20$ cm in the low corona.

The heights, h , of the microwave structures can be inferred from their angular displacements from underlying photospheric features. Very Large Array observations indicate that 2 cm emission overlies sunspots at heights $h \sim 5,000$ km. and that the 6 cm emission marks the legs of magnetic dipoles at $h \sim 30,000$ km above the photosphere. As illustrated in Figure 1, the 20 cm emission comes from the hot, dense plasma trapped within coronal loops with total extents of about 100,000 km. [Lang and Willson (1983); Lang et al. (1983); Shevgoankar and Kundu (1984); Kundu and Lang (1985)]

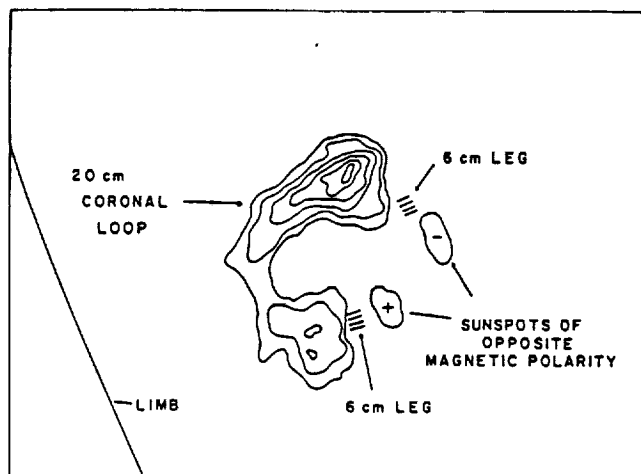


Figure 1. A Very Large Array synthesis map of a coronal loop at 20 centimeters wavelength. The contours mark levels of equal brightness temperature corresponding to 0.2, 0.4, ... 1.0 times the maximum value of 2.0×10^6 K. A schematic portrayal of the 6 cm microwave emission, which comes from the legs of magnetic dipoles, is also shown, together with the underlying sunspots that are detected at optical wavelengths.

One of the most satisfying observational results at 6 cm wavelength has been the detection of circularly polarized horseshoe structures predicted by the theory of gyroresonant emission from individual sunspots (see figure 2 and Kundu and Lang (1985)). The circular polarization maps at 6 cm reveal highly polarized (up to 100 percent) structures that lie above the curved magnetic fields of sunspot penumbrae. There is no detectable circular polarization above the central sunspot umbrae where the magnetic fields project radially upward into the hot coronal regions. Values of a longitudinal magnetic field strength of $H = 600$ to 900 Gauss are inferred from the fact that the 6 cm radiation is emitted at the second or third harmonic of the gyrofrequency. These magnetic field strengths apply to the legs of coronal loops.

We have also carried out simultaneous observations of solar active regions with Very Large Array (VLA) and the Solar Maximum Mission (SMM) satellite. The VLA observations at 20 cm wavelength can be compared with the soft X-ray polychromator (XRP) data from SMM (see figure 3). Physical parameters such as electron temperature,



Figure 2. A Westbork Synthesis Radio Telescope synthesis map of circular polarization at 6 cm wavelength superposed on a $H\alpha$ photograph from the observatory at Athens. The contours are in steps of 1.5×10^5 K. The circularly-polarized horseshoe structure that rings the sunspot umbra is due to gyroresonant emission in the curved magnetic fields of the sunspot penumbra.

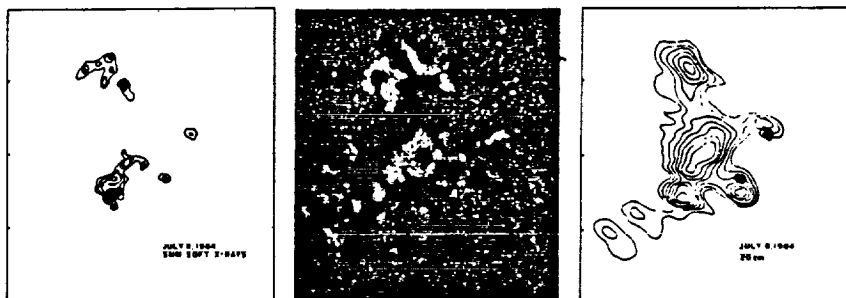


Figure 3. Plots the soft X-ray, $H\alpha$ and 20 cm (right) emission of a solar active region taken on the same day. The most intense radio emission is spatially correlated with the most intense $H\alpha$ and soft X-ray radiation, but there is intense 20 cm emission associated with the sunspots where there is no detectable $H\alpha$ or soft X-ray emission. There is a $60''$ spacing between fiducial marks on the axes.

ORIGINAL PAGE IS
OF POOR QUALITY

T_e , and electron density, N_e , can be independently inferred and compared at two wavelengths. For instance, the intense 20 cm emission from the apex of coronal loops can be interpreted in terms of thermal bremsstrahlung with an electron temperature and emission measure that are consistent with those inferred from bright X-ray sources at the same regions. However, there is intense 20 cm emission above and near sunspots where there is no detectable X-ray emission (see figure 3). The 20 cm emission from these regions requires an extra source of opacity that may be attributed to gyroresonance absorption. Although this effect has been previously noticed at 6 cm, Schmahl et al. (1980), this is the first time that it has been observed at the longer 20 cm wavelength. We also notice the excellent correlation between bright H α plage, intense X-ray emission and intense 20 cm emission over a range of 10^8 in wavelength.

I B. Quiescent Microwave Emission at Closely Spaced Wavelengths

As previously mentioned, the gyroresonant radiation of thermal electrons accelerated by magnetic fields can compete with the bremsstrahlung of thermal electrons accelerated in the electric field of ions. The discovery of circularly polarized ring-shaped or horse-shoe structures above individual sunspots at 6 cm wavelength (see Figure 2) showed that gyroemission dominates the radiation from the legs of magnetic dipoles; these results have played an important role in theoretical models of the quiescent radio emission from solar active regions.

The thermal electrons gyrate around the magnetic fields, emitting cyclotron lines at harmonics of the gyrofrequency. The frequency, ν , of the cyclotron lines therefore provides a sensitive measurement of the longitudinal magnetic field strength, H , through the relation $\nu = 2.8 \times 10^6 n \text{ MHz}$, where the harmonic number $n = 2, 3, 4, \dots$. However, because the magnetic field strength in a coronal loop decreases uniformly with height, it was thought that the individual cyclotron lines would merge to form a smooth continuum.

Theoretical speculations have nevertheless led to two hypothetical situations in which individual cyclotron lines might be observed. The presence of neutral current sheets might lead to enhanced emission from relatively thin coronal layers where the magnetic field

is constant, Syrovatskii and Kuznetsov (1980); Kuznetsov and Syrovatskii (1981); Somov and Syrovatskii (1982). The individual cyclotron lines might then be detected if the region of current sheet emission was resolved and appropriate spectral data were obtained. Alternatively, the thermal cyclotron emission from a dipolar loop might be detected through spatial and polarization structures that are sensitive to both observation frequency and the angle of observation, Holman and Kundu (1985).

Preliminary Very Large Array observations at three closely spaced wavelengths near 21 cm showed significant brightness changes that suggested cyclotron line emission from the apex of a coronal loop where the magnetic field strength is relatively constant. These results were substantiated in greater detail, Willson (1985), when observations at ten closely spaced frequencies revealed the spectral shape of a cyclotron line that could not be attributed to alternative emission mechanisms (see Figure 4). The brightness spectrum was attributed to cyclotron emission from a narrow layer where current sheets resulted in enhanced temperatures in regions of relatively constant magnetic field.

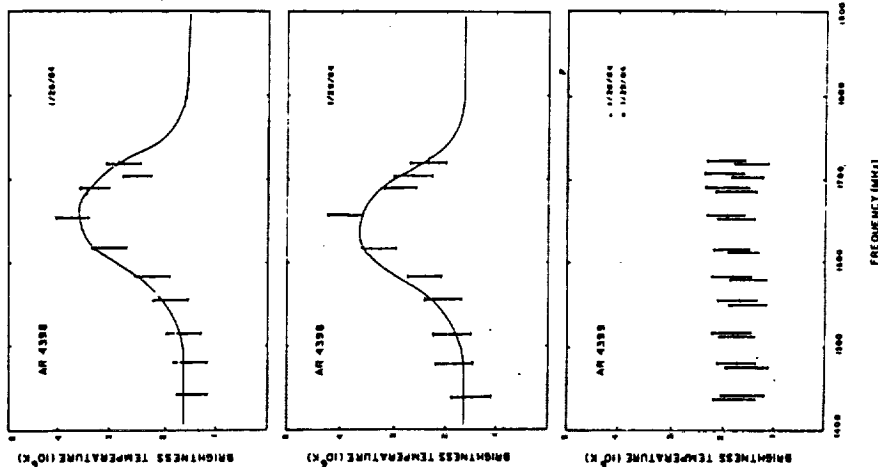


Figure 4. The maximum brightness temperature observed from a coronal loop at ten closely-spaced frequencies near 1446 MHz (20cm) showing a thermal cyclotron line from active region AR 4389 on two successive days, together with optically thick thermal bremsstrahlung spectra from active region AR 4399 on the same days.

The discovery of individual cyclotron lines provides a sensitive new diagnostic tool for specifying the magnetic and plasma properties of coronal loops. For example, a change in the magnetic field strength of only 20 Gauss produces a 170 MHz shift in the central frequency of a cyclotron line near 1420 MHz (or 21 cm wavelength). Measurements of the central frequency therefore specify the magnetic field strength with unprecedented precision.

I C. Thermal and Nonthermal Emission Mechanisms for Quiescent Microwave Emission

The quiescent microwave emission from solar active regions has generally been attributed to thermal radiation from hot electrons, Kundu and Lang (1985). Thermal bremsstrahlung and/or thermal gyroresonance effects dominate both the 6 cm and the 20 cm emission from the legs of coronal loops.

Nonthermal microwave emission has been recently suggested by the detection of high brightness temperatures in regions where the magnetic fields are weak, Webb et al. (1983); Akhmedov et al. (1985) - see figures 5 and 6. Thermal bremsstrahlung cannot account for the radiation because the temperatures are too high and the electron

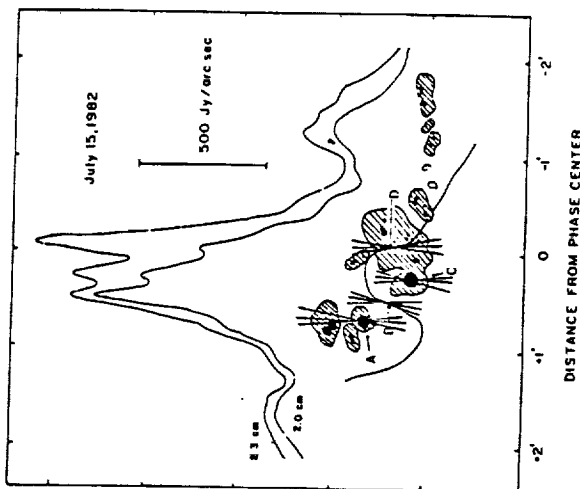


Figure 5. One-dimensional fan beam scans of AR 3084 taken with the RATAN 600 at wavelengths of 2.0 and 2.3 centimeters. Sources A and C are associated with sunspots; sources B and D are associated with filaments.

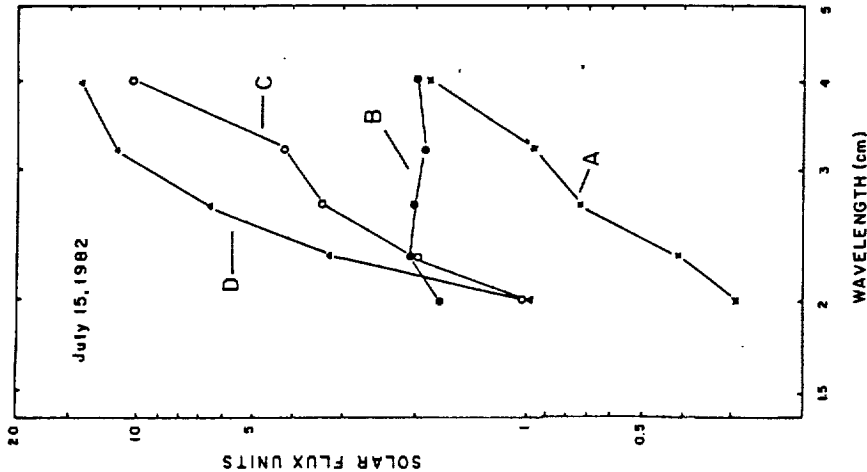


Figure 6. The radiation spectra of the four sources shown in Figure 5. The steep spectrum of the filament-associated source D is attributed to the gyrosynchrotron radiation of mildly relativistic electrons, whereas the flat spectrum of source B is attributed to thermal bremsstrahlung. The sunspot-associated sources A and C are attributed to gyroresonant emission.

densities are too low. Thermal gyroemission is similarly ruled out because the weak magnetic fields require a high harmonic of the gyrofrequency where the optical depth is far too small to account for the high brightness temperatures. The nonthermal radiation might be explained by the gyrosynchrotron emission of subrelativistic electrons, Akhmedov et al. (1985); Chiuderi-Drago and Melozzi (1984); but the acceleration mechanism is difficult to explain because of the short lifetime of the electrons.

II. MICROWAVE BURSTS FROM SOLAR ACTIVE REGIONS

The 27 antennae of the Very Large Array are interconnected electronically to provide a total of 356 interferometer pairs. Signals recorded every three seconds of time therefore provide sufficient data to construct snapshot synthesis maps with angular resolutions of a few seconds of arc without relying on the Earth's rotation to provide variable interferometric baselines. Snapshot maps of total intensity, I , and circular polarization, or Stokes parameter V , can be made at time intervals as short as three seconds. These maps can be used to detect changes in the configuration of coronal magnetic fields and temperature enhancements within coronal loops that are important triggering

agents for solar bursts.

The origin and prediction of these powerful bursts is one of the most important and interesting problems of solar physics. It has long been known that solar eruptions are intimately connected with the magnetic fields in active regions, for the ultimate source of energy for these bursts must be magnetic energy. It has only recently been realized, however, that evolving magnetic fields in the solar corona may play a dominant role in triggering solar eruptions.

Snapshot maps of the impulsive phase of 20 cm bursts indicate, for example, that the microwave energy is released near the apex of coronal loops, while the underlying optical flares occur near the footpoints of these loops. The examples shown in Figure 7 indicate that the 20 cm bursts are displayed by about 40,000 km above the solar photosphere. The loop plasma is impulsively heated at the loop tops where most of the electrons remain trapped, but some high-speed electrons escape to the lower parts of the loop detected at H α wavelengths.

Theoretical considerations indicate that loops emerging into the

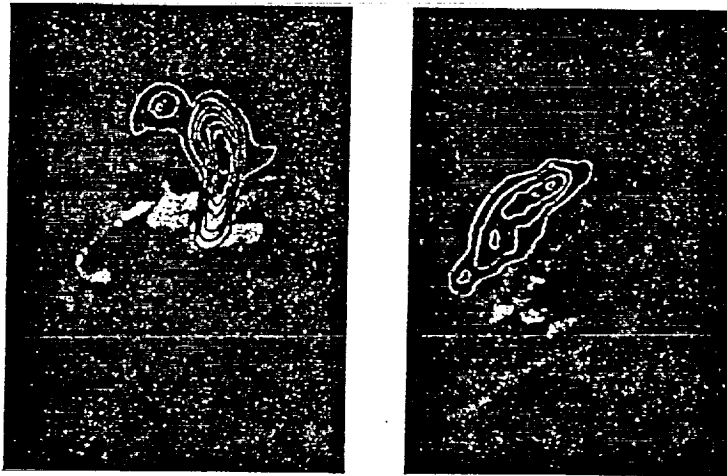


Figure 7. Ten second V.L.A. synthesis maps (white contours) of the impulsive phase of two solar bursts at 20 cm wavelength superposed on H α photographs of the optical flares taken at the same time at the Big Bear Solar Observatory. The 20 cm bursts originate near the tops of coronal loops that are about 40,000 kilometers above the flaring region seen at optical wavelengths. The contours mark levels of equal brightness corresponding to 0.2, 0.4, ... 1.0 times the maximum value of 10^8 K. The angular scale can be inferred from the 30" arrows, and the western solar limb is visible on both photographs.

ORIGINAL PAGE IS
OF POOR QUALITY

corona, magnetic shear within these loops, and interacting coronal loops can trigger solar bursts and supply their energy, Heyvaerts et al. (1977); Spicer (1977); Hood and Priest (1979); Syrovatski and Kuznetsov (1980); Kuznetsov and Syrovatski (1981); Spicer (1981); Emslie (1982); Somov and Syrovatskii (1982); Priest (1983). Very Large Array solar observations have played a crucial role in demonstrating that many of these theoretical effects actually take place on the Sun, Kundu and Lang (1985). These observations indicate that no single theoretical model is versatile enough to explain the diverse ways in which magnetic energy is dissipated in solar bursts. They nevertheless indicate that preburst changes can be ordered into three major categories - changes within a single coronal loop, the emergence of coronal loops, and interaction between coronal loops, Lang and Willson (1983, 1984); Willson and Lang (1983); Kundu (1984); Kundu and Lang (1985).

Our recent Very Large Array observations have revealed two new approaches to an understanding of the excitation and eruption of solar bursts. They include the observation of preburst heating and magnetic triggering in coronal loops (following Section II A), and the observation of coherent burst mechanisms at closely spaced frequencies (following Section II B).

II A. Preburst Heating and Magnetic Triggering

Interferometric observations at microwave wavelengths first indicated that preburst activity is associated with brightness and polarization changes that precede solar bursts on time scales of tens of minutes; but these observations had inadequate resolution to determine the sources of this activity. The high two-dimensional angular resolution provided by the Very Large Array has recently shown that the intensity or brightness increases are associated with preburst heating in coronal loops, Lang and Willson (1984); Willson (1984) and that the changes in circular polarization are associated with changes in the coronal magnetic field, Lang and Willson (1984); Willson and Lang (1984); Kundu (1984); Kundu and Lang (1985). Both the preburst heating in coronal loops and the changes in coronal magnetic fields may trigger solar eruptions.

There is evidence for sequential triggering of microwave bursts in

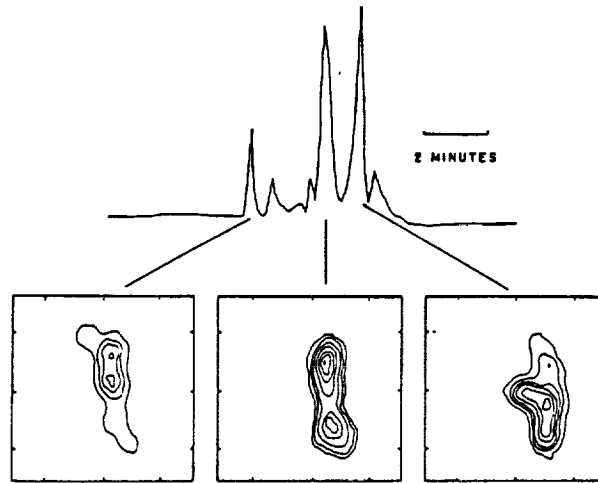


Figure 8. The time profile of successive impulsive bursts at 20 cm wavelength (top) is compared with ten second V.L.A. synthesis maps at the same wavelength (bottom). Here the contour intervals are in steps of 1.0×10^7 K and there is a $30''$ spacing between the fiducial marks on the axis. Although the successive weak bursts were emitted from the same coronal loop or arcade of loops, the successive intense bursts arose from spatially separated loops or arcades of loops.

different loops within magnetically complicated regions. VLA 20 cm maps of total intensity (Figure 8) show that successive intense bursts can originate in adjacent coronal loops, whereas successive weaker bursts are located in the same coronal loop. The 20 cm maps of circular polarization indicate that the feet or legs of the loop-like feature shown in Figure 8 originate in regions of opposite magnetic polarity.

As illustrated in Figure 9, single coronal loops or arcades of loops often begin to heat up and change structure about 15 minutes before the eruption of impulsive bursts. Radio and soft X-ray data have been combined for this example to derive a peak electron temperature of $T_e = 2.5 \times 10^7$ K and an average electron density of $N_e = 10^{10} \text{ cm}^{-3}$ during the heating phase. This heating may be related to the development of current sheets at the apex or tops of coronal loops.

New bipolar loops can also emerge and interact with preexisting ones. When the polarity of the new emerging flux differs from that of the preexisting flux, current sheets are produced that trigger the emission

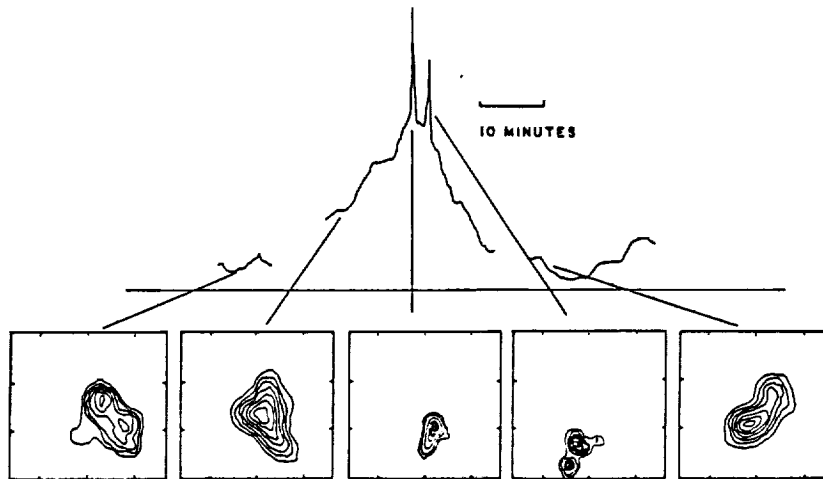


Figure 9. The time profile of a solar burst at 20 centimeters wavelength (top) suggests preburst heating within a coronal loop prior to the emission of two impulsive microwave bursts. The ten second V.L.A. synthesis maps (bottom) suggest that adjacent coronal loops were successively excited or that a coronal loop twisted in space. The outermost contour and contour interval are both equal to 4×10^5 K, and there is a $60''$ spacing between the fiducial marks on the axes.

of bursts. Two oppositely polarized bipolar loops may also interact and reconnect, Kundu (1984); Kundu and Lang (1985). A current sheet can develop at the interface of the two closed loops, thereby triggering the burst onset.

II B. Burst Emission at Closely Spaced Wavelengths and Coherent Mechanisms

Microwave bursts from the Sun are characterized by compact (angular sizes $\theta \leq 10''$), highly circularly polarized (degrees of circular polarization $\rho_c \geq 50\%$) sources with high brightness temperatures, T_B , in excess of 10^7 K, Lang and Willson (1984); Willson and Lang (1984). The high brightness temperatures and high degrees of circular polarization have generally been attributed to the gyrosynchrotron radiation of mildly relativistic electrons with energies of 100 to 500 keV (see Kundu and Lang (1985) for a review).

Recently, however, it has been suggested that electron-cyclotron maser emission may play a role in solar microwave bursts, Holman et al. (1980); Melrose and Dulk (1982). Such a coherent emission mechan-

ism has been invoked to explain intense ($T_B \leq 10^{12}$ K), narrow-band, millisecond spikes that have been detected from the Sun at decimeter wavelengths, Droge (1977); Slottje (1978).

The long integration times ($\tau \geq 10$ seconds), broad bandwidths ($\Delta\nu \geq 50$ MHz), and large beamwidths ($\theta \geq 30''$) of most radio telescopes nevertheless preclude the detection of coherent burst emission. Rapidly varying emission is smoothed by the long time constants, leading to large upper limits to burst duration. This provides unrealistically large upper limits to the source size from the argument that nothing can move faster than the velocity of light. Large upper limits to source size are also constrained by the large antenna beamwidths. As a result, the brightness temperatures of the burst emission may be seriously underestimated. Narrow-band coherent emission is also smoothed in frequency by the large bandwidths.

Although the high angular resolution of the Very Large Array provides the possibility of isolating and perhaps even resolving individual coherent emitters, previous multi-frequency observations have been made over such widely spaced frequencies that the narrow-band features characteristic of coherent emission processes could not be detected. We have recently used the Very Large Array with narrow bandwidths ($\Delta\nu=12.5$ MHz) and closely spaced frequencies (30 MHz) near 1440 MHz (or 20.7 cm) to isolate a coronal loop that exhibited narrow-band burst emission, Lang and Willson (1984); Willson (1985) - see figure 10). The impulsive burst emission was nearly 100% circularly polarized and originated in a loop-like structure 10" or less in angular size. One burst exhibited a factor of two difference in brightness temperature (1.5×10^8 K and 0.8×10^8 K) at two wavelengths separated by only 32 MHz (burst 7 of Figure 10 at 1658 MHz and 1690 MHz). The high circular polarization and narrow bandwidth ($\Delta\nu/\nu \leq 10^{-2}$) of this burst are comparable to those expected from gyrosynchrotron masers, Holman et al. (1980) or electron-cyclotron masers, Melrose and Dulk (1982). Although the burst source was apparently resolved, the 10 second integration time of the VLA may have smoothed or integrated several briefer, spatially-separated coherent spikes.

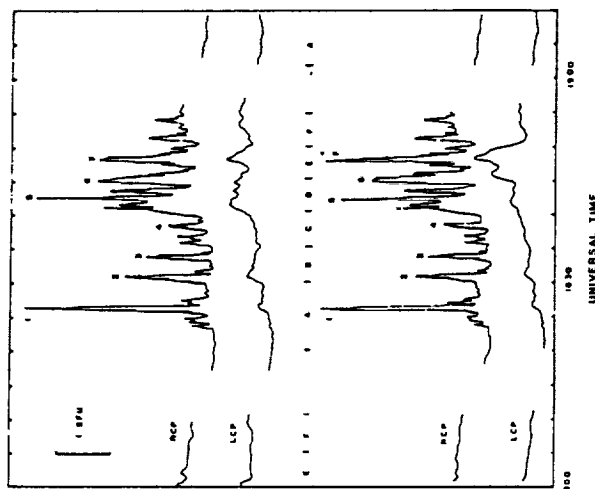


Figure 10. A sequence of right circularly polarized (RCP) impulsive bursts from a solar active region observed at wavelengths near 20 cm. The top and bottom profiles are separated by only 30 MHz; burst 7 has a factor of two difference in brightness temperature over this narrow frequency interval; suggesting coherent burst emission.

III. MICROWAVE EMISSION FROM NEARBY STARS OF LATE SPECTRAL TYPE

Nearby main-sequence stars of late spectral type exhibit a variety of phenomena that are closely related to our understanding of solar active regions including dark spots, activity cycles and bursts at ultraviolet, optical, radio and X-ray wavelengths. These stars also emit quiescent X-ray emission whose absolute luminosity is as much as one hundred times that of the Sun. They may therefore have large-scale coronal loops and intense magnetic fields. The solar analogy suggests that the magnetic fields and coronal plasma of these nearby stars will be detected as slowly varying microwave emission, and that their stellar bursts may exhibit coherent microwave emission similar to that suspected for the Sun.

Nearby dwarf M flare stars do, in fact, exhibit quiescent, or non-flaring microwave emission that is slowly variable with time scales of tens of minutes to hours [Linsky and Gary (1983); Pallavicini, Willson and Lang (1985)]. Brightness temperatures of 10^7 to 10^8 K are inferred if the microwave-emitting source covers the entire visible surface of the star. The detected emission might then be explained as the gyroresonant emission of thermal electrons gyrating in gigantic

ORIGINAL PAGE IS
OF POOR QUALITY

coronal loops that exceed the stars in size. Alternatively, the slowly-varying stellar microwave emission might be attributed to the gyrosynchrotron emission of energetic electrons in magnetic fields associated with smaller coronal loops of star spots.

The dwarf M flare stars also exhibit intense, highly circularly polarized microwave bursts that are similar to those emitted by the Sun. Both the high circular polarization and the high brightness temperatures might be explained by electron-cyclotron maser emission, Melrose and Dulk (1982). As discussed in the preceding Section IIB, a similar coherent burst mechanism may have to be invoked to explain microwave bursts from the Sun.

Another class of microwave-emitting stars is the RS CVn binary stars. Their microwave emission is intense, highly variable and often circularly polarized [Mutel and Lestrade (1985); Pallavicini, Willson and Lang (1985).] There is a slowly varying component that varies on time scales of hours and days. Bursts of short duration that are close to 100% circularly polarized have occasionally been observed; speculation about the origin of these bursts have involved electron-cyclotron masers and expanding coronal loops. Very Long Baseline Interferometry (VLBI) has been used to resolve a few of the RS CVn microwave sources, indicating that they are comparable with the binary separation and/or an individual stellar diameter (or smaller) in size, Mutel et al. (1984, 1985).

Observations of the dwarf M star AD Leonis with high time resolution have provided dramatic evidence for coherent burst emission, Lang et al. (1983). A microwave stellar eruption from AD Leonis was composed of highly circularly polarized (100%) spikes with rise times of less than 200 milliseconds. An upper limit to the linear size of the emitting region is 6×10^9 cm, the distance that light travels in 200 milliseconds. If the emitting region is symmetrical, it has an area that is less than 3 percent of the star's surface area, and its brightness temperature exceeds 10^{13} K. The high brightness temperature requires a coherent burst mechanism. Both the high degree of circular polarization and the high brightness temperature may be explained by electron-cyclotron maser emission.

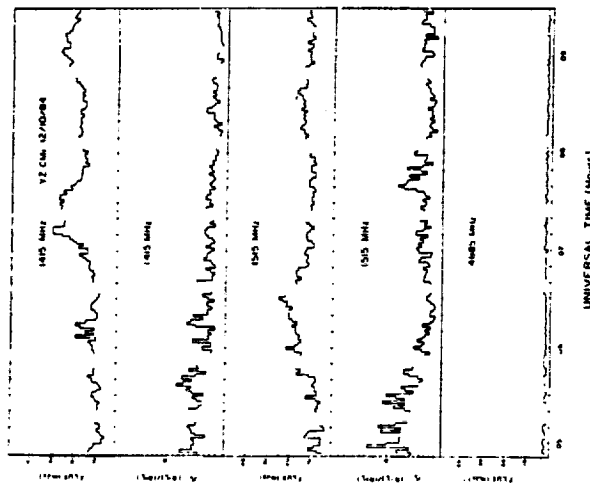


Figure 11. Slowly-varying emission from the dwarf M flare star YZ Canis Minoris at two closely spaced frequencies of 1415 and 1515 MHz and at 4885 MHz. The emission at the two nearby frequencies peaks at different times, suggesting a coherent emission mechanism with a bandwidth of less than 100 MHz. There are no detectable variations at 4885 MHz.

VLA observations of the slowly varying emission from the dwarf M flare star YZ Canis Minoris indicate that its microwave emission peaks at different times at two frequencies near 1420 MHz (21 cm) that are separated by only 100 MHz (Figures 11 and 12). This emission exhibits narrow-band characteristics that are suggestive of coherent emission mechanisms, Lang and Willson (1985). Moreover, the mechanism appears to be confined to the stellar corona, and the intensity is far in excess of that expected from gyroresonance radiation.

IV. CONCLUSIONS

Multiple-wavelength VLA observations of the quiescent microwave emission from solar active regions at widely spaced wavelengths specify the three-dimensional structure of the magnetic field and plasma in the low corona. Gyroresonance effects dominate the 6 cm emission from the legs of magnetic dipoles; whereas thermal radiation from the ubiquitous coronal loops is detected at 20 cm wavelength. Individual cyclotron lines have been detected at the apex of coronal loops, providing sensitive probes of the magnetic field strength. Nonthermal radiation mechanisms are required to explain intense microwave emission with a steep radiation spectrum in regions of relatively weak magnetic

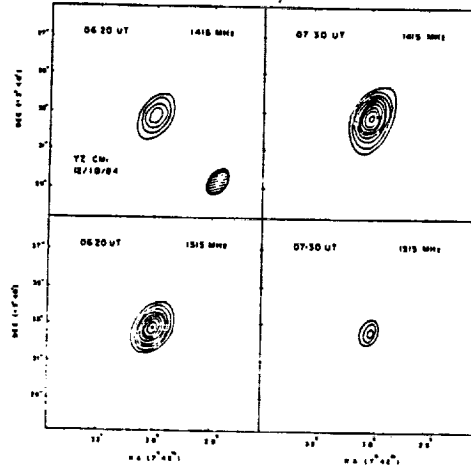


Figure 12. VLA snapshot maps of the emission from the dwarf M flare star YZ Canis Minoris. The unresolved emission peaks at different times at two frequencies separated by only 100 MHz, suggesting a coherent burst mechanism. The contours are at intervals of 4, 8, 12, ... Jy/beam area, with maximum values of 14 and 22 at 0620 UT and 1415 and 1515 MHz, respectively, and 25 and 10 at 0730 for the same respective frequencies.

fields.

Snapshot synthesis maps provide evidence for the excitation of solar bursts by preburst heating within coronal loops or by magnetic triggering due to emerging coronal loops or interacting coronal loops. Narrow band, highly circularly polarized solar bursts require coherent emission mechanisms like gyrosynchrotron masers or electron-cyclotron masers. Coherent mechanisms are also required to explain both stellar bursts and the slowly varying microwave emission from some dwarf M flare stars.

Radio astronomical studies of the Sun and other active stars at Tufts University are supported under Air Force Office of Scientific Research grant AFOSR-83-0019 and by Solar Maximum Mission NASA grant NAG 5-501. Investigations of flare stars at Tufts University are supported by NASA grant NAG 5-477.

REFERENCES

- Akhmedov, Sh.B., Borovik, V.N., Gelfreikh, G.B., Bogod, V.M., Korzhavin, A.N., Petrovo, A.E., Dikij, V.N., Lang, K.R. and Willson, R.F. (1985). The Structure of a Solar Active Region from RATAN 600 and Very Large Array Observations. *Ap. J.* in press.
- Chiuderi-Drago, F. and Melozzi, M. (1984). Non-Thermal Radio Sources in Solar Active Regions. *Astr. Ap.* 131, 103-110.
- Droge, F. (1977). Millisecond Fine Structures of Solar Burst Radiation in the Range 0.2-1.4 GHz. *Astr. Ap.* 57, 285-290.
- Emslie, A.G. (1982). An Interacting Loop Model for Solar Flare Bursts. *Ap. Lett.* 22, 41-47.
- Hayvaerts, J., Priest, E.R. and Rust, D.M. (1977). An Emergin Flux Model for Solar Flare Phenomenon. *Ap. J.* 216, 123-130.
- Holman, G.D., Eichler, D. and Kundu, M.R. (1980). An Interpretation of Solar Flare Microwave Spikes as Gyrosynchrotron Masering. In: *IAU Symp. No. 86: Radiophysics of the Sun*, M.R. Kundu and T. Gergeley (eds.). Reidel, Dordrecht, pp. 457-459.
- Holman, G.D. and Kundu, M.R. (1985). The Microwave Structure of Hot Coronal Loops. *Ap. J.* in press.
- Hood, A.W. and Priest, E.R. (1979). Kink Instability of Solar Coronal Loops as the Cause of Solar Flares. *Solar Ph-s.* 64, 287-301.
- Kundu M.R. (1984). Observational Evidence for Magnetic Reconnection in Microwave Solar Bursts. In: *Proc. IAU Symp. No. 107*. M.R. Kundu and G.D. Holman (eds.). Reidel, Boston, pp. 185-190.
- Kundu, M.R. and Lang, K.R. (1985). The Sun and Nearby Stars: Microwave Observations at High Resolution. *Science* 228, 9-15.
- Kuznetsov, V.D. and Syrovatskii, S.I. (1981). On the Possibility of Observations of Current Sheets in Radio Band. *Solar Phys.* 69, 361-372.
- Lang, K.R., Bookbinder, J., Golub, L. and Davis, M. (1983). Bright, Rapid, Highly Polarized Radio Spikes from the M Dwarf AD Leonis. *Ap. J. (Letters)* 272, L15-L18.
- Lang, K.R. and Willson, R.F. (1983). Multiple Wavelength Observations of Flaring Active Regions. *Adv. Space Res.* 2, No. 11, 91-100.
- Lang, K.R. and Willson, R.F. (1984). Observations of Flare Build Up in Coronal Loops on the Sun and Solar-Type Stars, *Adv. Space Res.* 4, 105.
- Lang, K.R. and Willson, R.F. (1985). Narrow-Band, Slowly Varying Decimetric Radiation from the Dwarf M Star YZ Canis Minoris. *Ap. J. (Letters)* in press.

- Lang, K.R., Willson, R.F. and Gaizauskas, V. (1983). Very Large Array Observations of Solar Active Regions III. Multiple Wavelength Observations. *Ap. J.* 267, 455-464.
- Lang, K.R., Willson, R.F. and Rayrole, J. (1982). Very Large Array Observations of Coronal Loops at 20 cm Wavelength. *Ap. J.* 258, 384-387.
- Linsky, J.L. and Gary, D.E. (1983). Microwave Emission from the Coronae of Late-Type Dwarf Stars. *Ap. J.* 274, 776-783.
- Marsh, K.A. and Hurford, G.J. (1980). Two-Dimensional VLA Maps of Solar Bursts at 15 and 23 GHz with Arcsec Resolution. *Ap. J. (Letters)* 240, L111-L114.
- McConnell, D. and Kundu, M.R. (1983). VLA Observations of a Solar Active Region and Coronal Loops. *Ap. J.* 269, 698-705.
- Melrose, D.B. and Duld, G. (1982). Electron-Cyclotron Masers as the Source of Certain Solar and Stellar Radio Bursts. *Ap. J.* 259, 844-858.
- Melrose, D.B. and Dulk, G.A. (1984). Radio Frequency Heating of the Coronal Plasma During Flares. *Ap. J.* 282, 308-315.
- Mutel, R.L., Doiron, D.J., Lestrade, J.F. and Phillips, R.B. (1984). VLBI Observations of the RS Canium Venaticorum Binary Systems UX Arietis and HR 1099 at 1.69 GHz. *Ap. J.* 278, 220-223.
- Mutel, R.L., Lestrade, J.F., Preston, R.A., and Phillips, R.B. (1985). Dual Polarization VLBI Observations of Stellar Binary Systems at 5 GHz. *Ap. J.* 289, 262-268.
- Pallavicini, R., Willson, R. and Lang, K.R. (1985). Microwave Observations of Late-Type Stars with the Very Large Array. *Astr. Ap.* 149, 95-101.
- Priest, E.R. (1983). Magnetic Theories of Solar Flares. *Solar Phys.* 86, 33-45.
- Schmahl, E.J., Kundu, M.R., Strong, K.T., Bentley, R.D., Smith, J.B. and Krall, K.R. (1982). Active Region Magnetic Fields Inferred from Simultaneous VLA Microwave Maps, X-ray Spectroheliograms and Magnetograms. *Solar Phys.* 80, 233-249.
- Shevgaonkar, R.K. and Kundu, M.R. (1984). Three-Dimensional Structures of Two Solar Active Regions from VLA Observations at 2, 6 and 20 Centimeter Wavelengths. *Ap. J.* 283, 413-420.
- Slottje, C. (1978). Millisecond Microwave Spikes in a Solar Flare. *Nature* 275, 520-521.
- Somov, B.V. and Syrovatskii, S.I. (1982). Thermal Trigger for Solar Flares and Coronal Loops Formation. *Solar Phys.* 75, 237-244.

Spicer, D.S. (1977). An Unstable Arch Model of a Solar Flare. *Solar Phys.* 53, 305-345.

Spicer, D.S. (1981). Loop Models of Solar Flares: Revisions and Comparisons. *Solar Phys.* 70, 149-172.

Syrovatskii, B.V. and Kuznetsov, V.D. (1980). On the Possibility of Radio Observations of Current Sheets on the Sun. In: *Radio Physics of the Sun*. IAU Symp. No. 86. M.R. Kundu and T. Gergely (eds.). Reidel, Dordrecht, 445-455.

Webb, D.F., Davis, J.M., Kundu, M.R. and Velusamy T. (1983). X-Ray and Microwave Observations of Active Regions. *Solar Phys.* 85, 267-283.

Willson, R.F. (1985). VLA Observations of Solar Active Regions at Closely Spaced Frequencies: Evidence for Thermal Cyclotron Line Emission. *Ap. J.* in press.

Willson, R.F. (1985). VLA Observation of Narrow Band Decimetric Burst Emission, *Solar Phys.* in press.

Willson, R.F. and Lang, K.R. (1983). Very Large Array Observations of Solar Active Regions IV. Structure and Evolution of Radio Bursts from 20 cm Loops. *Ap. J.* 279, 427-437.

Zheleznyakov, V.V. and Tikhomirov, Yu. V. (1984). Microwave Radiation from Magnetic Stars. *Ap. Space Sci.* 102, 189-209.

C. SOLAR BURST PRECURSORS AND ENERGY BUILD-UP AT MICROWAVE WAVELENGTHS

Kenneth R. Lang and Robert F. Willson

Department of Physics, Tufts University, Medford, MA 02155,
U.S.A.

ABSTRACT

We summarize high-resolution microwave observations (VLA) of heating and magnetic triggering in coronal loops. Magnetic changes that precede solar eruptions on time scales of tens of minutes involve primarily emerging coronal loops and the interaction of two or more loops. Thermal cyclotron lines have been detected in coronal loops, suggesting the presence of hot current sheets that enhance emission from relatively thin layers of enhanced temperature and constant magnetic field. These current sheets may play a role in the excitation of solar bursts. A filament-associated source with a high brightness temperature and steep radiation spectrum occurs above a region of apparently weak photospheric field. This source might be attributed to currents that enhance coronal magnetic fields. Compact ($\phi = 5''$) transient sources with lifetimes of 30 to 60 minutes have also been detected in regions of apparently weak photospheric field. We conclude by comparing VLA observations of coronal loops with simultaneous SMM-XRP observations.

MAGNETIC CHANGES AND PREBURST HEATING

The VLA has recently been used to detect changes in the configuration of coronal magnetic fields and temperature enhancements within coronal loops that are important in the excitation of solar bursts. It has long been known that solar eruptions are intimately connected with the magnetic fields in active regions, for the ultimate source of energy for these bursts must be magnetic energy. It has only recently been realized, however, that evolving magnetic fields in the solar corona may play a dominant role in triggering solar eruptions /1/.



Fig. 1. The ten second V.L.A. synthesis maps of the impulsive phase of two solar bursts at 20 cm wavelength superposed on H α photographs of the optical flares taken at the same time at the Big Bear Solar Observatory. The 20 cm bursts originate near the tops of coronal loops that are about 40,000 kilometers above the flaring region seen at optical wavelengths. The western solar limb is visible in both photographs.

Preflare changes in active regions are detected as increases in the intensity and polarization of the microwave emission at centimeter wavelengths. These increases precede solar eruptions on time scales of 10 minutes to an hour. The high angular resolution provided by the Very Large Array (VLA) has shown that these increases are related to preburst heating in coronal loops and to changes in the coronal magnetic field topology /2/. The VLA snapshot maps have also made possible tests of flare models that could not be carried out at optical wavelengths. For instance, the region of microwave energy release occurs at the

apex of coronal loops, while the optical flares occur at the loop footpoints (See Fig. 1). The VLA results indicate that preburst changes can be ordered into three major categories: (I) changes within a single coronal loop, (II) the emergence of coronal loops, and (III) interaction between coronal loops. As illustrated in Figure 2, coronal loops or arcades of loops often begin to heat up and change structure about 15 minutes before the eruption of impulsive bursts. Examples of the other types of magnetic interaction detected by the University of Maryland and Tufts groups are given in the review by Kundu and Lang /2/.

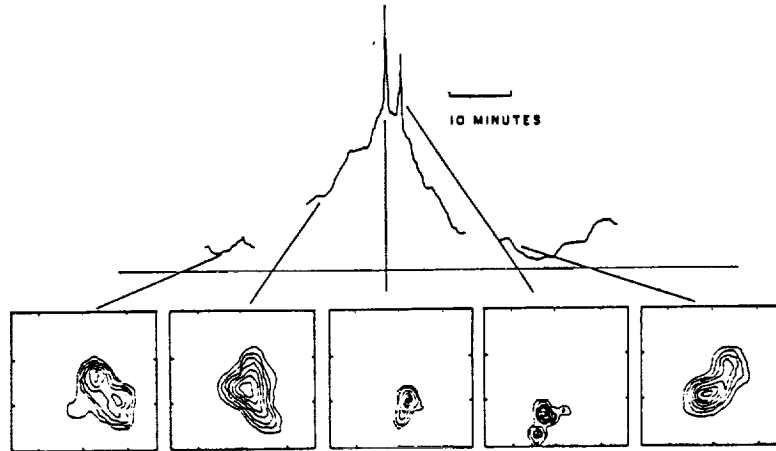


Fig. 2. The time profile of a solar burst at 20 cm wavelength suggests heating within a coronal loop prior to the emission of two impulsive microwave bursts. Radio and X-ray data have been combined to derive a peak electron temperature T_e of 2.5×10^7 K and an average electron density N_e of 10^{10} cm^{-3} during the heating phase. The changing orientation illustrated in the 10 second VLA snapshot maps could be related to the shear of photospheric fields.

THERMAL CYCLOTRON LINES AND EVIDENCE FOR CURRENTS

Theoretical work has shown that individual cyclotron lines might be detected as narrow-band enhancements in the radio-frequency spectra of solar active regions /3/. The spectra of individual cyclotron lines have subsequently been observed at wavelengths near 20 cm when the apex of a coronal loop is resolved /4/ - see Figure 3. This is because the magnetic field strength is relatively constant near the loop apex; the cyclotron lines would merge into a continuum along the loop legs where the magnetic field strength decreases uniformly with height. Neutral current sheets might also play a role, leading to intense radio emission from a thin layer near the loop apex. Both a uniform field and a steep temperature gradient in the uniform region are probably required to detect the cyclotron lines. In any event, observations of individual cyclotron lines indicate magnetic field strengths of $H = 145 \pm 5$ G at the apex of some coronal loops. Observations of individual cyclotron lines provide an unusually accurate method of specifying the coronal magnetic field strength, while also suggesting the presence of currents.

Evidence for current amplification of the coronal magnetic field may be provided by sources of high brightness temperature and steep radiation spectrum above regions of apparently-weak magnetic field /5/. An example is the filament associated source D whose spectrum is shown in Figure 4. If this emission is due to thermal gyroradiation, strong magnetic fields are required to produce gyroradiation at the first few harmonics of the gyrofrequency. Higher harmonics produce insufficient optical depth to account for the high brightness temperatures. The strong magnetic fields could be obtained if currents amplify the magnetic field in the low corona to values greater than those expected from extrapolations from the photosphere. The emission could alternatively be due to nonthermal radiation in weak magnetic fields. Nonthermal synchrotron radiation from mildly relativistic electrons is one possibility, but some as yet unspecified mechanism must be continuously accelerating the electrons.

COMPACT VARIABLE SOURCES

We have recently discovered compact, variable highly-polarized sources in regions of apparently-weak photospheric magnetic field /6/. Our subsequent VLA observations have confirmed the existence of compact, variable 2 cm sources that are not associated with active regions, but these sources had no detectable circular polarization.

The 2 cm maps showed two compact ($\theta = 5''$), highly circularly polarized ($\rho_c = 80$ to 90%) sources that vary on time scales of 30 to 60 minutes. The left circularly polarized source varied in maximum brightness temperature from $T_B = 2.0 \times 10^5$ K to $T_B < 0.5 \times 10^5$ K.

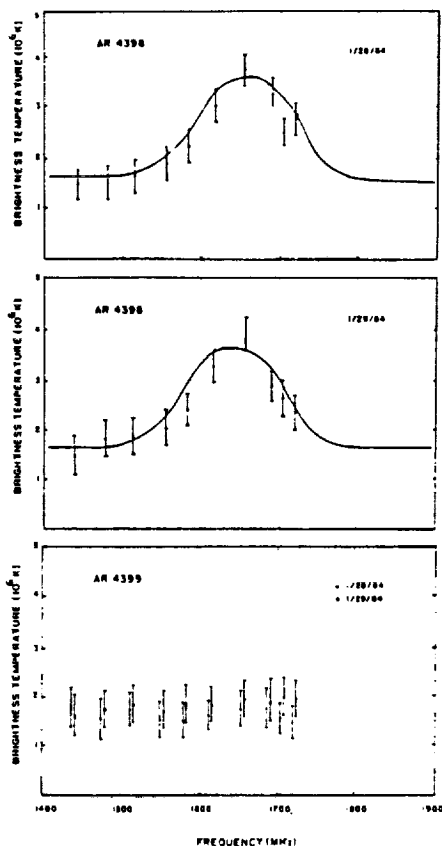


Fig. 3.

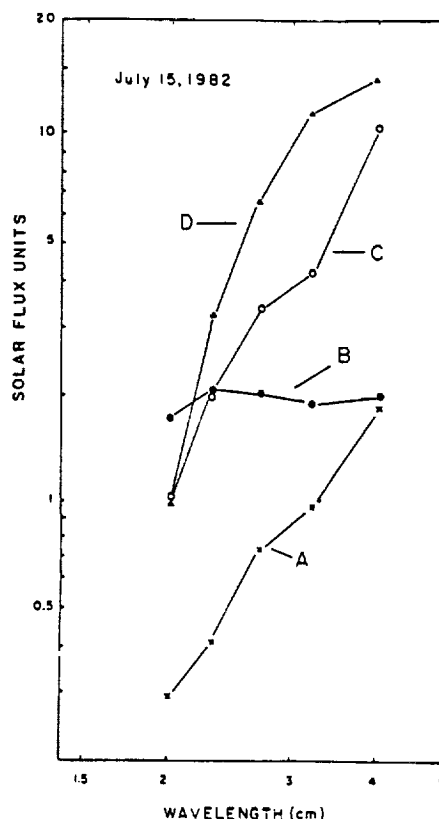


Fig. 4.

Fig. 3. VLA data at ten closely-spaced frequencies near 1440 MHz (20 cm) showing thermal cyclotron line spectra from active region AR 4398 on successive days, together with optically-thick thermal bremsstrahlung spectra from active region AR 4399 on the same days.

Fig. 4. The radiation spectra for the three types of sources usually detected at short centimeter wavelengths. The most common type of source is the sunspot-associated component (A and C) that is attributed to thermal gyroresonance radiation in the legs of coronal loops that are connected to the underlying sunspots. Source D is a filament-associated component located above a magnetic neutral line in regions of apparently-weak magnetic field. It may be due to thermal gyroradiation in current-amplified magnetic fields. The filament-associated source B has the flat spectrum of optically-thin thermal bremsstrahlung.

Comparisons with Mr. Wilson magnetograms indicate that the two compact, variable sources were located in regions of apparently-weak photospheric magnetic field ($H < 80$ G), and that they did not overlie sunspots. The high polarization of these sources is therefore somewhat enigmatic, for the polarization of thermal radiation requires strong magnetic fields of $H = 2,000$ G.

The enigmatic presence of highly polarized sources in regions of apparently-weak photospheric magnetic field may be explained by any one of three hypothesis. First, the photospheric field may have strengths of up to 2,000 G in compact regions that are not readily detected by the photospheric magnetograms. Alternatively, the magnetic field in the transition region or the low corona may be amplified by currents to a strength above that in the underlying photosphere. If either of these hypothesis is true, then the high circular polarization of the 2 cm sources can be attributed to either thermal gyroradiation or the propagation of thermal bremsstrahlung in the presence of a magnetic field of strength $H = 2,000$ G. A third hypothesis is that the compact 2 cm sources are due to non-thermal gyrosynchrotron radiation of mildly relativistic electrons in relatively weak magnetic fields of strength $H = 50$ G.

ONGOING COMPARISONS OF VLA AND SMM-XRP DATA

We are continuing with a comparison of 20 cm coronal loop data (VLA) with soft X-ray data obtained with the SMM satellite. In some instances, there is radiation at 20 centimeters

wavelength near sunspots where no X-ray radiation is detected /7/. In other cases, the 20 centimeter radiation appears at the apex of coronal loops, but with a slightly lower brightness temperature, $T_B = 1.4$ to 1.7×10^6 K, than the electron temperature, $T_e = 3.0 \times 10^6$ K, inferred from the X-ray data. This may be explained by a low temperature plasma with $T_e = 10^5$ K that lowers the effective brightness temperature of the radio bremsstrahlung while not affecting the X-ray data that only detects the 10^6 K plasma /8/.

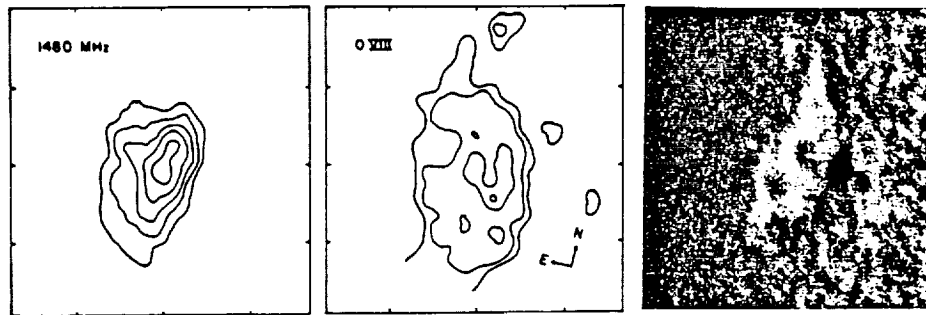


Fig. 5. A comparison of the 20 cm emission (V.L.A.-left), soft X-ray (S.M.M.-middle) and H α (SOON-right) emission of an active region on the same day. The angular spacing between fiducial marks on the axes is 60 arc-seconds.

As illustrated in Figure 5, there are other instances in which the 20-cm radiation and the soft X-ray emission have the same angular extent. In this case, the maximum brightness temperature of the radio emission has the same value as the electron temperature, $T_e = 3 \times 10^6$ K, inferred from the X-ray data. At first sight it would seem that the 20-cm emission is the thermal bremsstrahlung of the X-ray emitting plasma (electron density $N_e = 2 \times 10^{10} \text{ cm}^{-3}$), but in this instance we have also detected a cyclotron line. Preliminary modeling indicates a thin layer of $T_e = 4 \times 10^6$ K with a magnetic field strength of $H = 145$ or 187 G (harmonic $n = 4$ or 3). The thermal electrons that give rise to the X-ray radiation therefore also seem to produce strong gyroresonant radiation at 20 centimeters wavelength.

ACKNOWLEDGEMENTS

Radio astronomical studies of the Sun at Tufts University are supported under grant AFOSR-83-0019 with the Air Force Office of Scientific Research and by contract N00014-86-K-0068 with the Office of Naval Research (ONR). Comparisons of VLA and Solar Maximum Mission satellite data are supported under NASA Guest Investigator grant NAG 5-501.

REFERENCES

1. K.R. Lang and R.F. Willson, V.L.A. observations of flare build-up in coronal loops, Advances in Space Research 4, No. 7, 105 (1984).
2. M.R. Kundu and Kenneth R. Lang, The Sun and nearby stars: microwave observations at high resolution, Science, 228, 9 (1985).
3. V.S. Kuznetsov and S.I. Syrovatskii, On the possibility of observations of current sheets in the radio band, Solar Physics, 69, 361 (1981).
4. R.F. Willson, V.L.A. observations of solar active regions at closely spaced frequencies: evidence for thermal cyclotron line emission, Astrophysical Journal, 298, 911 (1985).
5. S.B. Akmedov, et al., Structure of a solar active region from RATAN 600 and Very Large Array observations, Astrophysical Journal, 301, 460 (1986).
6. R.F. Willson and K.R. Lang, VLA observations of compact, variable sources on the Sun, Astrophysical Journal (1986) - to be published.
7. K.R. Lang, R.F. Willson, K.T. Strong and K.L. Smith, Simultaneous Solar Maximum Mission and Very Large Array observations of solar active regions, Astrophysical Journal (1986) - to be submitted.
8. K.R. Lang, R.F. Willson, K.T. Strong and K.L. Smith, Physical parameters of solar active regions inferred from thermal cyclotron lines and soft X-ray spectral lines, Astrophysical Journal (1986) - to be submitted.

D. VLA¹ OBSERVATIONS OF COMPACT, VARIABLE SOURCES ON THE SUN

ROBERT F. WILLSON AND KENNETH R. LANG

Department of Physics and Astronomy, Tufts University

Received 1985 September 24; accepted 1986 February 12

ABSTRACT

Very Large Array (VLA) observations of a solar active region at 2 cm wavelength have revealed a new class of compact, variable sources on the Sun. The compact sources vary on two different time scales of 10–20 s and 30–60 minutes. They are small (angular size $\theta = 5''$), hot (brightness temperatures $T_B = 0.5\text{--}3 \times 10^5$ K), and highly circularly polarized (degrees of circular polarization $\rho_c = 80\%\text{--}90\%$). This emission originates in regions of low magnetic field strength $H \leq 80$ G. The high circular polarization must nevertheless be associated with magnetic fields, and a plausible explanation for the source variability is variations in the magnetic fields on the two time scales. Alternatively, the variability might be attributed to a variable nonthermal electron density, perhaps resulting from a variable acceleration mechanism. The compact sources are attributed to gyrosynchrotron emission from mildly relativistic electrons with a power-law spectrum.

Subject headings: interferometry — polarization — radiation mechanisms — Sun: activity — Sun: radio radiation

I. INTRODUCTION

The radiation mechanisms of quiescent (nonflaring) microwave emission from solar active regions at 6 cm and 20 cm wavelength are now well understood. This emission is attributed to the gyroresonant radiation or the bremsstrahlung of thermal electrons at the legs or apex of coronal loops, or both (Lang, Willson, and Gaizauskas 1983; Lang and Willson 1983; Shevgaonkar and Kundu 1984; Kundu and Lang 1985). In contrast, the quiescent emission of solar active regions at 2 cm wavelength is poorly understood.

There are only two published reports of 2 cm VLA observations of solar active regions (Lang, Willson, and Gaizauskas 1983; Shevgaonkar and Kundu 1984). Both papers report the presence of several (2–6) compact (angular sizes $\theta \leq 15''$), highly polarized (degrees of circular polarization $\rho_c = 80\%\text{--}90\%$) sources at the feet of coronal loops and overlying sunspots. The brightness temperatures ($T_B \approx 10^5$ K) of these compact polarized sources suggests an origin in the transition region, while the high polarization is attributed to intense magnetic fields of strength $H \approx 2000$ G.

The relationship of the compact, highly polarized sources to the magnetic field geometry is controversial. Shevgaonkar and Kundu (1984) report the presence of two compact sources underlying larger 6 cm emission. This suggested that coronal loops diverge as they rise toward their apex, and contradicted loop models that assume a constant cross section (Rosner, Tucker, and Vaiana 1978). In contrast, Lang, Willson, and Gaizauskas (1983) find at least six compact 2 cm sources scattered over an area that is comparable to that of the 6 cm emission. They also notice that the 2 cm sources are not found everywhere over sunspots, suggesting an origin in the low corona rather than the transition region where uniformly strong magnetic fields are expected above umbrae.

Previous VLA observations of compact, highly polarized 2 cm sources were used to make synthesis maps over intervals

of 11–12 hr. These maps revealed long-lasting sources that overlie sunspots in regions of strong magnetic field. Our recent VLA observations at 2 cm wavelength have been used to make snapshot synthesis maps for time intervals as short as 10 s. These maps indicate the presence of variable compact sources that vary over intervals of ~ 20 s and ~ 30 minutes. The variable sources originate in regions of low magnetic field strength $H \leq 80$ G, but they are highly circularly polarized. These observations are discussed in greater detail in § II. The compact ($\theta \approx 5''$), highly circularly polarized ($\rho_c = 80\%\text{--}90\%$) sources have brightness temperatures $T_B = 0.5\text{--}3 \times 10^5$ K, and they vary in brightness on two different time scales of 10–20 s and 30–60 minutes. In § III we associate the high circular polarization with magnetic fields. Since the sources appear above regions of low magnetic field strength, the high circular polarization and high brightness temperatures cannot be explained by thermal radiation mechanisms. Here we explain the polarization and temperatures in terms of the nonthermal gyrosynchrotron emission from mildly relativistic electrons. The source variability is attributed to varying magnetic fields or a varying nonthermal electron density.

II. OBSERVATIONS

The VLA was used to observe the active region AR 4508 in the C configuration between 1530 and 2330 UT on 1984 June 4. The position of AR 4508 was N06 E57 at 1300 UT on this day. Wavelengths of 2.1 cm and 20.7 cm were used for alternate 15 minute periods, followed by 5 minute observations of the calibration source PKS 0528+134. In all cases, the bandwidth was 12.5 MHz. In the C configuration the synthesized beamwidths are ~ 1.72 and $2''$ at 2.1 and 20.7 cm, respectively. The data were sampled every 10 s and were calibrated using the standard solar calibration procedures at the VLA. These data were then used to make synthesis maps of both the total intensity, I , and circular polarization, V , at each wavelength. These maps were finally CLEANed to produce images having a dynamic range of $\sim 10:1$.

The synthesis maps of total intensity at both wavelengths are shown in Figure 1. The 20.7 cm map was made using the data taken during the entire 8 hr observation period, whereas

¹ The VLA is a facility of the National Radio Astronomy Observatory, which is operated by Associated Universities, Inc., under contract with the National Science Foundation.

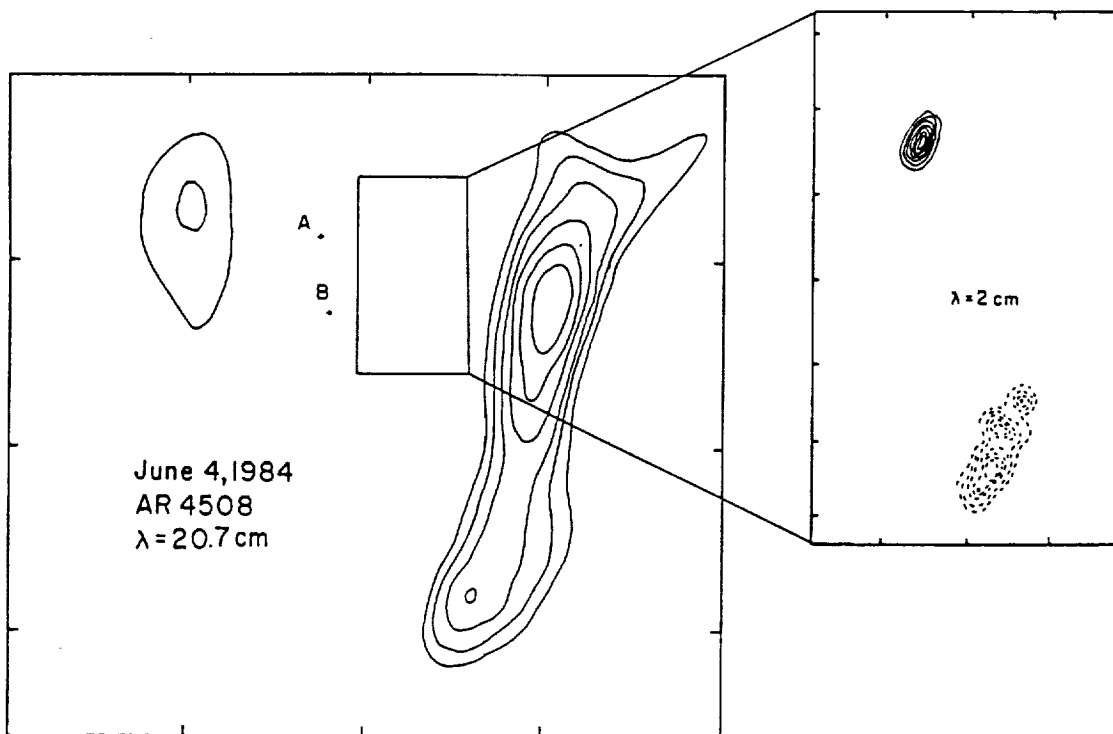


FIG. 1.—VLA synthesis maps of total intensity, I , at 20.7 cm for 8 hr of data and 2.1 cm (box) for 15 minutes of data (also see Fig. 2). The points marked "A" and "B" denote the positions of compact, variable 2 cm sources with lifetimes of 10–20 s (see Fig. 3). All of the compact 2 cm sources lie in regions of weak magnetic fields and do not overlie sunspots. The contours mark levels of equal brightness, and the fiducial marks on the axes are separated by $1''$ at 20 cm and $10''$ at 2 cm. The outermost contour and contour intervals are 4.5×10^5 K and 1.5×10^5 K at 20 cm and 6.1×10^4 K and 3.1×10^4 K at 2 cm.

the 2 cm map refers to a shorter 15 minute interval beginning at 1547 UT. The most intense 20 cm emission is contained within an elongated looplike structure of ~ 2.5 in extent which has a peak brightness temperature of 1.0×10^6 K. There was no detectable 20 cm circular polarization to a limit of 10% or less. A comparison with Kitt Peak and Mount Wilson magnetograms indicates that the extended 20 cm component lies along the magnetic neutral line in the western part of the active region. The weaker component lies $\sim 30''$ to the east of a pair of sunspots.

In contrast, the 2 cm map shows two compact ($\theta \approx 5''$), highly circularly polarized ($\rho_c = 80\%–90\%$) sources that vary on time scales of 30–60 minutes (Fig. 2). Comparisons with Mount Wilson magnetograms indicate that the two compact, variable sources appeared in regions of weak magnetic field with strengths $H \leq 80$ G, and that they did not overlie sunspots. The left circularly polarized sources (*solid contours*) varied in brightness temperature from $T_B = 2.0 \times 10^5$ K to $T_B \leq 0.5 \times 10^5$ K, while also moving systematically to the northwest with a total movement of $12''$ in 3 hr, or at a rate of ~ 0.8 km s^{-1} ($1'' = 725.3$ km on the Sun). The right circularly polarized source (*dashed contours*) ranged between 3.0 and 1.0×10^5 K.

Figure 3 shows 30 s snapshot maps of additional 2 cm compact sources with angular sizes $\theta \approx 4''$ and peak brightness temperatures of $T_B = 1.0–3.0 \times 10^5$ K. These sources are denoted by "A" and "B" in Figure 1. They also appeared in regions of weak magnetic field ($H \leq 80$ G) and did not overlie sunspots. An examination of 10 s snapshot maps indicates that sources A and B had respective lifetimes of 10 s and 20 s. The A source appeared at about 165740 UT and was unpolarized,

whereas the B source appeared at 173130 UT and had a dipolar structure. Source B suggests the emergence of a small dipolar loop with a lifetime of 20 s and a temperature characteristic of the transition region.

III. DISCUSSION

The high degree of circular polarization of the compact, transient 2 cm sources is somewhat enigmatic. This polarization cannot be accounted for by propagation effects (thermal bremsstrahlung) or gyroresonant absorption. The compact, transient 2 cm sources are in regions of weak magnetic field ($H \leq 80$ G) and do not overlie sunspots. The circular polarization of these sources cannot be explained by propagation effects of the thermal bremsstrahlung, for magnetic fields of $H \approx 2000$ G are required. Although gyroresonant absorption might account for the circular polarization, the weak magnetic field requires a very high harmonic of the gyrofrequency. The optical depth due to gyroresonant absorption is then negligibly small and the observed brightness temperatures $T_B \approx 10^5$ K cannot be accounted for by a plausible electron temperature. (The electron temperatures would be much too high.)

Conventional thermal radiation mechanisms like bremsstrahlung and gyroresonant, or cyclotron, radiation cannot explain the high circular polarization and high brightness temperature in the presence of weak photospheric magnetic fields. However, nonthermal gyrosynchrotron radiation might explain the observations. This mechanism has been invoked to explain 6 cm sources of high brightness temperature in regions of weak magnetic fields (Webb *et al.* 1983; Chiuderi Drago and Melozzi 1984), as well as a filament-associated source with a

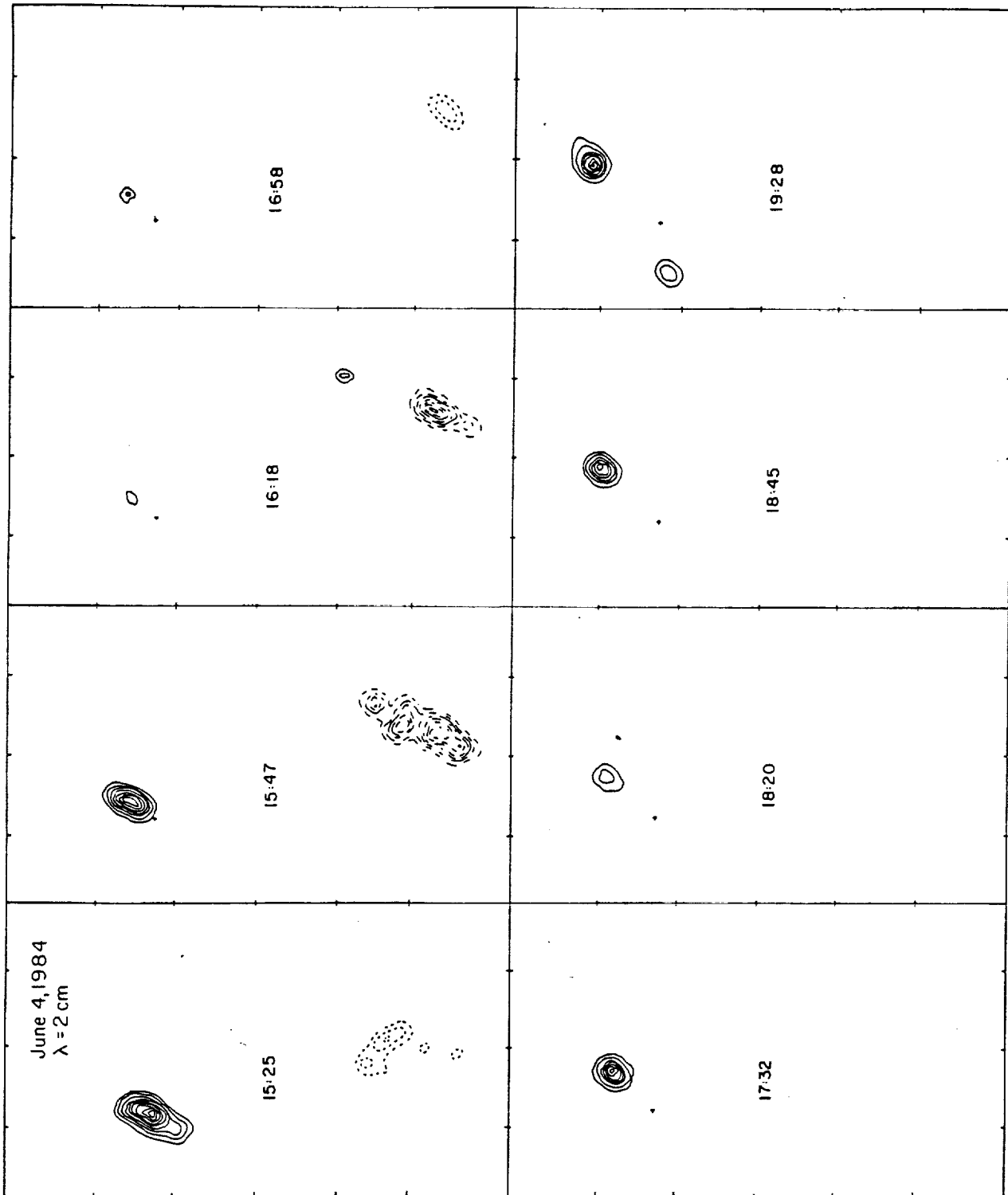


FIG. 2.—VLA synthesis maps of left circularly polarized (solid contours) and right circularly polarized (dashed contours) radiation at 2 cm wavelength. Each map begins at the UT time indicated. The map beginning at 1525 UT is for only 2 minutes of data, those beginning at 1618 and 1732 UT covered a 20 minute interval, and all of the other maps were for 15 minute intervals. The northern (top) source varied over time scales of 30 minutes, the southernmost (bottom) source had a lifetime of ~ 60 minutes, and the complex of sources just above the southernmost source lasted for ~ 30 minutes. Here the contours mark levels of equal brightness with an outermost contour of 6.1×10^4 K and a contour interval of 3.1×10^4 K. The fiducial marks on the axes are separated by $10''$.

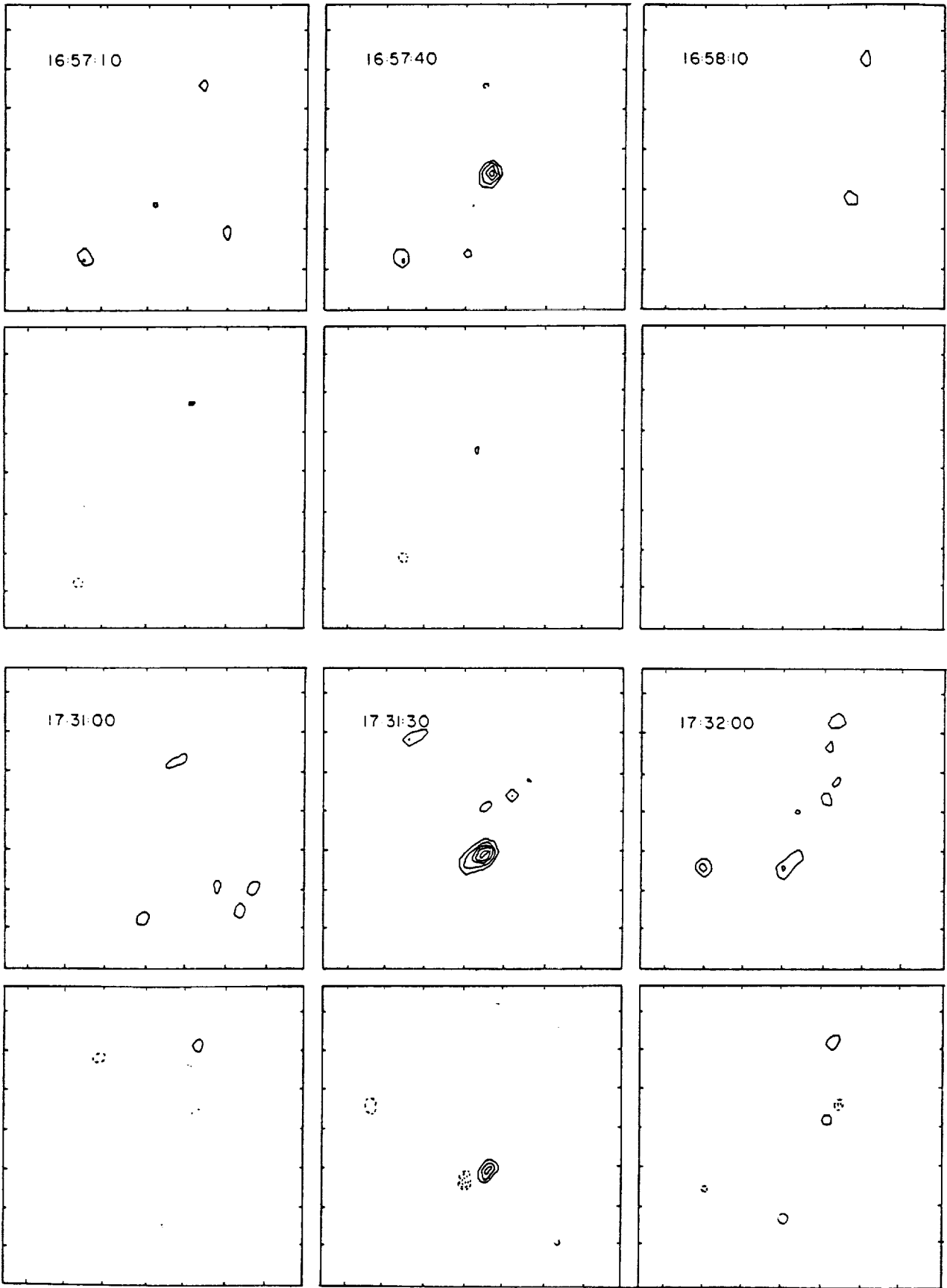


FIG. 3.—A series of 30 s snapshot maps of total intensity I (top) and circular polarization V (bottom). The maps reveal the presence of compact sources at 165740 and 173130 UT, respectively denoted by "A" and "B" in Fig. 1. An examination of 10 s snapshot maps indicates that compact sources A and B had respective lifetimes of 10 s and 20 s. Here the contour intervals mark levels of equal brightness temperature, and the fiducial marks on the axes are separated by $10''$. The outermost contour and the contour interval are 6.1×10^4 K and 3.1×10^4 K for the I maps and 1.5×10^4 K for the V maps. The solid and dashed contours of the V maps respectively refer to positive and negative values of V .

high brightness temperature and steep radiation spectrum (Akhmedov *et al.* 1986).

Simplified expressions for the gyrosynchrotron emission from mildly relativistic electrons with both a thermal (Maxwellian) and nonthermal (power-law) energy distribution have been given by Dulk and Marsh (1982). For nonthermal electrons with a power-law energy distribution of index δ , the degree of circular polarization, ρ_c , of the radiation and the effective temperature, T_{eff} , of the radiating electrons are given by

$$\rho_c = 0.20 \times 10^{0.5\delta} 10^{1.93 \cos \theta - 1.16 \cos^2 \theta} (v/v_H)^{-0.21 - 0.37 \sin \theta} \quad (1)$$

and

$$T_{\text{eff}} = 2.2 \times 10^9 10^{-0.31\delta} (\sin \theta)^{-0.36 - 0.06\delta} (v/v_H)^{0.50 + 0.085\delta}, \quad (2)$$

where θ is the angle between the line of sight and the direction of the magnetic field, the observing frequency is ν and the gyrofrequency $\nu_H = 2.8 \times 10^6$ Hz. For an observing frequency of $\nu = 15.0 \times 10^9$ Hz and a magnetic field strength of $H = 50$ G, we have $\nu/\nu_H = 107.1$, and for $\theta = 20^\circ$ – 40° we obtain:

$$\rho_c = 22\% - 36\%$$

and

$$T_{\text{eff}} = 1.1 \times 10^{10} \text{ K to } 1.5 \times 10^{10} \text{ K}$$

for an energy spectral index of $\delta = 3$.

The high effective temperatures permit brightness temperatures $T_B \approx 10^5$ K under the optically thin conditions (optical depth $\tau \ll 1$) that occur when one is observing at such high harmonics, n , of the gyrofrequency. (For our case, $\nu = n\nu_H = 2.8 \times 10^6 n$ Hz so that $n = 107$.) In contrast, the effective temperature of thermal electrons is equal to the kinetic temperature of 10^5 – 10^6 K, and the expected brightness temperatures are very much lower than those observed. For nonthermal electrons of density N_{nt} above some cutoff energy E_0 , we have

$$T_B = \tau T_{\text{eff}} = H L N_{nt} \frac{c^2}{k\nu^2} \times \left(\frac{\eta_\nu}{H N_{nt}} \right), \quad (3)$$

where E_0 is assumed to be $E_0 = 10$ keV = 1.6×10^{-8} ergs, and

$$\frac{\eta_\nu}{H N_{nt}} = 3.3 \times 10^{-24} 10^{-0.52\delta} (\sin \theta)^{-0.43 + 0.65\delta} \times (v/v_H)^{1.22 - 0.90\delta}. \quad (4)$$

If the magnetic field strength $H = 50$ G and the dimension along the line of sight is $L = 10^9$ cm, then a nonthermal electron density of $N_{nt} = 5 \times 10^6 \text{ cm}^{-3}$ give

$$\tau = 8.6 \times 10^{-6} \text{ to } 3.0 \times 10^{-5}$$

and

$$T_B = 1.2 \times 10^5 \text{ K to } 3.3 \times 10^5 \text{ K}.$$

These brightness temperatures are comparable to those observed.

The absence of nonthermal gyrosynchrotron radiation at 20 cm wavelength can be explained by the large optical depth in the overlying corona. With an electron temperature of $T_e = 10^6$ K and an electron density of $N_e = 5 \times 10^9 \text{ cm}^{-3}$, the optical depth due to thermal bremsstrahlung at 20 cm is $\tau = 20$. In this case, the nonthermal gyrosynchrotron radiation would be completely absorbed at 20 cm. Because the optical depth scales as the square of the wavelength, the corona would be optically thin at 2 cm wavelength.

Because the compact 2 cm sources are transient with lifetimes as short as 10 s, continual acceleration of the electrons is not required. The energy loss by synchrotron radiation with a power-law electron energy distribution has a half-life, T , for the total emitted radiation given by

$$T \approx \frac{10^8}{H^2} \text{ s}. \quad (5)$$

A magnetic field of strength $H = 50$ G, gives $T \approx 4 \times 10^4$ s or ~ 11 hr. But how are the electrons initially accelerated? Spicer (1979) and Shoub (1983) showed that large electric fields can be produced in the transition region as a result of the steep temperature gradient there. One possibility is that the electric fields become unstable and generate numerous nonthermal electrons. Spicer's calculations indicate that the number density of nonthermal electrons is $N_{nt} = 5 \times 10^6 \text{ cm}^{-3}$ for a thermal electron density of $N_e = 3 \times 10^9 \text{ cm}^{-3}$. This is consistent with the number of nonthermal electrons required to account for the compact, transient 2 cm sources.

But what causes the variability of the observed emission? According to equation (3), the observed brightness temperature decreases with decreasing magnetic field strength and decreasing nonthermal electron density. We have observed an apparent emergence and disappearance of a dipolar magnetic field in one case. A plausible explanation for the source variability is therefore variations in the magnetic fields. Alternatively, the variability might be attributed to a variable nonthermal electron density, perhaps resulting from a variable acceleration mechanism.

Yet another possibility is that currents amplify the magnetic fields, leading to magnetic field strengths of $H \approx 2000$ G in the transition region that are apparently not observed by photospheric magnetograms.

Radio astronomical studies of the Sun at Tufts University are supported under grant AFOSR-83-0019 with the Air Force Office of Scientific Research (AFOSR) and contract N0014-86-K-0068 with the Office of Naval Research (ONR). Comparisons of VLA and *Solar Maximum Mission (SMM)* data are supported by our NASA-SMM Guest Investigator grant NAG 5-501.

REFERENCES

- Akhmedov, Sh. B., *et al.* 1986, *Ap. J.*, **301**, 760.
 Chiuderi Drago, F., and Mellozzi, M. 1984, *Astr. Ap.*, **131**, 103.
 Dulk, G. A., and Marsh, K. A. 1982, *Ap. J.*, **259**, 350.
 Kundu, M. R., and Lang, K. R. 1985, *Science*, **228**, 9.
 Lang, K. R., and Willson, R. F. 1983, *Adv. Space Res.*, Vol. 2, No. 11, ed. Z. Svestka, D. M. Rust, and M. Dryer (Oxford: Pergamon), p. 91.
 Lang, K. R., Willson, R. F., and Gaizauskas, V. 1983, *Ap. J.*, **267**, 455.
 Rosner, R., Tucker, W. H., and Vaiana, G. S. 1978, *Ap. J.*, **283**, 413.
 Shevgaonkar, R. K., and Kundu, M. R. 1984, *Ap. J.*, **283**, 413.
 Shoub, E. C. 1983, *Ap. J.*, **266**, 339.
 Spicer, D. S. 1979, *Solar Phys.*, **62**, 295.
 Webb, D. F., Davis, J. M., Kundu, M. R., and Velusamy, T. 1983, *Solar Phys.*, **85**, 267.

KENNETH R. LANG and ROBERT F. WILLSON: Department of Physics and Astronomy, Robinson Hall, Tufts University, Medford, MA 02155

NASA Conference Publication 2442

Coronal and Prominence Plasmas

Edited by
A. I. Poland
NASA Goddard Space Flight Center
Greenbelt, Maryland

Proceedings of Workshops
Held at Goddard Space Flight Center
April 9-11, 1985
April 8-10, 1986

NASA

National Aeronautics
and Space Administration

Scientific and Technical
Information Branch

1986

E. CORONAL FLASMAS ON THE SUN AND NEARBY STARS

KENNETH R. LANG

Department of Physics and Astronomy
Tufts University
Medford, MA 02155

INTRODUCTION

The Very Large Array (VLA) has been used to observe solar microwave sources with second-of-arc angular resolution. Both the quiescent, or non-flaring, microwave sources and the flaring ones are usually resolved. They are often associated with the apex and/or legs of the ubiquitous coronal loops, which heretofore have been observable only with X-ray telescopes sent above the atmosphere. Multiple-wavelength VLA observations can specify the strength, evolution and structure of the magnetic fields in coronal loops, while also providing constraints on the electron density and electron temperature of the plasma trapped within the coronal loops.

VLA observations are providing new insights to the preburst heating and magnetic interaction that precede eruptions from solar active regions [Lang and Willson, (1983, 1984)]; but these interesting studies are not discussed here [see Kundu and Lang (1985) for a review]. We instead summarize our current understanding of the quiescent, or non-flaring, microwave emission from solar active regions. The next section briefly reviews the thermal radiation mechanisms that account for most of the quiescent emission, while also pointing out that current-amplified magnetic fields or non-thermal radiation may be required in some instances. This is followed by a discussion of the 20 cm radiation of coronal loops and the thermal cyclotron lines that accurately specify their magnetic field strength. The 20 cm and X-ray emission of the coronal plasma are then compared. We next discuss the coronae of nearby stars, where coherent radiation processes seem to prevail, and then conclude our summary with promising research opportunities for the future.

THERMAL RADIATION, CURRENTS AND NON-THERMAL RADIATION

The quiescent microwave emission of solar active regions has been attributed to the thermal radiation of hot electrons trapped within the strong magnetic fields of coronal loops. The microwave brightness temperature is then on the order of the million-degree electron temperature, and either thermal bremsstrahlung or thermal gyroresonant radiation dominate the emission. Bremsstrahlung, or braking radiation, is emitted when the thermal electrons are accelerated in the electric fields of ions and gyroresonant radiation is emitted when the thermal electrons are accelerated by magnetic fields.

Strong evidence for gyroresonant radiation at coronal levels above sunspots was provided by a comparison of microwave, EUV and X-ray observations [Kundu, Schmahl and Gerassimenko (1980); Pallavicini, Sakurai and Vaiana (1981)]. The near equality of the microwave brightness and electron temperatures indicated that the microwave emission was thermal, but the absence of detectable X-ray radiation above sunspots indicated a relatively low electron density there. This meant that the high microwave brightness temperature above sunspots could not be due to bremsstrahlung, but it could be explained by thermal gyroresonant radiation at the second or third harmonic of the gyrofrequency.

Thermal gyroradiation at coronal levels above sunspots was fully confirmed by the detection of circularly polarized ring-shaped or horseshoe structures [Allisandrakis and Kundu (1982); Lang and Willson (1982)] that were predicted using the theory of gyroresonant radiation in the curved magnetic fields above individual sunspots [Gel'freikh and Lubyshev(1979)]. These structures were observed at 6 cm wavelength where circular polarizations as high as 100% were detected. Bright sunspot-associated sources observed at 2 to 6 centimeters wavelength are now widely believed to be due to the gyroradiation of million-degree electrons spiralling about strong magnetic fields above sunspots.

But there is another class of compact, bright microwave sources in this wavelength range that are not associated with sunspots. They occur above regions of apparently-weak photospheric magnetic fields. For instance observations at 6 cm wavelength revealed sources with coronal brightness temperatures $T_B > 10^6$ K in regions away from sunspots [Schmahl et al. (1982); Webb, Davis, Kundu and Velusamy (1983)]. Force-free (potential) magnetic field extrapolations from the known photospheric values indicate that the magnetic field in the low solar corona is too weak to account for the observed emission by gyroradiation.

The situation is even worse at shorter wavelengths where stronger magnetic fields are required to produce gyroradiation at the first few harmonics of the gyrofrequency. (Higher harmonics produce insufficient optical depth to account for the high brightness temperatures.) Lang and Willson (1986a-this proceedings) and Willson and Lang (1986) report the presence of compact, bright 2-cm sources that require magnetic field strengths of $H \approx 2,000$ G in the low solar corona at regions away from sunspots if they are attributed to gyroresonance radiation.

Bright microwave sources in regions of apparently-weak photospheric fields can be explained by two different hypotheses. First, the emission could be thermal gyroradiation at the second or third harmonic of the gyrofrequency in strong magnetic fields. Currents might amplify the magnetic field in the low corona to values greater than those expected from extrapolations from the photosphere. Alternatively the photospheric magnetograms could be misleading, and strong magnetic fields could exist in isolated regions away from sunspots. Secondly, the emission could be nonthermal radiation in weak magnetic fields. Nonthermal synchrotron radiation from mildly relativistic electrons is one possibility, but some as yet unspecified mechanism must be continuously accelerating the electrons [Akhmedov et al. (1986), Chiuderi-Drago and Melozzi (1984); Willson and Lang (1986)].

Figure 1 provides the radiation spectra for the three types of sources usually detected at short centimeter wavelengths [see Akmedov et al. (1986) for greater details]. The most common type of source is the sunspot-associated component (A and C) that is attributed to thermal gyroresonance radiation in the legs of coronal loops that are connected to the underlying sunspots. Source D is a filament-associated component located above a magnetic neutral line in regions of apparently-weak magnetic field. Yet, this source has a steep radiation spectrum and high brightness temperature of $T_B > 7 \times 10^6$ K. It may be attributed to non-thermal radiation or to thermal gyroradiation in current-amplified magnetic fields. Then there is the filament-associated source B that has the flat spectrum of optically-thin thermal bremsstrahlung. Electron densities $N_e = 10^9$ to 10^{10} cm^{-3} are consistent with this interpretation, suggesting that in this case we are detecting the same thermal plasma that is observed at X-ray wavelengths from coronal loops. But this plasma is more commonly detected at the longer radio wavelength of 20 centimeters.

Individual cyclotron lines from AR 4398 are shown in Figure 3 together with the flat spectrum of the nearby active region AR 4399. The flat spectrum of AR 4399 is attributed to thermal bremsstrahlung, whereas the spectrum of AR 4398 can be explained by cyclotron line emission from a narrow layer of width $\Delta L = 10^8$ cm, electron density $N_e = 10^9$ cm⁻³ and a relatively high electron temperature $T_e = 4 \times 10^6$ K (solid line). Here the harmonic number $n = 4$ and the magnetic field strength $H = 145$ G. A key aspect of this discovery is the extraordinary precision in measuring the magnetic field strength; a change of only $\Delta H = 20$ G shifts the central frequency of the line by 170 MHz.

COMPARISON OF THE 20 CM AND X-RAY EMISSION

As previously mentioned, comparisons between the X-ray and short microwave (3 to 6 cm) radiation from solar active regions provided evidence for a new source of opacity at microwave wavelengths above sunspots. It has been attributed to gyroresonance effects in the legs of coronal loops connecting with underlying sunspots. Recent comparisons of the 6 cm radiation from the apex of coronal loops indicates that its brightness temperature is less than the electron temperature measured at X-ray wavelengths; this has been explained by a cool ($\approx 10^5$ K) external plasma [Holman (1986 - this proceedings); Webb, Holman, Davis and Kundu (1986)].

However, there have been no published comparisons of X-ray data with the 20 cm emission of the coronal plasma. In some instances, there is radiation at 20 centimeters wavelength near sunspots where no X-ray radiation is detected. The radio emission may be attributed to gyroresonant radiation of a low density plasma in magnetic fields of strength $H = 145$ to 290 G (harmonic $n = 4$ to 2), [see Lang, Willson, Strong and Smith (1986a) for greater details].

In other cases, the 20 centimeter radiation appears at the apex of coronal loops, but with a slightly lower brightness temperature, $T_B = 1.4$ to 1.7×10^6 K, than the electron temperature, $T_e = 3.0 \times 10^6$ K, inferred from the X-ray data. This may be explained by a low temperature plasma with $T_e = 10^5$ K that lowers the effective brightness temperature of the radio bremsstrahlung while not affecting the X-ray data that only detects the 10^6 K plasma [see Holman (1986 - this proceedings); Lang (1986 - this proceedings); and Lang, Willson, Strong and Smith (1986a) for greater details]. Because the line of sight through the low temperature plasma is greatest along the legs of coronal loops, it can reduce the size of the radio source below that of the X-ray emission. That is, the low temperature plasma can, under the right circumstances, confine the detectable radio radiation to the apex of coronal loops.

As illustrated in Figure 4, there are other instances in which the 20-cm radiation and the soft X-ray emission have the same angular extent. In this case, the maximum brightness temperature of the radio emission has the same value as the electron temperature, $T_e = 3 \times 10^6$ K, inferred from the X-ray data. At first sight it would seem that the 20-cm emission is the thermal bremsstrahlung of the X-ray emitting plasma (electron density $N_e = 2 \times 10^{10}$ cm⁻³), but in this instance we have also detected a cyclotron line. Preliminary modeling indicates a thin layer of $T_e = 4 \times 10^6$ K with a magnetic field strength of $H = 145$ or 187 G (harmonic $n = 4$ or 3). The thermal electrons that give rise to the X-ray radiation therefore also seem to produce strong gyroresonant radiation at 20 centimeters wavelength.

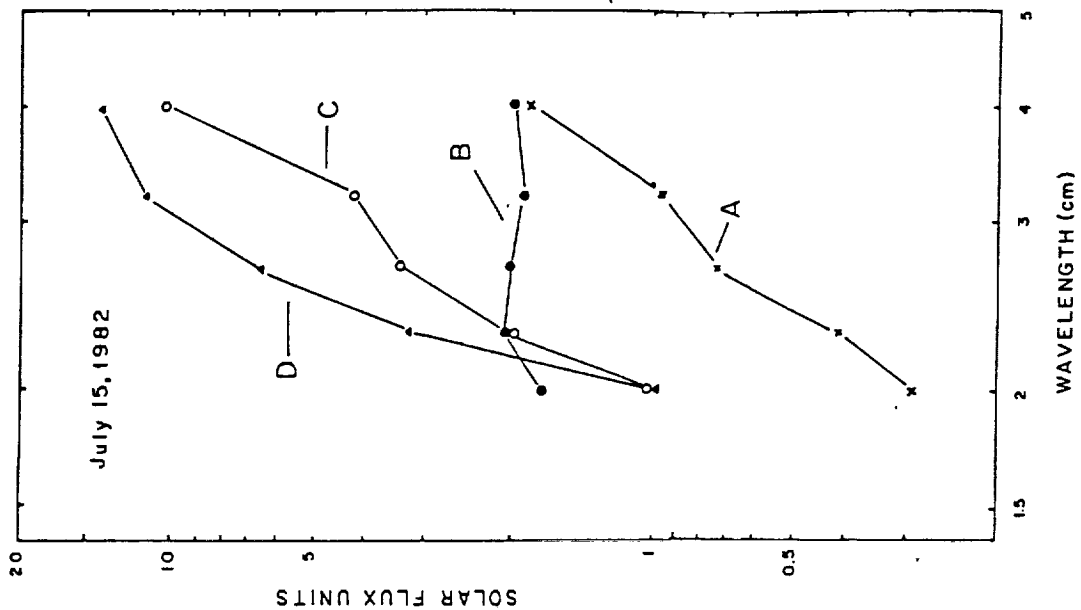


Figure 1. The radiation spectra of four sources associated with an active region. The steep spectrum of the filament-associated source D is attributed to the gyrosynchrotron radiation of mildly relativistic electrons whereas the flat spectrum of the source B is attributed to thermal bremsstrahlung. The sunspot-associated sources A and C are attributed to gyroresonance emission in the legs of coronal loops.

CORONAL LOOPS AT 20 CM WAVELENGTH AND THERMAL CYCLOTRON LINES

Radiation from a post-flare loop at 20 centimeters wavelength was reported by Velusamy and Kundu (1981); but there is a much more extensive literature regarding the quiescent 20-cm radiation of coronal loops [Lang, Willson and Rayrole (1982); Lang, Willson and Gaizauskas (1983); McConnell and Kundu (1983); Shevgaonkar and Kundu (1984); Kundu and Lang (1985); Kundu (1986 - this proceedings); Lang (1986 - this proceedings)]. The radiation at this longer wavelength often comes from the hot, dense plasma trapped within the coronal loop (see Figure 2 for a typical example). The 20-cm coronal loops have peak brightness temperatures of 1×10^6 to 4×10^6 K and extents of about 10^{10} cm. Their radio emission can be attributed to thermal bremsstrahlung or thermal gyroresonant radiation, or both.

Of special interest is the recent detection of thermal cyclotron lines near the apex of coronal loops at wavelengths near 20 centimeters [see Figure 3 and Willson (1985) for greater details]. These cyclotron lines are emitted at harmonics of the gyrofrequency, with a wavelength that depends only on the harmonic number and the magnetic field strength. However, because the magnetic field in the legs of coronal loops decrease uniformly with height, the individual cyclotron lines at short wavelengths will usually merge into a smooth continuum.

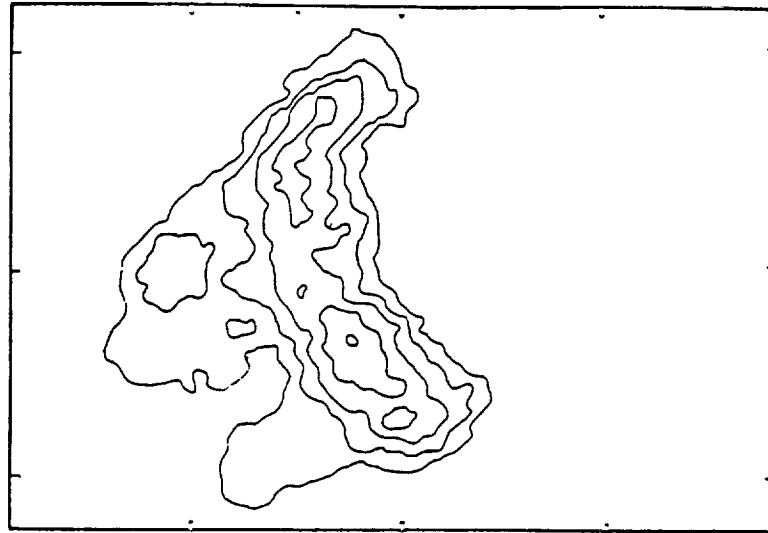


Figure 2. A typical radio wavelength (20 cm) V.L.A. map of the hot, million-degree plasma trapped in a coronal loop. The angular scale between fiducial marks on the axes is 60 arc-seconds.

At 20 centimeters wavelength we can observe the apex of coronal loops where the magnetic field is nearly constant and the spectrum of individual cyclotron lines can be resolved. This will be particularly true if currents or some other process confine the intense emission to a thin, hot layer within the loop apex.

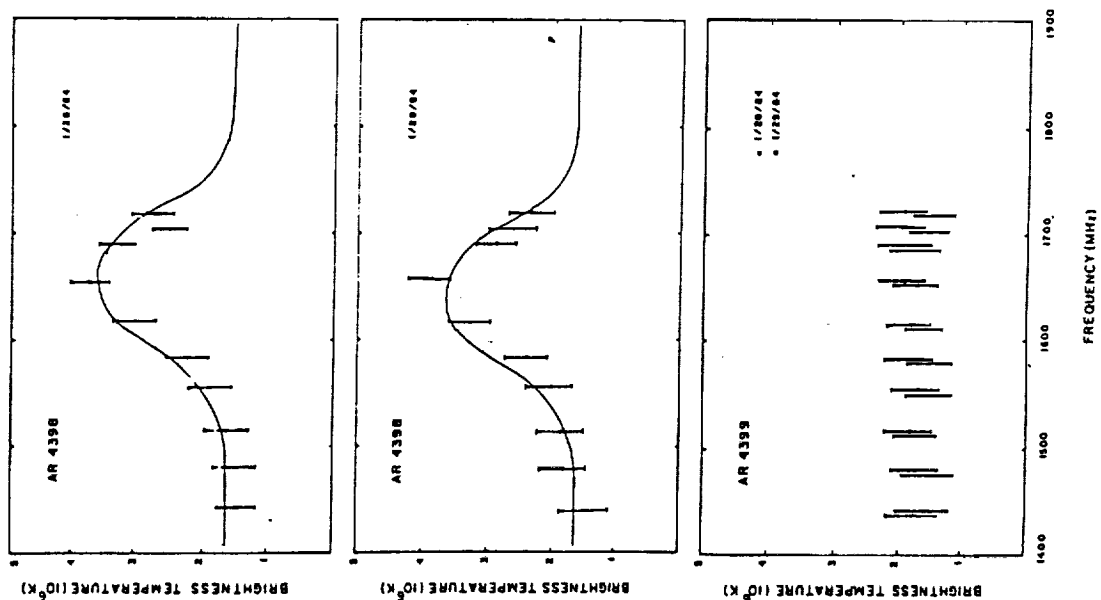


Figure 3. VLA data at ten closely-spaced frequencies near 1446 MHz (20 cm) showing thermal cyclotron line spectra from active region AR 4398 on successive days, together with optically-thick thermal bremsstrahlung spectra from active region AR 4399 on the same days.

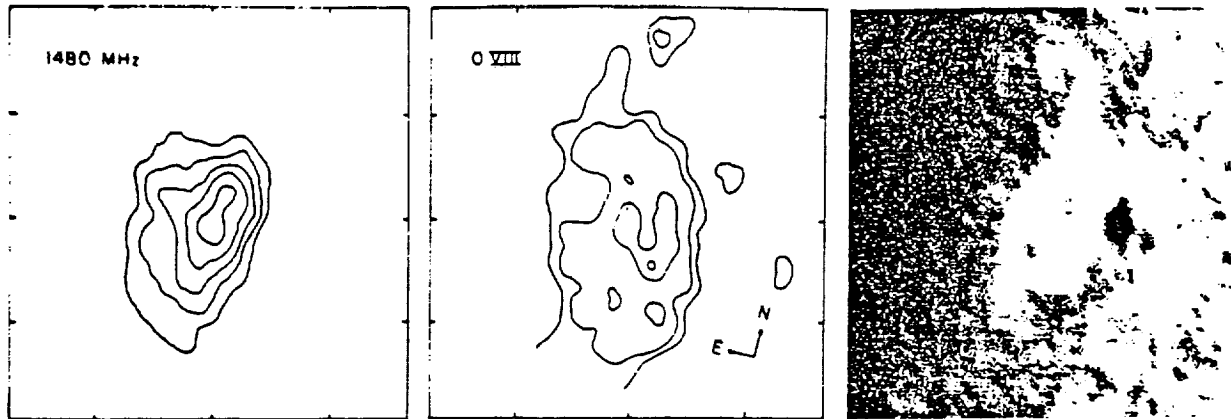


Figure 4. A comparison of the 20 cm emission (V.L.A.-left), soft-X-ray (S.M.M.-middle) and H α (SOON-right) emission of an active region on the same day. The angular spacing between fiducial marks on the axis is 60 arc-seconds.

CORONAE OF NEARBY STARS

Nearby dwarf M stars exhibit slowly-varying, quiescent microwave radiation and microwave bursts that have been detected with the Very Large Array (VLA) and the Arecibo Observatory. Observations with high resolution in frequency and time provide strong evidence for coherent radiation mechanisms in the coronae of these stars [Lang (1986b)]. Such mechanisms provide stringent constraints on the electron density and magnetic field strength in the stellar coronae.

Narrow-band, slowly varying radiation has been detected from the dwarf M star YZ Canis Minoris when using the VLA at wavelengths near 20 centimeters [Lang and Willson (1986b)]. White, Kundu and Jackson (1986) subsequently repeated this experiment, finding narrow-band bursts from the dwarf M stars AD Leonis and UV Ceti. The narrow-band structure cannot be explained by continuum emission processes such as thermal bremsstrahlung, thermal gyroresonant radiation or nonthermal gyrosynchrotron radiation. Although gyroresonant radiation can give rise to narrow-band cyclotron lines, it requires an implausibly large source that is hundreds of times larger than the star. The observations of narrow-band structure can apparently only be explained by coherent mechanisms like electron-cyclotron lines or coherent plasma radiation.

Independent evidence for coherent radiation mechanisms is provided by high-time-resolution observations of the dwarf M star AD Leonis at the Arecibo Observatory [Lang, Bookbinder and Golub (1983), Lang and Willson (1986c)]. As illustrated in Figure 5, quasi-periodic, highly polarized spikes are observed at 20 centimeters wavelength with rise times of less than 5 milliseconds. An upper limit to the linear size of the spike emitting region is $L < 1.5 \times 10^8$ cm, the distance

that light travels in 5 milliseconds. This size is only five hundredths of the estimated radius of AD Leonis. Provided that the emitter is symmetric, it has a brightness temperature greater than 10^{16} K. The high degrees of circular

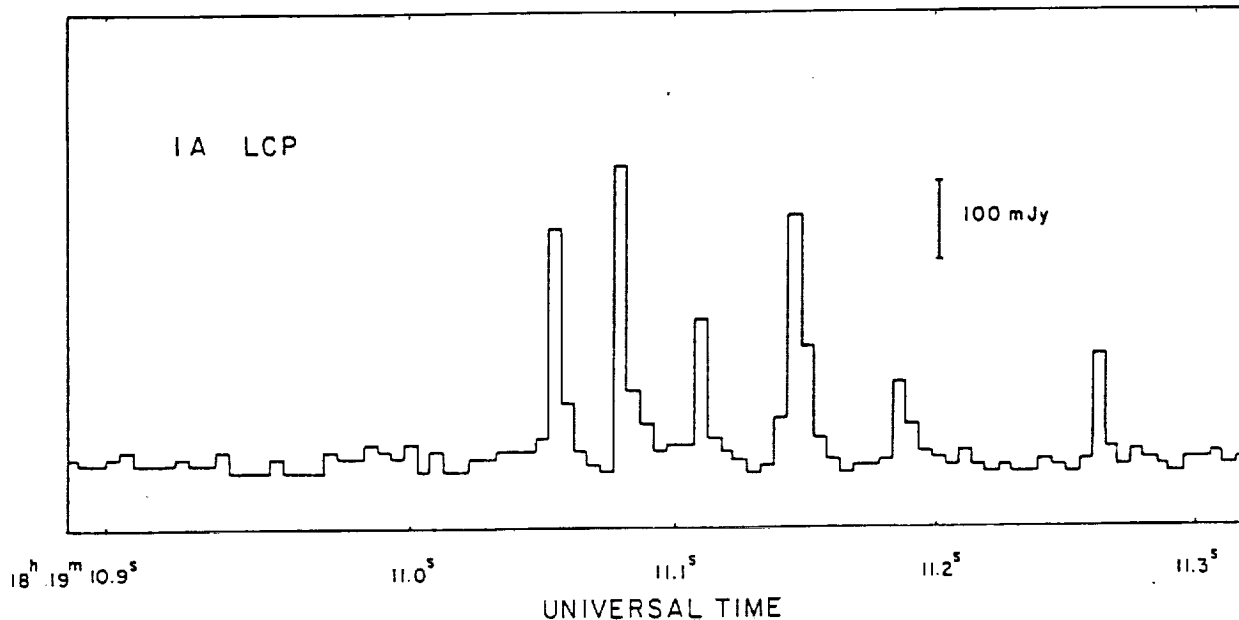


Figure 5. The total power detected at a frequency of 1415 MHz (21.2 cm) while tracking the dwarf M star AD Leonis. The left-hand circularly polarized (LCP) signal has been displayed with a 5 ms integration time. There are five quasi-periodic spikes with a mean periodicity of $T_p = 32 \pm 5$ ms and a total duration of $\tau_D = 150$ ms. Each of these spikes had a rise time of $\tau_R < 5$ ms, leading to an upper limit to the linear size $L < 1.5 \times 10^8$ cm for the spike emitter. A symmetric source of this size would have a brightness temperature of $T_B > 10^{16}$ K, requiring a coherent radiation mechanism.

polarization (up to 100%) indicate an intimate connection with the star's magnetic field, and the high brightness temperatures suggest a coherent radiation mechanism such as an electron-cyclotron maser or coherent plasma radiation.

The coherent process provides constraints on the electron density, N_e , and the magnetic field strength, H , in the stellar coronae [see Dulk (1985) for the relevant formulae]. If the electron-cyclotron maser emits at the second harmonic of the gyrofrequency, the longitudinal magnetic field strength $H = 250$ G and constraints on the plasma frequency imply an electron density of $N_e = 6 \times 10^9$ cm^{-3} . Coherent plasma radiation at the first or second harmonic of the plasma frequency respectively require $N_e = 2 \times 10^{10}$ cm^{-3} and $H \ll 500$ G or $N_e = 6 \times 10^9$ cm^{-3} and $H \ll 250$ G.

PROMISING DIRECTIONS FOR THE FUTURE

Future VLA observations at 20 centimeters wavelength will continue to provide diagnostic tools for the solar corona. Observations of thermal cyclotron lines offer a promising method of accurately determining the coronal magnetic field strength. Comparisons with soft X-ray spectral lines will help delineate the

electron density and temperature, while also specifying the radiation mechanisms. One promising approach that grew out of this conference involves simultaneous observations with the VLA and the Owens Valley Radio Observatory (OVRO). The OVRO will provide spectral information that is not obtainable with the VLA, whereas the high angular resolution of the VLA will remove ambiguities in the OVRO data. Future collaborations between the Tufts University group and the Observatoire de Paris - Nancay Radio Heliograph will provide new perspectives to coherent radiation processes on the Sun. The rapidly growing studies of the microwave radiation from dwarf M and RS CVn stars will continue to provide new insights to physical processes in stellar coronae. The full potential of these studies of the Sun and nearby stars will only be realized by the development of a solar-stellar synthesis radiotelescope. Such an instrument would be dedicated to solar and stellar observations with high angular, temporal and frequency resolution.

ACKNOWLEDGEMENTS

Radio astronomical studies of the Sun at Tufts University are supported under Air Force of Scientific Research grant AFOSR-83-0019 and contract N0014-86-K-0068 with the Office of Naval Research. Simultaneous VLA and Solar Maximum Mission observations of the Sun are supported by NASA grant NAG 5-501.

REFERENCES

- Akhmedov, S.B., et al., 1986, "Structure of a Solar Active Region from RATAN 600 and Very Large Array Observations," *Astrophys. J.*, 301, 460-464.
- Alissandrakis, C.E. and M.R. Kundu, 1982, "Observations of Ring Structure in a Sunspot Associated Source at 6 centimeter Wavelength", *Astrophys. J. (Letters)*, 253, L49-L52.
- Chiuderi-Drago, F. and M. Melozzi, 1984, "Non-Thermal Radio Sources in Solar Active Regions," *Astrophys. J.* 131, 103-110.
- Dulk, G.A., 1985 "Radio Emission from the Sun and Stars," *Ann. Rev. Astron. Ap.*, 23 169-180
- Dulk, G.A. and D.E. Gary, 1983, "The Sun at 1.4 GHz: Intensity and Polarization," *Astron. Astrophys.*, 124, 103-107
- Gel'frikh, G.B. and B.I. Lubyshev, 1979, "Structure of Local Sources of the S Component of Solar Radio Emission " *Sov. Astron. A.J.*, 23, 316.
- Holman, G.D., 1986, "Determining Magnetic and Plasma Structure of Coronal Loops from Microwave and Soft X-ray Observations",: this Proceedings.
- Kundu, M.R., 1986, "Three Dimensional Structure of Solar Active Regions," this Proceedings.
- Kundu, M.R. and K.R. Lang, 1985, "The Sun and Nearby Stars," *Science*, 228, 9-15.
- Kundu, M.R., E.J. Schmahl and M. Gerassimenko, 1980, "Microwave, EUV and X-ray Observations of Active Region Loops: Evidence for Gyroresonance Absorption in the Corona," *Astron. Astrophys.* 82, 265-271.
- Kundu, M.R. and T. Velusamy, 1980; " Observation with the VLA of a Stationary Loop Structure in the Sun at 6 cm Wavelength," *Astrophys. J. (Letters)*, 240, L62-L65.
- Lang, K.R., 1986a, "Coronal Diagnostics "-this Proceedings.
- Lang, K.R., 1986b, "Flare Stars and Solar Bursts: High Resolution in Time and Frequency," *Solar Phys.*, in press.
- Lang, K.R., J. Bookbinder, L. Golub and M. Davis, 1983, "Bright, Rapid, Highly Polarized Radio Spikes from the Dwarf AD Leo," *Astrophys. J. (Letters)*, 272, L15-L18.

- Lang, K.R. and R.F. Willson, 1982, "Polarized Horseshoes Around Sunspots at 6 Centimeter Wavelength.", *Astrophys. J. (Letters)*, 255 L111-L117.
- Lang, K.R. and R.F. Willson, 1983, "Multiple Wavelength Observations of Flaring Active Regions," *Adv.Space Res.* 2, No. 11, 91-100.
- Lang, K.R. and R.F. Willson, 1984, "V.L.A. Observations of Flare Build-Up in Coronal Loops," *Adv. Space Res.* 4, no. 7, 105-110.
- Lang, K.R. and R.F. Willson, 1986a, "Compact, Variable, Moving Sources on the Sun at 2 Centimeters Wavelength," *this Proceedings*.
- Lang, K.R. and R.F. Willson, 1986b, "Narrow-Band, Slowly Varying Decimetric Radiation from the Dwarf M Flare Star YZ Canis Minoris," *Astrophys. J. (Letters)*, 302, L17-L21.
- Lang, K.R. and R.F. Willson, 1986c, "Millisecond Radio Spikes from the Dwarf M Flare Star AD Leonis," *Astrophys. J.*, in press.
- Lang, K.R., R.F. Willson and V. Gaizauskas, 1983, "Very Large Array Observations of Solar Active Regions III. Multiple Wavelengths Observations," *Astrophys. J.* 267, 455-464.
- Lang, K.R., R.F. Willson and J. Rayrole, 1982, "Very Large Array Observations of Coronal Loops at 20 Centimeter Wavelength," *Astrophys. J.*, 258, 384-387.
- Lang, K.R., R.F. Willson, K.T. Strong and K.L. Smith, 1986a, "Simultaneous Solar Maximum Mission and Very Large Array Observations of Solar Active Regions", *Astrophys. J.*, to be submitted.
- Lang, K.R., R.F. Willson, K.T. Strong and K.L. Smith, 1986b, "Physical Parameters of Solar Active Regions Inferred from Thermal Cyclotron Lines and Soft X-ray Spectral Lines, *Astrophys. J.*, to be submitted.
- McConnell, D. and M.R. Kundu, 1983, "VLA Observations of a Solar Active Region and Coronal Loops," *Astrophys. J.*, 269, 698-705.
- Schmahl, E.J., et al., 1982, "Active Region Magnetic Fields Inferred from Simultaneous VLA Microwave Maps, X-ray Spectroheliograms, and Magnetograms", *Solar Phys.* 80, 233-249.
- Shevgaonkar, R.K. and M.R. Kundu, 1984, "Three-Dimensional Structures of Two Solar Active Regions from VLA Observations at 2, 6 and 20 Centimeter Wavelengths," *Astrophys. J.*, 283, 413-420.
- Strong, K.T., C.E. Alissandrakis and M.R. Kundu, 1984, "Interpretation of Microwave Active Region Structures Using SMM Soft X-ray Observations," *Astrophys. J.* 277, 865-873.
- Velusamy, T. and M.R. Kundu, 1981, "VLA Observations of Postflare Loops at 20 Centimeter Wavelength," *Astrophys. J. (Letters)*, 243, L103-L107.
- Webb, D.M. J.M. Davis, M.R. Kundu and T. Velusamy, 1983, "X-ray and Microwave Observations of Active Regions," *Solar Phys.* 85, 267-283.
- Webb, D.F., G.D. Holman, J.M. Davis and M.R. Kundu, 1986, "High-Spatial-Resolution Microwave and Soft X-ray Observations as Diagnostics of Solar Magnetic Loops", *Astrophys. J.*, submitted
- White, S.M., M.R. Kundu and P.D. Jackson, 1986, "Narrowband Radio Flares from Red Dwarf Stars," *Astrophys. J.*, submitted.
- Willson, R.F., 1985, "VLA Observations of Solar Active Regions at Closely Spaced Frequencies: Evidence for Thermal Cyclotron Line Emission," *Astrophys. J.*, 298, 911-917.
- Willson, R.F. and K.R. Lang, 1986, "VLA Observations of Compact, Variable Sources on the Sun," *Astrophys. J.*, in press.

F. CORONAL DIAGNOSTICS

KENNETH R. LANG

Department of Physics and Astronomy
Tufts University
Medford, MA 02155

INTRODUCTION

The relatively recent development of satellite-borne X-ray telescopes and ground-based aperture synthesis radio telescopes has led to an examination of the solar corona with unprecedented resolution in space, time and frequency. The high spatial and spectral resolution of the X-ray instruments aboard Skylab and the Solar Maximum Mission (SMM) satellite have, for instance, showed that coronal loops dominate the structure of the Sun's lower corona [see Vaiana and Rosner (1978) for a review]. Strong magnetic fields hold a hot, dense plasma within the ubiquitous coronal loops.

Observations of soft X-ray spectral lines indicate that the quiescent, or non-flaring, coronal loops have electron temperatures $T_e \sim 2$ to 4×10^6 K and electron densities $N_e \sim 10^9$ to 10^{11} cm⁻³ with total extents $L \sim 10^9$ to 10^{10} cm. Similar temperatures are inferred from radio-wavelength brightness temperatures that are comparable to the local electron temperatures.

The detailed temperature and magnetic structure of the quiescent, or non-flaring, coronal loops has been inferred from radio wavelength synthesis observations. Synthesis maps describe the two-dimensional distribution of source brightness and the two-dimensional structure of the magnetic field [see Kundu and Lang (1985) for a review]. The unique ability to specify the strength and structure of the coronal magnetic fields is an important aspect of the radio wavelength synthesis maps.

Our current understanding of coronal loops is summarized in this chapter. It includes observations from ground-based radio telescopes and from X-ray telescopes lofted above the atmosphere, as well as theoretical interpretations of these observations.

The remaining sections of this introductory overview highlight both the observational and theoretical results that are discussed in greater detail in the following papers. We begin by discussing the three-dimensional structure of coronal loops. Alternative radiation mechanisms are then described within the context of both the radio and X-ray emission. Various methods of determining the strength and structure of the coronal magnetic field are then described. The final sections of

NASA Conference Publication 2442

Coronal and Prominence Plasmas

Edited by
A. I. Poland
NASA Goddard Space Flight Center
Greenbelt, Maryland

Proceedings of Workshops
Held at Goddard Space Flight Center
April 9-11, 1985
April 8-10, 1986

NASA

National Aeronautics
and Space Administration

Scientific and Technical
Information Branch

1986

this introduction include the coronae of nearby stars and future prospects for radio diagnostics of coronal loops.

THREE DIMENSIONAL STRUCTURE OF CORONAL LOOPS

Observations at different radio wavelengths generally sample different levels within coronal loops, with longer wavelengths referring to higher levels. The heights of the radio structures can be inferred from their angular displacements from underlying photospheric features, and the two-dimensional maps at different radio wavelengths can be combined to specify the three-dimensional structure of coronal loops. The accuracy of these height determinations depends on the geometry of the magnetic field, and the accuracy is greatest near the limb.

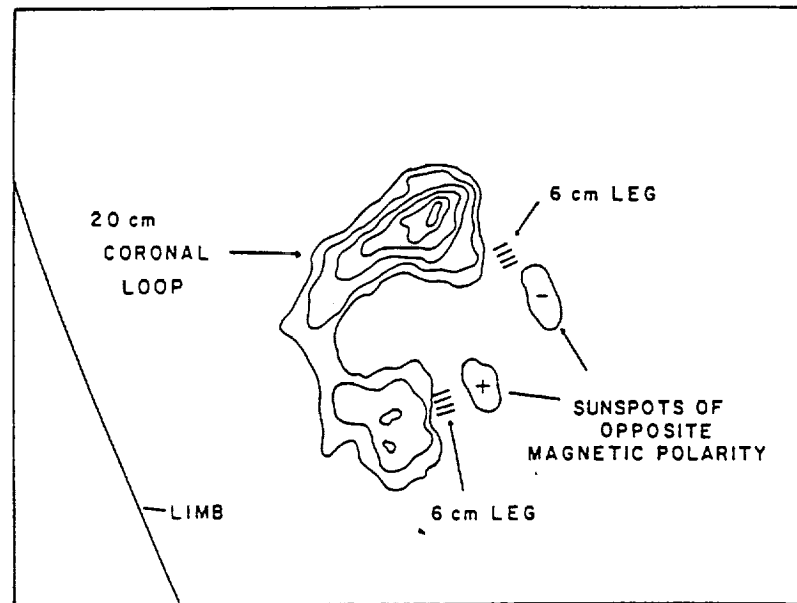


Figure 1. A VLA synthesis map of the total intensity, I , of the 20 cm emission from a coronal loop. The contours mark levels of equal brightness temperature corresponding to 0.2, 0.4, ...1.0 times the maximum brightness temperature of $T_B = 2 \times 10^6$ K. A schematic portrayal of the 6 cm emission, which comes from the legs of the magnetic loops, has been added together with the underlying sunspots that are detected at optical wavelengths.

Multiple-wavelength synthesis observations with the Very Large Array (VLA) have been carried out at wavelengths $\lambda = 20, 6$ and 2 cm (see Figure 1). The radiation at 20 cm can originate at both the apex and legs of coronal loops, and sometimes delineates the hot, dense plasma detected at X-ray wavelengths. The 20-cm coronal loops have brightness temperatures $T_B = 1 \times 10^6$ to 4×10^6 K and extents of $L = 10^9$ to 10^{10} cm. Magnetic field strengths of $H \sim 145$ G have been inferred from cyclotron lines at the apex of the 20-cm loops. Bright, highly polarized 6-cm cores often mark the legs of dipolar loops with $T_B = 2 \times 10^6$ to 5×10^6 K and heights $h \approx 10^9$ cm above the underlying sunspots. Values of H of ~ 600 to 900 G are inferred from the fact that these cores emit gyroradiation at the second or third harmonic of the gyrofrequency. The 2-cm emission has brightness temperatures of $T_B \approx 10^5$ K and often overlies sunspots at heights $h \approx 5 \times 10^8$ cm where H is $\approx 10^3$ G.

The 20-cm coronal loops have been discussed by Velusamy and Kundu (1981), Lang, Willson and Rayrole (1982), Dulk and Gary (1983), and McConnell and Kundu (1984). Multiple-wavelength VLA observations at 2, 6 and 20 cm have been presented by Lang, Willson and Gaizauskas (1983), Shevgaonkar and Kundu(1984), Kundu and Lang (1985) and Kundu (1986 - this proceedings). Most recently, Gary and Hurford (1986) have used microwave spectroscopy during a solar eclipse to delineate the physical conditions at a variety of levels within the legs and apex of a coronal loop (see Figure 2).

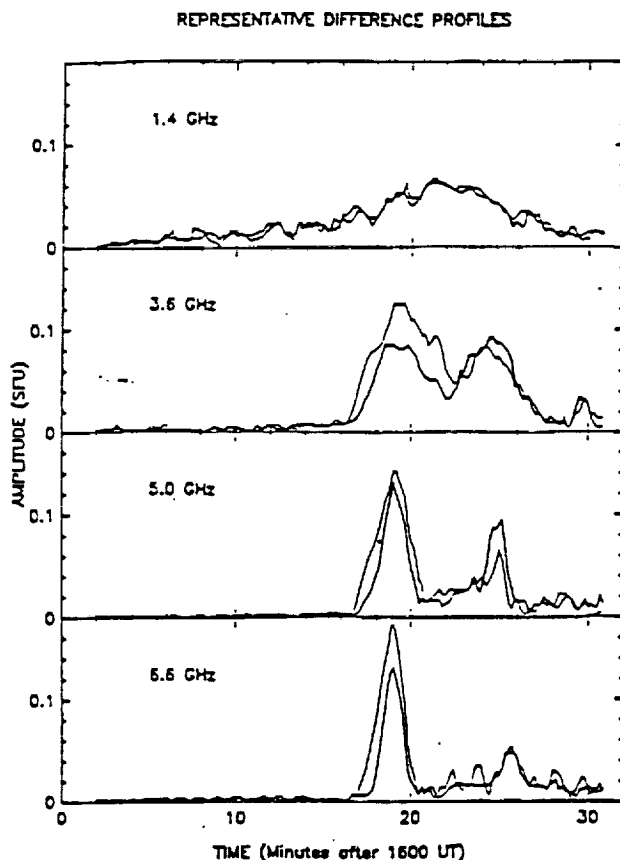


Figure 2. Differenced OVRO time profiles at four representative frequencies. Right hand circular (RH) polarization is shown by the heavy lines, and left hand (LH) polarization by the light lines. Below 3 GHz, the active region appears as a single board source. At higher frequencies, the region bifurcates into two main sources, becoming more localized to the sunspots as the observing frequency increases. The sense of polarization in the two spot sources is consistent with gyroresonance emission.

RADIATION MECHANISMS OF CORONAL LOOPS

The quiescent, or non-flaring, radiation of coronal loops is usually thermal in nature. The soft X-ray radiation is, for example, attributed to the thermal bremsstrahlung of hot million-degree electrons. However, at centimeter wavelengths there are two different thermal mechanisms: the bremsstrahlung of thermal electrons accelerated in the electric field of ions and the gyroresonant radiation of thermal electrons accelerated by magnetic fields can contribute to the emission. While the thermal bremsstrahlung emission is sensitive to the electron temperature and emission measure, gyroresonant emission is sensitive to the local magnetic field and electron temperature. It is this gyroresonant radiation which provides a sensitive measure of coronal magnetic field strength. Thus, it is important to distinguish which of these mechanisms is responsible for the emission from any given source at these wavelengths.

Strong evidence for thermal gyroradiation at coronal levels above sunspots has been provided by comparing the soft X-ray and centimeter-wavelength radiation of active regions [Kundu, Schmahl and Gerassimenko (1980); Pallavicini, Sakurai and Vaiana (1981); Schmahl et al. (1982)]. Although there is intense X-ray emission from the apex of coronal loops, the X-ray radiation often falls to undetectable levels in the legs of coronal loops above sunspots. Yet, intense radio radiation has sometimes been observed from both the apex and the legs of coronal loops. At other times radio emission has been detected from just the apex or just the legs of the loops, depending on the wavelength and observing conditions.

The near equality of the radio brightness and electron temperatures indicates that the radio emission from coronal loops is usually thermal. But the low electron densities inferred from the X-ray data above sunspots indicate that thermal bremsstrahlung is too weak to account for the intense radio radiation. The extra source of opacity has been attributed to gyroresonance absorption at the second or third harmonic of the gyrofrequency.

GYRORESONANT EMISSION



Figure 3. A Westerbork Synthesis Radio Telescope synthesis map of circular polarization at $\lambda = 6$ cm overlaid on an H α photograph obtained from the observatory at Athens. The contours are in steps of 1.5×10^5 K. The circularly polarized horseshoe structure that rings the sunspot umbra is due to gyroresonant emission in the curved magnetic fields of the sunspot penumbra.

Thermal gyroradiation at coronal levels above sunspots has been additionally confirmed by the detection of circularly polarized ring-shaped or horseshoe structures at 6 cm wavelength [Alissandrakis and Kundu (1982); Lang and Willson (1982)]. The highly-polarized (up to 100 percent) structures were predicted by the theory of gyroradiation in the curved magnetic fields above sunspot penumbrae [Gel'freikh and Lubyshev (1979)]. There is no detectable circular polarization above the central sunspot umbrae where the magnetic fields project radially upward into the hot coronal regions (see Figure 3). Depressions in the radio brightness temperature above sunspot umbrae have been attributed to cool material in these regions [Strong, Allisandrakis and Kundu(1984)].

At the longer, 20 cm, wavelength, emission is detected sometimes from both the apex and the legs of coronal loops (Lang, Willson, Strong, and Smith, 1986, and see Figure 4), and sometimes from just the apex (Webb et al., 1986). In the latter case, the electron densities and temperatures inferred from the X-ray spectral lines indicate that the plasma is optically thick at 20 cm, and hence that the observed brightness temperature should be equal to the electron temperature. However, the observed brightness temperature is a factor of 2 - 3 lower than the local electron temperature. Brosius and Holman (1986--this proceedings) and Holman (1986--this proceedings) explain this low brightness temperature in terms of a relatively cool, $<10^5$ K external plasma around the hot 2.5×10^6 K loops. Such material absorbs emissions primarily from the loop footpoints, where the optical depth along the line of sight is greatest. The loops and the external plasma are separated by a thin transition zone. The emission measure distributions for such models have been calculated, and have been found not only to agree well with recent observational emission measure curves for solar active region loops, but also to rise on both the cool and the hot side of the emission measure minimum. This is the first time that a theoretical emission measure curve for a single active region loop has been found to do this (cf. Antiochos and Noci, 1986).



Figure 4. A comparison of the soft X-ray (S.M.M.-left), H (SOON-middle) and 20 cm (V.L.A.-right) emission of an active region on the same day. The most intense soft X-ray emission is well correlated with intense 20 cm and H emission; but the 20 cm emission also extends across the areas near the sunspots where it is also intense. The angular spacing between fiducial marks on the axes is 60 arc-seconds.

Alternative radiation mechanisms may be required for intense radio emission from regions overlying weak photospheric magnetic fields. Observations of these regions have been reported by Akmedov et al. (1986), Lang (1986a-this proceedings), Lang and Willson (1986a-this proceedings), Webb, Davis, Kundu and Velusamy (1983), and Willson and Lang (1986). A possible explanation, first studied in detail by Chiuderi, Drago and Melozzi (1984), is the nonthermal synchrotron emission of mildly relativistic electrons; but some currently-unspecified mechanism must be accelerating the electrons. An equally plausible explanation is that currents amplify the magnetic field in the low solar corona to strengths that are a factor of ten larger than those inferred from magnetograms of the underlying photosphere. The observed radio emission might then be attributed to the gyroradiation of thermal electrons at the second and third harmonic of the gyrofrequency.

SPECIFYING THE CORONAL MAGNETIC FIELD

Measurements of the spectrum, polarization and angular size of active region sources at centimeter wavelengths have been pioneered by Soviet astronomers using the RATAN 600 [Radio Astronomy Telescope of the Academy of Sciences (Nauk)-see Akmedov et al. (1986)], and further developed and extended using the frequency-agile interferometer at the OVRO [Owens Valley Radio Observatory-see Hurford and Gary (1986) this proceedings]. By measuring both the angular size and the flux density at a variety of wavelengths, one can uniquely determine the brightness temperature spectrum of the sources. Circular polarization data can additionally be used to specify the magnetic field strength. Hurford and Gary (1986-this proceedings) have used this technique of microwave spectroscopy to measure the field distribution in the lower corona above sunspots.

In fact, both the strength and structure of the coronal magnetic field can be specified along the legs of coronal loops where gyroradiation dominates. The observations indicate that the magnetic fields systematically diverge and decrease in strength at higher heights (longer wavelengths) above single sunspots [see Hurford and Gary (1986) - this proceedings].

The magnetic field strength can also be inferred from individual cyclotron lines when gyroradiation dominates the emission. The observations at a single wavelength refer to a predetermined height where the radiation frequency is at one of the low harmonics of the gyrofrequency. Multiple-frequency observations provide information at a fixed height, regardless of field strength.

Holman and Kundu (1985) and Holman (1986 - proceedings) have pointed out that the emitting layers might be spatially resolved when a thin loop is observed. The magnetic field strength within each layer can then be inferred from the observing wavelength and the relevant harmonic. However, the cyclotron lines may overlap when the loop is thick or when a thin loop is observed along its legs.

The spectrum of an individual cyclotron line may also be obtained when observing at several wavelengths. For example, the spectra of individual cyclotron lines have been observed at wavelengths near 20 cm when the apex of a coronal loop is resolved [Willson (1985), Lang (1986a-this proceedings), Lang, Willson, Strong and Smith (1986)]. This is because the magnetic field strength is relatively constant near the loop apex; the cyclotron lines would merge into a continuum along the loop legs where the magnetic field strength decreases uniformly with height. Neutral current sheets might also play a role, leading to intense radio emission from a thin layer near the loop apex. Both a uniform field and a steep temperature gradient in the uniform region are probably required to detect the cyclotron lines. In any event observations of individual cyclotron lines indicate magnetic field strengths of $H = 145 \pm 5$ G at the apex of some coronal loops.

Solar bursts might also be used to infer the strength and configuration of coronal magnetic fields. Roberts, Edwin and Benz (1984) and Roberts (1984, 1986 - proceedings) have shown that bursts can impulsively generate magneto-acoustic oscillations in a coronal loop. These oscillations may be observed as quasi-periodic radio variations whose onset, duration and periodicity can be used to infer the height, size and magnetic field strength of the emitting region.

THE CORONAE OF NEARBY STARS

Nearby main-sequence stars of late spectral type exhibit quiescent, or non-flaring, X-ray emission whose absolute luminosity may be as much as 100 times that of the Sun [Vaiana et al. (1981)]. This suggests that these stars have hot stellar coronae with large-scale coronal loops and strong magnetic fields. The solar analogy suggests that these coronae might also be detected at radio wavelengths.

Nearby dwarf M flare stars do, in fact, exhibit slowly varying radio emission at 6 and 20 cm wavelength that is analogous to that of solar active regions. However, the X-ray observations rule out detectable thermal bremsstrahlung at radio wavelengths; the temperatures and emission measures inferred from the X-ray data indicate that the radio bremsstrahlung would be at least two orders of magnitude below detection thresholds. Moreover, thermal gyroradiation is an unlikely source of the intense 20 cm radiation from some of these stars; implausibly large coronal loops would have to be up to 10 times larger than the star with magnetic field strengths larger than 100 G at these remote distances. The most likely source of this slowly varying radiation in M-dwarf stars is gyrosynchrotron radiation from nonthermal electrons (Holman, 1986; Lang and Willson, 1986b).

In other words, the fact that we detect radio emission from these stars means that something unusual is happening on them. As an example, radio bursts from the dwarf M stars have been attributed to coherent emission mechanisms like electron-cyclotron masers or coherent plasma radiation [Melrose and Dulk (1982); Dulk (1985)].

Quasi-periodic and individual spikes have been detected from the dwarf M star AD Leonis at 20 cm wavelength [Lang et al. (1983), Lang and Willson (1986a), Lang (1986a)-this proceedings]. These spikes are up to 100% circularly polarized with rise times less than 5 milliseconds. The rapid rise time indicates that the emitter's size is less than 0.005 of the star's radius, and that a symmetric emitter has a brightness temperature in excess of 10^{16} K. Such a high brightness temperature requires a coherent radiation mechanism. Similar high brightness temperature spikes

have been observed during solar flares. Unlike solar flares, however, the underlying nonspiky emission from the AD Leonis flare is probably also coherent [Holman, Bookbinder and Golub (1985)].

Coherent emission is also suggested by the narrow-band, slowly varying, 20-cm emission from the dwarf M star YZ Canis Minoris [Lang and Willson (1986)], as well as narrow-band 20 cm flares from the red dwarf stars AD Leo and UV Ceti [White, Kundu and Jackson (1986)]. The narrow-band structure cannot be explained by continuum emission processes such as thermal bremsstrahlung, thermal gyroradiation, or nonthermal gyrosynchrotron radiation. Coherent radiation processes seem to be required.

If the radiation is emitted by an electron-cyclotron maser at the second harmonic of the gyrofrequency, then the magnetic field strength is $H = 250$ G, and constraints on the plasma frequency imply an electron density of $N_e \approx 6 \times 10^9$ cm^{-3} . Coherent plasma radiation at the first or second harmonic of the plasma frequency respectively require $N_e = 2 \times 10^{10}$ cm^{-3} and $H \ll 500$ G or $N_e = 6 \times 10^9$ cm^{-3} and $H \ll 250$ G. Thus, the coherent burst mechanisms suggest that the coronae of dwarf M stars have physical parameters similar to those of solar active regions.

FUTURE PROSPECTS FOR CORONAL DIAGNOSTICS

Probable observations of coherent radiation processes on nearby stars are stimulating further searches for coherent signatures in the Sun's radio radiation. In fact, narrow-band structure has been observed in a solar burst [Lang and Willson (1984): Lang (1986b)], and rapid spikes during some solar bursts have been interpreted in terms of electron-cyclotron masers [Holman, Eichler and Kundu (1980); Holman (1983)]. Future observations with high resolution in time and frequency at the VLA, OVRO and Nancay will help determine the role that coherent radiation processes play in solar active regions.

The next decade will also include detailed comparisons of radio and X-ray observations with model coronal loops that include both thermal bremsstrahlung and thermal gyroradiation. Coronal magnetic fields may be directly inferred from observations and models in which the expected radio emission is computed as a function of wavelength, polarization and viewing angle. A comparison of the observed radiation with theoretical expectations will determine magnetic field strengths, electron densities and electron temperatures.

The evolution of coronal loops has strong future potential. Of special interest are the preheating and magnetic changes that trigger solar bursts [see Kundu and Lang (1985) for a review]. Emerging coronal loops and the magnetic interaction of existing coronal loops will be particularly interesting topics.

Future studies of the evolution of the three-dimensional magnetic and plasma structure of coronal loops will lead to valuable new insights to the nature of solar active regions and eruptions on the Sun and nearby stars. Such insights can only be fully realized by the development of a solar-stellar synthesis radiotelescope. Such an instrument would be dedicated to solar and stellar observations with high angular, temporal and frequency resolution.

ACKNOWLEDGEMENTS

Radio astronomical studies of the Sun at Tufts University are supported under Air Force Office of Scientific Research grant AFOSR-83-0019 and contract N0014-86-K-0068 with the Office of Naval Research. Our simultaneous VLA and Solar Maximum Mission satellite observations of the Sun are supported under NASA grant NAG 5-501.

REFERENCES

- Akhmedov, S.B., et al., 1986, "Structure of a Solar Active Region from RATAN 600 and Very Large Array Observations," *Astrophys. J.*, 301, 460-464.
- Alissandrakis, C.E. and M.R. Kundu, 1982, "Observations of Ring Structure in a Sunspot Associated Source at 6 Centimeter Wavelength," *Astrophys. J. (Letters)*, 253, L49-L52.
- Alissandrakis, C.E. and M.R. Kundu, 1984, "Center-to-Limb Variation of a Sunspot-Associated Microwave Source," *Astron. Astrophys.*, 139, 271-284.
- Antiochos, S.K. and G. Noci, 1986 "The Structure of the Static Corona and Transition Region," *Astrophys. J.*, 301, 440-447
- Brosius, J.W. and G.D. Holman, 1986, "Theoretical Models of Free-Free Microwave Emission from Solar Magnetic Loops," this Proceedings.
- Chiuderi-Drago, F. and M. Melozzi, 1984, "Non-Thermal Radio Sources in Solar Active Regions," *Astron. Astrophys.* 131, 103-110.
- Dulk, G.A., 1985, "Radio Emission from the Sun and Stars," *Ann. Rev. Astron. Ap.*, 23, 169-180.
- Dulk, G.A. and D.E. Gary, 1983, "The Sun at 1.4 GHz: Intensity and Polarization," *Astron. Astrophys.* 124, 103-107.
- Gary, D.E. and G.J. Hurford, 1986, "Multi-Frequency Observations of a Solar Active Region During a Partial Eclipse, BBSO 259, submitted to *Astrophys. J.*
- Gel'frikh, G.B. and B.I. Lubyshev, 1979, "Structure of Local Sources of the S Component of Solar Radio Emission," *Sov. Astron. A.J.*, 23, 316-322.
- Holman, G.D., 1983, "Some Recent Results in the Interpretation of High Brightness Temperature Microwave Spike Emission," *Adv. Space Res.*, 2, No.11, 181-183
- Holman, G.D., 1986, "Coronal Heating and the X-ray and Microwave Emission from M-Dwarf Flare Stars," in Proceedings of the Fourth Cambridge Workshop on Cool Stars, Stellar Systems, and the Sun, eds. M. Zeilik and D.M. Gibson (Springer-Verlag), in press.
- Holman, G.D., 1986, "High-Spatial-Resolution Microwave and Related Observations as Diagnostics of Coronal Loops," - this Proceedings.
- Holman, G.D., J. Bookbinder and L. Golub, 1985, "Implications of the 1400 MHz Flare Emission from AD Leo for the Emission Mechanism and Flare Environment," in *Radio Stars*, ed. R.M. Hjellming and D.M. Gibson, (Dordrecht: Reidel), 35-37.
- Holman, G.D., D. Eichler and M.R. Kundu, 1980, "An Interpretation of Solar Flare Microspikes as Gyrosynchrotron Masering," in *Radio Physics of the Sun - I.A.U. Symposium No. 86*, ed. M.R. Kundu and T.E. Gergely, (Dordrecht: Reidel), 457-459.
- Holman, G.D. and M.R. Kundu, 1985, "The Microwave Structure of Hot Coronal Loops," *Astrophys. J.*, 292, 291-296.
- Hurford, G.J. and D.E. Gary, 1986, "Measurement of Coronal Fields Using Spatially Resolved Microwave Spectroscopy," - this Proceedings.
- Kundu, M.R., 1986, "Three Dimensional Structures of Solar Active Regions," this Proceedings."

- Kundu, M.R. and C.E. Alissandrakis, 1984, "Structure and Polarization of Active Region Microwave Emission," *Solar Phys.*, 94, 249-283.
- Kundu, M.R. and K.R. Lang, 1985, "The Sun and Nearby Stars," *Science*, 228, 9-15.
- Kundu, M.R., E.J. Schmahl and M. Gerassimenko, 1980, "Microwave, EUV and X-ray Observations of Active Region Loops: Evidence for Gyroresonance Absorption in the Corona," *Astron. Astrophys.* 82, 265-271.
- Kundu, M.R. and T. Velusamy, 1980, "Observation with the VLA of a Stationary Loop Structure in the Sun at 6 cm Wavelength," *Astrophys. J. (Letters)*, 240, L63-L65.
- Lang, K.R., 1986a, "Coronal Plasmas on the Sun and Nearby Stars," this Proceedings.
- Lang, K.R., 1986b, "Flare Stars and Solar Bursts: High Resolution in Time and Frequency," *Solar Phys.*, in press.
- Lang, K.R., J. Bookbinder, L. Golub and M. Davis, 1983, "Bright, Rapid, Highly Polarized Radio Spikes from the M Dwarf AD Leo," *Astrophys. J. (Letters)*, 272, L15-L18.
- Lang, K.R. and R.F. Willson, 1982, "Polarized Horseshoes Around Sunspots at 6 Centimeter Wavelength," *Astrophys. J. (Letters)*, 255, L111-L117.
- Lang, K.R. and R.F. Willson, 1983, "Multiple Wavelength Observations of Flaring Active Regions," *Adv. Space Res.* 2, No. 11, 91-100.
- Lang, K.R. and R.F. Willson, 1984, "V.L.A. Observations of Flare Build-Up in Coronal Loops," *Adv. Space Res.* 4, No. 7, 105-110.
- Lang, K.R. and R.F. Willson, 1986a, "Compact, Variable, Moving Sources on the Sun at 2 Centimeters Wavelength," this Proceedings.
- Lang, K.R. and R.F. Willson, 1986b, "Narrow-Band, Slowly Varying Decimetric Radiation from the Dwarf M Flare Star YZ Canis Minoris," *Astrophys. J. (Letters)*, 302, L17-L21.
- Lang, K.R. and R.F. Willson, 1986c, "Millisecond Radio Spikes from the Dwarf M Flare Star AD Leonis," *Astrophys. J.*, in press.
- Lang, K.R., R.F. Willson and V. Gaizauskas, 1983, "Very Large Array Observations of Solar Active Regions III. Multiple Wavelength Observations," *Astrophys. J.*, 267, 455-464.
- Lang, K.R., R.F. Willson and J. Rayrole, 1982, "Very Large Array Observations of Coronal Loops at 20 Centimeter Wavelength," *Astrophys. J.*, 258, 384-387.
- Lang, K.R., R.F. Willson, K.T. Strong and K.L. Smith, 1986a, "Physical Parameters of a Solar Active Region Inferred from Thermal Cyclotron Lines and Soft X-Ray Spectral Lines," *Astrophys. J.*, to be submitted.
- Lang, K.R., R.F. Willson, K.T. Strong and K. L. Smith, 1986b, "Simultaneous Solar Maximum Mission and Very Large Array Observations of Solar Active Regions," *Astrophys. J.*, to be submitted.
- McConnell, D. and M.R. Kundu, 1983, "VLA Observations of a Solar Active Region and Coronal Loops," *Astrophys. J.*, 269, 698-705.
- Melrose, D.B. and G.A. Dulk, 1982, "Electron-Cyclotron Masers as the Source of Certain Solar and Stellar Bursts," *Astrophys. J.*, 259, 844-858.
- Pallavicini, R., T. Sakurai and G.S. Vaiana, 1981, "X-Ray, EUV and Centimetric Observations of Solar Active Regions: an Empirical Model for Bright Radio Sources," *Astron. Astrophys.*, 98, 316-327.
- Roberts, B., 1984, "Waves in Inhomogeneous Media," in *The Hydrodynamics of the Sun*, ESA SP-220, November.
- Roberts, B., 1986, "Guided MHD Waves as a Coronal Diagnostic Tools," this Proceedings.
- Roberts, B., P.M. Edwin and A.O. Benz, 1984, "On Coronal Oscillations," *Astrophys. J.*, 279, 857-865.
- Schmahl, E.J., et al., 1982, "Active Region Magnetic Fields Inferred from Simultaneous VLA Microwave Maps, X-Ray Spectroheliograms, and Magnetograms," *Solar Physics* 80, 233-249.

- Shevgaonkar, R.K. and M.R. Kundu, 1984, "Three-Dimensional Structures of Two Solar Active Regions from VLA Observations at 2, 6 and 20 Centimeter Wavelengths" *Astrophys. J.*, 283, 413-420.
- Strong, K.T., C.E. Alissandrakis and M.R. Kundu, 1984, "Interpretation of Microwave Active Region Structures Using SMM Soft X-Ray Observations," *Astrophys. J.*, 277, 865-873.
- Vaiana, G.S. and R. Rosner, 1978, "Recent Advances in Coronal Physics," *Ann. Rev. Astron. Ap.* 16, 393-405.
- Vaiana, G.S., et al., 1981, "Results From An Extensive Einstein Stellar Survey," *Astrophys. J.*, 245, 163-182.
- Velusamy, T. and M.R. Kundu, 1981, "VLA Observations of Postflare Loops at 20 Centimeter Wavelength," *Astrophys. J. (Letters)*, 243, L103-L107.
- Webb, D.F., J.M. Davis, M.R. Kundu and T. Velusamy, 1983, "X-Ray and Microwave Observations of Active Regions," *Solar Phys.* 85, 267-283.
- Webb, D.F., G.D. Holman, J.M. Davis, M.R. Kundu and R.K. Shevgaonkar, 1986, "The Plasma and Magnetic Field Properties of Coronal Loops Observed At High Spatial Resolution," submitted to *Astrophys. J.*
- White, S.M., M.R. Kundu and P.D. Jackson, 1986, "Narrowband Radio Flares from Red Dwarf Stars," *Astrophys. J.*, submitted.
- Willson, R.F., 1983, "Possible Detection of Thermal Cyclotron Lines from Small Sources Within Solar Active Regions," *Solar Phys.*, 89, 103-113.
- Willson, R.F., 1985, "VLA Observations of Solar Active Regions at Closely Spaced Frequencies: Evidence for Thermal Cyclotron Line Emission," *Astrophys. J.*, 298, 911-917.

G. COMPACT, VARIABLE SOURCES ON THE SUN AT 2 CENTIMETER WAVELENGTH

ROBERT F. WILLSON and KENNETH R. LANG

Department of Physics and Astronomy, Tufts University, Medford, MA 02155, U.S.A.

(Received 14 May, in revised form 2 August, 1987)

Abstract. Very Large Array (VLA) observations of compact transient sources on the Sun at 2 cm wavelength are presented. These sources have angular sizes of $\theta \approx 5''-25''$, brightness temperatures of $T_B \approx 1-3 \times 10^5$ K, and lifetimes ranging between a few minutes to several hours. The emission originates in regions of diffuse plage and quiet Sun, where the photospheric magnetic fields are relatively weak ($H \leq 100$ G). In some cases the 2 cm radiation may be explained as the thermal bremsstrahlung of a dense ($N_e \leq 10^{10} \text{ cm}^{-3}$) plasma in the transition region. For other sources, the relatively high circular polarization ($\rho_c \approx 40-50\%$) suggests a nonthermal emission mechanism, such as the gyrosynchrotron radiation of mildly relativistic electron with a power-law spectrum.

1. Introduction

VLA observations of solar active regions have shown that the quiescent emission at 2 cm wavelength often originates in compact ($\theta < 5''$) highly circularly polarized ($\rho_c = 80-90\%$) sources in regions of strong magnetic fields near sunspots (Lang *et al.*, 1983; Shevgaonkar and Kundu, 1984). The observed brightness temperatures of $T_B = 10^5-10^6$ K suggest that this emission originates in the transition region or low solar corona. More recent observations have revealed a different class of 2 cm sources which are also compact and often highly circularly polarized but which originate in regions of apparently weak photospheric field (Akhmedov *et al.*, 1986; Willson and Lang, 1986). The nature of these sources is enigmatic because magnetic fields of $H \approx 1500-2000$ G are required if the observed brightness temperatures and degrees of circular polarization are to be attributed to thermal gyroresonance emission or to propagation effects (thermal bremsstrahlung). Alternatively, the 2 cm emission could be attributed to nonthermal radiation such as the gyrosynchrotron radiation of subrelativistic electrons in low magnetic fields.

These compact sources are also observed to vary on time-scales of a few tens of seconds to several hours. In one case Willson and Lang (1986) observed the apparent emergence and disappearance of a compact ($\theta < 10''$) dipolar loop which evolved on a time-scale of about 60 s. These variations could be due to fluctuations in the magnetic field strength or to a variable nonthermal electron density, possibly brought about by changes in the acceleration mechanism. The time-scales of the variations are similar to those observed at ultraviolet wavelengths from small sources in the transition region and to optical wavelength fluctuations of so-called ephemeral regions (Porter *et al.*, 1984; Martin *et al.*, 1985).

In this paper we discuss new VLA observations of the Sun at 2 cm wavelength. In

Section 2 we present these observations and show that compact, transient sources are detected in both regions of weak plage without sunspots as well as in regions of the quiet Sun. There also does not appear to be any clear association between these transient sources and the photospheric $H\alpha$ emission. In Section 3 we discuss these observations in light of both thermal and nonthermal radiation processes. We show that the unpolarized 2 cm emission could be attributed to the thermal bremsstrahlung of dense, compact sources in the transition region. The moderate circular polarization ($\rho_c = 40\text{--}50\%$) of other sources, however, suggests either a nonthermal emission mechanism such as gyrosynchrotron radiation or else unexpectedly high magnetic fields in the transition region or corona. Here we also comment on the possibility of detecting transient sources at other radio wavelengths.

2. Observations

The VLA was used (D configuration) to observe a region of diffuse plage on 1986 January 17. The position of this region was S 10 W 62 at 13:00 UT on this day. Observations (B configuration) were also made toward another plage region as well as toward two regions of quiet Sun on 1986 August 24. The plage was located at S 10 W 08 at 13:00 UT, and the two quiet-Sun regions were located at N 30 W 00 and S 30 W 00. On 1986 January 17, the region was observed during an eight hour period between 15:00 and 23:00 UT. The entire VLA was used to observe the Sun at 2.1 and 6.1 cm

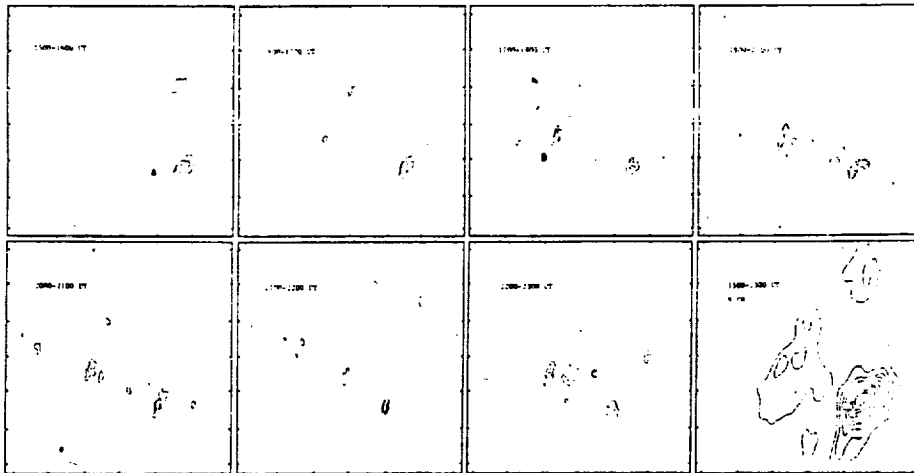


Fig. 1. VLA synthesis maps of the total intensity of the radiation from compact sources at 2.1 and 6.1 cm (lower right-hand box) during an eight hour period on 1986 January 17. Each map begins and ends at the time indicated. Here each box refers to the same area on the surface of the Sun, and the fiducial marks are separated by 60° . The contours mark levels of equal brightness temperature. At 2.1 cm, the outermost contour is drawn at 5.2×10^4 K with a contour interval of 1.8×10^4 K. The inner contour and contour interval of the 6 cm map are equal to 1.0×10^3 K.

for 20 m and 10 m, respectively, followed by successive 2 min observations on a nearby calibration source. On 1986 August 24, the plage and the northern and southern hemisphere quiet-Sun regions were observed at 2.1 cm for successive periods of 4.5, 2.5, and 2.5 hr, respectively, beginning at 15 : 00 UT. On both days the bandwidth was 12.5 MHz. At 2.1 cm the half-power beamwidth of the antennas is $\sim 3.5'$. At this wavelength the synthesized beamwidths in the *B* and *D* configurations are $\sim 0.4'' \times 0.5''$ and $4.2'' \times 4.6''$, respectively.

The right and left circularly polarized signals were sampled every 10 s and were calibrated using the standard VLA solar calibration procedures. These data were then used to produce CLEANED synthesis maps of the total intensity, I , and circular polarization, V , over an area of $\sim 5' \times 5'$ on the Sun on time-scales as short as 30 s.

In Figure 1 we show a series of 1–2 hour maps of total intensity for the plage region observed on 1986 January 17. Here each box refers to the same region on the Sun. This figure shows several compact 2 cm sources with angular sizes of $\theta_s < 25''$ and maximum brightness temperatures of $T_e \approx 2 \times 10^5$ K. These sources lie within more extended 6 cm emission whose peak brightness temperature is $T_B \approx 10^6$ K. Comparisons with a Kitt Peak magnetogram (taken at 16 : 05 UT) and SOON and Big Bear Solar Observatory $H\alpha$ pictures show that these sources were located in regions of diffuse plage with weak photospheric magnetic fields ($H \leq 100$ G) and no sunspots. The 2 cm sources were also unpolarized ($\rho_c = V/I \leq 15\%$) suggesting optically thick emission from regions where $T_e = T_B \approx 1-2 \times 10^5$ K.

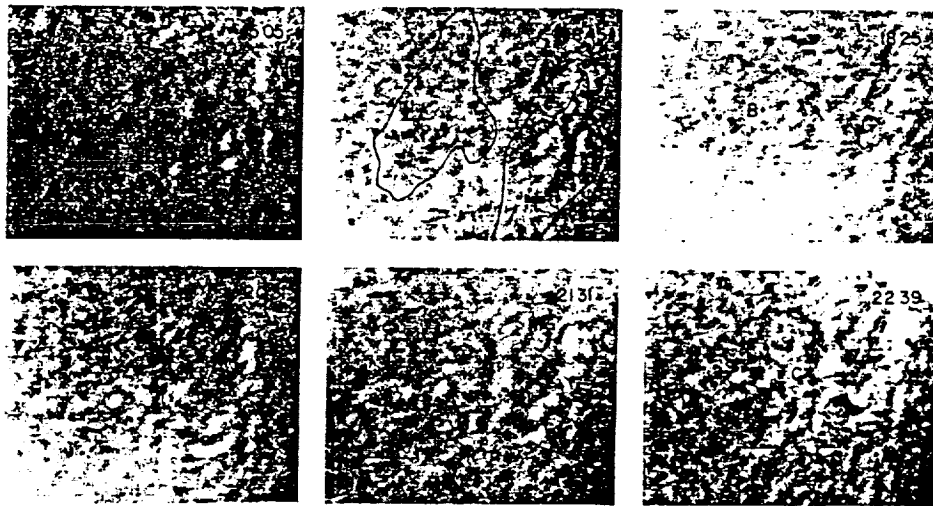


Fig. 2. A series of SOON $H\alpha$ images taken at the UT time indicated in the upper right-hand corner. The outermost contours of the 6 cm emission shown in Figure 1 are drawn on the image at 16 : 45 UT. The locations of the variable 2 cm sources *A*, *B*, and *C*, also shown in Figure 1, are indicated in the frames at 15 : 05, 18 : 25, and 22 : 39 UT, respectively.

It is clear from Figure 1 that these compact sources varied substantially in intensity on time-scales of hours. Source *B*, for example, appeared to emerge between $\sim 17:00$ and $19:00$ UT, and then faded and reappeared a few hours later. Likewise, source *C* emerged between $22:00$ and $23:00$ UT. A series of maps on hourly time-scales was also made for the 6 cm data, but they failed to reveal any significant changes in structure or intensity at this wavelength. Examination of $H\alpha$ images obtained by the SOON observatories also failed to reveal any obvious changes in the structure or brightness of the plage emission.

Figure 1 also shows that the most intense and long lasting source *A* appeared to move laterally towards the southeast during these observations. The angular displacement between the centroids of source *A* between $15:00$ and $23:00$ UT is $\sim 50''$, and corresponds to a transverse velocity of $\sim 1.3 \text{ km s}^{-1}$. Since the VLA was made to continuously track the same point on the Sun with an accuracy of $\sim 1''$, this shift in position cannot be attributed to systematic pointing errors.

In Figure 2 we show SOON $H\alpha$ images taken throughout the day. The universal time that the image was taken is given in the upper right-hand corner of each frame. Here

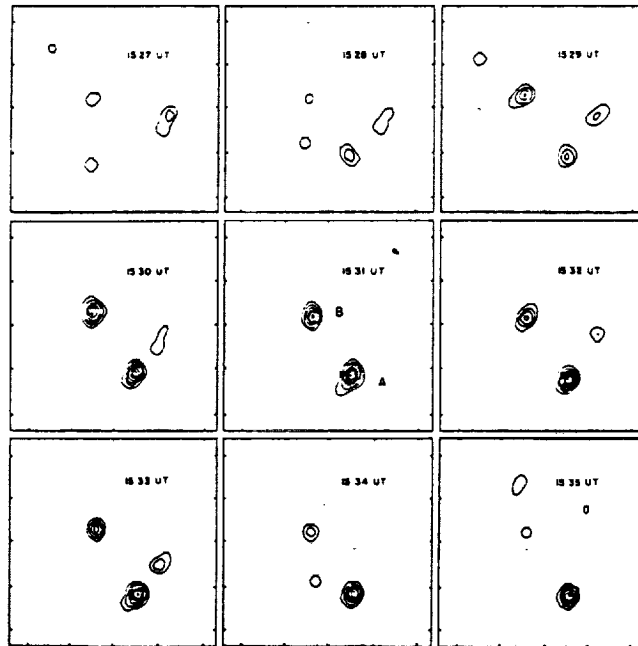


Fig. 3. VLA snapshot maps of the total intensity of compact variable sources at 2.1 cm wavelength. Each map is for 1 min of data beginning at the time indicated. These sources were located within a region of weak plage. The two sources *A* and *B* appear to have emerged together at $\sim 15:41$ UT. Source *A* lasted for ~ 12 min until $\sim 15:41$ UT, while source *B* lasted only until $\sim 15:34$ UT. Here the contours mark levels of equal brightness temperature with an outermost contour and contour interval of 3.5×10^4 K. The fiducial marks on the axes are separated by $10''$.

we have also superimposed the outer contours of the 6 cm emission on the image at 16:45 UT together with the locations of the 2 cm sources *A*, *B*, and *C*, shown in Figure 1. Source *A*, as well as the most intense 6 cm emission, might be associated with two patches of H α emission in the western half of the frame, but there is no such association for the variable sources *B* and *C*. Furthermore, although the H α data are not of the highest quality, it appears that there were no major changes in the intensity or structure of this diffuse H α emission during the day, unlike at 2 cm.

In Figure 3 we show a series of 60 snapshot maps of two compact variable sources detected within the diffuse plage region observed on 1986 August 24. The peak brightness temperatures and circular polarizations of the two sources, *A* and *B*, are

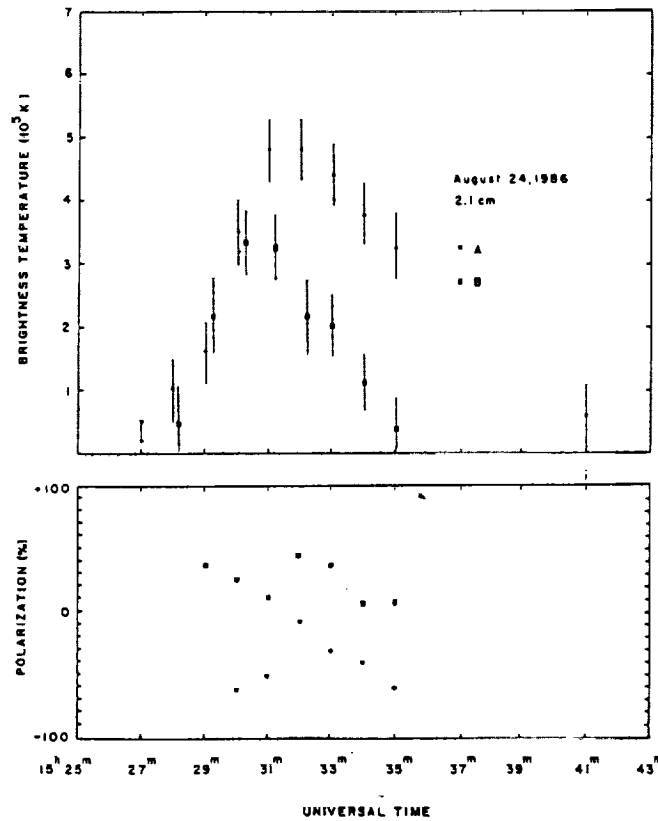


Fig. 4. Plots of the total intensity, $I = (RCP + LCP)/2$ (top) and circular polarization, $\rho_c = (RCP - LCP)/(RCP + LCP)$ (bottom), for the compact sources *A* and *B* shown in Figure 2.

plotted as a function of time in Figure 4. These data indicate that a bipolar region of about $10''$ in size emerged at $\sim 15:29$ UT and reached a maximum brightness a few minutes later. The weaker right circularly polarized source *B*, however, decreased in intensity more rapidly than the left circularly polarized source *A*, which lasted until

$\sim 15:41$ UT. Here the gap in the data between $15:35$ and $15:40$ UT corresponds to a calibration period. It is interesting to note the abrupt increase in circular polarization of source *B* to $\rho_c = 40\text{--}50\%$ between $15:32$ and $15:33$ UT, followed by an abrupt decrease at $15:34$ UT. Subsequent maps made on 1 min time intervals showed no evidence for the reappearance of sources at this position or for the emergence of any other sources ($T_B \leq 10^5$ K) during the following 4 hours that this region was observed.

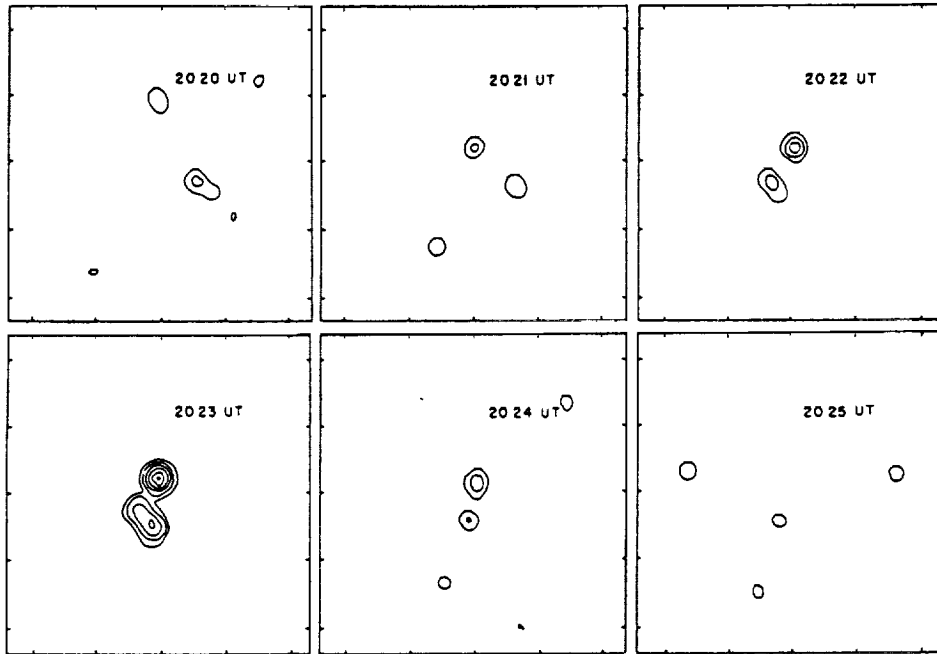


Fig. 5. VLA snapshot maps of the total intensity of a compact source at 2.1 cm wavelength. Each map is for 1 min of data, beginning at the time indicated. Here the fiducial marks are separated by $10''$. The contours mark levels of equal brightness-temperatures with an outermost contour and contour interval equal to 3.5×10^4 K.

In Figure 5 we show a series of snapshot maps depicting the emergence and decay of another 2 cm source located within a region of quiet Sun near the center of the disk (N30 W00). Again, the maps show the evolution of two compact sources on a time-scale of a few minutes. These sources, however, were, unlike those discussed previously, unpolarized ($\rho_c \leq 15\%$). Thus we cannot say whether these two sources represent the optically thick emission from the feet of a compact loop, or the unresolved emission from two separate loops.

Observations toward the quiet-Sun region in the southern hemisphere (S 30 W00) yielded no detectable emission ($T_B \leq 10^5$ K) during the 2.5 hours that this region was observed. Thus, only two cases of transient 2 cm emission were observed over an area of $\sim 5' \times 5''$ during the 9.5 hr period of observation.

3. Discussion

Our results have confirmed the presence of often highly circularly polarized 2 cm emission in regions of apparently weak photospheric magnetic fields. These sources are resolved with angular sizes of between 2" and 25" and undergo variations in intensity on time-scales of a few minutes to several hours. The inferred brightness temperatures of $T_B = 1-3 \times 10^5$ K are characteristic of the transition region. These sources are found both in plage regions without sunspots as well as in areas of quiet Sun. The fact that they are nearly always present within our relatively small field of view suggests they may be quite common on the Sun. The more rapidly varying 2 cm sources have temperatures, sizes, and lifetimes that are comparable to sources of rapid brightenings observed in the transition region at ultraviolet wavelengths (Vernazza *et al.*, 1975; Bruner and Lites, 1979; Athay *et al.*, 1980; Lites, 1981; Porter *et al.*, 1984). These brightenings occur frequently throughout active regions with lifetimes of 20 to 60 s, and appear to come from regions with angular sizes of $\leq 3''$. High-resolution EUV observations of small bipolar magnetic features, or ephemeral regions, indicate similar source characteristics (Roussel-Dupre *et al.*, 1984). Porter *et al.* (1984) suggest that the rapid brightenings may represent regions of small-scale heating in which magnetic loops emerge and reconnect with the existing magnetic field structure.

The high degree of circular polarization of the 2 cm sources is somewhat enigmatic. High circular polarization can be accounted for by propagation effects (thermal bremsstrahlung) or gyroresonant absorption in the presence of magnetic fields of $B \approx 2000$ G. Both explanations have been invoked to describe the compact 2 cm sources above sunspots (Lang *et al.*, 1983; Shevgaonkar and Kundu, 1984). However, the compact sources described here did not lie near sunspots and in fact lay above regions of apparently weak photosphere magnetic field ($B \leq 100$ G). Although gyroresonant absorption might account for the circular polarization, the weak magnetic field requires a very high harmonic ($n > 50$). The optical depth due to gyroresonant absorption is then negligibly small and cannot account for the observed brightness temperature of $T_B \approx 10^5$. Thermal bremsstrahlung, however, might explain the unpolarized sources (Figures 1 and 4) if the emission measure within the source is sufficiently high.

Recently, for example, Habbal *et al.* (1986) used the VLA to observe 20 cm emission from a number of so-called coronal bright points. These sources are variable on time-scales of a few minutes and have brightness temperatures between 1 and 5×10^5 K. These observations suggest that the radiation is dominated by emission in the transition region.

Some of these sources were also moderately circularly polarized with $\rho_c \leq 40\%$, yet there was no indication of exceptionally strong bipolar features underlying the radio emission. Habbal *et al.* (1986) interpreted these fluctuations in terms of density and temperature fluctuations in the transition region combined with plasma motions along changing magnetic fields. The 20 cm polarization was interpreted as a propagation effect in a thermal plasma with magnetic fields of between 50 and 200 G.

They showed the observed brightness temperature of a thermal plasma in the extraordinary and ordinary modes, T_{B_e} and T_{B_o} , could be expressed in terms of the coronal temperature, T_{cor} , the gas pressure, P_0 , and the conductive flux, F_c , in the transition region as

$$T_{B_{x,0}} = \frac{a_{x,0} T_{\text{cor}}}{a_{x,0} + 1},$$

where

$$a_{x,0} = \frac{1.95 \times 10^{-7} P_0^2}{v^2 (1 \mp v_H/v)^2 F_c}$$

and

$$P_0 = N_e T_e,$$

$$F_c = 1.1 \times 10^{-6} T_e^{5/2} \frac{dT_e}{dl}.$$

Here, v is the observing frequency, v_H is the gyrofrequency corresponding to a magnetic field H , N_e is the electron density, and T_e is the electron temperature.

The observed degree of circular polarization, ρ_c , is

$$\rho_c = \frac{T_{B_e} - T_{B_o}}{T_{B_e} + T_{B_o}}.$$

With $T_{\text{cor}} = 1.5 \times 10^6$ K, they showed that the observed brightness temperatures at 20 cm could be explained for $P_0^2/F_c \approx 2 \times 10^{24}$, consistent with quiet-Sun values (Withbroe and Noyes, 1977). For the same values, however, the predicted brightness temperatures at 2 cm wavelength are about a factor of 100 smaller and, therefore, cannot explain the present observations.

Under what conditions might we expect to observe the thermal bremsstrahlung from compact transient sources? Roussel-Dupré *et al.* (1984), for example, derive electron temperatures of $T_e = 1.6 \times 10^4 - 3 \times 10^5$ K and electron densities of $N_e = 10^{11} - 10^{12} \text{ cm}^{-3}$ from EUV observations of an ephemeral region. These regions are similar to the 2 cm sources in that they sometimes appear to move as they grow and evolve, typically with velocities of $\approx 0.5 \text{ km s}^{-1}$ (e.g., Martin *et al.*, 1985). For a pressure of $P_0 = 3 \text{ dyne cm}^{-2}$, a magnetic field strength of $H \leq 100$ G, and a conductive flux of $F_c = 2 \times 10^6 \text{ erg cm}^{-2} \text{ s}^{-1}$, typical of a quiet-Sun transition region, we would expect a brightness temperature of $T_{B_x} \approx T_{B_o} \approx 3 \times 10^5$ K at 2 cm wavelength. Therefore, if the transient microwave sources are related to ephemeral regions, or other regions of enhanced pressure, then their brightness temperatures could be attributed to a thermal plasma. However, we cannot explain the high degree of circular polarization ($\rho_c = 40-50\%$) unless there are unexpectedly high magnetic fields ($H \approx 2000$ G) in the regions where the 2 cm emission originates.

An alternative explanation, discussed by Willson and Lang (1986) is that the compact 2 cm sources arise from the nonthermal gyrosynchrotron-radiation of mildly relativistic electrons in relatively weak magnetic fields. This idea has also been suggested as the explanation for the high brightness temperatures ($T_b \geq 2 \times 10^6$ K) of 6 cm sources that are found close to neither enhanced X-ray emission nor sunspots (Webb *et al.*, 1983; Chiuderi Drago and Melozzi, 1984).

A fundamental difficulty with this model is the uncertain nature of the mechanism that accelerates electrons to near-relativistic energies. One possibility is that there are small-scale magnetic loops in the transition region or corona where electrons can be accelerated and confined in a magnetic bottle (e.g., Takakura and Kai, 1966; Brown and Hoyng, 1975). This so-called magnetic trap model has, for example, been successful in explaining the characteristics of hard X-ray and microwave bursts. It has been observed that the flux within small ($\theta \leq 3''$) knots in the photosphere can change on relatively rapid time-scales (Komle, 1979; Wilson and Simon, 1983; Topka and Tarbell, 1983; Simon and Wilson, 1985), and it is the evolution of these fields that might lead to the acceleration of electrons. These evolving fields might also give rise to isolated magnetic elements, or plasmoids (Cargill and Pneumann, 1984) which in turn might explain explosive events representing high-velocity mass ejections that have been observed at ultraviolet wavelengths (Karpen *et al.*, 1982).

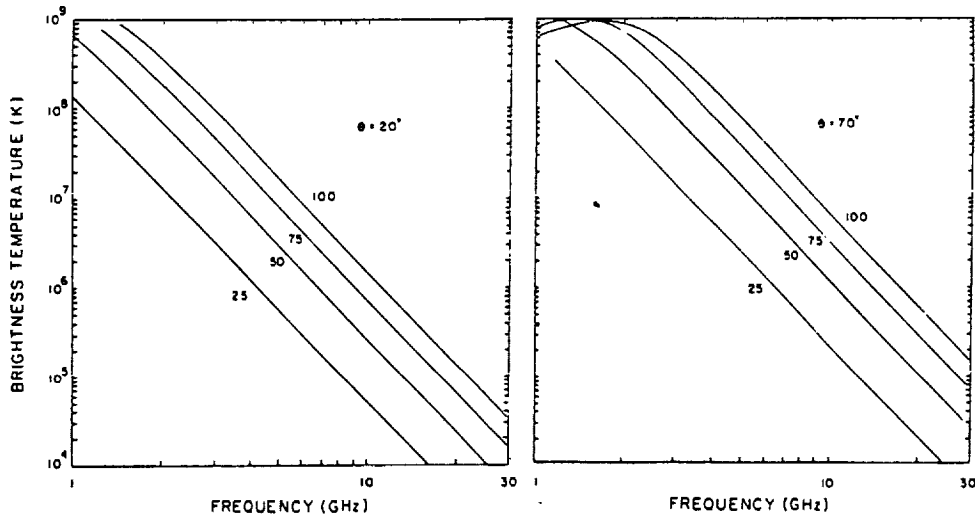


Fig. 6. Plots of the brightness temperature for nonthermal (power-law) radiation source. These spectra were generated assuming a power-law index of $\delta = 3.0$, a nonthermal electron density of $N = 5 \times 10^7 \text{ cm}^{-3}$, a path length $L = 5 \times 10^7 \text{ cm}$, viewing angles θ of 20° (left) and 70° (right) and magnetic field strengths of $H = 25, 50, 75,$ and 100 G .

In Figure 6 we show theoretical spectra of nonthermal (power-law) radiation from electrons in magnetic fields of $H = 25\text{--}100 \text{ G}$. These spectra were computed using the relationships given by Dulk and Marsh (1982) and Dulk (1984) for a power-law index

of $\delta = 3.0$, a nonthermal electron density of $N = 5 \times 10^7 \text{ cm}^{-3}$, a path length of $L = 5 \times 10^7 \text{ cm}$, viewing angles of $\theta = 20^\circ$ and 70° , and magnetic field strengths ranging between 25 and 100 G. These spectra indicate that brightness temperatures of $T_B > 10^5 \text{ K}$ can be produced at 2 cm wavelength in relatively low magnetic fields of $H > 75 \text{ G}$. With these values of δ , N , and L , the circular polarization may be as high as $\rho_c = 40\text{--}50\%$ for viewing angles of $\theta \approx 20^\circ$, and magnetic fields of $H > 75 \text{ G}$. The variable polarization of the compact source shown in Figures 3 and 4 may, therefore, reflect changes in some combination of the electron energy, density, or magnetic field strength as the source evolved.

Figure 6 also shows that the brightness temperature increases towards the longer wavelength, reaching $T_B \approx 10^9 \text{ K}$ at $\lambda = 20 \text{ cm}$. In this case, nonthermal emission from compact resources would also be detectable at the longer wavelengths (6 and 20 cm), available at the VLA. However, if the nonthermal emission is generated in the transition region, then the surrounding thermal plasma might significantly attenuate this emission at the longer wavelengths. This is because for a given electron density, temperature, and path length, the opacity of the thermal plasma increases as the square of the wavelength.

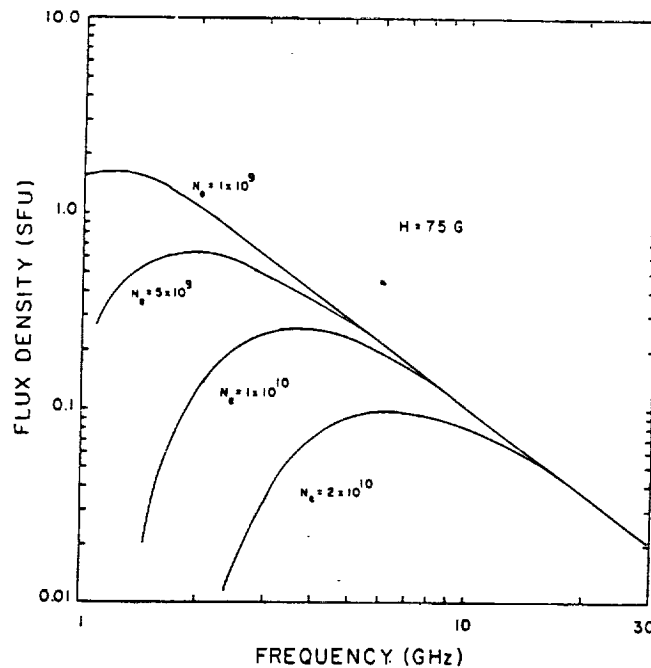


Fig. 7. Flux-density spectra of a nonthermal radiation source in the presence of a thermal plasma. These spectra were generated assuming a source size of $\theta = 5''$, a power law index of $\delta = 3.0$, a nonthermal electron density of $N = 5 \times 10^7 \text{ cm}^{-3}$, a path length of $L = 5 \times 10^7 \text{ cm}$, a magnetic field strength of $H = 75 \text{ G}$, a viewing angle of $\theta = 20^\circ$, and thermal electron densities ranging from $N_e = 1 \times 10^9 \text{ cm}^{-3}$ to $2 \times 10^{10} \text{ cm}^{-3}$. These plots indicate that the nonthermal emission may be significantly attenuated at the lower frequencies for $N_e > 5 \times 10^9 \text{ cm}^{-3}$.

In Figure 7 we show plots of the flux density of a nonthermal source embedded within such an absorbing plasma. Here, we assumed a constant source size of $\theta = 5''$, typical of the transient sources discussed in Section 2. These plots were generated by solving the equation of transfer for the brightness temperature using the density and temperature structure of the quiet-Sun transition region and corona as given by Vernazza *et al.* (1981). For a quiet-Sun transition region pressure of $N_e T_e = 10^{15} \text{ cm}^{-3} \text{ K}$, our calculations indicate that the nonthermal radiation would not be significantly attenuated. However, for higher densities of $N_e > 10^{10} \text{ cm}^{-3}$ and $T_e = 2 \times 10^5 \text{ K}$, the optical depth due to thermal absorption could be large enough to screen the nonthermal emission and effectively prevent the transient sources from being detected at the longer wavelengths. For example, the minimum 20 cm detectable flux of a source $5''$ in size during a 60 s integration (10:1 signal-to-noise ratio) at the VLA in the *A* or *B* configuration (synthesized beamwidths $\theta = 1.2''$ and $4.4''$, respectively) is ~ 0.015 SFU and 0.0015 SFU, respectively. This would therefore suggest that nonthermal transient sources originating in regions where $N_e \geq 2 \times 10^{10} \text{ cm}^{-3}$ would not be detectable at this wavelength with the VLA. Finally, as pointed out by Chiuderi Drago and Melozzi (1984), collisions with thermal electrons will decrease the energy of the nonthermal particles, thereby limiting the time that they radiate. For electron velocities of $v \geq 0.5c$ and thermal electron densities of $N_e \geq 10^{10} \text{ cm}^{-3}$, the so-called energy exchange time is less than 6 min, much shorter than the radiative lifetime of about 5 hours in a magnetic field of $H \leq 100 \text{ G}$. Simultaneous observations at several wavelengths of the brightness temperature and lifetimes of transient sources could, therefore, place useful constraints on their emission mechanism and place of origin.

Acknowledgements

The VLA is a facility of the National Radio Astronomy Observatory, which is operated by associated Universities, Inc., under contract with the National Science Foundation. Radio Astronomical studies of the Sun at Tufts University are supported under grant AFOSR-83-0019 with the Air Force Office of Scientific Research and contract N0014-86-K-0068 with the office of Naval Research (ONR). Comparisons of VLA and Solar Maximum Mission (SMM) data are supported by our NASA-SMM Guest Investigator grant NAG5-501.

References

- Akhmedov, Sh. B. *et al.*: 1986, *Astrophys. J.* **310**, 760.
 Athay, R. G., White, O. R., Lites, B. W., and Bruner, E. C.: 1980, *Solar Phys.* **66**, 357.
 Brown, J. C. and Hoyng, P.: 1975, *Astrophys. J.* **200**, 734.
 Bruner, E. C. and Lites, B. W.: 1979, *Astrophys. J.* **228**, 322.
 Cargill, P. J. and Pneuman, G. W.: 1984, *Astrophys. J.* **276**, 369.
 Chiuderi Drago, F. and Melozzi, M.: 1984, *Astron. Astrophys.* **131**, 103.
 Dulk, G. A.: 1985, *Ann. Rev. Astron. Astrophys.* **23**, 169.
 Dulk, G. A. and Marsh, K. A.: 1982, *Astrophys. J.* **259**, 350.
 Habbal, S. H., Ronan, R. S., Withbroe, G. L., Shevgaonkar, R. K., and Kundu, M. R.: 1986, *Astrophys. J.* **306**, 740.

- Karpen, J. T., Oran, E. S., Mariska, J. T., Boris, J. P., and Brueckner, G. E.: 1982, *Astrophys. J.* **261**, 375.
- Komle, N.: 1979, *Solar Phys.* **64**, 213.
- Lang, R. R., Willson, R. F., and Gaizauskas, V.: 1983, *Astrophys. J.* **267**, 455.
- Lites, B. W.: 1981, *Solar Phys.* **71**, 329.
- Martin, S. F., Livi, S. H. B., Wang J., and Shi, Z.: 1985, *NASA Conf. Publ.*, NASA CP-2374, p. 403.
- Porter, J. G., Toomre, J., and Gebbie, K. B.: 1984, *Astrophys. J.* **283**, 879.
- Roussel-Dupr e, R., Wrathall, J., Nicolas, K. R., Bartoe, J. D. F., and Brueckner, G. E.: 1984, *Astrophys. J.* **278**, 428.
- Shevgaonkar, R. K. and Kundu, M. R.: 1984, *Astrophys. J.* **283**, 413.
- Simon, G. W. and Wilson, P. R.: 1985, *Astrophys. J.* **295**, 241.
- Takakura, T. and Kai, K.: 1966, *Publ. Astron. Soc. Japan* **18**, 57.
- Topka, K. and Tarbell, T.: 1983, in S. Keil (ed.), *Small-Scale Dynamical Processes in Quiet Stellar Atmospheres*, Proc. Nat. Soc. Obs. Conf., Sunspot, N.M.: NSO, pp. 278-286.
- Vernazza, J. E., Avrett, E. H., and Loeser, R.: 1981, *Astrophys. J. Suppl.* **45**, 635.
- Vernazza, J. E., Foukal, P. V., Huber, M. C. E., Noyes, R. W., and Reeves, E. M.: 1975, *Astrophys. J.* **199**, L123.
- Webb, D. F., Davis, J. M., Kundu, M. R., and Velusamy, T.: 1983, *Solar Phys.* **85**, 267.
- Willson, R. F. and Lang, K. R.: 1986, *Astrophys. J.* **308**, 443.
- Wilson, P. R. and Simon, G. W.: 1983, *Astrophys. J.* **273**, 805.
- Withbroe, G. L. and Noyes, R. G.: 1977, *Ann. Rev. Astron. Astrophys.* **15**, 363.

H. VLA OBSERVATIONS OF A SOLAR NOISE STORM

KENNETH R. LANG AND ROBERT F. WILLSON
Department of Physics and Astronomy, Tufts University
Received 1986 October 6; accepted 1987 January 21

ABSTRACT

We present the first Very Large Array (VLA) observations of the Sun at 92 cm wavelength (328 MHz). A solar noise storm, which lasted at least 3 hr, was detected at this wavelength; it consisted of burstlike spikes superposed on a slowly varying background, and both storm components were $95\% \pm 5\%$ right-hand circularly polarized. A long-duration soft X-ray event preceded the radio radiation by 30 minutes, suggesting a disturbance moving outward at a velocity of $v = 78 \text{ km s}^{-1}$. The 92 cm noise storm was resolved with an angular resolution of $9''$ for time intervals as short as 13 s. During the onset and early phases, the storm consisted of four compact sources, each with an angular diameter of $40''$, oriented within an elongated source with angular dimensions of $40'' \times 200''$. During the subsequent hour the most intense emission was located in two $40''$ sources separated by $100''$. Snapshot maps revealed a persistent elongated source at successive peaks, with a scatter in the source position. A systematic position shift of $\Delta\theta, \geq 15''$ can be produced by Earth's ionosphere, but these effects can be removed by frequent observations of a nearby calibrator source. Our observations confirm previously reported trends for a decrease in source size at higher frequencies, but they suggest a hitherto unresolved complexity in source structure. The new VLA results are also consistent with previous observations of noise storm polarization and height. The VLA can potentially resolve both the burst and continuum components of noise storms, while also detecting the effects of anisotropic scattering in the corona. The high angular resolution and large collecting area of the VLA may either lead to the detection of the second harmonic of the storm plasma frequency or establish important limits to it.

Subject headings: interferometry — polarization — Sun: corona — Sun: radio radiation

I. INTRODUCTION

Noise storms are the most common phenomenon observed on the Sun at decimetric and metric wavelengths (see Elgaroy [1977] and Kai, Melrose, and Suzuki [1985] for reviews). Here we will present a brief synopsis of their properties, thereby providing a perspective for our subsequent observations and discussion.

The noise storms consist of a slowly varying, wide-band continuum radiation with superposed short-lived, narrow-band bursts. The background continuum, which is usually observed between 50 and 350 MHz, normally continues for a few hours and sometimes lasts for days. The noise storms are clearly associated with solar active regions, but there is no clear-cut association with solar flares.

Literally thousands of storm bursts are emitted, each with a bandwidth between 2 and 10 MHz and a duration of 0.1 to 2 s. These bursts have been designated type I bursts in order to distinguish them from other types of solar bursts. They are superposed upon a continuum that is not thought to be composed of numerous bursts.

Both the background continuum and the bursts are strongly circularly polarized (up to 100%), usually with the same sense and degree of polarization. This polarization is attributed to coronal magnetic fields that connect with underlying sunspots. The sense of circular polarization usually corresponds to the ordinary mode of wave propagation in the magnetic field of the nearest leading spot; right-handed circular polarization therefore corresponds to negative magnetic polarity with the magnetic field lines pointed in toward the Sun.

It is thought that noise storms are some kind of plasma radiation emitted at the plasma frequency, and this is consistent with circular polarization in the ordinary mode. The emission originates in the lower solar corona at altitudes of

between 0.1 and $0.5 R_{\odot}$ (solar radii) above the photosphere. Radiation at lower frequencies originates at higher altitudes where the electron density and plasma frequency are smaller than those at lower altitudes. The inferred electron density at a given altitude is greater than that of the quiet corona at this altitude, suggesting an origin in closed magnetic loops (coronal loops) that contain a high-density plasma.

II. OBSERVATIONS

a) Time Profile

The VLA was used to observe the solar active region AR 4732 in the A-configuration between 1300 UT and 2400 UT on 1986 May 29. The position of AR 4732 was 0N 40W on this day. The array was divided into two subarrays with 12 antennas operating at 92 cm wavelength (328 MHz) with a 3.12 MHz bandwidth, and 15 antennas operating at 21 cm wavelength (1420 MHz) with a 12.5 MHz bandwidth. The beamwidth of the individual antennas at 21 cm was $31.5''$ and included the active region AR 4731 located at 6S 50W at 1300 UT on May 29. The individual antennas had beamwidths of $138''$ at 92 cm, which includes the entire visible disk of the Sun, but AR 4731 and AR 4732 were the only active regions on the visible solar surface during our observations.

All four Stokes parameters were sampled every 6.67 s, and the data were calibrated by observing 3C 84 every 30 minutes. The flux density of 3C 84 was assumed to be 32.0 Jy and 8.0 Jy at 21 cm and 92 cm, respectively.

As illustrated in Figure 1, a noise storm was detected at 92 cm between about 1930 UT and 2400 UT. No noise storm was detected at 21 cm, but this is not surprising as plasma radiation at this wavelength would be absorbed in the overlying solar atmosphere. The 92 cm noise storm consisted of numerous burstlike spikes superposed on slowly varying emission.

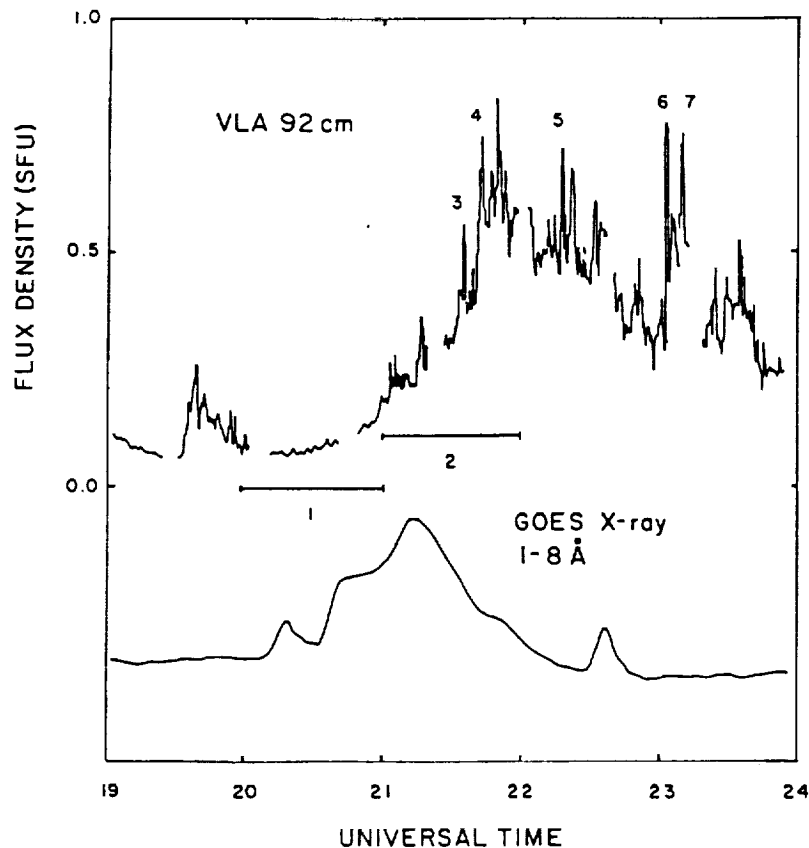


FIG. 1.—The time profile of a solar noise storm observed with one interferometer pair of the Very Large Array (VLA) at 92 cm wavelength (*top*) is compared with the soft X-ray emission detected by the *GOES* satellite (*bottom*). The separation of the two antennas was 0.8 km, providing an angular resolution of $240''$ at 92 cm during source transit. Here the data have been smoothed over 33.3 s. Spikelike bursts are superposed upon a slowly varying background: both of these components were $95\% \pm 5\%$ right-hand circularly polarized. VLA maps covering the intervals denoted by 1 and 2 are shown in Fig. 2, and VLA snapshot maps of the spikes denoted by 3, 4, 5, 6, and 7 are presented in Fig. 3. The X-ray emission precedes the 92 cm radiation by about 30 minutes. If we assume that the noise storm is excited by a disturbance that originates during the soft X-ray event at a distance of $0.2 R_{\odot}$, then that disturbance must travel outward at a velocity of $v \sim 78 \text{ km s}^{-1}$.

The burstlike spikes are analogous to type I bursts, but the observed data have relatively long integration times that probably integrate the emission of several type I bursts or chains of bursts. The slowly varying emission resembles the background continuum of a typical noise storm. Both the burstlike spikes and the slowly varying background emission were $95\% \pm 5\%$ right-hand circularly polarized.

A long-duration soft X-ray event (also shown in Fig. 1) may provide a clue to the triggering mechanism for the 92 cm noise storm that followed it by about 30 minutes. The noise storm may have been triggered by a disturbance moving outward from the source of the X-ray radiation. If the sources of radiation in the two spectral regions are separated by a distance of $0.2 R_{\odot}$, then the disturbance moves at a velocity of $v = 78 \text{ km s}^{-1}$.

b) Observations with High Angular Resolution

The VLA can provide angular resolutions that are more than an order of magnitude better than those of previous observations of solar noise storms. It is capable of $5''$ angular resolution at 92 cm wavelength (328 MHz). By way of comparison, the Culgoora and Nançay radioheliographs had respective beamwidths of ~ 2.0 and ~ 1.3 at 160 MHz.

As illustrated in Figure 2, the onset and first maximum of the 92 cm noise storm consisted of four compact sources, each about $40''$ in angular diameter, that were arranged within an

elongated $40'' \times 200''$ source. During the subsequent hour, the 92 cm emission was concentrated within the same elongated source, but it was most intense in two $40''$ sources separated by $100''$. For comparison, the tapered beamwidth of $9'' \times 9''$ is shown as a small black dot.

The VLA also has the capability of making snapshot maps at time intervals as short as 3 s. As an example, Figure 3 shows VLA snapshot maps of successive peaks in the emission of the 92 cm noise storm shown in Figure 1 (peaks 3, 4, 5, 6, and 7). These peaks originate in an elongated source that has a persistent, unchanging shape with half-power angular dimensions of about $40'' \times 120''$. The scatter in the locations of the most intensive emission is real, but there were no apparent trends in the location change.

Refraction in Earth's ionosphere will produce a systematic shift in source position. This shift is smallest at source transit and largest near the horizon. It is also relatively large at sunrise and at times of increased solar activity.

When theoretical formulae given by Komesaroff (1960) are combined with measurements of the ionosphere's electron density, Stewart and McLean (1982) obtain a noontime ionospheric shift of $\Delta\theta_r = 60''$ at 160 MHz. Because refraction scales as the inverse square of the observing frequency, we would expect $\Delta\theta_r = 15''$ at 92 cm (328 MHz). This is consistent with the observations of Erickson (1984) at 80 MHz and with those of Spoelstra (1983) at 600 MHz. The systematic position

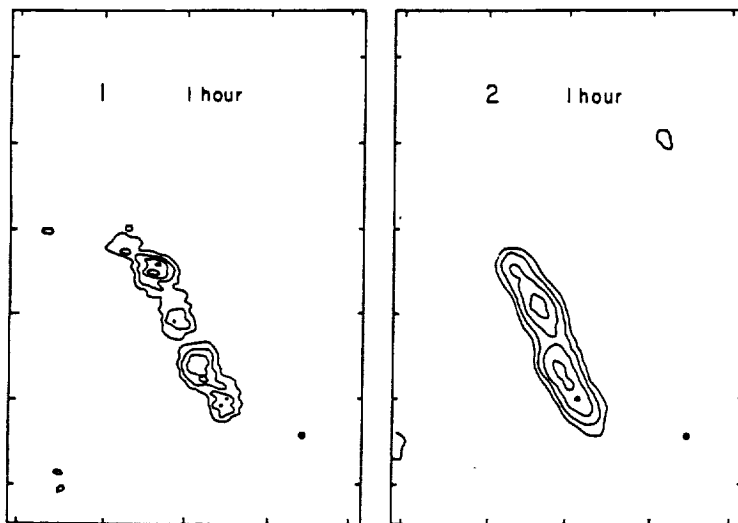


FIG. 2.—Very Large Array (VLA) synthesis maps for a 1 hr interval that includes the beginning of a solar noise storm (*left*) and for the subsequent 1 hr interval (*right*). These two intervals are respectively denoted by 1 and 2 in Fig. 1. Both the onset and early excitation of the 92 cm noise storm consist of four sources with angular diameters of $40''$ and a total angular extent of $200''$. Emission in the two central $40''$ sources became more intense later in the noise storm (see Fig. 3). The fiducial marks on the axes are separated by $100''$, and the contours mark levels of equal brightness temperature T_b , with an outermost contour of $T_b = 1.0 \times 10^6$ K and a contour interval of 7.2×10^5 K. The synthesized beamwidth is denoted by the black spot.

shift, $\Delta\theta$, can be automatically removed from future VLA data by frequent observations of a nearby calibrator source, but a smaller, random shift should remain because of the fluctuating component of the ionosphere's electron density.

III. DISCUSSION

a) Comparisons with Previous Results

Observations of noise storms with the Culgoora radioheliograph at two frequencies (80 and 160 MHz) and with the Clark Lake facility at several frequencies between 20 and 65 MHz suggest that the higher frequency radiation originates in more compact sources (Gergely and Kundu 1975; Stewart 1976; McLean 1981). This downward trend in source size with increasing frequency was also suggested by a small sample of storm sources observed with the Culgoora instrument at 80, 160, and 327 MHz (Sheridan *et al.* 1983). Characteristic half-power angular sizes of $\theta \sim 6'$, $3'$, and $1.5'$ were respectively obtained at 80, 160, and 327 MHz.

However, storm sources are also often unresolved with even the largest radio telescopes, and the telescope beamwidths exhibit a disturbingly similar downward trend with increasing frequency. There have been no systematic high-resolution investigations of the size and shape of solar noise storms because of the poor resolving power of the existing radio telescopes.

Although the new VLA observations are not inconsistent with previous observations of a decrease in source size at higher frequencies, they do suggest that complex source structure will be revealed at high resolution. Such complexity may well rule out a simple model in which noise storms originate within a conical column (diverging magnetic fields) whose size increases with height (McLean 1973, 1981).

The new VLA results are also consistent with previous polarization observations. The sense of circular polarization should correspond with that of the ordinary mode expected from plasma radiation in a strong magnetic field (Dulk and Nelson 1973; Stewart 1985). Right-handed circular polariz-

ation is therefore associated with negative magnetic polarity in which the magnetic field is directed away from the observer and into the Sun. Left-handed circular polarization is similarly associated with positive magnetic polarity in which the magnetic field is directed toward the observer.

Because our observed storm was $95\% \pm 5\%$ right-hand circularly polarized, it should originate in coronal magnetic fields that are connected with the dark, negative-polarity magnetogram features shown in Figure 4. Because the noise storm projects radially downward to the more central active region (AR 4732), the storm source is most likely associated with magnetic fields that connect to the dark, dominant leading spot of AR 4732. As a matter of fact, noise storms are usually related to the dominant, leading sunspot of the associated active region.

Thus the storm source is most likely plasma radiation on magnetic fields connected to the dark, leading spot of AR 4372. As illustrated in Figure 4, the angular size and distance of the noise storm are nevertheless larger than the angular separation of the leading and trailing spots of AR 4372. If the storm originates in closed magnetic loops, they may not be solely connected to the bipolar AR 4372. Large-scale magnetic fields may instead connect the leading spots of the two active regions AR 4371 and AR 4372. A similar model has been proposed by Kai and Sheridan (1974) for other noise storms. However, our observations cannot by themselves rule out the possibility of open magnetic field lines that extend out into the interplanetary medium.

The height of a noise storm can be found if we assume that it lies radially above the associated sunspot. Under this assumption, the average observed heights, h , at 160 MHz and 80 MHz were $h = 0.4 R_\odot$ and $h = 0.8 R_\odot$ above the photosphere (Stewart 1976). Noise storms at the higher frequencies of 327 MHz and 408 MHz have estimated heights of $h = 0.2 R_\odot$ and $h = 0.1 R_\odot$, respectively (Sheridan *et al.* 1983; Clavelier 1967).

Thus the average height of the noise storm source decreases with increasing frequency. Our observations also support this conclusion. The angular displacement of the noise storm from

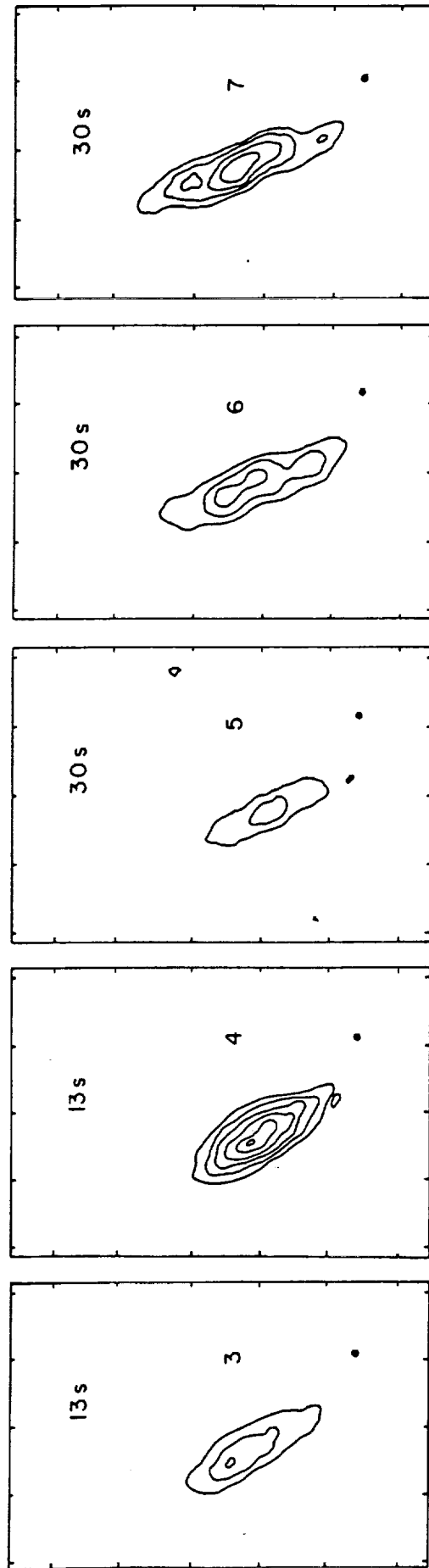


FIG. 3.—Very Large Array snapshot maps of successive peaks in a solar noise storm at 92 cm wavelength. These peaks are denoted by 3, 4, 5, 6, and 7 in Fig. 1. The snapshot maps, each lasting 13 s or 30 s, show no substantial change in the shape or size of the storm source over a period of 2 hr. Here the synthesized beamwidth is denoted by the black dot, and the fiducial marks on the axes are separated by 100". The contours mark levels of equal brightness temperature, T_b , with an outermost contour of $T_b = 3.8 \times 10^6$ K, a contour interval of 2.5×10^6 K, and a peak brightness temperature of $T_{b,p} = 1.6 \times 10^7$ K.

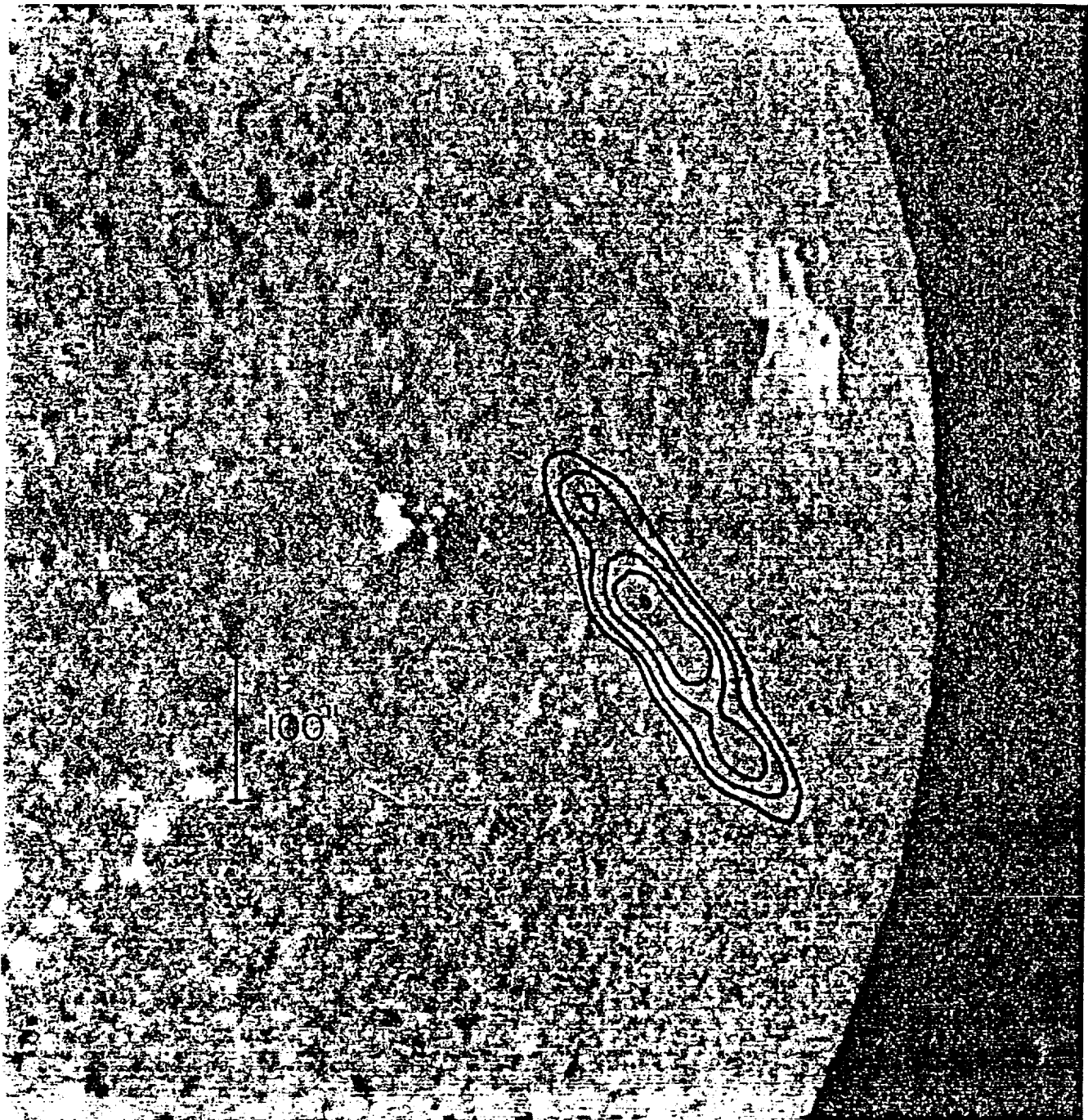


FIG. 4—A Very Large Array (VLA) synthesis map of a solar noise storm at 92 cm wavelength is superposed on a Kitt Peak National Observatory (KPNO) magnetogram taken on the same day. The VLA map covered the 1 hr time interval between 2300 and 2400 UT; its synthesized beamwidth is denoted by the black spot. The contours mark levels of equal brightness temperature, T_b , with an outermost contour of $T_b = 1.0 \times 10^6$ K and a contour interval of 7.2×10^5 K. Dark areas on the magnetogram correspond to negative magnetic polarity with the magnetic field lines pointing in toward the Sun, whereas light magnetogram areas correspond to outward regions of positive magnetic polarity. Two dipolar regions are shown on the magnetogram—AR 4731 near the limb and AR 4732. The 92 cm source is attributed to plasma radiation in the ordinary mode of wave propagation along magnetic field lines connected to the dark negative spot of AR 4732. The angular displacement between this spot and the 92 cm source corresponds to radial altitude of about $0.2 R_\odot$ above the photosphere. The magnetogram was kindly provided by Jack Harvey of the National Solar Observatory.

its associated spot is $\Delta\theta = 2.3$ (when corrected for ionospheric refraction), and this displacement corresponds to a radial height of $h = 1.0 \pm 0.2 \times 10^{10}$ cm $= 0.15 \pm 0.03 R_{\odot}$.

At our observing frequency of $\nu = 328$ MHz, we infer an electron density of $N_e = 1.4 \times 10^9$ cm $^{-3}$ for the height $h = 1.0 \times 10^{10}$ cm from the condition that $\nu = \nu_p$, where the plasma frequency $\nu_p = 8.9 \times 10^3 N_e^{1/2}$ Hz. The plasma radiation will dominate over thermal cyclotron radiation when $\nu = \nu_p \gg \nu_H$, where the gyrofrequency $\nu_H = 2.8 \times 10^6 H$ Hz and H is the magnetic field strength in gauss. Thus, we have $H \ll 100$ G in the storm source at a height of $h = 1.0 \times 10^{10}$ cm above the photosphere. The condition for suppression of the extraordinary mode of wave propagation, with the resultant escape of the ordinary mode, similarly requires $H \ll 100$ G at this height.

b) Future VLA Potential

The VLA can potentially resolve noise storm sources with an angular resolution of $5''$ at 92 cm wavelength. Snapshot synthesis maps can be made with this resolution for intervals as short as 3 s, which is comparable to the duration of chains of type I bursts. The observing bandwidth, $\Delta\nu$, can be comparable to that of type I bursts ($\Delta\nu \sim 6$ MHz), and an improvement in VLA integration time to 0.1 s would permit observations of individual type I bursts.

As illustrated in § II, the VLA has already been used to resolve noise storm sources with an angular diameter of $40''$. This diameter corresponds to a linear size, L , of $L = 3 \times 10^9$ cm at the Sun's distance. Waves moving at the velocity of light would cross this dimension in a time, $\tau = 0.1$ s. Because nothing can move faster than the velocity of light, the duration, τ , of a source with this dimension must be $\tau \geq 0.1$ s. The observed limit to the duration of individual type I bursts is also $\tau \geq 0.1$ s (Elgaroy 1977). The VLA resolution of $5''$ therefore seems to be fully capable of resolving the type I burst emitters.

The VLA can probably distinguish between the two principal components of noise storms, thereby resolving the sources of type I bursts and the background continuum for the first time. Future VLA observations will therefore probably determine if the two sources have comparable or different sizes, and if one of them resides within the other.

The VLA can also potentially detect the effects of scattering on field-aligned density inhomogeneities. This anisotropic scattering was first proposed to reconcile the narrow bandwidths and apparently large sizes of some type I bursts at 169 MHz (Bougeret and Steinberg 1977). As illustrated in § II, the 92 cm (328 MHz) VLA observations have resolved elongated sources that were predicted by the scattering theory.

Both the fundamental and the second harmonic of the plasma frequency might be detected if an intense noise storm is observed with both the VLA and a smaller patrol-type solar radio telescope. The fundamental plasma radiation is all that has been previously observed, primarily because of the low brightness temperature of the harmonic. The large collecting area and high angular resolution of the VLA will vastly improve detection thresholds. For instance, observations at twice the frequency of strong type I bursts indicate that the flux of the associated second harmonic emission is less than 0.001 of the fundamental (Jaeggi and Benz 1982). Future VLA observations should improve this limit by more than an order of magnitude, or else detect the second harmonic, thereby providing important constraints to theoretical explanations of noise storms (see Benz and Wentzel 1981).

We thank the staff of the Very Large Array and, in particular, Durga Bagri and Ray Gonzalez, for help with the observations. Radio astronomical studies of the Sun at Tufts University are supported under grant AFOSR-83-0019 with the Air Force Office of Scientific Research and contract N00014-86-K-0068 with the Office of Naval Research (ONR). Our simultaneous VLA and *Solar Maximum Mission (SMM)* observations of the Sun are supported by NASA grant NAG 5-501. Collaborative long-wavelength solar observations by Tufts University and the Observatoire de Paris are supported by National Science Foundation (NSF) grant INT-8602285 and Centre National de la Recherche Scientifique grant 920038. The Very Large Array is operated by Associated Universities, Inc., under contract with the National Science Foundation.

REFERENCES

- Benz, A. O., and Wentzel, D. G. 1981, *Astr. Ap.*, **94**, 100.
 Bougeret, J. L., and Steinberg, J. L. 1977, *Astr. Ap.*, **61**, 777.
 Clavelier, B. 1967, *Ann. d'Ap.*, **30**, 895.
 Dulk, G. A., and Nelson, G. J. 1973, *Proc. Astr. Soc. Australia*, **2**, 211.
 Elgaroy, O. 1977, *Solar Noise Storms* (New York: Pergamon Press).
 Erickson, W. C. 1984, *J. Ap. Astr.*, **5**, 55.
 Gergely, T. E., and Kundu, M. R. 1975, *Solar Phys.*, **41**, 163.
 Jaeggi, M., and Benz, A. O. 1982, *Astr. Ap.*, **107**, 88.
 Kai, K., Melrose, D. B., and Suzuki, S., 1985, in *Solar Radiophysics*, ed. D. J. McLean and N. R. Labrum (New York: Cambridge University Press), p. 415.
 Kai, K., and Sheridan, K. V. 1974, *Solar Phys.*, **35**, 181.
 Komesaroff, M. M. 1960, *Australian J. Phys.*, **13**, 153.
 McLean, D. J. 1973, *Proc. Astr. Soc. Australia*, **2**, 222.
 ———. 1981, *Proc. Astr. Soc. Australia*, **4**, 132.
 Sheridan, K. V., Labrum, N. R., Payten, W. J., Nelson, G. J., and Hill, E. R. 1983, *Solar Phys.*, **83**, 167.
 Spoelstra, T. A. T. 1983, *Astr. Ap.*, **120**, 313.
 Stewart, R. T. 1976, *Solar Phys.*, **50**, 437.
 ———. 1985, *Solar Phys.*, **96**, 381.
 Stewart, R. T., and McLean, D. J. 1982, *Proc. Astr. Soc. Australia*, **4**, 386.

KENNETH R. LANG and ROBERT F. WILLSON: Department of Physics and Astronomy, Robinson Hall, Tufts University, Medford, MA 02155

I. SIMULTANEOUS SMM FLAT CRYSTAL SPECTROMETER AND VERY LARGE ARRAY OBSERVATIONS OF SOLAR ACTIVE REGIONS

KENNETH R. LANG AND ROBERT F. WILLSON
Department of Physics and Astronomy, Tufts University

AND

KERMIT L. SMITH AND KEITH T. STRONG
Lockheed Palo Alto Research Laboratory
Received 1987 January 27; accepted 1987 May 4

ABSTRACT

We compare high-resolution images of the quiescent emission from two solar active regions at 20 cm (VLA) and soft X-ray (SMM FCS) wavelengths. There are regions where the X-ray coronal loops have been completely imaged at 20 cm wavelength. In other regions, the X-ray radiation was detected without detectable 20 cm radiation, and vice versa. The X-ray data were used to infer average electron temperatures, T_e , of about 3×10^6 K and average electron densities of about $2.5 \times 10^9 \text{ cm}^{-3}$ for the X-ray emitting plasma in the two active regions. The thermal bremsstrahlung of the X-ray emitting plasma is optically thin at 20 cm wavelength. The 20 cm brightness temperatures, T_B , were always less than T_e , which is consistent with optically thin bremsstrahlung. However, the thermal gyroresonance radiation from the X-ray emitting plasma ought to be optically thick at 20 cm wavelength. The low T_B can then be explained if a higher, cooler plasma covers the hotter X-ray emitting plasma. Thermal gyroresonance radiation must account for the intense 20 cm radiation near and above sunspots where no X-ray radiation is detected. The potential of 20 cm (VLA) and soft X-ray (SMM FCS) comparisons is discussed.

Subject headings: radiation mechanisms — Sun: corona — Sun: radio radiation — Sun: X-rays

1. INTRODUCTION

High-resolution observations with X-ray telescopes orbiting above the atmosphere have transformed our understanding of the solar corona. The corona is now viewed as a highly inhomogeneous distribution of closed magnetic loops that are anchored in the Sun, and open magnetic fields that extend out into interplanetary space (see Vaiana and Rosner [1978] for a review). The hot, dense plasma that is trapped within coronal loops gives rise to intense X-ray radiation, and observations of X-ray spectral lines can be used to infer the electron temperature, electron density, and emission measure of this plasma.

The development of aperture synthesis telescopes like the Very Large Array (VLA) has permitted ground-based microwave observations of the solar corona with angular resolutions that are comparable to those of X-ray telescopes. The high-resolution microwave observations can uniquely specify the strength and structure of the coronal magnetic field. VLA synthesis maps of the total intensity, I , describe the two-dimensional distribution of source brightness, whereas synthesis maps of circular polarization, or Stokes parameter V , can provide information about the coronal magnetic field (see Kundu and Lang [1985] for a review).

The microwave brightness temperature, T_B , of the quiescent, or nonflaring, corona is nearly equal to the coronal electron temperature, T_e , with $T_B \approx T_e \approx 10^6$ K. This suggests that the quiescent microwave emission is thermal. However, there are two possible thermal radiation mechanisms. They are thermal bremsstrahlung, or free-free emission, and thermal gyroresonance radiation, or cyclotron emission. In contrast, the quiescent X-ray emission of the solar corona is mainly due to thermal bremsstrahlung.

To identify the dominant thermal radiation mechanism at microwave wavelengths, one needs to know the electron temperature, the electron density and the magnetic field strength, as well as the thickness of the radiating layer, the scale length of the magnetic field, and the angle between the line of sight and the magnetic field. Thermal gyroresonance will generally dominate radiation at centimeter wavelengths when the electron density is relatively low and the magnetic field is strong.

Early evidence for thermal gyroresonance radiation at coronal levels above sunspots was provided by comparison of the soft X-ray and centimeter-wavelength radiation of active regions (Kundu, Schmahl, and Gerassimenko 1980; Pallavicini, Sakurai, and Vaiana 1981). Bright microwave radiation was found in the strong magnetic fields above sunspots, but the X-ray observations indicated a relatively low electron density in these regions. This meant that the high microwave brightness temperatures above sunspots could not be due to thermal bremsstrahlung, but it could be explained by thermal gyroresonant radiation at the second or third harmonic of the gyrofrequency.

These early low-resolution comparisons were fully confirmed when high-resolution synthesis maps at 6 cm wavelength were compared with simultaneous soft X-ray images obtained with the X-ray polychromator (XRP) aboard the *Solar Maximum Mission* (SMM) satellite (Chiuderi-Drago *et al.* 1982; Schmahl *et al.* 1982; Shibasaki *et al.* 1983; Strong, Alissandrakis, and Kundu 1984). Soft X-ray spectral lines were used to determine the electron temperature and electron density of the X-ray emitting plasma that coincided with the sunspot-associated 6 cm sources. These parameters were then used to compute the bremsstrahlung brightness temperature at 6 cm. Because the computed value was much less than the

observed brightness temperature, additional 6 cm opacity due to gyroresonance absorption above sunspots was required.

Thermal gyroresonance radiation at 6 cm in coronal regions above sunspots was additionally confirmed by the detection of circularly polarized ring-shaped or horseshoe-shaped structures (Alissandrakis and Kundu 1982; Lang and Willson 1982). The highly polarized (up to 100%) structures were predicted by the theory of cyclotron radiation in the curved magnetic fields above sunspots (Gel'freikh and Lubyshev 1979). Depressions in the 6 cm brightness temperature above sunspot umbrae have been attributed to cool material in these regions (Strong, Alissandrakis, and Kundu 1984).

What about the microwave counterpart of the intense X-ray sources? The brightest 6 cm sources are not usually associated with the brightest X-ray sources, and the detailed correspondence between the radiation at the two wavelengths is poor (Schmahl *et al.* 1982; Webb *et al.* 1983). However, this result is not particularly surprising. It would be expected if the dominant radiation mechanisms are different in the two wavelength domains. Thermal bremsstrahlung is often too optically thin to be detected at 6 cm wavelength where gyroresonant radiation dominates. Different structures are observed at the two wavelengths because 6 cm gyroresonance absorption occurs in the strong magnetic fields above sunspots, while the X-ray emission originates in coronal loops that stretch between sunspots of opposite magnetic polarity.

The hot temperatures, slow evolution, and long lifetime of X-ray coronal loops make them ideal candidates for aperture synthesis techniques. Of course, low-lying loops have occasionally been detected at 6 cm (Strong, Alissandrakis and Kundu 1984; Webb *et al.* 1987), but radiation at this wavelength originates at relatively low heights and is usually dominated by gyroresonance absorption. Higher levels are observed at 20 cm wavelength where the thermal bremsstrahlung of coronal loops can become optically thick. In fact, when VLA observations were extended to the longer 20 cm wavelength, quiescent looplike coronal features were discovered (Lang, Willson, and Rayrole 1982).

The coronal loops seen at 20 cm strongly resemble their X-ray counterparts (Lang and Willson 1983, 1984). They have million-degree temperatures and stretch across regions of opposite magnetic polarity in the underlying photosphere. The size and shape of the loops observed at 20 cm are also similar to those of arcades of X-ray coronal loops, with linear extents $L \approx 10^9$ – 10^{10} cm. In addition, the electron temperature and electron density inferred from X-ray observations of other loops are consistent with the idea that the microwave loops are due to thermal radiation from the X-ray emitting plasma. All of these similarities suggest that the microwave counterpart of X-ray coronal loops can be observed in VLA synthesis maps at 20 cm.

Numerous authors have now identified elongated, looplike features at 20 cm with coronal loops, but the exact radiation mechanism for the 20 cm emission remains controversial. Many authors have attributed this radiation to the optically thick thermal bremsstrahlung of a hot, dense plasma trapped within coronal magnetic loops that connect with underlying sunspots (Lang, Willson, and Rayrole 1982; Dulk and Gary 1983; Lang, Willson, and Gaizauskas 1983; Lang and Willson 1983, 1984; Gary and Hurford 1987; Holman 1986). Others reason that optically thick thermal gyroresonance radiation may dominate the 20 cm emission of coronal loops (McConnell and Kundu 1983; Shevgaonkar and Kundu 1984;

Lang *et al.* 1987). Both radiation mechanisms could play a role, with gyroresonance radiation becoming important at relatively high brightness temperatures or relatively low electron densities.

One can distinguish between the two thermal radiation mechanisms for the 20 cm emission from the coronal loops if the VLA synthesis maps are compared with simultaneous X-ray images. This has been done only twice. Chiuderi-Drago *et al.* (1982) used X-ray spectral lines from the *SMM* FCS to infer the electron temperature and emission measure of the X-ray emitting plasma, concluding that one 20 cm source is the optically thin bremsstrahlung of this plasma. The angular extent of the X-ray source was comparable to that of the 20 cm one, but the observations at both wavelengths were of relatively poor angular resolution. Another sunspot-associated 20 cm source had to be attributed to gyroresonance radiation, for there was no detectable X-ray radiation from this region. Webb *et al.* (1987) used X-ray data taken during a recent rocket flight to conclude that one of several 20 cm features was due to optically thick thermal bremsstrahlung associated with X-ray coronal loops. They noticed that the 20 cm radiation was concentrated at the tops of the X-ray loops and attributed this apparent concentration to absorption in a cool external plasma. However, such a concentration was not apparent in the data of Chiuderi-Drago *et al.* (1982).

In this paper, we present comparisons of high-resolution 20 cm maps from the VLA with simultaneous X-ray images from the *SMM* FCS. These comparisons are given in § II. In one instance, all of the X-ray emitting plasma was detected at 20 cm, and additional 20 cm emission was observed near sunspots where no X-ray radiation was detected. However, the 20 cm radiation was concentrated at the apex of the more extensive X-ray coronal loops of another active region. In § III, we discuss the absorption and radiation mechanisms for coronal loops at 20 cm. We next use X-ray measurements of electron temperature and electron density to place constraints on these mechanisms. The observed 20 cm features are then explained. Our results are summarized in § IV, where we also discuss the potential of future 20 cm (VLA) and soft X-ray (*SMM* FCS) comparisons.

II. OBSERVATIONS

We have used the VLA and the *SMM* FCS to observe solar active regions AR 4508 and AR 4532 on 1984 June 4 and 1984 July 8, respectively. The VLA was in the C-configuration on June 4 and in the hybrid C-D-configuration on July 8. In both instances, the signal wavelength was 20.7 cm (1446 MHz) and the bandwidths were 12.5 MHz. Active region AR 4508 was observed with the VLA between 1500 UT and 2300 UT on June 4; its position on the solar surface was 06° N and 57° E at 1300 UT on this day. Active region AR 4532 was observed between 1800 UT and 2300 UT on July 8; its position on the solar surface was 07° S and 18° E on this day. The flat crystal spectrometer (FCS) observed six prominent soft X-ray lines: OV III at 18.9 Å, Ne IX at 13.4 Å, Mg XI at 9.2 Å, Si XIII at 6.7 Å, S XV at 5.0 Å, and Fe XXV at 1.9 Å. The FCS observed AR 4508 and AR 4532 throughout the time the VLA was observing these regions.

The half-power beamwidth of the individual VLA antennas was about 30' at 20 cm wavelength, and the synthesized maps constructed from up to 325 interferometer pairs had beamwidths of 12'6 × 15'5 in the C-configuration and 12'6 × 36'0

in the C-D-configuration. The June 4 data were calibrated by 5 minute observations of the calibrator source PKS 0528 + 134 every 35 minutes, while the July 8 data were similarly calibrated with the source PKS 0742 + 103. The flux densities of PKS 0528 + 134 and PKS 0742 + 103 were 1.5 Jy and 3.3 Jy at 1446 MHz, respectively. The calibrated data for the entire observing period were used together with the standard CLEAN procedure to make synthesis maps of both the total intensity, I , and the circular polarization, or Stokes parameter, V . No solar bursts or flares were observed, and the synthesis maps therefore refer to the quiescent, or nonflaring, radio emission. That is, plots of the visibility data exhibited no variations that could be attributed to solar activity. There was no detectable circular polarization ($V/I \leq 15\%$) for both active regions.

The 14" collimated field of view of the FCS was rastered over a 7' x 7' field of view on June 4 and over a 4' x 4' field of view on July 8; in each case the pixel spacing was 10" x 10". X-ray images were obtained for each of the six spectral lines during the orbital day at a cadence of 410 s. All of the available data for each spectral line were then summed and averaged during each orbit to improve the statistical uncertainty on the count rate from each pixel. Significant emission was only detected from the three softest channels—O VIII, Ne IX, and Mg XI. The peak formation temperatures for these lines are 3×10^6 K, 4×10^6 K, and 7×10^6 K, respectively. The failure to detect emission in the harder, more energetic, channels indicates that the active regions were unperturbed by flaring activity during the periods of observation. The SMM bent crystal spectrometer (BCS) confirmed the absence of flares as no significant brightenings were observed in its Ca XIX channel during these observations.

The XRP also produced a white-light image that showed the sunspots, making it possible to align the X-ray images with the sunspots to an accuracy of 10". The VLA maps of the total intensity, I , at 20 cm were aligned with H α photographs of the same sunspots with a similar 10" accuracy. This enabled us to compare the soft X-ray and 20 cm data with the same field of view and angular scale. The 20 cm radiation of AR 4508 is concentrated in the central regions of a more extensive system of X-ray loops (Fig. 1). In this instance, the 20 cm radiation was aligned along the magnetic neutral line (Fig. 2). There is a sharp drop in the intensity of the radio emission along the edges of the magnetic neutral line where there ought to be a sharp gradient in the magnetic field strength.

However, all of the X-ray emitting plasma of AR 4532 was detected at 20 cm, and additional 20 cm emission was observed near and above sunspots where no X-ray radiation was detected. Intense X-ray radiation and intense 20 cm radiation were detected from coronal loops or arcades of loops that are connected with underlying sunspots (Fig. 3). These loops were about 60" across or about 5×10^9 cm in linear extent. Both X-ray and 20 cm radiation were also emitted from regions of bright plage. In addition, Lang *et al.* (1987) presented simultaneous FCS-VLA data in which an entire system of X-ray loops was completely imaged at 20 cm.

Thus, the same coronal loops are often detected at both 20 cm and X-ray wavelengths, with extra information at 20 cm near and above sunspots. Of course, the 20 cm coronal loops can also be limited to a smaller volume than their X-ray counterparts, but our FCS-VLA comparisons and other VLA observations suggest that this is not usually the case. We will now turn our attention to the absorption and radiation mechanisms that account for the 20 cm coronal loops.

III. DISCUSSION

Because the microwave brightness temperature, T_B , of the quiescent coronal loops is nearly equal to the electron temperature, T_e , the quiescent radiation from 20 cm loops is most likely thermal. The two possible thermal radiation mechanisms at 20 cm wavelength are thermal bremsstrahlung, or free-free emission, and thermal gyroresonance radiation, or cyclotron emission. In order to identify the dominant thermal radiation mechanism at 20 cm wavelength, we will evaluate the electron temperature, T_e , and the electron density, N_e , using the X-ray radiation that is attributed to thermal bremsstrahlung alone.

As previously mentioned, the active regions were so quiescent that they were only detectable in the three softest X-ray channels (O VIII, Ne IX, and Mg XI). Because the O VIII to Ne IX line intensity ratio is insensitive to temperature variations over the range typical of solar active regions, the ratios of the other two lines (O VIII to Mg XI and Ne IX to Mg XI) were used as temperature diagnostics. The temperatures inferred from the two ratios were averaged to obtain our estimate for the electron temperature.

An emission measure was inferred from the temperatures and the observed X-ray fluxes. The electron density was then calculated using a volume of 3×10^{27} cm³, which equals the product of the FCS pixel area and a typical soft X-ray scale height of 3×10^9 cm.

The mean electron temperatures, T_e , and electron densities, N_e , for AR 4508 were determined for the areas marked A, B, and C in Figure 4. These parameters are given in Table 1 together with the maximum observed brightness temperature, T_B , at 20 cm wavelength and the optical depth $\tau = T_B/T_e$. The mean T_e and N_e for AR 4532 were similarly inferred for the areas marked A, B, C, D, E, and F in Figure 5; they are given in Table 2 together with the relevant T_B and τ .

The mean values for different areas were then combined to give average values of $T_e = 3.0 \pm 0.2 \times 10^6$ K and $N_e = 2.7 \pm 0.3 \times 10^9$ cm⁻³ for AR 4508 and $T_e = 3.0 \pm 0.1 \times 10^6$ K and $N_e = 2.4 \pm 0.4 \times 10^9$ cm⁻³ for AR 4532. Here the uncertainties correspond to the standard deviation of the line ratios. These values of T_e and N_e are typical values for quiescent coronal loops in active regions.

TABLE 1
PHYSICAL PARAMETERS FOR AR 4508

Region	T_e (10 ⁶ K)	N_e (10 ⁹ cm ⁻³)	T_B (10 ⁶ K)	τ	W (10 ⁹ cm)
A	3.3	2.7	0.8	0.27	3
B	2.9	3.0	1.7	0.88	6
C	3.0	2.8	1.0	0.41	3
Average	3.1	2.8	1.2	0.52	4

TABLE 2
PHYSICAL PARAMETERS FOR AR 4532

Region	T_e (10 ⁶ K)	N_e (10 ⁹ cm ⁻³)	T_B (10 ⁶ K)	τ	W (10 ⁹ cm)
A	2.9	2.4	1.3	0.60	6
B	2.8	2.1	0.8	0.34	4
C	3.1	2.1	0.8	0.30	4
D	3.3	3.0	1.4	0.55	4
E	2.7	2.1	1.4	0.73	8
F	2.7	2.1	0.7	0.30	4
Average	2.9	2.3	1.1	0.47	5

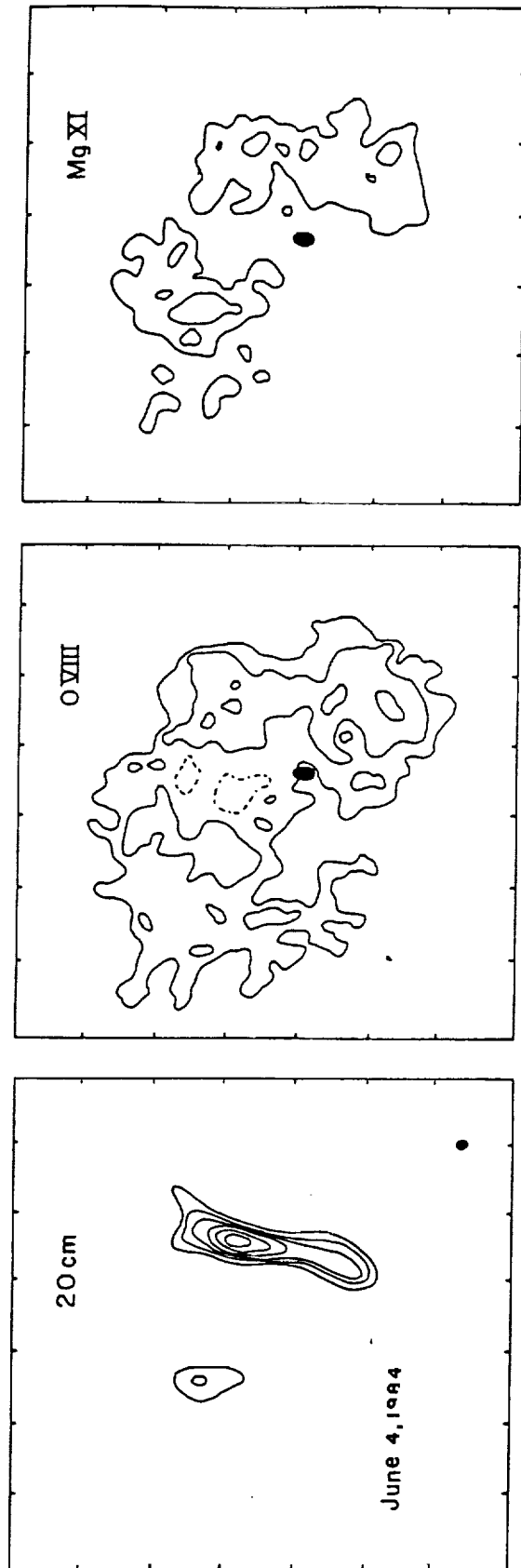


FIG. 1.—A comparison of a 20 cm VLA synthesis map of AR 4508 with SMM FCS images in the O VIII (18.9 Å) and Mg XI (9.2 Å) lines on 1984 June 4. The field of view of all three images is the same, and the angular scale can be inferred from the 60" spacing between fiducial marks on the axes. The contours of the 20 cm map mark levels of equal brightness temperature corresponding to 0.4, 0.5, 0.6 ... 1.0 times the maximum brightness temperature of 1.7×10^6 K. The contours of the O VIII image correspond to 4, 8, and 15 counts s^{-1} above the background level of 10 counts s^{-1} with a maximum signal of 20 counts s^{-1} . The contours of the Mg XI image are the same as those of O VIII with a background level of 5 counts s^{-1} and with a maximum signal of 15 counts s^{-1} . The small dark spot on the 20 cm map denotes the VLA beam, and the large dark spot on the O VIII and Mg XI images denotes the white light sunspot.

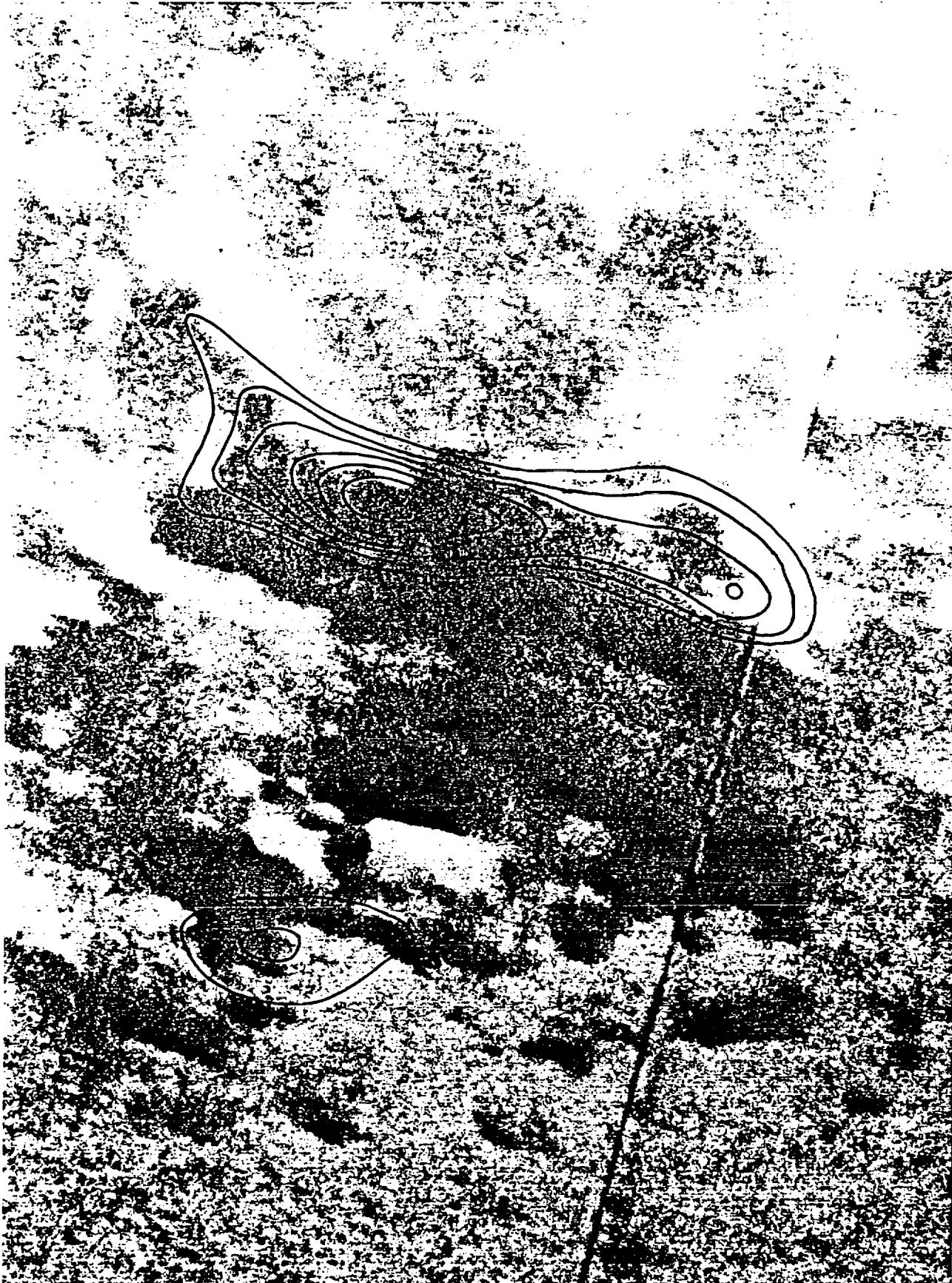


FIG. 2.—The 20 cm contours of equal brightness temperature (solid black lines) are superposed on a Kitt Peak National Observatory (KPNO) magnetogram of AR 4508 on 1984 June 4. The radio emission is concentrated along the magnetic neutral line that separates regions of negative (black) and positive (white) magnetic polarity. Sharp magnetic field gradients may exist along the neutral line. The KPNO magnetogram was kindly provided by Jack Harvey of the National Solar Observatory.

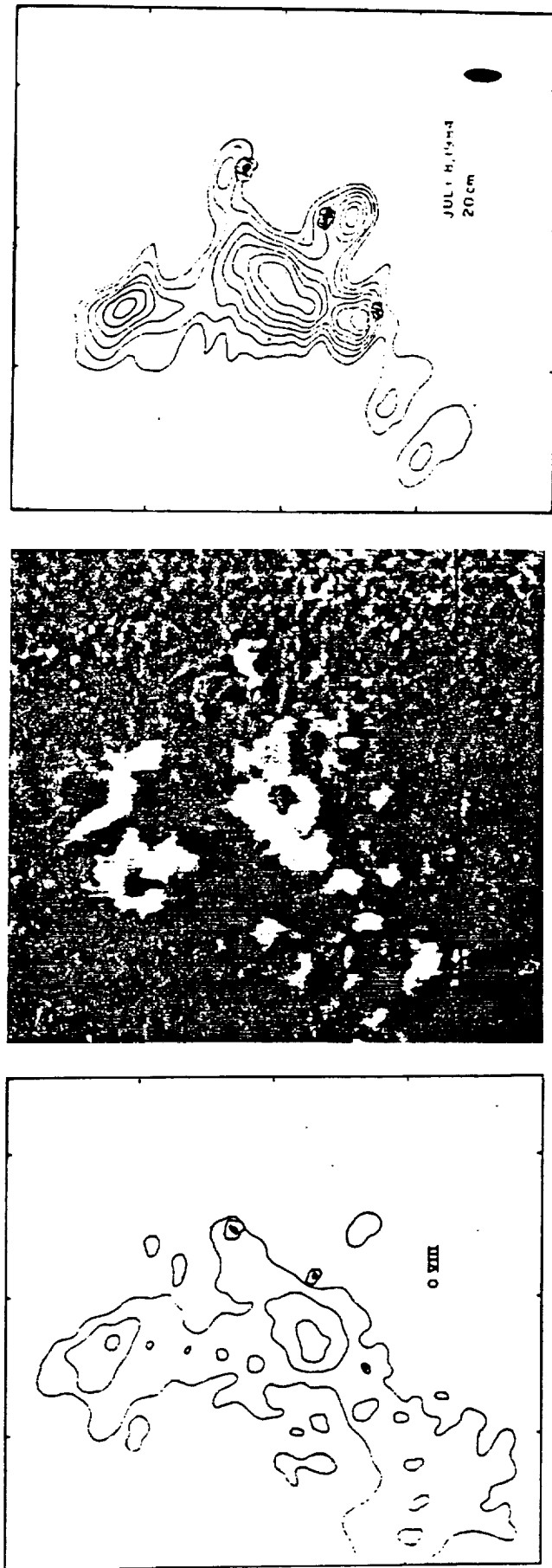


FIG. 3.—A comparison of soft X-ray (SMM FCS: *left*), $H\alpha$ (SOON: *middle*), and 20 cm (VLA: *right*) images of AR 4532 on 1984 July 8. The field of view of all three images is the same, and the angular scale can be inferred from the $120''$ spacing between the fiducial marks on the axes. The contours of the 20 cm map mark levels of equal brightness temperature corresponding to 0.4, 0.5, 0.6, ... 1.0 times the maximum brightness temperature of 1.4×10^6 K. The soft X-ray data were taken in the O VIII line (18.9 \AA) with contours corresponding to 4, 8, and 15 counts s^{-1} above a background level of 10 counts s^{-1} with a maximum signal of 20 counts s^{-1} . Here the sunspots are denoted by small black dots with a circle around them. The large black dot on the 20 cm map denotes the VLA beam.

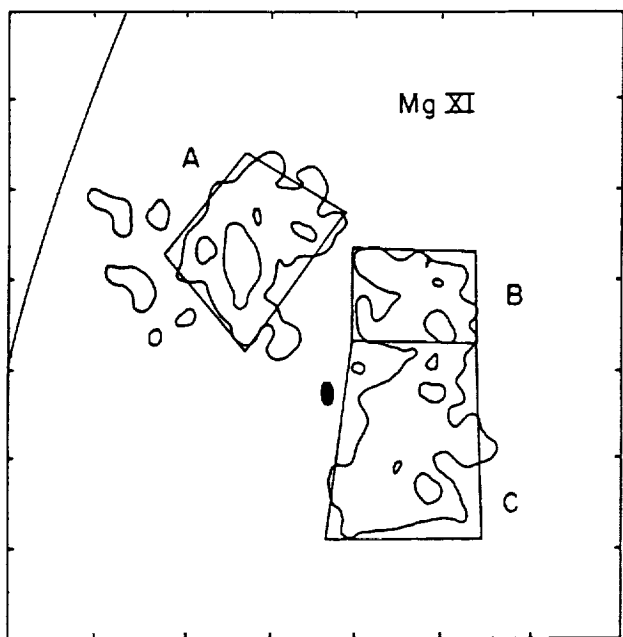


FIG. 4.—A soft X-ray map of AR 4508 taken in the Mg XI line (9.2 Å) with contours corresponding to 4, 8, and 15 counts s⁻¹. The ratios of the O VIII and Mg XI line intensities were used to determine the mean electron temperatures in the regions marked A, B, and C. These temperatures, the mean electron density, 20 cm brightness temperature, optical depth, and loop width are given in Table 1. The image represents the averaged sum of two maps taken at 17:03 UT and 18:37 UT on 1984 June 4. The solar limb is shown by the line in the upper left corner, and the black dot denotes the white light sunspot.

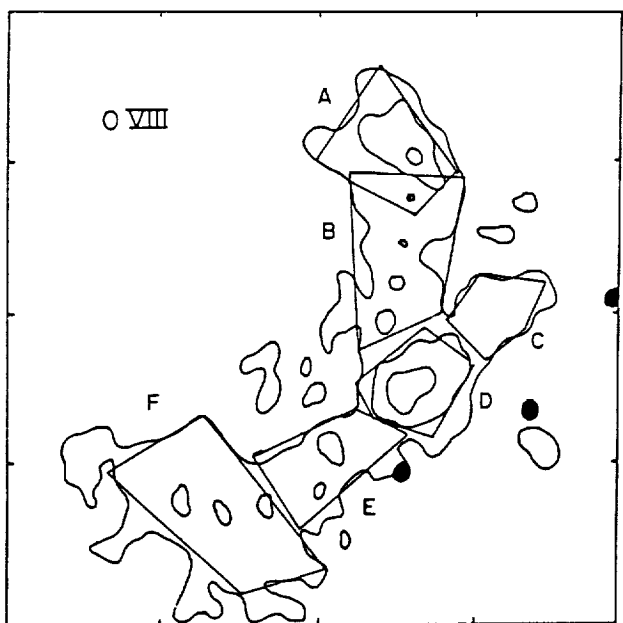


FIG. 5.—A soft X-ray map of AR 4532 taken in the O VIII line (18.9 Å) with contours corresponding to 4, 8, and 15 counts s⁻¹. The ratios of the O VIII and Mg XI line intensities were used to determine the mean electron temperature in the regions marked A, B, C, D, E, and F. These temperatures, the mean electron density, 20 cm brightness temperature, optical depth, and loop width are given in Table 2. The image represents the averaged sum of four maps taken at 18:06 UT, 19:40 UT, 21:15 UT, and 22:49 UT on 1984 July 8. There is no detectable X-ray emission associated with the white light sunspots (black dots), but these regions are associated with intense radiation at 20 cm wavelength (also see Fig. 3).

Within the uncertainties, the observed loops were isothermal. They also all had optical depths $\tau < 1$ (optically thin). We will therefore evaluate the loop width or thickness, W , that would give rise to optically thin thermal bremsstrahlung at our observing frequency of $\nu = 1446$ MHz (20.75 cm). According to Lang (1980):

$$W \leq \frac{102 \tau_{ff} \nu^2 T_e^{3/2}}{N_e^2 \ln(4.7 \times 10^{10} T_e / \nu)}, \quad (1)$$

or

$$W \leq \frac{2.13 \times 10^{20} \tau_{ff} T_e^{3/2}}{N_e^2 \ln(32.5 T_e)} \text{ cm},$$

where τ_{ff} is the optical depth for bremsstrahlung. The N_e and T_e obtained from the X-ray observations were substituted into equation (1) to provide the widths, W , given in Tables 1 and 2. The average values of W for the two active regions were $W \leq 4 \times 10^9$ cm and $W \leq 5 \times 10^9$ cm, which are certainly plausible.

In fact, the free-free optical depth, τ_{ff} , at 20 cm wavelength can be directly inferred from the X-ray measurements of electron temperature and emission measure, $N_e^2 W$. They imply $\tau_{ff} \approx 0.3$, suggesting that at least part of the 20 cm radiation is optically thin bremsstrahlung.

However, we will next evaluate the optical depth τ_{gr} for gyroresonance absorption by using the equation (Zheleznyakov 1970)

$$\tau_{gr} = 0.052 \frac{n^{2n}}{2^{n+1} n!} \frac{N_e}{\nu} (1.7 \times 10^{-10} T_e)^{n-1} L_H \times (1 \pm \cos \alpha)^2 \sin^{2n-2} \alpha, \quad (2)$$

where the magnetic scale length L_H has typical values of $L_H \sim 1 \times 10^9$ cm the angle between the line of sight and the direction of the magnetic field lines is α , and our observing frequency $\nu = 1446$ MHz and the harmonic n is related to ν through the relation

$$\nu = 2.8 \times 10^6 n H \text{ Hz}, \quad (3)$$

where the magnetic field strength is H .

When our average X-ray values of $N_e \sim 2.5 \times 10^9$ cm⁻³ and $T_e \sim 3 \times 10^6$ K are substituted into equation (2), we obtain optically thick conditions $\tau_{gr} \geq 1.0$ with low circular polarization at either the third or fourth harmonic ($n = 3$ or 4) and nearly transverse magnetic field lines ($\alpha = 60^\circ$ to 70°). Plausible magnetic field strengths of $H = 172$ G and 129 G are inferred for $n = 3$ and 4, respectively.

Thus we expect thermal gyroresonance radiation to be optically thick for plausible loop widths and magnetic scale lengths. This is consistent with the lack of any detectable circular polarization at 20 cm. The observed brightness temperature, T_B , at 20 cm wavelength should therefore be equal to the electron temperature with $T_B = T_e$, but the values of T_B are about 5 times smaller than T_e . To resolve this paradox, we call attention to an idea first proposed by Holman (1986).

To explain the restriction of one 20 cm loop to the apex of an X-ray loop, Holman argued that cooler material with $T_e \sim 10^5$ K exists either as a sheath around the loops or as part of an external medium. The 20 cm radiation emitted by the X-ray loops will be partly absorbed in the cooler, higher plasma, thereby reducing its brightness temperature. The cooler, higher material would, however, be invisible in X-rays because of its low temperature and relatively small emission measure.

If the cool plasma is part of an external medium that is more extensive than the X-ray loops, we would expect the observed 20 cm loops to be cospatial with the X-ray ones, but with a lowered brightness temperature. This is in fact observed for AR 4532. When the cool plasma is part of a sheath around the X-ray loops, the line of sight through the low-temperature plasma will be greatest at the loop edges and footpoints, and the observed 20 cm emission will be concentrated at the apexes of the X-ray coronal loops. This is observed for AR 4508.

What about the bright 20 cm radiation near and above sunspots? There is no detectable X-ray radiation in these regions, and this can be attributed to a low electron density, N_e . Because the optical depth for free-free absorption scales with N_e^2 while that for gyroresonance absorption scales with N_e , the low electron density favors gyroresonance absorption. The high magnetic field strength above sunspots also favors this process. We therefore attribute the 20 cm radiation near and above sunspots to thermal gyroresonance radiation.

IV. SUMMARY

The quiescent, or nonflaring, X-ray radiation of solar active regions is attributed to thermal bremsstrahlung, but the quiescent microwave radiation may be due to either thermal bremsstrahlung or thermal gyroresonant radiation. In the Introduction, we reviewed evidence for thermal gyroresonance radiation at 6 cm in coronal regions above sunspots. This evidence includes comparisons of 6 cm VLA maps with simultaneous soft X-ray data, as well as the detection of highly circularly polarized horseshoe-shaped structures above sunspots at 6 cm.

Although the thermal bremsstrahlung of coronal loops is usually optically thin at 6 cm, it might become optically thick at the longer 20 cm wavelength where looplike coronal structures are observed. These 20 cm coronal loops stretch between regions of opposite magnetic polarity in the underlying photosphere, and the temperatures, sizes, and shapes of the 20 cm coronal loops resemble those of soft X-ray coronal loops.

In this paper we have compared high-resolution 20 cm maps (VLA) with simultaneous high-resolution X-ray images (SMM FCS) of two active regions. The X-ray coronal loops in AR 4532 were completely imaged at 20 cm, while the 20 cm emission of AR 4508 was concentrated along the magnetic neutral line within more extended X-ray loops. The X-ray data were used to infer an average $T_e = 3.0 \pm 0.2 \times 10^6$ K and an average $N_e = 2.7 \pm 0.3 \times 10^9$ cm $^{-3}$ for AR 4532 and the average $T_e = 3.0 \pm 0.1 \times 10^6$ K and $N_e = 2.4 \pm 0.4 \times 10^9$ cm $^{-3}$ for AR 4508.

The microwave brightness temperatures, T_B , at 20 cm were always less than the average electron temperature, with optical depths $\tau = T_B/T_e$ of $0.2 \leq \tau \leq 0.5$. The X-ray values of T_e and

N_e indicate that thermal bremsstrahlung ought to be optically thin at 20 cm for plausible loop widths, but the thermal gyroresonance radiation can be optically thick at 20 cm for plausible magnetic field strengths and scale heights. Optically thick radiation is also consistent with the lack of detectable circular polarization at 20 cm. Thermal gyroresonance radiation must account for the intense 20 cm radiation near and above sunspots where no X-ray radiation is detected.

The unexpectedly low values of T_B can be explained if the X-ray emitting coronal loops lie beneath a higher, cooler plasma. The hot, dense plasma in the X-ray coronal loops would emit optically thick radiation at 20 cm wavelength, but the brightness temperature of this radiation would be reduced during subsequent propagation through the cooler, absorbing plasma. The observations of AR 4532 can be explained if the cooler plasma extends across and beyond the X-ray loops, while the AR 4508 results might be explained by the presence of a cool sheath around the X-ray loops. The cooler material would not be detected at X-ray wavelengths because of its low temperature and relatively small emission measure. The results given in this paper indicate that the structure and dominant radiation mechanisms in the low corona are much more complex and inhomogeneous than was previously thought. Systems of coronal loops within a single active region apparently have different temperatures and different radiation mechanisms that can be detected only by observations at both X-ray and 20 cm wavelength. Future comparisons of high-resolution images at these two wavelengths will lead to detailed information about the plasma and magnetic structure of the low solar corona. Physical parameters such as electron temperature, electron density, and magnetic field strength can be specified, and the detailed variation of these parameters within the coronal atmosphere can be determined. Such information will provide important constraints on theories and models of coronal loops as well as general theories for the structure and heating of solar active regions.

Radio astronomical studies of the Sun at Tufts University are supported under grant AFOSR-83-0019 with the Air Force Office of Scientific Research and contract N00014-86-K0068 with the Office of Naval Research (ONR). Simultaneous VLA and SMM FCS observations of the Sun are supported by NASA grant NAG 5-501. K.L.S. and K.T.S. are supported by NASA contract NAS 5-23758 and the Lockheed Independent Research Program. The XRP was built by a consortium of three groups: Lockheed Palo Alto Research Laboratory, Mullard Space Science Laboratory, and the Rutherford and Appleton Laboratories. The VLA is operated by Associated Universities, Inc., under contract with the National Science Foundation.

REFERENCES

- Alissandrakis, C. E., and Kundu, M. R. 1982, *Ap. J. (Letters)*, **253**, L49.
 Chiuderi-Drago, F., Bandiera, R., Falciani, R., Antonucci, E., Lang, K. R., Willson, R. F., Shibasaki, K., and Slotje, C. 1982, *Solar Phys.*, **80**, 71.
 Dulk, G. A., and Gary, D. E. 1983, *Astr. Ap.*, **124**, 103.
 Gary, D. E., and Hurford, G. J. 1987, *Ap. J.*, **317**, 522.
 Gelfriekh, G. B., and Lubyshv, B. I. 1979, *Soviet Astr.*, **23**, 316.
 Holman, G. D. 1986, "High-Spatial-Resolution Microwave and Related Observations as Diagnostics of Coronal Loops," to be published in *Coronal And Prominence Plasmas*.
 Kundu, M. R., and Lang, K. R. 1985, *Science*, **228**, 9.
 Kundu, M. R., Schmahl, E. J., and Gerassimenko, M. 1980, *Astr. Ap.*, **82**, 265.
 Lang, K. R. 1980, *Astrophysical Formulae* (2d ed.; New York: Springer Verlag).
 Lang, K. R., and Willson, R. F. 1982, *Ap. J. (Letters)*, **255**, L111.
 ———. 1983, *Adv. Space Res.*, **2**, No. 11, 91.
 ———. 1984, *Adv. Space Res.*, **4**, No. 7, 105.
 Lang, K. R., Willson, R. F., and Gaizauskas, V. 1983, *Ap. J.*, **267**, 455.
 Lang, K. R., Willson, R. F., and Rayrole, J. 1982, *Ap. J.*, **258**, 384.
 Lang, K. R., Willson, R. F., Smith, K. L., and Strong, K. T. 1987, "Solar Active Region Physical Parameters Inferred From A Thermal Cyclotron Line and Soft X-ray Spectral Lines," submitted to *Ap. J.*
 McConnell, D., and Kundu, M. R. 1983, *Ap. J.*, **269**, 698.
 Pallavicini, R., Sakurai, T., and Vaiana, G. S. 1981, *Astr. Ap.*, **98**, 316.
 Schmahl, E. J., Kundu, M. R., Strong, K. T., Bentley, R. D., Smith, J. B., and Krall, K. R., 1982, *Solar Phys.*, **80**, 233.

- Shevgaonkar, R. K., and Kundu, M. R. 1984, *Ap. J.*, **283**, 413.
Shibasaki, K., Chiuderi-Drago, F., Melozzi, M., Slottje, C., and Antonucci, E. 1983, *Solar Phys.*, **89**, 307.
Strong, K. T., Alissadrakis, C. E., and Kundu, M. R. 1984, *Ap. J.*, **277**, 865.
Vaiana, G. S., and Rosner, R. 1978, *Ann. Rev. Astr. Ap.*, **16**, 393.
Webb, D. F., Davis, J. M., Kundu, M. R., and Velusamy, T. 1983, *Solar Phys.*, **85**, 267.
- Webb, D. F., Holman, G. D., Davis, J. M., Kundu, M. R., and Shevgaonkar, R. K. 1987, *Ap. J.*, **315**, 716.
Willson, R. F. 1985, *Ap. J.*, **298**, 911.
Zheleznyakov, V. V. 1970, *Radio Emission of the Sun and Planets* New York: Pergamon), p. 454.

KENNETH R. LANG and ROBERT F. WILLSON: Department of Physics and Astronomy, Robinson Hall, Tufts University, Medford, MA 02155

KERMIT L. SMITH and KEITH T. STRONG: Code 602.6, Bldg. 7-XRP, Goddard Space Flight Center, Greenbelt, MD 20771

J. SOLAR ACTIVE REGION PHYSICAL PARAMETERS INFERRED FROM A THERMAL CYCLOTRON LINE AND SOFT X-RAY SPECTRAL LINES

KENNETH R. LANG AND ROBERT F. WILLSON
Department of Physics and Astronomy, Tufts University

AND

KERMIT L. SMITH AND KEITH T. STRONG
Lockheed Palo Alto Research Laboratory
Received 1987 January 27; accepted 1987 May 4

ABSTRACT

We present simultaneous high-resolution observations of coronal loops at 20 cm wavelength with the VLA and at soft X-ray wavelengths with the SMM FCS. The images at 20 cm and soft X-ray wavelengths have nearly identical sizes and ellipsoidal shapes, with a linear extent of about 5×10^9 cm. This emission stretches between and across regions of opposite magnetic polarity in the underlying photosphere. Complete X-ray coronal loops can therefore be imaged at 20 cm, and the VLA maps describe the radio wavelength counterpart of X-ray coronal loops. X-ray spectral lines were used to obtain values of electron temperature $T_e = 2.6 \pm 0.1 \times 10^6$ K and electron density $N_e = 3.1 \pm 0.3 \times 10^9$ cm⁻³ averaged over the emitting area. These parameters are used with plausible estimates for the loop thickness, magnetic scale height, and magnetic field strength to show that the plasma is optically thin to thermal bremsstrahlung, but that it might be optically thick to thermal gyroresonance radiation at 20 cm. The absence of detectable circular polarization is consistent with an optically thick plasma. The observed brightness temperature was roughly equal to the electron temperature of the coronal plasma. The VLA maps at 10 closely spaced frequencies between 1440 and 1720 MHz describe the same coronal loops or arcades of loops. A plot of the maximum brightness temperature of these loops as a function of observing frequency exhibits a linelike feature with a central frequency of 1650 MHz and a half-width of 80 MHz. This spectral feature is attributed to a thermal cyclotron line and indicates that the optical depth of thermal gyroresonance radiation must be greater than that of thermal bremsstrahlung at these frequencies. The X-ray values for T_e and N_e are combined with plausible values of magnetic scale height and optical depth for gyroresonance absorption to show that the harmonic of the gyrofrequency is 4. The central frequency and narrow width of the thermal cyclotron line are combined with this harmonic to show that the magnetic field strength of the coronal loops is 147 ± 5 G.

Subject headings: radiation mechanisms — Sun: corona — Sun: magnetic fields — Sun: radio radiation — Sun: X-rays

1. INTRODUCTION

Very Large Array (VLA) observations of solar active regions at 20 cm wavelength delineate looplike features that are probably the radio wavelength counterpart of the coronal loops seen at X-ray wavelengths. The 20 cm coronal loops stretch across regions of opposite magnetic polarity and have sizes, shapes, and temperatures that are similar to those of X-ray coronal loops (Lang, Willson, and Rayrole 1982; Lang, Willson, and Gaizauskas 1983; Lang and Willson 1983, 1984). Because the radio brightness temperatures are nearly equal to the electron temperatures of coronal loops, the radio radiation is most likely due to a thermal radiation mechanism.

The two possible thermal processes are thermal bremsstrahlung, or free-free emission, and thermal gyroresonance radiation, or cyclotron emission. The electron temperatures and electron densities inferred from X-ray observations of coronal loops can be consistent with either optically thin or optically thick thermal bremsstrahlung at 20 cm wavelength, but these parameters can also be combined with plausible estimates of the coronal magnetic field strength to show that thermal gyroresonance radiation can also become optically thick at this wavelength (McConnell and Kundu 1983; Shevgaonkar and Kundu 1984).

When thermal gyroresonance dominates, one might detect

individual cyclotron lines as narrow-band enhancements in the radio spectra of coronal loops. Theoreticians have predicted that such thermal cyclotron lines might be observed if the radiation is emitted from relatively thin layers in the corona where the magnetic field is nearly constant (Syrovatskii and Kuznetsov 1980; Zheleznyakov and Zlotnik 1980; Kuznetsov and Syrovatskii 1981). The spectrum of a linelike feature was subsequently observed at wavelengths near 20 cm when the apex of a coronal loop was resolved (Willson 1985). Observations of these lines provide an unusually accurate method of specifying the coronal magnetic field strength. The central frequency of the line must be a harmonic of the gyrofrequency, and the narrow linewidth provides tight constraints on that frequency and the relevant magnetic field strength.

Although there have been rapid recent developments in the observations of 20 cm coronal loops, there have been relatively few comparisons of simultaneous 20 cm and soft X-ray observations. Such comparisons can help specify the dominant 20 cm radiation mechanism, while also establishing the physical parameters of the coronal plasma. X-ray spectral lines can, for example, be used to calculate the electron temperature and electron density while the radio observations can uniquely specify the strength and structure of the magnetic field.

In this paper, we provide an example in which the coronal

radiation at 20 cm and X-ray wavelengths coincide. The observations are presented in § II, where we also present radio spectra that are attributed to a thermal cyclotron line. In § III, we provide values for the electron density, electron temperature, and magnetic field strength in these coronal loops and attribute the 20 cm radiation to thermal gyroresonance emission. The X-ray values of electron density and electron temperature are combined with the 20 cm brightness temperature and the cyclotron line to calculate the harmonic of the gyrofrequency. Our results are summarized in § IV.

II. OBSERVATIONS

We have used the VLA and the *SMM* FCS to observe the solar active region AR 4663 on 1985 June 7. The VLA was used in the B-configuration at 10 different wavelengths between 21.8 cm (1440 MHz) and 17.4 cm (1720 MHz) with bandwidths of 12.5 MHz between 1500 UT and 2400 UT on June 7, and the FCS observed five prominent soft X-ray lines (O VIII, Mg XI, Si XIII, S XV, and Fe XXV) between 1500 UT and 1940 UT on June 7. The position of AR 4663 on the solar surface was 01° N and 65° E at 1300 UT on June 7.

The half-power beamwidth of the individual VLA antennas ranged between $26'$ and $31'$, and the synthesized maps constructed from up to 325 interferometer pairs had beamwidths between $3''.0 \times 3''.5$ and $3''.6 \times 4''.2$. The active region was observed with the VLA at successive pairs of wavelengths for 5 minutes each, so that all 10 wavelengths could be observed in 25 minutes. This sequence of observations was followed by successive 2 minute observations of the calibrator source PKS 0552+398 whose flux density was 1.7 Jy at 1465 MHz. The calibrated data for the 9 hr interval were used with the standard CLEAN procedure to make synthesis maps of both the total intensity, I , and circular polarization or Stokes parameter V . No solar bursts or flares were observed during this interval, and the synthesis maps therefore refer to the quiescent, or nonflaring, radio emission. That is, plots of the visibility data exhibited no variations that could be attributed to solar activity. There was no detectable circular polarization ($V/I \leq 15\%$).

The $14''$ collimated field of view of the FCS was rastered over a $4' \times 4'$ area with a pixel spacing of $10'' \times 10''$. X-ray images were obtained simultaneously in the five soft X-ray emission lines every 990 s throughout the orbital day which lasts about 60 minutes. All of the available data for each spectral line during each orbit were then summed and averaged to improve the statistical uncertainty on the count rate from each pixel. Significant emission was detected in the two softest channels—O VIII and Mg XI. The peak formation temperatures for these lines are 3×10^6 K and 7×10^6 K, respectively. The failure to detect emission in the harder, more energetic channels indicates that the active region was unperturbed by any flaring throughout the period of observation. The *SMM* bent crystal spectrometer (BCS) confirmed the absence of flares as no significant brightenings were observed in its Ca XIX channel during these observations.

The FCS also produced a white-light image that showed the sunspots, making it possible to align the X-ray images with the sunspots to an accuracy of $10''$. The VLA maps of the total intensity, I , at 20 cm wavelength were aligned with H α photographs of the same sunspots with a similar $10''$ accuracy. This enabled us to compare the soft X-ray and 20 cm data for the same field of view and angular scale.

The 20.3 cm (1480 MHz) radiation and the soft X-ray (O VIII) emission originated in the same area (Fig. 1). Observations at

TABLE 1
SPECTRAL DATA FOR AR 4336

Frequency (MHz)	$T_{B,max}$ (10^6 K)
1440	1.7
1480	1.9
1515	2.0
1558	2.3
1585	2.2
1620	2.8
1658	3.8
1690	2.4
1705	2.0
1725	1.8

both wavelengths apparently describe the same coronal loops or arcades of loops. They are about $60''$ across, which corresponds to a linear extent, L , of about 5×10^9 cm. Both the radio and the X-ray emission are displaced toward the limb. If this displacement is attributed to a projection effect, then at a longitude of $\sim 65^\circ$ we infer a radial height of $h \approx 3 \times 10^9$ cm for both the radio and X-ray sources above the photosphere. Both sources stretch between and across regions of opposite magnetic polarity seen in magnetograms of the underlying photosphere (Fig. 2).

The radio-wavelength coronal loops exhibited the same ellipsoidal shape and extent at 10 closely spaced frequencies ranging from between 1440 MHz (20.8 cm) and 1725 MHz (17.4 cm) (Fig. 3). The maximum brightness temperatures are given in Table 1. The highest brightness temperature of $T_{B,max} = 3.8 \times 10^6$ K requires a hot spatially distinct region that was not detected with the soft X-rays. The failure to detect the associated X-ray emission places a 1σ limit of 3×10^{-3} to the volume emission measure of the hot plasma.

The maximum brightness temperatures are plotted as a function of observing frequency in Figure 4. This spectrum contains a linelike feature with a central frequency, $\nu = 1650$ MHz and a full width to half-maximum, $\Delta\nu$, of 80 MHz. As discussed in more detail in § III, we attribute this feature to a thermal cyclotron line and use it to obtain an estimate of the coronal magnetic field strength.

III. DISCUSSION

To identify the dominant thermal radiation mechanism at 20 cm, one needs to know the electron temperature, electron density, and the magnetic field strength. The X-ray data were therefore used to infer the mean electron temperature, T_e , and the mean electron density N_e , for the regions marked A, B, and C in Figure 5. As previously mentioned, the active region was quiescent and was only detectable in the two softest X-ray channels (O VIII and Mg XI). The ratios of the two lines (O VIII to Mg XI) were used as temperature diagnostics.

An emission measure was inferred from the temperature and the observed X-ray fluxes. The electron density was then calculated using a volume of 3×10^{27} cm 3 , which equals the product of the FCS pixel area and a typical soft X-ray scale height of 3×10^9 cm.

The mean temperatures and densities are given in Table 2. We obtain average values of $T_e = 2.6 \pm 0.1 \times 10^6$ K and $N_e = 3.1 \pm 0.3 \times 10^9$ cm $^{-3}$ when averaged over all the coronal loops or arcades of loops. Here, the uncertainties correspond to the maximum possible deviation that reproduces the flux in all the detected X-ray lines to within 1 standard deviation of

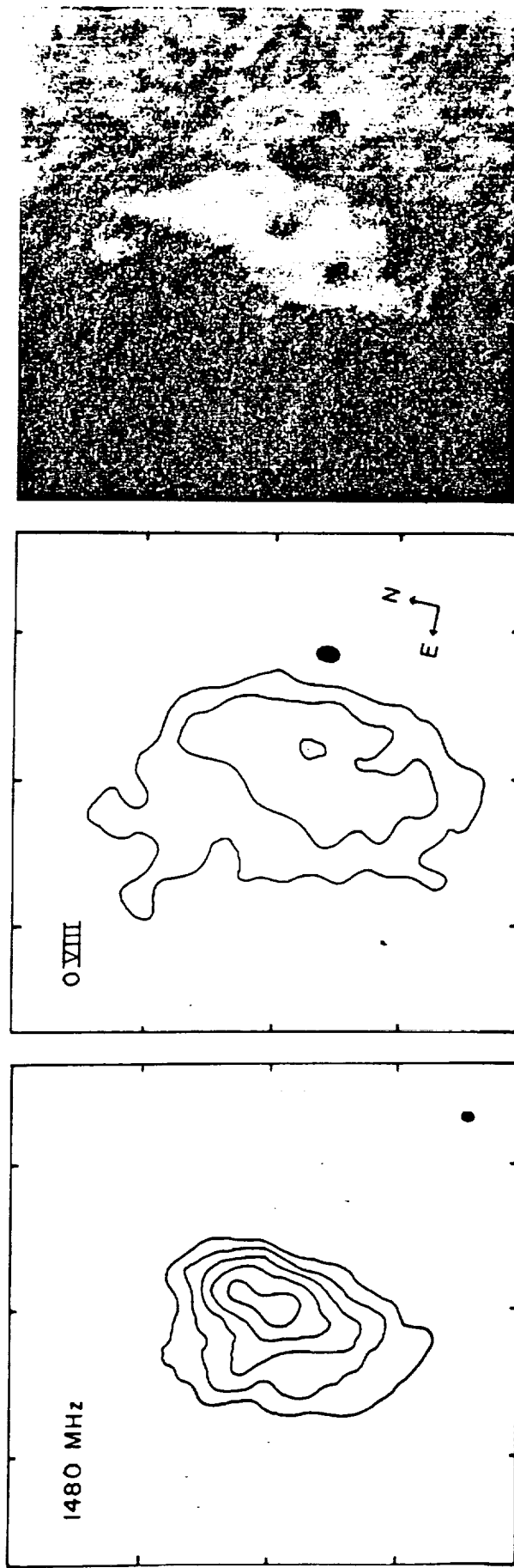


FIG. 1.—A comparison of 20 cm (VLA: left), soft X-ray (SMM: FCS-center) and H α (SOON: right) images of AR 4663 on 1985 June 7. The field of view of all three images is identical, and the identical angular scale can be inferred from the 60" spacing between fiducial marks on the axes. The contours of the 20 cm map mark levels of equal brightness temperature corresponding to 0.2, 0.4, ..., 1.0 times the maximum brightness temperature of 1.8×10^4 K. The soft X-ray data were taken in the O VIII line (18.9 Å) with contours corresponding to 3, 7, 14, and 24 counts s^{-1} above a background level of 10 counts s^{-1} with a maximum signal of 18 counts s^{-1} .

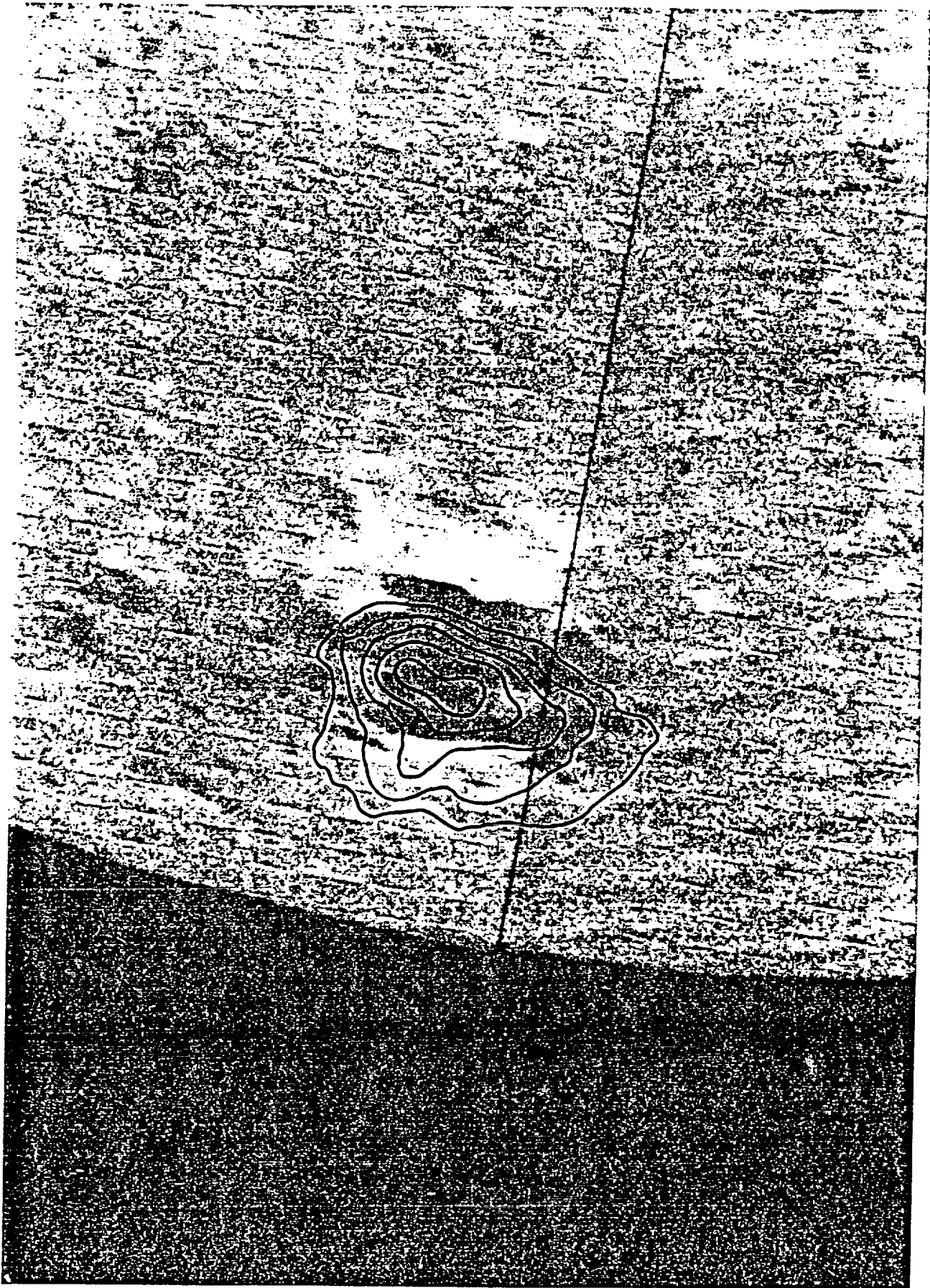


FIG. 2.—The 20 cm contours of equal brightness temperature (solid black lines) are superposed on a Kitt Peak National Observatory (KPNO) magnetogram of AR 4663 on 1985 June 7. The black magnetogram features indicate regions of negative magnetic polarity toward the Sun, while the white magnetogram areas are regions of positive magnetic polarity with magnetic field lines pointed out toward the observer. The KPNO magnetogram is courtesy of Jack Harvey of the National Solar Observatory.

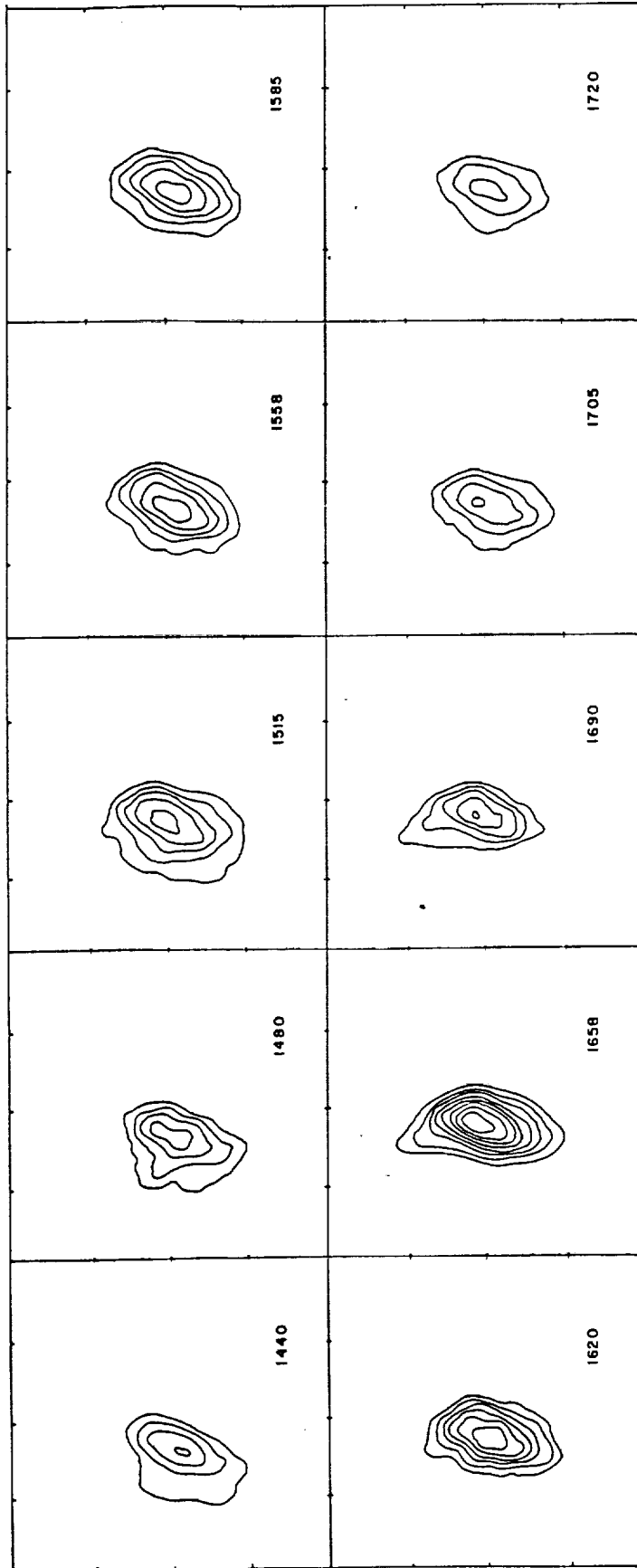


FIG. 3.—VLA synthesis maps of the total intensity, I , of AR 4663 at 10 closely spaced frequencies during a 9 hr period on 1985 June 7. The synthesized beamwidth was about $3'' \times 4''$, and the spacing between fiducial marks on the axes is $60''$. The map contours mark levels of equal brightness temperature, with an outermost contour of 7.6×10^4 K and a contour interval of 3.8×10^4 K. The maximum brightness temperatures are given in Table 1 and plotted in Fig. 4.

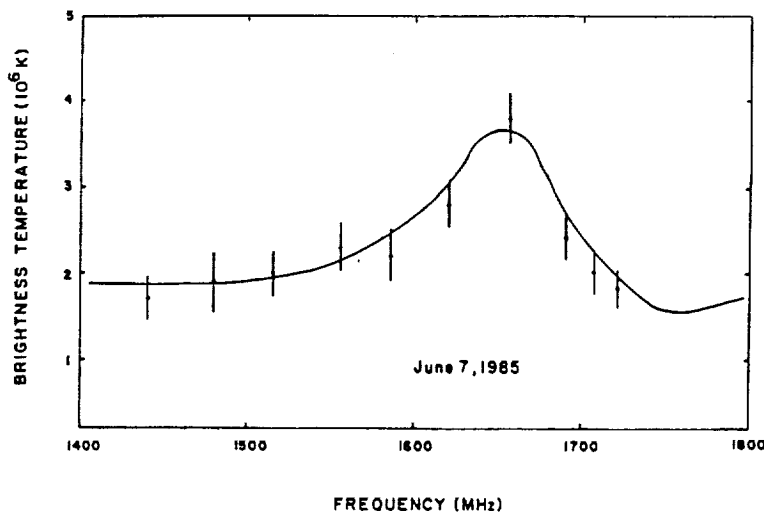


FIG. 4.—The maximum brightness temperature of the coronal loops of AR 4663 at 10 closely spaced frequencies on 1985 June 7. The maximum temperatures were inferred from the 9 hr synthesis maps shown in Fig. 3, and the error bars correspond to the peak-to-peak fluctuations in the background temperature of the synthesis maps.

the observed values. The inferred values of electron temperature and electron density are typical of those of quiescent coronal active region loops. Within the uncertainties, the observed loops were isothermal and isobaric, but there was a statistically uncertain tendency for a hotter temperature at the loop apex.

We may use the parameters derived from X-ray observations to estimate the optical depth and brightness temperature of the X-ray emitting plasma at radio wavelengths. Assuming an isothermal source of electron temperature, T_e , and optical depth,

τ , the observed radio brightness temperature, T_B , will be given by

$$T_B = \tau T_e \text{ for } \tau \ll 1 \text{ (optically thin)}$$

and (1)

$$T_B = [1 - \exp(-\tau)] T_e \text{ for } \tau \geq 1 \text{ (optically thick).}$$

The free-free optical depth, τ_{ff} , for an isothermal loop with electron temperature, T_e , and width or thickness, W , is (Lang 1980)

$$\tau_{ff} = 9.8 \times 10^{-3} \frac{N_e^2 W}{v^2 T_e^{3/2}} \ln \left(4.7 \times 10^{10} \frac{T_e}{v} \right), \quad (2)$$

where v is the observing frequency in Hz and N_e is the electron density in cm^{-3} . Using $v = 1.65 \times 10^9$ Hz, corresponding to the center of our linelike feature, together with the X-ray values of $T_e = 2.6 \times 10^6$ K and $N_e = 3.1 \times 10^9 \text{ cm}^{-3}$ and a typical loop thickness of $W \leq 3 \times 10^9$ cm in equation (2), we obtain $\tau_{ff} \leq 0.4$. Free-free emission might therefore be important for some of the radiation with brightness temperatures $T_B < T_e$, but not for the hotter, spatially distinct regions with $T_B \approx 3.8 \times 10^6$ K.

We must therefore examine the alternative possibility of thermal gyroresonance radiation. The optical depth, τ_{gr} , due to gyroresonance absorption is given by (Zheleznyakov 1970)

$$\tau_{gr} = 2\pi^2 \frac{n^{2n}}{2^{n+1}n!} \frac{v_p^2}{cv} \left(\frac{kT_e}{mc^2} \right)^{n-1} L_H (1 \pm \cos \alpha)^2 \sin^{2n-2\alpha}, \quad (3)$$

where $n = 1, 2, 3, \dots$ is the harmonic number, the plasma

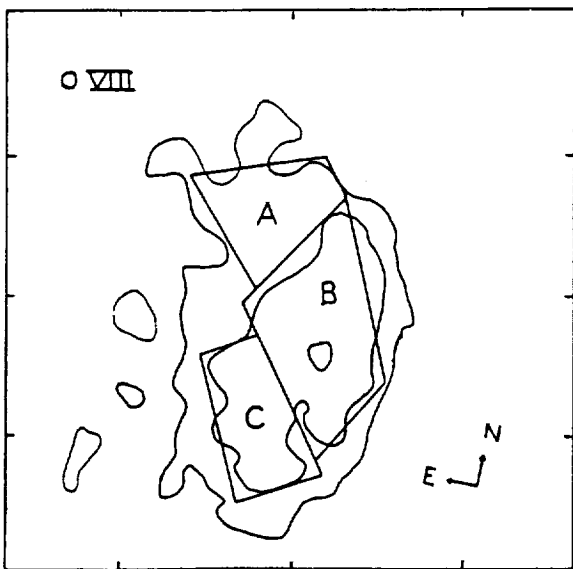


FIG. 5.—A soft X-ray map of AR 4663 taken in the O VIII line (18.9 Å) with contours corresponding to 3, 7, and 14 counts s^{-1} . The image represents the averaged sum of two maps taken at 15:11 UT and 19:55 UT on 1985 June 7. Each map took 590 s to accumulate. The ratio of the O VIII and Mg XI line intensities were used to determine the mean electron temperature in the regions marked A, B, and C. These temperatures are given together with estimates for the mean electron density in Table 2.

TABLE 2
PHYSICAL PARAMETERS FOR AR 4336

Region	T_e (10^6 K)	N_e (10^9 cm^{-3})
A.....	2.8	2.1
B.....	2.7	3.2
C.....	2.2	3.6
Average.....	2.6	3.1

ORIGINAL PAGE IS
OF POOR QUALITY

frequency $\nu_p = 8.9 \times 10^3 N_e^{1/2}$ Hz, the velocity of light $c = 2.9979 \times 10^{10}$ cm s⁻¹, Boltzmann's constant $k = 1.38 \times 10^{-16}$ ergs K⁻¹, the electron mass $m = 9.1 \times 10^{-28}$ g, the scale height of the magnetic field is L_H , and α is the angle between the line of sight and the direction of the magnetic field lines. Collecting terms, we obtain

$$\tau_{gr} = 0.052 \frac{n^{2n}}{2^{n+1}n!} \frac{N_e}{\nu} \times (1.7 \times 10^{-10} T_e)^{n-1} L_H (1 \pm \cos \alpha)^2 \sin^{2n-2\alpha}. \quad (4)$$

The harmonic n is related to the observing frequency ν and the magnetic field strength H through the relation

$$\nu = 2.8 \times 10^6 nH \text{ Hz}. \quad (5)$$

For gyroresonance absorption to dominate free-free absorption at our reference frequency $\nu = 1.65 \times 10^9$ Hz, the layers must be optically thick with $\tau_{gr} > \tau_{ff} \approx 0.4$.

Optically thick gyroresonance emission with low circular polarization can be obtained using the X-ray values of $N_e = 3.1 \times 10^9$ cm⁻³ and $T_e = 2.6 \times 10^6$ K in equation (4) with $n = 3$ or 4 and $\alpha = 60^\circ$ or 70° , respectively. We can then use equation (5) with $n = 3$ or 4 and $\nu = 1.65 \times 10^9$ Hz to obtain a magnetic field strength of $H = 196$ or 147 G, respectively. This is consistent with model calculations of the spectrum of another thermal cyclotron line (Willson 1985), but in the case presented here, we do not have to make ad hoc assumptions about N_e and T_e . Observations of these lines may provide an unusually accurate method of specifying the coronal magnetic field strength.

If the magnetic field strength is highly variable, the width of the cyclotron line will depend on this variation; but if the field is relatively constant, the width depends on Doppler broadening and the central frequency of the cyclotron line gives an accurate measurement of the field strength—provided the harmonic can be isolated. For instance, the observed line half-width is only 80 MHz, indicating that H is known with a precision of better than 5 G or $H = 147 \pm 5$ G if we assume $n = 4$.

However, these are general arguments based upon homogeneous, isothermal models. When Table 1 and Figure 4 are examined in greater detail, we notice that inhomogeneities are required. For example, the 20 cm brightness temperature, T_B , is usually lower than the electron temperature, T_e , suggesting that the radio emission from the hot, optically thick loops is partially absorbed in a cooler external plasma. In addition, the T_B at 1650 MHz is greater than T_e , suggesting a thin, hot gyroresonance layer similar to that proposed by Willson (1985). The detailed radio spectrum is probably due to a mixture of hot and cool loops whose average properties are inferred from X-ray observations.

Here we should point out that individual cyclotron lines are observed near the apex of coronal loops where the magnetic

field is relatively constant and a steep temperature gradient may exist. Neutral currents might also play a role, leading to intense radio emission from a relatively thin layer near the loop apex. The cyclotron lines from loop legs will, however, exhibit a great deal of spatial structure if the loops are thin enough (Holman and Kundu 1985). Observations of thin loops at an oblique angle with wavelengths of about 6 cm should lead to the spatial resolution of cyclotron-emitting layers along the loop legs, while observations of the loop apex at $\lambda \approx 20$ cm can resolve cyclotron lines in this region. Both techniques can provide a powerful diagnostic of the magnetic and thermal properties of coronal loops.

IV. SUMMARY

Simultaneous high-resolution observations of AR 4663 with the VLA and the SMM FCS indicate that the radiation at 20 cm and soft X-ray wavelengths originates from the same region, and that 20 cm VLA maps can image X-ray coronal loops. The X-ray spectral lines were used to infer an average electron temperature of about $2.9 \pm 0.1 \times 10^6$ K and an average electron density of $3.1 \pm 0.3 \times 10^9$ cm⁻³. These parameters were used to show that the layers emitting 20 cm radiation can be optically thick to either thermal bremsstrahlung or thermal gyroresonance radiation, depending upon unknown but plausible values of loop thickness, magnetic scale height, and magnetic field strength.

The absence of circular polarization suggests that these coronal loops are optically thick at wavelengths near 20 cm and the detection of a linelike feature in the radio spectrum indicates that gyroresonance absorption exceeds free-free absorption. This feature is attributed to a thermal cyclotron line. The X-ray values for T_e and N_e were combined with plausible values for gyroresonant optical depth and the magnetic scale height to show that the 20 cm radiation is probably at the fourth harmonic of the gyrofrequency. The central frequency and relatively narrow width of the thermal cyclotron line were combined with this harmonic to infer a magnetic field strength of 147 ± 5 G at the apexes of these coronal loops.

Radio astronomical studies of the Sun at Tufts University are supported under grant AFOSR-83-0019 with the Air Force Office of Scientific Research and contract N00014-86-K-0068 with the Office of Naval Research (ONR). Simultaneous VLA and SMM observations of the Sun are supported by NASA grant NAG 5-501. K.L.S. and K.T.S. are supported by NASA contract NAS 5-23758 and the Lockheed Independent Research Program. The FCS and BCS were built by a consortium of three groups: Lockheed Palo Alto Research Laboratory, Mullard Space Science Laboratory, and the Rutherford Appleton Laboratories. The VLA is operated by Associated Universities, Inc., under contract with the National Science Foundation.

REFERENCES

- Holman, G. O., and Kundu, M. R. 1985, *Ap. J.*, **292**, 291.
 Kuznetsov, V. S., and Syrovatskii, S. I. 1981, *Solar Phys.*, **69**, 391.
 Lang, K. R. 1980, *Astrophysical Formulae* (2d ed.; New York: Springer Verlag), p. 47.
 Lang, K. R., and Willson, R. F. 1983, *Adv. Space Res.*, **2**, No. 11, 91.
 ———. 1984, *Adv. Space Res.*, **4**, No. 7, 105.
 Lang, K. R., Willson, R. F., and Gaizauskas, V. 1983, *Ap. J.*, **267**, 455.
 Lang, K. R., Willson, R. F., and Rayrole, J. 1982, *Ap. J.*, **258**, 384.

McConnell, D., and Kundu, M. R. 1983, *Ap. J.*, 269, 698.

Shevgaonkar, R. K., and Kundu, M. R. 1984, *Ap. J.*, 283, 413.

Syrovatskii, S. I., and Kuznetsov, V. D. 1980, in *IAU Symposium 86, Radio Physics of the Sun*, ed. M. R. Kundu and T. E. Gergely (Dordrecht: Reidel), p. 109.

Willson, R. F. 1985, *Ap. J.*, 298, 911.

Zheleznyakov, V. V. 1970, *Radio Emission of the Sun and Planets* (New York: Pergamon), p. 454.

Zheleznyakov, V. V., and Zlotnik, E. Ya. 1980, in *IAU Symposium 86, Radio Physics of the Sun*, ed. M. R. Kundu and T. Gergely (Dordrecht: Reidel), p. 87.

KENNETH R. LANG and ROBERT F. WILLSON: Department of Physics and Astronomy, Robinson Hall, Tufts University, Medford, MA 02155

KERMIT L. SMITH and KEITH T. STRONG: Code 602.6, Bldg. 7-XRP, Goddard Space Flight Center, Greenbelt, MD 20771

K. High-resolution VLA maps of the quiescent corona at 90 cm wavelength

K.R. Lang^{2,*}, R.F. Willson¹, and G. Trottet²¹ Department of Physics and Astronomy, Tufts University, Medford, MA 02155, USA² Observatoire de Paris, Section d'Astrophysique de Meudon UA 324, F-92195 Meudon Principal Cedex, France

Received June 15, 1987; accepted February 25, 1988

Summary. We present the first Very Large Array (VLA) synthesis maps of the quiescent corona at 90 cm wavelength and compare them with optical solar features. When the quiet Sun is observed at 90 cm with moderate angular resolution of 100" to 200", structures are observed with angular extents, θ , of $\theta = 3'$ to $10'$ and brightness temperatures, T_B , of $T_B = 0.5$ to $5.7 \cdot 10^5$ K. Some of these structures are relatively stable over a two-day interval, with positions shifted westward by the amount expected from solar rotation; while others disappear or evolve during this interval. These intense, quiescent 90 cm sources are not associated with active regions; in contrast, simultaneous 20 cm observations reveal coronal loops that are associated with active regions. When the quiet Sun is observed with the VLA at 90 cm wavelength at high angular resolution of 15" to 30", compact components are detected with $\theta = 50''$ to $200''$ and $T_B = 2.1$ to $4.0 \cdot 10^5$ K. There is no systematic association of any of the 90 cm sources with any optical counterpart, including active regions, filaments, sunspots and the magnetic neutral line in the underlying photosphere. There is no intense 90 cm radiation in the polar regions where $T_B \leq 0.5 \cdot 10^5$ K, and this apparent depression is at least partly due to coronal holes. We confirm previous meter-wavelength results that indicate that noise storms are the only sources, other than flares, associated with active regions.

Key words: Sun: atmosphere – Sun: corona – Sun: coronal holes – Sun: coronal loops – Sun: magnetic field – Sun: noise storms – Sun: radio radiation

1. Introduction

The radio emission of the quiescent, or non-flaring, corona is dominated by different structures at different wavelengths. The most intense quiescent radiation at 20 cm wavelength is due to a hot, dense plasma trapped within relatively compact coronal loops associated with individual active regions (Kundu and Lang, 1985; Lang et al., 1987a, b). In contrast, the most intense emission of the quiescent corona at meter wavelengths (80 and 160 MHz) is not associated with active regions or with bright regions in the centimeter maps (Sheridan and McLean, 1985). This emission

might be associated with relatively large coronal loops or with extended magnetic structures such as coronal streamers.

This paper presents the first VLA images of the quiescent corona at 90 cm wavelength. It therefore refers to a spectral region located between the shorter 20 cm region and the longer meter wavelength one. Our 90 cm observations are presented in Sect. 2, where they are also compared with optical features. Our conclusions are summarized in Sect. 3.

2. Observations

The half-power beamwidth of the VLA's 25-meter telescopes is 32' at 20 cm wavelength, and this is just equal to the angular extent of the Sun at mean Earth distance. So, the entire solar disk can be imaged at either 20 cm or 90 cm, but with a varying degree of completeness that depends on the array configuration. That is, the 27 individual telescopes can be moved in and out along the Y-shaped arms of the array, creating a radio zoom lens that provides higher angular resolution at the expense of more incomplete information on larger angular structures. For example, the synthesized half-power beamwidth, θ , at 20 cm is $\theta \approx 1'', 4'', 13''$ and $44''$ for the A, B, C and D configurations, respectively, while the corresponding values at 90 cm are $\theta \approx 5'', 18'', 60''$ and $200''$.

The VLA was used to observe the Sun in the C–D hybrid configuration between 2013 UT on 20 February 1987 and 0015 UT on 21 February 1987 and between 1905 UT on 22 February 1987 and 0020 UT on 23 February 1987. The array was divided into two subarrays with 15 antennas operating at 90 cm wavelength (333 MHz) with 3.125 MHz bandwidth and 12 antennas operating at 20.7 cm wavelength (1446 MHz) with 12.5 MHz bandwidth. The beamwidth of the individual antennae was 138' at 90 cm and 32' at 20.7 cm.

All four Stokes parameters were sampled every 6.67 s, and the data were calibrated by observing 3C 48 for five minutes every 70 min. The flux density of 3C 48 was assumed to be 47.0 Jy and 14.6 Jy at 90 cm and 20.7 cm respectively.

In order to construct reliable 90 cm synthesis maps, we had to delete data from the shortest baselines at the end of the day. These data, which corresponded to fringe spacings of 36' and 48', were omitted because the large correlated flux exceeded the dynamic range of the correlators. There were no such problems at the beginning of our observations because the projected baselines were longer with correspondingly smaller fringe spacings and correlated fluxes. Shadowing of the antennae at the end of the day

Send offprint requests to: K.R. Lang

* Currently on sabbatical leave at the Observatoire de Paris, Meudon

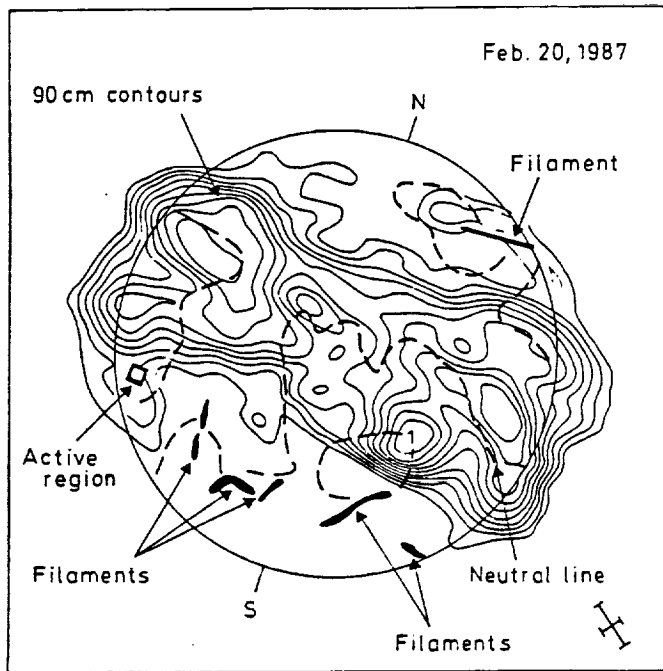


Fig. 1. Four-hour VLA synthesis map of the Sun at 90 cm wavelength on 20 February 1987 is compared with optical solar features including active regions (squares), filaments (solid lines) and the magnetic neutral line (dashed line). The most intense 90 cm emission is not systematically associated with any optical counterpart. There is no intense 90 cm radiation in the polar regions, and this is at least partly due to polar coronal holes. The array was in the C-D hybrid configuration with a synthesized beamwidth denoted by the crosses. The contours mark levels of equal brightness temperature, T_B , with an outermost contour of $T_B = 5.5 \cdot 10^4$ K, a contour interval of $5.5 \cdot 10^4$ K, and a peak brightness temperature of $T_B = 5.7 \cdot 10^5$ K. All of the sources are positive and all of the optical data have been extracted from Solar Geophysical Data (1987)

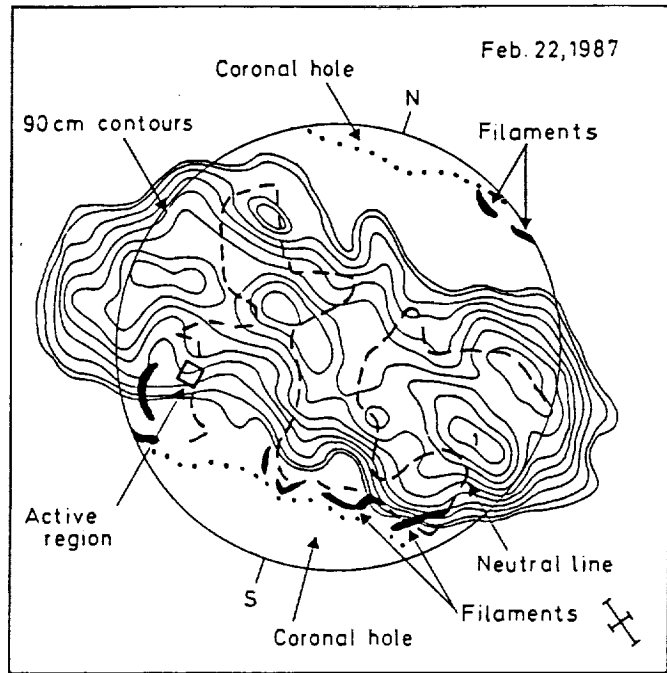


Fig. 2. Four-hour VLA synthesis map of the Sun at 90 cm wavelength on 22 February 1987 is compared with optical solar features including active regions (squares), coronal hole boundaries (dotted lines), filaments (solid lines) and the magnetic neutral line (dashed line). The most intense 90 cm emission is not systematically associated with any optical counterpart. There is no intense 90 cm radiation in the polar regions, and this is at least partly due to polar coronal holes. The array was in the C-D hybrid configuration with a synthesized beamwidth denoted by the crosses. The contours mark levels of equal brightness temperatures, T_B , with an outermost contour of $T_B = 5.5 \cdot 10^4$ K, a contour interval of $5.5 \cdot 10^4$ K, and a peak brightness temperature of $T_B = 5.5 \cdot 10^5$ K. All of the sources are positive, all of the optical data have been extracted from Solar Geophysical Data (1987) and the coronal hole boundaries have been inferred from the He 10830 map supplied by Jack Harvey

can also produce erroneous fringe amplitude changes and incorrect images.

The calibrated and edited data were used together with the standard CLEAN procedure to produce the synthesis maps shown in Figs. 1 and 2. Each map refers to 4 h of observation with a synthesized beamwidth of $113'' \times 237''$. All of the sources shown in each cleaned map were also present in the dirty map, so the cleaning procedure did not introduce any artifacts. The level of negative residuals was 15 to 20% of the dirty map maximum.

The most intense 20 cm emission on both days was associated with an active region with strong photospheric magnetic fields. We attribute this emission to the coronal loops that have been previously detected in the low corona at 20 cm and soft X-ray wavelengths. The association of intense 20 cm emission with coronal loops in active regions has now been documented by numerous VLA observations (see Lang et al., 1987a, b and references within it), so we do not give our 20 cm maps here.

In contrast to the 20 cm coronal loops, the most intense 90 cm radiation of the quiescent, or non-flaring, corona (see Figs. 1 and 2) is not related to active regions. The 90 cm sources are concentrated near the equatorial regions and provide a distinctly inhomogeneous component to the quiescent corona. The 90 cm structures have brightness temperatures, T_B , of $T_B = 0.5$ to $5.7 \cdot 10^5$ K, which are slightly less than those of the 20 cm coronal

loops, but that are comparable to the brightness temperature $T_B \approx 6 \cdot 10^5$ K of the entire quiet Sun (Sheridan and McLean, 1985).

In several cases, the 90 cm sources shown in Figs. 1 and 2 remain, within the uncertainty of measurements, at the longitudes expected from solar rotation (see source 1), but some of the latitudes also apparently change and some sources have disappeared, changed shape or emerged during the two-day interval. These results suggest that the large-scale structures detected at 90 cm wavelength are both inhomogeneous and variable on time scales of a few days.

Assuming an angular radius $\theta \approx 4'$ and a brightness temperature of $T_B \approx 5 \cdot 10^5$ K, we can use the Rayleigh-Jeans law to show that the flux density, S , in a typical intense 90 cm source is $S \approx 1$ s.f.u., where 1 s.f.u. = 10^4 Jy (see Lang, 1980). But there are at least five such sources, so their combined flux density is 5 s.f.u., or roughly half the 10 s.f.u. flux density of the quiet Sun at this wavelength (Sheridan and McLean, 1985). Thus, as much as half the total flux density of the quiescent corona at 90 cm wavelength may be emitted from undetected structures. This essentially follows from the fact that the intense 90 cm sources have a brightness temperature comparable to the entire quiet Sun at this wavelength, so if they occupy roughly half the surface area of the Sun they account for roughly half the total flux density.

A comparison of the 90 cm sources with optical features (Figs. 1, 2) indicates that the intense, quiescent 90 cm emission is not systematically associated with any optical counterpart, at least for our observations. Although the north-west filament on 20 February 1987 is apparently associated with an extended 90 cm source, the other filaments on this day and on 22 February are not associated with detectable 90 cm emission. All of the 90 cm sources on these days are concentrated within equatorial regions away from active regions and sunspots. There is a noticeable depression, or lack of intense 90 cm emission, at the poles, and this is at least partly due to polar coronal holes.

Some of the extended 90 cm sources lie on or near the neutral line, but other sources do not. Moreover, some minima in brightness temperature also lie on or near that line, and the 90 cm emission certainly does not trace out all of the neutral line. So, relations with that line may be due to chance, and there is no systematic association with it.

When the VLA zeroes in for a closer look, the 90 cm structures are resolved into compact components. For example, the VLA was used to observe the Sun in the B configuration between 1545 UT and 2230 UT on 23 August 1986. An array of 13 antennas operating at 90 cm wavelength with a bandwidth of 3.125 MHz was used to produce the synthesis map shown in Fig. 3. In this case, the data were calibrated by observing 3C 286 (90 cm flux 29.0 Jy) for 5 min every 40 min, and the synthesized beamwidth was $16'' \times 29''$.

Components with angular dimensions, θ , of $\theta = 50''$ to $200''$ and brightness temperatures, T_b , of $T_b = 2.1$ to $4.0 \cdot 10^5$ K were detected. As indicated in Fig. 3, these sources are not directly related to the active regions that would have been detected if we had simultaneous VLA observations at 20 cm wavelength.

The only possible optical counterpart of the intense compact 90 cm sources is the inversion line (magnetic neutral line) of the photospheric magnetic field, but these sources do not trace out the full magnetic neutral line. If the quiescent 90 cm sources are related to the magnetic neutral line, some additional factor is causing them to be concentrated over only small parts of it. This factor is apparently unrelated to Hz filaments; an examination of Meudon data (DASOP) indicated no detectable Hz filament or plage at the latitudes of the enhanced 90 cm emission, either on the day of observation or on three rotations before or after that day.

There is, however, one source of 90 cm radiation that is associated with active regions: it is the ubiquitous noise storms. This nonthermal radiation is the most common type of activity observed on the Sun at decimetric and metric wavelengths. The noise storms might be confused with quiescent radiation because of their long durations (hours to days); but they are actually sources of continued activity, apparently located in large magnetic arches that connect active regions with their surroundings (Mercier et al., 1984). Metric wavelength observations of noise storms provided some of the first evidence for stable magnetic connections between solar active regions and more distant areas on the Sun (Lantos-Jarry, 1970; Daigne et al., 1971).

When the VLA is used to resolve a noise storm at 90 cm wavelength, it is indeed found near the apex of large-scale magnetic loops that apparently connect two active regions (Lang and Willson, 1987). Intense radiation at 183 cm wavelength is also associated with this loop system (see Fig. 4). This radiation could be due to low-level noise storm activity, for such noise storm continua are an important source of slowly varying radiation at 183 cm wavelength (Alissandrakis et al., 1985; Lantos et al., 1987). Other extended quiescent coronal features at 183 cm, such as the one near the center of the map shown in Fig. 4, resemble those

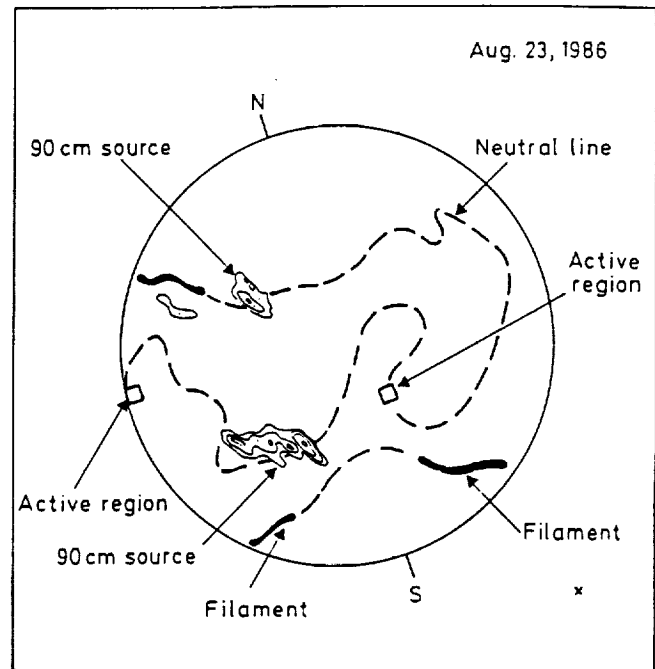


Fig. 3. A VLA synthesis map at 90 cm wavelength during a $6^h 45$ min period on 23 August 1986 is compared with optical solar features including active regions (squares), filaments (solid lines) and the probable magnetic neutral line (dashed line). At least three compact 90 cm sources have been detected with angular dimensions of $50'' \times 200''$. Here the 90 cm contours mark levels of equal brightness temperature, T_b , with an outermost contour of $T_b = 2.1 \cdot 10^5$ K, a contour interval of $4.1 \cdot 10^4$ K and a peak brightness temperature of $T_b = 4.0 \cdot 10^5$ K. The VLA was in the B configuration with a $16'' \times 29''$ synthesized beamwidth denoted by the small solid cross in the lower right corner. All of the optical data have been extracted from Solar Geophysical Data (1986)

found at 90 cm with the VLA, with no apparent correlation with any optical counterpart and comparable brightness temperatures.

Our results are in accord with previous observations which showed that intense quiescent emission at meter wavelengths (80 and 169 MHz) is not associated with active regions (Axisa et al., 1971; Sheridan and McLean, 1985). A statistical study of numerous one-dimensional Nançay scans at 169 MHz indicated, however, that the longitudes of many quiescent sources are associated with filament corridors as seen on Hz synoptic maps and not on daily maps (Axisa et al., 1971). In contrast, fewer two-dimensional maps at the same frequency show a poor apparent association with filaments and a possible association with the magnetic neutral line in the underlying photosphere (Alissandrakis et al., 1985; Lantos et al., 1987). Our observations do not confirm either result, indicating no systematic association with any optical counterpart; but we can not rule out such associations, particularly during different parts of the solar cycle.

Correlations of radio sources with optical counterparts are confused by nonradial divergence, refraction effects and solar tilt. There are additional uncertainties due to random correlations with the long magnetic neutral line; its placement on the solar surface differs by several degrees depending on the technique used. A deeper understanding of the quiescent coronal sources is likely to come from multiple-wavelength observations in the radio part of the electromagnetic spectrum.

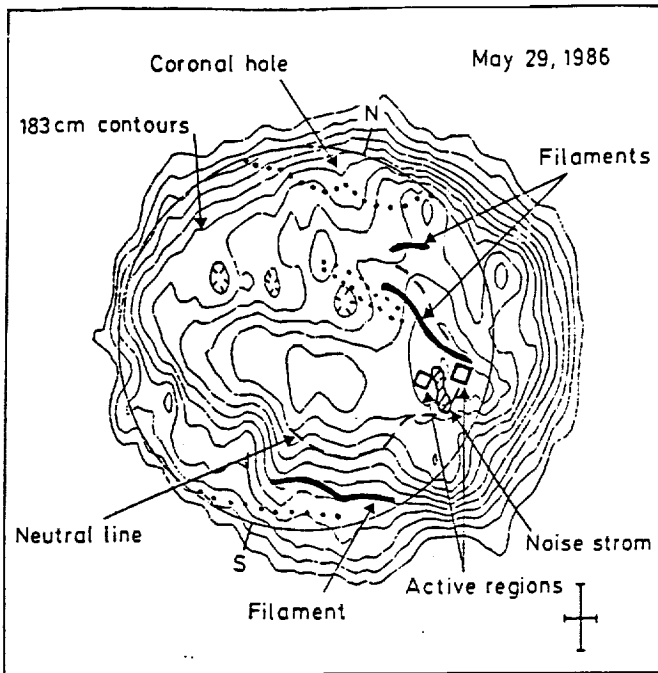


Fig. 4. A Nançay Radioheliograph synthesis map at 183 cm wavelength during an 8 h period is compared with a 90 cm noise storm (VLA-hatched area) and various optical solar features including active regions (squares), coronal hole boundaries (dotted lines), filaments (solid lines) and the magnetic neutral line (dashed line). The 90 cm noise storm emission apparently comes from large-scale magnetic loops that connect active regions, and the apex of these loops is probably associated with a maximum in the intensity of the 183 cm radiation. Here the 183 cm contours mark levels of equal brightness temperature, T_{B} , with an outermost contour of $T_{\text{B}} = 2.0 \cdot 10^5$ K, a contour interval of $5.0 \cdot 10^4$ K and a peak brightness temperature of $7.5 \cdot 10^5$ K. A detailed understanding of these sources will require greater angular resolution and spectral information. The 1.2×4.5 synthesized beamwidth is denoted by crosses in the lower right corner, and all of the optical data have been extracted from Solar Geophysical Data (1986)

3. Conclusions

The quiescent corona at 90 cm wavelength is very inhomogeneous and variable, with the most intense emission concentrated within structures near the equatorial regions. This emission may be the thermal bremsstrahlung of a coronal plasma that might be confined in large-scale magnetic structures. The 90 cm sources are not systematically associated with any optical counterpart including active regions, filaments, sunspots and the magnetic neutral

line, at least for the observations presented here. There is no intense 90 cm radiation in the polar regions, and this is at least partly due to coronal holes. More compact 90 cm sources in the quiescent corona also show no systematic correlation with optical counterparts. Associations with the magnetic neutral line are uncertain, and future multiple-wavelength radio observations might provide new insights to the paradoxical quiescent coronal structures.

Acknowledgements. Radio astronomical studies of the Sun at Tufts University are supported under grant AFOSR-83-0019 with the Air Force Office of Scientific Research and contract N00014-86-K-0068 with the Office of Naval Research. Collaborative long-wavelength solar observations by Tufts University and the Observatoire de Paris are supported by National Science Foundation grant INT-8602285 and Centre National de la Recherche Scientifique grant 920038. The Very Large Array is operated by Associated Universities Inc., under contract with the National Science Foundation. We thank C.E. Alissandrakis, K.-L. Klein, P. Lantos, C. Mercier and M. Pick for useful discussions.

References

- Alissandrakis, C.E., Lantos, P., Nicolaidis, E.: 1985, *Solar Phys.* 97, 267
- Axisa, F., Avignon, Y., Martres, M.J., Pick, M., Simon, P.: 1971, *Solar Phys.* 19, 110
- Daigne, G., Lantos-Jarry, M.F., Pick, M.: 1971, in *Solar Magnetic Fields*, ed. Howard, p. 609
- Kundu, M.R., Lang, K.R.: 1985, *Science* 228, 9
- Lang, K.R.: 1980, in *Astrophysical Formulae*, 2nd ed., New York, Springer-Verlag, p. 23
- Lang, K.R., Willson, R.F.: 1987, *Astrophys. J.* 319, 514
- Lang, K.R., Willson, R.F., Smith, K.L., Strong, K.T.: 1987a, b, *Astrophys. J.* 322, 1035, 1044
- Lantos, P., Alissandrakis, C.E., Gergely, T., Kundu, M.R.: 1987, *Solar Phys.* 112, 325
- Lantos-Jarry, M.F.: 1970, *Solar Phys.* 15, 40
- Mercier, C., Elgaroy, O., Tlamicha, A., Zlobek, P.: 1984, *Solar Phys.* 92, 375
- Saito, K.: 1970, *Ann. Tokyo Astron. Obs. Ser.* 2, 12, 53
- Sheridan, K.V., Labrum, N.R., Payten, W.J., Nelson, G.J., Hill, E.R.: 1983, *Solar Phys.* 83, 167
- Sheridan, K.V., McLean, D.J.: 1985, in *The Quiet Sun at Metre Wavelengths*, *Solar Radiophysics*, eds. D.J. McLean, N.R. Labrum, New York, Cambridge University Press, p. 443
- Solar Geophysical Data: 1986, 1987, Part 1, No 503, p. 53, No 506, p. 47, No 512, p. 50, 52

ROBERT F. WILLSON
Department of Physics and Astronomy
Tufts University
Medford, Ma 02155

ABSTRACT

We summarize recent high resolution microwave observations of the coronae of the Sun and other nearby active stars. VLA observations near 20 cm wavelength have been combined with simultaneous soft X-ray (SMM-XRP) observations to obtain the electron density and temperature in coronal loops and to specify the radiation mechanism within the emitting plasma. Observations near 90 cm wavelength outline large-scale coronal structures that may connect areas of weak magnetic fields. VLA observations of a solar noise storm at 90 cm have resolved the burst-emitting region into a number of compact components. These observations confirm previously reported trends for a decrease in burst size at shorter wavelengths, and they also suggest a hitherto unresolved complexity in source structure. The results of a search for 6 cm microwave emission from stars with short rotation periods and high magnetic fields or intense X-ray emission indicate that these properties alone do not guarantee the stars will be radio emitters. VLA and Arecibo observations of the dwarf M flare stars VZ Canis Minoris and AD Leonis reveal both slowly-varying and impulsive narrow-band emission, suggesting a nonthermal radiation mechanism such as plasma emission or electron-cyclotron maser emission.

1. INTRODUCTION

Recent high resolution microwave observations of the Sun have provided new insights to the structure of the solar corona and transition region. These include such things as the three-dimensional structure and magnetic field strengths of coronal loops, the preburst heating and magnetic triggering of loops, and the evolution of solar microwave bursts (see Kundu and Lang 1985 and Dulk 1985, for recent reviews). These results have come about through the unprecedented spatial resolution of radio synthesis instruments such as the Very Large Array (VLA) which can produce microwave images on angular scales of few seconds of arc and on timescales as short as a few seconds. The high sensitivity of the VLA, and the Arecibo Observatory also makes it possible to detect quiescent and burst emission from nearby stars. These observations can be used to specify the magnetic field strength in stellar coronae, to resolve the components of binary star systems, and to place stringent limits on the size of burst-emitting regions.

**SOLAR AND STELLAR CORONAL
STRUCTURE AND DYNAMICS**
A Festschrift in Honor of Dr. John W. Evans

PROCEEDINGS OF THE NINTH SACRAMENTO
PEAK SUMMER SYMPOSIUM, SUNSPOT, NM
17 – 21 AUGUST 1987

Sponsored by:
The National Solar Observatory
The NASA Solar Maximum Mission
The U. S. Air Force

Edited by:

Richard C. Altrock
Air Force Geophysics Laboratory
Sunspot, New Mexico

JULY 1988
NATIONAL SOLAR OBSERVATORY/SACRAMENTO PEAK
SUNSPOT, NEW MEXICO 88349

In this paper we discuss some recent VLA and Arecibo observations of the Sun and other active stars. We begin by discussing simultaneous VLA-SMM observations of coronal loops for which the microwave and soft X-ray data were combined to specify the radiation mechanisms of the emitting plasma. We then discuss observations of quiescent and burst emission from the Sun at 90 cm. Finally, we present the results of a recent VLA survey of active stars and discuss observations of narrow-band burst emission that provides evidence for non-thermal, coherent emission processes in stellar coronae.

3. MICROWAVE OBSERVATIONS OF THE SOLAR CORONA

3.1 Simultaneous Microwave and Soft X-ray Observations of Coronal Loops.

VLA observations of active regions at 20 cm wavelength outline coronal loops that appear to stretch between areas of opposite magnetic polarity in the photosphere (Lang, Willson and Rayrole 1982; Lang, Willson and Gaizauskas 1983). These loops have lengths ($L=10^9 - 10^{10}$ cm), temperatures ($T = 1 - 3 \times 10^6$ K) and shapes that are similar to those inferred from X-ray observations of the Sun. Although the soft X-ray emission is attributed to the thermal bremsstrahlung of a hot dense plasma, there are two possible thermal emission mechanisms at centimeter wavelengths. These are the thermal bremsstrahlung of electrons accelerated in the electric fields of ions, and the gyroresonant emission of electrons accelerated in coronal magnetic fields. Although both mechanisms are sensitive to the electron temperature and electron density, only gyroresonant emission provides a direct estimate of the magnetic field strength.

In order to determine which of these two competing mechanisms is the dominant one, it is necessary to know the temperature, density, magnetic field strength, and scale height of the coronal loop. X-ray observations provide estimates of T_e and N_e , so that comparisons of simultaneous X-ray and microwave observations might be used to specify the dominant microwave emission mechanism, and also establish the physical properties of the coronal plasma.

In Figure 1 we compare a 20 cm VLA synthesis map of an active region with a Solar Maximum Mission Flat Crystal Spectrometer (FCS) image in the O VIII line and with an H α image (Lang et al. 1987a). This figure shows that all of the X-ray emitting plasma was detected at 20 cm, with additional 20 cm emission above and near sunspots where no X-ray radiation was detected. Both X-ray and 20 cm emission was detected from coronal loops or arcades of loops that have sizes of $\sim 5 \times 10^9$ cm. The emission measure and electron temperature were inferred from ratios of different line intensities, and the electron density was calculated using a volume of 3×10^{27} cm³, which equals the product of the FCS projected area and a typical scale height of 3×10^9 cm. Our analysis indicates that the electron temperature and density were fairly uniform throughout the region, with $T_e = 2.7 - 3.1 \times 10^6$ K indicate that thermal bremsstrahlung ought to be optically thin for plausible loop widths, and that thermal gyroresonance radiation can be optically thick for plausible magnetic fields strength of $H > 130$ gauss.

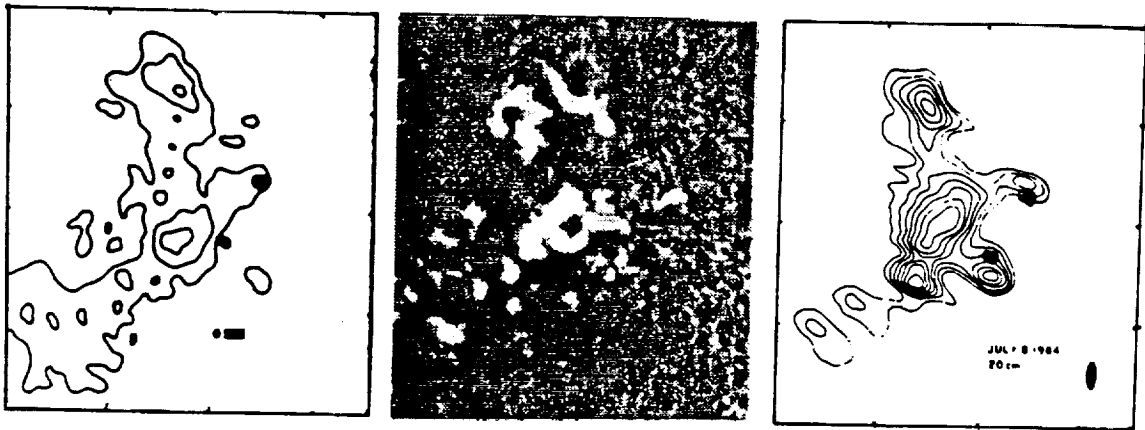


Figure 1. A comparison of soft x-ray (SMM-FCS-left), H α (SOON-middle) and 20 cm (VLA-right) images of AR 4532 on 1984 July 8. The angular scale can be inferred from the 120" spacing between the fiducial marks on the axes. The contours of the 20 cm map mark levels of equal brightness temperature corresponding to 0.4, 0.5 ... 1.0 times the maximum brightness temperature of 1.4×10^6 K. The soft X-ray data were taken in the O VIII line (18.9 Å) with contours corresponding to 4, 8 and 15 counts s $^{-1}$.

Conclusive evidence for the importance of thermal gyroresonance emission comes from observations of sharp line-like enhancements in the microwave brightness temperature spectra of some active regions (Willson 1985; Lang et al 1987b). It has been predicted that thermal cyclotron lines might be observed if the radiation is emitted from hot, thin regions, or current sheets where the magnetic field is relatively constant (Syrovatskii 1977; Zheleznyakov and Zlotnik 1980; Kuznetsov and Syrovatskii 1981). Figure 2 shows a comparison between a 20 cm loop and SMM and H α images for another active region, while Figure 3 shows the brightness temperature spectrum at 10 different frequencies, as measured at the top of the loop. The peak brightness-temperature at $\nu = 1650$ MHz is higher than the electron temperature inferred from the X-ray data ($T_e = 2.6 \times 10^6$ K) while the brightness temperature at neighboring frequencies is lower. If the spectral feature is attributed to a thermal cyclotron line, then it indicates that the optical depth of thermal gyroresonance radiation must be greater than that of thermal bremsstrahlung at these frequencies, and that the coronal loop is inhomogeneous, with higher temperatures in some parts of the loop. The central frequency and narrow width of the line-like feature suggest that the magnetic field strength in this hotter layer is $H = 196 \pm 5$ or 147 ± 5 gauss, if the cyclotron radiation is generated at the third or fourth harmonic of the gyrofrequency, respectively.

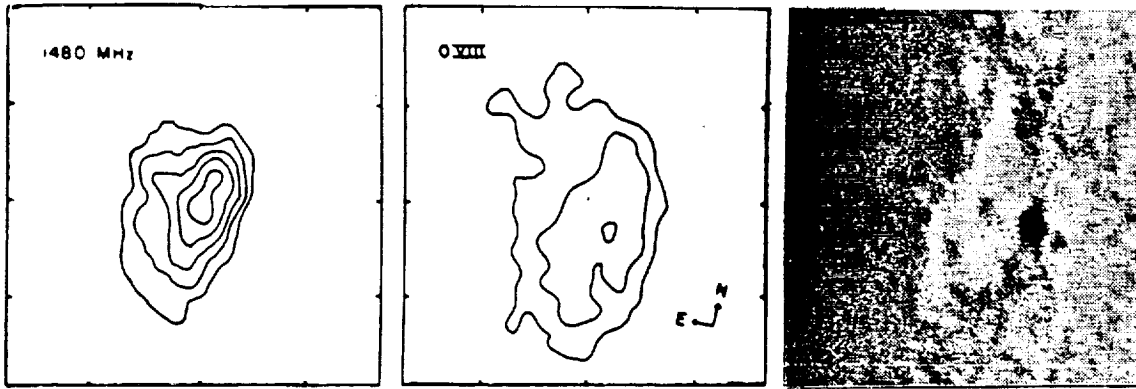


Figure 2. A comparison of 20 cm (VLA-left), soft X-ray (SMM-FCS-center) and H α (SOON-right) images of AR 4663 on 1985 June 7. The field of view of all three images is identical, and the angular scale can be inferred from the 60" spacing between fiducial marks on the axes. The contours of the 20 cm map mark levels of equal brightness temperature corresponding to 0.2, 0.4, ... 1.0 times the maximum brightness temperature of 1.8×10^6 K. The soft X-ray data were taken in the OVIII line (18.9 Å) with contours corresponding to 3, 7, 14 and 24 counts s^{-1} above a background level of 10 counts s^{-1} with a maximum signal of 18 counts s^{-1} .

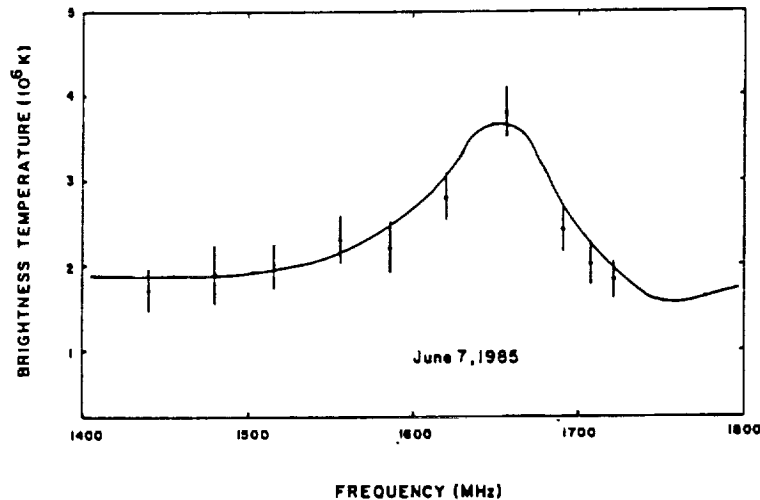


Figure 3. The maximum brightness temperatures of the coronal loop of AR 4663 at 10 closely spaced frequencies.

3.2 Large-Scale Coronal Loops at 90 cm Wavelength.

Recent developments at the VLA have made it possible to observe the Sun at 90 cm wavelength. When the VLA is in the most extended configuration the angular resolution is about 5 seconds of arc or about a factor of 20 better than that available on other instruments at this wavelength. In Figure 4 we show full-disk synthesis maps of the Sun at 20 cm and 90 cm on February 20, 1987. During these observations, the

VLA was in the C-D hybrid configuration which provided synthesized beamwidths of $\sim 26'' \times 54''$ at 20 cm and $\sim 113'' \times 237''$ at 90 cm (crosses).

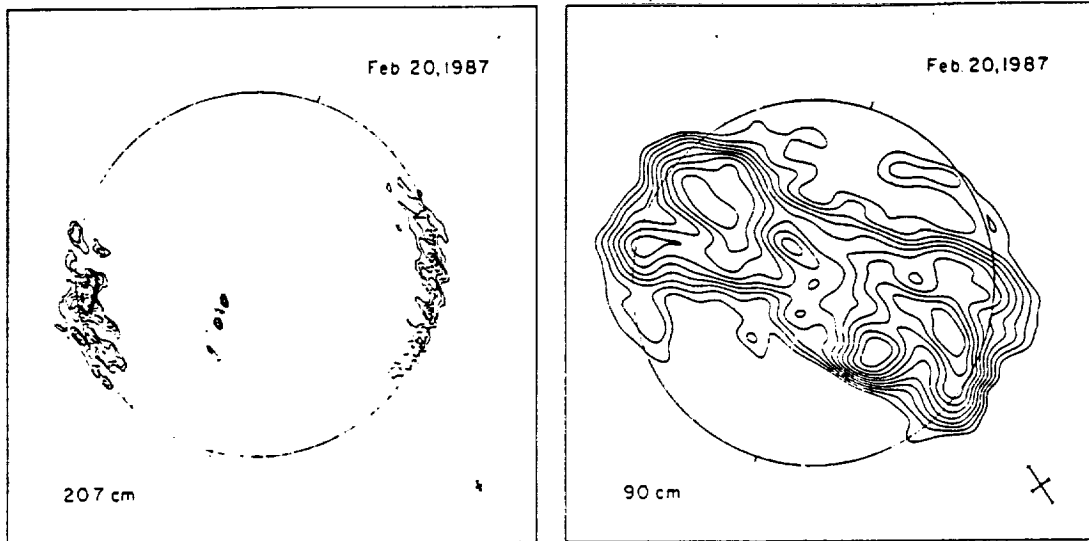


Figure 4. Four-hour VLA synthesis maps of the Sun at 20.7 cm (left) and 90 cm (right) wavelength on 20 February 1987. The contours mark levels of equal brightness temperature, T_B . The 20.7 cm map has an outermost contour of $T_B = 1.3 \times 10^5$ K a contour interval of 6.5×10^4 K and peak brightness temperature of $T_B = 6.5 \times 10^5$ K. The 90 cm map has an outermost contour of $T_B = 5.5 \times 10^4$ K a contour interval of 5.5×10^4 K, and a peak brightness temperature of $T_B = 5.7 \times 10^5$ K. The circles denote the edge of the optically-visible solar disk, and the Sun's north-south axis is denoted by the two short lines that intersect each circle.

A comparison with a Kitt Peak magnetogram shows that the 20 cm emission was associated with bipolar active regions (sizes 2'-3') with strong magnetic fields similar to the situation described in the previous section. The emission at 90 cm however indicates six or seven elongated structures with angular extents ranging between 3' and 10'. These sources have no obvious association with strong magnetic fields or other optical features. Since observations at longer wavelengths generally refer to greater heights in the solar atmosphere, these results suggest that the coronal region where the 90 cm emission originates is highly structured, but that it is concentrated in more extended loops that connect areas of less intense magnetic fields. In this sense, high resolution full-disk 90 cm maps may act as "coronagrams" that outline the structure of global magnetic fields, just as Kitt peak magnetograms delineate more intense, smaller scale photospheric fields. A comparison of the 90 cm map with one made two days later reveals that some of the sources have evolved or even disappeared during the day between observations. These observations indicate that the middle corona is dynamic, with evolutionary timescales of a few days or less.

3.3 Observations of a Solar Noise Storm.

We have also used the VLA at 90 cm to study a solar noise storm (Lang and Willson 1987). Noise storms are, in fact, the most common type of solar activity at decimetric and metric wavelengths (see eq. Elgaroy 1977 and Kai, Melrose and Suzuki 1985). They consist of thousands of narrow-band, impulsive spikes or bursts superimposed on a wide-band continuum. The continuum is usually observed between ~ 50 and 350 MHz and normally lasts for a few hours to several days.

In Figure 5 we show a plot of the noise storm intensity together with a plot of the 1-8 Å GOES X-ray flux. The noise storm consisted of many burst-like spikes superimposed on a slowly-varying component. The most intense 90 cm emission followed a soft X-ray burst by about 30 minutes, and may have been triggered by an outward moving disturbance from the source of the X-ray event. The radio spikes are similar to Type I bursts but the relatively long VLA integration time of 6.7 seconds may have averaged the emission of several Type I bursts or chains of bursts. Both the spikes and the slowly varying emission were $95 \pm 5\%$ right hand circularly polarized.

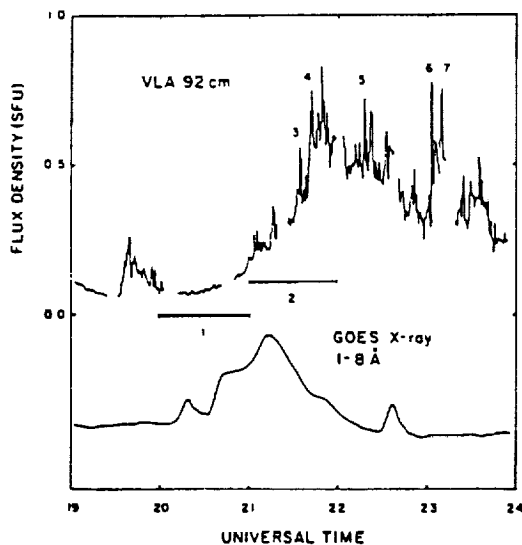


Figure 5. The time profile of a solar noise storm observed with one interferometer pair of the VLA at 92 cm wavelength (top) is compared with the soft X-ray emission detected by the GOES satellite (bottom). The data have been smoothed over 33.2 s. Spike-like bursts are superimposed upon a slowly-varying background; both of these components were $95 \pm 5\%$ right-hand circularly polarized.

A series of VLA snapshot maps made at successive peaks (Figure 6) depict the evolution of the noise storm. The peaks originate in an elongated region that has a nearly constant shape with a half-power size of $\sim 40'' \times 120''$. Figure 7 shows that these sources were located between widely separated active regions (separation $\sim 6'$) seen in the underlying photosphere.

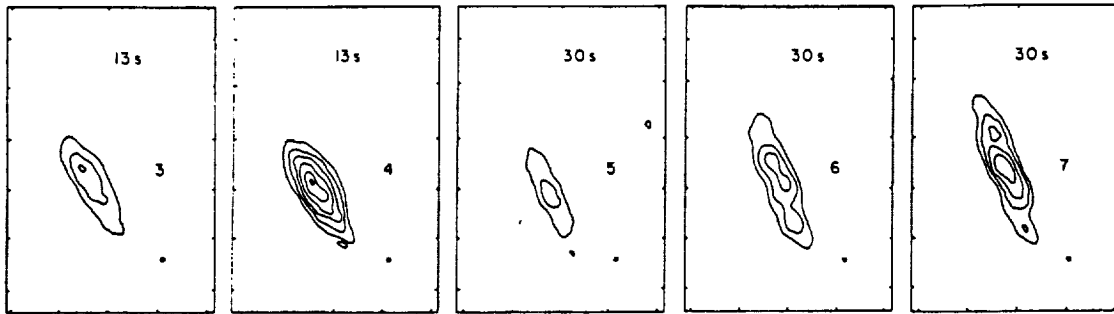


Figure 6. VLA snapshot maps of successive peaks in a solar noise storm at 92 cm wavelength. These peaks are denoted by 3,4,5,6 and 7 in Figure 5. The contours mark levels of equal brightness temperature, T_B , with an outermost contour of $T_B = 3.8 \times 10^6$ K, a contour interval of 2.5×10^6 K, and a peak brightness temperature of $T_B = 1.0 \times 10^7$ K.

Previous observations of solar noise storms suggest that sense of circular polarization should correspond to the ordinary mode of wave propagation expected from plasma radiation in a strong magnetic field (Dulk and Nelson 1973; Stewart 1985). The high right handed circularly polarized source might therefore originate in coronal magnetic fields that are associated with the leading negative polarity sunspot shown in Figure 7. If this is the case, and if the source projects radially upward from this spot, then from the limbward projection of the source we infer a height of $h = 0.15 \pm 0.03 R_\odot$ for the noise storm. Under the assumption that the radiation is emitted at the fundamental of the plasma frequency ν_p , we infer an electron density of $N_e = 1.4 \times 10^9 \text{ cm}^{-3}$, and a magnetic field strength of $H \ll 100$ gauss, if $\nu_H \ll \nu_p$, where $\nu_H = 2.8 \times 10^6$ Hz is the gyrofrequency.



Figure 7. A Very Large Array (VLA) synthesis map of solar noise storm at 92 cm wavelength is superimposed on a Kitt Peak National Observatory (KPNO) magnetogram taken on the same day. The VLA map covered the one hour time interval between 2300 and 2400 UT. Its synthesized beamwidth is denoted by the black spot. The contours mark levels of equal brightness temperature, T_B , with an outermost contour of $T_B = 1.0 \times 10^6$ K and a contour interval of 7.2×10^5 K. The magnetogram was kindly provided by Jack Harvey of the National Solar Observatory.

ORIGINAL PAGE IS
OF POOR QUALITY

4. MICROWAVE OBSERVATIONS OF THE CORONAE OF ACTIVE LATE-TYPE STARS

4.1 A VLA Survey of Active Cool Stars at 6 cm Wavelength

Observations using the High Energy Astronomical Observatory (HEAO-1) and Einstein (HEAO-B) satellites indicate that most active cool stars of spectral type F-M are intense X-ray emitters (see Rosner, Golub and Vaina 1985) for a recent review). If the solar analogy applies, then there stars must also have hot ($T_e = 10^6 - 10^8$ K) coronae with large-scale loops and intense photospheric magnetic fields. The coronal X-ray luminosity appears to increase with the square of the stellar rotation rate (Pallavicini et al 1981) and this correlation is probably related to the internal dynamo mechanism that generates the stellar magnetic field. Chromospheric activity also increases with the rotational velocity, but it additionally depends on spectral type, or equivalently, with the depth of the convection zone (Noyes et. al 1984).

If these stars have large-scale magnetic loops, then quiescent microwave emission might also be detected from thermal or non-thermal electrons trapped in these loops. Quiescent emission has in fact been detected from at least one class of late-type stars, the dwarf M flare stars using the VLA (Gary and Linsky 1981; Topka and Marsh 1982; Linsky and Gary 1983; Pallavicini, Willson and Lang 1985; Willson, Lang and Foster 1987).

The radiation mechanism that gives rise to this emission is somewhat controversial. The emission from the star EQ Peg has been interpreted as thermal gyroresonance radiation by electrons spiralling in regions of high magnetic field (Gary and Linsky 1981; Topka and Marsh 1982). This interpretation is suggested by the analogy with the Sun, in which intense, highly circularly polarized centimeter wavelength emission is usually observed from magnetic field regions overlying sunspots. However, for coronal temperatures of $T_e = 10^6 - 10^7$ K, this explanation requires magnetic field strengths of several hundreds gauss in loops that are many times larger than the star, and photospheric magnetic field strengths that may be at least an order of magnitude higher than observed on late-type stars. An alternative explanation is gyrosynchrotron-radiation from non-thermal electrons accelerated more or less continuously in weaker magnetic fields above starspots (Pallavicini, Willson and Lang 1985; Willson, Lang and Foster 1987).

Since it would be interesting to correlate intrinsic properties of the stars with microwave emission, we have recently begun a 6 cm VLA survey of nearby active stars of spectral type F,G, and K (Table 1). All of these stars exhibit chromospheric activity and many of them rotate faster than the Sun. Some of them also have strong photospheric magnetic fields, and some exhibit chromospheric variability, indicative of stellar activity cycles. The results of our initial observations are summarized in Table 1, where we give the rotation period, distance, and when available the photospheric magnetic field strength and X-ray luminosity, and either the flux or 3σ upper limits. Of the 18 stars observed, two were detected, namely BY Draconis and BD + 26° 730. Both are members of the BY Draconis class of stars,

and both show evidence of long-term photometric variations, suggestive of activity cycles (Phillips and Hartmann 1978). BY Draconis was ~ 8% left hand circularly polarized, while ED + 260730 was less than 5% circularly polarized. BD 260730 also systematically increased in intensity by about a factor of two during our observation period of 60 minutes, but there was no evidence for narrow-band emission as has been observed from some active stars (see section 4.2). Our preliminary results indicate that in general, rapid rotation and or high surface magnetic fields are not sufficient to yield detectable radio emission, suggesting that these fields do not extend far out into the corona, or that the coronal loops do not have a high enough density of thermal or nonthermal particles. (see Willson and Lang (1987) for a detailed discussion of these results).

Table 1. Results of a 6 cm VLA Survey of Active Cool Stars

STAR NAME	Sp. CL.	θ (days) ^a	D (pc)	H (gauss)	L_x (10^{26} erg s ⁻¹)	τ (mJy)
9 Oct	G2	7.7	20.4			< 0.16
HD 4628	G2	38	6.9			< 0.17
HD 16160	G3	45	7.2			< 0.16
ϵ Ori	G2	11.3	3.1	2850 ^d	200 ^h	< 0.15
HD 25988	F7	2.6	27			< 0.15
HD + 260730	K5	-	-			2.5 - 7.5
GL 202	M8	2.6	15.6			< 0.15
HD 45099	G1	7.3	12.0			< 0.18
GL 311	G1.5	3.7	15.6			< 0.15
HD 82895	G8	18.1	5.2			< 0.16
GL 417	G2	5.3	23.9			< 0.15
β Com	G0	12.4	8.3		2000	< 0.15
HD 152391	q8	11.1	14.9			< 0.17
J6 Oph	K1, K5	22.9	5.4	2080 ^d		< 0.15
HD 156026	K5	18.0	5.4			< 0.16
HD 190007	K2	29.3	14.1			< 0.14
RY Dra	K6	-	15.6		3200 ^d	3.8
61 Cyg	K5, K7	38.48	3.4	3240 ^d	~30 ^h	< 0.19

Refs. a) March (1984)
 b) Johnson (1981)
 c) Valina et al (1981)
 d) Golub (1983)
 e) Hayes et al (1984)

4.2 Observations of Narrow Band Microwave Bursts from Stars.

The high sensitivity of instruments such as the VLA and Arecibo has made it possible to study burst emission from active stars. These bursts are often highly circularly polarized, suggesting an intimate connection with stellar magnetic fields. Brightness temperatures of $T_B > 10^{10}$ K are often inferred from observations of millisecond spikes observed from the dwarf M flare star AD Leonis (Lang et al 1983; Lang and Willson 1986b). These characteristics are suggestive of a coherent radiation mechanism.

Conclusive evidence of a coherent mechanism came when observers began to study the dynamic spectra of stellar microwave bursts and found that some showed evidence of narrow-band characteristics. Lang and Willson (1986a) found that variations in the 20 cm flux from YZ Canis Minoris had a fractional bandwidth of $\Delta\nu/\nu_0 < 0.03$. Similar results were obtained for the stars AD Leonis and L726-8A by White, Kundu and Jackson (1986). Dynamical spectra in both time and frequency for one burst emitted by the flare star IV Ceti showed no variations as a function of frequency across a band of 41 MHz, while another circularly polarized exhibited complex frequency structure with narrow-band components of $\Delta\nu < 3.0$ MHz. (Bastian and Bookbinder (1987)).

In Figure 8 we show our most recent Arecibo observations of burst emission from AD Leonis. These observations were made at wavelengths near 20 cm using a 64 channel autocorrelator and a bandwidth of 40 MHz (For a description of our observing technique, see Willson and Lang (1987)). Here, the time resolution of the data is 1.25 seconds. This burst was ~ 100% right circularly polarized and consisted of a number of individual components each with a lifetime of few seconds. The intensity of the burst decreases rapidly with increasing frequency, with spectral indices, α , ($S_\nu \propto \nu^\alpha$) ranging from -55 to -70. Such high spectral indices cannot be accounted for by an incoherent emission process such as gyrosynchrotron radiation which predicts more broad-band emission.

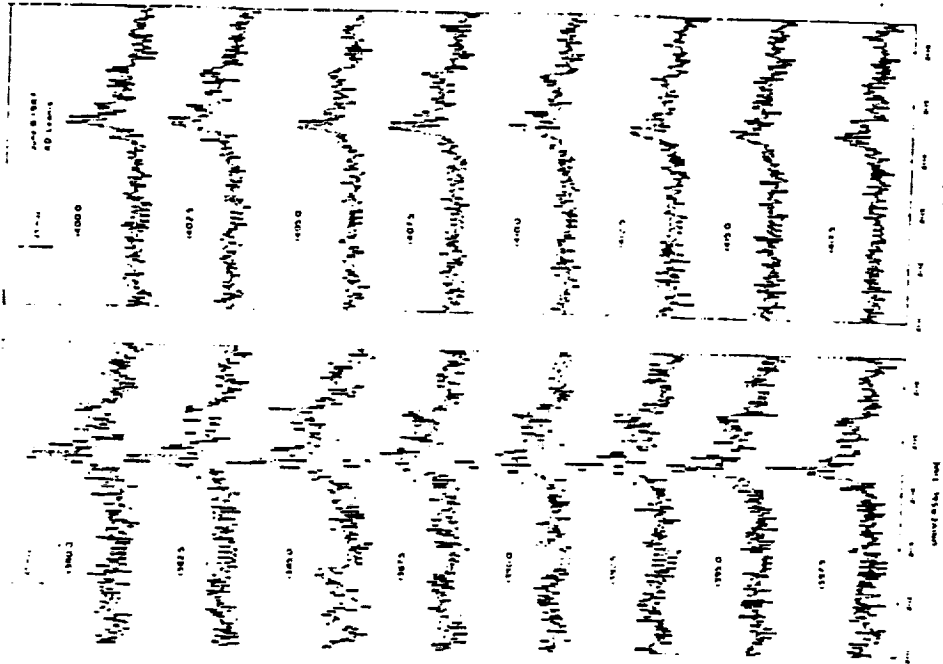


Figure 8. The right circularly polarized intensity of a 20 cm burst observed from AD Leonis over a 40 MHz bandwidth. Each channel is ~ 2.5 MHz wide and is centered at the given frequency, in MHz.

Finally, in Figure 9 and 10 we show recent VLA dynamical spectral observations of YZ Canis Minoris (Lang and Willson 1988). In Figure 9 we plot the left and right circularly polarized signals which represent the averages of 15 contiguous frequency channels covering a bandwidth of ~ 50 MHz. Here the data have been averaged over a time interval of 1.5 minutes. This figure shows that the emission is nearly 100% left circularly polarized and variable on timescales of tens of minutes. In Figure 10 we show spectra for different intervals denoted on each plot. These spectra indicate that, in some cases, the emission has a relatively-narrow bandwidth ($\Delta\nu < 50$ MHz) whose central frequency shifts with time. The total intensity at other times appears to be broad-band with $\Delta\nu > 50$ MHz, but these spectra could represent the average of many narrow-band emission. The interesting aspect of the narrow-band emission is that it persists for relatively long time intervals of ten minutes with a well defined bandwidth and central frequency. Coherent emission processes such as an electron-cyclotron maser emission or plasma

plasma radiation can produce narrow band radiation at the first or second harmonic of the gyrofrequency or plasma frequency, but if the magnetic field or electron-density change significantly within the source during the periods of observation, then the average emission profile will be smeared, resulting in wide-band spectrum. The fact that the narrow-band emission persisted for ten minutes therefore is surprising and suggests that these parameters remained remarkably constant in the stellar corona.

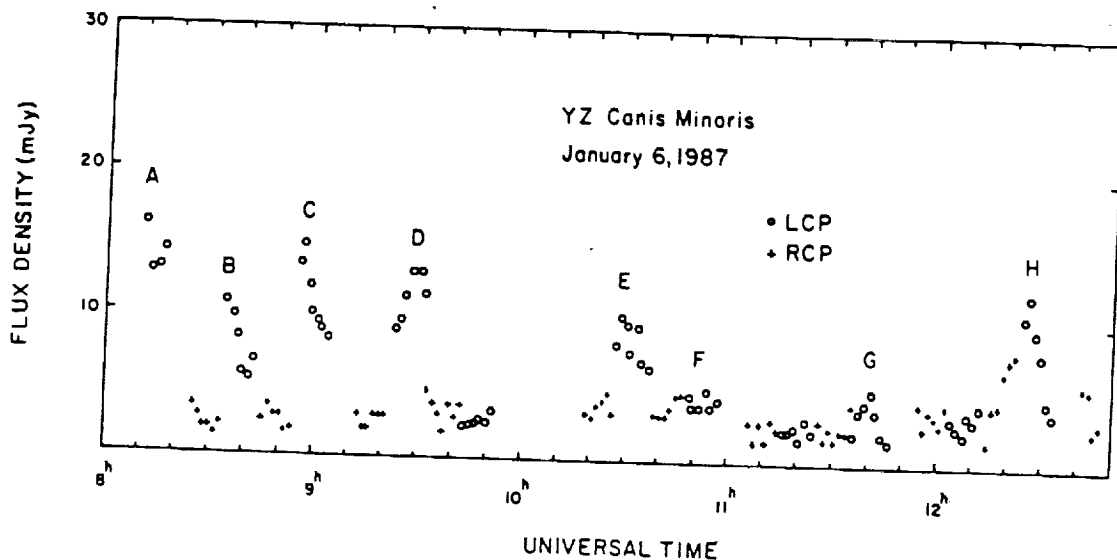


Figure 9. The right and left circularly polarized intensity of the radiation observed from YZ Canis Minoris, plotted as a function of time. The oppositely polarized signals were alternately recorded for 10 minutes intervals within a 50 MHz bandwidth centered on 1464.0 MHz. Here the data have been averaged over a time interval of 1.5 minutes. Frequency spectra of the slowly varying LCP radiation marked by the letters A, E, G and H are shown in Figure 10.

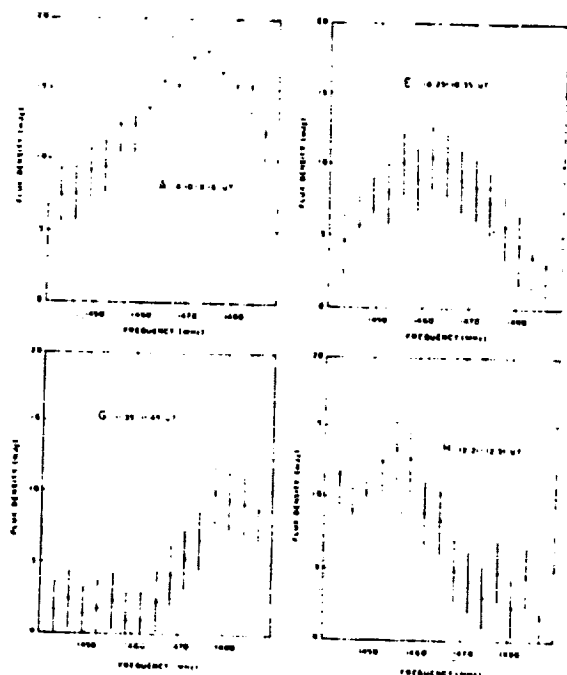


Figure 10. Frequency spectra of the left circularly polarized emission from YZ Canis Minoris for the intervals marked A, E, G and H in Figure 9. Each of the 15 frequency channels is 3.125 MHz wide. The error bars denote the 3σ noise level for the relevant time interval and bandwidth. These spectra all show evidence for narrow band radiation with $\Delta\nu < 30$ MHz. At other times, the radiation appears to have a width greater than the 50 MHz bandwidth.

ORIGINAL PAGE IS
OF POOR QUALITY

Acknowledgements

All of these observations were made in collaboration with Kenneth R. Lang at Tufts University. Radio Astronomical studies of the Sun and other active stars at Tufts University are supported under grant AFOSR-93-0019 with the Air Force Office of Scientific Research and by contract N00014-86-K-0068 with the office of Naval Research (ONR). Investigations of dwarf flare stars at Tufts are also supported by NASA grant NAG 5-477. The Very Large Array is operated by Associated Universities, Inc., under contract with the National Science Foundation. The Arecibo Observatory is part of the National Astronomy and Ionosphere Center which is operated by Cornell University under contract with the National Science Foundation.

References

- Bastian, T.S., and Bookbinder, J.A., 1987, *Nature*, 326, 678.
Dulk, G.A. 1985, *Ann. Rev. Astron. Ap.*, 23, 169.
Dulk, G.A., and Nelson, G.J. 1973, *Proc. Astr. Soc. Austr.* 2, 211.
Elgaroy, O. 1977, *Solar Noise Storms*. (New York; Pergamon Press).
Activity in Red Dwarf Stars ed. M. Rodono
Gary, D.E., and Linsky, J.L., 1981, *Ap. J.* 250, 284.
Golub, L., 1983 in *IAU Colloquium 71*, and P.B. Byrne (Dordrecht: Reidel).
Johnson, H.M., 1981, *Ap.J.*, 243, 234.
Kuznetsov, V.S., and Syrovatskii, S.I. 1981, *Solar Phys.*, 69, 391.
Kai, K., Melrose, D.B., and Suzuki, S. 1985, "Storms", in *Solar Radiophysics*, eds. D.J. McClean and N.R. Labrum (New York: Cambridge University Press) pp. 415-441.
Kundu, M.R., and Lang, K.R. 1985, *Science*, 228, 9.
Lang, K.R., and Willson, R.F., 1986a *Ap. J. (Letters)*, 302, L17.
Lang, K.R., and Willson, R.F., 1986b, *Ap.J.*, 305, 363.
Lang, K.R., and Willson, R.F. 1987, *Ap.J.* 319, 514.
Lang, K.R., and Willson, R.F. 1988, *Ap.J.* (in press).
Lang, K.R., Willson, R.F., and Rayrole, J. 1982, *Ap.J.* 258, 384.
Lang, K.R., Willson, R.F., and Gaizauskas, V. 1983, *Ap.J.*, 267, 455.
Lang, K.R., Bookbinder, J., Golub, L. and Davis, M.M. 1983, *Ap. J. (Letters)*, 272, L15.
Lang, K.R., Willson, R.F., Smith, K., and Strong, K.T. 1987a, *Ap.J.*, (in press).
Lang, K.R., Willson, R.F., Smith, K., and Strong, K.T. 1987b, *Ap.J.*, (in press).
Marcy, G.W., 1984, *Ap.J.*, 276, 286.
Noyes, R.W., Hartmann, L., Baliunas, S., Duncan, D., and Vaughan, A.H. 1984, *Ap. J.*, 279, 763.
Pallavicini, R.P., Golub, L., Rosner, R., Vaina, G.S., Ayres, T., and Linsky, J.L. 1981, *Ap.J.* 248, 279.
Pallavicini, R., Willson, R.F., and Lang, K.R., 1985, *Astron. Ap.*, 149, 95.
Phillips, M.J., and Hartmann, L. 1978, *Ap.J.*, 224, 82.
Rosner, R., Golub, L., and Vaina, G.S., 1985, *Ann. Rev. Astron. Ap.*, 23, 413.
Stewart, R.T. 1985, *Solar Phys.* 96, 381.
Syrovatskii, V.D. 1977, *Astr. Zh (letters)*, 3, 133.
Topka, K., and Marsh, K.A., 1982, *Ap.J.*, 254, 641.
Vaina, G.S., et al., 1981, *Ap.J.*, 244, 163.
White, S., Kundu, M.R., and Jackson, J. 1986, *Ap.J.*, 311, 814.
Willson, R.F. 1985, *Ap.J.*, 298, 911.
Willson, R.F., and Lang, K.R. 1987. (in preparation).
Willson, R.F., Lang, K.R., and Foster, P. 1987, *Astron. Ap.* (submitted).
Zhelznaykov, V.V., and Zlotnik, E. Ya., 1980, in *IAU Symposium 86, Radio Physics of the Sun*, eds. M.R. Kundu and T. Gergely (Dordrecht: Reidel) p. 87.

M. SIMULTANEOUS VLA-SATELLITE
OBSERVATIONS OF THE SUN*

Kenneth R. Lang**
D.A.S.O.P.
Observatoire de Paris - Meudon
92195 MEUDON PRINCIPAL CEDEX
FRANCE

*Presented at the XXVII COSPAR (Committee on
Space Research) meeting in Helsinki, Finland
during Workshop XV - Scientific Planning for
the Next Solar Maximum and Beyond on 26 July
1988.

**On sabbatical leave from the Department of
Physics and Astronomy, Robinson Hall,
Tufts University, MEDFORD, MA 02155, U.S.A.

ABSTRACT

The Very Large Array (VLA) and satellite-borne telescopes can be used in the 1990s to provide unique observations of the quiescent and active corona with comparable resolution in time and space. Recently available 90-cm VLA data specify closed and open magnetic structures in the low solar corona, providing unique information about the initiating source of coronal mass ejections observed by satellite coronagraphs. The physical properties of quiescent coronal loops can be inferred from combined soft X-ray (electron density and temperature) and 20-cm VLA (magnetic field strength and structure) data. Systems of coronal loops within a single active region have different temperatures and different radiation mechanisms that can only be detected by observations in both spectral domains. The combined VLA-satellite observations will also specify magnetic interaction and particle acceleration before and during flares, including magnetic triggering in the corona (VLA) and preflare heating (VLA-satellite).

INTRODUCTION

The Very Large Array (VLA) can provide unique information about large-scale magnetic structures, coronal holes, and coronal loops. Newly-developed receiving systems at 92-cm wavelength permit observations of quiescent and active emission from filaments and coronal holes, while 20-cm observations provide similar information for coronal loops within active regions.

FILAMENTS AND CORONAL HOLES

The first VLA synthesis maps of the quiescent corona at 92-cm wavelength (327 MHz) revealed intense, elongated structures that were not systematically associated with any optical counterpart, including active regions, filaments, sunspots and magnetic neutral lines /1/. Filaments are sometimes associated with enhanced 92-cm emission, however, and there is a reduction in brightness over polar coronal holes at this wavelength /1/, /2/.

The ubiquitous noise storms are the only source of intense 92-cm radiation associated with solar active regions. These storms are apparently located in large-scale magnetic loops that connect with more distant areas on the Sun /3/. Individual noise storm bursts and the background continuum can be resolved in both space and time by using simultaneous observations with the VLA and the Nancay Radioheliograph /4/. Such information will provide important constraints to our future understanding of noise storms and related activity on the Sun.

Recent VLA synthesis maps indicate that intense, quiescent 92-cm radiation is definitely associated with the large-scale magnetic structures detected as dark filaments in H α photographs (see Fig. 1, 2). Such an association was first suggested by a statistical study of numerous one-dimensional scans of moderate angular resolution at meter wavelengths (169 MHz) /5/, but subsequent two-dimensional maps at this wavelength suggested that extended quiescent filaments have no radio counterpart /6/, /7/. The results shown in Figures 1 and 2 indicate that this is not

always the case at 92-cm.

Future VLA observations of large-scale magnetic structures can be used to test models for the origin of coronal mass ejections. These outward-moving magnetic bubbles are currently thought to be initiated by global magnetic changes; associated chromospheric activity, detected as erupting prominences or H α flares, is thought to be the result, rather than the cause, of these changes /8/. Such models have been derived from observations with satellite-borne coronagraphs whose occulting disks block the visible photosphere and the low corona. VLA observations at 92-cm wavelength can enhance and extend future coronagraph investigations by observing the formation of coronal mass ejections in the low solar corona at both the limb and across the entire solar disk.

Reductions or depressions in the 92-cm radiation are apparently associated with coronal holes in both the polar and equatorial regions (see /1/ and Fig. 1). Future VLA observations can therefore provide new insights to the formation and evolution of coronal holes and the high-speed solar wind that probably originates in them. Comparisons with satellite observations may resolve current uncertainties about the density and temperature of these coronal holes /9/.

Although intense, quiescent 92-cm sources are not associated with active regions, the quiescent emission at 20-cm wavelength is dominated by radiation from coronal loops that are often anchored within single active regions. These magnetic loops are smaller than the large-scale magnetic structures detected at the longer wavelength; but the 20-cm loops dominate the coronal structure of active regions and store the magnetic energy that is released during powerful eruptions from them /10/, /11/.

When the 20-cm VLA results are combined with satellite observations of spectral lines at soft X-ray wavelengths, the physical properties and dominant radiation mechanisms can be specified /12/. There are coronal structures that are detected at 20-cm but remain invisible at X-ray wavelengths and vice versa (see Fig. 3). Future VLA data will also uniquely specify the strength and structure of the coronal magnetic fields.

Observations of the 20-cm loops during the coming solar maximum will help establish magnetic changes that probably trigger solar eruptions /13/, /14/. The magnetic interaction of coronal loops apparently involves reconnection processes that release stored magnetic energy and accelerate particles near their tops (see Fig. 4). Simultaneous satellite observations at soft and hard X-ray wavelengths will help unravel the detailed triggering and acceleration mechanism.

ACKNOWLEDGEMENTS

Radio astronomical studies of the Sun at Tufts University are supported under grant AFOSR-83-0019 with the Air Force Office of Scientific Research and contract N00014-86-K-0068 with the Office of Naval Research. Collaborative long-wavelength solar observations by Tufts University and the Observatoire de Paris are supported by National Science Foundation grant INT-8602285 and Centre National de la Recherche

Scientifique grant 920038. Simultaneous SMM and VLA observations of the Sun are supported by NASA grant NAG 5-501. The Very Large Array is operated by Associated Universities Inc., under contract with the National Science Foundation.

REFERENCES

1. K. R. Lang, R. F. Willson, and G. Trottet, High-resolution VLA maps of the quiescent corona at 90-cm wavelength, Astron. Astrophys. in press (1988).
2. R. K. Shevgaonkar, M. R. Kundu, and P. D. Jackson, Variability of Metric Emission from the Sun, Astrophys. J., submitted (1988).
3. K.R. Lang, and R. F. Willson, Astrophys. J. 319, 514-519 (1987). Also see M. F. Lantos-Jarry, Solar Phys., 15, 40 (1970).
4. A. Kerdraon, G. Trottet, K. R. Lang, and R. F. Willson, High-resolution VLA-Nancay observations of the Sun, this issue.
5. F. Axisa, Y. Avignon, M. J. Martres, M. Pick, and P. Simon, Solar Phys. 19, 110-127 (1971).
6. C. E. Alissandrakis, P. Lantos, and E. Nicolaidis, Solar Phys., 97, 267-282 (1985).
7. P. Lantos, C. E. Alissandrakis, T. Gergely, and M. R. Kundu, Solar Phys., 112, 325-340 (1987).
8. A. J. Hundhausen, The origin and propagation of coronal mass ejections, Solar Wind Six, in press (1988).
9. G. A. Dulk, K. V. Sheridan, S. F. Smerd, and G. L. Withbroe, Solar Phys. 52, 349-367 (1977).
10. K. R. Lang, and R. F. Willson, Adv. Space Res., 2, No. 11, 91-## (1983).
11. K. R. Lang, and R. F. Willson, Adv. Space Res. 4, No. 7, 105-### (1984).
12. K. R. Lang, R. F. Willson, K. L. Smith, and K. T. Strong, Astrophys. J., 322, 1035-1043, 1044-1051 (1987).
13. M. R. Kundu, and K. R. Lang, Science, 228, 9-15 (1985).
14. K. R. Lang, and R. F. Willson, Adv. Space Res. 6, No. 6, ###-### (1986).

FIGURE LEGENDS

Fig. 1. Three-hour VLA synthesis map at 92-cm wavelength (327.0 MHz) on 15 May, 1988 between 13 h and 16 h U.T. The regions of enhanced 92-cm emission are well correlated with dark filaments shown in a H α photograph taken on the same day (see Figure 2). The elongated filaments have similar shapes at 92-cm and H α wavelengths. Active regions (squares) are not associated with enhanced 92-cm radiation; but they dominate the intense radiation at 20-cm wavelength and are observed as bright H α features. Regions of depressed 92-cm emission are at least partly due to equatorial coronal holes. The contours mark levels of equal brightness temperature, T_b , with an outermost contour of $T_b = 7.8 \times 10^4$ K, a contour interval of 7.8×10^4 K, and a peak brightness temperature of $T_b = 7.8 \times 10^5$ K. The synthesized beamwidth is denoted by the small black spot in the lower left-hand corner; it has angular dimensions of 80" x 55" at a position angle of -20° .

Fig. 2. An H α spectroheliogram taken at 6 h and 36 m U.T. on 15 May 1988 at the Observatoire de Paris, Meudon. Five dark filaments are well correlated with regions of enhanced emission at 92-cm wavelength (see Figure 1); the elongated shape of the longer filaments is also detected in the radio data. Areas of bright H α emission (plage-active regions) are not associated with enhanced 92-cm emission; but they dominate the radiation at 20-cm wavelength.

Fig. 3. A comparison of soft X-ray (Solar Maximum Mission Satellite) and 20 cm (Very Large Array) images of AR 4532 on 1984 July 8. The field of view of all two images is the same, and the angular scale can be inferred from the 120" spacing between the fiducial marks on the axes. The contours of the 20 cm map mark levels of equal brightness temperature corresponding to 0.4, 0.5, 0.6...1.0 times the maximum brightness temperature of 1.4×10^6 K. The soft X-ray data were taken in the 0 VIII line (18.9 A) with contours corresponding to 4, 8, and 15 counts s $^{-1}$ above a background level of 10 counts s $^{-1}$ with a maximum signal of 20 counts s $^{-1}$. Here the sunspots are denoted by small black dots with a circle around them.

Fig. 4. A VLA snapshot map during a 10-second interval at 20 cm wavelength catches a powerful eruption at the site of particle acceleration. The energetic particles originate at the apex of coronal loops; some of them travel to the Earth where they interfere with radio communication and high-flying aircraft. The VLA contours are superposed on an H α photograph of flare emission at lower levels in the solar atmosphere.

VLA 3 hour synthesis map
visible solar disk at 327 MHz

MAY 15, 1988

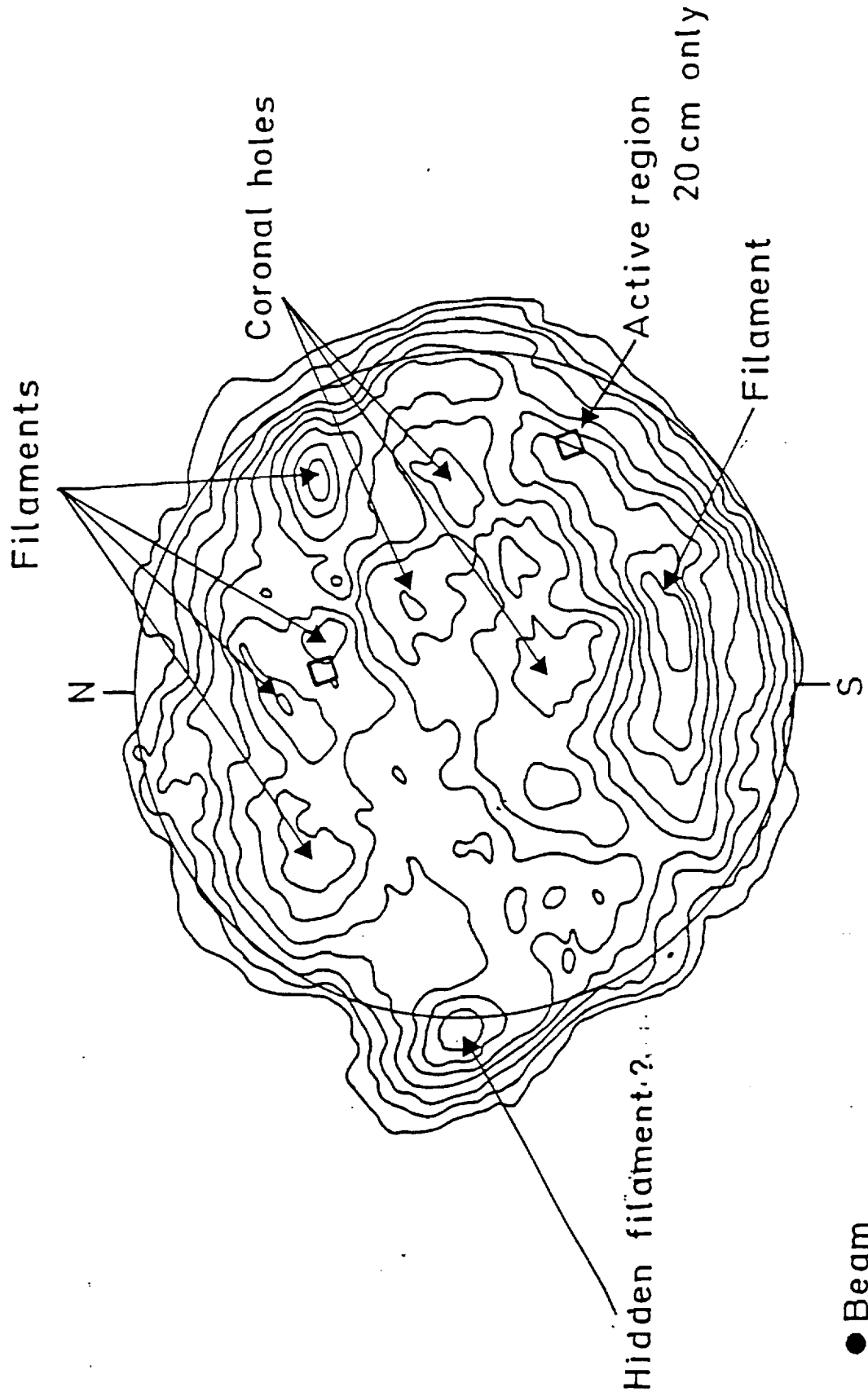


FIG. 1.

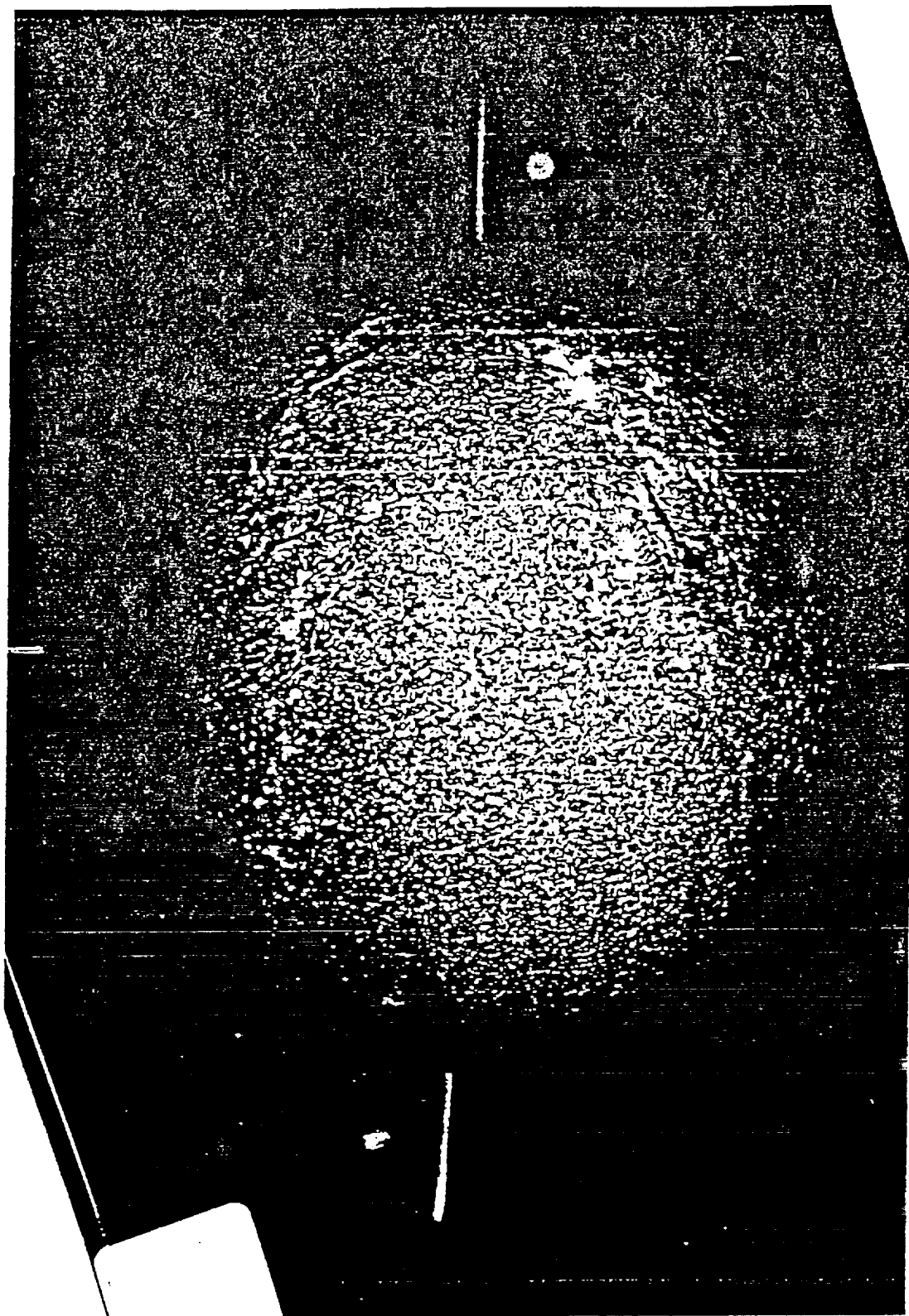
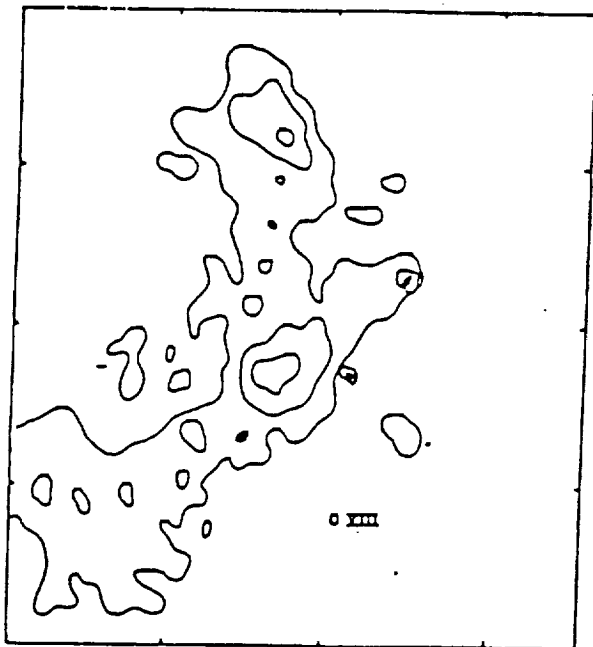
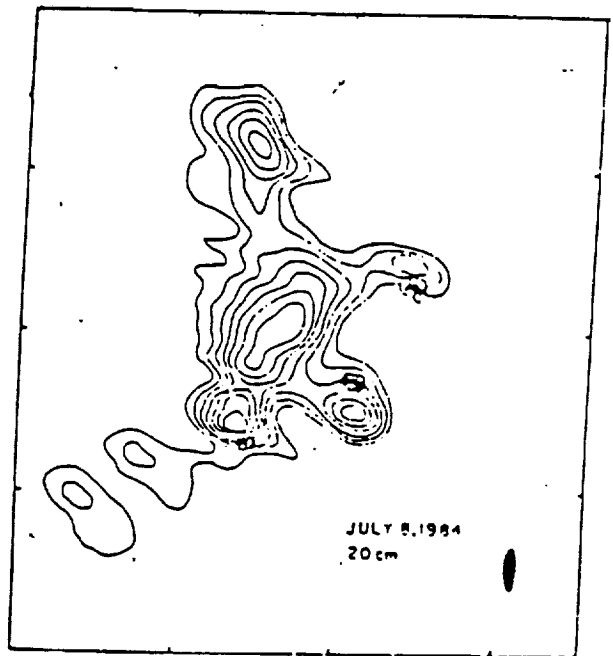


Fig. 2.



X - Rays
SMM SATELLITE



RADIO RADIATION
VERY LARGE ARRAY

Fig. 3.

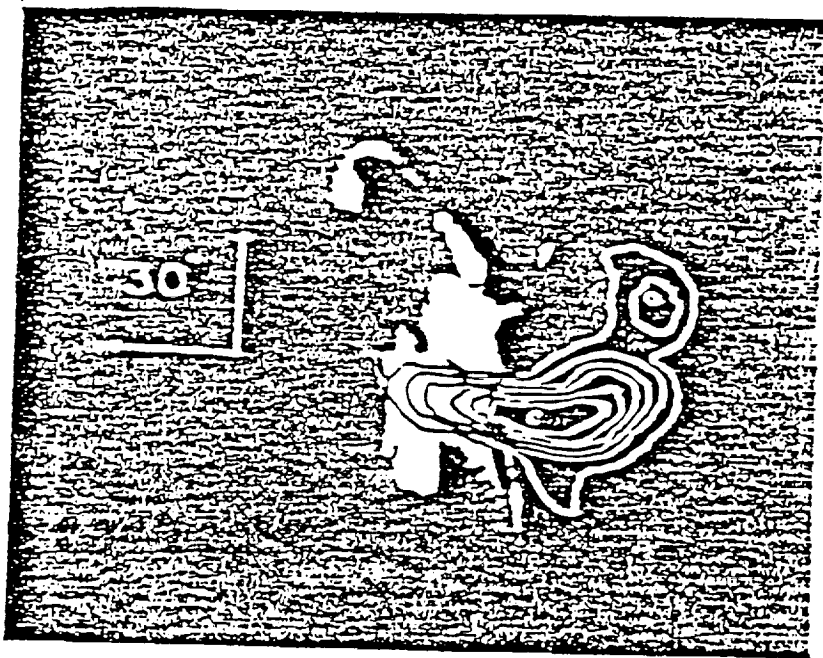


Fig. 4.

N. HIGH RESOLUTION VLA - NANCAY OBSERVATIONS OF THE SUN *

Alain Kerdraon and Gérard Trottet
D.A.S.O.P.
Observatoire de Paris - Meudon; CNRS-UA 324
92195 MEUDON PRINCIPAL CEDEX
FRANCE

Kenneth R. Lang ** and Robert F. Willson
Department of Physics and Astronomy
Robinson Hall
Tufts University
MEDFORD, MA 02155
U.S.A.

* Presented at the XXVII COSPAR (Committee on Space Research) meeting in Helsinki, Finland, during Workshop XV - Scientific Planning for the Next Solar Maximum and Beyond on 26 July 1988.

** On sabbatical leave from Tufts University at the Observatoire de Paris - Meudon.

A B S T R A C T

The Very Large Array (VLA) and the Nançay Radioheliograph (NR) can be used in the 1990s to provide unique observations of the quiescent and active corona. The combined data can specify the evolution and magnetic structure at a variety of heights in the quiescent corona, from compact to extended structures such as loops, streamers and coronal holes. The scientific potential of simultaneous VLA - NR research is illustrated by observations of solar noise storms with hitherto unavailable resolution in space (VLA), time (NR). Unique information will also be provided for other types of solar bursts, leading to an improved understanding of solar activity during the coming maximum.

NOISE STORMS

Noise storms are the most common type of solar activity observed at metric wavelengths. They consist of a slowly-varying, wide-band continuum radiation with superposed short-lived, narrow-band bursts. These bursts have been designated Type I bursts to distinguish them from other types of solar bursts. The background continuum, which is usually observed between 50 and 350 MHz, normally continues for a few hours, while individual bursts have bandwidths between 2 and 10 MHz and durations of 0.1 to 2 seconds /1/.

Both the background continuum and the bursts are usually strongly circularly polarized (up to 100 %), but unpolarized bursts are occasionally observed. The sense of circular polarization is constant throughout the storm; it is attributed to the ordinary mode of plasma radiation in a strong magnetic field /3/.

Noise storms have been extensively studied with the Culgoora and Nançay radioheliographs, whose respective beamwidths are $\theta \sim 2.0$ and 1.3 at 160 MHz. The resolved storm sources have sizes that tend to increase with height, and radiation at lower frequencies originates at higher altitudes

(see Fig. 1 and /4/). These sources appear to be located in large-scale magnetic loops extending high into the corona from one or more active region /5/, /6/; suggesting plasma radiation within the legs of magnetic loops whose field lines diverge with height /7/, /8/. At a given frequency, successive Type I bursts may come from either a fixed or different locations /9/, /10/, and can have a variety of sizes /11/.

Storm sources were nevertheless often unresolved with the Culgoora and Nançay instruments, for they were often operating at the limits of their capability. The Very Large Array (VLA) now provides a substantial improvement in angular resolution, θ with $\theta \approx 5''$ at 92 cm wavelength (327 MHz) in the A configuration. It has been used to fully resolve one noise storm that had an elongated shape (40" x 200"), and contained four compact components, each 40" across, during the onset and early stages /12/. Such complexity may rule out the simple conical model, or at least involve its extension to include magnetic flux tubes or scattering on field-aligned density inhomogeneities.

Because the VLA has limited integration times of $\tau \geq 3.3$ sec., simultaneous observations with the Nançay Radioheliograph ($\tau \geq 0.02$ sec.) are required to isolate individual bursts and to discriminate between the bursts and background continuum. We have therefore begun such observations during the period of common solar visibility (13 h to 16 h U.T.). This collaborative program will continue throughout the coming maximum in solar activity, thereby enhancing the scientific return of both ground-based and balloon or satellite-borne instruments.

Simultaneous observations of a solar noise storm were carried out on 27 June 1987 with the VLA in the A configuration and operating at a signal frequency of 333.0 MHz with a bandwidth of 3.125 MHz; the Nançay Radioheliograph (NR) operated at 327.0 MHz with a 700 kHz bandwidth. The integrated signal from all the VLA interferometer pairs was plotted as a function of time and compared with a similar NR record to determine bursts that were detected by both telescopes.

The VLA was then used to make successive 10-second snapshot maps for intervals of several minutes centered at the common burst time. Two examples are shown in Fig. 2. The unpolarized and polarized bursts both have elongated shapes, but they originate in different sources that are separated by 60". The unpolarized burst (degree of circular polarization $g_c \approx 10\%$) consists of a single elongated source with angular dimensions of 30" x 80", whereas the polarized one ($g_c \approx 70\%$) contained two components separated by $\approx 20''$ and embedded within an elongated 40" x 60" structure. Although previous observers have established similar overall source sizes, the VLA has determined the elongated shape, source complexity and separate burst positions for the first time.

The NR has been used to determine the time profiles shown in Fig. 3. The unpolarized burst has a rapid rise and exponential decay; its most intense component is resolved in time with a duration of ≈ 2 sec. The time of the VLA snapshot map for one of them is designated by the horizontal bar. Successive 10-second snapshot maps throughout the two-minute interval indicate that the entire chain of bursts came from the same elongated source located at the same position. Subsequent highly-polarized chains of Type I bursts may originate in other sources, however, and the unpolarized burst definitely does.

PHYSICS OF SOLAR BURSTS

These previously-unpublished noise storm results illustrate the scientific potential of simultaneous VLA-NR observations of solar activity. They will be extended during the coming maximum to include other types of solar bursts, thereby providing constraints to theoretical models. The dynamical evolution of the source size is, for example, required as an input to models of the gradual and impulsive phases of solar flares. VLA-NR observations with high resolution in time, space and frequency are also required to provide fresh insights to the physics of burst phenomena such as pulsations /13/.

ACKNOWLEDGEMENTS

ACKNOWLEDGEMENTS

Radio astronomical studies of the Sun at Tufts University are supported under grant AFOSR-83-0019 with the Air Force Office of Scientific Research and contract N00014-86-K-0068 with the Office of Naval Research.

Collaborative long-wavelength solar observations by Tufts University and the Observatoire de Paris are supported by National Science Foundation grant INT-8602285 and Centre National de la Recherche Scientifique grant 920038. Simultaneous SMM and VLA observations of the Sun are supported by NASA grant NAG 5-501. The Very Large Array is operated by Associated Universities Inc., under contract with the National Science Foundation. The Nançay Radioheliograph is supported by INSU. (Institut National des Sciences de l'Univers) by CNRS (Centre National de la Recherche Scientifique) and by Paris Observatory.

REFERENCES

1. O. Elgaroy, Solar Noise Storms, (New York : Pergamon Press, 1977).
2. C. Mercier, O. Elgaroy, A. Tlámicha, and P. Zlobec, Solar Phys., 92 375-381 (1984).
3. K. Kai, P.B. Melrose, and S. Suzuki, Storms, in Solar Radiophysics, ed. D.J. McLean and N.R. Labrum (New York : Cambridge University Press, 1985), pp. 415-442.
4. J.V. Sheridan, N.R. Labrum, W.J. Payten, G.J. Nelson, and E.R. Hill, Solar Phys., 83 167-177(1983).
5. M.F. Lantos-Jarry, Solar Phys. 15, 40-47 (1970).
6. P. Lantos, A. Kerdraon, G.G. Rapley, and R.D. Bentley, Astron. Astrophys. 101, 33-38 (1981).
7. D.J. McLean, Proc. Astron. Soc. Austr. 4, 132-138 (1981).
8. K.V. Sheridan, Storm-Source structure from two-dimensional radio-heliograph observations at meter wavelengths, in Solar Radio Storms, ed. A.O. Benz and P. Zlobec (Osservatorio Astronomico : Trieste, 1982), pp. 12-25.
9. A. Kerdraon, and C. Mercier, New observational results on noise storms, in Solar Radio Storms, ed. A.O. Benz and P. Zlobec (Osservatorio Astronomico : Trieste, 1982), pp. 27-37.
10. R.A. Duncan, Solar Phys. 97, 137-182 (1985).
11. A. Kerdraon, Astron. Astrophys. 71, 266-268 (1979).
12. K.R. Lang, and R.F. Willson, Astrophys. J. 319, 514-519 (1987).
13. G. Trottet, A. Kerdraon, A.O. Benz, and R. Treumann, Astron. Astrophys. 93, 129-132 (1981).

FIGURE LEGENDS

Fig. 1. Multiple-frequency observations of a solar noise storm with the Nançay Radioheliograph on 3 February 1986 at 150 and 164 MHz (small solid circle), 327 MHz (dashed circle) and 408 MHz (dark spot). The square denotes the position of the associated active region in the underlying photosphere. The noise storm is displaced away from a radial projection above the active region. Lower frequencies are emitted in higher regions, and the source size tends to increase with height.

Fig. 2. Very Large Array (VLA) synthesis maps for ten second intervals during a polarized burst ($\sim 50\%$ - right) and an unpolarized burst (left) on 27 June 1987. The two intervals began at 14h 30m 36.0s and 14h 46m 16s U.T., respectively. The fiducial marks on the axes are separated by $60''$, and the contours mark levels of equal brightness temperature, T_B , with an outermost contour and contour interval of 4.4×10^7 K. The peak brightness temperatures for the two intervals are 6.2×10^8 K and 3.1×10^8 K, respectively. The synthesized beam is denoted by the black spot in the lower left-hand corner; it has an angular extent of $\theta \approx 6''$. The time profiles for the two bursts are given in Figure 3.

Fig. 3. Intensity plotted as a function of time for an unpolarized burst (top) and a polarized burst ($\sim 50\%$ - bottom) with 0.5 second time resolution over two minutes on 27 June 1987. These time profiles were taken with the Nançay Radioheliograph at the same observing frequency as the VLA (~ 327 MHz) and included the times of the 10 second VLA maps shown in Figure 2.

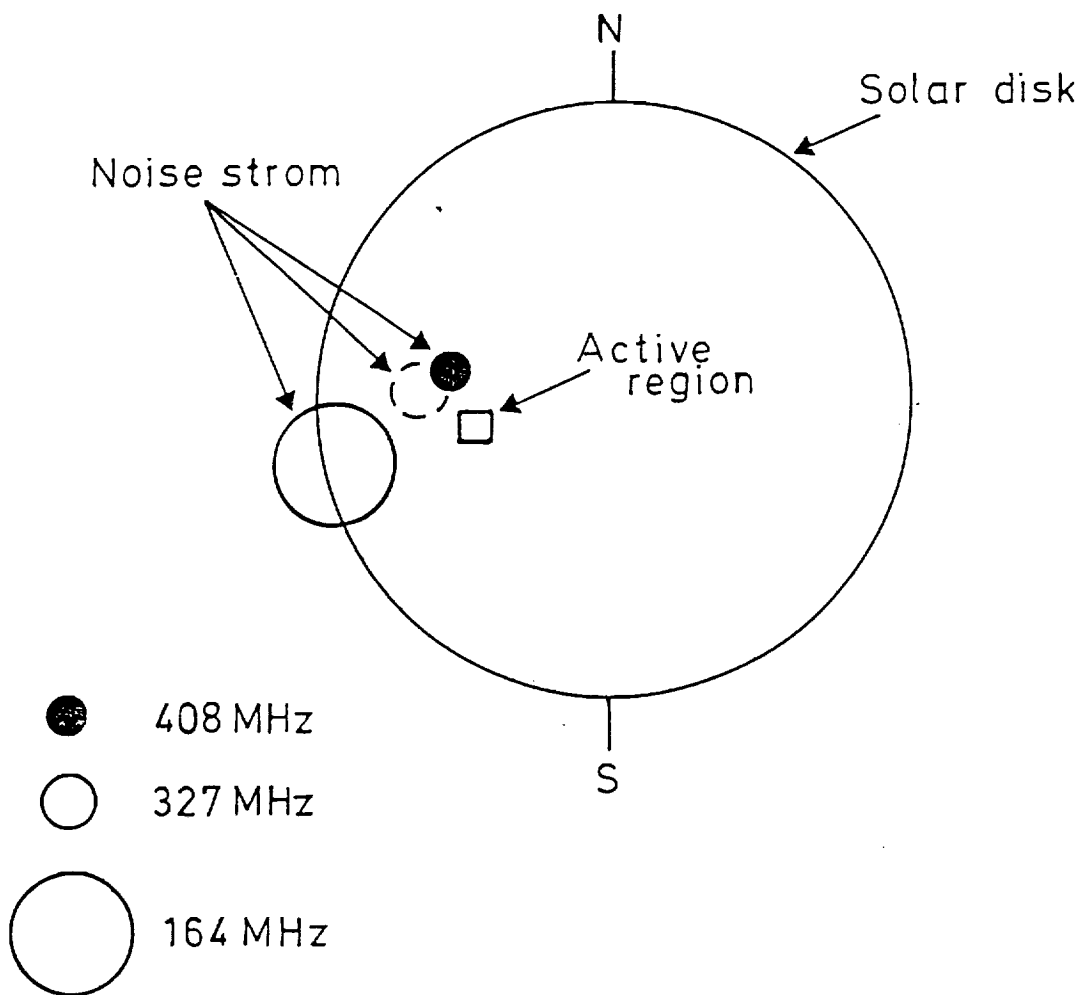
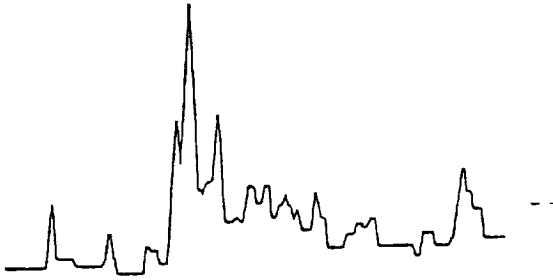


Figure 1

NANÇAY RADIOHELIOGRAPH
TIME PROFILES AT 327 MHz

unpolarized burst



polarized burst

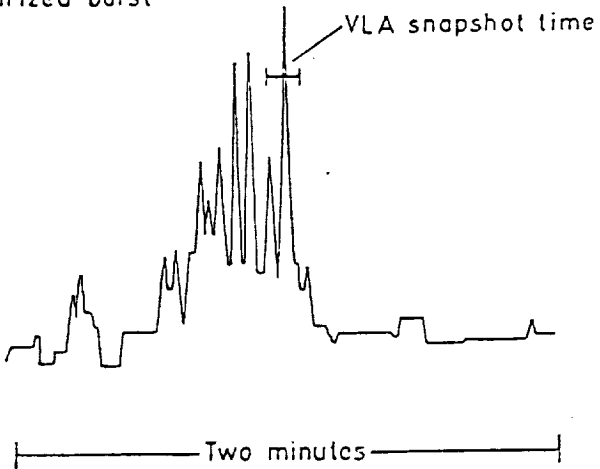


Figure 3

VLA 10 SECOND SNAPSHOTS

UNPOLARIZED

POLARIZED

● BEAM

60"

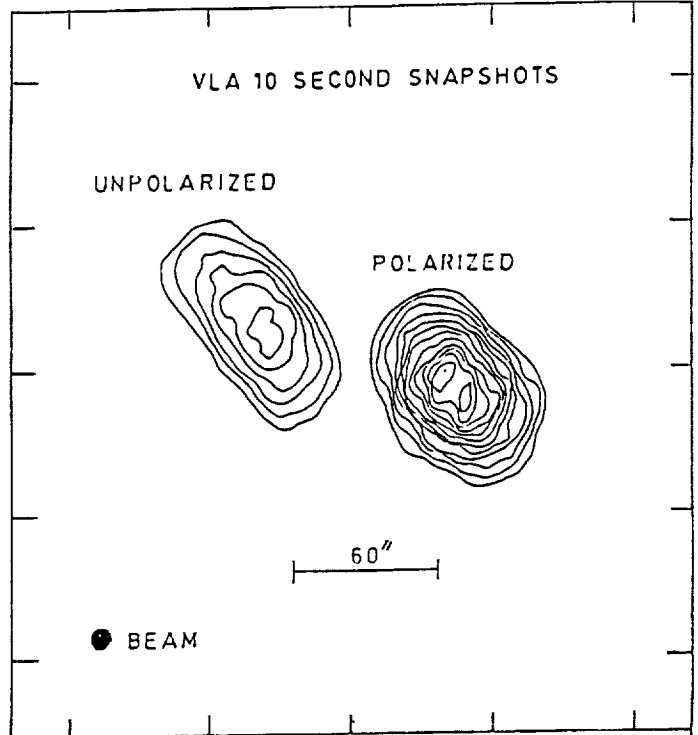


Figure 2

ORIGINAL PAGE IS
OF POOR QUALITY

O. TIME-CORRELATED BURSTS FROM WIDELY SEPARATED SOLAR ACTIVE REGIONS AT 91.6 CENTIMETER WAVELENGTH

KENNETH R. LANG AND ROBERT F. WILLSON

Department of Physics and Astronomy, Tufts University

Received 1989 March 10; accepted 1989 June 28

ABSTRACT

VLA synthesis maps at 20.7 cm wavelength, VLA snapshot maps at 91.6 cm wavelength, and NSO-Kitt Peak photospheric magnetograms indicate that time-correlated radio bursts can occur in active regions on opposite sides of the solar equator. These regions are apparently linked by large-scale, transequatorial magnetic loops that are at least 2.6×10^5 km (or $6'$) long. Energetic electrons accelerated during a radio burst in one active region probably move along this magnetic conduit at velocities of about one-third the velocity of light, thereby triggering radio bursts in the other active region.

Subject headings: Sun: corona — Sun: flares — Sun: magnetic fields — Sun: radio radiation — Sun: X-rays

I. INTRODUCTION

Evidence for correlated radio bursts from widely separated regions on the Sun was presented by Kai (1969) when he showed a type III burst can be followed within 10 s by a reverse-slope type III burst at distances $L > 10^5$ km. This suggested that electron beams are channeled along a large-scale magnetic loop at relativistic speeds $v \sim 0.3c$, first moving upward from the primary acceleration sight and then downward in a remote leg of the loop. Tang and Moore (1982) demonstrated that two large flares produced H α brightenings in quiet regions more than 10^5 km away from the flaring active region, and that these remote brightenings were accompanied by reverse-slope type III bursts. They suggested that the H α brightenings were initiated by the nonthermal electrons producing the secondary radio burst.

Rust and Webb (1977) had, in the meantime, shown that active region flares can be associated with sudden X-ray enhancements of large-scale loops or arcades of loops that extend outside the flaring active regions to distances $L > 10^5$ km, but that subsequent H α brightenings at the remote end of the interconnecting X-ray loop suggested shocklike excitation velocities of 300–1200 km s $^{-1}$.

Secondary microwave bursts caused by a distant primary one have also been reported by Kundu, Rust, and Bobrowsky (1983) and Nakajima *et al.* (1985); they respectively observed remote unpolarized microwave bursts accompanied by H α brightening and remote polarized bursts with no H α counterpart. In both cases, the relativistic velocity required by the measured time delay and the spatial separation indicated that the secondary burst was excited by high-energy electrons produced in the primary burst sight.

Simnett and Dennis (1987) have more recently shown that rapid (≤ 100 s) soft X-ray bursts can be produced in widely separated active regions connected by extensive coronal magnetic loops. Kundu, Schmahl, and Fu (1989), observing with the VLA at 6 and 21 cm, have inferred the presence of a large-scale ($L > 10^5$ km), transequatorial arch from near-simultaneous changes in the microwave emission of two widely separated active regions. In the latter case, a coronal instability associated with a filament disruption was supposed to produce simultaneous effects in the two active regions.

In this *Letter* we also present evidence for interactive bursts

from active regions on opposite sides of the solar equator. Our 91.6 cm VLA observations, presented in § II, provide high-resolution, two-dimensional structural information about these large-scale interactions, while the simultaneous 20.7 cm VLA data and photospheric magnetograms provide information about the underlying active regions. In § III we note that secondary soft X-ray emission was also detected and interpret our observations in terms of energetic electrons that are channeled along large-scale, otherwise invisible magnetic loops connecting active regions on either side of the solar equator.

II. OBSERVATIONS

The Sun was observed with the VLA in the C/D hybrid configuration between 1315 and 1610 UT on 1988 May 15 using 27 antennas at 20.7 cm wavelength (1446 MHz) and 19 antennas at 91.6 cm wavelength (327.5 MHz) with respective bandwidths of 12.5 and 3.125 MHz. The individual antenna beamwidths were $138'$ and $32'$ at 91.6 and 20.7 cm, respectively; we were therefore able to make full-disk synthesis maps at both wavelengths with respective synthesized beamwidths of $55'' \times 80''$ and $12.4'' \times 18''$. The 20%–25% uncertainty in the absolute calibration of the solar brightness temperatures has been discussed by Lang and Willson (1989). Although all four Stokes parameters were sampled every 3.3 s, there was no detectable polarization at either wavelength, so our 3 hr synthesis maps refer to the total intensity, I . Their contours mark levels of equal brightness temperature, T_B .

These maps are shown in Figure 1. The 20.7 cm emission is concentrated within small-scale (angular sizes $\theta \approx 1'$) sources above individual active regions in which bright H α plage is also found. The outermost contour and contour interval of the 20.7 cm map are equal to $T_B = 2.5 \times 10^5$ K, with a peak brightness temperature of $T_B = 2.5 \times 10^6$ K. The 20.7 cm brightness temperatures are therefore similar to the electron temperatures of the hot plasma trapped within coronal loops above active regions, suggesting that these loops are optically thick to thermal bremsstrahlung (Lang, Willson, and Gai-zauskas 1983). Such optically thick loops would account for the lack of detectable circular polarization.

In contrast to the 20.7 cm emission, the most intense 91.6 cm radiation is concentrated within large-scale ($\theta \approx 3'$) structures that are not associated with active regions; the quiet Sun, 91.6

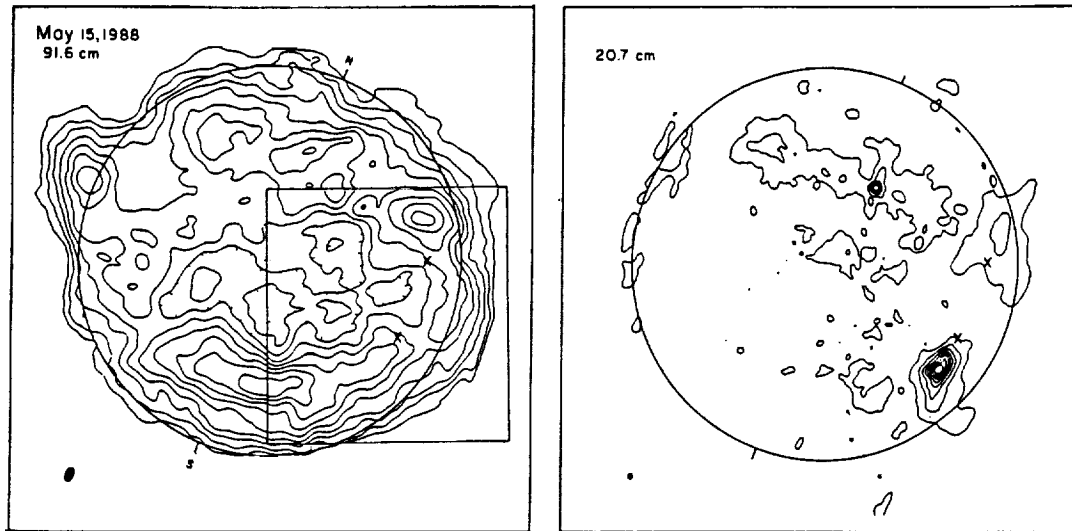


FIG. 1.—Very Large Array (VLA) 3 hr synthesis maps of the total intensity, I , from the visible solar disk at 91.6 cm (left) and 20.7 cm (right). The circle denotes the visible solar limb, the tick marks denote solar north and south, and the synthesized beamwidths are denoted by the dark spots in the lower left-hand corners. The boxed area of the 91.6 cm map denotes the field of view for the 3.3 s synthesis maps shown in Fig. 3; they illustrate interacting flare emission from the two places marked by X on opposite sides of the solar equator.

cm emission is instead associated with dark, elongated filaments (also see Lang and Willson 1989). The contours of the 91.6 cm map mark levels of equal brightness temperature, T_B , with an outermost contour of $T_B = 7.8 \times 10^4$ K, a contour interval of 7.8×10^4 K, and a peak brightness temperature of $T_B = 7.8 \times 10^5$ K.

The boxed area of the 91.6 cm map denotes the field of view for the snapshot maps shown in Figure 3; it contains two X marks that denote the location of the two groups of bursts whose temporal evolution is shown in Figure 2. The 91.6 cm time profiles indicates these two groups, beginning at ~ 1537 and ~ 1540 UT. The second group was associated with a weak

soft X-ray flare (dashed line, class B1.5). Both groups were also detected at 122 cm wavelength using the Air Force Solar Patrol Telescope at the Sagamore Hill observatory, but with more intense emission than at 91.6 cm, indicating nonthermal radiation with a positive spectral index in both cases. The Sagamore Hill radio data were supplied by Ed Cliver. The only available H α data (SOON) showed H α brightening at 1537 UT in AR 5014 (S17 W57 at 00 UT on May 15). The SOON H α data were supplied by Judy Nelson of the Goddard Space Flight Center. Active region AR 5014 was also active on the days before and after May 15 (see *Solar Geophysical Data H α flare reports*). There was no detectable circular polarization for

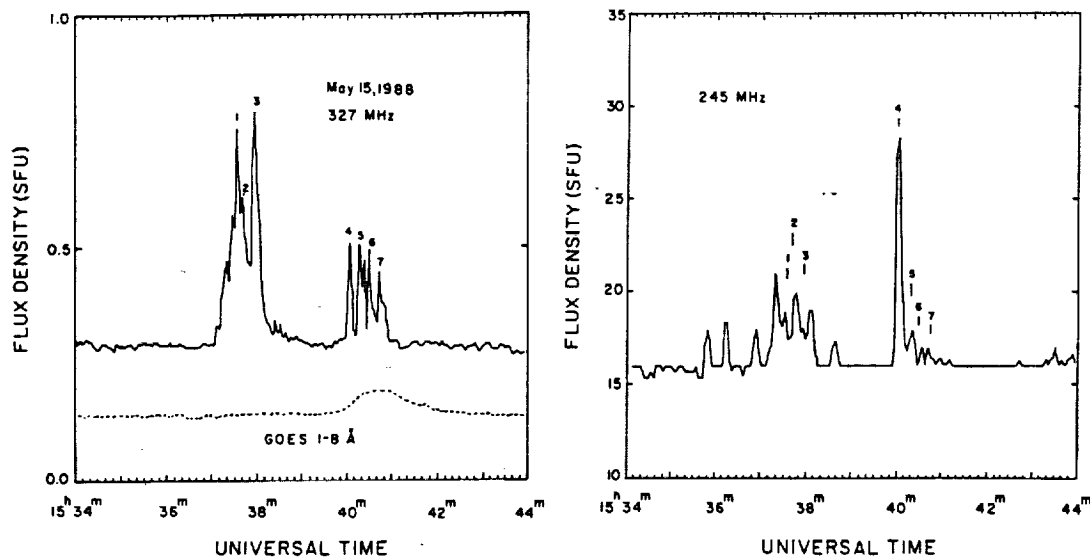


FIG. 2.—The time profile of the 91.6 cm (327 MHz—left) emission detected with one of the short VLA baselines (fringe spacing of about 5') is compared with that observed at 122 cm (245 MHz—right) over the same time interval on 1988 May 15 with the Air Force Solar Patrol telescope at the Sagamore Hill Radio Observatory. A plot of the GOES satellite soft X-ray flux is also shown as a dashed line. The numbers above the individual bursts refer to the times of the VLA 3.3 snapshot maps shown in Fig. 3.

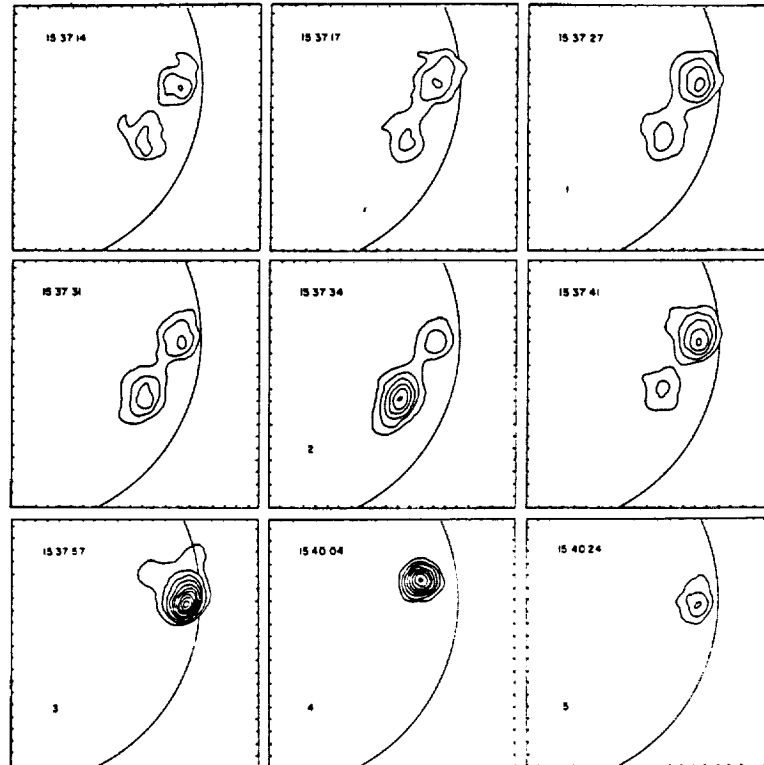


FIG. 3.—Very Large Array 3.3 s snapshot maps at 91.6 cm (327 MHz) for different times during the burst shown in Fig. 2. The locations of the bursts correspond to the crosses on the 90 cm synthesis map shown in Fig. 1. Note how the burst location shifts between the two regions, suggesting activation in the legs of one or more large-scale magnetic loops that cross the solar equator.

the 91.6 cm bursts (degree of circular polarization $\rho_c < 8\%$), suggesting type III bursts rather than type I, and there was no detectable burst emission at 20.7 cm (flux $S < 0.2$ SFU).

In Figure 3 we show 3.3 s snapshot maps of the individual bursts numbered in Figure 2. During the early states of the first group of bursts, emission was found in both northern and southern sources, each about 2.5 in size with a peak brightness temperature of $T_b \sim 3 \times 10^6$ K and an angular separation of about 5.5. Here the contour intervals are in units of equal brightness temperature, T_b , with an outermost contour and contour interval of 1×10^6 K. The angular scale may be inferred from the 1' spacing between the fiducial marks on the axes.

The locations of the northern and southern burst sources are denoted by crosses in Figure 1; they are displaced equatorward from two active regions shown in the 20.7 cm map, suggesting emission from the legs of large-scale coronal loops that straddle the equator and join the two active regions.

The presence of a large-scale magnetic conduit that links active regions on two sides of the solar equator is also inferred from subsequent burst emission that was localized first in the northern source, then in the southern one and thereafter in the northern region again. Such hypothetical, and otherwise invisible, transequatorial loops are further suggested by the photospheric magnetogram on 1988 May 15 (Fig. 4 [Pl. L5]); it indicates that large areas of opposite leading magnetic polarity underlie the northern and southern burst sources.

III. DISCUSSION

Our interpretation of correlated burst emission over widely separated areas does not differ substantially from that of Kai

(1969), Tang and Moore (1982), Kundu, Rust, and Bobrowsky (1983), and Nakajima *et al.* (1985). Examination of the NSO-Kitt Peak magnetogram for 1988 May 15 indicates that the positions of the two burst sources (designated by two X marks in Fig. 1) are displaced equatorward from two active regions; designated AR 5012 and AR 5014, near the northwest and southwest limb, respectively. We propose that the two active regions are linked by one or more large-scale, otherwise invisible magnetic loops that stretch across the solar equator connecting regions separated by 6', over a distance of at least 2.6×10^5 km. Some triggering agent travels across this distance, producing bursts with time delays of ~ 3 –6 s at velocities up to 10^5 km s $^{-1}$, or about one-third the velocity of light. Energetic electrons are probably accelerated during a burst in one active region and hurled at these velocities along large-scale magnetic loops to produce bursts in another active region located at the other footpoint of the loop.

Radio astronomical studies of the Sun at Tufts University are supported under grant AFOSR-89-0147 with the Air Force Office of Scientific Research. The Very Large Array is operated by Associated Universities, Inc., under contract with the National Science Foundation. The data presented in this Letter were taken during collaborative long-wavelength solar observations by Tufts University and the Observatoire de Paris-Meudon, under the support of National Science Foundation grant INT-8602285 and Centre National de la Recherche Scientifique grant 920038.

REFERENCES

- Kai, K. 1969, *Proc. Astr. Soc. Australia*, **1**, 186.
Kundu, M. R., Rust, D. M., and Bobrowsky, M. 1983, *Ap. J.*, **265**, 1084.
Kundu, M. R., Schmahl, E. J., and Fu, Q.-J. 1989, *Ap. J.*, **336**, 1078.
Lang, K. R., and Willson, R. F. 1989, *Ap. J. (Letters)*, **344**, L73.
Lang, K. R., Willson, R. F., and Gaizauskas, V. 1983, *Ap. J.*, **267**, 455.
Nakajima, H., Dennis, B. R., Hoyng, P., Nelson, G., Kosugi, T., and Kai, K. 1985, *Ap. J.*, **288**, 806.
Rust, D. M., and Webb, D. F. 1977, *Solar Phys.*, **54**, 403.
Simnett, G. F., and Dennis, B. R. 1987, in *Rapid Fluctuations in Solar Flares*, ed. B. R. Dennis and L. E. Orwig (NASA Conf. Pub. 2449), p. 123.
Tang, F., and Moore, R. L. 1982, *Solar Phys.*, **77**, 263.

KENNETH R. LANG and ROBERT F. WILLSON: Department of Physics and Astronomy, Robinson Hall, Tufts University, Medford, MA 02155

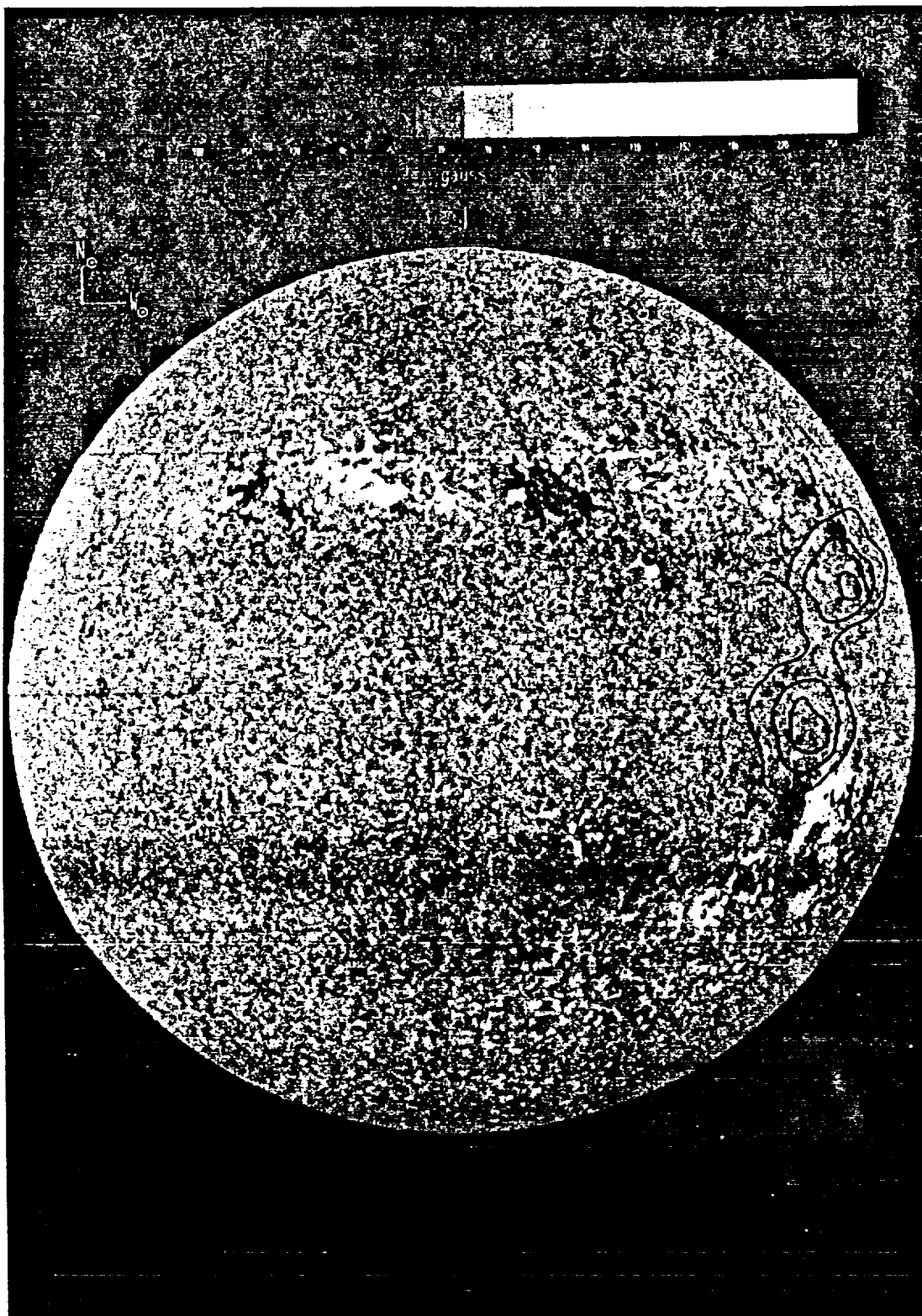


FIG. 4.—The contours of a 3.3 s VLA snapshot map showing the 91.6 cm burst emission at 153731 UT is overlaid on a National Solar Observatory (NSO)-Kitt Peak magnetogram. This comparison indicates that the hypothetical transequatorial loops connecting 91.6 cm burst locations may also connect underlying photospheric regions of opposite leading magnetic polarity. Magnetogram courtesy of Jack Harvey.

LANG AND WILLSON (see 344, L79)

P. RADIO EMISSION FROM QUIESCENT SOLAR FILAMENTS AT 91.6 CENTIMETER WAVELENGTH

KENNETH R. LANG AND ROBERT F. WILLSON

Department of Physics and Astronomy, Tufts University

Received 1989 March 10; accepted 1989 June 28

ABSTRACT

Full-disk VLA synthesis maps of the quiet Sun at 91.6 cm wavelength reveal large-scale (angular size $\theta \sim 3'$), hot (brightness temperatures $T_B \sim 3 \times 10^5$ K) structures that overlie dark H α filaments. The similarity between the shape, position, elongation, and orientation of the radio and optical features suggests their close association. We interpret the 91.6 cm emission in terms of the thermal bremsstrahlung of a hot sheath that envelops the cooler H α filament. A power-law gradient in pressure provides a better match to the observations than a constant pressure model. Variable physical parameters of the sheath, such as width, electron density, and electron temperature, can explain controversial reports of the detection of, or failure to detect, the meter-wavelength counterpart of H α filaments.

Subject headings: Sun: corona — Sun: magnetic fields — Sun: prominences — Sun: radio radiation

I. INTRODUCTION

Filaments are cooler than the surrounding corona and therefore appear as depressions in the quiet Sun background at centimeter wavelengths (Gary 1986; Kundu, Melozzi, and Shevgaonkar 1986); the cool filaments can also appear as depressions at millimeter wavelengths (Schmahl, Bobrowsky, and Kundu 1981). Regions that overlie filaments can now be detected using the VLA at the longer 91.6 cm wavelength; the higher temperatures produce regions of increased emission when compared with the surrounding quiet Sun background.

Previous observations have, however, led to an ongoing controversy about the optical counterparts of the quiescent, or nonflaring, solar radiation at meter wavelengths. A statistical study of numerous one-dimensional Nançay scans suggested that many quiescent meter-wavelength sources are associated with filament corridors as seen on H α synoptic maps (Axisa *et al.* 1971), but subsequent two-dimensional maps indicated that most filaments have no radio counterpart at meter wavelengths (Alissandrakis, Lantos, and Nicolaidis 1985; Lantos *et al.* 1987).

The VLA provides an order-of-magnitude improvement in angular resolution over all previous meter-wavelength investigations of the quiet Sun and might therefore help resolve this controversy. The first VLA observations of the quiescent corona at 92 cm wavelength indicated no systematic association of any of the radio sources with any optical counterpart, including active regions, filaments, sunspots and the magnetic neutral line in the underlying photosphere (Lang, Willson, and Trotter 1987). Full-disk VLA observations by Shevgaonkar, Kundu, and Jackson (1988) indicated that the 90 cm sources may be identified as streamers above H α filaments. However, our comparison of their data with H α observations (*Solar Geophysical Data*) indicates that many of the intense 90 cm sources do not overlie H α filaments.

One probable source of confusion is noise storms, the most common form of solar activity at meter wavelengths. The numerous type I bursts and background continuum of noise storms have been associated with coronal loop structures detected during the *Skylab* mission at soft X-ray wavelengths (Stewart and Vorpahl 1977; Gergely *et al.* 1980) as well as with

large-scale EUV loops (Stewart, Brueckner, and Dere 1986). VLA observations at 91.6 cm wavelength confirm the location of noise storms in large-scale magnetic loops that either overlie coronal loops within individual active regions or connect these regions with more distant areas on the Sun (Lang and Willson 1987); such conclusions were also anticipated by metric wavelength observations with the Nançay Radioheliograph (Lantos-Jarry 1970; Mercier *et al.* 1984). Detection of the meter-wavelength counterpart of filaments requires observations when the intense noise storms are not present.

In this *Letter* we present VLA 91.6 cm synthesis maps during quiescent periods without any noise storm activity. In § II we show that there is an excellent association of some 91.6 cm sources with H α filaments. The radio filaments are enhanced over the surrounding quiescent emission, rather than depressed. Not all H α filaments, however, exhibit detectable 91.6 cm counterparts. In § III we interpret some quiescent 91.6 cm sources in terms of the thermal radiation of a sheath overlying a H α filament, and with temperatures intermediate between those of its H α counterpart and the surrounding corona.

II. OBSERVATIONS

The Sun was observed with the VLA in the C/D hybrid configuration between 1315 and 1610 UT on 1988 May 15 using 27 antennas at 20.7 cm wavelength (1446 MHz) and 19 antennas at 91.6 cm wavelength (327.5 MHz) with respective bandwidths of 12.5 and 3.125 MHz. The full-disk synthesis maps at 20.7 cm are given elsewhere (Lang and Willson 1989), where they are used to identify active regions that interact via large-scale, transequatorial magnetic loops. Here we focus on the full-disk 91.6 cm synthesis map shown in Figure 1 (Plate L4) (*left*). Although all four Stokes parameters were sampled, there was no detectable circular polarization, so our 3 hr synthesis map refers to the total intensity, *I*. Burst data have been removed prior to making this synthesis map.

All the data were calibrated by observing 3C 48 for 5 minutes every 40 minutes; the flux density of 3C 48 was assumed to be 47.0 and 14.6 Jy at 91.6 and 20.7 cm, respectively.

Because the VLA lacks enough short baselines to adequately

sample the full solar disk at 91.6 cm, the 3 hr dirty, or uncleaned, map exhibited a negative ring surrounding the radio disk. This artifact has been previously discussed by Shevgaonkar, Kundu, and Jackson (1988). It was removed by using the maximum entropy algorithm (MEM) on the dirty map together with an assumed full-disk model that accounted for the missing short-baseline flux. This procedure has been discussed by Cornwell (1986) and Bastian (1988).

The MEM method converged after 15 iterations to indicate a total solar flux of 15–17 SFU, depending on the assumed size of the solar disk at 91.6 cm wavelength (we varied its radius between 1.50 and 1.20 R_{\odot}). This flux is 3–5 SFU lower than the 20 SFU value that is extrapolated from spectral data obtained on 1988 May 15 at the Sagamore Hill Radio Observatory (data courtesy of Ed Cliver).

Uncertainties in the absolute calibration of the VLA solar observations have been discussed by Kundu, Schmahl, and Fu (1989) and by Shevgaonkar, Kundu, and Jackson (1988). One uncertainty results from a software error in the program that applies the system temperatures of solar calibration antennas to other antennas (Ray Gonzalez, private communication). This uncertainty results in an underestimate of brightness temperatures by a factor of 1.8, and our data have been corrected for this error. Another uncertainty is attributed to measurements of the high-temperature noise diodes on the solar calibration antennas; they are not measured regularly enough at the VLA to assure accurate measurements of the system temperature. The lower total solar flux that we derived from the maximum entropy procedure probably reflects this uncertainty in the system temperature, and our inferred brightness temperatures may therefore be in error by 20%–25%. This is reflected in the stated uncertainties of our measurements and the error bars of the plots of them.

The contours of the resulting map (Fig. 1, *left*) mark levels of equal brightness temperature, T_b , with an outermost contour of $T_b = 7.8 \times 10^4$ K, a contour interval of 7.8×10^4 K, and peak brightness temperature of $T_b = 7.8 \times 10^5$ K. The mean brightness temperatures of the elongated sources marked A and B are, for example, estimated to be $T_b \sim 3 \times 10^5$ K above the surrounding quiet Sun level of $T_b \sim 4 \times 10^5$ K, with an uncertainty of 20%.

An H α photograph taken on the same day (1988 May 15) is also shown in Figure 1 (*right*); it contains several dark, elongated filaments. Two of these have counterparts in the 91.6 cm map with similar shapes, positions, elongations, and orientations; they are designated by the letters A and B in the 91.6 cm map. The smaller filaments seen in the north central regions also seem to have 91.6 cm counterparts, but there is no increased 91.6 cm emission in the vicinity of the dark filaments that lie near the northeast and southeast limbs (marked C and E on the 91.6 cm map).

The intense 91.6 cm emission detected near the equator on the east limb (marked D) may be due to a coronal streamer. Sacramento Peak coronagraph data (*Solar Geophysical Data*) show coronal material in this region, as well as those that have no detectable 91.6 cm radiation. No underlying active regions or filaments were visible as the Sun rotated and the limb region turned into view during the following days.

Depressions in the 91.6 cm radiation are found in the central equatorial regions (*hatched regions*). They may be at least partly due to coronal holes, but the only available He 10830 data, taken on May 14, do not exhibit a detectable equatorial coronal hole. Examination of the 91.6 cm maps for shorter

time scales showed no evidence for variable features on time scales of a few tens of minutes, so our data does not confirm reports of such variations by Shevgaonkar, Kundu, and Jackson (1988).

III. DISCUSSION

The similarity in shape, position, elongation, and orientation strongly suggests that the radio emission from sources A and B is associated with the underlying dark filaments detected in the H α photograph, but the radio emission could also be associated with bright H α plage and their associated higher magnetic fields. The most intense emission from source A coincides with a dark filament rather than plage, and the most intense part of source B corresponds to the largest part of the underlying filament. Moreover, the weaker emission from both sources has the same shape and orientation as the associated narrow, elongated filaments. We therefore attribute the radio emission to these filaments, while noticing that H α plage might also play a role in enhanced 91.6 cm emission.

We therefore interpret the regions of increased 91.6 cm emission around filaments (sources A and B) in terms of a hot sheath that envelops the cooler H α filaments; such a surrounding sheath is suggested by the fact that the radio wavelength features are similar in shape to, but wider, longer and hotter than, their optical counterparts. The mean 91.6 cm brightness temperatures of $T_b \sim 3 \times 10^5$ K, for example, lie between the electron temperatures of the cool H α filaments and the electron temperature of the surrounding corona.

In order to gain a quantitative view of the transition sheath, we compare our observations with the data and models given by Kundu, Melozzi, and Shevgaonkar (1986). Their VLA observations at the shorter 6 and 20 cm wavelengths indicated radio depressions above H α filaments, in comparison with the hot surrounding corona, but a transition sheath was indicated by the fact that the radio filaments are larger in size than their optical counterparts and that the brightness temperature, T_b , of the radio filaments increases with wavelength from $T_b \sim 1.5 \times 10^4$ K at 6 cm to $T_b \sim 5 \times 10^4$ K at 20 cm. Our higher brightness temperature of $T_b \sim 3 \times 10^5$ K at the longer 91.6 cm wavelength can be explained by the larger optical depth of thermal bremsstrahlung from the transition sheath at longer wavelengths, and the fact that the 91.6 cm sheath is seen in emission can be explained by the relatively low optical depth of the low-density corona.

To be exact, we have assumed that the variation of temperature with height in the transition sheath is that given by Kundu, Melozzi, and Shevgaonkar (1986); their data resulted from an assumed balance between the thermal energy conducted in from the corona and the energy radiated away. These temperatures, T , were then combined with three pressure models to infer the electron density, N , and the equation of transfer was solved assuming free-free emission with these values of temperature and density. The three models were a constant pressure model $P = NT = 3 \times 10^{14}$ cm $^{-3}$ K, and two power-law models $P = NT = aT^n$, with $a = 2.5 \times 10^{17}$, $n = -0.58$, and $a = 4 \times 10^{17}$, $n = -0.62$. The calculated brightness temperatures of two models are shown in Figure 2 together with our measurements at 91.6 cm and those of other observers at shorter wavelengths. This figure indicates that the brightness temperature of the constant pressure model is too high at both 20 cm and 90 cm, with respective values of $T_b \sim 9 \times 10^4$ K and $T_b \sim 6 \times 10^5$ K. The power-law models are more in accord with the observational data; at 20 cm and 90

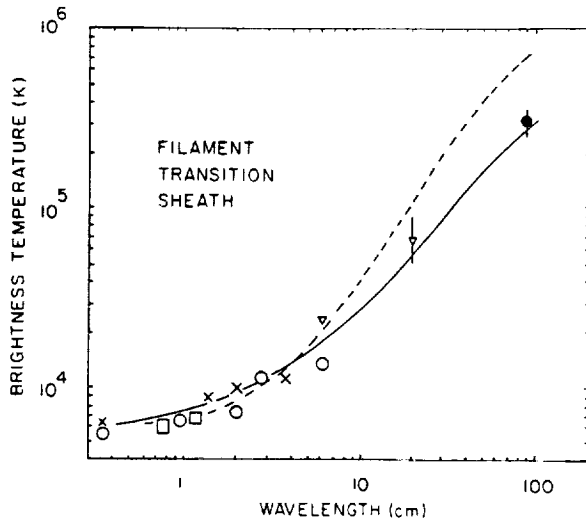


FIG. 2.—Calculated brightness temperatures for a constant pressure $P = 3 \times 10^{14} \text{ cm}^{-3} \text{ K}$ (dashed line) and a power-law pressure $P = 2.5 \times 10^{17} T^{-0.58}$ with $dT/dh = 0$ at height $h = 0$ (solid line). The observed temperature at 91.6 cm (filled circle) is from this Letter, whereas the other values (crosses, open circles, open squares, and open triangles) are from Kundu, Melozzi, and Shevgaonkar (1986) with their 6 and 20 cm measurements increased by a factor of 1.7 due to the detection of a software calibration error. The brightness temperatures refer to mean values over the radio source.

cm they both produce respective values of $T_B \sim 5 \times 10^4 \text{ K}$ and $T_B \sim 3 \times 10^5 \text{ K}$.

So, the observed 91.6 cm structures that are associated with

these H α filaments may be interpreted as the thermal bremsstrahlung of a hot (electron temperature $T_e \approx 3 \times 10^5 \text{ K}$) sheath that envelops a H α filament. Such a sheath acts as the boundary between the filament and the surrounding 10^6 K corona. A loop thickness of $L \approx 10^9 \text{ cm}$, or about 1/50 of the $10' \approx 5 \times 10^{10} \text{ cm}$ extent of the radio sources A and B, may be assumed; such a thickness is consistent with the models of Kundu, Melozzi, and Shevgaonkar (1986). If the hypothesized sheath were substantially thinner than the assumed thickness of $L \approx 10^9 \text{ cm}$, then the optical depth for thermal bremsstrahlung would be much smaller, and the optically thin sheath might not be detectable. And if the electron density of the sheath was only slightly higher, then its plasma frequency would exceed our observing frequency, and the sheath radiation could not propagate out to be observed. Variable physical parameters of the sheath might therefore easily explain why the elusive meter-wavelength counterpart of H α filaments is only sometimes observed; just the right thickness, electron density, and electron temperature are required for detection.

Radio astronomical studies of the Sun at Tufts University are supported under grant AFOSR-89-0147 with the Air Force Office of Scientific Research. The Very Large Array is operated by Associated Universities, Inc., under contract with the National Science Foundation. The data presented in this Letter were taken during collaborative long-wavelength solar observations by Tufts University and the Observatoire de Paris-Meudon, under the support of National Science Foundation grant INT-8602285 and Centre National de la Recherche Scientifique grant 920038.

REFERENCES

- Alissandrakis, C. E., Lantos, P., and Nicolaidis, E. 1985, *Solar Phys.*, **97**, 267.
 Axisa, F., Avignon, Y., Martres, M. J., Pick, M., and Simon, P. 1971, *Solar Phys.*, **19**, 110.
 Bastian, T. 1988, Ph.D. thesis, University of Colorado.
 Cornwall, T. 1986, in "Synthesis Imaging" (NRAO Summer School Course Notes), p. 117.
 Gary, D. E. 1986, in *Coronal and Prominence Plasmas*, ed. A. I. Poland (NASA Conf. Pub. 2442), p. 121.
 Gergely, T. E., Kundu, M. R., Golub, L., and Webb, D. 1980, in *IAU Symposium 86, Radio Physics of the Sun*, ed. M. R. Kundu and T. E. Gergely (Dordrecht: Reidel), p. 435.
 Kundu, M. R., Melozzi, M., and Shevgaonkar, R. K. 1986, *Astr. Ap.*, **167**, 166.
 Kundu, M. R., Schmahl, E. J., and Fu, Q.-J. 1989, *Ap. J.*, **336**, 1078.
 Lang, K. R., and Willson, R. F. 1987, *Ap. J.*, **319**, 514.
 ———, 1989, *Ap. J. (Letters)*, **344**, L77.
 Lang, K. R., Willson, R. F., and Trotter, G. 1988, *Astr. Ap.*, **199**, 325.
 Lantos, P., Alissandrakis, C. E., Gergely, T., and Kundu, M. R. 1987, *Solar Phys.*, **112**, 325.
 Lantos-Jarry, M. F. 1970, *Solar Phys.*, **15**, 40.
 Mercier, C., Elgaroy, O., Tiamicha, A., and Zlobec, P. 1984, *Solar Phys.*, **92**, 375.
 Schmahl, E. J., Bobrowsky, M., and Kundu, M. R. 1981, *Solar Phys.*, **71**, 311.
 Shevgaonkar, R. K., Kundu, M. R., and Jackson, P. D. 1988, *Ap. J.*, **329**, 982.
 Stewart, R. T., Brueckner, G. E., and Dere, K. P. 1986, *Solar Phys.*, **106**, 107.
 Stewart, R. T., and Vorpahl, J. 1977, *Solar Phys.*, **55**, 111.

KENNETH R. LANG and ROBERT F. WILLSON: Department of Physics and Astronomy, Robinson Hall, Tufts University, Medford, MA 02155

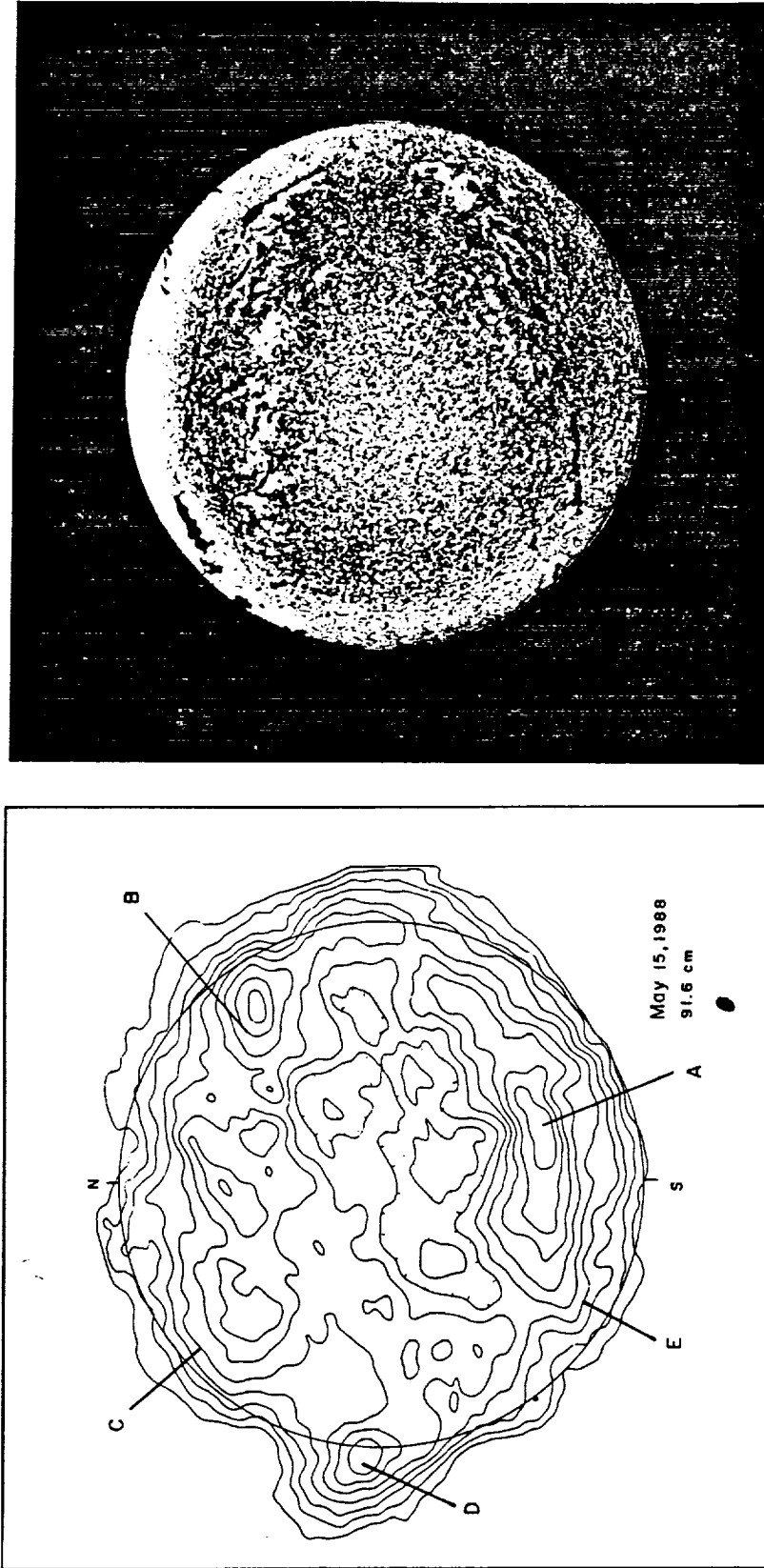


FIG. 1.—A 3 hr Very Large Array (VLA) synthesis map of the total intensity, I , from the visible solar disk at 91.6 cm (left) is compared with an H α photograph (right) taken at the Boulder Solar Observatory at 1415 UT on the same day (1988 May 15, courtesy of Patrick McIntosh and Helen Coffey). The synthesized beamwidth is denoted by the small black spot in the lower right-hand corner; it has angular dimension of $80'' \times 55''$ at a position angle of -20° . The circle in the 91.6 cm map denotes the visible solar limb, and the tick marks denote solar north and south. Radio wavelength emission from dark, elongated filaments in the H α photo are designated by A and B in the 91.6 cm map. Filaments C and E did not correspond to enhanced 91.6 cm emission, while source D probably coincides with a coronal streamer. The hatched regions in the central equatorial regions correspond to depressions in the 91.6 cm emission.

LANG AND WILLSON (see 344, L73)

IV. PUBLISHED PAPERS

Q. IMPULSIVE MICROWAVE BURST AND SOLAR NOISE STORM EMISSION RESOLVED WITH THE VLA

ROBERT F. WILLSON AND KENNETH R. LANG
Department of Physics and Astronomy, Tufts University

AND

MARGARET LIGGETT
Solar Astronomy, California Institute of Technology
Received 1989 April 7; accepted 1989 August 22

ABSTRACT

The Very Large Array (VLA) was used to study the evolution of a microwave burst at 20.7 cm wavelength and a type I noise storm at 91.6 cm wavelength. Snapshot maps of the 20.7 cm emission show that the precursor, impulsive and postburst phases originated in spatially separated sources, suggesting successive activation in different coronal loops. Our observations show that a higher-lying 91.6 cm continuum source began to brighten and change shape ~ 30 minutes before the onset of the 20.7 cm burst, possibly indicating an interaction between magnetic loops in these two spectral regions. Comparisons with off-band H α images show that these changes may have been associated with the disappearance of one of the active region filaments. The 91.6 cm level increased again a few minutes after the microwave burst, and this was immediately followed by the onset of a type I noise storm. The sizes ($\theta = 1'.5-2'$) and brightness temperatures ($T_B = 2-10 \times 10^7$ K) of the 20.7 cm burst sources were compared with those predicted by multithermal and nonthermal models of microwave burst emission in which the magnetic field strength and temperature are allowed to vary throughout the source. Our results indicate that the multithermal model gives a better fit to the data, with magnetic field strengths of $B = 75-120$ G at the locations of the bursts. These values are consistent with those inferred from potential magnetic field extrapolations into the corona, using Kitt Peak photospheric magnetograms as boundary conditions.

Subject headings: interferometry — polarization — Sun: corona — Sun: radio radiation

I. INTRODUCTION

During the past decade, high-resolution, VLA observations of the Sun have provided valuable new insights to the physical processes responsible for solar radio bursts. For example, observations at 20 cm wavelength indicate that the regions of energy release are usually located at the apex of coronal loops, while bursts at shorter wavelengths are generally located along the legs or feet of loops (Marsh and Hurford 1980; Alissandrakis and Kundu 1978; Lang and Willson 1984, 1986; Willson 1983; Willson and Lang 1984). In some cases, preburst changes in the active regions are detected as increases in the intensity and polarization of the microwave emission on time scales of a few minutes before the bursts (Kundu *et al.* 1982; Willson 1984; Kundu and Lang 1985). These changes may be related to preburst heating in coronal loops and to the reconfiguration of coronal magnetic field structures which subsequently trigger the impulsive phase. Recently, improvements at the VLA have made it possible to study bursts at 90 cm wavelength with an angular resolution of $\sim 5''$ when the array is in the most extended configuration. At this wavelength, solar noise storms are the most common type of solar activity, although other types of bursts, such as type III may also be detected (Willson *et al.* 1989). A typical noise storm consists of a slowly varying, wide-band continuum with superposed impulsive bursts (Elgaroy 1977). The first VLA observations of a solar noise storm showed that it had an elongated shape ($\sim 40'' \times 200''$) and contained four compact sources of $\sim 40''$ in size (Lang and Willson 1987). The high-degree and sense of circular polarization ($\rho_c \approx 95\%$) was consistent with previous low-resolution observations which suggested that noise storm

emission is fundamental plasma radiation (Elgaroy 1977 and references therein). The noise storm followed a soft X-ray burst by ~ 20 minutes, suggesting an outwardly moving disturbance or triggering event originating from lower in the corona. Recent VLA observations by Habbal, Ellman, and Gonzalez (1989) did not show any clear correlation between the temporal evolution of the emission at 20 and 90 cm, but in this paper we provide evidence for interaction between magnetic loops detected in the two spectral regions.

There is an uncertainty about which flare-related phenomena are associated with noise storms. Numerous studies (Dodson and Doselman 1951; Das and Sethumadhaven 1953; Davies 1953; Wild and Zirin 1956; McClean 1973) have suggested that noise storms are associated with eruptive prominences while Webb and Kundu (1978) have discussed examples of noise storms that were related to eruptive filaments and long-duration X-ray events outside active regions. Lantos *et al.* (1981) have also presented evidence for an association between a noise storm, a long-duration X-ray event, and a coronal transient. From an analysis of *Skylab* EUV data, Stewart, Brueckner, and Dere (1986) found that the occurrence of major type I metric noise storms is highly correlated with strong changes in the coronal magnetic field structure and with newly emerging flux. They concluded that storms are caused by large-scale rearrangement of coronal fields connecting active regions, rather than by changes of fields within isolated active regions. Theoretical investigations also suggest that emerging flux in regions of strong preexisting coronal magnetic fields may play an important role in the triggering of type I noise storms (McClean 1981; Spicer, Benz, and Huba 1981; Stewart 1985).

Thus, there is evidence that both microwave and decimetric bursts can be triggered by the interactions of magnetic loops. Simultaneous observations at these wavelengths may therefore provide insight to where in a loop or system of loops these interactions actually begin while also providing constraints to models of microwave burst emission and noise storms.

II. OBSERVATIONS

a) Impulsive Microwave Burst at 20.7 cm Wavelength

i) Time Profiles

The VLA (C/D hybrid configuration) was used to observe the Sun between 1315 UT and 1622 UT on 1988 June 24. Observations were made using the entire array simultaneously at wavelengths of 20.7 cm (1446 MHz) and 91.6 cm (327.5 MHz) with respective bandwidths of 12.5 MHz and 0.781 MHz. During these observations, all 27 antennas were operating at 20.7 cm wavelength and 22 were operating at 91.6 cm wavelength. At these wavelengths the antenna beamwidths are $\sim 32'$ (20.7 cm) and $145'$ (91.6 cm) with zero-hour angle synthesized beamwidths of $\sim 12''.5 \times 22''$ and $55'' \times 97''$. The data were sampled every 3.3 s and calibrated from observations of 3C 48 every 40 minutes. These data were then used to make CLEANed maps of the total intensity, I , and circular polarization or Stokes parameter V , at both wavelengths on intervals as short as 3.3 s.

On 1988 June 24, the most active region on the Sun was AR 5047, located near the southwest limb (S17 W52 at 1600 UT). This region had produced dozens of H α flares and soft X-rays during the previous few days, including several X-class events (Solar Geophysical Data). At ~ 1600 UT the region produced one X2.4 burst which we detected at 20.7 cm at the VLA. This event was followed ~ 40 minutes later by an X5.6-class soft X-ray burst, but our observations had ended by that time. Unfortunately the *Solar Maximum Mission Satellite* (SMM) was in the nighttime part of its orbit during the X2.4 burst and thus could not provide complementary soft and hard X-ray data. However, at ~ 1720 UT, the Coronal Polarimeter (C/P) aboard the SMM did detect a coronal mass ejection above the southwest limb. Since there were no other active regions in the vicinity of AR 5047, the CME was almost certainly associated with one of the two X flares (J. Burckpile, private communication, 1988).

In Figure 1 we show time profiles of the visibility amplitudes between 1600 and 1620 UT at 20.7 cm and 91.6 cm wavelengths as observed on one of the shortest VLA baselines (fringe spacing of 250" at 91.6 cm and 55" at 20.7 cm.) The 20.7 cm burst profile exhibits two impulsive ($\tau < 10$ s) spikes (160626 and ~ 160647 UT) two faint precursors which precede the impulsive phase by a few minutes, and finally a secondary peak (~ 160810 UT) that occurs after the start of the gradual decay phase.

In Figure 2 we show a plot of the GOES X-ray emission during this same time interval as well as profiles of total flux at eight wavelengths between 1.94 cm (15400 UT) and 122 cm (245 MHz) as recorded by the San Vito station of the Air Force Solar Radio Patrol (courtesy of Ed Cliver). Note that the duration of the microwave burst is considerably shorter than that of the soft X-ray burst. In fact, the GOES data showed that the soft X-ray emission had not yet reached its preburst level before the second X-flare began at ~ 1645 UT. In this figure the original 1 s time resolution radio data have been averaged over 3 s in order to provide a more direct comparison with the

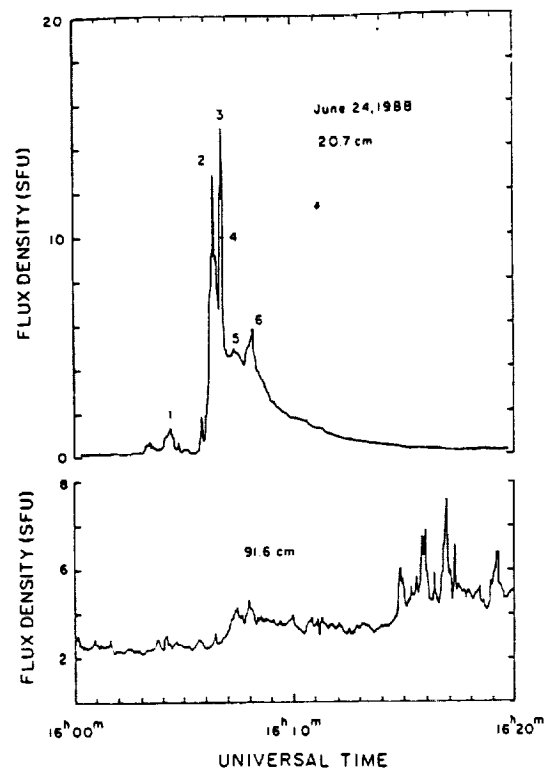


FIG. 1.—Time profiles of a solar burst observed by one interferometer pair of the VLA at 20.7 cm (1446 MHz) and 91.6 cm (327.5 MHz) during a 20 minute interval on 1988 June 24. Snapshot maps of the components (1–6) of the 20.7 cm burst are shown in Fig. 4. VLA maps of the 91.6 cm emission are shown in Figs. 7–9.

3.3 s VLA data. Notice that although the profiles are similar, the peak flux at 21 cm is about a factor of 3 higher than shown on the plot of visibility amplitude in Figure 1. This indicates that the burst emission was larger than the 55" resolution VLA baseline on which the correlated flux was measured.

Microwave spectra measured at different times during the burst are also shown in Figure 2. They indicate that the flux decreases sharply at the longer wavelengths, with a spectral index of $\alpha \approx 0.8$ – 0.9 below the spectral peak. In the case of the two impulsive 20.7 cm spikes, the frequency of maximum emission may lie above the highest observed frequency of 15,400 MHz. These data also indicate that the microwave burst emission probably does not extend much below ~ 1415 MHz. The absence of any obvious counterpart at 606, 410, and 245 MHz may be due to Razin suppression or free-free absorption by thermal plasma, both of which reduce the intensity of microwave bursts at long wavelengths (e.g., Dulk 1985). The gradual increase in intensity at 606 MHz starting at ~ 1608 UT, and which appears to have a relatively narrow bandwidth, might be attributed to a decimetric type IV continuum burst. Such bursts are, for example, known to begin a few minutes after impulsive microwave bursts (e.g., Kundu 1965; Dulk 1985). The emission at 410 MHz and 245 MHz which exhibits a gradual increase with superposed impulsive bursts may be associated with what we believe to be a type I noise storm detected at 327 MHz with the VLA (see § IIb). In § III we use the higher frequency data, together with our VLA results, to estimate the magnetic field strength in the burst sources and to test different models of burst emission.

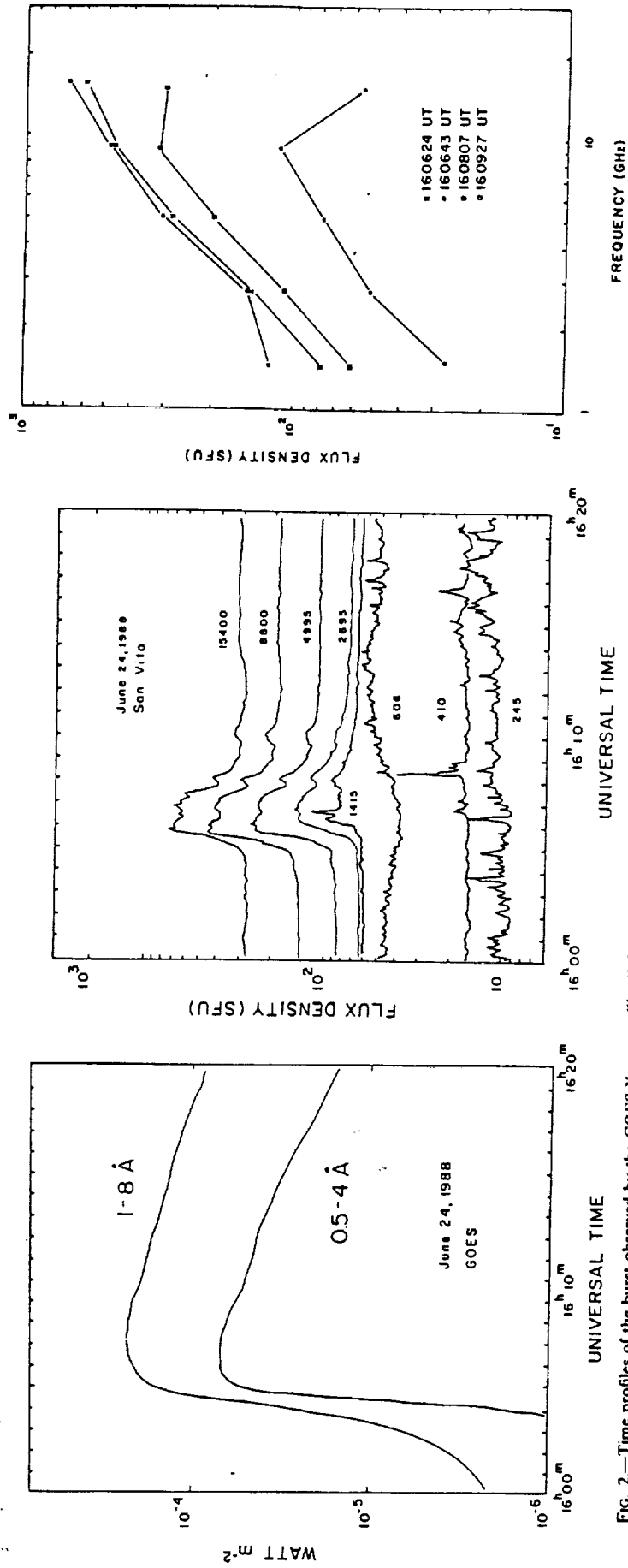


FIG. 2.—Time profiles of the burst observed by the GOES X-ray satellite (*left*) and by the San Vito station of the Air Force Solar Radio Patrol (*middle*) together with microwave spectra during the impulsive and decay phases (*right*).

ORIGINAL PAGE IS
OF POOR QUALITY

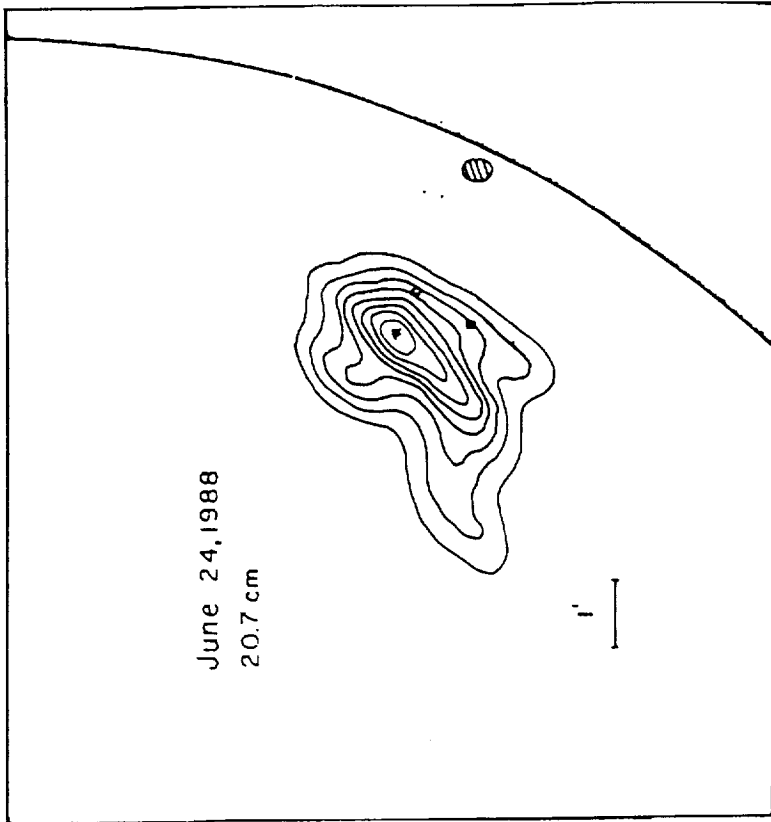


FIG. 3.—A VLA synthesis map of total intensity at 20.7 cm wavelength (*right*) is compared with a KITT Peak magnetogram (*left*) taken on the same day. Potential magnetic field lines extrapolated into the corona are superposed on the magnetogram. The VLA map was produced using data taken during the 2.5 hour interval prior to the microwave burst shown in Fig. 1. The angular scale may be inferred from the 60" spacing between fiducial marks on the axes. The contour intervals are in units of equal brightness temperature, T_b , with an outermost contour and contour interval of $T_b = 3.6 \times 10^5$ K. The circle, cross, and square mark, respectively, the locations of burst emission during the precursor, impulsive, and postimpulsive phases. Snapshot maps of these different phases are shown in Fig. 4. The hatched eclipse near the solar limb denotes the position of the 91.6 cm source shown in Fig. 7.

ii) *VLA Maps of Quiescent 20.7 cm Emission*

In Figure 3 we compare a 20.7 cm VLA synthesis map of total intensity with a Kitt Peak magnetogram taken on the same day (courtesy of Jack Harvey and Kermit Smith). This map was made using data from 1315–1555 UT, and therefore represents the quiescent emission leading up to the impulsive burst. Here we also show magnetic field lines that have been extrapolated into the corona using a computer code kindly provided by T. Sakurai. This program, described in detail by Sakurai (1981), solves Laplace's equation to calculate potential magnetic field lines using photospheric fields as boundary conditions. Since Kitt Peak magnetograms are known to saturate above ~ 100 G, the strong umbral fields ($B \approx 2400$ – 2600 G) were corrected by using sunspot strengths and sizes obtained from Mount Wilson, in a manner described by Gary and Hurford (1988) who made similar comparisons with VLA data.

As shown in the figure, the most intense 20.7 cm emission is concentrated in a looplike structure ($\theta \approx 2' \times 3'$) that lies along an arcade of magnetic loops connecting the underlying sunspots. Its peak brightness temperature is $T_b \approx 3 \times 10^6$ K, and there was no detectable circular polarization, ($\rho_c < 10\%$), suggesting optically thick thermal emission. Maps made for time intervals ranging from 10 minutes to one hour revealed no significant changes in structure, brightness, or polarization, indicating that the 20.7 cm source was stable during the several hours before the 20.7 cm burst. In this figure, the circle, cross, and square mark, respectively, the locations of burst emission during the precursor, impulsive and post impulsive phases of the 20.7 cm burst shown in Figure 1 (see next section).

iii) *VLA Maps of the 20.7 cm Burst*

Figure 4 shows 3.3 s 20.7 cm wavelength maps of total intensity at the peaks of the faint precursor and impulsive spikes

and during the decay phase. In order to more clearly distinguish the burst and quiescent emission, we first subtracted the preburst visibility function at 1602 UT from the subsequent burst data. As shown, the precursor has an elongated shape whose peak lies $\sim 1'$ west of the quiescent 20.7 cm source (denoted by a cross in the figure). Its peak brightness temperature is $T_b \sim 4 \times 10^6$ K, and there was no detectable circular polarization.

Maps depicting the evolution of the main burst show that the peaks of the two impulsive spikes (160626 and 160647 UT) lie at the same position as the quiescent emission. Each burst has a half-power angular size of ~ 1.5 and a peak brightness temperature of $T_b \approx 10^8$ K. There is no indication of circular polarization above an instrumental uncertainty of $\rho_c \approx 15\%$ – 20% .

Notice that after ~ 1607 UT the emission, including the gradual decay phase and the secondary impulsive burst at 160807 UT, lies $\sim 2'$ south of the first two impulsive peaks. In fact the maps show that this southern component began to emerge within ~ 3 s after the second impulsive spike at 160647 UT, suggesting successive activation in an adjacent set of loops. Although the burst is located near the limb, our maps after 160807 UT showed no evidence for systematic changes in position or size, as would be expected if the postburst source were expanding or moving outward into the corona at any velocity $v \geq 10$ km s $^{-1}$.

In Figure 5 we show a Big Bear Observatory H α photograph taken during the decay phase of the 20.7 cm burst. This photograph shows a number of H α flare ribbons which mark at least two sets of flare loops. Inspection of a time sequence of images shows that the pair of flare kernels, denoted by a_1 and a_2 , and located in the eastern half of AR 5047 appeared at ~ 1600 UT, or several minutes before the first 20.7 cm precursor

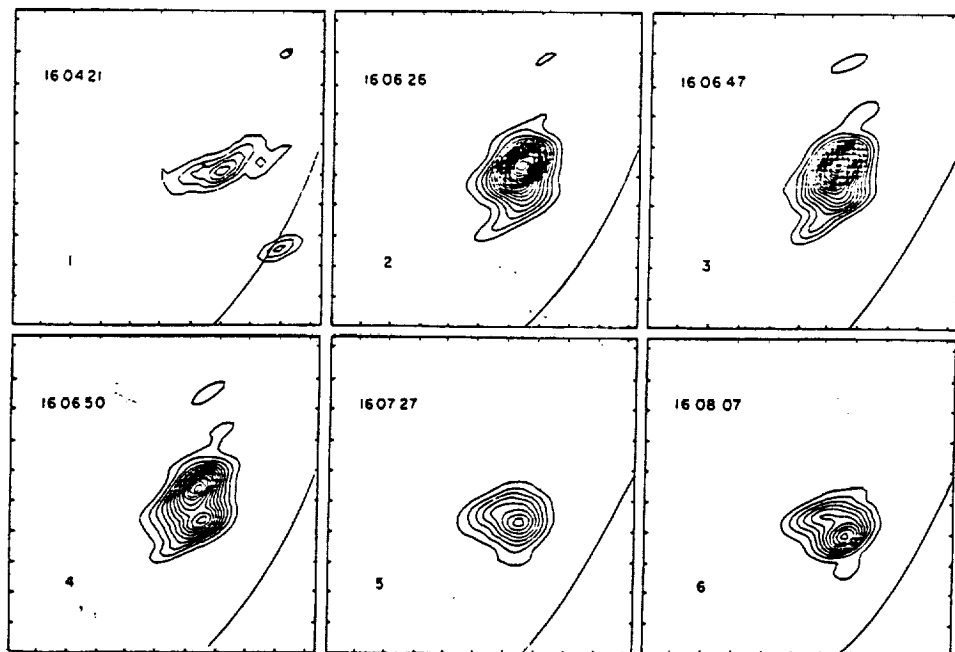


FIG. 4.—VLA snapshot maps of the total intensity, I , at 20.7 wavelength during 3.3 s intervals at the times denoted by 1–6 in Fig. 1. The precursor (1) had no detectable circular polarization and is spatially separated from the subsequent impulsive bursts (2 and 3). The cross denotes the peak of the impulsive bursts in (1), and of the peak of the quiescent emission shown in Fig. 3. The sources are resolved with a synthesized beamwidth of $12'' \times 30''$; the angular scale may be inferred from the $60''$ spacing between the fiducial marks on the axes. The contour intervals are in units of equal brightness temperature, T_b , with an outermost contour and contour interval of $T_b = 4.4 \times 10^5$ K ($T_{b, \text{min}} = 4.4 \times 10^6$ K) for (1) and an outermost contour and contour interval of $T_b = 5.5 \times 10^6$ K ($T_{b, \text{min}} = 1.0 \times 10^8, 1.3 \times 10^8, 7.7 \times 10^7, 4.4 \times 10^7, 5.5 \times 10^7$ for 2,3,4,5, and 6, respectively).

sor. It is interesting to note that other observations have shown that $H\alpha$ emission can precede the impulsive phase by a few minutes to tens of minutes, possibly indicating magnetic triggering in adjacent loops (Martin 1980; Rust *et al.* 1981; Webb 1983). The second pair of kernels, b_1 and b_2 , located in the western part of the region, appeared at ~ 1605 UT, or about the same time as the impulsive emission. A coregistration of the snapshot maps with this image shows that the peak of the impulsive microwave emission is located about midway between b_1 and b_2 . If these kernels represent the footprints of a flaring loop, then the location of the 20.7 cm burst peak suggests that the energy release occurred near the loop top.

b) Activity at 91.6 cm Wavelength

i) Time Profile

Figure 6 shows plots of the correlated flux and circular polarization between 1400 and 1620 UT. There are two groups of type I bursts, one preceding (1448–1507 UT), the other following (1615–1620 UT) the 20.7 cm burst. These bursts are superposed upon a slowly varying background level that is punctuated by hundreds of low-intensity spikes whose durations are almost always less than the 3.3 s VLA integration time. We also draw attention to the gradual increase of the background intensity starting at ~ 1525 UT, and to the more pronounced jump at ~ 1607 UT, or ~ 1 minute after the second impulsive 20.7 cm burst (Fig. 1). Although the bottom half of Figure 6 suggests a steady increase in circular polarization, we believe that this is an instrumental effect which is due to the gradual resolution of large-scale unpolarized structure on this baseline. Longer baselines, for example, show system-

atically higher and more constant degrees of circular polarization, while synthesis maps (excluding bursts) show no systematic trends in the polarization of the dominant left circularly polarized ($\rho_c \approx 90\%$) source associated with AR 5047 (see next section). We include the plot of ρ_c only in order to illustrate relatively rapid changes in polarization (which could not be due to change in resolution) such as occur during the first group of type I bursts.

ii) Noise Storm Resolved and Preburst Enhancement

Figure 7 shows a sequence of maps depicting the evolution of the 91.6 cm emission from 1315–1600 UT, excluding the 20 minute interval between 1448–1507 UT, containing bursts. Figure 7(a), for example, represents the slowly varying source before the slow rise in intensity shown in Figure 6. During this time the emission is resolved by the $1' \times 2'$ synthesized beam and concentrated in an elliptical source of $\sim 3' \times 5'$ in size whose center is shifted limbward by $\sim 3'$ with respect to the active region and the 20.7 cm loop. The source has a peak brightness temperature of $T_B \approx 3.5 \times 10^7$ K and is 85% left circularly polarized. Maps made on shorter time intervals showed no significant changes in size or brightness temperature, indicating that the 91.6 cm source was also relatively stable during this period. Figure 7 however shows that between 1545–1600 UT the source began to brighten and extend to the north, reaching a brightness temperature of $T_B \sim 5 \times 10^7$ K at 1600 UT. Since there were no impulsive bursts during this period (Fig. 6) this sequence of maps depicts a gradual evolution of the continuum source, rather than a rapid evolution caused by bursting sources.



FIG. 5.—A Big Bear Observatory off-band $H\alpha$ ($H\alpha + 0.6 \text{ \AA}$) filtergram taken at 161109 UT showing the location of flare kernels following the microwave burst. The kernels a_1 and a_2 appeared ~ 5 minutes before the impulsive phase of the burst; b_1 and b_2 were nearly coincident with it. The cross denotes the location of the impulsive source (2), shown in Fig. 4.

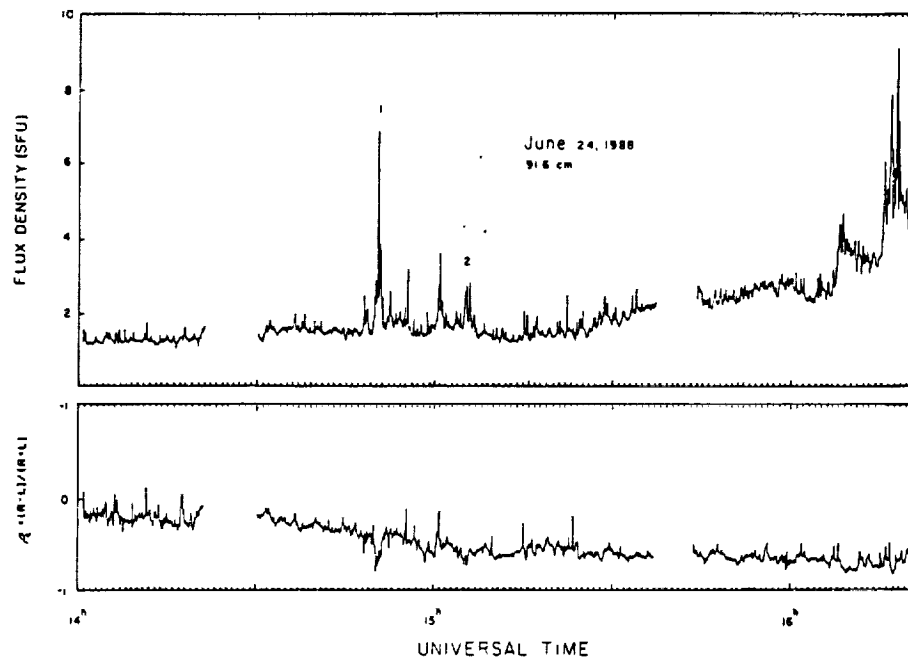


FIG. 6.—Time profile of the total intensity, I (top), and circular polarization, ρ_c (bottom) observed with one interferometer pair at 91.6 cm wavelength on 1988 June 24. Here the data are plotted with a time resolution of 3.3 s. Spike-like bursts are superposed upon a slowly varying background that begins to increase ~ 30 minutes before an intense microwave burst.

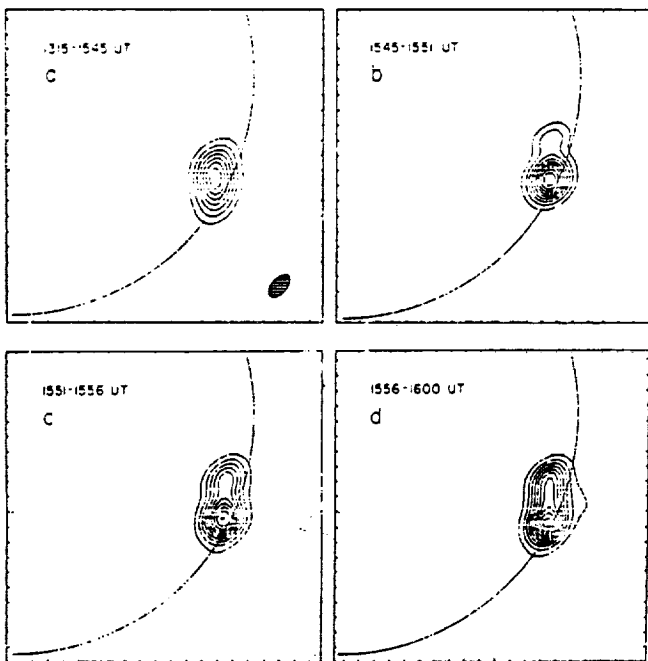


FIG. 7.—VLA synthesis maps of total intensity, I , at 91.6 cm wavelength between the indicated time intervals. The synthesized beam is shown in the upper left hand panel. It has an angular size of $65^\circ \times 114^\circ$. The angular scale may be inferred from the $60''$ spacing between the fiducial marks on the axes. The 91.6 cm source is seen to begin to change shape and elongate, ~ 15 minutes prior to the impulsive 20 cm burst shown in Fig. 1. The polarization remained nearly constant at $\rho_c \approx 85\%$ (LCP) throughout this time interval. The contour intervals are in units of equal brightness temperature, T_b , with an outermost contour and contour interval of 5×10^6 K.

The high brightness temperatures and degree of circular polarization suggest that the emission is nonthermal and associated with active-region magnetic fields. By way of comparison, VLA observations of the solar corona at 90 cm, reveal large-scale ($\theta \approx 3'-5'$) unpolarized structures with brightness temperatures of $T_b = 0.5-5 \times 10^5$ K (Lang, Willson, and Trotter 1988; Shevgaonkar, Kundu, and Jackson 1988; Lang and Willson 1989). These sources are not systematically associated with active regions and may delineate large-scale magnetic loops or filament sheaths whose brightness temperature can be attributed to thermal bremsstrahlung emission.

The 91.6 cm source discussed here may in fact be the continuum emission of a type I noise storm (Elgaroy 1977). In this case, the sense of circular polarization should correspond to the ordinary mode expected of plasma radiation in a unipolar flux tube (Kerdraon and Mercier 1982). We therefore expect the left circularly polarized emission to be associated with the leading spot of positive magnetic polarity shown in Figure 3. In fact, our potential magnetic field extrapolation indicates that the 91.6 cm sources lie within either a large-scale loop extending beyond the field of view or along open magnetic field lines which are anchored to photospheric fields of the leading spot of positive polarity. We may then estimate the height of the 91.6 cm source if it assumed to lie radially above the leading spot. From the position of the spot (S17 W52) and the angular displacement of the source shown in Figure 7(a), ($\Delta\theta \approx 3'$) we infer a height of $h = 0.18 \pm 0.03 R_\odot$. This is in agreement with the height inferred by Lang and Willson (1987) for a noise storm observed at 327 MHz using the VLA. Although it has been reported that noise storm centers are not located radially above the associated active regions (Kerdraon and Mercier 1982) the center of the quiescent source (from 1300–1545 UT) does appear to project nearly radially above the leading spot in the active region. The brightening at its northern end may represent newly accelerated particles radi-

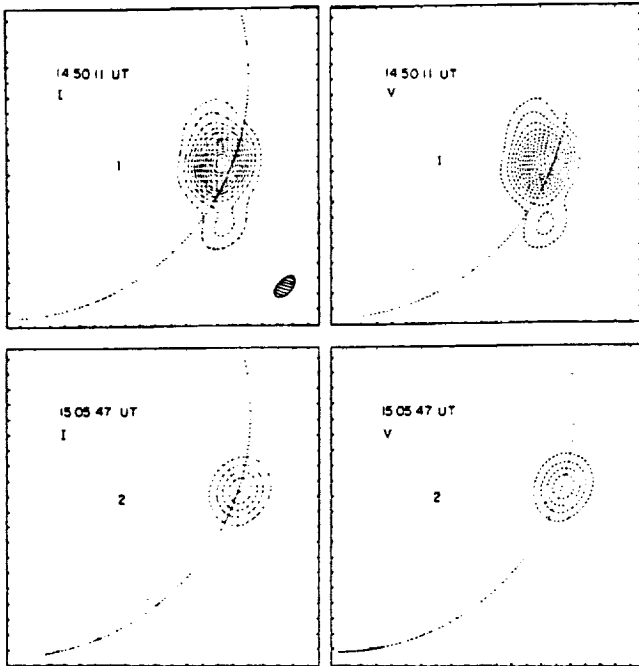


FIG. 8.—VLA 3.3 s snapshot maps at 91.6 cm wavelength of total intensity, I , and Stokes parameter, V , at the peaks of two impulsive bursts shown in Fig. 6. The synthesized beamwidth is shown in the upper left hand panel. It has an angular size of $55'' \times 90''$. The angular scale may be inferred from the $60''$ spacing between the fiducial marks on the axes. The contour intervals are in units of equal brightness temperature, T_b , with an outermost contour and contour interval of 5×10^6 K.

ating in this part of a diverging flux tube that bends upward and crosses the equator, possible connecting to a distant active region.

iii) Impulsive Bursts

Snapshot maps of the 91.6 cm impulsive emission are shown in Figures 8 and 9. Here, the preburst visibility level has also been subtracted before making these maps. The emission from groups of bursts shown in Figure 6 originates in an elliptical source ($\theta \approx 3'' \times 5''$) whose position is coincident with that of the slowly varying sources shown in Figure 7. In all cases, the emission was 90%–100% left circularly polarized, with peak brightness temperatures of $T_b = 1.5\text{--}5 \times 10^7$ K. These values are characteristic of type I bursts, but the 3.3 s observations may have integrated the emission of several such bursts or chains of bursts which have durations, τ of less than ~ 1 s (Elgaroy 1977). In this case the true brightness temperatures would exceed those observed, by a factor of approximately $(3.3/\tau)^2$.

Although the structure of the 91 cm emission varies from peak to peak, there was no evidence for a systematic shift in position of successive bursts for either group at any velocity $v \geq 150 \text{ km s}^{-1}$. Van Nieukoop (1986), for example, found that at 243 MHz, some groups of type I bursts showed a systematic angular displacement with time, suggesting disturbances moving with apparent velocities of up to $15,000 \text{ km s}^{-1}$.

The coincidence in position as well as the similarity in the degree of circular polarization of the continuum and type I burst suggests that both are emitted in a region of about the same magnetic field strength and density. Our magnetic field extrapolations indicate a magnetic field strength of $B \approx 10$ G at the position of the 91.6 cm burst. If the type I emission propagates in the ordinary mode at the fundamental of plasma

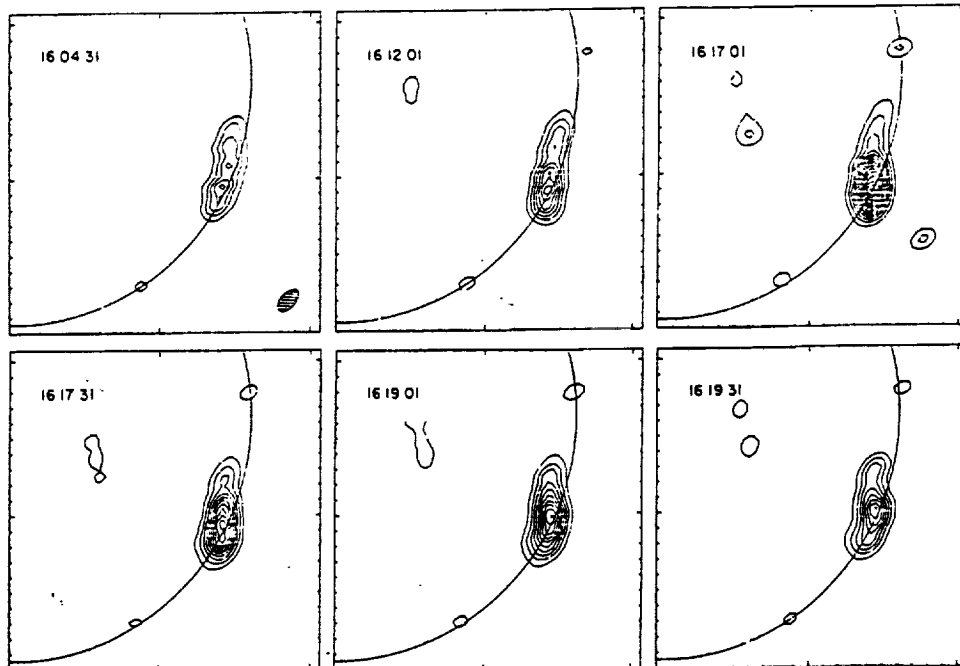


FIG. 9.—VLA snapshot maps of the total intensity, I , at 91.6 cm wavelength during 3.3 s intervals at the times indicated. The 91.6 cm source is shifted with respect to the 20.7 cm one (Fig. 3) by an angle $\theta \approx 3'$ towards the limb. The synthesized beamwidth is shown in the upper left hand panel. It has an angular size of $50'' \times 95''$. The angular scale may be inferred from the $60''$ spacing between the fiducial marks on the axes. The contour intervals are in units of equal brightness temperature, T_b , with an outermost contour and contour interval of 3.2×10^6 K.

frequency, v_p , (Dulk 1985; Kai, Melrose, and Suzuki 1985; Melrose 1985, 1987) then $v_{\text{obs}} > v_p > v_B$, where $v_B = 2.8 \times 10^6$ B is the gyrofrequency. At $v_{\text{obs}} = 327.5$ MHz, this corresponds to an electron density of $N_e = 1.3 \times 10^9 \text{ cm}^{-3}$ and $B < 116$ G, which is consistent with our field extrapolations.

III. DISCUSSION

a) Correlated Activity at 20.7 cm, 91 cm and Optical Wavelengths

Our data at 20.7 cm and 91.6 cm wavelength show intriguing correlations between activity at these two wavelengths. For example, our 91.6 cm maps (Fig. 7) indicate that the region emitting the storm continuum began to increase in size and intensity about 30 minutes before the impulsive 20.7 cm burst. Although a group of type I bursts occurred earlier at the same location, they apparently did not initiate this increase. The 91.6 cm continuum level again abruptly increased a few minutes after the 20.7 cm burst, and this was followed ~ 15 minutes later by another group of type I bursts. These results may suggest a feed-back mechanism in which interactions of large-scale loops trigger burst activity in lower lying loops and vice versa.

The onset of the increase 91.6 cm (Fig. 7) may have also been related to changes in one of the active regions filaments. In Figure 10 we show two Big Bear Solar Observatory off-band H α (H α -0.6 Å) filtergrams illustrating that a portion of one end of the filament, marked A, disappeared sometime between 1537 UT and 1543 UT. Later frames (after 1600 UT) show the presence of filament material in that area. The time gap (1537–1543 UT) was due to a gap in the data leaving one not knowing whether there was a true eruption and reappearance of this portion of the filament or, if line of sight motion in the filament was greater than 30 km s^{-1} , it might not have been visible at this wavelength. More subtle changes at the other end of the filament (marked B) can be seen on BBSO filtergrams between 1546–1548 UT. Various small motions and weak brightenings were noted at both ends of this filament from 1505 UT. The filament lies in the vicinity of the two H α kernels (a_1 and a_2 in Fig. 5) that appeared at 1600 UT, but is displaced from the sunspot that marks the footpoints for the open magnetic field lines that thread the 91.6 cm emission.

Filaments have long been known to exhibit preflare activity, often showing upward motions or reconfiguration tens of minutes before flare onset (Martin and Ramsey 1972; Webb, Krieger, and Rust 1976). These activations are often accompanied by changes in the photosphere or chromosphere which have been taken as evidence for the evolution or emergence of magnetic flux (Rust 1976; Kundu and Woodgate 1986). The newly formed magnetic loops can then interact with existing magnetic fields, thereby providing the triggering mechanism for microwave bursts (Heyvaerts, Priest, and Rust 1977). Filament activity can also apparently result in the production of nonthermal electrons. Webb and Kundu (1978) found a close temporal and spatial association between erupting filaments and noise storm continua, while Webb, Krieger, and Rust (1976) showed that X-ray and microwave gradual rise and fall peaks follow the end of filament disappearances by tens of minutes. Finally, preburst activity at 6 cm wavelength, including an increase in intensity and polarization, has also been associated with motions and changes in a nearby filament (Kundu *et al.* 1985).

At least one theoretical model has been proposed that

relates noise storms to changes in magnetic fields, and presumably to filament activity (Spicer, Benz, and Huba 1981). In this model shock waves are generated at the boundary of newly emerging flux and the ambient corona, thereby accelerating the particles that produce the type I bursts. Although this model may explain our observations, confirmation may have to wait until VLA images of noise storm sources are correlated with simultaneous high time resolution magnetograms which resolve changes in photospheric magnetic fields.

b) Estimates of Magnetic Field Strength in the 20.7 cm Burst Sources

In this section we combine our measurements of the sizes and brightness temperatures of the 20.7 cm burst components with the solar radio patrol data shown in Figure 2 to estimate the magnetic field strength in these sources. In particular we consider two models of burst emission developed by Dulk and Dennis (1982), called multithermal and nonthermal models, which make specific predictions about the size and brightness temperature of a microwave burst source as a function of frequency. These models assume that the impulsive emission at hard X-rays and microwaves comes from the same population of electrons and that the source can be described as a set of loops which confine the highest energy electrons to a compact core. In the multithermal model, the average electron temperature, T , and magnetic field strength, B , both decrease with radius from the center of the core according to the power laws

$$T = T_{\text{max}} \left(\frac{r}{r_{\text{min}}} \right)^{-\alpha_T}$$

$$B = B_{\text{max}} \left(\frac{r}{r_{\text{min}}} \right)^{-\alpha_B}$$

where r_{min} is the core radius ($r > r_{\text{min}}$). T_{max} and B_{max} are the maximum temperature and magnetic field strength in the core, and α_T and α_B are related to the X-ray photon number index, α_x , and the microwave spectral index, α_m , by

$$\alpha_T = \frac{6}{2\alpha_x - 3}$$

$$\alpha_B = \frac{7\alpha_T \alpha_m - 24\alpha_T - \alpha_m + 22}{18 - 22\alpha_m}$$

Here, α_m is obtained from the optically thick region of the microwave spectrum (at $\nu < \nu_{\text{max}}$) where the flux density increases with frequency as $S \propto \nu^\delta \propto A \nu^2 T_{\text{eff}}$ and where A is the projected area of the source and T_{eff} is the effective brightness temperature.

For the nonthermal model, it is assumed that the energy electron distribution is a power law of index $\delta = \alpha_x - 0.5$ and that only the magnetic field strength varies with distance from the core. In this case the microwave spectral index is related to α_B by

$$\alpha_m = 2.9 - \frac{(0.9\alpha_B + 2)(1.2 + \delta)}{\alpha_B(0.2 + \delta) - 1}$$

Using the equations for a gyrosynchrotron-emitting source given by Dulk, Melrose, and White (1979) and Dulk and Marsh (1982), Dulk and Dennis (1982) derive expressions for the flux, brightness temperature, size and magnetic field strength as a function of frequency for both the multithermal and nonthermal models. For both models, one must know the

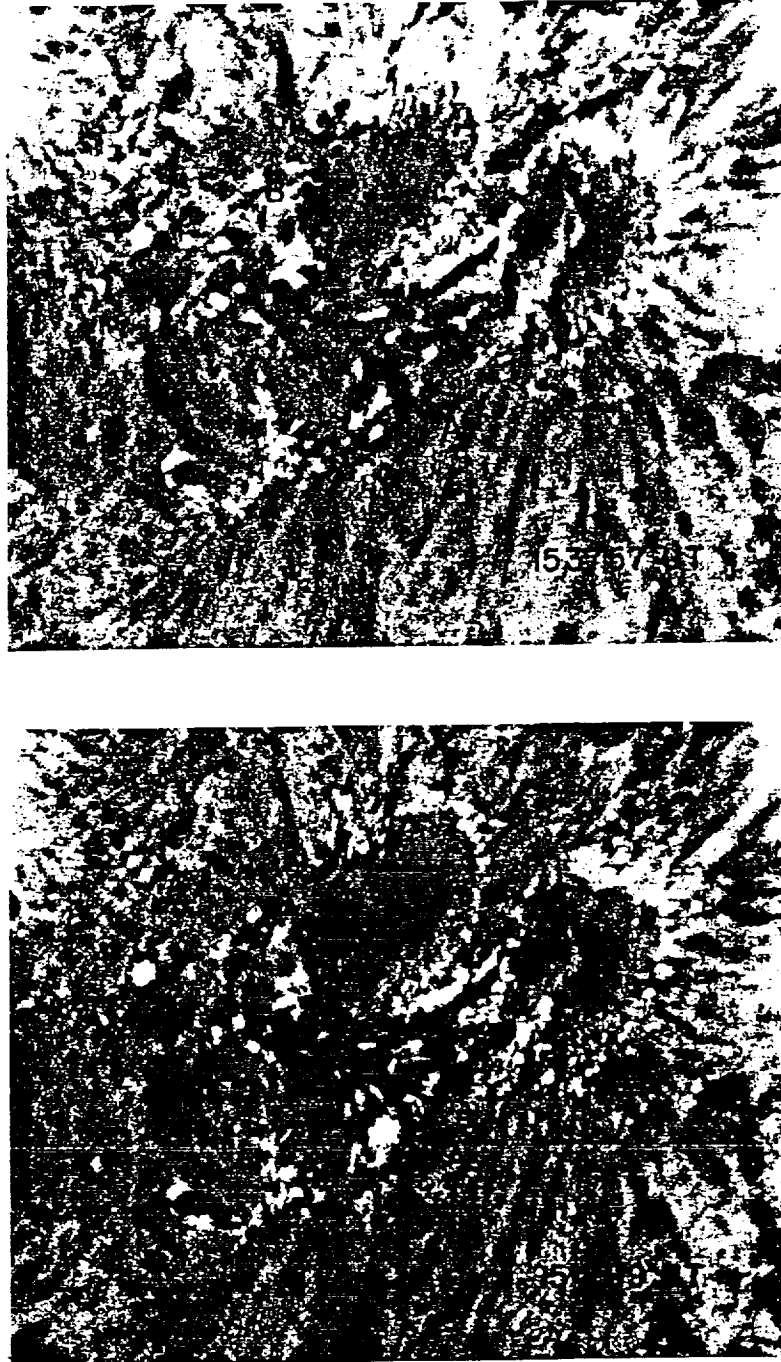


FIG. 10.—Big Bear Observatory off-band H α ($H\alpha - 0.6 \text{ \AA}$) images showing the disappearance of a section of filament (A) between 153757 UT and 154319 UT.

flux, $S_{\nu_{\max}}$, at the turnover frequency, ν_{\max} , the hard X-ray spectral index, α_x , and the core size, r_{\min} . For the multithermal model, one must also know the effective brightness temperature T_{\max} , at the peak frequency corresponding to $r = r_{\min}$. Since there were no hard X-ray observations during this burst, we have made calculations for a range of values of $\alpha_x = 3.5-7.0$, which are consistent with those inferred from other observations (e.g., Dennis 1989). For the multithermal model, we assumed a core temperature of $T_{\max} = 5 \times 10^8 \text{ K}$, a value that is somewhat higher than the brightness temperature observed during the impulsive phase. For this model the core radius at a

given time was derived using this T_{\max} and the observed flux density at the peak frequency (see eq. 11 of Dulk and Dennis 1982). Since the nonthermal emission does not depend on T_{\max} , we could not calculate the nonthermal core radius in this way. Instead, we followed the procedure outlined by Dulk and Dennis (1982) and assumed a set of values ranging from $r_{\min} = 2-15 \times 10^8 \text{ cm}$, corresponding to core angular sizes of $\theta = 5.5-40''$. These sizes bracket the range of burst sizes we recently observed at 2 cm and 3.5 cm wavelength using the VLA (Willson *et al.* 1990).

The results of our calculations are given in Table 1. Here we

TABLE I
OBSERVED AND DERIVED PARAMETERS FOR DIFFERENT TIMES DURING THE 20.7 cm BURST

UT	T_p (K)	Angular size ($''$)	Spectral Index	S_{ν} (SFU)	ν_{\max} (GHz)	α_x	MULTITHERMAL MODEL			NONTHERMAL MODEL			
							B (G)	T_p (K)	Angular size ($''$)	δ	B (G)	T_p (K)	Angular size ($''$)
160626.....	1×10^8	1.0×1.5	0.85	600	≥ 15.4	5	42	1.1×10^8	1.3	6.0	155	1.1×10^8	1.3 ^a
160647.....	1.3×10^8	1.0×1.5	0.72	705	≥ 15.4	5.5	35	1.5×10^8	1.3	6.0	130	1.4×10^8	1.4 ^a
160807.....	5.5×10^7	1.4×1.5	0.92	327	~ 8.8	3.8	75	5.3×10^7	1.6	6.0	270	5.9×10^7	1.5 ^b
160927.....	2.2×10^7	1.5×2.0	0.80	117	~ 8.8	3.5	160	1.8×10^7	1.9	6.0	640	2.5×10^7	1.7 ^b

^a $r_{\min} = 1 \times 10^9$ cm.

^b $r_{\min} = 1.5 \times 10^9$ cm.

give the peak brightness temperature, half-power angular size, spectral index, and peak flux and frequency for each of four different 20.7 cm burst components, together with the magnetic field strength, angular size and brightness temperature for the best-fit multithermal and nonthermal models.

Our results show that for a given T_{\max} and r_{\min} , the multithermal model gives a satisfactory fit for spectral indices of $\alpha_x = 3.5$ – 5.5 and magnetic field strengths of $B = 35$ – 160 G. These values of B are consistent with those obtained from our potential field calculations which indicate field strengths of $B = 75$ – 120 G at the locations of the burst sources. However, the fact that the magnetic field strength in the nearly coplanar sources at 160807 and 160927 UT differ by about a factor of two may suggest that our assumption of a constant core temperature of $T_{\max} = 5 \times 10^8$ K is incorrect. With $T_{\max} = 1 \times 10^8$ K and $\delta = 5$ at 160927 UT, for example, we derive a magnetic field strength of $B = 115$ G, closer to the value inferred for the secondary impulsive peak at 160807 UT. These models also predict magnetic field strengths of $B = 10$ – 25 G and angular sizes of $\theta = 4$ – $8''$ at 91.6 cm. However, since the observed emission at this wavelength is probably due to plasma radiation and not to gyrosynchrotron emission (the long wavelength counterpart of the microwave burst is very likely attenuated by thermal plasma, see § II b[i]), the brightness temperatures and sizes of the 91.6 cm sources provide no useful constraints on these models.

For the same values of r_{\min} , the nonthermal model predicts consistently higher magnetic field strengths and smaller angular sizes than are observed at 20.7 cm. This is because the source size decreases less rapidly with frequency in the nonthermal model, than in the multithermal model. In order to get the observed sizes of 1.5, we require larger core sizes of $r_{\min} = 1$ – 1.5×10^9 cm (corresponding to angular sizes of $28''$ – $40''$). However with these larger values of r_{\min} , the nonthermal model predicts magnetic field strengths that are probably too high. At the turnover frequency of 15.4 GHz, for example, the expected core magnetic field strengths are $B_{\max} = 2500$ G, or about equal to the field strengths in some of the spots. In contrast, the corresponding core strengths in the multithermal models are $B_{\max} \approx 125$ – 220 G. In view of this difficulty, we therefore conclude that the multithermal model provides a better explanation for these data.

IV. SUMMARY

We may summarize our main results as follows:

1. The VLA snapshot maps show that the precursor, impulsive, and postimpulsive phases of the 20.7 cm burst are located

in spatially separated sources, suggesting activation in different coronal loops or systems of loops. The hot precursor source apparently interacted with an adjacent one, leading to the explosive release of energy during the impulsive phase. The system of coronal loops then seems to have relaxed to a more stable state when yet another nearby source emitted the decay phase. These results are similar to those obtained by Machado *et al.* (1988), who showed that X-ray flaring activity usually involves two or more interacting magnetic dipoles within an active region, with an initiating dipole impacting against an adjacent one.

2. The gradual enhancement of a 91.6 cm noise storm continuum source about 30 minutes before the microwave burst together with subsequent type I bursts suggests that some sort of feed-back mechanism may exist between activity in higher lying loops and lower lying ones. The additional observation of filament activity lends support to this idea, although further observations at radio, X-ray, and optical wavelengths are needed to confirm it.

3. The inhomogeneous source models of Dulk and Dennis (1982) were used to estimate the magnetic field strength in the 20.7 cm burst sources. The brightness temperatures and sizes of these sources, together with microwave data from solar radio patrol instruments are probably more consistent with a multithermal rather than a nonthermal gyrosynchrotron-emitting source. The derived magnetic field strengths at 20.7 cm for the nonthermal models are $B = 35$ – 160 G, with core field strengths of $B = 125$ – 220 G. The nonthermal models require core field strengths of $B = 2500$ G, which, though comparable to the strengths in the underlying sunspots, are considerably higher than expected for sources located in the solar corona.

Radio astronomical studies of the Sun at Tufts University are supported under grant AFOSR-89-0147 with the Air Force Office of Scientific Research.

We thank the referee for a number of helpful suggestions. We are grateful to Kermit Smith of Goddard Space Flight Center for providing the Kitt Peak magnetogram. We also thank Edward Cliver of the Air Force Geophysics Laboratory for providing the Air Force Solar Radio Patrol data and T. Sakurai for providing the magnetic field extrapolation program. Our simultaneous VLA and *Solar Maximum Mission* (SMM) observations of the Sun are supported by NASA grant NAG 5-501. The Very Large Array is operated by Associated Universities, Inc. under contract with the National Science Foundation.

REFERENCES

- Alissandrakis, C. E., and Kundu, M. R. 1978, *Ap. J.*, **222**, 342.
 Das, A. K., and Sethumadhaven, K. 1953, *Nature*, **172**, 446.
 Davies, R. D. 1953, *Nature*, **172**, 446.
 Dennis, B. R. 1989, *Solar Phys.*, **118**, 49.
 Dodson, H. W., and Doselman, R. W. 1951, *Ap. J.*, **113**, 519.
 Dulk, G. A. 1985, *Ann. Rev. Astr. Ap.*, **23**, 169.
 Dulk, G. A., and Dennis, B. R. 1982, *Ap. J.*, **260**, 875.
 Dulk, G. A., and Marsh, K. A. 1982, *Ap. J.*, **259**, 350.
 Elgaroy, E. O. 1977, *Solar Noise Storms* (Oxford: Pergamon Press).
 Gary, D. E., and Hurford, G. J. 1988, *Ap. J.*, **317**, 522.
 Habbal, S. R., Ellman, N. E., and Gonzalez, R. 1989, *Ap. J.*, in press.
 Heyvaerts, J., Priest, E. R., and Rust, D. M. 1977, *Ap. J.*, **216**, 123.
 Kai, K., Melrose, D. B., and Suzuki, S. 1985, in *Solar Radiophysics*, ed. D. J. McLean and N. R. Labrum (Cambridge: Cambridge University Press), p. 415.
 Kerdraon, A., and Mercier, C. 1982, in *Solar Noise Storms, Proceedings of the 4th Workshop on Solar Radio Noise Storms*, ed. A. O. Benz and P. Zlobec (Osservatorio Astronomico di Trieste), Trieste, p. 27.
 Kundu, M. R. 1965, *Solar Radio Astronomy* (New York: Interscience Publishing).
 Kundu, M., Gaizauskas, V., Woodgate, B., Schmahl, E. J., Jones, H., and Shine, R. A. 1985, *Ap. J. Suppl.*, **57**, 621.
 Kundu, M. R., and Lang, K. R. 1985, *Science*, **228**, 9.
 Kundu, M. R., Schmahl, E. J., Velusamy, T., and Vlahos, L. 1982, *Astr. Ap.*, **108**, 188.
 Kundu, M. R., and Woodgate, B. 1986, *Energetic Phenomena on the Sun*, ed. M. R. Kundu and B. Woodgate (Greenbelt: NASA CP-2439), Chap. 1.
 Lang, K. R., and Willson, R. F. 1984, *Adv. Space Res.*, Vol. 2(11), p. 91.
 ———. 1986, *Adv. Space Res.*, Vol. 4(7), p. 105.
 ———. 1987, *Ap. J.*, **319**, 514.
 ———. 1989, *Ap. J. (Letters)*, **344**, L73.
 Lang, K. R., Willson, R. F., and Trotter, G. 1988, *Astr. Ap.*, **199**, 325.
 Lantos, D., Kerdraon, A., Rapley, G. G., and Bentley, 1981, *Astr. Ap.*, **101**, 33.
 Machado, M. E., Moore, R. L., Hernandez, A. M., Rovira, M. G., Hagyard, M. J., and Smith, J. B. 1988, *Ap. J.*, **326**, 425.
 Marsh, K. A., and Hurford, G. J. 1980, *Ap. J. (Letters)*, **240**, L111.
 Martin, S. F. 1980, *Solar Phys.*, **68**, 217.
 Martin, S. F., and Ramsey, H. E. 1972, in *Solar Activity Observations and Predictions*, ed. P. McIntosh and M. Dryer (Cambridge: MIT Press), p. 371.
 McClean, D. J. 1973, *Proc. Astr. Soc. Austr.*, **2**, 222.
 ———. 1981, *Proc. Astr. Soc. Austr.*, **4**, 132.
 Melrose, D. B. 1985, in *Solar Radiophysics*, ed. D. J. McClean and N. R. Labrum (Cambridge: Cambridge University Press), p. 177.
 ———. 1987, *Solar Phys.*, **111**, 89.
 Mercier, C., Elgaroy, O., Tlamicha, A., and Zlobec, P. 1984, *Solar Phys.*, **92**, 375.
 Rust, D. M. 1976, *Phil. Trans. R. Soc. London, Ser. A.*, **281**, 427.
 Rust, D. M., Benz, A. O., Nelson, G. J., Pick, M., and Ruzdjak, V. 1981, *Ap. J. (Letters)*, **244**, L179.
 Sakurai, T. 1981, *Solar Phys.*, **76**, 301.
 Shevgaonkar, R. K., Kundu, M. R., and Jackson, P. D. 1988, *Ap. J.*, **329**, 982.
 Spicer, P. S., Benz, A. O., and Huba, J. D. 1981, *Astr. Ap.*, **105**, 221.
 Stewart, R. T. 1985, *Solar Phys.*, **96**, 381.
 Stewart, R. T., Brueckner, G. E., and Dere, K. P. 1986, *Solar Phys.*, **106**, 107.
 Van Nieukoop, J. 1986, *Solar Phys.*, **103**, 129.
 Webb, D. F. 1983, *A Study of Coronal Precursors of Solar Flares* (Technical Report AFGL-TR-83-0126).
 Webb, D. F., and Kundu, M. R. 1978, *Solar Phys.*, **57**, 155.
 Webb, D. F., Krieger, A. S., and Rust, D. M. 1976, *Solar Phys.*, **48**, 159.
 Wild, J. P., and Zirin, H. 1956, *Australian J. Phys.*, **9**, 315.
 Willson, R. F. 1983, *Solar Phys.*, **83**, 285.
 ———. 1984, *Solar Phys.*, **92**, 189.
 Willson, R. F., Kerdraon, A., Trotter, G., and Lang, K. R. 1990, *Ap. J.*, submitted.
 Willson, R. F., and Lang, K. R. 1984, *Ap. J.*, **279**, 427.

MARGARET LIGGETT: Solar Astronomy, California Institute of Technology, Pasadena, CA 91125

ROBERT F. WILLSON and KENNETH R. LANG: Department of Physics and Astronomy, Robinson Hall, Tufts University, Medford, MA 02155

YU ISSN 0351-2651
HOBUD7 13(1) 93(1989)

R. RADIO EMISSION FROM QUIESCENT FILAMENTS

Kenneth R. Lang
Tufts Universtiy, Medford, MA, USA

UDC 523.987.2-77
conference paper

Hvar Obs.Bull. 13 (1989) 93-111

93

Lang: Radio emission from quiescent filaments

ABSTRACT

Full-disk VLA synthesis maps of the quiet Sun indicate that filaments can be seen in emission at 91.6-cm wavelength; they are detected in absorption at shorter microwave wavelengths. The 91.6-cm emission has a brightness temperature of $T_B = 3 \times 10^5$ K. It is hotter, wider and longer than the underlying filament detected at H α wavelengths, but the similarity between the shape, position, elongation and orientation of the radio and optical features suggests their close association. The 91.6-cm emission is attributed to the thermal br \ddot{u} msstrahlung of a hot transition sheath that envelopes the H α filament and acts as an interface between the cool, dense H α filament and the hotter, rarefied corona. The transition sheath is seen in emission because of the lower optical depth of the corona at 90-cm wavelength, and the width of this sheet is 10^9 cm. A power law gradient in pressure provides a better match to the observations than a constant pressure model; definitive tests of theoretical models await simultaneous multi-wavelength studies of filaments at different observing angles. When the thermal br \ddot{u} msstrahlung is optically thin, the magnetic field strength in the transition sheath can be inferred from the observed circular polarization. Variable physical parameters of the sheath, such as width, electron density, and electron temperature, can explain controversial reports of the detection of, or the failure to detect, the meter-wavelength counterpart of H α filaments.

Subject headings: Sun: filaments - Sun: prominences - Sun: radio radiation
Sun: coronal loops - Sun: magnetic fields

94

Hvar Obs.Bull. 13 (1989) 93-111

I. INTRODUCTION

Filaments are cooler than the surrounding corona, and therefore appear as depressions in the quiet Sun background at centimeter wavelengths (Gary, 1986; Kundu, Melozzi and Shevgaonkar, 1986); the cool filaments can also appear as depressions at millimeter wavelengths (Schmahl, Bobrowsky and Kundu, 1981). Regions that overlie filaments can now be detected using the VLA at the longer 91.6-cm wavelength; the higher temperatures produce regions of increased emission when compared with the surrounding quiet Sun background.

Previous observations have, however, led to an ongoing controversy about the optical counterparts of the quiescent, or non-flaring, solar radiation at meter wavelengths. A statistical study of numerous one-dimensional Nancay scans suggested that many quiescent meter-wavelength sources are associated with filament corridors as seen on H α synoptic maps (Axisa et al., 1971), but subsequent two-dimensional maps indicated that most filaments have no radio counterpart at meter wavelengths (Alissandrakis, Lantos and Nicolaidis, 1985; Lantos et al., 1987).

The VLA provides an order-of-magnitude improvement in angular resolution over all previous meter-wavelength investigations of the quiet Sun and might therefore help resolve this controversy. The first VLA observations of the quiescent coronal at 92-cm wavelength indicated no systematic association of any of the radio sources with any optical counterpart, including active regions, filaments, sunspots and the magnetic neutral line in the underlying photosphere (Lang, Willson, and Trotter, 1987). Full disk VLA observations by Shevgaonkar, Kundu, and Jackson (1988) indicated that the 90-cm sources may be indentified as streamers above H α filaments. However, our comparison of

Lang: Radio emission from quiescent filaments

their data with H α observations (Solar Geophysical Data) indicates that many of the intense 90-cm sources do not overlie H α filaments.

One probable source of confusion is noise storms, the most common form of solar activity at meter wavelengths. The numerous type I bursts and background continuum of noise storms have been associated with coronal loop structures detected during Skylab at soft X-ray wavelengths (Stewart and Vorpahl, 1977; Gergely, Kundu, Golub and Webb, 1980) as well as with large-scale EUV loops (Stewart, Brueckner and Dere, 1986). VLA observations at 91.6-cm wavelength confirm the location of noise storms in large-scale magnetic loops that either overlie coronal loops within individual active regions or connect these regions with more distant areas on the Sun (Lang and Willson, 1987); such conclusions were also anticipated by metric wavelength observations with the Nancay Radioheliograph (Lantos-Jarry, 1970; Mercier et al., 1984). Detection of the meter-wavelength counterpart of filaments requires observations when the intense noise storms are not present.

In this paper we present VLA 91.6-cm synthesis maps during quiescent periods without any noise storm activity. In Section II we show that there is an excellent association of some 91.6-cm sources with H α filaments. The radio filaments are enhanced over the surrounding quiescent emission, rather than depressed. Not all H α filaments, however, exhibit detectable 91.6-cm counterparts. In Section III we interpret some quiescent 91.6-cm sources in terms of the thermal radiation of a sheath overlying a H α filament, and with temperatures intermediate between those of its H α counterpart and the surrounding corona.

Lang: Radio emission from quiescent filaments
II. OBSERVATIONS

The Sun was observed with the VLA in the C/D hybrid configuration between 1315 and 1610 UT on 15 May 1988 using 27 antennas at 20.7-cm wavelength (1446 MHz) and 19 antennas at 91.6-cm wavelength (327.5 MHz) with respective bandwidths of 12.5 and 3.125 MHz. The full-disk synthesis maps at 20.7-cm are given elsewhere (Lang and Willson, 1989a), where they are used to identify active regions that interact via large-scale, trans-equatorial magnetic loops. Here we focus on the full-disk 91.6-cm synthesis map shown in Figure 1 (left). Although all four Stokes parameters were sampled, there was no detectable circular polarization, so our three-hour synthesis map refers to the total intensity, I. Burst data have been removed prior to making this synthesis map. The details of calibration procedures are given in Lang and Willson (1989b).

The contours of the resulting map (Figure 1, left) mark levels of equal brightness temperature, T_B , with an outermost contour of $T_B = 7.8 \times 10^4$ K, a contour interval of 7.8×10^4 K, and peak brightness temperature of $T_B = 7.8 \times 10^5$ K. The mean brightness temperatures of the elongated sources marked A and B are, for example, estimated to be $T_B \sim 3 \times 10^5$ K above the surrounding quiet Sun level of $T_B \sim 4 \times 10^5$ K, with an uncertainty of 20 percent.

An H α photograph taken on the same day (15 May 1988) is also shown in Figure 1 (right); it contains several dark, elongated filaments. Two of these have counterparts in the 91.6-cm map with similar shapes, positions, elongations and orientations; they are designated by the letters A and B in the 91.6-cm map. The smaller filaments seen in the north-central regions also seem to have 91.6-cm counterparts, but there is no increased 91.6-cm emission in the vicinity of the dark filaments that lie near the north-east and south-east limbs (marked C and E on the 91.6-cm map).

Lang: Radio emission from quiescent filaments

The intense 91.6-cm emission detected near the equator on the east limb (marked D) may be due to a coronal streamer. Sacramento Peak coronagraph data (Solar Geophysical Data) show coronal material in this region, as well as those that have no detectable 91.6-cm radiation. No underlying active regions or filaments were visible as the Sun rotated and the limb region turned in to view during the following days.

Depressions in the 91.6-cm radiation are found in the central equatorial regions (hatched regions). They may be at least partly due to coronal holes, but the only available He 10830 data, taken on 14 May, do not exhibit a detectable equatorial coronal hole. Examination of the 91.6-cm maps for shorter time scales showed no evidence for variable features on time scales of a few tens of minutes.

III. DISCUSSION

The similarity in shape, position, elongation and orientation strongly suggests that the radio emission from sources A and B is associated with the underlying dark filaments detected in the H α photograph, but the radio emission could also be associated with bright H α plage and their associated higher magnetic fields. The most intense emission from source A coincides with a dark filament rather than plage, and the most intense part of source B corresponds to the largest part of the underlying filament. Moreover, the weaker emission from both sources has the same shape and orientation as the associated narrow, elongated filaments. We therefore attribute the radio emission to these filaments, while noticing that H α plage might also play a role in enhanced 91.6-cm emission.

We therefore interpret the regions of increased 91.6-cm emission around filaments (sources A and B) in terms of a hot sheath that envelops the cooler H α filaments; such a surrounding sheath is suggested by the fact that the radio wavelength features are similar in shape to, but wider, longer and hotter than, their optical counterparts. The mean 91.6-cm brightness temperatures of $T_B \sim 3 \times 10^5$ K, for example, lie between the electron temperatures of the cool H α filaments and the electron temperature of the surrounding corona.

In order to gain a quantitative view of the transition sheath, we compare our observations with the data and models given by Kundu, Melozzi and Shevgaonkar (1986). Their VLA observations at the shorter 6 and 20 cm wavelengths indicated radio depressions above H α filaments, in comparison with the hot surrounding corona, but a transition sheath was indicated by the fact that the radio filaments are larger in size than their optical counterparts and that the brightness temperature, T_B , of the radio filaments

Lang: Radio emission from quiescent filaments

increases with wavelength from $T_B \sim 1.5 \times 10^4$ K at 6 cm to $T_B \sim 5 \times 10^4$ K at 20 cm. Our higher brightness temperature of $T_B \sim 3 \times 10^5$ K at the longer 91.6-cm wavelength can be explained by the larger optical depth of thermal bremsstrahlung from the transition sheath at longer wavelengths, and the fact that the 91.6-cm sheath is seen in emission can be explained by the relatively low optical depth of the low-density corona. The brightness temperature contribution of the corona has been taken into account by subtracting the background solar disk temperature in obtaining our filament brightness temperature of $T_B \sim 3 \times 10^5$ K. If the transition sheath is observed as optically thin bremsstrahlung during future observations, the magnetic field strength can be inferred from the observed circular polarization.

We have assumed that the variation of temperature with height in the transition sheath is that given by Kundu, Melozzi and Shevgaonkar (1986); their data resulted from an assumed balance between the thermal energy conducted in from the corona and the energy radiated away. These temperatures, T , were then combined with three pressure models to infer the electron density, N , and the equation of transfer was solved assuming free-free emission with these values of temperature and density. The three models were a constant pressure model $P = NT = 3 \times 10^{14} \text{ cm}^{-3} \text{ K}$, and two power law models $P = NT = aT^n$, with $a = 2.5 \times 10^{17}$, $n = -0.58$ and $a = 4 \times 10^{17}$, $n = -0.62$. The calculated brightness temperatures of these two models are shown in Figure 2 together with our measurements at 91.6 cm and those of other observers at shorter wavelengths. This figure indicates that the brightness temperature of the constant pressure model is too high at both 20 cm and 90 cm, with respective values of $T_B \sim 9 \times 10^4$ K and $T_B \sim 6 \times 10^5$ K. The power law models are more in accord with the observational data; at 20 cm

Lang: Radio emission from quiescent filaments

and 90 cm they both produce respective values of $T_B \sim 5 \times 10^4$ K and $T_B \sim 3 \times 10^5$ K. Also note that the 20 cm point is an average of several observations for different observing angles, so this difference cannot account for the result. Detailed model comparisons await future multi-wavelength studies of the same filament at the same time for different observing angles.

So, the observed 91.6-cm structures that are associated with these H α filaments may be interpreted as the thermal bremsstrahlung of a hot (electron temperature $T_e = 3 \times 10^5$ K) sheath that envelops a H α filament. Such a sheath acts as the boundary between the filament and the surrounding million-degree corona. A loop thickness of $L = 10^9$ cm, or about one fiftieth of the $10' = 5 \times 10^{10}$ cm extent of the radio sources A and B, has been inferred by deconvolving the observed radio width, to take into account the beamwidth, and using the convolution relation to subtract the observed width of the H α filament. Such a thickness is consistent with the models of Kundu, Melozzi and Shevgaonkar (1986). If the hypothesized sheath were substantially thinner than the assumed thickness of $L = 10^9$ cm, then the optical depth for thermal bremsstrahlung would be much smaller, and the optically-thin sheath might not be detectable. And if the electron density of the sheath was only slightly higher, then its plasma frequency would exceed our observing frequency, and the sheath radiation could not propagate out to be observed. Variable physical parameters of the sheath might therefore easily explain why the elusive meter-wavelength counterpart of H α filaments is only sometimes observed; just the right thickness, electron density and electron temperature are required for detection.

Lang: Radio emission from quiescent filaments

Discussion

Chiuderi Drago: In the figure that you have shown, Kundu et al. report the observed brightness temperature corrected for the coronal emission $T_c \tau_c$. Did you apply this correction to your data? If not, the data can not be compared. In the positive case, which coronal parameters did you use to calculate $T_c \tau_c$?

Lang: Our point for the brightness temperature of filament emission at 92 cm wavelength is the observed data corrected for the observed background emission of the corona as seen against the quiet Sun away the filament. We have not applied the Kundu et al. correction to our data. We assumed that they knew what they were doing in correcting their own data.

Lang: Radio emission from quiescent filaments

ACKNOWLEDGMENTS

Radio astronomical studies of the Sun at Tufts University are supported under grant AFOSR-89-0147 with the Air Force Office of Scientific Research. The Very Large Array is operated by Associated Universities, Inc., under contract with the National Science Foundation. The data presented in this paper were taken during collaborative long-wavelength solar observations by Tufts University and the Observatoire de Paris - Meudon, under the support of National Science Foundation grant INT-8602285 and Centre National de la Recherche Scientifique grant 920038.

Lang: Radio emission from quiescent filaments

REFERENCES

- Alissandrakis, C.E., Lantos, P., and Nicolaidis, E. 1985, Solar Phys., 97, 267.
- Axisa, F., Avignon, Y., Martres, M.J., Pick, M., and Simon, P. 1971, Solar Phys., 19, 110.
- Gary, D.E. 1986, in Coronal and Prominence Plasmas, ed. A.I. Poland (NASA Conf. Pub. 2442), p. 121.
- Gergely, T.E., and Kundu, M.R. 1980, in Radio Physics of the Sun. IAU Symposium No. 86, ed. M.R. Kundu and T.E. Gergely, p. 435.
- Kundu, M.R., Melozzi, M., and Shevgaonkar, R.K., 1986, Astron. Ap., 167, 166.
- Lang, K.R., and Willson, R.F. 1987, Ap.J., 319, 514.
- Lang, K.R., and Willson, R.F. 1989a, Ap. J. (Letters) 344, L 77.
- Lang, K.R., and Willson, R.F. 1989b, Ap. J. (Letters) 344, L 73.
- Lang, K.R., Willson, R.F., and Trottet, G. 1988, Astron. Ap., 199, 325.
- Lantos, P., Alissandrakis, C.E., Gergely, T., and Kundu, M.R. 1987, Solar Phys., 112, 325.
- Lantos - Jarry, M.F. 1970, Solar Phys., 15, 40.
- Mercier, C., Elgaroy, O., Tiamicha, A. and Zlobec, P. 1984, Solar Phys., 92, 375.

Lang: Radio emission from quiescent filaments

Schmahl, E.J., Bobrowsky, M., and Kundu, M.R. 1981, Solar Phys., 71, 311.

Stewart, R.T., Brueckner, G.E., and Dere, K.P. 1986, Solar Phys., 106, 107.

Stewart, R.T., and Vorpahl, J. 1977, Solar Phys., 55, 111.

Lang: Radio emission from quiescent filaments

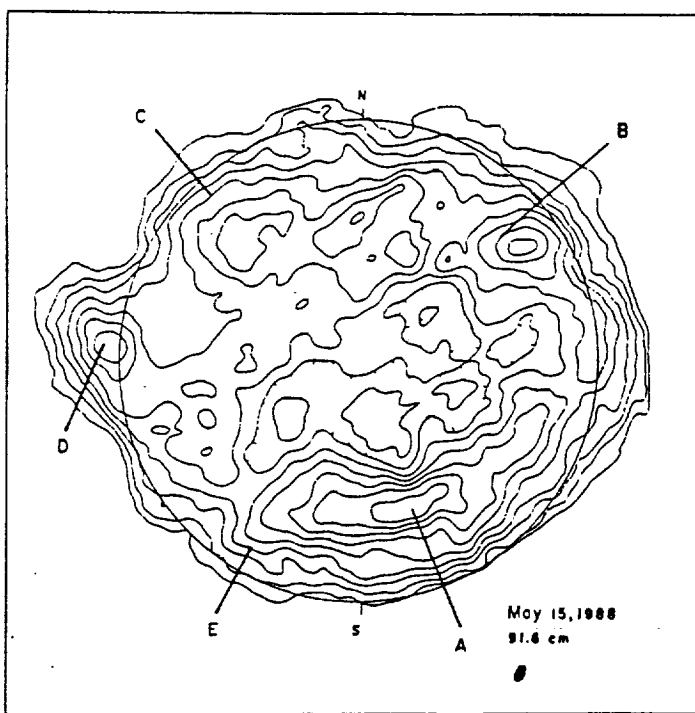


Figure 1.

Lang: Radio emission from quiescent filaments

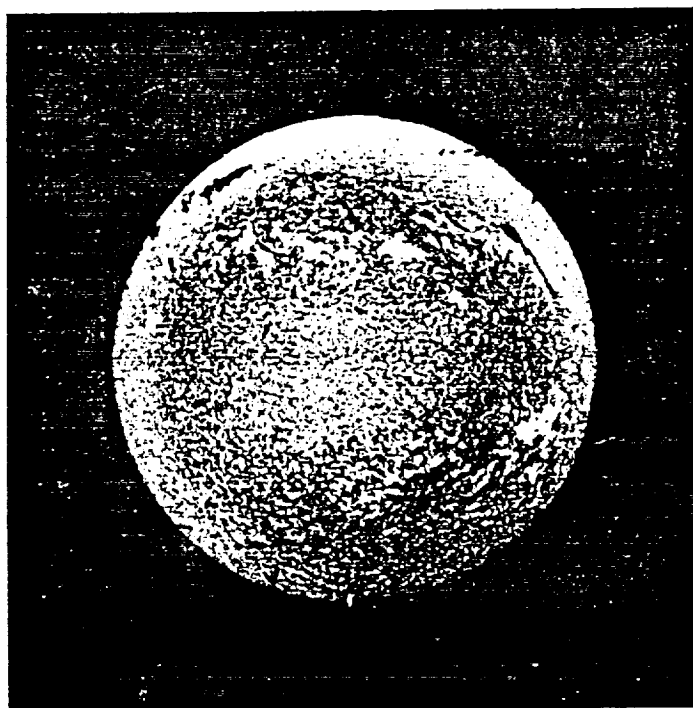


Figure 1.

Hvar Obs.Bull. 13 (1989) 93-111

107

**ORIGINAL PAGE IS
OF POOR QUALITY**

Lang: Radio emission from quiescent filaments

FIG. 1. A three-hour Very Large Array (VLA) synthesis map of the total intensity, I , from the visible solar disk at 91.6-cm (left) is compared with an $H\alpha$ photograph (right) taken at Boulder Solar Observatory - at 1415 UT on the same day (15 May 1988, courtesy of Pat McIntosh). The synthesized beamwidth is denoted by the small black spot in the lower right-hand corner; it has angular dimension of $80'' \times 55''$ at a position angle of -20° . The circle in the 91.6-cm map denotes the visible solar limb, and the tick marks denote solar north and south. Radio wavelength emission from dark, elongated filaments in the $H\alpha$ photo are designated by A and B in the 91.6-cm map. Filaments C and E did not correspond to enhanced 91.6-cm emission while source D probably coincides with a coronal streamer. The hatched regions in the central equatorial regions correspond to depressions in the 91.6-cm emission.

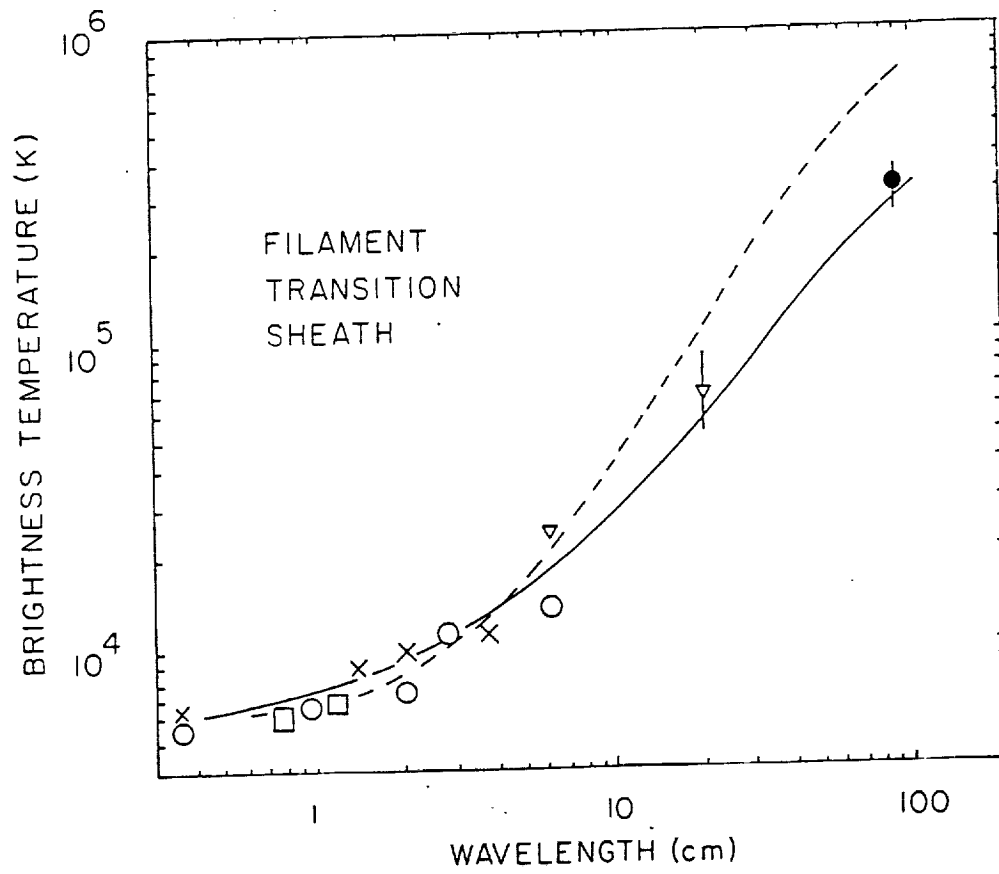


Figure 2.

Lang: Radio emission from quiescent filaments

FIG. 2. Calculated brightness temperatures for a constant pressure $P = 3 \times 10^{14} \text{ cm}^{-3} \text{ K}$ (dashed line) and a power law pressure $P = 2.5 \times 10^{17} \text{ T}^{-0.58}$ with $dT/dh = 0$ at height $h = 0$. The observed temperature at 91.6-cm (filled circle) is from this paper, whereas the other values (crosses, open circles, open squares and open triangles) are from Kundu, Melozzi and Shevgaonkar (1986) with their 6 and 20 cm measurements increased by a factor of 1.7 due to the detection of a software calibration error. The brightness temperatures refer to mean values over the radio source.

S.- FLARE STARS AT RADIO WAVELENGTHS

KENNETH R. LANG
Department of Physics and Astronomy
Tufts University
Medford, MA 02155
U.S.A.

ABSTRACT. The radio emission from dMe flare stars is discussed using Very Large Array and Arecibo observations as examples. Active flare stars emit weak, unpolarized, quiescent radio radiation that may be always present. Although thermal bremsstrahlung and/or thermal gyroresonance radiation account for the slowly-varying, quiescent radio radiation of solar active regions, these processes cannot account for the long-wavelength quiescent radiation observed from nearby dMe flare stars. It has been attributed to nonthermal gyrosynchrotron radiation, but some as yet unexplained mechanism must be continually producing the energetic electrons. Long-duration (hours), narrow-band ($\Delta\nu/\nu < 0.1$) radiation is also emitted from some nearby dMe stars at 20 cm wavelength. Such radiation may be attributed to coherent plasma radiation or to coherent electron-cyclotron masers. Impulsive stellar flares exhibit rapid variations (< 100 msec) that require radio sources that are smaller than the star in size, and high brightness temperatures $T_B > 10^{15}$ K that are also explained by coherent radiation processes. Quasi-periodic temporal fluctuations suggest pulsations during some radio flares. Evidence for frequency structure and positive or negative frequency drifts during radio flares from dMe stars is also presented.

1. INTRODUCTION

Pioneering single-dish observations in the 1970s showed that dwarf M flare stars occasionally emit radio bursts with extremely high flux densities and brightness temperatures of $T_B > 10^{12}$ to 10^{15} K if the radio source is comparable to the star in size (see Lang and Willson (1986b) and Kundu and Shevgaonkar (1988) for some historical details). Such powerful radio flares are extremely rare, sporadic and brief, however, leading many to suspect that they might be confused with terrestrial interference. Moreover, identification by correlation with optical flares could not be relied on, for different radiation mechanisms often dominate in the two spectral domains.

Interferometric observations with the Very Large Array (VLA) have unambiguously differentiated stellar radio emission from terrestrial interference, and the large collecting area of both the VLA and the Arecibo Observatory have enabled detection of the relatively weak radio flares that are presumably more frequent than the more powerful ones. One survey, for example, indicates that flaring emission can be detected for about 40% of flare stars nearer than 10 parsecs and visible with the VLA (White, Kundu and Jackson, 1990). Under the assumption that the radio source size is equal to the stellar radius, brightness temperatures of $T_B = 10^8$ to 10^{10} K and $T_B = 10^9$ to 10^{11} K have been inferred for the detected stars at 6 cm and 20 cm wavelength, respectively.

Although the observed radio luminosity from stellar flares is only about one thousandth the luminosity observed at X-ray or optical wavelengths, the radio emission is still thousands of times more powerful than solar radio flares, and it serves as an important diagnostic tool for studies of stellar coronae. Such studies have been carried out in detail for the most active dwarf M flare stars listed in Table 1. They are all nearby dMe stars that show evidence for chromospheric activity in the form of Ca II, Mg II and H α emission lines.

Table 1. Accurate 6 cm positions, spectral type, Sp, quiescent flux density, S_{Q6} , at 6 centimeters wavelength, peak flaring flux density, S_{F20} , at 20 centimeters wavelength, distance, D, in parsecs, and the logarithm of the quiescent X-ray luminosity, $\log L_x$, for radio-active flare stars.

Star	R.A.(1950.0) h m s	Dec.(1950.0) ° ' "	Sp	S_{Q6} (mJy)	S_{F20} (mJy)	D (pc)	$\log L_x$ (erg s ⁻¹)
L 726-8A**	01 36 33.314	- 18 12 23.20	dM5.5e	1.0	20	2.7	27.5
UV Ceti**	01 36 33.404	- 18 12 21.56	dM6e	3.2	100	2.7	27.5
YY Gem	07 31 25.691	+31 58 47.23	dM1e	0.4	1	14.5	29.5
YZ CMi	07 42 02.962	+03 40 30.39	dM4.5e	0.5	20	6.0	28.5
AD Leo	10 16 52.604	+20 07 17.59	dM3.5e	1.1	100	4.9	29.0
Wolf 630A,B	16 52 46.455	- 08 15 13.715	dM4.5e	0.9	3	6.2	
AT Mic†	20 38 44.4	- 32 36 49.5	dM4.5e	3.6	6	8.8	29.3
AU Mic	20 42 04.558	- 31 31 17.50	dM0e	0.8	26	8.8	29.8
EQ Peg A††	23 29 20.910	+19 39 41.11	dM5e	0.3	25	6.4	

*Adapted from Kundu et al. (1987), and Jackson, Kundu and White (1989) for the 6 cm data, with positions accurate to 0".1 or better.

**The separation and position angle of L 726-8A and L 726-8B (UV Ceti) is $2''.080 \pm 0''.080$ at $38^\circ.0 \pm 1^\circ.9$.

†Southern component of a fully resolved binary whose components are both active radio emitters; the northern component lies about 3".6 away at a position angle of about 15°.

††Quiescent emission from both component of EQ Peg A, B has been previously detected with respective 6 cm fluxes of 0.7 and 0.4 mJy and an angular separation of about 3".0 (see Gary (1985)).

This review will focus on these radio-active dMe stars. They include the very few cases in which we can detect the relatively weak (a few mJy), quiescent radio flux of the star (see Section 2). Long-duration, narrow-band radio flares (Section 3) have also been observed from several of these stars; they are unlike anything observed on the Sun.

Powerful (up to 200 mJy), impulsive (a few minutes) radio flares are also emitted by these stars. Such flares exhibit rapid variations (Section 4.1), quasi-periodic fluctuations (Section 4.2), both narrow-band and broad-band features (Section 5) and positive and negative frequency drifts (Section 5).

Figures 1 and 2 illustrate such flares for the dMe star EQ Pegasi. They are often up to 100% circularly polarized. Successive oppositely polarized flares have been detected for EQ Pegasi (Fig. 2) and AD Leonis (Willson, Lang and Foster (1988)), suggesting the presence of both magnetic polarities; but YZ Canis Minoris always exhibits left-handed circular polarization that remains the same over a wide range of wavelength (6 cm to 90 cm), suggesting a global, dipolar magnetic field that is viewed pole-on (Kundu and Shevgaonkar (1988)).

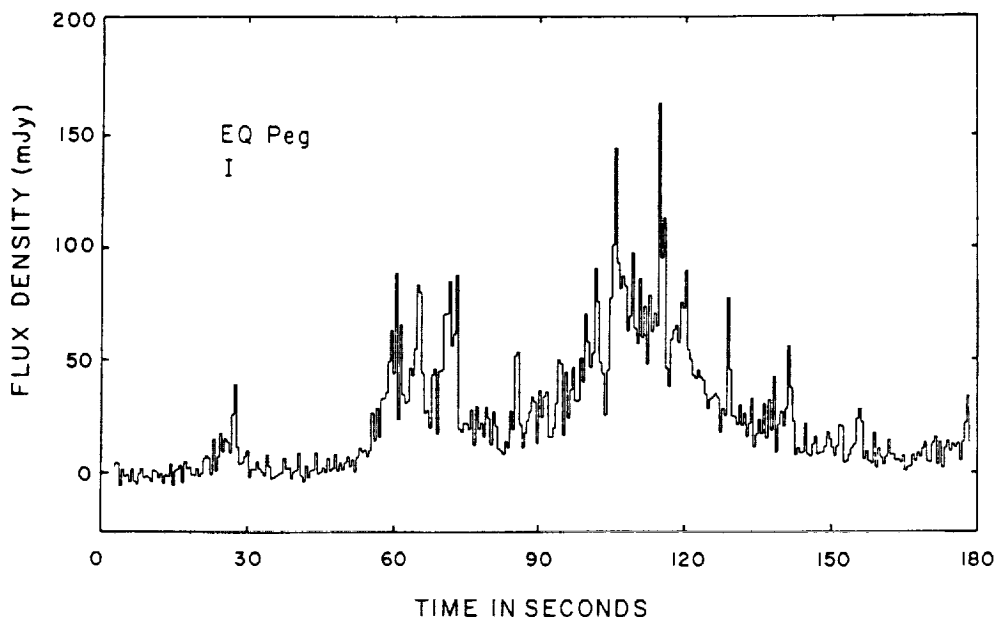


Figure 1. A previously unpublished VLA observation of the total intensity, I, at 1420 MHz (21 cm) from the dwarf M star EQ Pegasi. The flaring emission has a total duration of minutes, with components on shorter time scales of seconds or less. The radiation is up to 100 percent circularly polarized (see Fig. 2).

2. QUIESCENT RADIO EMISSION FROM dMe FLARE STARS

Unpolarized radio radiation that is nearly always present, and shows only slow variations with time, has been termed quiescent radio emission to distinguish it from the highly variable, brief radio flares that are often highly circularly polarized. The quiescent emission has flux densities of a few mJy at 6 cm wavelength (see Table 1 and Gary (1985)). It was at first attributed to thermal radiation from the same electron population that gives rise to the stellar X-ray emission (also see Table 1). If this were the case, it would be consistent with the Sun's slowly varying radiation at centimeter wavelengths; the solar radiation is due to either thermal bremsstrahlung or the thermal gyroresonance radiation of hot (10^6 K) electrons trapped within coronal loops that radiate strongly at X-ray wavelengths.

Nevertheless, thermal emission from the stellar coronae observed in X-rays cannot easily account for the quiescent radiation. Thermal bremsstrahlung of the X-ray plasma is so optically thin at 6 cm wavelength that its flux density is one or two orders of magnitude below the detection limit of the VLA - even when the X-ray plasma covers the entire surface of the nearest flare star.

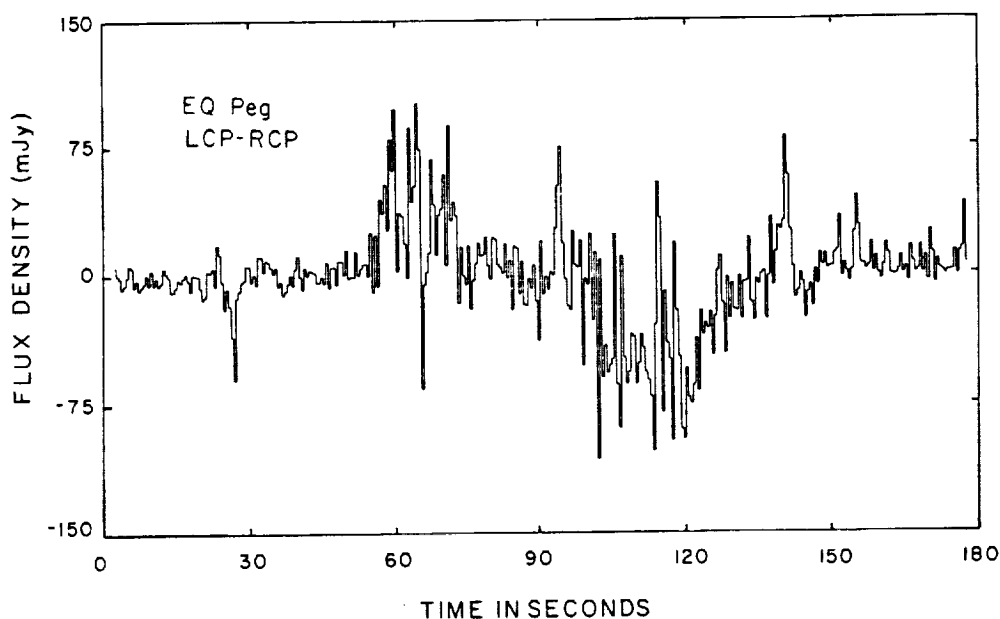


Figure 2. The difference between the left-hand circularly polarized (LCP) and right-hand-circularly polarized (RCP) radiation from the dwarf M star EQ Pegasi at 1420 MHz (21 cm). Up to 100 percent circularly polarized radiation is emitted with opposite senses, or directions, for successive bursts (courtesy of Robert F. Willson).

The optical depth can be enhanced for the gyroresonance of thermal electrons in relatively strong magnetic fields. Short-wavelength (< 6 cm) quiescent emission might then be explained by optically thick gyroresonant radiation of the high-temperature tail of the X-ray emitting plasma (Gudel and Benz, 1989). In this case, the radio data require electrons that are at a higher temperature than the average X-ray emitting electrons, and they are probably emitted from a source that is much larger than the star. The maximum observed flux density, S , is given by the Rayleigh-Jeans law, and the radius of the emitting source is therefore given by:

$$R^2 = 10^{13} \frac{SD^2}{\nu^2 T} \text{ cm}^2,$$

where S is the source flux density in Jy, D is the distance in cm, T is the temperature in K, and the observing frequency is $\nu = 2.8 \times 10^6 nH$ Hz for the n th harmonic in a magnetic field of strength H . Radii comparable to those of the dwarf M stars are only obtained for low flux densities, $S = 1$ mJy, short wavelengths, $\lambda < 6$ cm, high temperatures $T > 10^7$ K, and nearby dMe flare stars, $D < 10$ pc.

Thermal gyroresonance radiation cannot explain the long-wavelength, $\lambda > 20$ cm, quiescent radiation where higher flux densities of $S = 2$ to 20 mJy have been observed (Lang and Willson, 1986 a, Bastian and Brokbinder, 1987, Gudel and Benz, 1989). The radio source would have to be tens to hundreds of times larger than the star with implausibly intense magnetic fields at these remote locations. This long-wavelength radio emission has been attributed to nonthermal gyrosynchrotron radiation.

The gyrosynchrotron hypothesis requires a hotter corona with smaller sizes and lower densities than the gyroresonance model, but there must be a currently - unexplained, steady source of energetic electrons. Both models have been discussed by Kundu et al. (1987); because the gravitational scale height is comparable to the height of the stellar coronae, magnetic structures are required to confine the radio-emitting plasma. The coronae of nearby dMe flare stars therefore bear a closer resemblance to the Earth's magnetosphere than to the Sun's corona. We do not know if the relevant magnetic structures on the flare stars are due to several small active regions or to a global dipolar field, and we do not know how the radio-emitting electrons interact with the X-ray emitting plasma. The long-wavelength quiescent radiation might alternatively be due to continued, low-level, narrow-band, coherent radiation that resembles radio flares from these stars.

3. LONG-DURATION, NARROW-BAND EMISSION

Relatively intense ($S = 100$ mJy), narrow-band ($\Delta\nu/\nu < 0.1$) radiation lasting for several hours has been observed at 20 cm wavelength in several flare stars (Lang and Willson, 1986; White, Kundu and Jackson, 1986; Kundu et al., 1987; Lang and Willson, 1988). These

long-duration events are slowly variable, so they might be more energetic version of the process that accounts for the quiescent radiation. However, the long-duration, narrow-band radiation is highly circularly polarized, so its polarization bears a closer resemblance to the stellar flares than to the unpolarized quiescent radiation.

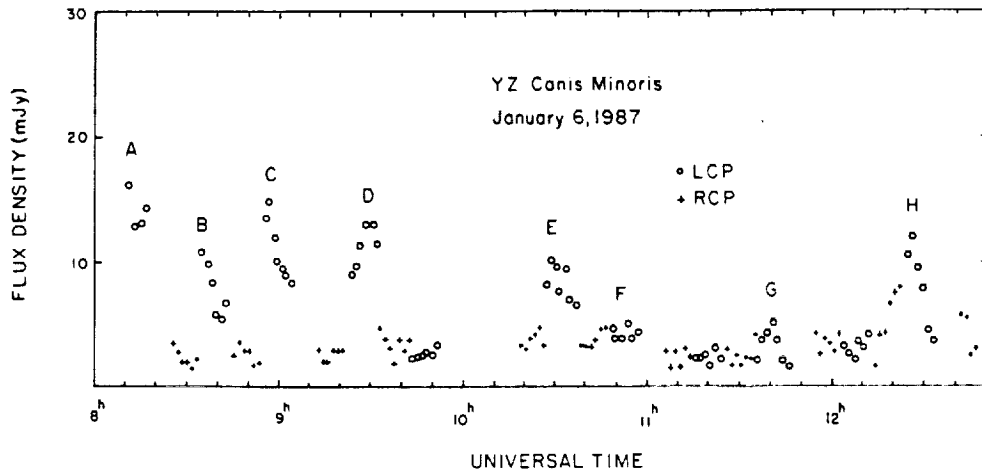


Figure 3. A five-hour VLA observation of the total intensity of the radiation from the dwarf M star YZ Canis Minoris in a 50 MHz bandwidth centered at 1464.9 MHz. The radiation is 100 percent left-hand circularly polarized. Its narrow-band frequency structure is illustrated in Fig. 4. (adapted from Lang and Willson (1986a)).

The long-duration, narrow-band highly polarized radiation (see Figures 3 and 4) is unlike any flares observed on the Sun, and cannot be easily explained using the solar analogy. The energy release mechanism lasts at least an order of magnitude longer than solar flares, and is difficult to understand if magnetic reconnection is the source of energy for the stellar flares (White, Kundu and Jackson, 1986). The narrow-band structure cannot be attributed to continuum emission processes such as thermal bremsstrahlung, thermal gyroresonant radiation, or nonthermal gyrosynchrotron radiation; it may be due to coherent mechanisms like electron-cyclotron masers or coherent plasma radiation. Both mechanisms require a magnetic field to produce the high circular polarization - either at the site of radiation production or during subsequent propagation of initially unpolarized radiation.

The coherent radiation processes provide constraints on the physical conditions in the coronae of flare stars (Lang, 1986). An upper limit to the electron density in the source is given by the requirement that the observing frequency must be greater than the

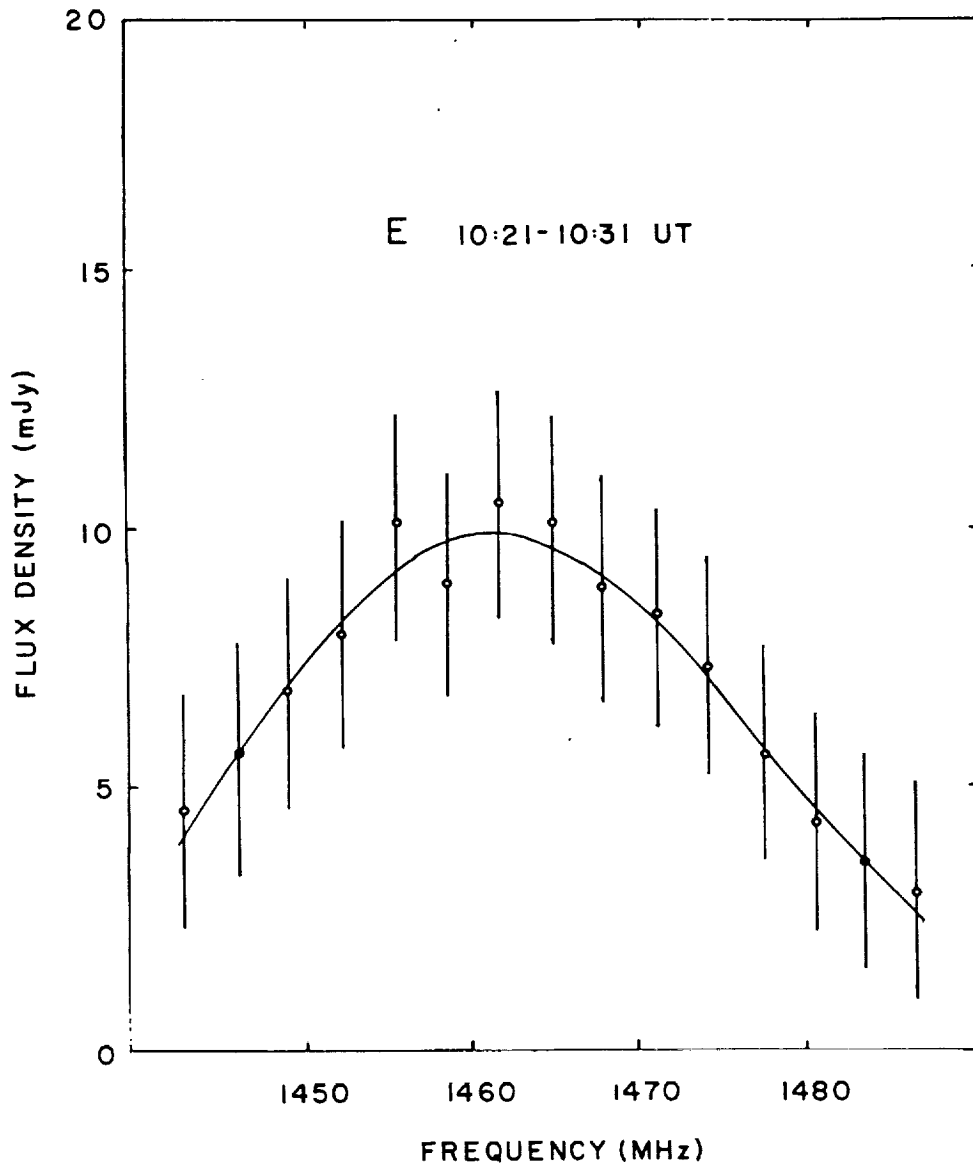


Figure 4. Frequency spectrum of the left circularly polarized radiation from YZ Canis Minoris for the interval marked E in Figure 1. Here the total intensity is plotted for 15 contiguous channels, each 3.125 MHz wide, for the 10-second interval. These data, as well as those for other intervals lettered in Fig. 3, show evidence for narrow-band radiation with a bandwidth $\Delta\nu < 30$ MHz, or $\Delta\nu/\nu = 0.02$. (Adapted from Lang and Willson (1986a)).

plasma frequency for the radiation to propagate out and reach the observer; at 20-cm wavelength this requires $N_e < 2.5 \times 10^{10} \text{ cm}^{-3}$. If an electron-cyclotron maser emits at the second or third harmonic of the gyrofrequency, then a coronal magnetic field strength of $H = 250 \text{ G}$ or 167 G is required to explain the 20 cm radiation. Coherent plasma radiation at the second harmonic of the plasma frequency requires an electron density of $N_e = 6 \times 10^9 \text{ cm}^{-3}$. If coherent plasma radiation dominates, then the plasma frequency must be larger than the electron gyrofrequency, thereby providing an upper limit to the magnetic field strength $H < 250 \text{ G}$.

4. TEMPORAL STRUCTURE OF RADIO FLARES

4.1 Rapid Variations

Radio flares from the dMe star AD Leonis near 20 cm wavelength consist of rapid (< 100 milliseconds), highly-polarized (up to 100% left-hand circularly polarized) spikes whose rise times provide stringent limits to the size and brightness temperature of the radio source. Such rapid variations were first observed by Lang et al. (1983) using the Arecibo Observatory (see Figure 5). They have been confirmed by Bastian et al. (1990) using the same radio telescope, and by Gudel, et al. (1989) whose simultaneous observations with the radio telescopes in Effelsberg, Jodrell Bank and Arecibo substantiated the common origin of the radiation and eliminated any remaining doubts about its stellar origin (the time coincidence of flares observed at the three sites was within 0.4 seconds).

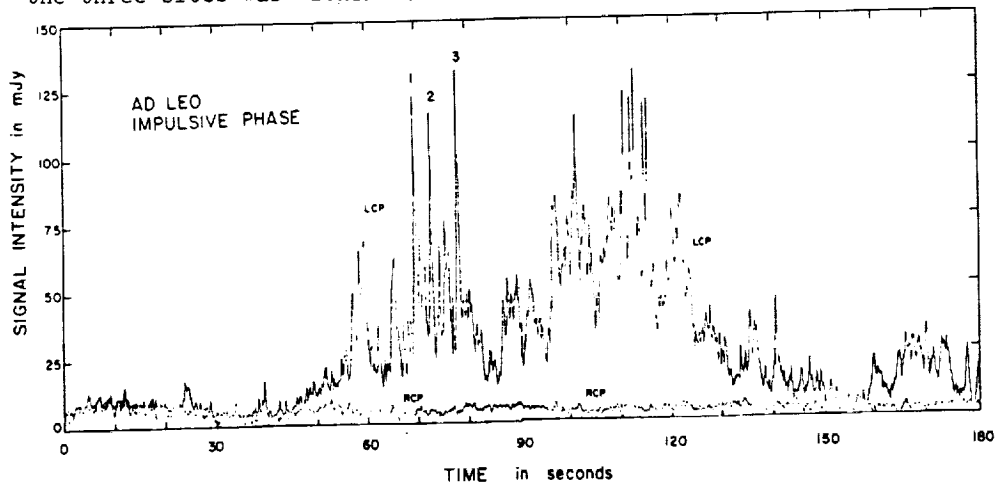


Figure 5. These observations, taken at 1400 MHz (21 cm) with the Arecibo Observatory, indicate that highly left-circularly polarized (LCP) radiation from the dwarf M star AD Leonis consists of rapid spikes whose duration $\tau < 100$ milliseconds. The emitting source must be much smaller than the star in size. (Adapted from Lang et al. (1983)).

The spikes labeled 1,2 and 3 in Figure 5 have rise times $\tau < 200$ milliseconds, and upper limits of $\tau < 20$ milliseconds have been observed. An upper limit to the linear size, L , of the emitting region is provided by the distance that light travels in time, τ , or $L < c \times \tau$. A light-travel time of 20 milliseconds indicates $L < 6,000$ km, which is less than 1% of the stellar diameter. If the burst emitter is symmetric, it has an area less than 0.0003 of the stellar surface area, and the brightness temperature, T_B , is $T_B > 10^{15}$ K.

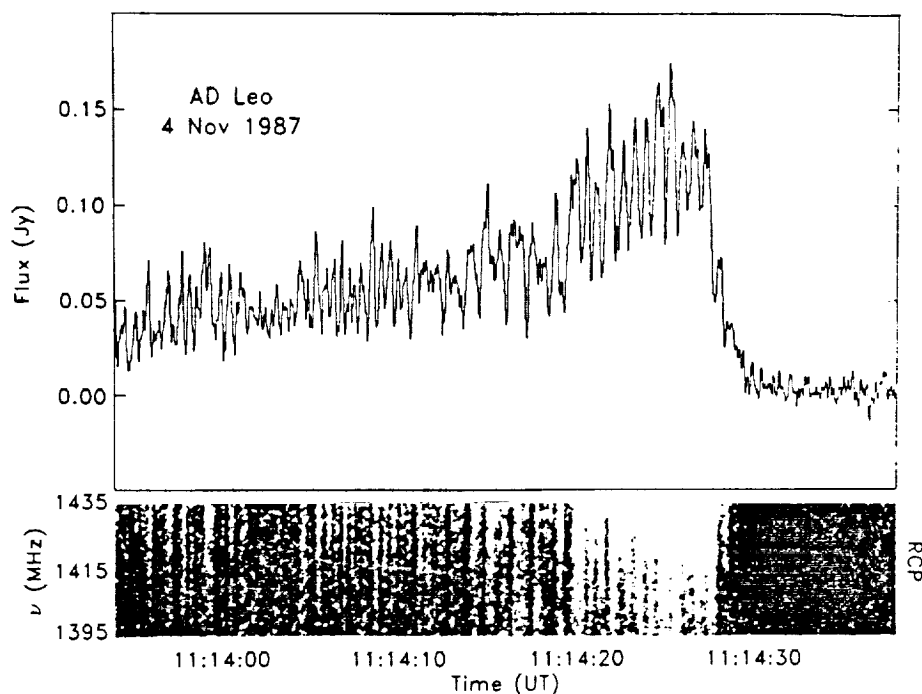


Figure 6. Observations of AD Leonis at 1415 MHz (21 cm) with the Arecibo Observatory indicate quasi-periodic pulsations with an amplitude modulation of ≈ 50 percent and a period of ≈ 0.7 seconds (top). The dynamic spectrum (bottom) indicates that the pulsations are broad-band with bandwidths $\Delta\nu > 40$ MHz. (Adapted from Bastian et al. (1990)).

4.2. Quasi-Periodic Fluctuations

Radio flare emission from AD Leonis has also been resolved into a multitude of broad-band, quasi-periodic fluctuations called pulsations. Such pulsations have been reported by Lang and Willson (1986), Gudel et al. (1989) and Bastian et al. (1990); and example is shown in Figure 6. The typical interval between pulses is about 1 second, which

is comparable to that of solar decimetric pulsations. The AD Leo pulsations are up to 100% circularly polarized; they are coherent across the observing bandwidths of up to 100 MHz. They might be attributed to oscillations in a coronal loop with dimensions of about 5,000 km, which is close to the upper size limit inferred from the light-travel time.

5. FREQUENCY STRUCTURE OF RADIO FLARES

Observations of the radio radiation intensity as a function of both time and frequency (dynamic spectra) can independently confirm the small size of the radio emitter and provide insights to the relevant plasma processes. Dynamic spectra of UV Ceti near 20 cm wavelength (Bastian and Bookbinder, 1987) indicated, for example, both broadband (> 40 MHz) and narrow-band ($\Delta\nu/\nu < 0.002$) features. The narrow-band emission is most likely due to a coherent radiation mechanism. A spectral component with a width, $\Delta\nu$, of 0.2 percent of the central frequency, ν , puts an upper limit on the source diameter of 200 km, assuming a scale height of one stellar radius, the largest reasonable. If an electron-cyclotron maser is responsible, the magnetic field strength $H \approx 250$ G and the electron density $N_e < 10^9$ cm $^{-3}$.

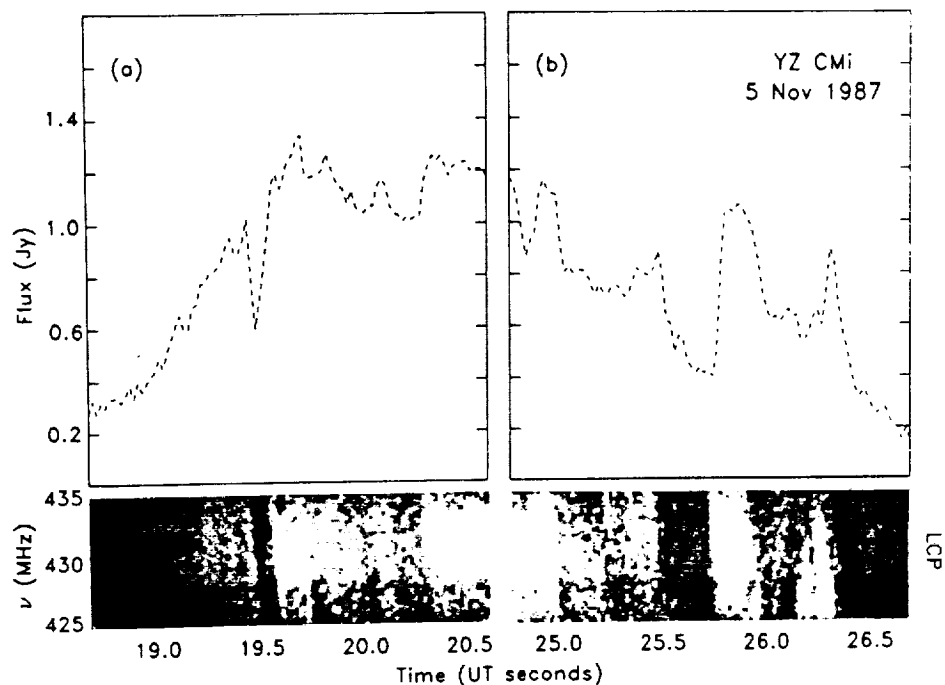


Figure 7. These Arecibo observations of the dynamic spectra (lower panel) of the 430 MHz (70 cm) radiation from the dwarf M star YZ Canis Minoris indicate a sudden reduction feature, in (a), with a drift in frequency of 250 MHz/s from high to low frequencies, as well as other narrowband and drifting features in (b). (Adapted from Bastian et al. (1990)).

Dynamic spectra of the radio radiation from the dMe flare stars AD Leo, YZ Cmi and UV Ceti show considerable complexity, with both narrow-band and broad-band features, and both positive and negative frequency drifts (Bastian and Bookbinder, 1987; Jackson, Kundu, and White, 1987; Bastian et al., 1990). The example shown in Figure 7 has a negative drift of 250 MHz per second from high to low frequencies. Such a negative drift is commonly observed in the Sun (eg. type II and type III bursts) suggesting electron beams or shock waves that propagate outwards in the stellar corona. But positive frequency drifts have also been observed for flare stars, suggesting a disturbance that propagates downward in the stellar corona and progressively excites plasma radiation at higher frequencies (larger electron densities).

Thus, there is clear evidence for apparent frequency drifts and narrow-band features in radio flares from dMe stars, but their interpretation is currently open to question. They could be due to the propagation of an exciter, group delays or some other cause.

6. DISCUSSION

To sum up, the quiescent radio radiation from dMe stars might be due to exceptionally hot thermal electrons, nonthermal electrons, or near continual coherent flaring. The high brightness temperatures, strong circular polarization and narrow frequency extent of long-duration radio events require a coherent plasma process, as does the more impulsive stellar radio flares. The cyclotron maser could explain many aspects of the flaring emission (Dulk, 1985), but several other coherent radiation processes might be involved (Kuijpers, 1989; Mullan, 1989). When the correct radiation mechanisms are identified, perhaps as the result of future observations with broader bandwidths, we can accurately specify the physical parameters in the stellar coronae.

Different processes probably dominate at different wavelengths, as they do on the Sun, and both solar and stellar flares must be related to magnetic fields. Past theoretical studies of solar radio radiation can therefore provide a useful background for exploring plausible radiation mechanisms. However, the direct analogy of the Sun as a radio flare star is probably a mistake; the Sun is the wrong spectral type, and its radio flares are so weak that they would be undetectable at the distance of the nearest star. In addition, solar flares have near-simultaneous signatures at optical, radio and X-ray wavelengths, while flaring radio emission from the dMe stars is often undetectable in other regions of the electromagnetic spectrum (see for instance Kundu et al. (1989)). The available evidence therefore indicates that radio flares from dwarf M flare stars are physically very different from those occurring on the Sun.

7. ACKNOWLEDGMENTS

Radio astronomical studies of the Sun and other nearby active stars at Tufts University are supported under grant AFOSR-89-0147 with the Air Force Office of Scientific Research. Related solar observations are supported by NASA grant NAG 5-501. The Arecibo Observatory is part of the National Astronomy and Ionosphere Center, which is operated by Cornell University under contract with the National Science Foundation (N.S.F.). The Very Large Array is operated by Associated Universities, Inc., under contract with the N.S.F.

8. REFERENCES

- Bastian, T.S. and Bookbinder, J.A. (1987) 'First dynamic spectra of stellar microwave flares', *Nature*, 326, 678-680.
- Bastian, T.S., Bookbinder, J., Dulk, G.A. and Davis, M. (1990) 'Dynamic spectra of radio bursts from flare stars', *Astrophysical Journal*, April 10, 1990 issue.
- Dulk, G.A. (1985), 'Radio emission from the sun and stars', *Annual Review of Astronomy and Astrophysics* 23, 169-224.
- Gary, D.E. (1985) 'Quiescent stellar radio emission', in R.M. Hjellming and D.M. Gibson (eds.), *Radio Stars*, D. Reidel, Boston, pp. 185-196.
- Güdel, M. and Benz, A.O. (1989) 'Broad-band spectrum of dMe star radio emission', *Astronomy and Astrophysics Letters*, 211, L5-L8.
- Güdel, M., Benz, A.O., Bastian, T.S., Fürst, E., Simnett, G.M. and Davis, R.J. (1989) 'Broadband spectral observation of a dMe star radio flare', *Astronomy and Astrophysics Letters* 220, L5-L8.
- Jackson, P.D., Kundu, M.R. and White, S.M., (1987) 'Dynamic spectrum of a radio flare on UV Ceti', *Astrophysical Journal Letters* 316, L85-L90.
- Jackson, P.D., Kundu, M.R. and White, S.M. (1989) 'Quiescent and flaring radio emission from the flare stars AD Leonis, EQ Pegasi, UV Ceti, Wolf 630, YY Geminorum, and YZ Canis Minoris', *Astronomy and Astrophysics* 210, 284-294 .
- Kuijpers, J. (1989) 'Radio emission from stellar flares', *Solar Physics* 121, 163-185.
- Kundu, M.R., Jackson, P.D., White, S.M., and Melozzi, M. (1987) 'Microwave observations of the flare stars UV Ceti, AT Microscopii, and AU Microscopii', *Astrophysical Journal* 312, 822-829.
- Kundu, M.R., Pallavicini, R., White, S.M., and Jackson, P.D. (1985) 'Co-ordinated VLA and EXOSAT observations of the flare stars UV Ceti, EQ Pegasi, YZ Canis Minoris and AD Leonis', *Astronomy and Astrophysics* 195, 159-171.
- Kundu, M.R. and Shevgaonkar, R.K. (1988) 'Detection of the dMe flare star YZ Canis Minoris simultaneously at 20 and 90 centimeter wavelengths', *Astrophysical Journal* 334, 1001-1007.

- Lang, K.R. (1986) 'Radio wavelength observations of magnetic fields on active dwarf M, RS CVn and magnetic stars', *Advances in Space Research* 6, No. 8, 109-112.
- Lang, K.R., Bookbinder, J., Golub, L. and Davis, M.M. (1983) 'Bright, rapid, highly-polarized radio spikes from the M dwarf AD Leonis', *Astrophysical Journal (Letters)* 272, L15-L18.
- Lang, K.R. and Willson, R.F. (1986a) 'Narrow-band, slowly varying decimetric radiation from the dwarf M flare star YZ Canis Minoris', *Astrophysical Journal (Letters)* 302, L17-L21.
- Lang, K.R. and Willson, R.F. (1986b) 'Millisecond radio spikes from the dwarf M flare star AD Leonis', *Astrophysical Journal* 305, 363-368.
- Lang, K.R. and Willson, R.F. (1988) 'Narrow-band, slowly varying decimetric radiation from the dwarf M flare star YZ Canis Minoris II', *Astrophysical Journal* 326, 300-304.
- Mullan, D.J. (1989) 'Solar and stellar flares: questions and answers', *Solar Physics* 121, 239-259.
- White, S.M., Jackson, P.D., and Kundu, M.R. (1989) 'A VLA survey of nearby flare stars', *Astrophysical Journal Supplement*, December 15, 1989.
- White, S.M., Kundu, M.R., and Jackson, P.D. (1986) 'Narrow-band radio flares from red dwarf stars', *Astrophysical Journal* 311, 814 - 818.
- Willson, R.F., Lang, K.R., and Foster, P. (1988) 'VLA observations of dwarf M flare stars and magnetic stars', *Astronomy and Astrophysics* 199, 255-261.

RODONO: Can you spend a few words on the correlation between microwave and hard X-ray flares on the Sun and stars?

LANG: Although the solar analogy would predict a correlation between microwave and hard X-ray emission, such a correlation will not exist on many flare stars because their radio emission is not continuum synchrotron radiation. The radio emission of dwarf M flares is often narrow-band ($\Delta f/f < 0.02$), high brightness temperature ($T_B > 10^{15}$ K), and sometimes of long total duration (hours). However, simultaneous observations across the electromagnetic spectrum from X-ray to optical to radio should be encouraged to search for correlations and to increase the net observational time on these stars.

PALLAVICINI: I would like to comment on the question just raised by Dr. Rodono. On the Sun, there is a very good correlation between X-ray and radio microwave emission both during the impulsive phase and during the gradual phase of flares. This apparently is not the case for flare stars. We have carried out a detailed comparison of EXOSAT and VLA observations of 4 flare stars (cf. Kundu, Pallavicini, White and Jackson 1988, Astron. Ap. 195, 159), and we have found virtually no correlation between the two data sets. This shows that there are other processes going on on stars as Dr. Lang just pointed out.

BROMAGE: This is a comment. As Professor Rodono said, it is necessary for investigating the impulsive phase, to observe hard X-rays, greater than 20-30 keV. There has not been any possibility of observing such flares so far.

LANG: The GRO satellite will provide such an opportunity after it is launched next June. I would expect a possible correlation of hard X-rays with short centimeter radiation or millimeter radiation.

BENZ: The energy radiated in radio emission by a typical (dMe) radio burst is at most 10^{26} erg. If it is a coherent emission process such as cyclotron maser, the electron energy may be as low as 10^{28} erg. This is a small number compared to the observed energies in the optical and soft X-ray regimes. Thus the absence of correlation is less surprising.

LANG: I agree. The energy emitted during radio flares is less than that radiated at optical and soft X-ray wavelengths, and this difference may become less for coherent emission, but the difference in any event does support a lack of correlation, and different radiation mechanisms for the radio and other spectral regions.

T. VLA OBSERVATIONS OF THE CORONAL PLASMA

KENNETH R. LANG
Department of Physics and Astronomy
Tufts University
Medford, MA 02155
U.S.A.

ABSTRACT. VLA observations at 20-cm wavelength specify the brightness temperature and magnetic structure of plasma constrained within coronal loops in solar active regions. Comparisons with simultaneous SMM observations at soft X-ray wavelengths lead to measurements of physical parameters like electron density, electron temperature and magnetic field strength. Such comparisons also indicate coronal loops can be detected at either radio or X-ray wavelengths while remaining invisible in the other spectral domain, and that the dominant radiation mechanisms can be thermal bremsstrahlung or thermal gyroresonance radiation. VLA observations at the longer 90-cm wavelength reveal the thermal emission of a hot transition sheath enveloping a cooler, underlying H α filament seen in absorption. The 20-cm VLA observations indicate that the precursor, impulsive and post-flare components of solar flares originate in spatially separated and resolved sources.

I. INTRODUCTION.

This paper provides a brief overview of recent discoveries by the Tufts University group using the Very Large Array (VLA) to study the coronal plasma under the support of the AFOSR and NASA (Section 5). More detailed accounts can be found in the references given in this introduction and in Section 6. Ground-based VLA observations at 20-cm wavelength can detect the hot coronal plasma previously detected by space-borne X-ray telescopes; detailed comparisons of simultaneous data (SMM and VLA) indicate that physical parameters can be obtained (Section 2), but that some coronal loops are invisible in either spectral domain (Lang, Willson, Smith and Strong 1987a,b). At the longer 91.6-cm wavelength, the VLA detects more extensive emission interpreted as a hot 10^5 K interface between cool, dense H α filaments and the hotter enveloping rarefied corona (Section 3, Lang and Willson, 1989). The unparalleled spatial resolution of the VLA at 20-cm wavelength has shown that the precursor, impulsive and post-flare components of solar bursts originate in nearby, but separate, coronal loops or systems of loops (Section 4, Willson, Lang and Liggett, 1990).

501

E. R. Priest and V. Krishan (eds.), Basic Plasma Processes on the Sun, 501-507.
© 1990 IAU. Printed in the Netherlands.

2. QUIESCENT 20 CM AND X-RAY EMISSION FROM CORONAL LOOPS

The development of aperture synthesis telescopes like the Very Large Array (VLA) has permitted ground-based observations of coronal loops at 20-cm wavelength; the quiescent, or non-flaring, loop emission has brightness temperatures, T_B , comparable to the million-degree coronal electron temperature. A comparison with simultaneous soft X-ray images of comparable angular resolution and field of view (Fig. 1) indicates that X-ray coronal loops can be imaged at 20 cm.

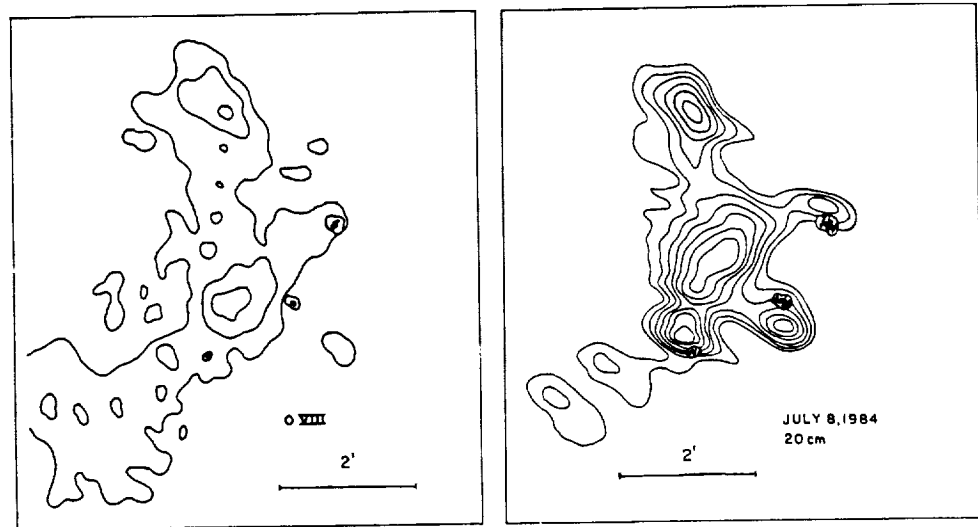


Figure 1. A comparison of soft X-ray (SMM FCS - left) and 20-cm (VLA-right) images of an active region. Here the sunspots are denoted by small black dots with a circle around them (cf. Lang et al. (1987a)). Soft X-ray spectral lines have been used to determine the electron temperature, T_e , and electron density, N_e , of the X-ray emitting plasma that spatially coincides with the 20-cm radiation; for the data shown in Fig. 1, average values of $T_e = 3.0 \pm 0.1 \times 10^6$ K and $N_e = 2.4 \pm 0.4 \times 10^9$ cm $^{-3}$ were obtained. The quiescent X-ray radiation is attributed to thermal bremsstrahlung. The 20-cm emission is optically thin with optical depths $\tau = T_e/T_B = 0.3$. The thermal bremsstrahlung of the X-ray emitting plasma ought to be optically thin at 20 cm, but its thermal gyroresonance radiation should be optically thick at this wavelength. Thermal gyroresonance radiation must account for the intense 20-cm radiation near and above sunspots where no X-ray radiation is detected (also see Fig. 1).

3. QUIESCENT 90 CM EMISSION FROM FILAMENTS

Although 20-cm VLA observations of the quiet Sun reveal the ubiquitous coronal loops anchored within solar active regions, the VLA results at the longer 91.6-cm wavelength reveal quiescent emission from more extensive structures (angular sizes $\theta = 3'$) that are not associated with active regions (Fig. 2 right and left). The 91.6-cm features are similar in shape, position, elongation and orientation to dark H α filaments; but the radio structures are wider and longer, and they are detected in emission rather than absorption. This 91.6-cm emission has been interpreted as the thermal bremsstrahlung of a hot (10^5 K), transition sheath that envelopes the cooler H α filaments and acts as an interface with the hotter surrounding corona. This transition sheath has been previously detected in absorption with lower brightness temperatures at shorter wavelengths of 6 and 20 cm (Rao and Kundu, 1980; Kundu, Melozzi, and Shevgaonkar, 1986).

Variable physical parameters of the transition sheath can explain controversial reports of the detection of, or the failure to detect, the meter-wavelength counterpart of H α filaments. If the sheath were substantially thinner, then the optical depth would not be large enough for detection of its 91.6-cm bremsstrahlung; and if the electron density of the sheath was much higher than $N_e = 10^9 \text{ cm}^{-3}$, then its plasma frequency would exceed our observing frequency and the sheath radiation could not propagate out to be observed.

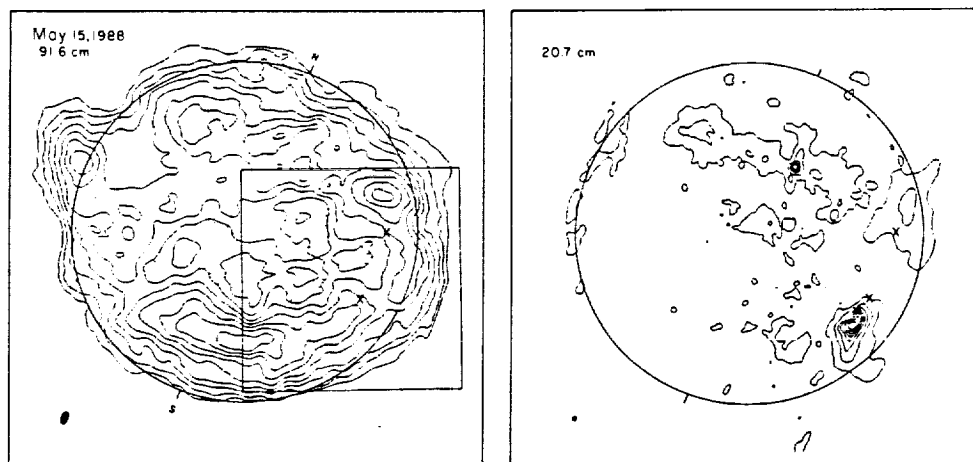


Figure 2. The quiescent 91.6 cm (left) and 20.7 cm (right) emission from the Sun. The 20.7-cm contours delineate active-region coronal loops with a peak brightness temperature of $T_B = 2.5 \times 10^6 \text{ K}$, while the 91.6-cm contours show more elongated structures that are not associated with active regions and have a peak $T_B = 7.8 \times 10^5 \text{ K}$. (Adapted from Lang and Willson (1989)).

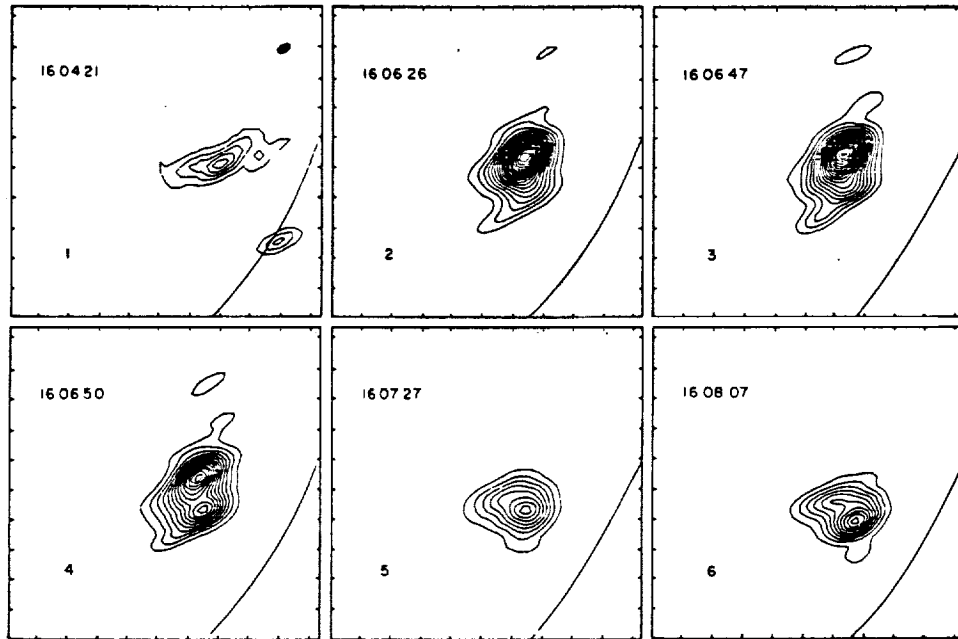


Figure 4. VLA snapshot maps of the total intensity, I , at 20.7-cm wavelength during 3.3-second intervals at the times denoted by 1 to 6 in Fig. 3. The precursor (1) is spatially separated from the subsequent impulsive bursts (2 and 3). The post-burst, or decay, phase (5, 6) originates in another spatially separate source that first becomes detectable during the end (4) of the second impulsive burst (3). The angular scale can be inferred from the 60" spacing between the fiducial marks on the axes. The contour intervals are in units of equal brightness temperature, T_B , with an outermost contour and contour interval of $T_B = 4.4 \times 10^5$ K for 1, and $T_B = 5.5 \times 10^6$ K for the others five images. The maximum value is $T_{B\max} = 4.4 \times 10^6$, 1.0×10^8 , 1.3×10^8 , 7.7×10^7 , 4.4×10^7 and 5.5×10^7 K for 1, 2, 3, 4, 5 and 6 respectively. (Adapted from Willson, Lang and Liggett (1990)).

These results suggest that solar flares are triggered by interacting coronal loops; emerging coronal loops may interact with adjacent ones, leading to the explosive release of magnetic energy stored within them. Evidence for the magnetic triggering of solar flares by interacting and reconnecting coronal loops has been provided by previous VLA observations at 20 cm and 6 cm wavelength (Kundu et al., 1982; Kundu and Lang, 1985). The system of coronal loops then relaxes to a spatially-different configuration during the decay phase.

5. ACKNOWLEDGMENTS.

Radio astronomical studies of the Sun at Tufts University are supported under grant AFOSR-89-0147 with the Air Force Office of Scientific Research. Related solar observations are supported by NASA grant NAG 5-501. The Very Large Array is operated by Associated Universities, Inc., under contract with the N.S.F.

6. REFERENCES.

- Kundu, M.R., Melozzi, M., and Shevgaonkar, R.K. (1986) 'A study of solar filaments from high resolution microwave observations', *Astronomy and Astrophysics* 167, 166-172.
- Kundu, M.R. and Lang, K.R. (1985) 'The Sun and nearby stars - microwave observations at high resolution', *Science* 228, 9-15.
- Kundu, M.R., Schmahl, E.J., Velusamy, T. and Vlahos, L. (1982). 'Radio imaging of solar flares using the Very Large Array - new insight in flare processes', *Astronomy and Astrophysics* 108, 188-194.
- Lang, K.R. and Willson, R.F. (1989) 'Radio emission from quiescent solar filaments at 91.6 centimeter wavelength', *Astrophysical Journal (Letters)* 344, L73-L75.
- Lang, K.R., Willson, R.F., Smith, K.L. and Strong, K.T. (1987a) 'Simultaneous SMM flat crystal spectrometer and Very Large Array observations of solar active regions', *Astrophysical Journal* 322, 1035-1043.
- Lang, K.R., Willson, R.F., Smith, K.L., and Strong, K.T. (1987b) 'Solar active region physical parameters inferred from a thermal cyclotron line and soft X-ray spectral lines', *Astrophysical Journal* 322, 1044-1051.
- Rao, A.P. and Kundu, M.R. (1980) 'Synthesized map of a solar filament at 6 cm with $\approx 15''$ resolution', *Astronomy and Astrophysics* 86, 373-376.
- Willson, R.F., Lang, K.R., and Liggett, M. (1990) 'Impulsive microwave burst and solar noise storm emission resolved with the VLA', *Astrophysical Journal*, February 20, 1990.

DISCUSSION

CHIUDERI DRAGO: The filament brightness temperatures given by Kundu *et al.* are not the observed ones, but they have been corrected for the coronal contribution. The coronal parameters used by Kundu *et al.* correspond to a coronal pressure $p \approx 0.2$ dyne/cm², one order of magnitude larger than the pressure at the top of the transition region, in their "variable pressure model" - this inconsistency does not affect very much the data at short ($\lambda < 21$ cm) wavelengths, but it would affect very much the T_b at 90 cm. If the parameters you used for the coronal contribution subtraction are the same as those used by Kundu *et al.*, the agreement with the "variable pressure model" gives an inconsistency. If you take, for the computation of the coronal contribution, parameters in agreement with the variable pressure model, then you cannot compare your data with the Kundu *et al.* ones.

VAN BALLEGOIJEN: Have you ever observed polarization in filament radio emission?

LANG: Our observations of filament emission at 90 cm wavelength were unpolarized, probably because the thermal radiation of the 10^5 K plasma was optically thick. However, these were the first such observations. So, when the Sun becomes less active, we hope to observe some emission that is optically thin and circularly polarized. This will let us determine the shape and strength of the filament magnetic field for the first time. We also hope to carry out strict tests of the theory by observing the same filament at several wavelengths, say 2, 6, 20 and 90 cm, and for varying angles between the line of sight and the magnetic field.

GELFREIKH: How do the size and shape of the radio (90 cm) filaments compare with optical ($H\alpha$) filaments?

LANG: The 90 cm filaments have the same size, shape, position and elongation as the underlying $H\alpha$ filaments, but the radio emission is wider and longer. The transition sheath is thought to be about 100 km thick. We should be able to measure this thickness in future.

U. VLA-PHOENIX OBSERVATIONS OF A NARROW-BAND DECIMETRIC BURST

Robert F. Willson
Dept. Of Physics and Astronomy
Tufts University
Medford, MA 02155
USA

Arnold. O. Benz
Institute of Astronomy
ETH, CH-8092
Zurich
Switzerland

ABSTRACT We discuss observations of a highly-circularly polarized multiply-impulsive microwave burst detected by the Very Large Array and the Phoenix Digital Radio Spectrometer. The VLA was used to resolve the burst in two dimensions, while PHOENIX provided high time resolution information about its spectral properties. During part of the burst, positive frequency drifts were detected, suggesting inwardly propagating beams of electrons emitting Type III-like radiation.

1. INTRODUCTION

It is generally believed that gyrosynchrotron radiation from nonthermal electrons can explain the properties of most solar microwave bursts, including their brightness temperature, polarization and bandwidth. Recent observation using wide-band dynamic spectrographs have, however, discovered multiply-impulsive ($\tau < 100$ msec) bursts including spikes, pulsations and decimetric type III bursts whose narrow bandwidths and frequency drifts require a different explanation such as plasma radiation or electron-cyclotron maser emission (eg. Stähli and Benz 1987). Practically nothing is known about the spatial properties of these events since they have only been detected with single dish instruments with poor angular resolution. Here we discuss some spatially resolved observations of a narrow band decimetric burst using the VLA and the Phoenix Digital Radiospectrometer.

2. COORDINATED OBSERVATIONS OF MICROWAVE BURSTS

The Very Large Array was used to observe the Sun between 1300-2300 UT on June 25 and 27, 1989 as part of the Max 91 Campaign. Observations were made simultaneously at 1446 MHz (20.7 cm) and 327 MHz (91.6 cm) with a time resolution of 1.67 s. They were coordinated with observations at the Nancay Radioheliograph (164 and 327 MHz) and with the PHOENIX Digital Radio Spectrometer (ten frequencies each between 301 and 356 MHz and 1265 and 1525 MHz- 20 msec time resolution) in order to study the spatial, temporal and spectral properties of decimetric bursts.

Figure 1a shows an example of a burst detected by the VLA and PHOENIX at 1446 MHz. It consists of several impulsive spikes, each of 20-30 seconds in duration, covering a period of a few minutes. There was no

evidence for burst emission at 327 MHz, nor was there a soft or hard X-ray burst detected by the SMM or GOES satellites. Snapshot maps (Fig. 1b) show that the bursts are compact ($\theta = 25\text{--}30''$) and highly circularly polarized ($\rho = 90\text{--}100\%$). Co-registration of these maps with a SOON H α image taken at 1617 UT showed that the burst was located above a faint optical flare lying between two active regions (\sim N25, E21)

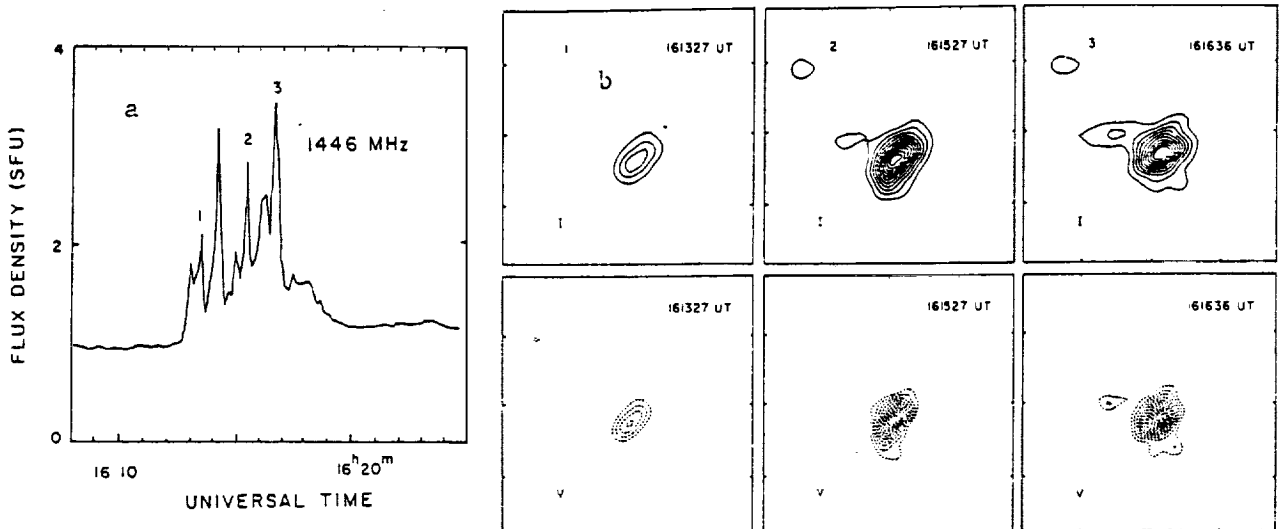


Figure 1. a) Time profile of the burst detected with one of the short VLA baselines on 1989 June 25. b) VLA 3.3 s snapshot maps at times 1, 2 and 3 shown in Fig. 1a. The brightness temperature contours for the I and V maps are drawn at intervals of $T_b = 8 \times 10^5$ and 4×10^5 K, respectively. Fiducial marks on the axes are drawn every $60''$.

The PHOENIX spectral data showed that the emission drifted from high to low frequencies near the time of the most intense peak (3) ($\sim +750$ MHz/sec) suggesting an inwardly-propagating beam of electrons. Broad-band emission was detected at most other times. Although the positions of the bursts shifted from peak to peak ($\Delta\theta \sim 10''$), these changes were not systematic, as would be expected for a source moving through the corona. Nevertheless, this event may be related to the decimetric type III events (Stähli and Benz 1987) whose narrow bandwidths and frequency drifts suggest a coherent emission mechanism, such as plasma radiation or electron-cyclotron maser emission.

3. ACKNOWLEDGEMENTS

Radio astronomical studies of the Sun at Tufts University are supported under grant AFOSR-89-0147 with the Air Force Office of Scientific Research, and by NASA grant NAG-5-501.

4. REFERENCE

- Stähli, M., and Benz, A.O. (1987) 'Microwave Emission of Solar Electron Beams', *Astronomy and Astrophysics* 175, 271-276.

V. MULTIPLE-WAVELENGTH ANALYSIS OF ENERGY RELEASE DURING A SOLAR FLARE: THERMAL AND NONTHERMAL ELECTRON POPULATIONS

ROBERT F. WILLSON,¹ KARL-LUDWIG KLEIN,² ALAIN KERDRAON,² KENNETH R. LANG,¹ AND
GERARD TROTTET²

Received 1989 September 25; accepted 1990 January 15

ABSTRACT

Collaborative solar investigations by Tufts University and the Observatoire de Paris have resulted in simultaneous radio observations with the Very Large Array (VLA) and the Nançay Radioheliograph (NR), comparisons of this radio data with X-ray observations, and theoretical interpretations of the dominant radiation mechanisms during a weak impulsive solar flare observed on 1988 May 28. The VLA has mapped the flaring structures at time intervals of 3.3 s, showing that the preflash and flash-phase components of the impulsive emission originate in spatially separated sources. The 20.7 cm preflash source is ascribed to thermal gyroresonance emission from coronal loops with typical magnetic field strengths of up to 270 G; this emission is associated with heating and exhibits no detectable hard X-ray radiation above 30 keV. The flash-phase 20.7 cm source and the hard X-ray emission are attributed to nonthermal electrons in the coronal and chromospheric portions of a magnetic loop. The combination of imaging observations at 20.7 and 91.6 cm excludes emission from a confined hot plasma during the flash phase.

Subject headings: radiation mechanisms — Sun: corona — Sun: flares — Sun: radio radiation

I. INTRODUCTION

Energy release during solar flares proceeds through several, observationally distinguishable steps: soft X-ray and radio wave signatures of interacting magnetic structures and of the heating of coronal loops can be observed during the preflare phase, i.e., minutes before the onset of the impulsive energy release revealed by the hard X-ray onset (see reviews by Priest *et al.* 1986; Van Hoven and Hurford 1986; Kundu 1986). The frequent presence of suprathermal electrons in the corona during the preflare phase is revealed by decimeter-wave emission (Benz *et al.* 1983). During large bursts, the impulsive phase, which starts with the first detectable hard X-ray emission above about 30 keV, has been shown to consist of two parts, termed preflash phase and flash phase, respectively. Preflash emission is characterized by weak hard X-ray emission and by metric type III bursts. At the transition from the preflash phase to the flash phase, the hard X-ray spectrum starts hardening, the decimetric-to-metric radio wave emission is shifted to higher frequencies, and the full scale of electromagnetic emission from energetic particles, going from γ -rays to radio waves, appears nearly simultaneously (Benz *et al.* 1983; Raoult *et al.* 1985; Klein *et al.* 1987). Observational evidence in different wavelength ranges suggests that the interaction between magnetic structures is necessary to trigger the flash phase (Raoult *et al.* 1985; Machado *et al.* 1988).

There is general agreement—and observational evidence (e.g., Lin *et al.* 1981; Kattenberg *et al.* 1981)—that any physically reasonable process of energy release will both heat the plasma and produce suprathermal particles. However, the relative contribution of the two populations to the observed hard X-ray and microwave emission in the different parts of the impulsive phase is unknown. Fürst, Benz, and Hirth (1982) and Alissandrakis, Schadee, and Kundu (1988) argued that the microwave emission of the weak flares they studied was incom-

patible with bremsstrahlung from the soft X-ray emitting plasma ($T \approx 10^7$ K), but they did not discuss the potential role of a high-temperature plasma ($T \geq 10^8$ K). Quantitative analyses of the problem were carried out through the modeling of hard X-ray and microwave emissions (see the recent review by Pick, Klein, and Trottet 1989). When studying the correlation of peak fluxes in the two spectral ranges, most authors (Gary 1985; Kai 1986; Lu and Petrosian 1989) have recently favored the nonthermal over the thermal model (Batchelor *et al.* 1985; but see Batchelor 1989). More detailed analyses of individual events, using temporal, spectral, or spatial information, however, tried to include both thermal and nonthermal electron populations (Böhme *et al.* 1977; Klein, Trottet, and Magun 1986; Holman, Kundu, and Kane 1989). These studies did not lead to a unique conclusion on the role of the two electron populations, and they did not analyze the transition between the preflash and the flash phase.

In this paper we reconsider the analysis of different electron populations in the case of a weak impulsive flare with simple spatial structure. VLA observations at 20.7 and 91.6 cm, and soft and hard X-ray data from the spectrometers aboard the *GOES* and *SMM* (HXRBS) spacecraft, are used. The times and techniques of relevant observations are given in § II, and an overview of the radio observations of the active region is contained in § III. Section IV focuses on the flare observations: 20.7 cm emission during the preflash phase is spatially separated from the subsequent flash phase component. The preflash peak at 20.7 cm has no counterpart in the hard X-ray emission, while during the flash phase the radio emission is closely associated with that at hard X-ray wavelengths. These observations are interpreted in § V: thermal gyroresonance emission is shown to be the most probable process for the preflash emission at 20.7 cm wavelength, while the radio and hard X-ray observations during the remainder of the impulsive phase are shown to be inconsistent with a confined thermal electron population, but are more readily explained by the injection of nonthermal electrons. In our concluding section,

¹ Department of Physics and Astronomy, Tufts University.

² Observatoire de Paris, Section d'Astrophysique de Meudon.

we place these observations and their interpretation within the context of current research on energy release during solar flares.

II. OBSERVATIONS

The observations reported below were carried out conjointly with the Very Large Array (VLA), the Nançay Radioheliograph (NR; The Radioheliograph Group 1989), the hard X-ray burst spectrometer HXRBS on board the *Solar Maximum Mission* (SMM) Satellite (Orwig, Frost, and Dennis 1980), and the soft X-ray telescope aboard the *GOES* satellite. The VLA observations were made from 1435 UT to 1630 UT on 1988 May 28 in the C/D array. In this configuration, the outermost antennas of the southeast and southwest arms are located at a distance of 0.59 km from the array center, while the most remote antenna of the north arm is located at 1.9 km from the center. The NR observed the Sun from 0755 UT to 1449 UT. The characteristics of the instruments are summarized in Table 1. At all wavelengths, the beamwidths of the individual antennas cover the whole Sun.

The VLA data were calibrated using standard solar calibration procedures; uncertainties in this calibration have been discussed by Kundu, Schmahl, and Fu (1989) and by Shevgaonkar, Kundu, and Jackson (1988). One uncertainty results from a software error in the program that applies the system temperatures of solar calibration antennas to other antennas (Ray Gonzales, private communication). This uncertainty results in an underestimate of brightness temperatures by a factor of 1.8, and our data have been corrected for this error. Another uncertainty is attributed to measurements of the high-temperature noise diodes on the solar calibration antennas; they are not measured regularly enough at the VLA to assure accurate measurements of the system temperature. This problem leads to an uncertainty of no more than 20%–25% in the inferred brightness temperatures.

The brightness temperatures were derived from a flux cali-

TABLE 1

SUMMARY OF INSTRUMENTAL CHARACTERISTICS

Observed frequency (MHz)	Beam (FWHM)	Bandwidth (MHz)	Sampling time (s)
Very Large Array			
1446	23" × 40"	12.5	3.33
327.5	75 × 135	0.781	3.33
Nançay Radioheliograph			
435	72	0.7	0.25
408	78	0.7	0.25
327	96	0.7	0.25
236.6	132	0.7	0.25
164	96/192	0.7	0.05/0.25

bration with the radio source 3C 48, which was observed for 5 minutes every 40 minutes; its flux density is 14.6 Jy and 47.0 Jy at 20.7 cm and 91.6 cm, respectively (VLA calibrator list).

The calibrated VLA data were used together with the standard CLEAN procedure to make synthesis maps of the total intensity, I , and the circular polarization, or Stokes parameter V , for both the 2 hr observing interval and for 3 s snapshot intervals during the radio bursts, or flares.

The NR provides six independent data sets, at 164 MHz with both the east-west and north-south branches, and at four further frequencies (see Table 1) with the north-south branch.

III. OVERVIEW OF THE RADIO OBSERVATIONS

During the entire observing period covered by the two radio instruments, a noise storm continuum and type I bursts were visible at all frequencies up to 435 MHz. This emission dominates the 2 hr VLA synthesis map of total intensity at 91.6 cm (Fig. 1, left). It has an extent of $3.7 \times 7'$, a peak brightness

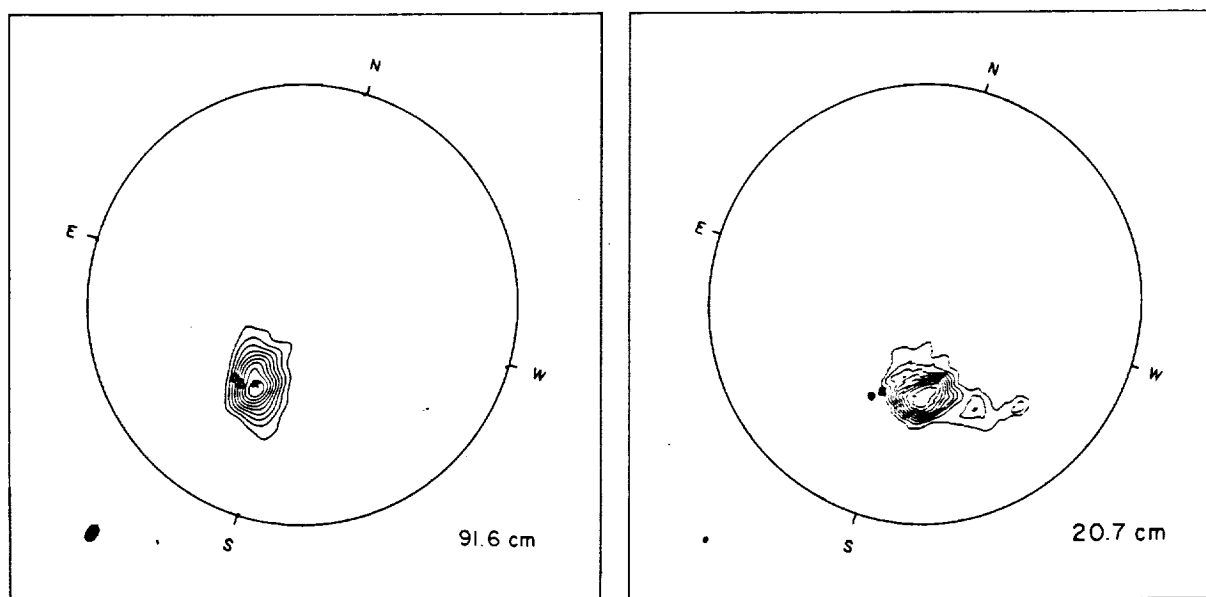


FIG. 1.—Two hour VLA synthesis maps at 91.6 cm (left) and 20.7 cm (right). Peak brightness temperature and contour intervals are 2.1×10^7 K, and 2.16×10^6 K (91.6 cm) and 2.9×10^6 K and 2.9×10^5 K (20.7 cm), respectively. The 91.6 cm emission is dominated by noise storm activity that is 90% right-hand circularly polarized, whereas the 20.7 cm map shows the quiescent, or nonflaring, emission of AR 5027. The 91.6 cm figure also shows the positions of the noise storm at 66, 91.6, and 183 cm, respectively designated by an open circle, cross and triangle (Nançay Radioheliograph); the filled circle and open square in the 20.7 cm image denote the positions of two bursts, designated as sources A and B, respectively. The synthesized beams at the two wavelengths are given as filled ellipses in the lower left-hand corner of each image, and the large circle denotes the limits of the photosphere.

temperature of $T_b = 2 \times 10^7$ K, and it is 90% right-hand circularly polarized. The open circle, cross, and triangle show the noise storm centroid at 66 and 91.5 cm, inferred from the rotation of the fringe pattern of the NR during the 7 hr observing period, and the average position at 183 cm measured with both branches of the radioheliograph. The dispersion of the noise storm source positions with wavelength is seen to be small, as is expected for a source close to disk center. The NR observations indicate a double source structure in the north-south direction, which is consistent with the elongated shape observed at 91.6 cm with the VLA. The two sources are more than 90% right-hand polarized at all observed frequencies. Comparison of the sense of polarization with the large-scale photospheric field pattern obtained from the Stanford magnetogram (*Solar-Geophysical Data*) indicates the association of the noise storm source with a region of negative magnetic polarity, which suggests radio emission in the ordinary mode. This is usually assumed to be the case in noise storms (e.g., Elgarøy 1977; Mercier *et al.* 1984).

Figure 1 (right) shows the 2 hr total intensity VLA synthesis map at 20.7 cm wavelength. The emission comes predominantly from an extended source ($3' \times 9'$) associated with the quiescent emission of active region AR 5027 (S29 W12). A weaker structure extends northward toward active region AR 5025 (S18 W12). The peak brightness temperature in the map is 2.9×10^6 K. No circular polarization was detected. The filled circle and open square in Figure 1 indicate the locations of the 20.7 cm bursts associated with a radio flare occurring around 14:49:20 UT; they are respectively designated source A and B in the subsequent text.

The remainder of this paper will discuss this flare-associated radio burst.

IV. FLARE-ASSOCIATED OBSERVATIONS

Figure 2 shows the time history, with 3.3 s integration time, of the flux densities at 20.7 and 91.6 cm (VLA), the hard X-ray count rate above 25 keV (HXRBS on board *SMM*, courtesy B. Dennis), and the soft X-ray flux in the 0.5–4 Å band as observed with the *GOES* satellite. The 20.7 cm and hard X-ray emissions are associated with a flare detected at H α and soft X-ray wavelengths (importance SN/C1.3) located at S26 W01 (*Solar-Geophysical Data* 531 II). The flare-associated emission starts at 14:49:30 UT in hard X-rays above 30 keV and at 91.6 cm, 10 s earlier at 20.7 cm and in the first HXRBS channel (below 30 keV). The hard X-ray and radio bursts fade together, vanishing at about 14:50:10 UT. The enhanced 91.6 cm brightness between 14:49:00 UT and 14:49:20 UT (designated 5 in Fig. 2) is not associated with the flare but is due to the noise storm discussed in the previous section. The soft X-ray burst has its most rapid rise during the hard X-ray and radio bursts and attains its maximum about 40 s after the impulsive peaks in these wavelength ranges. The time history of the radio and soft X-ray emissions is typical for such flares (see Fürst, Benz, and Hirth 1982).

Figure 3 shows 3.3 s snapshot maps of total and circularly polarized brightness at 20.7 cm at three instants of the burst, together with the synthesized beam (hatched ellipse). Two sources can be distinguished: The first peak (marked 1 in Fig. 2) arises from a source termed A (Fig. 3, top), the second and third peak (marked 2 and 3 in Fig. 2) are from a source B displaced about 40" from A (Fig. 3, middle). Besides their positions, A and B have other distinctive characteristics:

1. A is not associated with a detectable hard X-ray peak, but

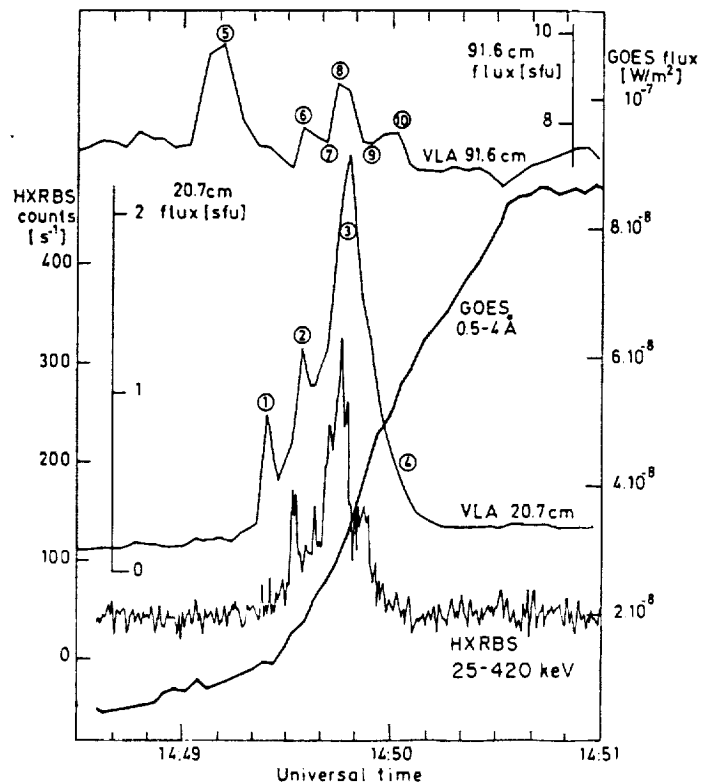


FIG. 2.—Time profiles of emission observed simultaneously at radio (VLA; 91.6 cm, 20.7 cm), hard X-ray (HXRBS/SMM; channels 1–15, $h\nu = 25$ –420 keV), and soft X-ray (*GOES*; 0.5–4 Å) wavelengths. Radio and soft X-ray data have been plotted with the same 3.3 s integration time, whereas 1 s integration was performed on the hard X-ray count rate in order to demonstrate that no essential feature of the burst has been lost in the VLA data. Although the first 20.7 cm peak (designated 1) is not detected at hard X-rays, the rest of the burst profiles (2 and 3) in the two spectral domains are very similar. The 91.6 cm profile shows fluctuating emission from a noise storm center (peak 5) that is spatially separated from the subsequent burst emission. The soft X-ray data show a gradual increase, with some low-level fluctuations around the time of the first impulsive emission (1) at 20.7 cm. VLA snapshot maps for the times marked 1, 3, and 4 are given in Fig. 3, while those for the times marked 7, 8, and 9 are given in Fig. 5.

with smoothly rising low-energy emission; the radio source is unpolarized.

2. B appears and vanishes with the hard X-ray emission above 30 keV. It has a bipolar structure with a maximum circular polarization of about 20%. The source shape and polarization are conserved throughout the burst.

Source A is not visible during the phase of brightest emission (14:49:34–14:49:57 UT) but is detected again, together with B, at the end of the event (time marked 4 in Fig. 2, synthesis map in Fig. 3, bottom). A test consisting of convolving source A with the 40" beam during the presence of source B shows that A would go undetected as long as $T_b(A) < 0.5 \times T_b(B)$, where $T_b(X)$ denotes the brightness temperature of source X.

In Figure 4 (Plate 15) we compare a 3.3 s snapshot map of the 20.7 cm burst at 14:49:54 UT with a SOON H α image taken at 14:50:10 UT. Here the uncertainty in the coregistration of the two images is $\pm 10''$. This figure shows that the microwave burst is displaced $\approx 1'$ east-southeast from the compact ($\theta \leq 30''$) H α flare kernels located at the eastern end of the active region. The size of the 20.7 cm source (half-intensity level) is about twice that of the optical flare. The angular displacement of the microwave emission with respect

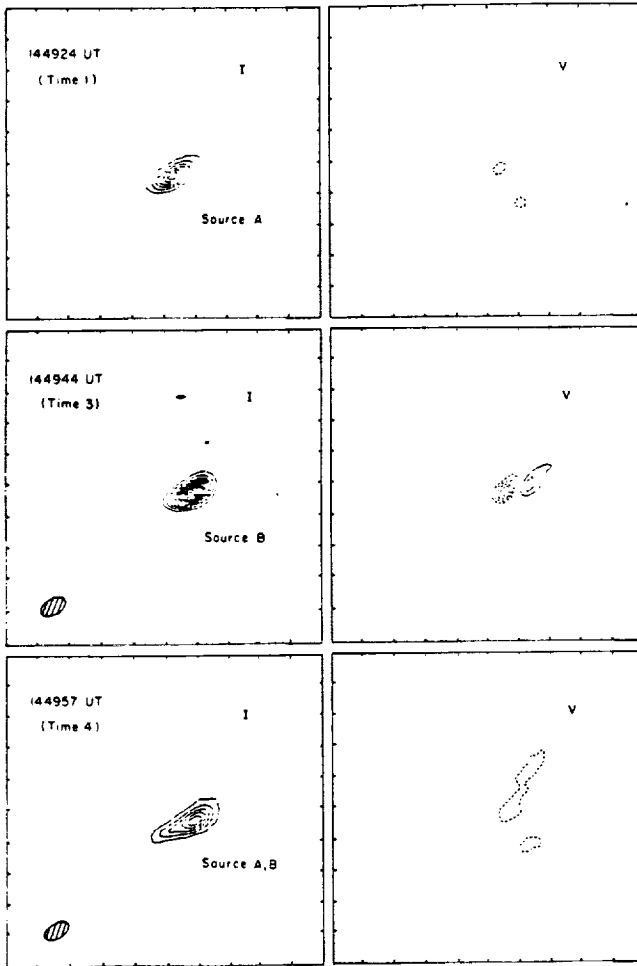


FIG. 3.—Three second VLA snapshot maps of the total intensity, *I*, and circular polarization, *V*, at 20.7 cm for the times denoted 1–4 in Fig. 2. They illustrate an unpolarized source A at time 1, a dipolar source B at time 3, and both sources A and B at a later time 4. Peak brightness temperature and contour intervals for the *I* maps are 2.0×10^7 K and 1.1×10^6 K, respectively. The outermost contour and contour interval of the *V* maps are equal to 5.5×10^5 K. The synthesized beam is denoted by the hatched ellipse in the lower left-hand corner. The angular scale may be inferred from the 60° fiducial marks on the axes.

to the H α flare may be attributed to a projection effect (due by the greater height of the 20.7 cm source above the photosphere) if the source lies within a coronal loop that bends toward the east limb. A microwave source that lies radially above the flaring region would produce mostly a southward displacement, contrary to observation.

The 91.6 cm emission at time 5 in Figure 2 was highly circularly polarized (95%–100%) noise storm radiation whose spatial position and structure were identical to those of the 2 hr synthesis map shown in Figure 1 (*left*). Figure 5 shows 91.6 cm VLA snapshot maps for the time intervals 7–9 in Figure 2. Burst component 6 at 91.6 cm (Fig. 2) showed the same structure and position as burst 8. Peak 10 is an unpolarized burst from a position slightly southward of the western source seen at time 8. The less intense peaks at time 7 and 9 (also Fig. 2) were spatially identical and separated from burst sources 6, 8, and 10. At the times of peaks 6 and 8, two sources (C and D) with opposite polarization are observed. Component C of this burst was $55\% \pm 5\%$ (left-hand) circularly polarized at 91.6 cm

wavelength, while component D was nearly completely right-hand polarized. In the valleys of the total flux (time 7 and 9) only source D is visible in polarization. When measured in the valleys, the brightness temperature of source D decreases with time. No accurate determination of the brightness temperature of D is possible at the times of the peaks because the emission from C dominates the signal, but there seems to be a weak brightening of D at the time of peak 8. We infer from these maps that we observed one source (C), which was the seat of two partially polarized bursts (peaks 6, 8), one displaced unpolarized source bursting later (peak 10), and a third, totally polarized source (D). The brightness of D essentially decreases slowly between the first peak (6) and the time when the last snapshot map was taken. The bipolar structure at peaks 6 and 8 may hence be ascribed to the existence of two spatially separated sources which exhibit different temporal evolution, rather than to a single magnetic loop.

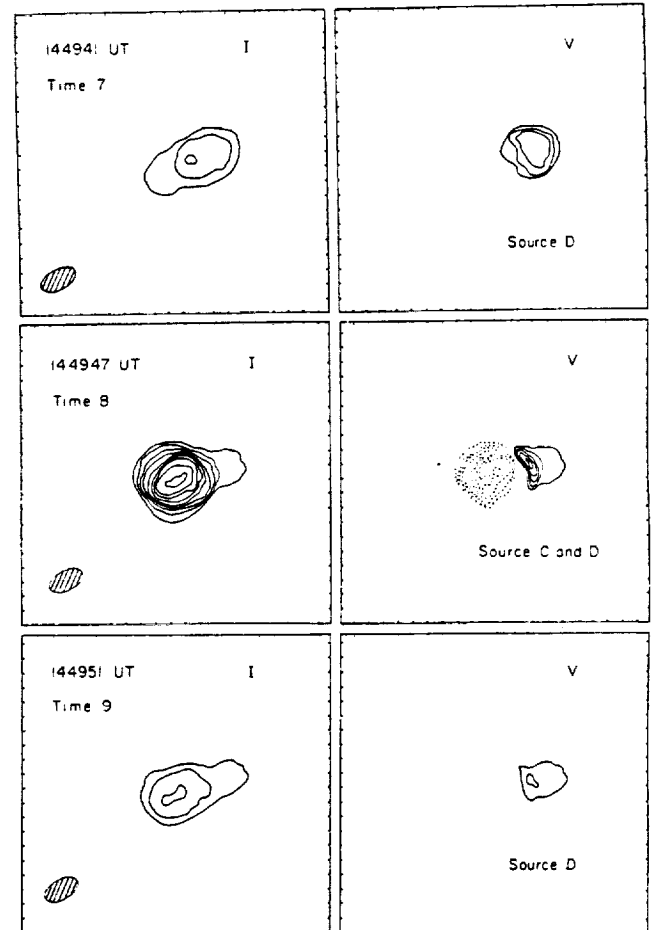


FIG. 5.—Three second VLA snapshot maps of the total intensity, *I*, and circular polarization, *V*, at 91.6 cm wavelength for the times denoted 6–10 in Fig. 2. They illustrate the same extended dipolar source (C and D) at the peaks 6, 8, or 10, and the same compact, unipolar source D at the valley 7 or 9. Peak brightness temperature and contour intervals for the *I* maps are 2.5×10^7 K and 2.75×10^6 K, respectively. The outermost contour and contour interval of the *V* maps are equal to 2.7×10^5 K and 1.37×10^5 K, respectively. The synthesized beam is denoted by the hatched ellipse in the lower left-hand corner. The angular scale may be inferred from the 60° fiducial marks on the axes.

ORIGINAL PAGE IS
OF POOR QUALITY

V. INTERPRETATION OF THE FLARE-ASSOCIATED EMISSION

a) Flare-associated Emission at 91.6 cm

The lack of spatially resolved spectral observations in the decimeter-to-meter waveband precludes any detailed discussion of the 91.6 cm emission associated with the impulsive burst. The only spectral information available stems from single-frequency records at Sagamore Hill (*Solar-Geophysical Data* 527 I) and at Nançay (only paper records available). Sagamore Hill reports both type V and type IV from 1443 to 1453 UT. The impulsive nature of the emission seen at the VLA and on Nançay records suggests type III/V activity. This is also consistent with the similarity of the 91.6 cm time history and those at 20.7 cm and hard X-rays (Raoult *et al.* 1985; Suzuki and Dulk 1985). Assuming this spectral identification is correct, peaks 6, 8, and 10 are ascribed to type III electron beams, and the smoothly varying source D is ascribed to a type V continuum. The simultaneous start and end, to within the VLA time resolution, of these emissions and those of source B (see § Vb) at 20.7 cm and hard X-ray wavelengths, indicates a common injection of nonthermal electrons into different magnetic structures (see Raoult *et al.* 1985). This does not imply a peak-to-peak correspondence. Peak 10, which occurs in the decay phase of the 20.7 cm burst at a site displaced from the preceding peak, has no clearly associated hard X-ray feature. The data set of Raoult *et al.* (1989), who study the relative timing of microwave bursts and metric type III emission, shows a similar behavior in the decay phase of microwave bursts.

The main objection against the type III/V interpretation of the 91.6 cm emission is the high degree of circular polarization. Opposite polarization of the type III and continuum sources has been observed at longer wavelengths (Suzuki and Dulk 1985), but with much lower degrees of polarization than in the present case. From one-dimensional images provided by the NR, Mercier (1989) finds that the degree of circular polarization of Type III bursts is most often below 30% in the 300–500 MHz range. If interpreted as plasma emission, the high polarization of source D suggests fundamental emission, so that

ordinary mode polarization is expected at 91.6 cm, while the extraordinary mode is most likely for the underlying 20.7 cm gyrosynchrotron source. However, the bipolar sources at the two frequencies show the same sense of polarization. This implies that the underlying 20.7 cm source is situated in an oppositely directed magnetic field. Altogether the available information is confusing, and one cannot exclude the alternative interpretation of gyromagnetic emission, e.g., a cyclotron maser, for sources C and D. Whatever is the nature of the burst-associated emission at 91.6 cm, it reveals the injection of nonthermal electrons in the middle corona at the time of the hard X-ray burst into a structure which is larger than the 20.7 cm burst source. This will be an important constraint to the interpretation of the 20.7 cm and hard X-ray emission in § Vd.

b) Measured Source Parameters at 20.7 cm and X-Ray Wavelengths

Measured quantities of the 20.7 cm and X-ray sources are summarized in Table 2. Column (1) gives the starting time of the sampling interval. Dimensions are given when sources A and B are clearly separated. Instants where both sources are observed are denoted by "A + B". The soft X-ray temperature and emission measure have been inferred from the two channels of the GOES detector using the formalism of Thomas, Starr, and Crannell (1985), which accounts for both bremsstrahlung continuum and the contribution of lines. In calculating these parameters, the preburst emission was first subtracted from the subsequent GOES data. The formal values of T, EM, and N given in Table 2 are those obtained from our calculations, but they are probably not determined to better than one significant figure. The hard X-ray spectral index γ likewise probably lies within ± 0.5 from the given value. The temperature is essentially constant during the radio and hard X-ray burst, while the emission measure smoothly rises from 2 to $9 \times 10^{47} \text{ cm}^{-3}$ between 14:49:19 UT and 14:49:50 UT. The injection spectrum [power law $F(E)dE \sim E^{-\gamma}dE$] and number of nonthermal electrons are derived from power-law fits to the observed hard X-ray spectrum using the thick-target

TABLE 2
MEASURED PARAMETERS OF X-RAY AND RADIO SOURCES

TIME (1)	VLA 20.7 cm		GOES		HXRBS			
	T_b (K) (2)	Size (3)	T (K) (4)	EM (cm^{-3}) (5)	γ (6)	N (≥ 25 keV) (7)	T (K) (8)	EM (cm^{-3}) (9)
Source A								
14:49:21.....	1.1×10^6	...	8.6×10^6	1.8×10^{47}
14:49:24.....	6.6×10^6	$30'' \times 60''$	8.0×10^6	2.0×10^{47}	...	$< 10^{31}$
14:49:27.....	3.3×10^6	...	8.3×10^6	2.6×10^{47}
Source B								
14:49:31.....	4.4×10^6	A + B	8.3×10^6	3.3×10^{47}
14:49:34.....	9.9×10^6	A + B	8.1×10^6	3.9×10^{47}	5.9	5.0×10^{34}	1.5×10^8	2.2×10^{44}
14:49:37.....	7.7×10^6	...	8.3×10^6	4.6×10^{47}	7.4	1.8×10^{35}	9.9×10^7	9.9×10^{44}
14:49:41.....	9.9×10^6	...	8.1×10^6	5.6×10^{47}	5.0	5.2×10^{34}	2.3×10^8	1.7×10^{44}
14:49:44.....	1.5×10^7	$30'' \times 60''$	8.1×10^6	5.6×10^{47}	5.5	1.3×10^{35}	1.8×10^8	4.2×10^{44}
14:49:47.....	1.9×10^7	...	8.0×10^6	6.5×10^{47}	5.9	1.2×10^{35}	1.6×10^8	3.6×10^{44}
14:49:51.....	1.1×10^7	...	8.1×10^6	8.6×10^{47}
14:49:54.....	9.9×10^6
14:49:57.....	5.5×10^6	A + B
14:50:01.....	3.3×10^6	A + B
14:50:04.....	2.2×10^6

expressions of, e.g., Lin and Hudson (1976). The number of electrons is the product of the injected particle flux and the integration time of 3.3 s. The temperatures and emission measures in the last column are derived from an isothermal hard X-ray model (e.g., Batchelor *et al.* 1985, and references therein).

c) Interpretation of the 20.7 cm Emission of Source A

The lack of circular polarization and of any detectable hard X-ray emission above 30 keV suggests that the 20.7 cm emission from source A comes from a Maxwellian electron population with moderate temperature ($T < 10^7$ K). This is also consistent with the absence of a counterpart to source A at 91.6 cm. The failure to detect hard X-ray emission implies that less than 10^{-3} photons $\text{keV}^{-1} \text{cm}^{-2} \text{s}^{-1}$ are emitted at 30 keV (Dennis *et al.* 1988: HXRBS Event listing). This puts an upper limit of the order of 10^{31} to the number of nonthermal electrons above 25 keV. Although this number would be sufficient to produce the observed brightness temperature in a magnetic field of the order of 100 G through gyrosynchrotron radiation, the nondetection of circular polarization is incompatible with such an interpretation.

Thermal microwave radiation is either bremsstrahlung or gyromagnetic emission. The electron temperatures inferred from the soft X-ray observations (Table 2) show that a moderately hot plasma does exist at the time of source A. However, the temporal evolutions of the radio and soft X-ray emissions are clearly different, which suggests that either the sources seen in these wavelength ranges are not the same, or that the radio brightness temperature depends sensitively on a parameter, such as the magnetic field, that does not affect the soft X-ray flux.

i) The Radiation Mechanism

The radio data yield an upper limit of the electron density, which is attained when the plasma frequency equals the observed frequency of 1500 MHz ($N_e = 2.8 \times 10^{10} \text{cm}^{-3}$), and a lower limit of the electron temperature, given by the brightness temperature ($T = 7 \times 10^6$ K). Assuming that the source dimension along the line of sight does not exceed 2×10^9 cm, one finds that the observed 20.7 cm emission is compatible with the free-free mechanism if the electron density is at least 10^{10}cm^{-3} . The opacity of the radio emission is increased in the presence of a magnetic field. We compute the optical depth of a plasma with $T = 7 \times 10^6$ K, assuming gyroresonance emission from the top of the loop or loops seen at 20.7 cm, which implies a viewing angle close to 90° . Using equations 27 and 28 of Dulk (1985), the source is found to be optically thick at the third or fourth harmonic of the gyrofrequency in the extraordinary mode, at the second harmonic in the ordinary mode, for scale heights of the magnetic field above 10^7 cm and an electron density of the order of $2 \times 10^9 \text{cm}^{-3}$. Unpolarized emission will hence be observed from the summit of a nearly isothermal magnetic loop with a magnetic field that increases along the line of sight from roughly 130 G or 180 G at the top to 270 G. The 20.7 cm data do not allow us to decide whether source A emits predominantly free-free or gyroresonance emission. However, it will be shown below that the high electron density required by the free-free interpretation is inconsistent with the soft X-ray observations.

ii) Temporal Evolution

In light of the foregoing analysis, the temporal evolution of the radio emission from source A reflects either the rapid changes of the magnetic field, if the radiation process is gyro-

magnetic, or the heat exchange of the radio source with the cool lower atmospheric layers.

The upper limits of the temperature and density inferred from the radio observations yield a radiative cooling time $\tau_r \approx 10^7(T_e/N_e)$ greater than 2500 s. Thus, radiative cooling does not explain the observed rapid changes in source A.

Conductive cooling operates on a shorter time scale. The classical Spitzer-Härm theory, which is valid as long as the collisional mean free path of the electrons is smaller than 1% of the temperature scale height (e.g., Duijveman 1983, and references therein), is inapplicable in the case under discussion: When $T > 7 \times 10^6$ K, the density would have to be greater than 10^{12}cm^{-3} in order that the mean free path of the electrons be smaller than 1% of the characteristic scale length of the temperature required by the observed 4 s cooling time (e.g., Duijveman 1983). At such an electron density, no 1500 MHz emission would escape from the source.

An upper limit for the heat flux out of the loop is given by the free-streaming value (e.g., Duijveman 1983, eq. [8]). A conductive cooling time of 3 s is then achieved in a loop at 7×10^6 K. The free streaming will be inhibited if turbulence at the interface between the hot and the cool plasma confines the bulk of the hot plasma. The typical velocity of heat transport is then $5c_s$ (Smith 1986), where c_s is the sound velocity in the hot plasma. If source A as seen by the VLA represents a single loop, a cooling time of roughly 20 s will result from this interpretation, and the observed 4 s decay time would require a shorter loop length around 10^9 cm. In summary, conductive cooling can explain the fading of the emission from source A. This implies either that heat is transported in a nearly free-streaming situation or that the radio source observed by the VLA comprises several smaller magnetic loops. The heat transport interpretation appears more attractive than the hypothesis of transient variation of the magnetic field. No direct diagnostic tool has allowed us so far to probe the magnetic field on second time scales. Detailed radio spectra might give essential information on the field strength, but we do not have such observations in the present case. However, the radio observations suggest that the magnetic field configuration is not destroyed during the burst, because source A is seen again at the end of the impulsive phase. Furthermore, the dissipation of a magnetic field of 100 G in a volume of 10^{28}cm^{-3} would dump 4×10^{30} ergs into the plasma on a time scale of 4 s, and it is difficult to understand why this energy release would only appear as a small fluctuation superposed on a smoothly rising soft X-ray flux. Thus, the hypothesis that the temporal evolution of source A reflects that of the magnetic field cannot be corroborated.

iii) Relation with the Soft X-Ray Emitting Plasma

The thermal interpretation of source A poses the question of consistency of the observations at 20.7 cm wavelength and in soft X-rays. The 20.7 cm brightness temperature evolves on a 4 s time scale, while the bulk of the soft X-ray emission exhibits a smooth increase of the emission measure with an e -folding time around 20 s, with a low level of fluctuations at the shorter wavelengths around the time of source A (see Fig. 2). The different time histories in the radio and soft X-ray bands suggest that the sources are spatially distinct.

The 20.7 cm brightness temperature comprises a peak with a 4 s decay constant, which may be superposed on a smoothly rising emission similar to the soft X-ray and the low-energy hard X-ray flux in the first HXRBS channel (Fig. 2). The bulk

of the soft X-ray emission exhibits a smooth increase of the emission measure with an e -folding time around 20 s, and a low level of fluctuations at the shorter wavelengths around the time of source A (see Fig. 2). The different time histories of the 20.7 cm peak and of the soft X-ray emission suggests that at least part of the radio emission comes from a source which is spatially distinct from the soft X-ray emitting region.

The contribution of the soft X-ray emitting plasma to the 20.7 cm radiation of source A can be estimated from the soft X-ray emission measure and temperature in Table 2, together with the measured surface of the radio source ($4 \times 10^{18} \text{ cm}^2$, if one assumes that the large beam broadens the source by 40%). This yields a brightness temperature of $(1.5 \times 10^6 \text{ K})/\mu$ (μ is the refractive index), i.e., at least 20% of the peak brightness temperature of source A. This would agree with a slowly rising component underlying peak 1 in Figure 2. The peak of the 20.7 cm emission itself then would come from a cooler plasma ($T \leq 5 \times 10^6 \text{ K}$), which would hardly be visible in the GOES data. On the other hand, if the whole of the emission of source A is attributed to a plasma distinct from the soft X-ray emitting plasma, the contribution of source A to the soft X-ray emission is estimated as follows: if the radio source observed with the VLA consists of a semicircular nest of loops with the projected dimension measured at 20.7 cm, a volume of $2 \times 10^{28} \text{ cm}^3$ is derived, which together with an electron density of $5 \times 10^9 \text{ cm}^{-3}$ in source A yields an emission measure of $5 \times 10^{47} \text{ cm}^{-3}$. With a temperature of $7 \times 10^6 \text{ K}$, the soft X-ray emission would be 10^{-7} W m^{-2} and $5 \times 10^{-9} \text{ W m}^{-2}$ respectively, in the long- and short-wavelength ranges of GOES. These values comprise the bremsstrahlung continuum emission (Tucker and Koren 1971) and an estimated line contribution of 55% and 25%, respectively, in the two channels (Thomas, Starr, and Crannell 1985, Fig. 5). During the emission of source A, GOES measured excess fluxes which are slightly higher than these values. The thermal gyroresonance emission of source A hence appears consistent with the soft X-ray data, while the bremsstrahlung interpretation would require densities that should make source A a brighter soft X-ray emitter than actually observed. The fact that the 20.7 cm peak has no clear counterpart in the soft X-ray flux may be due to either of the following:

1. The magnetic field in the soft X-ray loops is low ($H \leq 130 \text{ G}$), and the density is below $5 \times 10^9 \text{ cm}^{-3}$, when a detection threshold of $T_b = 10^6 \text{ K}$ is assumed, or below $3 \times 10^9 \text{ cm}^{-3}$ for a threshold of $5 \times 10^5 \text{ K}$. This implies that the bulk of the observed soft X-ray emission comes from a tenuous plasma in loops larger than those observed at 20.7 cm.

2. The bulk of the soft X-ray emission comes from dense structures ($N_e > 2.8 \times 10^{10} \text{ cm}^{-3}$), where 20.7 cm waves do not propagate. The simultaneous existence of hot structures with low and high density in flaring active regions is well established by X-ray observations with angular resolution (e.g., Hernandez *et al.* 1986).

In summary, the 20.7 cm observations of source A are consistent with thermal gyroresonance emission from a loop or a nest of loops with typical field strengths of 270 to 130 G. Since no spatially resolved X-ray observations are available, we cannot decide whether or not the soft X-ray source contributes to a smoothly evolving emission underlying the spike seen at 20.7 cm. The site of the radio spike itself must be spatially distinct from the soft X-ray source. The most probable interpretation of the fading of the spike is conductive cooling.

d) Interpretation of the 20.7 cm Emission of Source B

Source B is different from A by its position, its polarization characteristics, and by its close association with hard X-ray emission. The two latter points suggest gyromagnetic emission from an energetic electron population, either a very hot plasma ($T \geq 10^8 \text{ K}$) or a suprathermal electron population. We compute the spatial distribution of the brightness temperature for both cases, using the gyrosynchrotron model of Klein and Trotter (1984) with the approximations of Klein (1987), and a power-law and relativistic Maxwellian distribution of the energetic electrons. The magnetic loop is represented by a collection of dipolar field lines, with the observer being situated in the meridional plane of the dipole (see Fig. 1 of Klein and Trotter 1984, with $\Lambda = 0$). The geometry of the radio source is fixed by the VLA observations. The dimensions of the model loop are given in Table 3. No variation of the source parameters were assumed perpendicular to the line of sight.

i) Nonthermal Electrons

We suppose that hard X-ray and microwave emission result from a common injection of electrons in the magnetic loop. Like Hernandez *et al.* (1986), we assume that equal numbers of particles travel upward and downward. Those injected downward give rise to the hard X-ray emission in the chromosphere, while those going upward generate radio waves in the coronal part of the loop and hard X-rays when penetrating into the chromospheric layers of the opposite leg of the loop. The number of electrons seen at 20.7 cm is then half the number derived from the hard X-ray observations. We suppose further that the electron distribution is isotropic in the corona and that the slope of the instantaneous energy spectrum of these particles is the same as that of the injection spectrum derived from the thick target hard X-ray emission. We adopt values of the electron population which are situated between those derived from the hard X-rays at 14:49:44 UT and 14:49:47 UT; these values are listed in Table 3.

Once the energy spectrum is fixed, the resulting emission depends on the magnetic field strength and—through their influence on free-free absorption and Razin suppression—on the temperature and density of the thermal electrons in the loop. We restrict, somewhat arbitrarily, the variation of the

TABLE 3
PARAMETERS OF MODEL SOURCE B
A. LOOP GEOMETRY

Parameter	Value
Height (cm)	2.4×10^9
Depth (cm)	1.3×10^9
Width (cm)	2.2×10^9
Volume (cm ³)	1.4×10^{28}

B. PLASMA PARAMETERS

PARAMETER	NONTHERMAL MODEL		THERMAL MODEL
	High H	Low H	
H_{top} (G)	105	32	20
H_{bottom} (G)	368	112	70
N_e (cm ⁻³)	1.5×10^{10}	2×10^9	1.8×10^8
T (K)	2.0×10^6	2×10^6	1.7×10^8
γ	5.7	5.7	...
n ($\geq 25 \text{ keV}$) (cm ⁻³) ...	4.4×10^6	4.4×10^6	...

field strength, H , in the coronal part of the loop to $H_{\text{bottom}} = 3.5 \times H_{\text{top}}$. It will turn out that the emission comes mainly from the legs of the coronal loop, so that the magnetic field strength at the top is of no crucial importance. It then appears that the observed brightness distribution can be represented by a wide set of parameters, ranging from a tenuous plasma where gyrosynchrotron radiation is efficiently emitted even in a rather weak field, to dense and/or cool plasmas, where the brightness is reduced by Razin suppression and free-free absorption, such that the observed brightness temperature can then only be produced if the magnetic field is intense.

Typical parameter sets which fit the observations after convolution with a Gaussian beam of $40''$ are given in Table 3 for two extreme cases, referred to as "High H " and "Low H ," where H denotes the magnetic field strength. The two cases can in principle be distinguished observationally: the low magnetic field case produces a higher degree of circular polarization at a given frequency and a lower brightness at high frequencies than the strong field case. However, the polarization criterion does not effectively constrain the models, because the degree of circular polarization may be lowered by field inhomogeneities and effects of propagation which are not accessible to observations (see discussion by Alissandrakis and Preka-Papadema 1984). The spectral criterion cannot be fully exploited either, because short-wavelength observations of the burst are not available. Nevertheless, the model has to take into account that the 91.6 cm observations show no significant contribution from the electron population radiating the 20.7 cm emission. The source at long wavelengths is much larger than at 20.7 cm, and the emission is highly polarized and of similar brightness temperature as the 20.7 cm source. If there were an optically thick low-frequency counterpart of the 20.7 cm emission, bright and weakly polarized radiation from essentially the same source as seen at 20.7 cm should be observable at 91.6 cm. The failure to detect this signature suggests that Razin suppression or free-free absorption reduce the contribution of the gyrosynchrotron spectrum to the 91.6 cm emission. This can happen, e.g., when the thermal electron density in the radio-emitting loop is above $1.5 \times 10^9 \text{ cm}^{-3}$, so that no 91.6 cm radiation can escape.

Figure 6 compares computed and observed brightness temperature distributions at the peak of the burst. For the purpose of illustration the "High H " mode of Table 3 is chosen. The computed 20.7 cm brightness temperature (Fig. 5, top, solid line) attains its highest value in the legs of the coronal loop, while the circular polarization (dashed line) is more pronounced in the feet of the loop, where the radiation propagates nearly parallel to the magnetic field. The circular polarization is computed assuming quasi-parallel propagation. This approximation breaks down close to the top of the loop, where the wavevector is perpendicular to the magnetic field. It was assumed that no circularly polarized emission arises from this region. For comparison with the observations, the computed brightness temperature profile is convolved with a Gaussian beam of $40''$ FWHM. The convolved brightness profile is shown in Figure 6 (middle), where it is favorably compared with the observed one (bottom). The convolution with the large beam makes the bright legs disappear, giving a brightness distribution with a peak at the top of the loop ($T_b = 1.7 \times 10^7 \text{ K}$). The circular polarization, after convolution with the beam, gives two peaks of roughly $4 \times 10^6 \text{ K}$ in the legs of the loop, corresponding to a degree of polarization of 30%. This is about 1.5 times the observed value. The symmetry of the uncon-

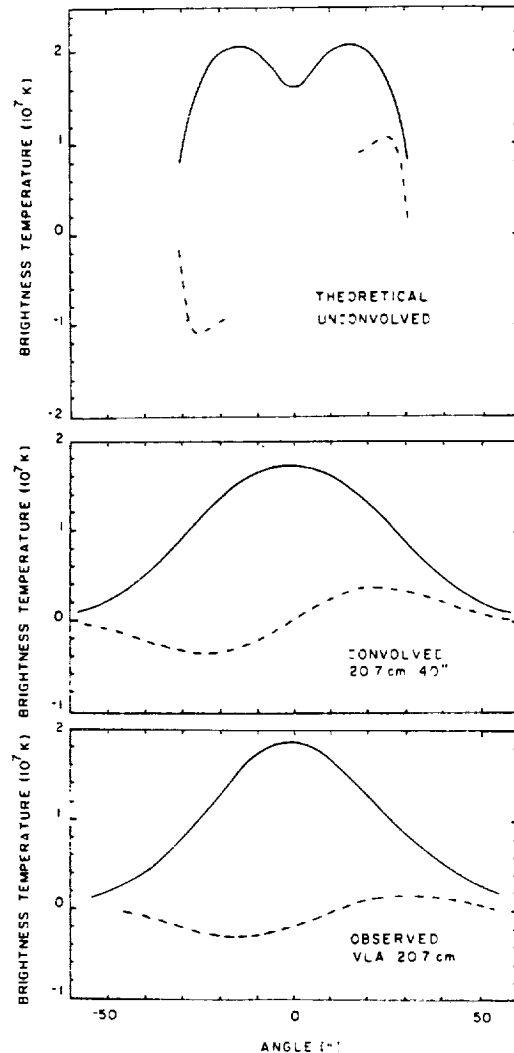


FIG. 6.—The computed spatial distribution of brightness temperature due to gyrosynchrotron radiation at 20.7 cm from a homogeneous and isotropic power-law electron spectrum in a magnetic loop (top) (solid line: total intensity I , dashed line: circular polarization V ; parameters of the "High H " model of Table 3). The convolved distribution (middle) expected from the VLA (beamwidth $40''$ across the long axis of the source) represents the observed distribution (bottom). Notice that the presence or absence of intense emission from the legs or apex of magnetic loops depends on the source parameters as well as on the observing beamwidth.

convolved source is a consequence of our assumption that the observer is located in the meridional plane of the dipole. However, the asymmetry between the legs of the loop, which would be seen by an observer outside this plane (see figures in Alissandrakis and Preka-Papadema 1984, and Klein and Trotter 1984), would not generate any observational difference after convolution with the large beam, but it would decrease the observed degree of polarization. The circular polarization is expected to be overestimated in the model computations anyway, because the assumed magnetic field structure is very regular, and depolarizing effects during propagation cannot be taken into account. It hence appears that radiation from a nonthermal electron population in a dense and/or cool magnetic loop is compatible with the whole set of available radio and hard X-ray observations.

ii) Maxwellian Plasma

When the hard X-ray and 20.7 cm emission are assumed to come from the same isothermal plasma, the magnetic field structure is the only free parameter left. The density of the hot plasma is determined by the emission measure derived from the hard X-ray observations, and the source volume is inferred from the 20.7 cm images (Table 3). A very tenuous source results ($N_e = 1.5 \times 10^8 \text{ cm}^{-3}$), which is not uncommon in thermal microwave models (see Batchelor *et al.* 1985, Table 2). The observed brightness temperature distribution at 20.7 cm is well represented by a Maxwellian plasma with the magnetic field parameters given in the last column of Table 3. However, the long-wavelength spectrum expected from the thermal model is not easily reconciled with the 91.6 cm observations: the thermal plasma would be optically thick at 91.6 cm but sufficiently tenuous to enable the propagation of radiation at this wavelength. One thus expects a brightness temperature of roughly 10^8 K and very weak polarization from a source similar to that at 20.7 cm, contrary to what is observed. The only way to reconcile the radio and hard X-ray observations with emission from a hot plasma would be to locate the 20.7 cm source in an underdense structure so that the bright long-wavelength emission is totally absorbed in the ambient corona.

VI. DISCUSSION

In this paper, we have discussed observations of a weak impulsive flare. Since the lack of spatially resolved observations in the soft X-ray domain precludes any examination of the global energy balance of this flare, we will restrict our discussion to the hard X-ray and radio observations.

The 20.7 cm observations reveal the presence of two spatially distinct sources during the burst:

1. The radio emission during the early onset of the hard X-ray burst (detected only below 30 keV) originates from a source A. This preflash emission is most probably thermal gyroresonance emission from a $7 \times 10^6 \text{ K}$ plasma in a magnetic field of 130–270 G. This interpretation is consistent with the absence of detectable circular polarization, of a simultaneous hard X-ray peak and of burst emission at 91.6 cm.

2. From the onset to the end of the flash phase, the predominant 20.7 cm emission arises from a source B, which is different from A both in position and in polarization. The flash phase comprises several peaks observed in hard X-rays above 30 keV and at 20.7 cm and 91.6 cm.

As is again seen at the end of the impulsive phase, the preflash source A probably exists throughout the burst. Nevertheless, the large beam of the VLA in the C/D configuration does not enable us to determine whether the time history of source A resembles that of the dominant impulsive source B. Former VLA observations (Willson 1983; Holman, Kundu, and Kane 1989; Willson, Lang, and Liggett 1990) showed also that the

precursor, impulsive, and decay phases of other flaring active regions originated in spatially separated sources. These findings are in agreement with results at metric (Raoult *et al.* 1985) and X-ray wavelengths (Hernandez *et al.* 1986; Machado *et al.* 1988). These sets of observations suggest that a destabilized coronal triggering source interacts with adjacent coronal loops, leading to the explosive release of energy during the flash phase.

While in the burst discussed in the present paper preflash emission at 20.7 cm seems to be consistent with a thermal electron population, the flash phase emission is in conflict with a perfectly confined hot plasma. The decimetric observations turn out to be a crucial criterion for distinguishing the two populations: while, in order to be detectable at high photon energies, the thermal plasma must have a temperature of at least 10^8 K , the low emission measure required, together with the measured dimension of the radio source, implies a low electron density (see Batchelor *et al.* 1985, Table 2, for other examples of weak hard X-ray bursts). If the high-energy tail of the hot electron population were confined around the apex of the loop by ion conduction fronts, bright, weakly polarized gyrosynchrotron emission should be seen at 91.6 cm at the location of the 20.7 cm source. This has not been observed in the present case. Hence, if the energetic electrons yielding the hard X-ray and radio emission originate from bulk energization of coronal plasma, they cannot be part of a confined Maxwellian. On the other hand, the injection of energetic electrons into different structures, where they emit hard X-ray, microwave, and decimetric emission through different mechanisms, might be easier to understand in terms of a process which generates a population of suprathermal electrons. This is consistent with the quantitative analysis of § V. The present work suggests that the acceleration of electrons is the main process responsible for the hard X-ray and radio emission associated with the flash phase.

Radio astronomical studies of the Sun at Tufts University are supported under grant AFOSR-89-0147 with the Air Force Office of Scientific Research. Simultaneous Very Large Array and *Solar Maximum Mission* observations of the Sun are supported by NASA grant 5-501 to Tufts University. The VLA is operated by Associated Universities, Inc., under contract with the National Science Foundation (NSF). Collaborative solar observations by Tufts University and the Observatoire de Paris are supported by NSF grant INT-8602285 and Centre National de la Recherche Scientifique (CNRS) grant 920038. The authors are indebted to B. R. Dennis for providing the hard X-ray spectral data and to C. Alissandrakis and J. Kuijpers for helpful discussions. We also thank R. Schwartz and G. Labow for their help with the analysis of the HXRBS data.

REFERENCES

- Alissandrakis, C. E., and Preka-Papadema, P. 1984, *Astr. Ap.*, **139**, 507.
 Alissandrakis, C. E., Schadee, A., and Kundu, M. R. 1988, *Astr. Ap.*, **195**, 290.
 Batchelor, D. A. 1989, *Ap. J.*, **340**, 607.
 Batchelor, D. A., Crannell, C. J., Wiehl, H. J., and Magun, A. 1985, *Ap. J.*, **295**, 258.
 Benz, A. O., Barrow, C. H., Dennis, B. R., Pick, M., Raoult, A., and Simnett, G. 1983, *Solar Phys.*, **83**, 267.
 Böhme, A., Fürstenberg, F., Hildebrandt, J., Saal, O., Krüger, A., Hoyng, P., and Stevens, G. A. 1977, *Solar Phys.*, **53**, 139.
 Dennis, B. R., *et al.* 1988, *NASA-TM 4036*.
 Duijveman, A. 1983, *Solar Phys.*, **84**, 189.
 Dulk, G. A. 1985, *Ann. Rev. Astr. Ap.*, **23**, 169.
 Elgarøy, Ø. 1977, *Solar Noise Storms* (Oxford: Pergamon Press).
 Fürst, E., Benz, A. O., and Hirth, W. 1982, *Astr. Ap.*, **107**, 178.
 Gary, D. E. 1985, *Ap. J.*, **297**, 799.
 Hernandez, A. M., Machado, M. E., Vilmer, N., and Trotter, G. 1986, *Astr. Ap.*, **167**, 77.
 Holman, G., Kundu, M. R., and Kane, S. R. 1989, *Ap. J.*, **345**, 1050.
 Kai, K. 1986, *Solar Phys.*, **104**, 235.
 Kattenberg, A., Allaart, M., de Jager, C., Schadee, A., Schrijver, J., Shibasaki, K., Svestka, Z., and van Tend, W. 1981, *Solar Phys.*, **88**, 315.
 Klein, K.-L. 1987, *Astr. Ap.*, **183**, 341.
 Klein, K.-L., Pick, M., Magun, A., and Dennis, B. R. 1987, *Solar Phys.*, **111**, 225.
 Klein, K.-L., and Trotter, G. 1984, *Astr. Ap.*, **141**, 67.
 Klein, K.-L., Trotter, G., and Magun, A. 1986, *Solar Phys.*, **104**, 243.
 Kundu, M. R. 1986, *Adv. Space Res.*, **6**, No. 6, 93.
 Kundu, M. R., Schmahl, E. J., and Fu, Q.-J. 1989, *Ap. J.*, **336**, 1078.

- Lin, R. P., and Hudson, H. S. 1976, *Solar Phys.*, **50**, 153.
 Lin, R. P., Schwartz, R. A., Pelling, R. M., and Hurley, K. C. 1981, *Ap. J. (Letters)*, **251**, L109.
 Lu, E. T., and Petrosian, V. 1989, *Ap. J.*, **338**, 1122.
 Machado, M. E., Moore, R. L., Hernandez, A. M., Rovira, M. G., Hagyard, M. J., and Smith, J. B. 1988, *Ap. J.*, **326**, 425.
 Mercier, C. 1989, *Solar Phys.*, in press.
 Mercier, C., Elgarøy, Ø., Tlamicha, A., and Zlobec, P. 1984, *Solar Phys.*, **92**, 375.
 Orwig, L. E., Frost, K. J., and Dennis, B. R. 1980, *Solar Phys.*, **65**, 25.
 Pick, M., Klein, K.-L., and Trottet, G. 1989, *Ap. J. Suppl.*, in press.
 Priest, E. R., Gaizauskas, V., Hagyard, M. J., Schmahl, E. J., and Webb, D. F. 1986, in *Energetic Phenomena on the Sun*, ed. M. Kundu and B. Woodgate (NASA CP-2439), p. 1.
 The Radioheliograph Group 1989, *Solar Phys.*, **120**, 193.
 Raoult, A., Correia, E., Lantos, P., Kaufmann, P., Klein, K.-L., and de Genouillac, G. 1989, *Solar Phys.*, **120**, 125.
 Raoult, A., Pick, M., Dennis, B. R., and Kane, S. R. 1985, *Ap. J.*, **299**, 1027.
 Shevgaonkar, R. K., Kundu, M. R., and Jackson, P. D. 1988, *Ap. J.*, **329**, 982.
 Smith, D. F. 1986, *Ap. J.*, **302**, 836.
 Suzuki, S., and Dulk, G. A. 1985, in *Radiophysics of the Sun*, ed. D. J. McLean and N. R. Labrum (Cambridge: Cambridge University Press), p. 289.
 Thomas, R. J., Starr, R., and Crannell, C. J. 1985, *Solar Phys.*, **95**, 323.
 Tucker, W. H., and Koren, M. 1971, *Ap. J.*, **168**, 283.
 Van Hoven, G., and Hurford, G. J. 1986, *Adv. Space Res.*, **6**, No. 6, 83.
 Willson, R. F. 1983, *Solar Phys.*, **83**, 285.
 Willson, R. F., Lang, K. R., and Liggett, M. 1990, *Ap. J.*, **350**, 856.

ALAIN KERDRAON, KARL-LUDWIG KLEIN, and GÉRARD TROTTET: Observatoire de Paris, Section d'Astrophysique de Meudon, CNRS UA 324, F-91925 Meudon Principal Cédex, France

KENNETH R. LANG and ROBERT F. WILLSON: Department of Physics and Astronomy, Robinson Hall, Tufts University, Medford, MA 02155

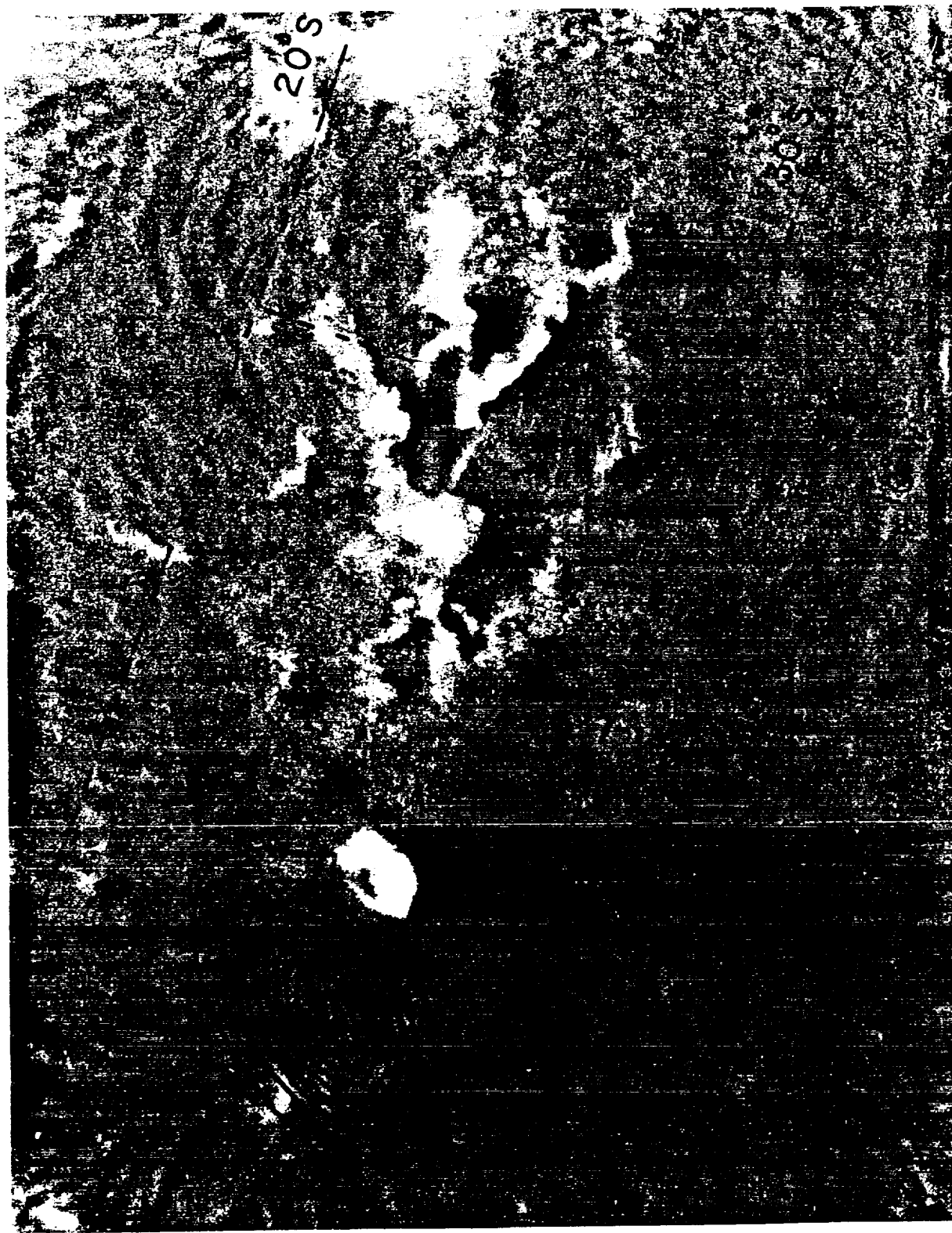


FIG. 4.—A VLA 3.3 s snapshot map of the 20.7 cm burst at 14:49:54 UT is compared with a SOON Hz image taken at 14:50:10 UT. The contours of the snapshot map denote levels of equal brightness temperature, with an outermost contour and contour interval of $T_b = 1.1 \times 10^6$ K. The dashed lines denote heliocentric latitude and longitude, and the angular scale may be determined from the 1' horizontal bar. The two arrows show the locations of Hz kernels which are displaced westward from the position of the 20.7 cm burst.

WILLSON *et al.* (see 357, 664)

W. VLA STUDIES OF LARGE-SCALE CORONAL LOOPS

Robert F. Willson
Department of Physics and Astronomy
Tufts University
Medford MA. 02155 USA

ABSTRACT: VLA observations at 20 and 91 cm delineate the structure of large-scale, otherwise-invisible coronal loops that have been previously observed at X-ray wavelengths. These loops may serve as conduits for relativistic electrons that propagate over large distances and trigger bursts in widely-spaced active regions.

Observations of Large-Scale Quiescent Loops

Full-disk VLA maps at 91 cm wavelength have shown that the most intense quiescent emission is contained in large-scale structures that are sometimes associated with dark H α filaments (Lang and Willson 1989) or with coronal streamers (Shevgaonkar, Kundu and Jackson 1988). One such example is shown in Figure 1 where we compare a full-disk 91 cm VLA map (28 May 1988) with a Kitt Peak magnetogram taken on the same day. This figure shows an extended ($\theta \approx 18'$, $L \approx 8 \times 10^{10}$ cm) loop-like structure which appears to join active regions on opposite sides of the equator. Active region B was the site of a long-lived noise storm and an impulsive 20 cm burst whose characteristics have been discussed by Willson et al. (1990).

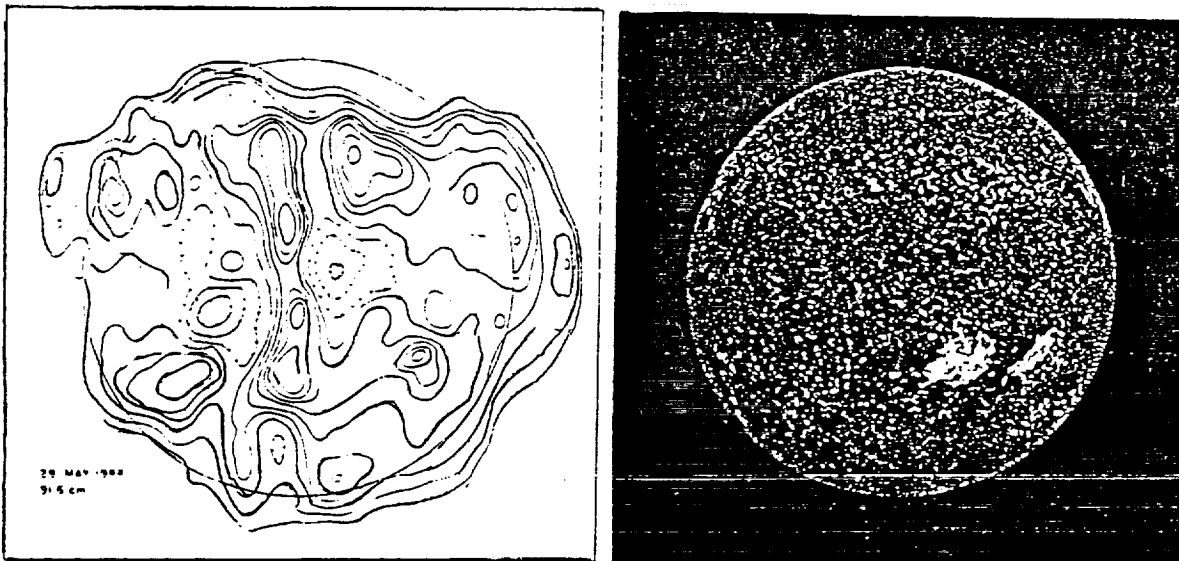


Fig. 1. A VLA 91 cm map (left) is compared with a Kitt Peak magnetogram (right) on the same day. A large-scale loop appears to join two active regions, A and B, on opposite sides of the equator.

Observations of Correlated Bursts From Different Active Regions

VLA observations at 91 cm wavelength have also provided evidence for triggering of burst emission across extended loops joining different active regions. In Figure 2 we show time profiles of a burst detected on 1988 June 8 with the VLA at 20.7 cm and 91.6 cm, at soft X-rays (0.5-4.0 A) with the GOES satellite and at hard X-rays (25-420 keV) with the Hard X-ray Burst Spectrometer (HXRBS) aboard the SMM Satellite.

Several 20.7 cm burst components can be identified, including a relatively weak "precursor" (A) that began at about the same time as the soft X-ray burst (163310 UT), and three impulsive bursts (B, C and D) which appear several minutes later. The 91.6 cm data show at least four impulsive peaks (E, F, G and H) three of which (E, F, and H) coincide with peaks at 20.7 cm. Hard X-ray emission was detected only at the times of peaks B, C and F.

VLA 3.3 second snapshot maps shown in Figure 2 indicate that bursts A and D occurred

ORIGINAL PAGE IS
OF POOR QUALITY

above the limbward active region AR 5032, while B and C were located above AR 5040, $\approx 5'$ to the northeast.

Snapshot maps of the 91 cm emission indicate that the bursts E-H were located above and between these two active regions. In Figure 2 we also show potential field lines that have been extrapolated to coronal heights using Kitt Peak photospheric fields. These calculations show that there are small-scale loops connecting regions of opposite magnetic polarity within individual active regions, as well as large-scale loops connecting different active regions. The most intense 91 cm peak at 163544 UT, in fact, appears to lie along a set of closed loops joining the two bursting active regions AR 5032 and AR 5040. Other 91 cm sources, including E, G and H appear to lie predominantly along open magnetic field lines whose footpoints originate in AR 5032. The fact that these regions appear to be magnetically connected suggests that electrons accelerated above one active region (AR 5032, the site of the gradual 20.7 cm burst A) may have travelled along large-scale loops to trigger secondary, impulsive, bursts in a neighboring active region (AR 5040). Other examples of sympathetic flare triggering by electron streams which may have travelled from the primary to the secondary flare site, have been discussed by Nakajima et al (1985).

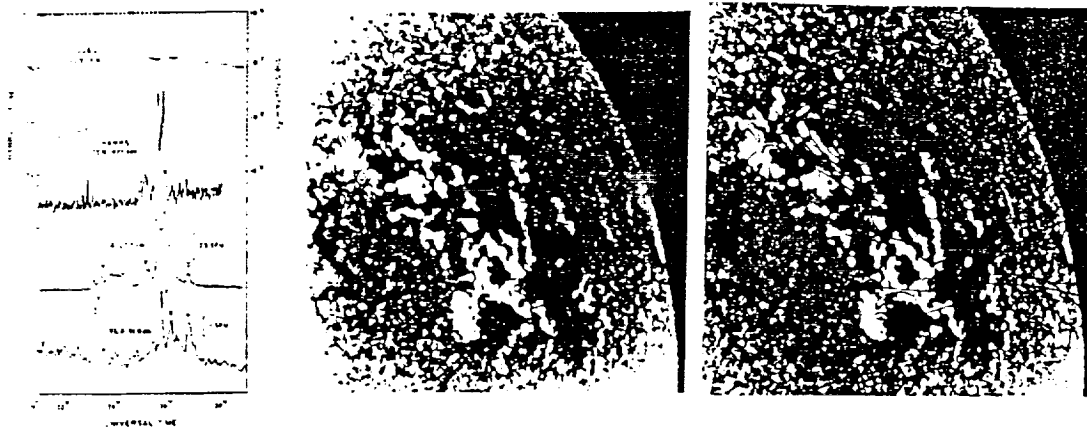


Fig. 2. Time profiles observed at radio (VLA; 91.6 cm and 20.7 cm), hard X-ray (HXRBS/SMM $h\nu=25-420$ keV) and soft X-ray (GOES 0.5-4.0 Å) wavelengths on 1988 June 8 (left). VLA 3.3 second snapshot maps at different times at 20.7 cm (middle) and 91.6 cm (right) are overlaid on a Kitt Peak magnetogram taken at 154235 UT on 1988 June 8. The results of potential field calculations (right) show large-scale loops that interconnect the active regions that were the sites of 20 cm bursts.

Acknowledgements

Radio astronomical studies of the Sun at Tufts University are supported under grant AFOSR-89-0147 with the Air Force Office of Scientific Research. Simultaneous Very Large Array and *Solar Maximum Mission* observations of the Sun are supported by NASA grant 5-501 to Tufts University.

References

- Lang, K.R., and Willson, R.F. 1989, *Ap.J. (Letters)*, 344, L77.
 Nakajima, H., Dennis, B.R., Hoyng, P., Nelson, G., Kosugi, T., and Kai, K. 1985, *Ap.J.*, 288, 806.
 Shevgaonkar, R.K., Kundu, M.R., and Jackson, P.D. 1988, *Ap.J.*, 329, 982.
 Willson, R.F., Klein, K.L., Kerdraon, A., Lang, K.R., and Trotter, G. 1990, *Ap.J.*, 357, 662.

**x. MULTI-WAVEBAND SMM-VLA OBSERVATIONS
OF AN M2 FLARE
AND AN ASSOCIATED CORONAL MASS EJECTION**

Robert F. Willson¹, Joan T. Schmelz², Raymond D. Gonzalez³,
Kenneth R. Lang¹, and Kermit L. Smith⁴

¹ Department of Physics and Astronomy Tufts University

² Applied Research Corporation under subcontract to Lockheed

³ National Radio Astronomy Observatory

⁴ Lockheed Palo Alto Research Laboratory

Abstract

An M2 flare and an associated Coronal Mass Ejection (CME) were observed by instruments on the Solar Maximum Mission as well as by the Very Large Array and other ground-based observatories on 1988 September 30 as part of the International Solar Month campaign. The multi-waveband data show a gradual, slowly changing event which lasted several hours. The microwave burst emission originates in compact ($\theta = 10'' - 30''$), moderately circularly polarized ($\rho_c \leq 60\%$) sources ($T_b = 0.5 - 20 \times 10^6$ K) located near the sites of bright H α and soft X-ray emission. These data were combined with estimates of electron temperature ($T_e = 1.5 \times 10^7$ K) and emission measure (EM $\approx 2.0 \times 10^{49}$ cm $^{-3}$) obtained from Ca XIX and Fe XXV spectra to show that the microwave emission can be attributed to thermal gyrosynchrotron radiation in regions where the magnetic field strength is $H = 425\text{-}650$ G. The CME was observed by both ground- and space-based coronagraphs and a good estimate of the acceleration at low altitudes could be measured: 0.0620 ± 0.0233 km s $^{-2}$. From these observations, the flare and CME start times appear to be simultaneous. The event can be described by a "cartoon" where a global magnetic disturbance both triggers the flare and opens the field lines allowing the filament cavity to rise. After the mass ejection, the open field lines begin to reconnect. The low-lying loops are heated first and the deposited energy travels down to the surface and appears as bright H α parallel ribbons. Higher

and higher loops are heated until reconnection is complete.

I Introduction

Multiple-wavelength VLA observations of solar radio bursts may be used to determine the size and location of sites of energy release at different heights in the corona and to provide information about preburst heating and magnetic interactions of coronal loops that sometimes precedes these events (eg. Willson 1983; Kundu and Shevgaonkar 1985; Shevgaonkar and Kundu 1985; Dulk, Bastian and Kane 1986). Comparisons of VLA time profiles and images with those obtained at soft and hard X-ray wavelengths and at H α may also be used to constrain radiation mechanisms and plasma parameters (i.e. electron temperature, electron density and magnetic field strength) in flaring loops, while also allowing studies of the spatial and temporal relationships of different flare plasmas during the preburst, impulsive and post-flare phases (Schmahl et al. 1990; Willson et al 1990).

In this paper, we discuss multi-waveband VLA and Solar Maximum Mission (SMM) observations of an X-ray burst and an associated coronal mass ejection (CME) which occurred on 1988 September 30. These observations were made during the International Solar Month (September 1988), an unprecedented opportunity for coordinated multi-waveband observations of the Sun in a phase of the solar cycle that has not been well studied. This worldwide campaign was endorsed by NASA, the Soviet Space Research Institute, and SCOSTEP, the International Science Committee on Solar-Terrestrial Physics. At least 26 satellite and ground-based observatories operated by researchers in 18 different countries participated in the campaign, insuring routine broadband coverage of the target active regions.

The coordinated observations of International Solar Month focused on different goals throughout September, depending on solar activity. When high activity was forecast, the SMM and VLA observing strategy was designed to obtain high spatial and temporal resolution data from the flaring active region. These data could address such issues as preburst heating, magnetic interaction in coronal loops, burst emission mechanisms, flare parameters, and the relationship between burst activity and other flare-related phenomena such as CME's.

In Section II, we present VLA snapshot maps of the preburst, impulsive, and decay phases of the event at several centimeter wavelengths. These multiple-wavelength images allowed us to study the spatial structure of the emission at different heights in the corona, and to derive estimates of the magnetic field strength along different directions through the bursting source. In this section, we also present SMM X-Ray Polychromator (XRP) soft X-ray images as well as light curves and spectra of the flaring plasma. The soft X-ray images were used to study the structural evolution of the coronal plasma, while the spectra provided estimates of its electron temperature and emission measure. Finally, we describe observations of a CME associated with the flare. In Section III, we combine the SMM, VLA and other ground-based observations to estimate the magnetic field strength in the microwave-emitting sources and compare the evolution of an expanding X-ray arch, a dark filament, and the CME. Section IV summarizes our conclusions.

II Observations

Active region AR 5171 (S26 E25 at 1300 UT) was chosen as the International Solar Month target for 1988 September 30, having produced a number of M-class GOES flares during the preceding several days. (GOES, the Geostationary Operational Environmental Satellite, has a full disk X-ray monitor with a soft X-ray channel (1-8 A) and a harder channel (0.5-4 A)). At ≈ 1900 UT, an M2 flare erupted from the region which was detected with several instruments on SMM, the VLA, and other ground-based observatories participating in the campaign. The GOES data shown in Figure 1 indicate a simple burst profile, consisting of a relatively slow rise (≈ 5 -10 minutes) followed by a gradual decay lasting several hours. In this figure, the times of the VLA and SMM observations are also shown. The VLA observed the preburst, impulsive and decay phases of the flare. SMM, which had been tracking the region for two days, was eclipsed by the earth until 1907 UT and, therefore, missed the impulsive phase.

a Radio Observations

The VLA observed AR 5171 in the D configuration between 1815 and 2300 UT on 1988 September 30. The observations were made at wavelengths of 2.0, 3.6, 6.1, and 20.7 cm (14934, 8484, 4816, and 1496 MHz) with bandwidths of 12.5 MHz. At these four respective wavelengths, the individual antenna beamwidths are 3.2', 6.0', 9.7', and 32' with synthesized beamwidths of $\approx 5''$, 10'', 16'' and 40''. Our observing sequence consisted of consecutive 8-10 minute observations at 2, 3.6 and 6.1 cm, with a 5-7 minute observation

at 20.7 cm about every 90 minutes. This strategy allowed us to image both the quiescent active region and emission from different phases of the relatively long-lasting burst.

The gains and phases of the antennas were calibrated every 35 minutes using two-minute observations of PKS 1252+119, with 3C286 used to establish the flux density scale at all wavelengths. All four Stokes parameters were sampled every 3.3 s in order to study rapid changes in the structure and polarization. The data were calibrated using the standard VLA reduction programs and then used to make CLEANed maps at all wavelengths. Uncertainties in the calibration of solar observations at the VLA have been discussed by Kundu, Schmahl and Fu (1989), Shevgaonkar, Kundu and Jackson (1989), and Lang and Willson (1989).

This burst was also detected by the Sagamore Hill and Palehua stations of the Radio Solar Telescope Network (RSTN), operated by the US Air Force. The total solar flux is measured at eight wavelengths between 122 and 1.94 cm. The 122-cm data (Figure 1) show intense burst emission before and during the M2 flare which may be attributed to a Type I noise storm. Unfortunately, these data provide no spatial information and, because the VLA was not operating at 90 cm, we cannot say whether this long-wavelength activity was associated with the X-ray burst or the CME. However, recent simultaneous VLA observations of another event at 20.7 and 91.6 cm did show that a noise storm continuum source began to increase in intensity about 30 minutes prior to the onset of an impulsive burst, possibly indicating an interaction between large- and small-scale coronal loops (Willson, Lang and Liggett 1990).

b SMM Observations

The XRP (Acton et al. 1980) Flat Crystal Spectrometer (FCS) can be centered on resonance lines between 1.5 to 20.0 Å. These lines are sensitive to different plasma temperatures and ratios of the line fluxes can be used to determine various physical parameters of the plasma. The wavelength drive which scans the crystals and centers them on different spectral lines could, unfortunately, not move freely in September. The strategy adopted was to park the drive at the Fe XVII resonance line (peak formation temperature $T_e = 5 \times 10^6$ K) at 15.01 Å, the most sensitive line for active region studies. The FCS was centered on AR 5171 and rastered continuously over a $4' \times 4'$ field of view in steps of $10''$ or $15''$. Successive images provide a time history of the active region.

Temperature and emission measure estimates of the flaring plasma are available from the XRP Bent Crystal Spectrometer (BCS), a non-imaging instrument with a $6' \times 6'$ (FWHM) field of view. The BCS monitors the high-temperature ($T_e \geq 10^7$ K) component of the plasma through light curves and spectra of Ca XVIII-XIX lines (peak formation temperature $T_e = 35 \times 10^6$ K) near 3.18 Å and Fe XXIV-XXV lines (peak formation temperature $T_e = 70 \times 10^6$ K) at 1.91 Å. The electron temperature can be determined from the ratio of the dielectronic satellite line flux to the collisionally excited resonance line flux for each ion: k/w in Ca XVIII/Ca XIX and j/w in Fe XXIV/Fe XXV (using the notation of Gabriel 1972). The emission measure can then be found by using the ion emissivity curves

with the derived electron temperature. The atomic physics calculations of Bely-Dubau et al. (1982 and references therein) were used to derive these plasma parameters.

The SMM Coronagraph/Polarimeter (C/P) was built and operated by the High Altitude Observatory and described in detail by MacQueen et al. (1980). It imaged the solar corona between 1.5 and 6 R_{\odot} using a broadband green filter. On 1988 September 30, the first C/P image of the southeast limb after the M2 flare revealed only the relatively quiet corona. The CME was detected in an image taken at 1936 UT and its evolving structure was observed in two subsequent images (1944 and 2001 UT) before it moved out of the C/P field of view. These images were, unfortunately, not ideal since the CME was at the edge of the field of view in two of the images and a portion was blocked by the occulting disk pylon shadow in the third. Nevertheless, measurements of the CME properties could be made and, thus, the event is interesting because of the multi-waveband data taken of the associated flare.

III Results

a Preburst Active Region Emission

Because of the large number of short interferometer spacings in the D configuration, we were able to make snapshot maps of the preburst emission with a reasonably high dynamic range of about 20 to 1. Figure 2 shows maps of total intensity, I , and circular polarization, V , and Table 1 gives the peak brightness temperature, size and degree of circular

polarization at all wavelengths. Here, the uncertainties in the values of the brightness temperatures are approximately 15-20 percent. As shown in Figure 2, the emission at 3.6, 6.1 and 20.7 cm is contained in a single component whose size systematically increases and whose polarization decreases with increasing wavelength. These systematic variations are also apparent at 2.0 cm, except that there is an additional component that has no counterpart at longer wavelengths. The peak brightness temperatures (Table 1) are typical of those observed in quiescent active regions (e.g., Lang, Willson and Gaizauskas 1983); and unless the actual brightness temperatures of the quiescent emission are abnormally low, this suggests that there was no significant preburst heating on timescales of a few tens of minutes before the burst, as has been observed for some active regions (Willson 1984; Kundu, Velusamy and White 1987). Such enhanced emission, for example, could occur because of the emergence or reorientation of magnetic flux resulting in the heating of the plasma and the triggering of bursts (Heyvaerts et al. 1977; Priest et al. 1986 and references therein).

The VLA maps have been coaligned with an $H\alpha$ image and a Kitt Peak magnetogram (provided courtesy of Jack Harvey) of the active region. In Figure 3, we mark the locations of the sunspots and regions of bright plage as found on a Solar Optical Observing Network (SOON) $H\alpha$ image made at 1841 UT. Figure 3 shows contours of the longitudinal magnetic fields obtained from the Kitt Peak magnetogram taken earlier in the day (1454 UT). Here we also show the configuration of magnetic field lines that have been extrapolated into the corona using the Kitt Peak data and sunspot field measurements from the Mt. Wilson

Observatory as boundary conditions. The method of extrapolation used for these calculations has been discussed by Sakurai (1981) who kindly provided us with his computer code.

A comparison of Figures 2 and 3 shows that the emission at 2, 3.6 and 6.1 cm is associated with relatively short magnetic loops connecting the dominant leading spot ($B \approx 2400$ G) of positive polarity to the smaller negative polarity ($B \approx 1000$ G) spots located $\approx 30''$ to the south. The more extended 20.7-cm emission is partly associated with these short loops, but mostly extends in the direction of the large-scale loops connecting the spots with regions of weaker magnetic fields ($B \approx 500$ G) to the southeast. The relatively high degree of (right hand) circular polarization of the 2-cm ($\rho_c \approx 90\%$) and 3.6-cm ($\rho_c \approx 60\%$) emission suggests optically thin emission that is probably attributable to extraordinary-mode gyroresonance emission from the legs of loops anchored to the dominant spot. This quiescent active region emission will be discussed in greater detail in a future paper (Willson et al. 1990).

SMM began tracking AR 5171 at ≈ 1300 UT on 28 September 1988 as the region was rotating over the east limb. Several hours later, AR 5171 produced two M flares and recovered quickly to a semi-quiescent state, producing only small events before the VLA observations. The bulk of the Fe XVII X-ray emission is associated with the large-scale loops in the southeast. This is not surprising, as previous simultaneous VLA-XRP observations show a close correspondence between the structure of coronal loops at 20 cm and at X-ray wavelengths (Lang et al. 1987a,b). In addition, there is another more compact

source located $\approx 30''$ south of the sunspots. The southward (or limbward) shift can be attributed to a projection effect due to the greater height of the soft X-ray emission above the underlying spots.

b Burst Emission

Figures 4a and 4b show a series of VLA snapshot maps of total intensity, I , and circular polarization, V , which depict the evolution of the burst during the impulsive phase. The maps at 6.1, 3.6 and 2 cm represent 10 s of data, beginning at the time indicated. Maps made at shorter intervals (3.3 s) showed no detectable changes in structure. Table 2 gives the peak brightness temperature, size, and degree of circular polarization of these sources. The maps at 6.1 cm made near the peak of the soft X-ray emission show that the source has an elongated structure with an angular size of $\approx 20'' \times 38''$ at the half intensity level. Its centroid lies $\approx 30''$ south of the preburst 6-cm peak, suggesting that the energy release took place in an adjacent source. There was no detectable change in the location of the 6-cm burst peak, although there is some indication of either a lengthening of the source or the emergence of a separate peak to the southeast. The peak brightness temperature of $T_b \approx 20 \times 10^6$ K is somewhat higher than the electron temperature inferred from the BCS spectra and the GOES data (see below).

The 3.6-cm maps show that, initially, there were two components, A and B, both of which were displaced eastward from the peak of the 6-cm burst. By ≈ 1900 UT, compo-

nent A had disappeared, while component B had intensified. Component A had a circular polarization of $\approx 50\%$ (RCP) while the peak of component B was only weakly polarized. The 2-cm maps made a few minutes after the peak of the impulsive phase indicate a single component (size $\approx 10''$) whose center lies $\approx 15''$ north of the 3.6-cm peak B. It shows circular polarization ($\rho_c \approx 25\%$ RCP) whose sense coincides with that at 6 and 3.6 cm, but which is smaller than at these other two wavelengths.

The electron temperature of the flaring plasma can be determined as a function of time from the k/w line ratio observed in the BCS Ca XIX spectra. The flux ratio as a function of temperature has been determined by Bely-Dubau et al. (1982). At 1907 UT, just after the impulsive phase of the M2 flare (as SMM moved out of the earth's shadow), the electron temperature determined by the k/w ratio was about 14×10^6 K with a statistical error of about $\pm 0.3 \times 10^6$ K. As shown in Figure 5, the temperature fell gradually, typical for long duration X-ray events, to 11×10^6 K at 1940 when SMM entered the South Atlantic Anomaly. The volume emission measure increased from 0.05 to 0.15×10^{50} cm⁻³ in this period. The results from the j/w line ratio observed in the BCS Fe XXV spectra gave slightly higher temperatures and lower emission measures; the GOES data show the opposite effect. This indicates that flaring plasma was produced at a range of temperatures and each ratio is most sensitive to a slightly different value.

c Evolution of the X-ray Plasma and Postburst Motion

At 1936 UT, C/P detected a faint coronal mass ejection above the southeast limb at a position angle of ≈ 150 degrees. A second image (1944 UT) shows a bright loop with a dark feature trailing the front. The outer edge of the loop is determined in these images and a third (2001 UT) at a uniform position angle of 145 degrees. From these three images, a height-time diagram was constructed and a linear speed (projected onto the plane of the sky) of $378 \pm 17 \text{ km s}^{-1}$ is determined for the CME. A linear extrapolation of this speed yields a start time of ≈ 1905 UT (A.J. Hundhausen, private communication). The location of this event in the C/P field of view and the extrapolated initiation time of the mass ejection establish its association with the M2 flare from AR 5171. A careful examination of the Mauna Loa Mark III K-Coronameter data for 1988 September 30 reveals two images of the event as it developed between $1.2 R_{\odot}$ and the lower radius of the C/P field of view. Figure 1 shows that a constant acceleration trajectory, rather than a constant speed trajectory, best fits the five data points. This quadratic fit gives an extrapolated start time of 1857 ± 0001 UT and an acceleration of $0.0620 \pm 0.0233 \text{ km s}^{-2}$.

Figures 6 and 7 show the evolution of the Fe XVII X-ray emission and the SOON H α emission. Also shown in Figure 6 are the locations of the microwave burst peaks. Near the peak of the impulsive phase (1912-1922 UT), the X-ray emission is dominated by two relatively compact ($\approx 45''$) sources, X₁ and X₂ which lie respectively, southwest and southeast of the major sunspot. These limbward-shifted sources may represent loops whose feet are marked by the underlying H α emission. There are two other peaks, X₃ and X₄, located

in the eastern portion of the active region, which are also shifted with respect to the $H\alpha$ emission. After 1922 UT, the peaks X_1 and X_2 appear to merge, forming a large-scale loop that extends across much of the active region. The 2-, 3.6- and 6-cm sources are located close to the $H\alpha$ kernels near the sunspots and under this large-scale X-ray loop. During the flare decay, the X-ray emission begins to move limbward with an apparent projected speed of $\approx 7 \text{ km s}^{-1}$ (Figure 7). By 2309 UT, it has disappeared from the field of view, leaving a hole or depression $\approx 1'$ south of the preburst, spot-associated X-ray component. These data suggest the outward movement of a post-flare loop or the successive brightening of a set of loops at different altitudes. Svestka et al. (1982), Svestka (1984), and de Jager and Svestka (1985) have discussed similar observations of post-flare X-ray loops which appeared to ascend into the corona following intense flares and, in one case, a coronal mass ejection. They attributed these observations to coronal heating and particle acceleration caused by successive magnetic field line reconnection.

Inspection of the SOON $H\alpha$ film indicated a limbward motion of the filament lying above the flare ribbon following the burst. Comparison of these images (Figure 7) shows a close correspondence between the position, overall shape, and orientation of the filament and X-ray loop. Analysis of subsequent $H\alpha$ images shows that the filament also appears to move laterally across the Sun together with the X-ray loops. Figure 8 shows the trajectory of the loops/filament system as measured from the bright $H\alpha$ flare ribbon shown in Figure 6. The filament first appears at about 2014 UT with an initial limbward velocity (on the plane of the sky) of about 10 km s^{-1} . It soon decelerated to zero velocity ($v = -8.2$

$\times 10^{-4} \text{ km sec}^{-2}$) and became undetectable in the $\text{H}\alpha$ images taken after 2230 UT. The X-ray loops show a clear, limbward displacement (relative to the flare peak) in the first image taken after SMM emerged from the earth's shadow at 2042 UT. The loops display a decelerating motion similar to that of the filament until they disappear out of the XRP field of view at approximately 2300 UT.

In contrast, the 20-cm emission peak during the early decay phase (2011-2018 UT) is coincident with that of the preburst source (Figure 9), suggesting energy release in the same region. A later map shows that, by 2138 UT, the peak has shifted $\approx 40''$ north while also developing a discernible "tongue" extending to the southeast. This new component could represent the microwave component of post-flare loops, often detected in X-rays after bursts (Velusamy and Kundu 1981). Although this southward extension was outside the 2-cm field of view, there was no evidence for 3.6- or 6.1-cm emission in this region ($T_b \leq 0.5 \times 10^6 \text{ K}$).

IV Discussion

a Interpretation of the Microwave Emission

In this section we will derive estimates of the magnetic field strength in the burst by comparing VLA brightness-temperature spectra with theoretical expectations from thermal and nonthermal distributions of electrons. A recent application of this technique was made by Gary and Hurford (1989) who used one-dimensional Owens Valley Radio Obser-

vatory interferometric observations to study the magnetic field structure of a simple solar microwave burst.

Our four-frequency observations are an improvement over some previous dual frequency studies (eg. Shevgaonkar and Kundu 1985; Dulk, Bastian and Kundu 1986) because they cover a wider range of wavelengths and therefore provide better constraints on radiation mechanisms and plasma parameters. A homogeneous source emitting thermal gyrosynchrotron radiation, for example, will have a constant brightness temperature, T_b , equal to the electron temperature, T_e , at frequencies $\nu \leq \nu_t$ where the emission is optically thick. At higher frequencies, corresponding to optically thin emission, T_b will decrease rapidly with frequency as $\approx \nu^{-10}$ (see Dulk and Marsh 1982, Dulk 1985). The turnover frequency depends critically on the magnetic field strength, B , the electron temperature, T_e , and the angle, θ , between B and the line of sight. For a nonthermal distribution of electrons, the brightness temperature will have a maximum at a single frequency, ν_{peak} , whose value depends on B , δ , the energy spectral index, and the column density of nonthermal electrons, $N_{nt}L$. Here, N_{nt} is the number density of electrons with energy $E \geq E_0$, usually taken as 10 keV, and L is the path length through the source. The degree of circular polarization, ρ_c , for both thermal and nonthermal gyrosynchrotron emission also depends on these physical parameters. Given independent estimates of these quantities, the problem reduces to adjusting the magnetic field strength to give satisfactory agreement between the observed and modeled brightness-temperature spectra.

Figure 10 shows brightness-temperature spectra along three lines of sight through the

source. Because the wavelengths were observed sequentially, we must assume that the brightness temperatures at the other wavelengths could be scaled by the variations in total flux density, S_λ , as given by the RSTN data. That is, for any two times t_1 and t_2 , $T_{b\lambda}(t_1) = T_{b\lambda}(t_2) * S_\lambda(t_1) / S_\lambda(t_2)$. This method is valid if the size of the emitting region does not change with time, as appears to be the case for the relatively simple sources at 2 and 6 cm and at 3.6 cm after 1918 UT.

As shown in Figure 10, the observed brightness temperatures at 6.1 and 20.7 cm are 1) comparable to the electron temperatures ($T_e = 6-18 \times 10^6$ K) derived from synchrotron-emitting distributions.

To test this idea, we used the equations of Dulk (1985) to calculate theoretical brightness-temperature spectra from both thermal and nonthermal gyro-synchrotron emission for a range of B , T_e , δ , and θ . For both models, a source thickness of $L = 4.3 \times 10^9$ cm, corresponding to the approximate angular size ($\theta \approx 1'$) of the 6-cm emission, was assumed. The electron density was taken to be $N_e = (EM/L^3)^{0.5}$, where the emission measure was obtained from the BCS data. With $EM \approx 0.5-1.5 \times 10^{49} \text{ cm}^{-3}$, and $L = 4.3 \times 10^9$ cm, $N_e \approx 0.8-1.4 \times 10^{10} \text{ cm}^{-3}$, a value consistent with those typically found in flaring loops. Included in our thermal model calculations is the contribution from thermal bremsstrahlung radiation, using the equation for optical depth given by Lang (1974). The SMM Hard X-Ray Burst Spectrometer data could, in principle, have been used to derive both δ and n_{nt} by

fitting the observed photon energy distribution as a function of energy. However, because SMM was eclipsed by the earth until the very end of the impulsive phase, the data show no significant emission above the second energy channel ($E \geq 50$ keV) and standard fitting was not possible (B.R. Dennis, private communication). This suggests that the hard X-ray emission was largely the high-energy tail of a low temperature thermal distribution or, at least, that the number of nonthermal electrons in this event was low. From the relationship between photon and electron energy given by Lin and Hudson (1976), an upper limit of 10^{-2} photons/cm²/sec/keV between 50 and 70 keV gives an upper limit to the total number of thick-target electrons with $E \geq 10$ keV equal $N_{nt} \leq 10^{34}$ and 1.5×10^{35} , respectively for $\delta = 4.5$ and 6.0 .

The results of our calculations indicate that the brightness temperatures and polarization can be fit by a thermal spectrum with magnetic field strengths of 425-650 G, electron temperatures of $T_e = 7-18 \times 10^6$ K, and observing angles of $\theta \approx 60^\circ$. Spectrum A, for example, could be well fit with $B = 425$ G and $T_e = 18 \times 10^6$ K, values that are, respectively, somewhat lower and higher than along the direction of the 3.6-cm peak A ($B = 475$ G, $T_e = 12 \times 10^6$ K). Spectrum C, corresponding to the 3.6-cm peak at ≈ 1918 UT, shows that the brightness temperature at this wavelength ($T_b = 6.1 \times 10^6$ K) is approximately equal to that at 6 cm and 20.7 cm. A satisfactory fit to these data was found for a magnetic field strength of $B = 650$ G, except that the emission at 2 cm ($T_b = 0.36 \times 10^6$ K) was attributed not to thermal gyrosynchrotron emission, but to optically thin ($\tau \approx 0.04$) thermal bremsstrahlung radiation. The low degree of circular polarization of the 2-cm

emission ($\rho_c \approx 25\%$) results from a propagation effect which increases the optical depth of the extraordinary mode of thermal bremsstrahlung over that of the ordinary mode in a magnetoactive plasma (Ratcliffe 1962).

As shown by other recent multi-wavelength studies (Schmahl, Kundu and Dennis 1985; Gary and Tang 1985; Dulk, Bastian and Kane 1986), nonthermal gyrosynchrotron radiation might also explain the brightness temperatures of solar microwave bursts. For example, with $\delta = 3.5$ and $N_{nt}L = 2.5 \times 10^{15}$ corresponding to a thickness of $1 - 4 \times 10^8$ cm ($\theta = 5''$) the predicted brightness temperatures at 6.1, 3.8 and 2.0 cm are 13×10^6 , 1.8×10^6 and 0.18×10^6 K, in good agreement with those for spectrum A. However, the predicted brightness temperature at 20.7 cm is 6.8×10^8 K, about a factor of 40 higher than observed. A higher magnetic field strength or larger column density of nonthermal particles would increase T_b at all wavelengths. Absorption by a thermal gas with $T_e = 7 \times 10^6$ K, $N_e = 1.2 \times 10^{10}$ cm $^{-3}$, and $L = 5 \times 10^9$ cm would decrease the predicted brightness temperature by only a factor of 18 at 20.7 cm. For this reason, we believe that the microwave burst emission is probably better explained by thermal, rather than nonthermal, gyrosynchrotron emission.

We note that Gary and Hurford (1989) have also interpreted the microwave emission from a relatively simple burst in terms of a thermal model with a somewhat higher electron temperature and magnetic field strength derived here. For this event they showed that the spectrum could be well-fit by a homogeneous, though expanding, thermal source with a peak electron temperature of $T_e = 7.1 \times 10^7$ K and a magnetic field strength of $B \approx 770$ G.

Comparisons with GOES soft X-ray data also showed that the electron density increased by an order of magnitude during the burst, in contrast to smaller changes in N_e that we find for our event.

b Evolution of the Expanding X-ray Arch, the Dark Filament, and the CME

Recent work by Simnett and Harrison (1985) and Harrison et al. (1989) investigates the relative timing of flares and associated CMEs. Earlier models (Wu et al. 1983, Maxwell et al. 1985) have assumed that flares preceded and drove mass ejections but these more recent revisionist models suggest quite the opposite: that the CME may precede and actually trigger the flare. The 1988 September 30 event is, in fact, a good candidate to test this cause-effect relationship between the flare and the CME. It is one of about a dozen events where both C/P and K-coronameter data were available (A.J. Hundhausen, private communication). With the combined data set, the development of the mass ejection can be tracked beginning at a much lower height in the corona. For these few events, linear fit seems to be a very poor representation of the CME velocity at low altitudes; using this fit extrapolated to $1 R_\odot$ would give an incorrect start time because 1) the CME was accelerating at low altitudes and 2) the CME was building up below the C/P field of view and did not start from $1 R_\odot$. These negative effects (MacQueen 1985) are minimized for this event; As in Figure 1, a constant acceleration trajectory, rather than a constant speed trajectory, is a much better representation of the data.

We find, as did Hundhausen (private communication), that, within the uncertainties of the measured quantities, that the start of the flare and the initiation of the mass ejection are nearly coincident: 1) the extrapolated CME start time is approximately 1857 UT with an error on the *fit* of \pm one minute; 2) the start time recorded at the Holoman SOON site in $H\alpha$ was 1857 UT; 3) the Palehua SOON site could record the start time as only *before* 1900 UT; 4) the Ramey SOON site recorded *before* 1910 UT; 5) the Sagamore Hill RSTN station recorded a burst beginning *before* 1904 UT; and 5) the GOES soft X-ray event began at 1858 UT.

Based on this result, it seem that neither the CME nor the flare “came first.” We suggest, on the other hand, a slightly different scenario in the form of a “cartoon” which is put together in part from Hundhausen (1987) and Zirin (1988) which (with some modifications) describes both the relative timing and morphology of 1988 September 30 event: As the magnetic field loops attempt to redistribute themselves to a more relaxed configuration, the global disturbance both triggers the flare and opens the field lines. The filament cavity along the neutral line, which is normally buoyant but is held down by the magnetic pressure of the loops on top of it, begins to rise, plowing through coronal material which builds up ahead of the cavity. This configuration: 1) the built up material, 2) the cavity, and 3) the filament or prominence becomes the “three-part” structure of a “typical” CME: 1) a bright outer loop surrounding 2) a dark cavity with 3) bright material at the center. After the CME is ejected, the open field lines begin to reconnect. In the “typical” two-ribbon flare scenario, this reconnection first heats the low-lying loop archades, injecting

energy into each flux tube; this energy reaches the loop footpoints and is revealed in H α images as two (ideally) parallel bright ribbons. As reconnection continues, higher loops are heated; these loops would (again ideally) have footpoints further from the neutral line and the bright parallel ribbons in the H α image would appear to move apart.

There is some evidence of the global magnetic disturbance before the 1988 September 30 event: There appears to be a precursor in the GOES light curve (Figure 1), peaking at about 1740 UT, as well as an event at 245 MHz in the RSTN data, peaking about an hour later. The GOES event was untagged (according the Solar Geophysical Data) and it was not observed by FCS or BCS which were tracking the region (if the event had been from AR 5171, FCS and BCS would have detected it easily). Also, the VLA saw no preflare heating during the 245 MHz event. This enhanced emission may be the result of a change in the large-scale structure of the global magnetic field or from a footpoint hidden behind the limb (Harrison 1986). We favor the first possibility since it is likely that the entire loop structure was large enough to be outside the BCS field of view but not large enough to extend behind the limb since the region was only 25° from central meridian. Either scenario, however, would be consistent with Harrison (1986).

Although many CMEs show a distinct and striking three-part structure, this is not always the case. In fact, only about half of the CMEs observed by C/P show this “classic” structure (Hundhausen 1987). In the photographs of the 1988 September 30 CME, only the fuzzy faint outer loop and trailing dark cavity can be seen. As the field lines opened up, the buoyant cavity began to rise and collect material in front of it but the active region

filament does not seem to have escaped: The filament, as well as the X-ray arch, are still at the site of the M2 flare (Figure 6) at this time. It is not until over an hour later, when the CME is well beyond the C/P field of view, that the filament begins to move (Figures 7 and 8). Because this active region was well on the disk, the proper motion of both the filament and the loops is well measured. They are moving together, toward the limb in the direction of the CME, with an initial speed (in the plane of the sky) of about 10 km s^{-1} . Then the filament/loop system decelerates and virtually stops at approximately 2230 UT. If we assume a simple loop geometry and that these loops expand radially away from the surface, the total velocity of about 25 km s^{-1} is not high enough to escape the Sun's gravitational field. Quite the opposite is true for the CME: assuming the same simple loop geometry and radial expansion, the total initial velocity is about 900 km s^{-1} , well above the escape velocity of the photosphere.

It seems, however, that the X-ray loops may not actually be moving but that the FCS images show a successive brightening of a set of loops at different altitudes as in the above, "ideal," two ribbon flare scenario. Each X-ray images shows its brightest point at the peak of the loop system. This brightening is evidence of reconnection at higher and higher altitudes. (Unfortunately, there is not a good estimate of the temperature at this point since the FCS was able to image only in Fe XVII.) The report from the Holoman observatory SOON site actually described the event and a "parallel ribbon" flare. It seems, therefore, that the cartoon outlined above is a reasonable, generic description of the 1988 September 30 event; it is not perfect since no filament was observed as part of the CME but then,

many events are probably only slightly different from the “typical” event described by this cartoon.

V Conclusions

The M2 flare of 1988 September 30 during International Solar Month was well observed by SMM, the VLA, and other ground-based instruments. The primary energy release at the short microwave wavelengths took place in a set of compact loops located near the sites of the brightest $H\alpha$ and soft X-ray emission. There was no evidence for preburst heating of the coronal plasma on timescales of a few tens of minutes before the burst. Microwave spectra, together with estimates of electron temperature and emission measure derived from BCS data, suggest that the microwave emission can be attributed to thermal gyrosynchrotron radiation in regions of magnetic field strength $H = 425 - 650$ G. The inferred values of H are in reasonable accord with those obtained from coronal magnetic field extrapolations. Although the associated CME was rather unspectacular, the width, speed, and (in conjunction with Mauna Loa coronameter observations) acceleration of this event could be measured. This is one of the few mass ejections for which an unambiguous initiation time is obtained. Although only a single event, the resulting near-coincidence of the CME and the flare initiation times must seriously question earlier models of CME dynamics where the flare provides the “driver” for the mass ejection. Taken in conjunction with other multi-waveband data, we believe the event to be rather interesting. We propose that this event seems to be well described by a “cartoon” where a global magnetic distur-

bance opens the field lines allowing the filament cavity to rise and plow through coronal material. This configuration becomes the bright outer loop surrounding the dark cavity which is observed by the K-coronameter and C/P. After the CME is ejected, the open field lines begin to reconnect. The low-lying loop archades heat first and the deposited energy travels down to the photosphere and appears as bright $H\alpha$ parallel ribbons. As reconnection continues, higher and higher loops are heated until the system is stable again, a process which took several hours.

ACKNOWLEDGEMENTS

Radio astronomical studies of the Sun at Tufts University are supported under grant AFOSR-89-0147 with the Air Force Office of Scientific Research. Simultaneous Very Large Array and Solar Maximum Mission observations of the Sun are supported by NASA grant 5-501. JTS and KLS acknowledge support by NASA contracts NAS5-30431 and NAS5-28713 and the Lockheed Independent Research Program. JTS thanks Dr. O.C. St. Cyr and Dr. A.J. Hundhausen for helpful discussions on CMEs and Dr. J.L.R. Saba for reading this manuscript. NRAO is operated by Associated Universities, Inc., under contract with the National Science Foundation. The XRP data used in this work were available only because of the repair of the SMM spacecraft by the crew of the Challenger on mission 41-C. The pilot for that mission, and the commander of Challenger's last flight was Francis R. Scobee. This work is dedicated to his memory.

References

- Acton, L.W., et al. 1980, *Solar Phys.*, **65**, 53.
- Bely-Dubau, F., Dubau, J., Faucher, P., and Gabriel, A.H. 1982, *MNRAS*, **198**, 239.
- de Jager, C., and Svestka, Z. 1985, *Solar Phys.*, **100**, 435.
- Dulk, G.A. 1985, *Ann. Rev. Astron. Astrophys.*, **23**, 169.
- Dulk, G.A., and Marsh, K.A. 1982, *Ap. J.*, **259**, 350.
- Dulk, G.A., Bastian, T.S., and Kane, S.R. 1986, *Ap. J.*, bf 300, 438.
- Gabriel, A.H. 1972, *MNRAS*, **162**, 99.
- Gary, D.E., and Tang, F. 1985, *Ap.J.*, **288**, 385.
- Gary, D.E., and Hurford, G.J. 1989, *Ap.J.*, **399**, 1115.
- Harrison, et al. 1989, *JGR*, in press.
- Heyvaerts, J., Priest, E.R., and Rust, D.M. 1977, *Ap. J.*, **216**, 123.
- Hundhausen, A. 1987, *Proc. of the 6th Inter. Solar Wind Conference*, **1**, 181.
- Kahler, S. 1987, *Rev. Geophys.*, **25**, 663.
- Kundu, M.R., and Shevgaonkar, R.K. 1985, *Ap. J.*, **291**, 860.
- Kundu, M.R., Velusamy, T., and White, S.M. 1987, *Ap. J.*, **321**, 593.
- Kundu, M.R., Schmahl, E.J., and Fu, Q.-J. 1989, *Ap. J.*, **336**, 1078.
- Lang, K.R. 1974, *Astrophysical Formulae*, (New York: Springer Verlag).
- Lang, K.R., Willson, R.F., and Gaizauskas, V. 1983, *Ap. J.*, **267**, 455.
- Lang, K.R., Willson, R.F., Smith, K.L., and Strong, K.T. 1987a, *Ap. J.*, **322**, 1035.
- Lang, K.R., Willson, R.F., Smith, K.L., and Strong, K.T. 1987b, *Ap. J.*, **322**, 1044.

- Lang, K.R., and Willson, R.F. 1989, *Ap. J. (Letters)*, **344**, L73.
- Lin, R. P., and Hudson, H.S. 1976, *Solar Phys.*, **50**, 153.
- MacQueen, R.M. 1985, *Solar Phys.*, **95**, 359.
- MacQueen, R.M., et al. 1980, *Solar Phys.*, **65**, 91.
- Maxwell, A., Dryer, M., and McIntosh, P. 1985 *Solar Phys.*, **97**, 401.
- Priest, E. R. et al. 1986, *Energetic Phenomena on the Sun*, NASA CP-2439, ch. 1, M.R. Kundu and B. Woodgate, eds.
- Ratcliffe, J.A. 1962, *The Magneto-ionic Theory*, (Cambridge: Cambridge University Press).
- Sakurai, T. 1981, *Solar Phys*, **76**, 301.
- Schmahl, E.J., Kundu, M.R., and Dennis, B.R. 1985, *Ap. J.*, **299**, 1017.
- Schmahl, E.J., Schmelz, J.T., Saba, J.L.R., Strong, K.T., and Kundu, M.R. 1990, *Ap.J.*, **358**, 654.
- Shevgaonkar, R.K., and Kundu, M.R. 1985, *Ap. J.*, **292**, 733.
- Shevgaonkar, R.K., Kundu, M.R., and Jackson, P.D. 1989, *Solar Phys.*, **71**, 311.
- Simnett, G.M., and Harrison, R.A. 1984, *Adv. Space. Res.*, **4**, 279.
- Svestka, A. 1984, *Solar Phys.*, **94**, 171.
- Svestka, Z., et al. 1982, *Solar Phys.*, **75**, 305.
- Willson, R.F. 1983, *Solar Phys.*, **83**, 285.
- Willson, R.F. 1984, *Solar Phys.*, **92**, 189.
- Willson, R.F., Lang, K.R., and Liggett, M. 1990, *Ap.J.*, **350**, 856.

Willson, R.F., Schmelz, J.T., Lang, K.R., and Brosius, J.W. 1990, (in Preparation).

Willson, R.F., Klein, K.-L., Kerdraon, A., Lang, K.R., and Trottet, G. 1990, *Ap. J.*, **357**, 662.

Wu, S.T., Wang, S., Dryer, M., Poland, A.I., Wolfson, C.J., Orwig, L.E., and Maxwell, A. 1983, *Solar Phys.*, **85**, 351.

Zirin, H. 1988, 1962, *Astrophysics of the Sun*, (Cambridge: Cambridge University Press).

Table 1:

Wavelength (cm)	<u>Parameters of the Preburst Emission</u>		
	Brightness Temperature (K)	Polarization (%)	Angular Size (")
2.0	5.0×10^5	90	12 x 25
3.6	2.1×10^6	60	20 x 40
6.1	1.4×10^6	40	30 x 75
20.7	2.2×10^6	≤ 10	170 x 175

Table 2:

UT Time	<u>Parameters of the Burst Sources</u>			
	Wavelength (cm)	Brightness Temperature (K)	Size (")	Polarization (%)
190018	6.1	6.5×10^6	26 x 37	30
190438	6.1	1.6×10^7	25 x 39	30
190838	6.1	1.8×10^7	25 x 30	20
191138A	3.6	3.2×10^6	15 x 18	55
191138B	3.6	2.5×10^6	12 x 15	≤ 10
191438A	3.6	2.1×10^6	12 x 17	50
191438B	3.6	4.7×10^6	12 x 14	≤ 10
191838B	3.6	6.1×10^6	12 x 14	≈ 15
192138	2.0	1.6×10^6	10 x 12	25
192408	2.0	2.2×10^6	10 x 12	27
192728	2.0	1.6×10^6	10 x 12	60
201100	20.7	4.6×10^6	100 x 130	≤ 15
213800	20.7	3.1×10^6	125 x 150	≤ 15

FIGURE LEGENDS

Fig. 1. (Bottom) Time profiles of the burst obtained by the 0.5-4.0 A detector on GOES and by the Sagamore Hill station of the Air Force Solar Radio Patrol at 245 MHz. The times and bands that the VLA observed are shown at the top. The times of the SMM orbits are given at the bottom. Here the VLA band designations of U,X,C and L correspond to wavelengths of 2, 3.6, 6.1 and 20.7 cm, respectively. (Top) Time-height plot of the CME as detected by the Mauna Loa Mark III K Coronometer (M) and by the SMM Coronagraph/Polarimeter (S). The solid and dashed lines represent, respectively, constant speed and constant acceleration fits to the data.

Fig. 2. VLA maps of total intensity, I , and Stokes parameter, V , showing the preburst emission at 2, 3.6, 6.1 and 20.7 cm wavelength. The fiducial marks on the axes are drawn at 60" intervals. The direction of the north and east solar limbs are denoted by arrows. The box on the 20.7 cm map marks the 3' field of view of the maps at the shorter wavelengths. The contours mark levels of equal brightness temperature, with an outermost contour and contour interval of $T_b = 3.1 \times 10^5$ K, 2.7×10^5 K, 1.7×10^5 K and 3.6×10^4 K at 20.7, 6.1, 3.6 and 2.0 cm. The peak brightness temperatures at these four respective wavelengths are $T_b = 2.2 \times 10^6$ K, 1.4×10^6 K, 2.1×10^6 K and 5.0×10^6 K.

Fig. 3. a) A drawing showing the locations of the sunspots and brightest regions of plage as obtained from a SOON $H\alpha$ image of AR 5171 at 1841 UT. For comparison, the

6.1 cm preburst map shown in Figure 4 is superposed. b) Potential magnetic field lines superposed on contours ($B= 200,400,600$ G) of the photospheric fields as obtained from a Kitt Peak magnetogram. c) An XRP-FCS image of Fe XVII emission made during the preburst interval from 1738-1758 UT. The contours correspond to 10,20,30... counts s^{-1} .

Fig. 4. VLA snapshot maps of I (a) and V (b) at 6.1, 3.6, and 2.0 cm wavelength. The contours mark levels of equal brightness temperature, with an outermost contour and contour interval of $T_b= 1.3 \times 10^6$, 3.6×10^5 , and 2.0×10^5 K for the maps at 6.1, 3.6 and 2.0 cm, respectively. The fiducial marks on the axes are drawn every $30''$.

Fig. 5. Plots of the electron temperature and emission measure derived from analysis of the BCS Ca XIX spectra. The error bars denote $1-\sigma$ uncertainties in the measurements.

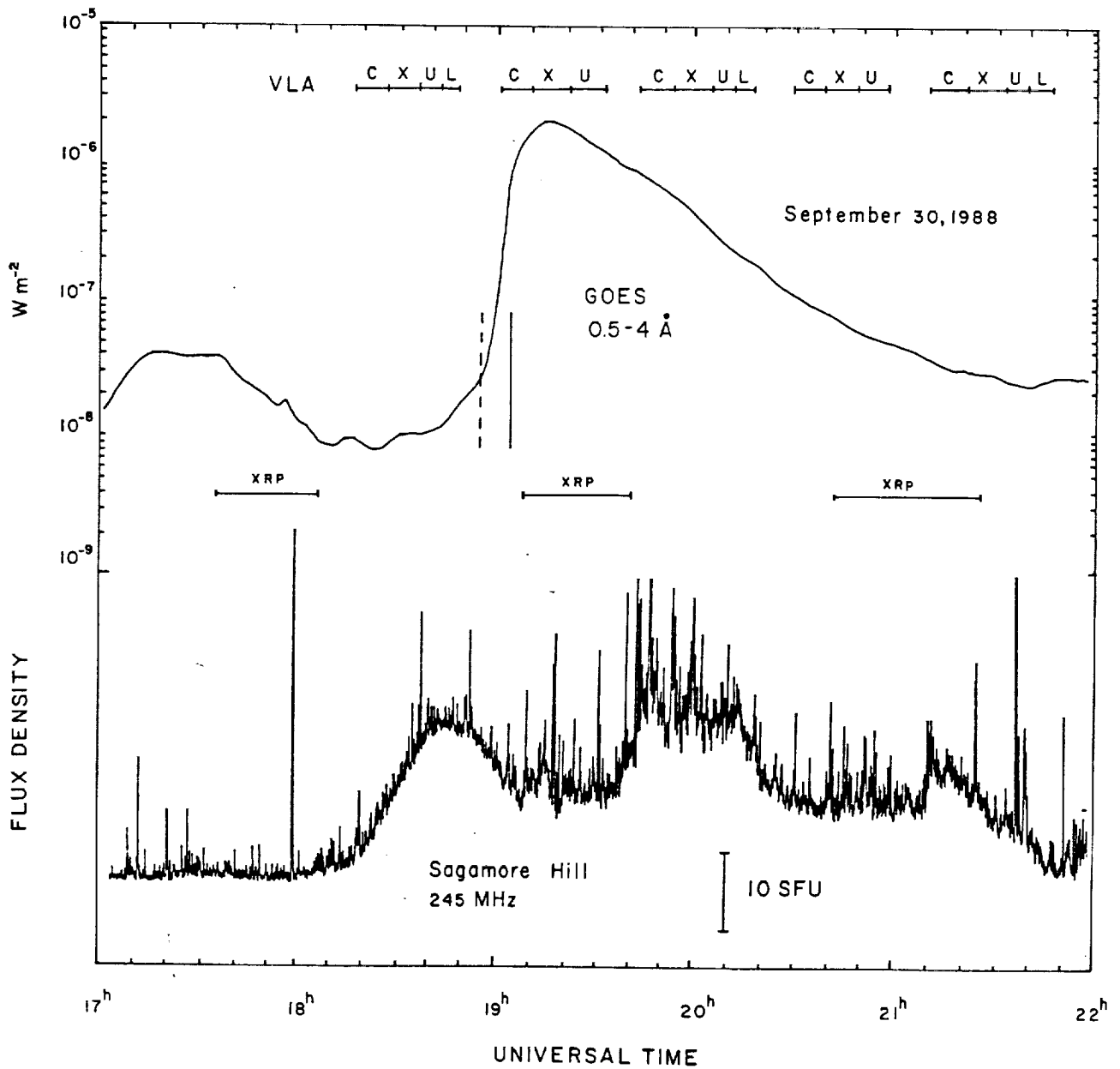
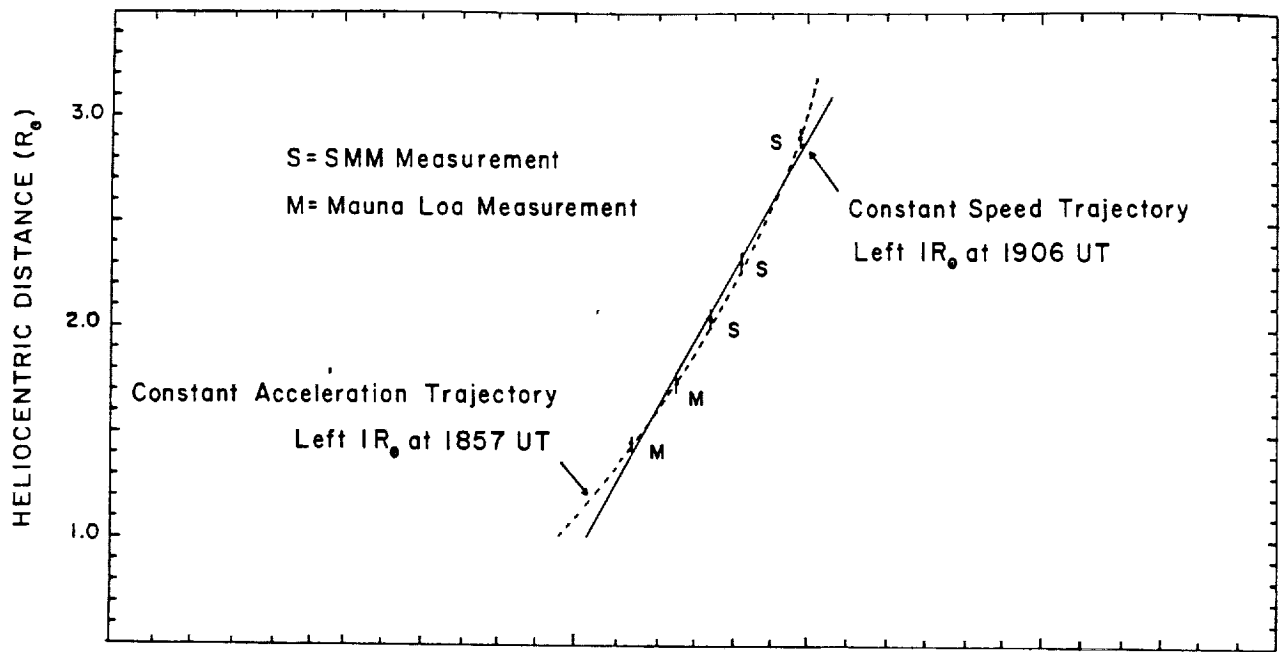
Fig. 6. A SOON $H\alpha$ image (top left) showing the location of the optical flare emission is compared with a sequence of XRP Fe XVII images depicting the evolution of the soft X-ray plasma. The locations of the VLA burst sources at 2.0, 3.6, 6.1 and 20.7 cm (Figures 4 and 8) are superposed on the optical image. The contour levels of the XRP maps correspond to 100,200,400,600,800,1000,1400,1800,2200,2600 and 3000 counts sec^{-1} above the background level. The angular scale can be inferred from the $10''$ spacing between the fiducial marks. The dashed line in the upper left-hand panel denotes the outermost contour of the 20.7 cm map at 2011 UT (see Figure 9).

Fig. 7. A comparison of H α (top left) and soft X-ray (XRP-Fe XVII) images during the decay phase of the burst. A dark filament appearing to move outward with a projected speed of $\approx 7 \text{ km s}^{-1}$ is coincident with an expanding X-ray loop which eventually disappears from the field of view. The contour levels of the Fe XVII image from 2046-2056 UT correspond to 100, 200, ... counts s^{-1} above the background level. The contour levels of the later maps are drawn at 10, 20 ... counts s^{-1} above the background level.

Fig. 8. The lateral displacement of the H α filament relative to the bright flare ribbon taken at 192210 UT (Figure 6). The error bars correspond to an uncertainty of $\approx 5''$ in determining the position of the leading edge of the filament on each SOON image. A quadratic fit to the data (solid line) yields a velocity and deceleration of $v = 10.2 \text{ km sec}^{-1}$ and $\dot{v} = -8.2 \times 10^{-4} \text{ km sec}^{-2}$, respectively.

Fig. 9. A comparison of SOON H α images (top) and VLA 20.7 cm maps during the post-impulsive phase. Here the contours mark levels of equal brightness temperature with an outermost contour of $6.2 \times 10^5 \text{ K}$ and a contour interval of $3.1 \times 10^5 \text{ K}$. The angular scale can be inferred from the $60''$ spacing between the fiducial marks on the axes. Note that the 20.7 cm emission has developed a distinct southeastward extension during the same time that the dark filament is seen to move outward.

Fig. 10. Brightness temperature spectra for three lines of sight through the microwave burst source. Spectra 1, 2, and 3 refer, respectively, to the peaks of the 6 cm source at 190838 UT, the 3.6 cm source A at 191138 UT, and the 3.6 cm peak B at 191738 UT. Theoretical spectra of the combined thermal gyrosynchrotron radiation and thermal bremsstrahlung emission for different values of magnetic field strength and electron density are also shown. These spectra were computed for an angle $\theta = 65^\circ$ and electron densities of $N_e = 1.2 \times 10^{10} \text{ cm}^{-3}$ (1 and 2) and $1.5 \times 10^{10} \text{ cm}^{-3}$ (3).



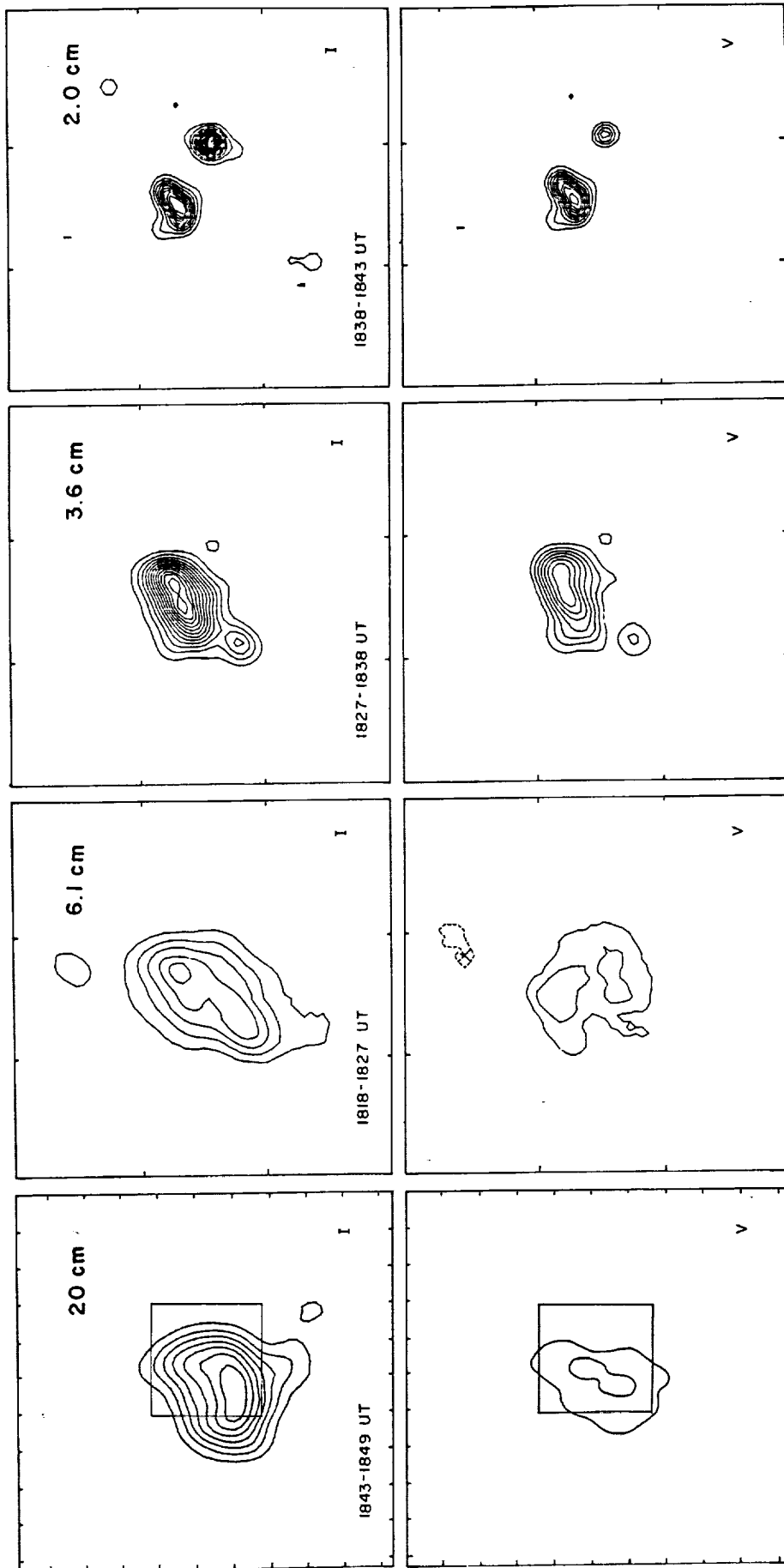


FIG. 2.

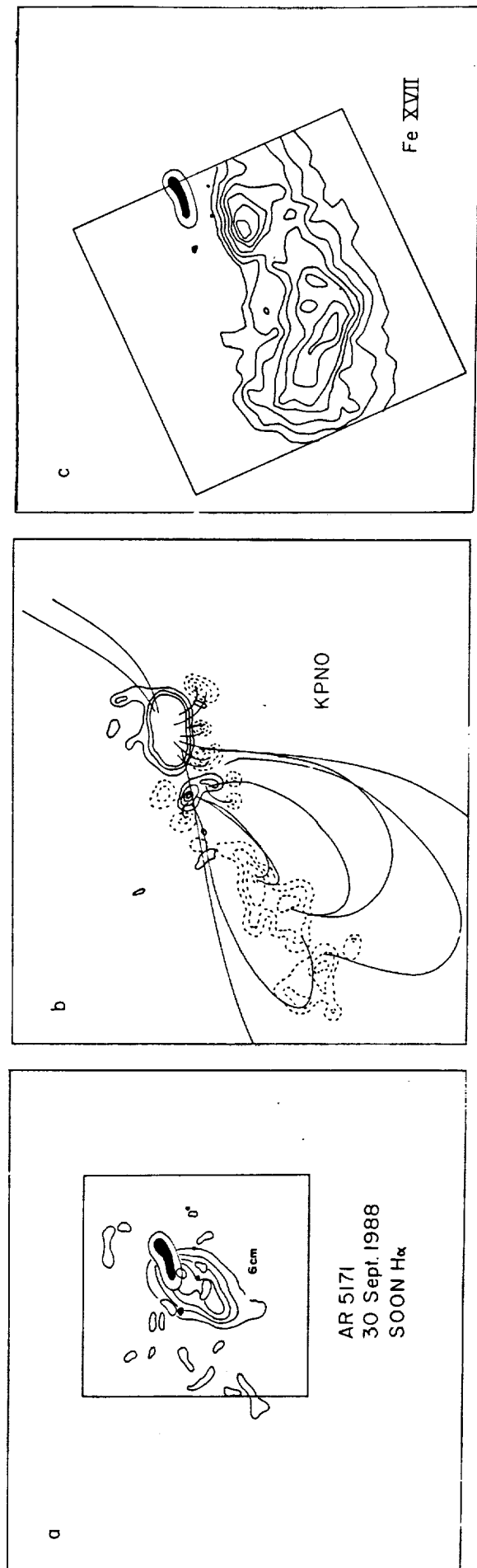
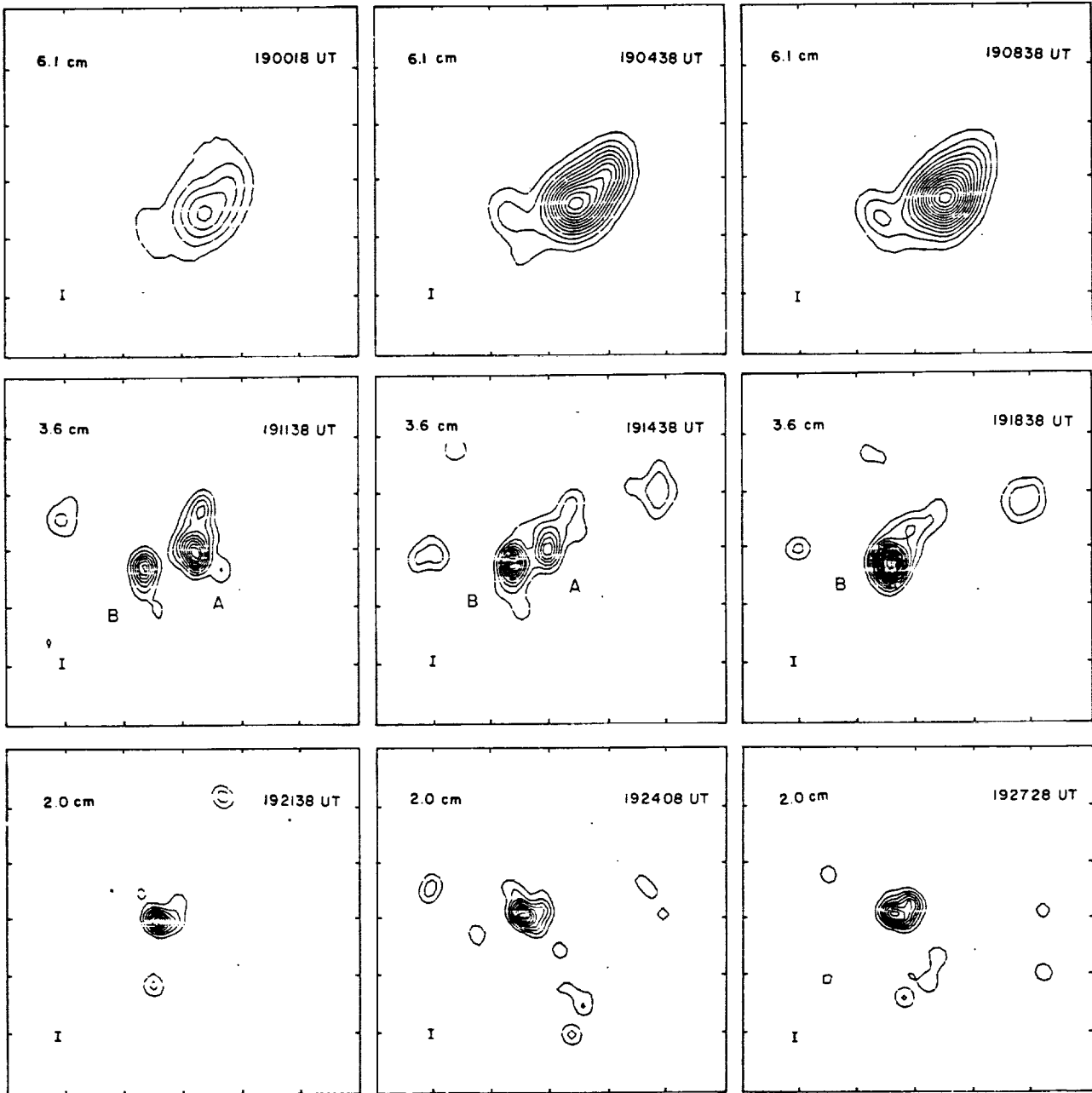


Fig. 3.



248
Fig. 4a

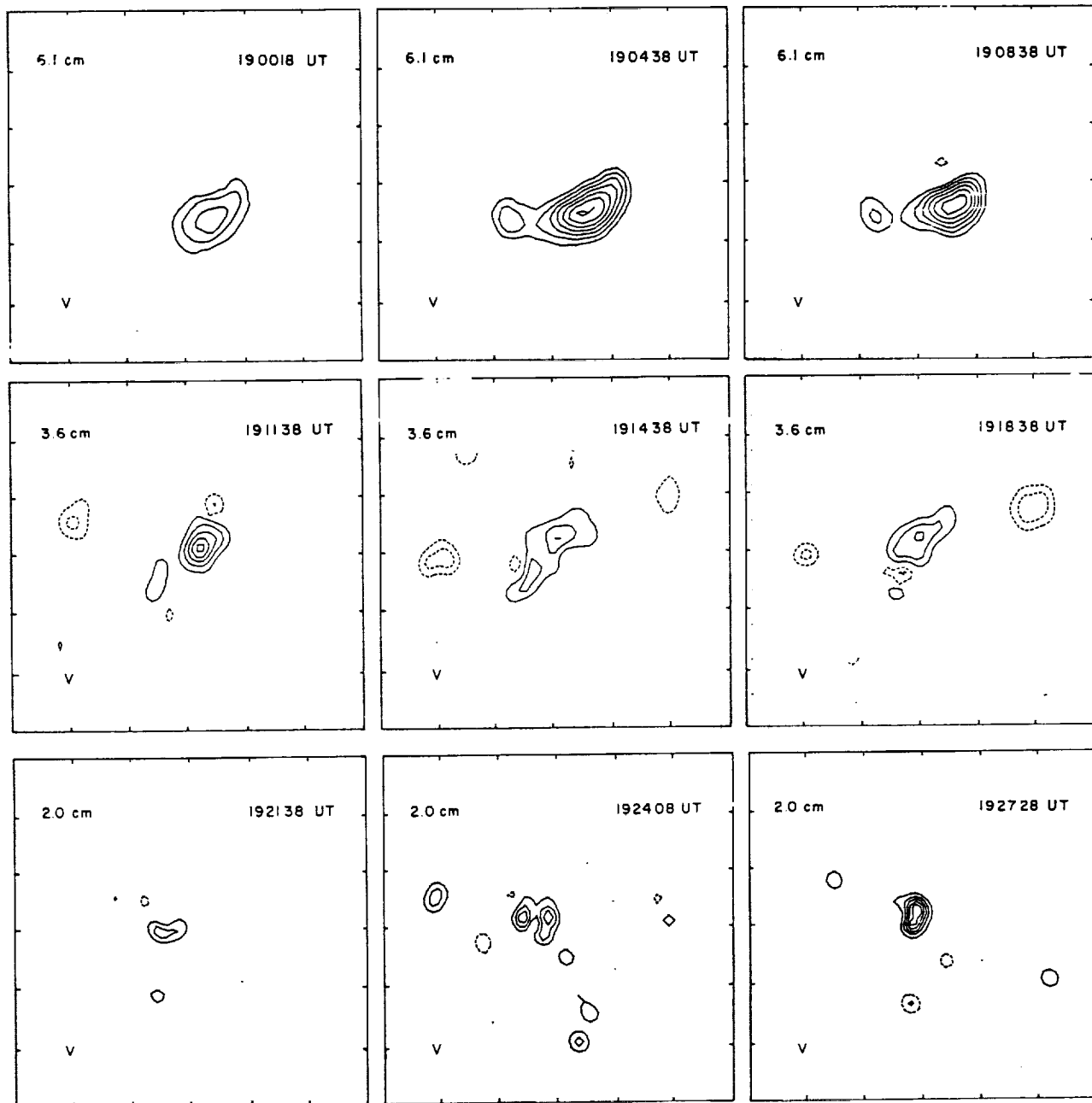


Fig. 4b

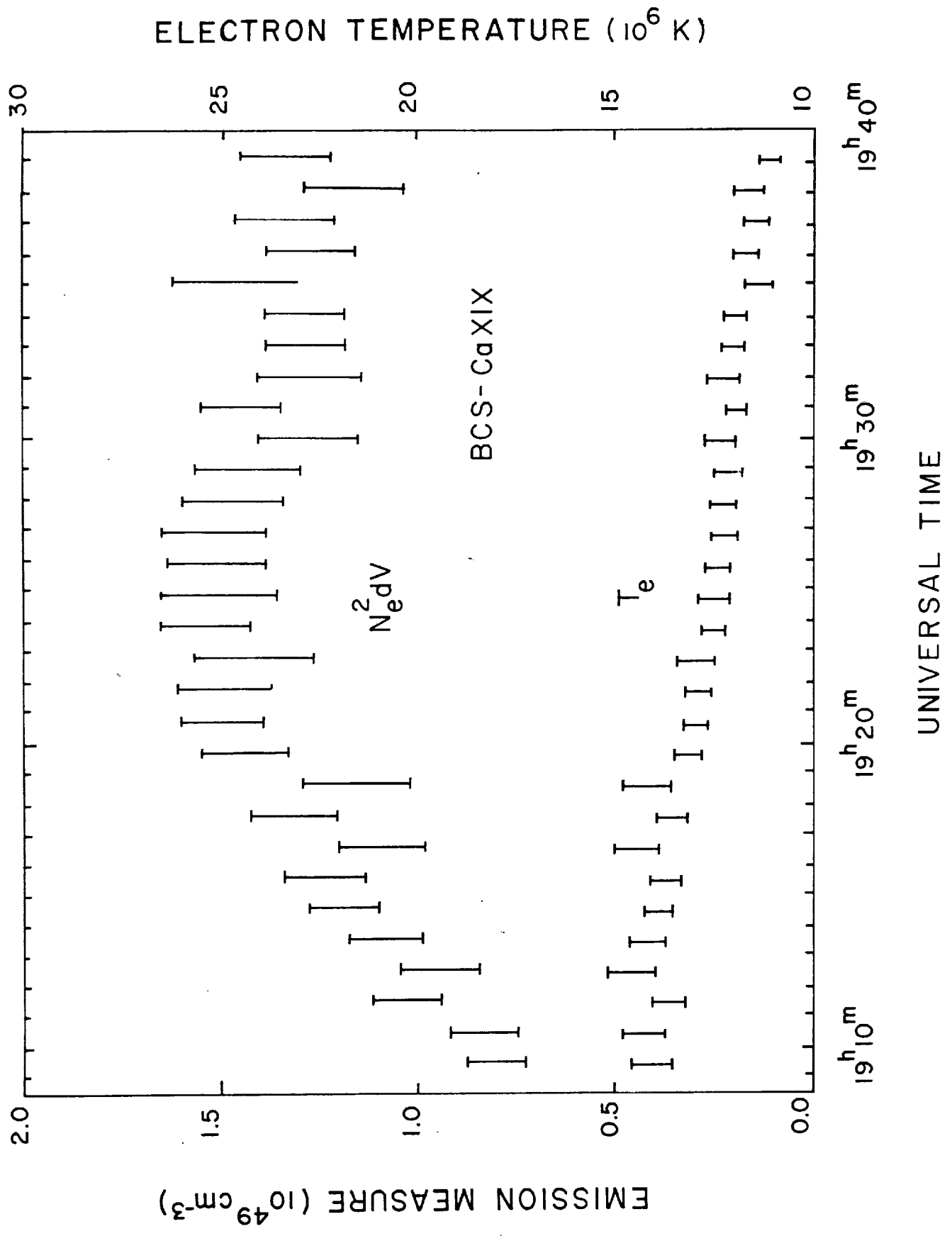


FIG. 5.

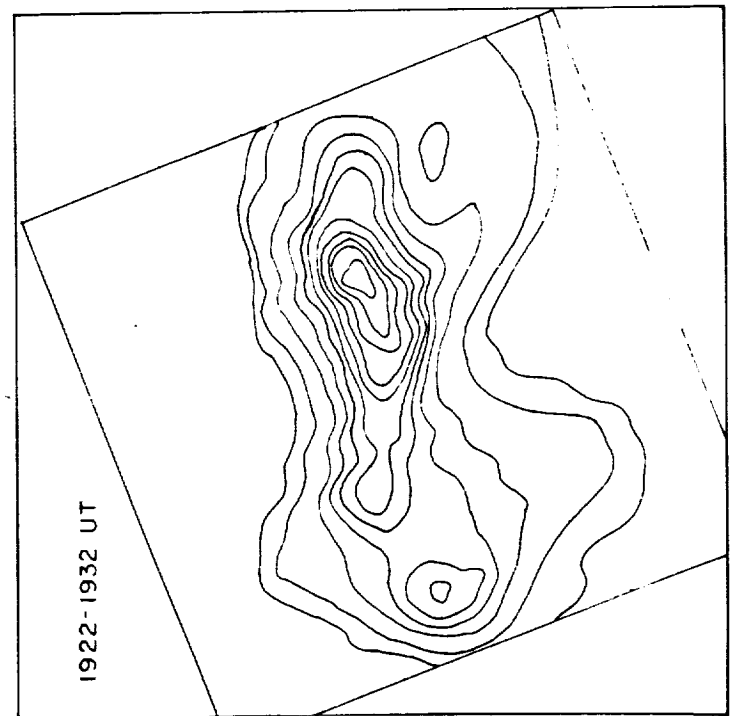
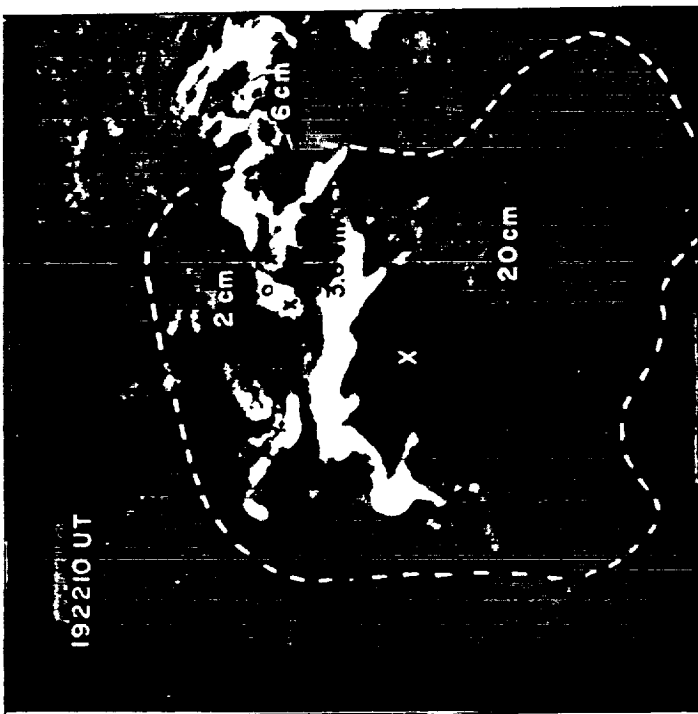
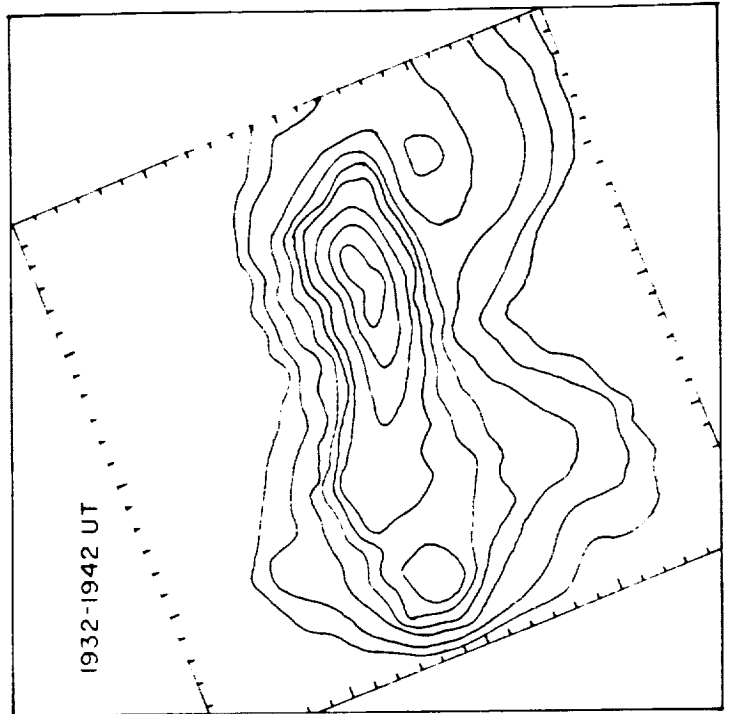
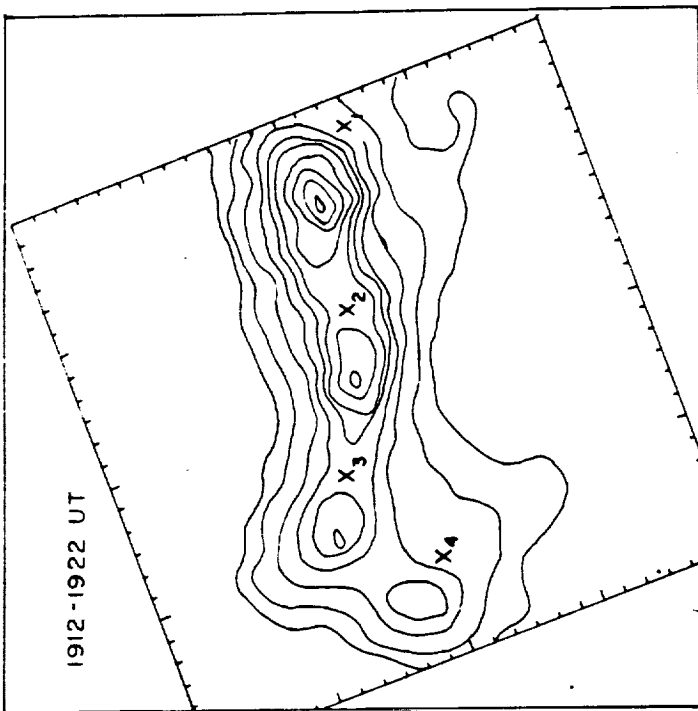
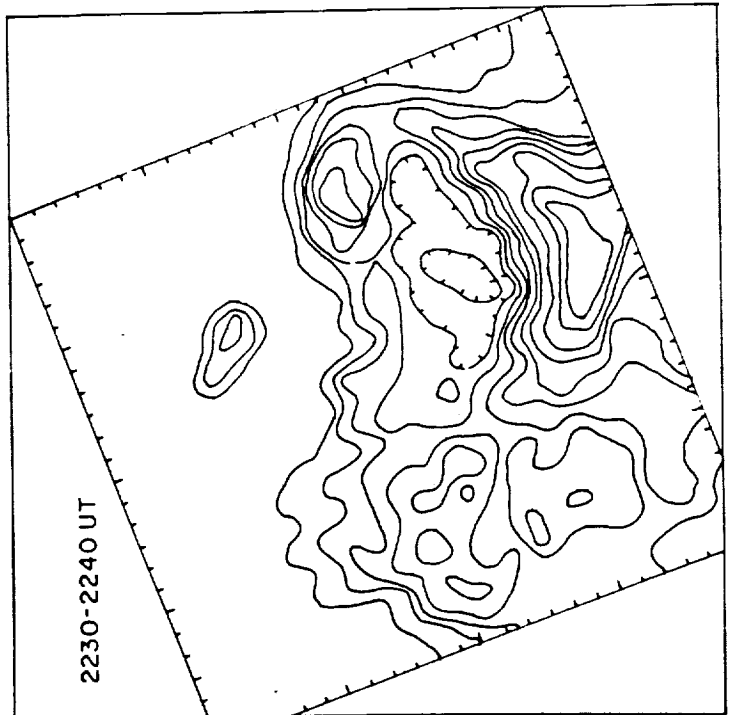
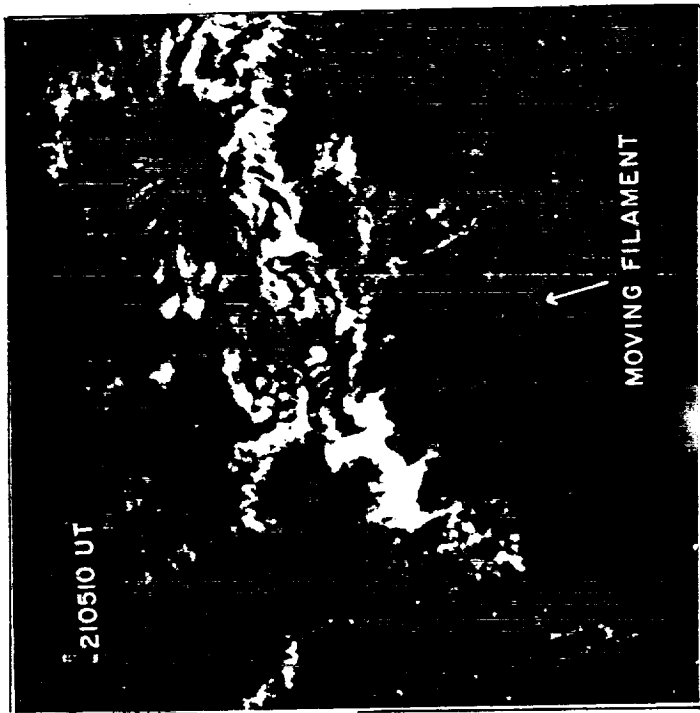
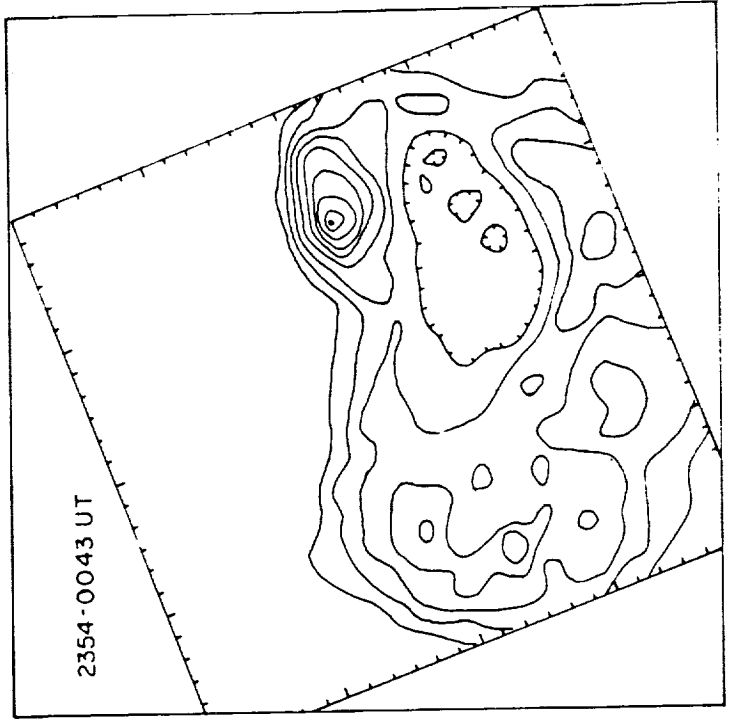
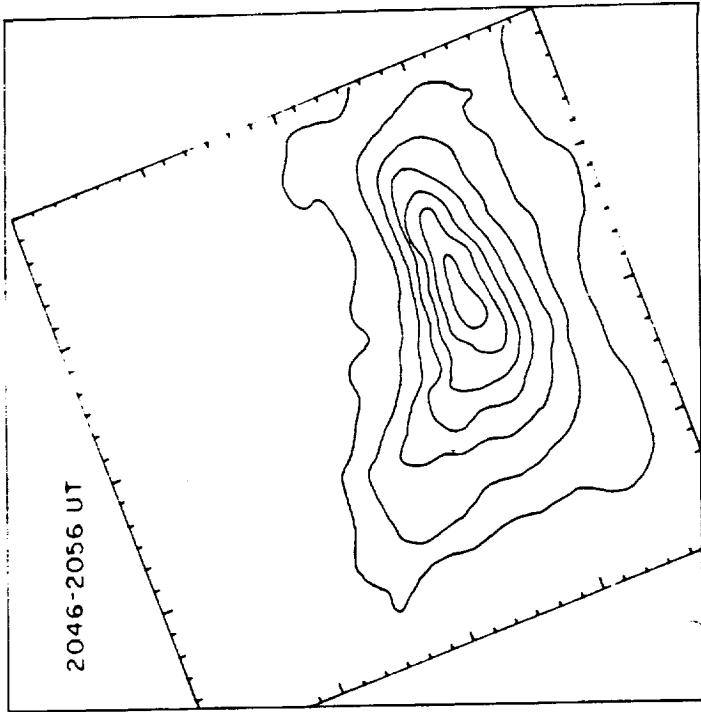


FIG. 6.



P. 7

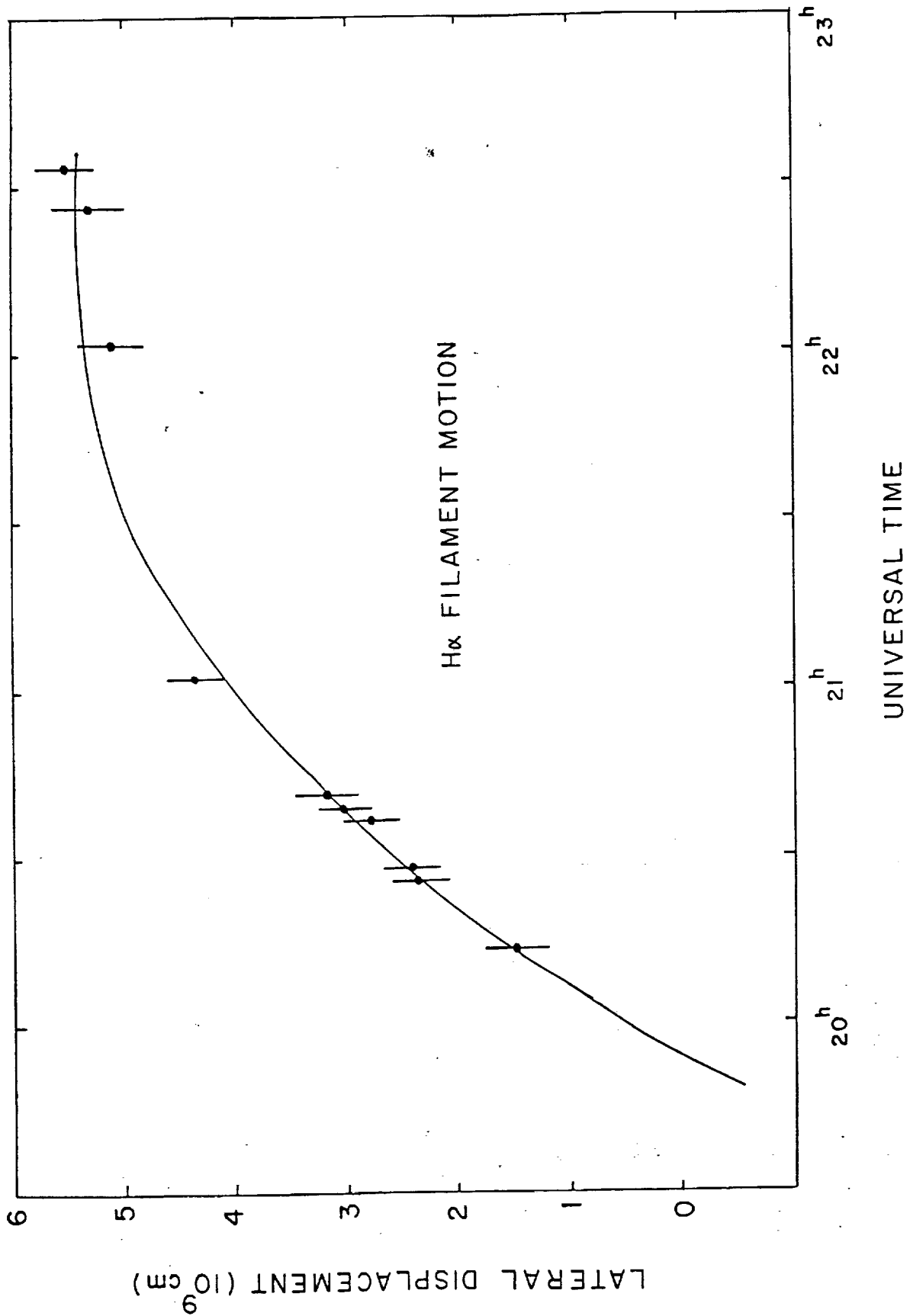


FIG. 8.

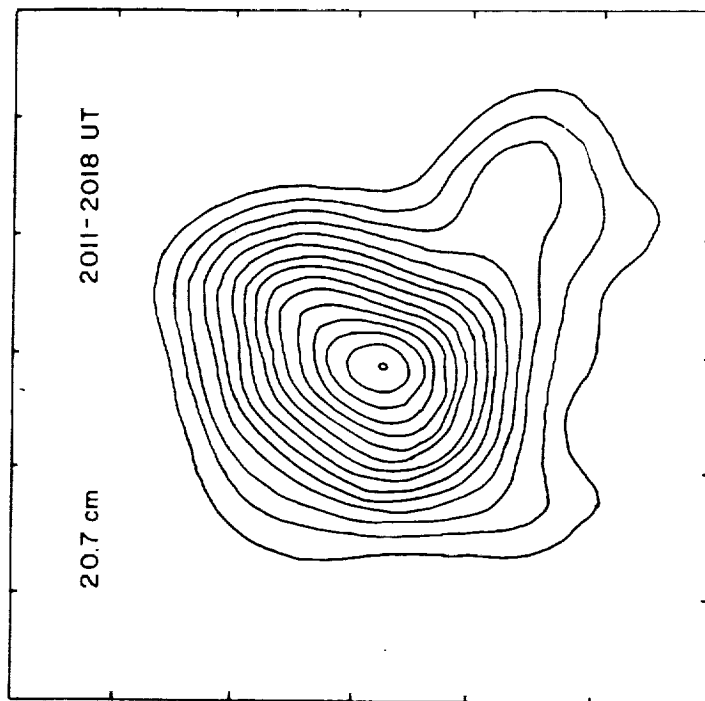
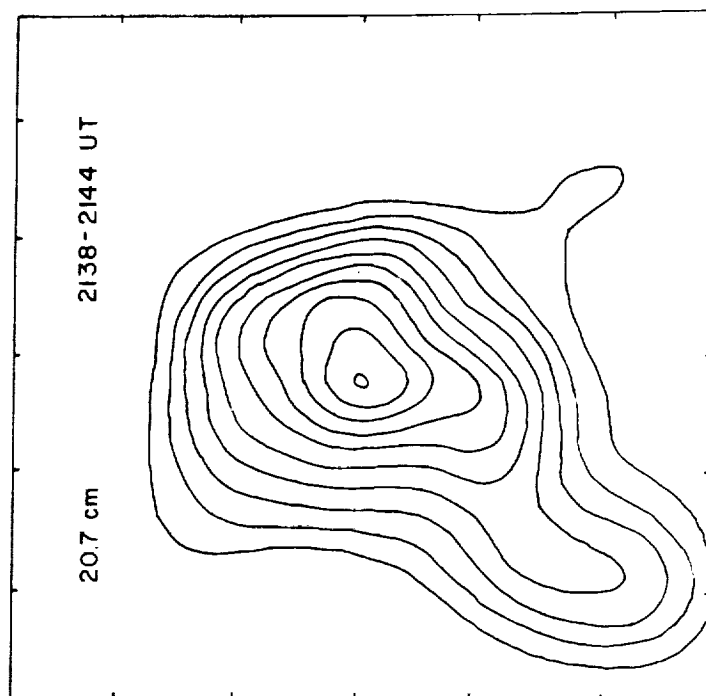
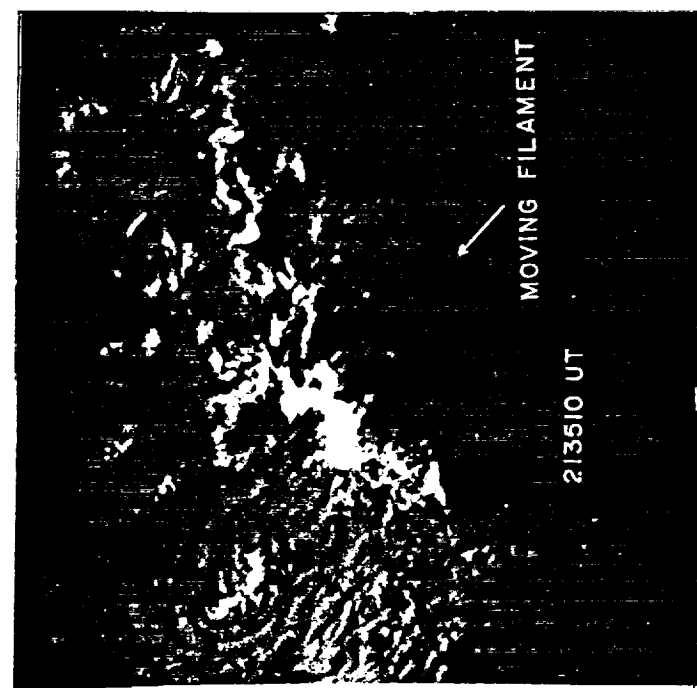


Fig. 9.

ORIGINAL PAGE IS
OF POOR QUALITY

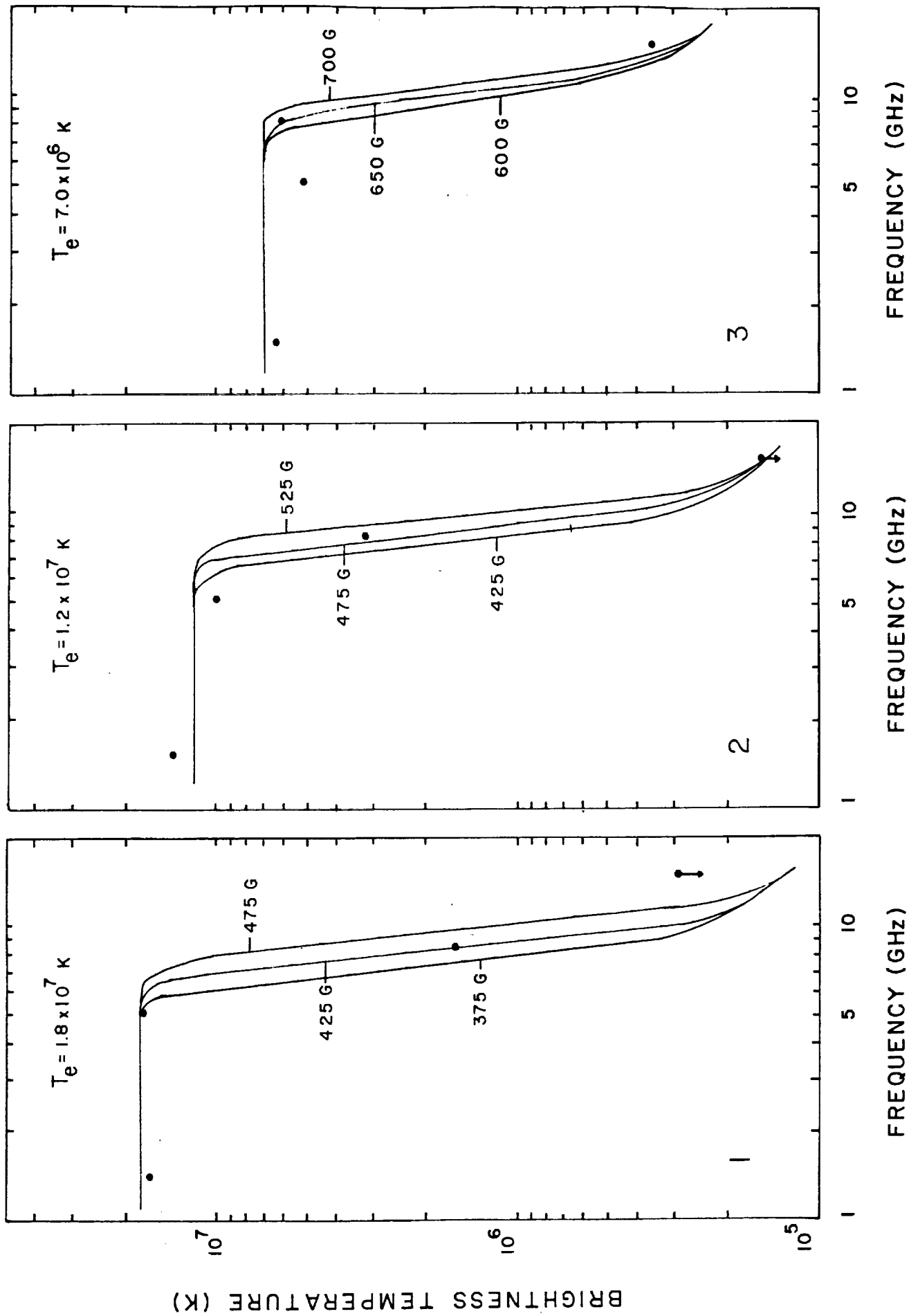


Fig. 10

v. CoMStOC IV: Multiwaveband
Observations of Sunspot and
Plage-Associated Coronal Emission

J.W. Brosius, R.F. Willson, G.D. Holman, and J.T. Schmelz

Abstract

We obtained simultaneous observations of an active region located near central meridian with the Very Large Array, the Solar Maximum Mission X-Ray Polychromator (XRP), and the Beijing Observatory magnetograph on 18 December 1987, during the Coronal Magnetic Structures Observing Campaign (CoMStOC). The active region contains a sunspot with a nearby region of opposite polarity, and a trailing area of plage. An asymmetric loop-like structure connects the south-east portion of the sunspot with the nearby region of opposite polarity. Both 6- and 20-cm emission lie along this structure, rather than over the sunspot, with higher frequency emission originating closer to the footpoint inside the sunspot. The 20-cm emission is due to a superposition of 2nd and 3rd harmonic gyroemission, where the field strength is 160 G – 300 G, while the 6 cm emission is due to 3rd harmonic gyroemission from a region where the magnetic field strength ranges from 547 G – 583 G. A high value of the Alfvén speed, $\sim 40,000$ km/sec, is obtained at the location of the 6-cm source, and somewhat lower values, $\sim 10,000 - 20,000$ km/sec, are obtained at the location of the 20-cm emission. At the location of the 6-cm source, the plasma temperature diminishes with height from 2.5×10^6 K at the height of ~ 5000 km to 1.3×10^6 K at $\sim 15,000$ km.

The X-ray data associated with the plage were used to predict the brightness temperature structure due to free-free emission in the 6- and 20-cm wavebands. The predicted 6-cm brightness temperature in the plage is low, consistent with our lack of observed 6-cm plage emission. The predicted 20-cm brightness temperature is consistent with that observed at 20 cm in the central portions of the plage; however, the observed high polarization requires the presence of cool, absorbing plasma overlying the hot plasma observed by XRP. The most likely model involves polarization inversion occurring in a quasi-transverse layer in the magnetic field above the plage.

1 Introduction

Observations of coronal loops with the VLA show that emission at different wavelengths originates at different heights, with longer wavelengths corresponding to higher levels. Synthesis maps at 20-cm wavelength, for example, outline loop-like structures that stretch across regions of opposite magnetic polarity (Lang, Willson, and Rayrole 1982) while observations at shorter wavelengths (2 and 6 cm) generally indicate sources that lie along the legs of loops (Alissandrakis and Kundu 1982; Lang and Willson 1982; Lang, Willson and Gaizauskas 1983; Strong, Alissandrakis and Kundu 1984). The 20-cm loops are similar to their X-ray counterparts, for the loops detected have similar sizes, shapes and brightness temperatures.

Although the X-ray emission is attributed to thermal bremsstrahlung and atomic line emission from hot ($T_e \sim 2 \times 10^6$ K) coronal plasma, the microwave emission may be due to either thermal bremsstrahlung or to gyroresonance emission of thermal electrons spiralling along coronal magnetic field lines. In order to determine which of these mechanisms is dominant, it is necessary to know the electron temperature and emission measure so that the brightness temperature at a particular wavelength can be calculated and compared with the observed values. Observations of soft X-ray spectral lines obtained by the X-ray Polychromator (XRP) aboard the Solar Maximum Mission (SMM) satellite, for example, can yield estimates of the electron temperature, emission measure, and density in quiescent loops. These parameters have been combined with plausible estimates for the magnetic scale height and the harmonic to show that the microwave-emitting plasma can be optically thick to either thermal bremsstrahlung or gyroresonance emission at 20-cm wavelength (Lang, Willson, and Rayrole 1982; McConnell and Kundu 1983; Shevgaonkar and Kundu 1984; Gary and Hurford 1987).

Direct comparison of 6-cm and soft X-ray emission has confirmed the importance of gyroresonance emission at this wavelength. However the brightest 6-cm sources are usually not associated with the brightest X-ray sources and the detailed correspondence between the radiation at these two wavelengths is poor (Schmahl et al. 1982; Webb et al. 1983). The reason for this is that 6-cm gyroresonance absorption typically occurs in the strong magnetic fields above sunspots, while the bremsstrahlung-emitting X-ray emission is usually most intense between regions of opposite magnetic polarity. The thermal bremsstrahlung is often too optically thin to be detected at 6 cm where gyroresonance radiation dominates.

More recent comparisons between simultaneous 20-cm and XRP images have shown better agreement between the emission at these wavelengths, although there are significant differences (Webb et al. 1987; Lang et al. 1987a,b; Nitta et al. 1990 - CoMStOC I). The 20-cm maps suggest the presence of both cool and hot plasmas

in different regions that are not detected in X-rays and there is X-ray emitting plasma that remains invisible at 20 cm. Although thermal bremsstrahlung could explain the bulk of the 20-cm emission, the detection of a line-like enhancement in the brightness spectrum at the apex of one coronal loop suggests the dominance of gyroresonance emission in that part of the loop (Willson 1985).

In this paper we describe the results of simultaneous VLA and XRP observations of a solar active region obtained during the Coronal Magnetic Structures Observing Campaign (CoMStOC). The primary objective of CoMStOC was to obtain quantitative information about the plasma and magnetic field structure above solar active regions by comparing the microwave and soft X-ray data with theoretical models (Holman and Kundu 1985, Brosius and Holman 1988, Brosius and Holman 1989) and magnetic field measurements. In Section 2 we present and discuss the coordinated observations: VLA observations at four different frequencies in each of the 6- and 20-cm wavebands, simultaneous XRP spectral and image data, and a simultaneous photospheric longitudinal magnetogram from Beijing Observatory. In Section 3 we further analyze and interpret the VLA, XRP, and magnetograph observations in terms of physical models. In Section 4 we summarize and discuss our conclusions and their implications.

2 Observations and Data Analysis

2.1 VLA Observations

The VLA (B configuration) was used to observe the active region AR 4906 (S34.5, E17.7 at 1300 UT) between 1440 UT and 2300 UT on 18 December 1987. The entire array of 27 antennas was used at four frequencies in the 20-cm band (1375, 1420, 1550, and 1665 MHz) and four in the 6 cm band (4600, 4700, 4800, and 4900 MHz) with bandwidths of 12.5 MHz. The half-power beamwidth of the individual antennas ranged between 29' and 34'.7 at 20 cm, with synthesized beamwidths of 4". At 6 cm, the primary beamwidths ranged from 9'.7 to 10'.4, with synthesized beamwidths of 1". One pair of frequencies was observed for about 5 minutes, so that all eight could be observed in about twenty minutes. The data were sampled every 10 s and calibrated using observations of PKS1655+078. Corrections were made for the difference in the signals from high temperature noise diodes located on four of the antennas. The temperatures of these sources were measured across each band prior to the observations. The data were edited and calibrated with the standard solar procedures at the VLA, and used to make synthesis maps of both the total intensity, I , and Stokes parameter, V , during the 8.5 hour interval at all eight frequencies. Examination of the fringe visibility on several baselines indicated

no variations that could be attributed to solar bursts or interference.

Individual maps at the four 6-cm frequencies show no discernible differences in position, structure, or brightness temperature. Therefore, in Figure 1b, we show a frequency-averaged I map at 6 cm. The emission is concentrated in an elliptical source of about $16'' \times 28''$ in size (half-intensity level) which is located $\sim 20''$ southeast of the center of the dominant leading sunspot. Its peak brightness temperature is $T_B = 2.5 \times 10^6$ K and it is $\sim 60\%$ right-hand circularly polarized near the long edges of the source (see Fig. 6). The sense of circular polarization coincides with the positive polarity of the spot. In Section 3 we show by both modeling and potential field extrapolation that the 6-cm emission is most likely attributable to 3rd harmonic gyroresonance emission. The polarization arises because the extraordinary mode is more optically thick than the ordinary mode at the edges of the source.

At 20 cm there are two main components (Fig. 1a): source A is located $25''$ southeast of the 6-cm emission, and source B is located $2'.5$ to the east, in the plage. The peak brightness temperatures of sources A and B are, respectively, $\sim 2 \times 10^6$ K and $\sim 1.4 \times 10^6$ K. Source B is $\sim 50\%$ left-hand circularly polarized while source A has no detectable polarization to a limit of 10-20%. Individual maps at the four 20-cm frequencies (Fig. 2) show that there is a systematic difference in the structure of the 20-cm emission at these frequencies. For example, a third component (C), located to the north of component A, becomes less intense with increasing frequency, as component B decreases in size. These systematic trends are consistent with the absence of components B and C at 6 cm. In addition, the more sharply defined peak of source A systematically shifts by $\sim 10''$ in the direction of the 6 cm source from 1375 MHz to 1665 MHz. This is a manifestation of gyroresonance as the dominant emission mechanism: as the observing frequency changes, the magnetic field strength required to stimulate gyroresonance emission also changes; the appropriate field strength is at a slightly different location, resulting in a shift of the radio source with observing frequency.

In the B-configuration VLA, the fringe spacings range between $\sim 4''.5$ and $225''$ at 20 cm and $1''.3$ and $66''$ at 6 cm, so that extended, low brightness structures will be resolved out. Since the standard CLEAN algorithms used to produce the maps presented here are not best suited to recovering such extended emission, we also used the Maximum Entropy Method (Cornwell 1986; Bastian 1988??) to produce maps at all wavelengths. This allows us to determine whether larger-scale ($\theta \geq 4'$ at 20 cm and $\theta \geq 1'$ at 6 cm) features were in fact present. This method uses the fringe visibility data on all baselines, together with the CLEANed maps as default images, to restore any "missing" flux and large-scale structure that has been resolved out. The results of our analyses, however, showed no significant changes in structure or brightness temperature ($\leq 15\%$) between the MEM and CLEANed maps. The only discernible difference was that the MEM maps tended to be slightly wider

and smoother, so that the systematic shifts in the maxima of the 20 cm emission were less obvious. We did not find any evidence for extended, low-brightness 6 cm emission in the region of the 20 cm plage-associated source with any brightness temperature $\geq 0.4 \times 10^6$ K. In CoMStOC I (Nitta et al. 1991), for example, a significant difference was observed between the CLEANED and MEM images for a 6-cm source on the limb. Because there were no significant differences in the results from the two methods for our data, and because of the uncertainty in comparing the MEM results with, for example, the fluxes from single-dish flux measurements (T. Bastian, private communication) we have decided to use the CLEANed maps in the following analyses.

2.2 XRP Observations

The XRP Flat Crystal Spectrometer (Acton et al. 1980), collimated to 14" FWHM, can build images by rastering over a portion of a 4' \times 4' area with a minimum pixel spacing of 5", or scan a series of spectral lines at one or more spatial locations. XRP mapped AR 4906 (Figure 1c) in the Fe XVII resonance line at 15.01 Å, the most sensitive line at active region temperatures. This map shows two peaks of emission: the weaker source on the right (microwave source A) lies between the sunspot and a nearby region of opposite polarity; the stronger source on the left (microwave source B) is associated with the trailing area of plage.

A spectroscopic scan (between 13 Å and 19 Å) was done at the brightest Fe XVII pixel (marked with a "+" in Fig. 1c) in the SMM orbit beginning at 0343 UT on 1987 December 18. Analysis of these spectral data follows the procedure outlined in CoMStOC I. The emissivity calculations from Mewe, Gronenschild, and van den Oord (1985) and the coronal abundances of Meyer (1985) were used to calculate the electron temperatures from five selected line flux ratios. These ratios vary by a factor of 10 or more in the range $2\text{-}4 \times 10^6$ K; this steep gradient makes a ratio sensitive to small changes in temperature and relatively insensitive to systematic uncertainties such as relative flux calibrations, elemental abundance variations, or errors in the atomic parameters. (See CoMStOC I for a detailed discussion of these calculations and possible sources of error.) These values and their uncertainties (statistical only) are listed in Table 1. The uncertainties in the weighted mean include systematic as well as statistical uncertainties. The column emission measure corresponding to each temperature in Table 1 was computed using the O VIII line flux, which has an emissivity curve with a broad, flat response in the range of interest; therefore, the emission measure determined using this line is relatively insensitive to changes in temperature. Once again, the uncertainties on the individual entries are statistical only (dominated by the uncertainty in the O VIII line flux) while the weighted mean includes systematic as well as statistical uncertainties.

XRP mapped AR 4906 at the peaks of five bright resonance lines—O VIII, Ne IX, Fe XVII, Mg XI, and Fe XVIII—in the SMM orbit beginning at 1134 UT on 1987 December 18. Ratios of these images can be used to determine the spatial structure of the plasma parameters across the region (as was done in CoMStOC I). AR 4906 was relatively weak, however, and, although Fe XVII was observed throughout the region, significant counts were observed in only one other line, O VIII, and only near the brightest, central areas of the plage. The O VIII/Fe XVII flux ratio varies by only a factor of about five in the temperature range $2\text{--}4 \times 10^6$ K, making it more sensitive to errors in flux calibration, elemental abundance, and atomic parameters than the line ratios available at the brightest Fe XVII pixel. Even though the map data and spectroscopic scan data were taken 8 hours apart, the electron temperature and emission measure obtained with the O VIII/Fe XVII flux ratio from the spectroscopic scan data at the location of the Fe XVII peak flux are equal to the electron temperature and emission measure obtained with the O VIII/Fe XVII flux ratio from the map data at the same location. This indicates that the active region was stable during our observation period. Also, GOES soft X-ray data show no significant activity at or between the times of these observations.

As was found in CoMStOC I, our analysis of the spectroscopic scan data leads us to conclude that the Fe XVII emissivity is inconsistent with that of the other lines, here by a factor of ~ 2.75 . This issue is discussed in greater detail in CoMStOC I and CoMStOC II (Schmelz et al. 1991). This factor is somewhat higher than in CoMStOC I, where it was found to be in the range 2.0 – 2.5. The difference is within the uncertainty of the measurements, however. Here we apply the Fe XVII emissivity correction factor of 2.75 obtained with the spectroscopic scan data to the emission line map data, in order to obtain maps of the temperature and emission measure from the O VIII/Fe XVII map flux ratios (Figures 1e and 1f). Predicted microwave brightness temperatures at 20 cm and 6 cm are also shown (Figures 1g and 1h) and discussed further in Section 3.3. These maps were smoothed with a 3×3 boxcar to remove statistical noise, and the calculations were done only for those pixels with significant count rates, $\geq 3 \sigma$, in both lines.

It is difficult to obtain a meaningful, quantitative estimate of the error in the map temperatures and emission measures other than to note that they are expected to be larger than at the Fe XVII peak (Table 1). We can look at their sensitivity to the Fe XVII correction factor, however. If no correction factor had been applied, at the Fe XVII peak the O VIII/Fe XVII ratio would have given a temperature of 1.97×10^6 K and log emission measure of 29.30. For a correction factor of 2.0, the temperature and log emission measure are found to be 2.55×10^6 K and 28.90. As will be discussed in Section 3.3, these variations have only a small effect upon the predicted brightness temperature at 20 cm, but a significant effect upon the predicted brightness temperature at 6 cm.

2.3 Beijing Magnetogram

Figure 1d shows a photospheric longitudinal magnetogram of AR 4906 on 18 December 1987 from the Beijing Observatory (courtesy of H. Zhang and H. Wang). The maximum line-of-sight umbral magnetic field strength is ~ 2600 G with a noise level of ~ 100 G. Comparison of the umbral field strength with data taken at the Mt. Wilson Observatory shows good agreement, indicating that the magnetogram did not saturate. (Saturation is frequently a problem with Kitt Peak magnetograms.) Just left (east) of the sunspot is a nearby region of opposite polarity with a maximum, inward directed field of ~ 790 G. Farther to the left is the trailing plage with a maximum field of ~ 930 G. The numbers on the x- and y-axes represent the distance from disk center on the plane of the sky in units of 10,000 km. (One arcsec is equivalent to 725 km.) In these units the solar radius is 69.6. Because the active region was so close to disk center, the approximate sizes of or distances between various active region features can simply be read off of the figure.

Figure 1d also shows field lines obtained with the potential field extrapolation code developed by Sakurai (1982); this code solves Laplace's equation to calculate current-free magnetic field lines using the line-of-sight photospheric fields as boundary conditions. Most of the field lines emanating from the sunspot terminate in regions of very weak opposite polarity; however, a cluster of lines in the lower left portion of the spot terminates in and around the nearby, relatively strong region of opposite polarity. These field lines outline a loop-like structure (or bundle of loops) which is quite asymmetric. For several representative field lines, we list pairs of total extrapolated photospheric magnetic field strengths (in Gauss), where the first element in the pair corresponds to the footpoint inside the sunspot and the second corresponds to the footpoint in or around the nearby region of opposite polarity: (1800,33), (1500,280), (1400,550). The corresponding photospheric foot point separations for the above field lines are 5.06, 4.64, and 3.80×10^4 km.

3 Results

3.1 Analysis of the Sunspot

An overlay of the intensity maps in the 20 cm waveband (Fig. 2) with the photospheric longitudinal magnetogram reveals that the 20 cm intensity contours of source A do not cover the entire sunspot. The potential field extrapolations (see below and Fig. 3) show that magnetic fields which are high enough to produce 2nd harmonic gyroemission at all four frequencies in the 20 cm waveband (245 - 297 G) occur at heights of 5000 - 15000 km, where coronal temperatures ($> 10^6$

K) and densities ($\sim 10^9 \text{ cm}^{-3}$) are expected to persist (Papagiannis and Kogut 1975, Hildebrandt et al. 1987). Indeed, 2nd harmonic gyroemission is expected to emanate from the portion of the sunspot for which the observed brightness temperature is less than the lowest observed intensity contour ($5.3 \times 10^5 \text{ K}$). Ways to obtain brightness temperatures this low from the 2nd harmonic gyroemission mechanism are (i) the density in the emission region is extremely low ($< 10^5 \text{ cm}^{-3}$ for a $2 \times 10^6 \text{ K}$ plasma), (ii) the temperature in the emission region is less than $5.3 \times 10^5 \text{ K}$, or (iii) both the temperature and the density in the emission region are low. To obtain a density less than 10^5 cm^{-3} in the corona over a large fraction ($\sim 1/3$) of a sunspot area seems unlikely, but it cannot be ruled out. Thus we find that a lower temperature and/or density exists over a portion of both the sunspot umbra and penumbra on the side of the sunspot away from the center of AR 4906 than on the side of the sunspot toward the center of AR 4906. This is consistent with Gary and Hurford (1987), who concluded that the plasma temperature and/or density are lower on the sides of sunspots away from the centers of active regions, and with Strong, Alissandrakis, and Kundu (1984), who concluded that low temperature plasma was present over the umbra of a sunspot which they observed with the Westerbork Synthesis Radio Telescope.

We modified the Sakurai code to obtain the total extrapolated magnetic field strength in a grid of locations all at the same specified height above the photosphere. We used the high resolution Beijing magnetogram (discarding a portion of the magnetogram which consists entirely of noise) to calculate the extrapolated field in a 64×34 grid with a spacing of 3500 km ($4''.8$ in the plane of the sky) in each of the x and y directions. The resolution of the magnetogram is 512×512 , with a pixel spacing of 526 km ($0''.73$) in x and 370 km ($0''.51$) in y . We selected such a coarse grid in order to maintain a reasonable computation time. This grid spacing is comparable to the VLA resolution at 20 cm and is better than the XRP resolution.

Contour maps of the extrapolated coronal potential field at heights of 0 , 5000 , 10000 , and 15000 km above the photosphere are shown in Figure 3. The physical dimensions of the extrapolated maps are smaller than the dimensions of the Beijing magnetogram because we focused on the portion of the magnetogram which contains features visible in radio and/or X-rays. At the photosphere, the maximum longitudinal field strength in the sunspot is $B_z \text{ max} = 2627 \text{ G}$, and the maximum total field strength is $B \text{ max} = 2732 \text{ G}$. These two parameters are not cospatial: the location of $B \text{ max}$ depends only upon the total magnetic field strength, but the location of $B_z \text{ max}$ depends upon both the total magnetic field strength and the angle between the curved sunspot field lines and the line of sight. At a height of 5000 km above the photosphere, the sunspot has $B_z \text{ max} = 1165 \text{ G}$ and $B \text{ max} = 1220 \text{ G}$. At 10000 km , $B_z \text{ max} = 645 \text{ G}$ and $B \text{ max} = 683 \text{ G}$, and at 15000 km , $B_z \text{ max} = 405 \text{ G}$ and $B \text{ max} = 430 \text{ G}$. The vertical gradient of the total magnetic field strength near the center of the umbra for heights between 0 and 5000 km above the photosphere

is ~ 0.30 G/km. This is less than but comparable to the gradient of $0.41 - 0.67$ G/km obtained by Henze et al. (1982) for the longitudinal magnetic field in the transition region and photosphere of a sunspot umbra. We also find that the average horizontal gradient in the total photospheric magnetic field strength is ~ 0.11 G/km. Knowing the height variation of the maximum total extrapolated sunspot field, and assuming that this field can be described by that of a vertically oriented point dipole buried below the photosphere, we obtain a depth of 1.76×10^4 km and a dipole moment of 7.45×10^{15} G-km³.

With the depth and moment obtained above for the vertically oriented point dipole buried below the photosphere, we calculated contours of constant magnetic field strength which extend well into the corona. Figure 4(a) shows magnetic field contours corresponding to the 1st through 5th harmonics of 1665 MHz, and (b) shows contours for the same harmonics of 4900 MHz. Using these figures, along with Figure 3 (showing extrapolated contours at various heights), we compared the sunspot field due to the single point dipole with the field calculated with the Sakurai code. If the extrapolated sunspot potential field can be well approximated by that of a simple point dipole, it simplifies the calculation of microwave emission from sunspot models. Specifically, we compared the radii in the x-direction of several field strength contours in the point dipole field with the radii of these same contours in the four extrapolated maps of Figure 3. At these four heights, the contours are equal to better than 10% for magnetic fields $\gtrsim 300$ G. The shape of the field contours in the extrapolated maps become distorted for fields less than ~ 300 G, so comparison becomes difficult. The radii at which the distortion effects become significant are ~ 27000 km at the photosphere, ~ 26000 km at a height of 5000 km, ~ 22000 km at 10000 km, and ~ 17000 km at 15000 km. The potential field of the vertically oriented point dipole buried below the photosphere is a good approximation of the extrapolated potential field within this three-dimensional structure.

The extrapolated potential field deviates from that of the simple point dipole outside of the region obtained above because of the presence of other nearby strong fields which distort the simple dipole field. As far as modeling microwave emission from a sunspot is concerned, however, the simple point dipole is a reasonable approximation for a large part of the sunspot microwave emission volume. Using it, along with the model sunspot atmosphere described in Brosius and Holman (1989), we obtained theoretical I and V maps for frequencies of 1665 MHz (Fig. 5a) and 4900 MHz (Fig. 5b). The failure of this simple model to reproduce the sunspot microwave structure provides insight into the temperature, density, and field structure above the sunspot. Specifically, it supports our earlier contention that the coronal temperature and/or density must be relatively low over large portions of the sunspot, and it also suggests that we need microwave emission from some coronal structure other than a simple sunspot in order to explain the observed 6 and 20 cm I and V structure.

3.2 Analysis of the Loop Structure Connecting the Sunspot with the Nearby Region of Opposite Polarity

An overlay of the intensity maps in the 20-cm waveband (Fig. 2) with the magnetogram field lines (Fig. 1d) reveals that the peak of source A in all four of the 20-cm intensity maps lies along the loop structure joining the sunspot with the nearby region of opposite polarity. Figure 6 shows the locations of the centers of the 20-cm peak intensity contours, along with the 6-cm I and V sources, on the magnetogram. The higher the frequency, the farther down the leg of the loop (on the side of the sunspot) the intensity peak occurs. The separation of the intensity peaks at 1375 and 1665 MHz is ~ 10 arcsec. Compared with the synthesized half-power beamwidth of $4''$, this shift is real. Assuming the emission in the 20 cm peaks to be dominated by 2nd harmonic gyroemission, we estimate a magnetic field gradient ~ 0.0068 G/km along the loop in the plane of the sky. Assuming 3rd harmonic, the field gradient is ~ 0.0047 G/km. Both of these gradients are factors of 2 to 3 less than the gradients calculated along the individual extrapolated field lines which pass through the 20-cm emission peaks. Furthermore, the diameters of the peak contours for the four frequencies in the 20-cm waveband range from $\sim 12''$ to $\sim 23''$, and we find that, where the extrapolated field lines overlap these 20-cm contours, magnetic field strengths appropriate for both 2nd and 3rd harmonic gyroemission occur. Thus, based upon the potential field extrapolation, the peak emission region (the area within the peak contour) at each frequency in the 20-cm waveband is comprised of a superposition of 2nd and 3rd harmonic gyroemission arising from the loop structure joining the sunspot with the nearby region of opposite polarity. This implies magnetic field strengths ranging from 160 G to 300 G in the 20-cm source region.

An overlay of the averaged intensity map at 6 cm (Fig. 1b) with the magnetogram field lines (Fig. 1d) shows that the 6-cm emission is also associated with the loop structure joining the sunspot with the nearby region of opposite polarity. (Again, see Fig. 6.) This emission originates farther down the leg of the loop (on the side toward the sunspot) than do any of the 20-cm emission peaks. This is expected since much higher fields are required for gyroresonance emission at 6 cm than at 20 cm. The polarization structure shows two V sources – one on either side of the I source – such that the I and V sources all lie roughly along the length of the loop. The polarization is $\sim 60\%$ close to the edges of the I source. Such structure appears in the microwave loop models of Holman and Kundu (1985). This polarization structure arises from the gyroresonance emission mechanism, since the ordinary mode of a given harmonic becomes optically thin toward the harmonic edge more rapidly than does the extraordinary mode. Assuming the emission in the 6 cm peak to be dominated by 3rd harmonic gyroemission (see next paragraph), we estimate an average magnetic field gradient (between the 6- and 20-cm source regions) ~ 0.020

G/km along the loop in the plane of the sky. This is less than but comparable to the average field gradient ~ 0.028 G/km calculated along the individual extrapolated field lines which pass through the 6- and 20-cm emission peaks.

In principle, the harmonic number of the 6-cm emission can be determined by comparing the observations with models. We reproduced the observed 6-cm I and V sources (see Fig. 7) by assuming that the emission arises from a simple dipole loop model. The height of the loop apex (16000 km), the footpoint separation (50000 km), and the loop thickness at the apex (7700 km) were all estimated from the extrapolated potential field lines. While our simple dipole loop model does not accurately portray the asymmetry of the extrapolated field lines, we are only interested in reproducing the emission from one leg of the loop, so the magnetic field structure of the loop elsewhere is of little consequence. The loop temperature, taken to be constant throughout the loop, is equal to the 6-cm peak brightness temperature of 2.5×10^6 K. (No significant polarization is observed at the location of the 6 cm brightness temperature peak, indicating that both the X- and O-modes are fully thick and, hence, that their respective brightness temperatures are equal to the electron temperature.) The density is selected so that the brightness temperature calculated for the portion of the loop away from the desired 6-cm source remains less than the lowest observed 6-cm brightness temperature contour, as observed. Both thermal bremsstrahlung and thermal gyroemission were included in the calculations and theoretical I and V maps at 6 cm were calculated for cases in which (i) the 2nd harmonic, (ii) the 3rd harmonic, and (iii) the 4th harmonic emission region was in the footpoint at a height of ~ 5000 km. The 6-cm I and V structure and magnitude could be produced with both the 2nd and 3rd harmonic, but could not be produced with the 4th. For 2nd harmonic, the density required is low: $\sim 5 \times 10^6$ cm $^{-3}$. If the density were higher, the overlying 3rd harmonic emission region will yield too high a brightness temperature from a large area of the loop and would destroy the desired V structure. For 3rd harmonic, the density is $\sim 10^9$ cm $^{-3}$. This is reasonable in light of the sunspot atmosphere model of Hildebrandt et al. (1987) where a density of $\sim 8 \times 10^8$ cm $^{-3}$ occurs ~ 5000 km above the photosphere. The emission measure for the model loop with density $\sim 10^9$ cm $^{-3}$ is $\sim 10^{27}$ cm $^{-5}$, less than but comparable to the value of $\sim 10^{28}$ cm $^{-5}$ estimated from the very weak Fe XVII flux measured by XRP at the location of the 6-cm source (and assuming $T_e = 2.5 \times 10^6$ K). The corresponding value for the model loop with density $\sim 5 \times 10^6$ cm $^{-3}$ is $\sim 2 \times 10^{22}$ cm $^{-5}$, substantially less than the observed value. Thus our model, combined with XRP observations, indicates that the observed 6-cm I and V structure is indeed due to 3rd harmonic gyroemission. Accounting for the four frequencies at which the 6-cm emission was observed, this translates into magnetic field strengths ranging from 547 G to 583 G. At the location of the 6-cm source the potential field extrapolation yields a field ~ 600 G at a height ~ 5000 km, consistent with our deduced values.

Our magnetic field and density results can be used to estimate the Alfvén speed and its variation within the loop. The magnetic field strength required for the highest frequency source in the 6-cm band, 583 G, gives an electron gyrofrequency of 1.63 GHz. The 6-cm source model is reasonably consistent with the observations when the electron density is between $5 \times 10^8 \text{ cm}^{-3}$ and $2 \times 10^9 \text{ cm}^{-3}$, giving a plasma frequency of 0.2 – 0.4 GHz. Hence, the ratio of the gyrofrequency to the plasma frequency is found to be in the range 4 – 8 and the Alfvén speed falls within the 28,000 km/sec – 57,000 km/sec range. (The estimated density of $1 \times 10^9 \text{ cm}^{-3}$ gives an Alfvén speed of 40,000 km/sec.) The 160 G – 300 G range for the magnetic field strength in the 20-cm source region gives an electron gyrofrequency ranging from 0.45 GHz to 0.84 GHz. The electron density is not as well established. With an estimated value of $1 \times 10^9 \text{ cm}^{-3}$, the ratio of the gyrofrequency to the plasma frequency ranges from 1.5 to 3, and the Alfvén speed ranges from 10,000 km/sec to 20,000 km/sec. Hence, the Alfvén speed in this coronal loop is highest near the sunspot and decreases away from the sunspot toward the apex of the loop.

At the location of the 6-cm peak, where the brightness temperature is $\sim 2.5 \times 10^6$ K, the 20-cm brightness temperature is lower, $\sim 1.3 \times 10^6$ K. Because lower frequencies require lower fields for the thermal gyroemission mechanism and, because the magnetic field diminishes with increasing height in the atmosphere, the 20-cm emission must originate higher in the atmosphere than the 6-cm emission. Indeed, fields high enough for 20-cm 2nd harmonic gyroemission (245 - 297 G) occur over the 6-cm source at heights in excess of 15,000 km. In order to obtain a brightness temperature $\sim 1.3 \times 10^6$ K from 2nd harmonic gyroresonance emission, we require that either (i) the 2nd harmonic is optically thin in a plasma where the temperature is greater than 1.3×10^6 K, or (ii) the 2nd harmonic is optically thick in a plasma where the temperature is equal to 1.3×10^6 K. If the 2nd harmonic gyroemission region is optically thin, one can expect to observe polarization because the ordinary mode is less optically thick than the extraordinary mode. This is not observed in the 20-cm emission at the 6-cm source. We conclude that the observed 20-cm brightness temperature of $\sim 1.3 \times 10^6$ K is due to optically thick 2nd harmonic gyroemission in a region where $T_e \sim 1.3 \times 10^6$ K. This means that the plasma temperature at the height of formation of the 6-cm emission is higher than the plasma temperature at the height of formation of the 20-cm emission. Thus, at the location of the 6-cm intensity peak, the plasma temperature diminishes with height. Note, however, that this lower temperature plasma is outside and above (higher up than) the loop structure connecting the sunspot with the nearby region of opposite polarity.

3.3 Analysis of the Plage

The electron temperature and column emission measure values obtained from the XRP data can be used to compute the thermal bremsstrahlung microwave emission from the X-ray emitting plasma. The optical depth due to thermal bremsstrahlung absorption is

$$\tau_{X,O} = \frac{9.786 \times 10^{-21} (EM) \ln(47T_e/\nu)}{n_\nu T_e^{1.5} (\nu \mp \nu_B \cos \theta)^2}, \quad (1)$$

where T_e is the electron temperature in K, EM is the emission measure in cm^{-5} , ν is the observation frequency in GHz, n_ν is the index of refraction (~ 1 for plasma and field conditions here), ν_B is the electron gyrofrequency ($\nu_B = 2.8 \times 10^{-3} B$, where B is in Gauss and ν_B is in GHz), θ is the angle between the field and the line of sight, and the minus sign refers to the extraordinary mode while the plus sign refers to the ordinary mode. The free-free brightness temperature predicted for each mode can be calculated using

$$TPRED_{B,X,O} = T_e [1 - \exp(-\tau_{X,O})]. \quad (2)$$

For an unmagnetized plasma, the optical depth, and hence the predicted brightness temperature, of the two modes is the same. The intensity I and Stokes parameter V are calculated from the X- and O-mode brightness temperatures as

$$IPRED = \frac{1}{2} (TPRED_{B,X} + TPRED_{B,O}), \quad (3)$$

and

$$VPRED = \frac{1}{2} (TPRED_{B,X} - TPRED_{B,O}), \quad (4)$$

where the fractional polarization is given by

$$\rho_c PRED = V/I. \quad (5)$$

At the location of the Fe XVII X-ray flux peak, where the XRP spectroscopic scan data used to generate Table 1 were obtained, the temperature of the plasma observed by XRP was $2.95 \pm 0.20 \times 10^6$ K and the log of the column emission measure was 28.85 ± 0.19 . For an unmagnetized plasma, these values entered into Equations (1), (2), and (3) ($V = 0$ for an unmagnetized plasma) yield the predicted intensities listed in Table 2. The uncertainties associated with $IPRED$ are due to the error bars associated with the temperature and emission measure, as listed in Table 1. At this same location in the plage, the VLA observed an intensity $I_{20}OBS \sim 1.2 \times 10^6$ K at all four frequencies in the 20-cm waveband, and $I_6OBS < 0.42 \times 10^6$ K in the 6-cm waveband. Our predicted intensities in the 6-cm waveband are all consistent with the VLA observations. Our predicted intensities in the 20-cm waveband are about 1.4 to 1.9 times higher than the corresponding observed intensities. Thus it

appears that thermal bremsstrahlung plays a significant role in the observed plage emission.

Although we have found that thermal bremsstrahlung plays a significant role in the plage emission, the picture becomes considerably more complex when the observed polarization is considered. Table 3 lists the observed intensity, fractional polarization, Stokes parameter V , and brightness temperatures of the left-hand (L-) and right-hand (R-) modes for each of the four frequencies in the 20-cm waveband at the location of the XRP spectroscopic scan. The extraordinary mode corresponds to the right-hand (R-) component for outward directed fields, and to the left-hand (L-) component for inward directed fields; the ordinary mode corresponds to the L-component for outward directed fields, and to the R-component for inward directed fields. The L-mode brightness temperature is consistent with the predicted free-free brightness temperature (Table 2), for which an unmagnetized plasma yields the same brightness temperature in both modes. However, the observed R-mode brightness temperature is considerably lower, by a factor of 2 to 4, than its corresponding predicted value. Thus, some mechanism is required to explain the reduction of the expected R-mode brightness temperature to its observed value. The only way to reduce the expected brightness temperatures of $\sim 2 \times 10^6$ K to values $\sim 7 \times 10^5$ K is to have cooler absorbing plasma along the line of sight between the emission region and the observer.

It is not possible to produce the observed polarization by simply embedding the free-free emitting plasma in a magnetic field. Assuming a field ~ 100 G (so that gyroresonance absorption remains unimportant) and an angle between the field and the line of sight $\sim 45^\circ$ leads to a polarization $\sim 14\%$. Fields ~ 500 G are required for the free-free mechanism to produce $\sim 50\%$ circular polarization, but fields this high also require that gyroresonance absorption be taken into account. Indeed, at the location of the XRP spectroscopic scan, the extrapolated coronal magnetic fields are ~ 300 G at a height of 5000 km and ~ 200 G at 10,000 km (see Figure 3), quite sufficient for 2nd and 3rd harmonic gyroemission in the 20-cm waveband. While 2nd or 3rd harmonic gyroemission is certainly capable of producing polarizations $\sim 50\%$, it is not capable of reducing an expected high R-mode brightness temperature to a low value unless the 2nd or 3rd harmonic gyroemission regions themselves contain plasma which is cooler than the expected free-free brightness temperature. Thus we conclude that overlying cool, absorbing plasma is required in order to explain the discrepancy between the observed and predicted R-mode brightness temperature values. This cool plasma will also absorb L-mode emission, however, reducing its brightness temperature by at least the same amount by which it reduced the R-mode brightness temperature. For inward directed fields, which we have at the location of the XRP scan in the plage, the L-mode corresponds to extraordinary mode, for which the optical depth in a given layer is greater than that for the ordinary mode. Thus the L-mode will be attenuated even more than the R-mode,

which corresponds to O-mode emission. Thus, although the R-mode brightness temperature discrepancy is explained, the resulting L-mode brightness temperature discrepancy requires further modeling.

One possible model which explains the discrepancy between the observed and the predicted polarization is that the hot plasma observed by XRP consists of two overlying sources separated by an intervening layer of cooler plasma. The lowest layer contains the highest column emission measure and, hence, is responsible for the majority of the predicted free-free microwave emission. The intervening layer of cooler plasma absorbs out the microwave emission from this lower hot layer, leaving only the microwave emission from the uppermost hot layer to be detected by the VLA (see Figure 8a). The uppermost hot layer, optically thin to thermal bremsstrahlung, is embedded in a magnetic field such that thermal gyroemission, capable of producing the observed high polarization, produces the observed 20-cm microwave emission. The cool intervening layer must have a temperature less than 5×10^5 K in order to reduce the predicted R-mode brightness temperature at 1665 MHz from 1.75×10^6 K to its observed value of 5×10^5 K. If, for example, the cool absorbing plasma has a temperature of 105 K, it needs $\log EM = 27.5$ to get $\tau_{f-f} \sim 5$ at 1665 MHz. This means that if the cool absorbing layer forms a sheath ~ 3500 km thick, it needs a density $\sim 3 \times 10^9$ cm $^{-3}$ in order to be an effective absorber. If gyroresonance absorption contributes to the opacity of this cool layer, then the required emission measure is lower. In order for the uppermost hot layer to both emit strongly in the 20-cm waveband and produce polarization as high as $\sim 50\%$, the layer must contain magnetic fields sufficiently high for gyroemission. For 2nd harmonic gyroemission in the 20-cm waveband, fields between 245 and 297 Gauss are required; for 3rd harmonic gyroemission, fields between 164 and 197 Gauss are required; for 4th harmonic gyroemission, fields between 122 and 148 G are required. From our potential field extrapolation at the location of the XRP spectroscopic scan, we find field strengths ~ 300 G at a height of 5000 km above the photosphere, field strengths ~ 200 G at a height of 10,000 km above the photosphere, and field strengths ~ 140 G at a height of 15,000 km above the photosphere. Thus the requisite magnetic field strengths are present in the corona, indicating that the observed 20-cm emission could originate in a gyroresonance emission layer between heights of ~ 5000 and $\sim 15,000$ km. Since the radiation is emitted primarily in the X-mode and the longitudinal field direction is inward, the emitted radiation will be left-hand polarized.

The optical depth of the uppermost hot layer $\tau_{UHLX,O}$ can be estimated by solving

$$T_{BX,O} = T_c \exp(-\tau_{UHLX,O}) + T[1 - \exp(-\tau_{UHLX,O})] \quad (6)$$

for $\tau_{UHLX,O}$, where $T_{BX,O}$ are the observed X- (L-) and O- (R-) mode brightness temperatures at a particular frequency, T_c is the brightness temperature of the optically thick, underlying cool absorbing plasma ($T_c < 5 \times 10^5$ K), and T is

the electron temperature of the uppermost hot layer ($T > 2 \times 10^6$ K). Solving for τ_{UHLX}, O we obtain

$$\tau_{UHLX}, O = \ln[(T - T_c)/(T - T_{B,X}, O)]. \quad (7)$$

Assuming $T = 3 \times 10^6$ K and $T_c = 1 \times 10^5$ K, we obtain $\tau_{UHLX} = 0.80$ and $\tau_{UHL}O = 0.15$ for the observed brightness temperatures at 1665 MHz. These values become $\tau_{UHLX} = 0.73$, $\tau_{UHL}O = 0.077$ for $T_c = 3 \times 10^5$ K. Assuming $T = 3 \times 10^6$ K and $T_c = 2 \times 10^4$ K, we obtain $\tau_{UHLX} = 0.83$, $\tau_{UHL}O = 0.26$ for the averaged observed brightness temperatures in the 20 cm waveband. Now the optical depth due to gyroresonance absorption can be written (e.g., Kundu 1965, Zheleznyakov 1970)

$$\tau = 0.052 \frac{s^2 s}{2s + 1s!} n_e \nu^{-1} L_B (1.77 \times 10^{-10} T_e)^s - 1 (1 \pm \cos \theta) 2 \sin 2s - 2\theta, \quad (8)$$

where s is the harmonic number, n_e is the electron density, ν is the frequency, L_B is the magnetic scale height ($B/\nabla B$), T_e is the electron temperature, θ is the angle between the field and the line of sight, and the plus sign refers to X-mode while the minus sign refers to O-mode. Since the X-mode optical depth due to gyroabsorption is proportional to $(1 + \cos \theta)2$, and the O-mode optical depth due to gyroabsorption is proportional to $(1 - \cos \theta)2$, the ratio

$$\tau_{UHLX}/\tau_{UHL}O = (1 + \cos \theta)2/(1 - \cos \theta)2 \quad (9)$$

yields the angle between the field and the line of sight which is required in order to produce the calculated X- and O- mode optical depths in the upper hot layer. For the three cases discussed above, the calculated angles are 66°, 59°, and 74°, respectively. These angles are comparable to the angles obtained from the extrapolated coronal magnetic field at and near the location of the XRP spectroscopic scan. Here θ is 58° at the height at which the field strength is appropriate for 2nd harmonic gyroemission, and 57° at the height at which the field strength is appropriate for 3rd and 4th harmonic gyroemission. At other nearby locations the angles in the extrapolated field range from 38° to 77° for the same harmonics.

The magnetic scale height L_B can also be calculated from the potential field extrapolation. It is 0.94×10^9 cm in the 2nd harmonic gyroemission region, 1.4×10^9 cm in the 3rd harmonic gyroemission region, and 1.8×10^9 cm in the 4th harmonic gyroemission region. Using $\tau_{UHLX} \sim 0.8$, $T_e = 3 \times 10^6$ K, $\nu \sim 1500$ MHz, and $\theta \sim 60^\circ$, we calculate the electron density n_e required in the upper hot layer if the emission process is due to 2nd harmonic gyroemission ($n_e = 3.0 \times 10^4 \text{ cm}^{-3}$), 3rd harmonic gyroemission ($n_e = 6.8 \times 10^6 \text{ cm}^{-3}$), and 4th harmonic gyroemission ($n_e = 1.2 \times 10^9 \text{ cm}^{-3}$). The latter two values of the electron density will allow polarization inversion of the 20 cm emission to occur in the quasi-transverse layer of the extrapolated coronal magnetic field (see below), resulting in the emission of R-mode dominated, rather than the observed L-mode dominated, emission. Such is

not the case for the density corresponding to the 2nd harmonic gyroemission region. It is low enough that polarization inversion will not take place in the quasi-transverse layer, and the resulting emission is dominated by the L-mode, as observed. This density is admittedly much lower than canonical low coronal values.

A second possible model is that the absorption by the cooler overlying plasma takes place in a gyroresonance absorption layer, but that no substantial new microwave emission source exists higher up. Because the X-mode gyroresonance absorption coefficient is higher than the O-mode gyroresonance absorption coefficient, the optical depth of the X-mode in the absorbing plasma is higher than that of the O-mode. If both modes were fully optically thick in the cool absorbing layer, then all of the 20-cm emission from the hot plasma below would be absorbed, and we would again be dealing with the model discussed in the previous paragraphs. However, if both modes are not fully thick, the X-mode is more attenuated by the cool absorbing plasma than the O-mode, resulting in the emission of O-mode-dominated microwave emission. The inward direction of the photospheric magnetic field and the left-hand polarization of the 20-cm emission indicate that the physical polarization is X-mode, however. Nevertheless, the microwave emission can undergo a polarization inversion upon traversing a quasi-transverse (QT) layer in the coronal magnetic field (see Fig. 8b). This QT layer occurs where the angle between the magnetic field and the line of sight (direction of wave propagation) goes through 90°, i.e., the longitudinal field component B_z goes through zero and reverses. Previous studies have provided evidence for such polarization inversions (Kundu et al. 1977, Webb et al. 1983). The observed polarization is inverted when coupling between the polarization modes is weak.

Zheleznyakov (1970), using the WKB method, obtains the following expression for the coupling parameter, given here in the notation of Bandiera (1982):

$$C = \frac{2 \ln 2 (m_e c)^4}{\pi^2 e^5} \frac{\omega^4}{N_e B^3} \left| \frac{d\theta}{ds} \right|, \quad (10)$$

where m_e and e are the rest mass and charge on an electron, c is the speed of light, ω is the observation angular frequency, N_e is the electron number density, B is the magnetic field strength, and $d\theta/ds$ is the gradient of the angle between the field and the line of sight along the ray path; all units are in CGS. The microwave emission undergoes a polarization inversion when $C \ll 1$, or

$$4.766 \times 10^{-18} \frac{\nu^4}{N_e B^3} \left| \frac{d\theta}{ds} \right| \ll 1. \quad (11)$$

In and near the location of the XRP spectroscopic scan, the Sakurai code yields a QT layer at a height of $\sim 75,000$ km. The average total magnetic field strength obtained from the code is 17 G, and the angular gradient along the line of sight is 1.1×10^{-10} rad/cm. Inserting these values into the expression for the coupling parameter and

using the highest observing frequency in the 20-cm waveband (1.665 GHz), we find that the polarization inversion will take place if the electron density in the QT layer greatly exceeds $8.4 \times 10^5 \text{ cm}^{-3}$. This is the value with which we compare our model coronal densities in order to determine whether or not polarization inversion takes place in the QT layer above the location of the XRP spectroscopic scan. The model plage electron density of Hildebrandt et al. (1987) at a height of 75,000 km is $1.4 \times 10^9 \text{ cm}^{-3}$, and the model electron densities in all of the coronal structures in Hildebrandt et al. (1987) and Pagagiannis and Kogut (1975) exceed $5.4 \times 10^7 \text{ cm}^{-3}$ at the same height. This indicates that it is reasonable to expect polarization inversion to occur for the 20-cm microwave emission from the plage: the 20-cm emission exiting the cool absorbing plasma, dominated by the O-mode, is inverted in the QT layer so that the O-mode emission becomes left-hand polarized, as required by the observations.

The optical depths of the cool absorbing layer $\tau_{CALX,O}$ can be estimated by solving

$$T_{BX,O} = T_{BPRED} \exp(-\tau_{CALX,O}) + T_c [1 - \exp(-\tau_{CALX,O})] \quad (12)$$

for $\tau_{CALX,O}$, where $T_{BX,O}$ are the observed X- (L-) and O- (R-) mode brightness temperatures at a particular frequency, T_{BPRED} is the free-free brightness temperature predicted from the X-ray observations, and T_c is the electron temperature of the cool absorbing layer. Solving for $\tau_{CALX,O}$ we obtain

$$\tau_{CALX,O} = \ln[(T_c - T_{BPRED}) / (T_c - T_{BX,O})]. \quad (13)$$

For the average observed brightness temperatures in the 20 cm waveband, we obtain $\tau_{CALX} = 1.44$ and $\tau_{CALO} = 0.18$ for $T_c = 3 \times 10^5 \text{ K}$ (with little variation for T_c between 1×10^5 and $4.5 \times 10^5 \text{ K}$), which leads to $\theta \sim 62^\circ$. This angle is comparable to the angles obtained above from the extrapolated field. Using $\tau_{XCAL} \sim 1.44$, $T_c = 3 \times 10^5 \text{ K}$, $\nu \sim 1500 \text{ MHz}$, and $\theta \sim 60^\circ$, we calculate the electron density n_e required in the cool absorbing layer if the absorption process is due to 2nd harmonic gyroabsorption ($n_e = 5.5 \times 10^5 \text{ cm}^{-3}$), 3rd harmonic gyroabsorption ($n_e = 1.2 \times 10^9 \text{ cm}^{-3}$), and 4th harmonic gyroabsorption ($n_e = 2.1 \times 10^{12} \text{ cm}^{-3}$).

If the absorption which causes the observed polarization takes place in the 4th harmonic gyroabsorption region, the required density must be extremely high. This leads to a high free-free optical depth, even for a path length $< 1 \text{ km}$. This would result in the emission of low brightness temperature, unpolarized radiation, so the absorption which causes the observed polarization cannot take place in the 4th harmonic region. If the absorption which causes the observed polarization takes place in the 3rd harmonic gyroabsorption region, the required density is $1.2 \times 10^9 \text{ cm}^{-3}$, and can be as low as $5.6 \times 10^8 \text{ cm}^{-3}$ (for $T_c = 5 \times 10^5 \text{ K}$). The physical size of this cool absorbing layer must extend from the height at which the field strength is appropriate for the 3rd harmonic of the highest observed frequency in

the 20 cm waveband (1665 MHz, or 198 G) to the height at which the field strength is appropriate for the 3rd harmonic of the lowest observed frequency in the 20 cm waveband (1375 MHz, or 164 G). This range of height is ~ 2000 km. For $T_e = 5 \times 10^5$ K, $n_e = 5.6 \times 10^8 \text{ cm}^{-3}$, and path length ~ 2000 km, we obtain $\tau_{f-f} \sim 0.01$, negligible compared to the 3rd harmonic gyroresonant optical depths. Assuming that the coronal density varies in hydrostatic equilibrium, the density at the height of the QT layer is sufficient for polarization inversion to occur (whether the temperature remains at the “cool” value or increases to a more canonical value). Thus the absorption which causes the observed polarization can take place in the 3rd harmonic region. If the absorption which causes the observed polarization takes place in the 2nd harmonic gyroabsorption region, the required density is $5.5 \times 10^5 \text{ cm}^{-3}$. This density, considerably less than canonical low coronal density values, is inadequate for polarization inversion to occur: unless the coronal density increases from $5.5 \times 10^5 \text{ cm}^{-3}$ at the height of the 2nd harmonic layer to a value much greater than $8.4 \times 10^5 \text{ cm}^{-3}$ at the height of the QT layer (a height separation of $\sim 70,000$ km), the necessary polarization inversion will not take place. We conclude that the absorption which produces the observed polarization at the location of the XRP spectroscopic scan most likely occurs in the 3rd harmonic gyroresonance absorption region.

Different conditions prevail at the location of the 20 cm intensity peak in the plage. Here, $\sim 30,000$ km west of the location of the XRP spectroscopic scan, the predicted and the observed 20 cm intensity peaks are cospatial. The predicted 20 cm brightness temperature is 2.2×10^6 K, while the observed 20 cm L-mode brightness temperature is 1.9×10^6 K, and the observed 20 cm R-mode brightness temperature is 0.9×10^6 K. The maximum predicted 6 cm brightness temperature is 7×10^5 K, while the observed 6 cm brightness temperature is $< 4.2 \times 10^5$ K.

Consider again the two models used above to explain the discrepancy between the observed and the predicted emission from the location of the XRP spectroscopic scan. In the hot/cool/hot layer model (Fig. 8a), the high predicted 20 cm brightness temperature of the plasma observed by XRP is reduced by optically thick cool, overlying plasma. Here, at the location of the observed/predicted 20 cm intensity peak, the cool absorbing plasma must be optically thick enough to reduce the predicted 6 cm brightness temperature of 7×10^5 K to at least the observed upper limit of 4.2×10^5 K. If, for example, the temperature of the cool absorbing layer is 1×10^5 K, then the 6 cm free-free optical depth must be $\tau_{f-f}(6\text{cm}) \sim 0.63$, requiring $\log EM = 27.55$. This yields a 20 cm free-free optical depth $\tau_{f-f}(20\text{cm}) \sim 7.3$. Above this cool layer is another hot layer, within which the magnetic field strength must be sufficient for gyroresonance emission. Assuming the cool absorbing layer is optically thick and produces microwave emission with a brightness temperature of 1×10^5 K, the required X- and O-mode opacities in the upper hot layer are $\tau X_{UHL} \sim 0.97$, $\tau O_{UHL} \sim 0.23$. The corresponding angle between the field and the line of sight is

$\theta \sim 70^\circ$, comparable to the angles found in the 2nd, 3rd, and 4th harmonic gyroemission regions at the location of the XRP spectroscopic scan. Here, however, the coronal potential field extrapolated from the observed photospheric longitudinal magnetogram does not yield fields sufficient for the gyroemission mechanism to operate. The total extrapolated photospheric field is less than 100 G, and between heights of 5000 and 15,000 km the total extrapolated field ranges from ~ 60 to ~ 90 G. In the hot/cool/QT layer model (Fig. 8b), the high predicted 20 cm brightness temperature of the plasma observed by XRP is partially reduced, and the low predicted polarization is raised to $\sim 40\%$, after passage through a cool absorbing layer in which the magnetic field strength is sufficient for gyroabsorption. Again, however, the extrapolated coronal magnetic field at the 20 cm peak is not high enough for gyroabsorption to operate. Furthermore, because the free-free optical depth of the cool absorbing layer must be low enough to permit the 20 cm emission to escape unaltered, the corresponding optical depth at 6 cm will be inadequate to reduce the predicted to the observed brightness temperature. It is possible, however, that some of the 6 cm flux was resolved out due to an extended source size.

Analysis of the observed and the predicted microwave emission from the location of the observed 20 cm intensity peak in the plage suggests quite strongly that the coronal potential magnetic field strength extrapolated from the photospheric longitudinal magnetogram is substantially less than the actual magnetic field in the corona. This is possibly a manifestation of instrumental insensitivity to photospheric longitudinal magnetic fields less than ~ 100 G. It is quite possible that compact, highly intense photospheric magnetic field regions were detected due to inadequate instrumental resolution. It also cannot be ruled out that electric currents, and hence non-potential magnetic fields, are present in the corona.

We note that the predicted 20-cm brightness temperatures are not very sensitive to the value of the Fe XVII correction factor, ranging from $1.7 - 2.2 \times 10^6$ K (at the location of the XRP spectroscopic scan) for a correction factor in the range 1 - 3. This is primarily because of the relatively high optical depth (~ 1) of the emission at 20 cm. At 6 cm, however, without the correction factor the predicted brightness temperature is 8×10^5 K, higher than the lowest significant brightness temperature of 4.2×10^5 K observed with the VLA. Hence, unless (a) the 6-cm emission was so extended that it was resolved out by the VLA, or (b) the hot/cool/hot layer model (which provides sufficient absorption at 6 cm) is the preferred model, these observations underscore the need for the correction to the Fe XVII emissivity. A correction factor of 1.7 or higher is required to bring the predicted brightness temperature below the sensitivity level of the VLA observations.

4 Conclusions

A number of important conclusions concerning the plasma and magnetic field structure of an active region, as well as the observational methods, result from this study:

(1) The temperature in the corona over an active region can diminish with height; this occurs over both the sunspot and the plage in AR 4906. A different line of reasoning leads to this conclusion for each of these structures. In the case of the sunspot, this conclusion is based upon the observation that the cospatial microwave emission in the 6- and 20-cm wavebands have substantially different brightness temperatures. The emission in both wavebands is attributed to thermal gyroemission in the high magnetic field of the sunspot. The 6-cm emission requires higher magnetic fields than does the 20-cm emission and, hence, originates lower in the sunspot atmosphere where the magnetic field strength is higher. Where the 6- and 20-cm emission overlap, the 6-cm brightness temperature is 2.5×10^6 K while the 20-cm brightness temperature is 1.3×10^6 K. Thus the sunspot atmosphere temperature diminishes from 2.5×10^6 K at the height of formation of the 6-cm emission to 1.3×10^6 K at the height of formation of the 20-cm emission. In the case of the plage, the conclusion is based upon the discrepancy between the observed brightness temperature at 20 cm in the right-hand polarized mode (R-mode) and the brightness temperature predicted from the electron temperature and column emission measure calculated with XRP line flux ratios. Specifically, the R-mode requires the presence of overlying cool, absorbing plasma in order to reduce its predicted brightness temperature of $T_{B,PRED} \sim 2 \times 10^6$ K to its observed brightness temperature of $T_{B,ROBS} \sim 0.7 \times 10^6$ K. The overlying, cool plasma must have a temperature less than 5×10^5 K.

(2) A loop or loop-like structure connects the sunspot with a nearby region of opposite polarity in the east. The peaks of the 6- and 20-cm emission lie along this loop, with higher frequency emission originating farther down the leg of the loop on the side of the sunspot. Based upon the potential field extrapolation, the 20-cm emission is due to a combination of 2nd and 3rd harmonic gyroemission, putting the magnetic field strength in this region in the range 160 – 300 G.

(3) Based upon a comparison of the 6-cm and XRP observations with calculations of the emission from a model loop, we deduced the plasma and magnetic field parameters at the location of the 6-cm source. An electron temperature $T_e = 2.5 \times 10^6$ K, an electron density $N_e \sim 1 \times 10^9$ cm⁻³, and a magnetic field strength of 583 G (3rd harmonic gyroemission at 4900 MHz) result. The potential field extrapolation yields this magnetic field strength at a height ~ 5000 km above the photosphere.

(4) Our results have allowed us to obtain good estimates of the Alfvén speed at two locations within the loop. At the location of the 6-cm source, near the sunspot, an Alfvén speed $\sim 40,000$ km/sec is obtained. Higher in the loop, at the location of the 20-cm emission, the Alfvén speed is found to range from 10,000 km/sec – 20,000 km/sec. At both locations the electron gyrofrequency exceeds the plasma frequency.

(5) The extrapolated potential sunspot field can be approximated by that of a vertically oriented point dipole for locations in which $B \gtrsim 300$ G. For locations in which $B < 300$ G, nearby pockets of magnetic field perturb the sunspot field from that of a point dipole.

(6) The electron temperature and/or density are lower over the western portion of the sunspot (away from the center of the active region) than they are over the eastern portion of the sunspot.

(7) In the plage, the ratios of X-ray emission lines are used to calculate the electron temperature and column emission measure. The most accurate determination of these parameters is at the location of the Fe XVII peak flux, where spectroscopic scan data were obtained. ...Fe XVII factor...

(8) Using the temperature and emission measure obtained from the XRP line flux ratios, a “predicted” brightness temperature is calculated at each microwave frequency using only the thermal bremsstrahlung emission mechanism. This places a lower limit on the expected brightness temperature in each of the X- and O-modes at the given frequency. The 6-cm predicted brightness temperature is less than the lowest observed 6-cm contour in the sunspot; it is thus consistent with the VLA’s lack of detection of 6-cm emission from the plage. This holds true as long as the Fe XVII correction factor is greater than 1.7.

(9) The predicted 20-cm brightness temperature is consistent with the observed 20 cm L-mode brightness temperature; however, the predicted 20-cm brightness temperature is much higher than the observed 20-cm R-mode brightness temperature. We are thus led to two possible models to explain the discrepancy between the predicted and the observed 20-cm emission from the plage. The first model has a layer of optically thick cool, absorbing plasma overlying the hot plasma from which the X-ray emission originates. On top of this cool layer is another hot layer; this second hot layer is optically thin to thermal bremsstrahlung but emits strong, polarized microwave emission owing to the fact that it is embedded in a magnetic field sufficient for gyroresonance emission at 20 cm. The second model has a layer of cool, but not fully thick, absorbing plasma overlying the hot plasma from which the predicted microwave emission originates. This cool plasma, embedded in a magnetic field sufficient for 20-cm gyroresonance absorption, attenuates the

X-mode more strongly than the O-mode. This results in the emission of right-hand polarized microwaves (R-mode), which is opposite to what is observed. However, the polarization is subsequently inverted in an overlying quasi-transverse layer in the magnetic field. This QT layer, required by the model, is found at a height of $\sim 75,000$ km above the photosphere in the extrapolated potential field over the plage. A similar result has been obtained from our analysis of the CoMStOC II data (Schmelz et al. 1991).

Acknowledgements. We gratefully acknowledge the assistance of Dr. Haimin Wang in the acquisition of the Beijing Observatory magnetogram. Radio astronomical studies of the Sun at Tufts University are supported under grant AFOSR-89-0147 with the Air Force Office of Scientific Research. Simultaneous VLA and SMM observations of the Sun are supported by NASA grant 5-501 to Tufts University. JTS acknowledges support by NASA contracts NAS5-30431 and NAS5-28713 and the Lockheed Independent Research Program. JWB and GDH acknowledge support by the SMM Guest Investigator Program and NASA RTOP 170-38-53-16. The success of the SMM CoMStOC observations depended on the efforts of many persons at the SMM Experimenters Operations Facility. The VLA is operated by Associated Universities Inc., under contract with the National Science Foundation. The XRP data used in this work were available only because of the repair of the SMM spacecraft by the crew of the Challenger on mission 41-C. The pilot for that mission, and the commander of Challenger's last flight, was Francis R. Scobee. This work is dedicated to his memory.

TABLE 1
Plasma Parameters from XRP Spectroscopic Scan Data

<u>Line Ratio</u>	<u>T_e (MK)(1)</u>	<u>$\log(\text{EM}) (\text{cm}^{-5})(2)$</u>
O VIII/Mg XI	3.01 ± 0.16	28.85 ± 0.08
O VIII/Fe XVIII	2.83 ± 0.19	28.87 ± 0.09
Ne IX/Fe XVIII	2.94 ± 0.22	28.85 ± 0.09
Mg XI/Fe XVIII	2.61 ± 0.50	28.89 ± 0.24
Fe XVII/Fe XVIII	3.12 ± 0.27	28.83 ± 0.06
weighted mean(3)	2.95 ± 0.20	28.85 ± 0.19

(1) The quoted uncertainties on the individual values of T_e reflect counting statistics only.

(2) The column emission measure is computed from the O VIII flux only; the quoted uncertainties on the individual values reflect counting statistics only.

(3) The quoted uncertainties on the weighted means of T_e and EM are the root mean squares of the statistical and systematic uncertainties. For temperature, the systematic uncertainty is estimated as the standard deviation of the individual values. For the emission measure, the systematic uncertainty is estimated as the standard deviation of the emission measures calculated for the O VIII, Ne IX, Mg XI, and Fe XVIII fluxes at the mean T_e .

TABLE 2
Predicted Microwave Intensities from XRP Spectroscopic Scan Data

<u>Frequency (MHz)</u>	<u>IPRED (MK)</u>
1375	2.17 ± 0.49
1420	2.10 ± 0.49
1550	1.91 ± 0.49
1665	1.75 ± 0.49
4600	$0.31 +0.17_{-0.11}$
4700	$0.30 +0.16_{-0.11}$
4800	$0.29 +0.16_{-0.10}$
4900	$0.28 +0.15_{-0.10}$

TABLE 3
Observed Microwave Emission at the Location of the XRP Spectroscopic Scan

ν (MHz)	$IOBS$ (MK)	$\rho_c OBS$ (%)	$VOBS$ (MK)	$T_{B,L} OBS$ (MK)	$T_{B,R} O$
1375	1.2	28	0.3	1.5	0.9
1420	1.1	41	0.4	1.5	0.7
1550	1.4	44	0.6	2.0	0.8
1665	1.1	54	0.6	1.7	0.5

References

- Acton, L. W., et al. 1980, *Solar Phys.*, **65**, 53.
- Alissandrakis, C. E., and Kundu, M. R. 1982, *Ap. J. (Letters)*, **253**, L49.
- Bandiera, R. 1982, *Astr. Ap.*, **112**, 52.
- Bastian, T. 1988, Ph.D. thesis, University of Colorado.
- Brosius, J. W., and Holman, G. D. 1988, *Ap. J.*, **327**, 417.
- Brosius, J. W., and Holman, G. D. 1989, *Ap. J.*, **342**, 1172.
- Cornwell, T. 1986, in *Synthesis Imaging* (NRAO Summer School Course Notes), p. 117.
- Gary, D. E., and Hurford, G. J. 1987, *Ap. J.*, **317**, 522.
- Henze, W., Jr., Tandberg-Hanssen, E., Hagyard, M. J., Woodgate, B. E., Shine, R. A., Beckers, J. M., Bruner, M., Gurman, J. B., Hyder, C. L., and West, E. A. 1982, *Solar Phys.*, **81**, 231.
- Hildebrandt, J., Kruger, A., Urpo, S., and Terasranta, H. 1987, *Observation and Interpretation of Solar S-Component Radiation at Millimeter Waves* (Helsinki Univ. of Technology Radio Lab., Rept. S170).
- Holman, G. D., and Kundu, M. R. 1985, *Ap. J.*, **292**, 291.
- Kundu, M. R. 1965, *Solar Radio Astronomy* (New York: Interscience).
- Kundu, M. R., Alissandrakis, C. E., Bregman, J. D., and Hin, A. C. 1977, *Ap. J.*, **213**, 278.
- Lang, K. R., and Willson, R. F. 1982, *Ap. J. (Letters)*, **255**, L111.
- Lang, K. R., Willson, R. F., and Gaizauskas, V. 1983, *Ap. J.*, **267**, 455.
- Lang, K. R., Willson, R. F., and Rayrole, J. 1982, *Ap. J.*, **258**, 384.
- Lang, K. R., Willson, R. F., Smith, K. L., and Strong, K. T. 1987, *Ap. J.*, **322**, 1035.

Lang, K. R., Willson, R. F., Smith, K. L., and Strong, K. T. 1987, *Ap. J.*, **322**, 1044.

McConnell, D., and Kundu, M. R. 1983, *Ap. J.*, **269**, 698.

Mewe, R., Gronenschild, E. H. B. M., and van den Oord, G. H. J. 1985, *Astr. Ap. Suppl.*, **62**, 197.

Meyer, J.-P. 1985, *Ap. J. Suppl.*, **57**, 173.

Nitta, N., White, S. M., Kundu, M. R., Gopalswamy, N., Holman, G. D., Brosius, J. W., Schmelz, J. T., Saba, J. L. R., and Strong, K. T. 1991, *Ap. J.*, in press (CoMStOC I).

Papagiannis, M. D., and Kogut, J. A. 1975, *Brightness Temperatures and Polarizations of Solar Active Regions at 3.8 cm - Theory and Observations* (AFCRL-TR-75-0430).

Sakurai, T. 1982, *Solar Phys.*, **76**, 301.

Schmahl, E. J., Kundu, M. R., Strong, K. T., Bentley, R. D., Smith, J. B., Jr., and Krall, K. R. 1982, *Solar Phys.*, **80**, 233.

Schmelz, J. T., Holman, G. D., Brosius, J. W., and Gonzalez, R. D. 1991, *Ap. J.*, in preparation (CoMStOC II).

Shevgaonkar, R. K., and Kundu, M. R. 1984, *Ap. J.*, **283**, 413.

Strong, K. T., Alissandrakis, C. E., and Kundu, M. R. 1984, *Ap. J.*, **277**, 865.

Webb, D. F., Davis, J. M., Kundu, M. R., and Velusamy, T. 1983, *Solar Phys.*, **85**, 267.

Webb, D. F., Holman, G. D., Davis, J. M., Kundu, M. R., and Shevgaonkar, R. K. 1987, *Ap. J.*, **315**, 716.

Willson, R. F. 1985, *Ap. J.*, **298**, 911.

Zheleznyakov, V. V. 1970, *Radio Emission of the Sun and Planets*, ed. J. S. Hey (Oxford: Pergamon Press).

Figure Captions

Figure 1. Observations of the CoMStOC IV active region, AR 4906. Celestial north is up, and west is to the right. All eight boxes cover the same field of view, for ease in coalignment. The tick spacing is one minute of arc, and the crosses mark the locations of the phase center of the VLA observations. (a) Frequency-averaged map of I (intensity) at 20 cm. The contour levels are 0.21, 0.41, 0.62, 0.83, 1.03, 1.24, 1.45, 1.66, 1.86, and 2.07×10^6 K. (b) Frequency-averaged map of I at 6 cm. The contour levels are 0.42, 0.63, 0.84, 1.05, 1.26, 1.47, 1.68, 1.89, and 2.10×10^6 K. (c) XRP soft X-ray map of AR 4906 in the bright Fe XVII line at 15.01 Å. The image was accumulated during a 4' square raster with 10" steps which took 10 min to complete. The map has been smoothed with a 3 x 3 boxcar to improve statistics. Contour levels are 10, 15, 20, 25, 30, and 35 counts/s. (d) Photospheric longitudinal magnetogram obtained from the Beijing Observatory, with superimposed magnetic field lines calculated with the potential field extrapolation code of Sakurai. The contour levels are 200 and 500 G, where the darker contours represent inward directed fields and the lighter contours represent outward directed fields. (e) Electron temperature and (f) log of the column emission measure calculated from line flux ratios of emission lines observed with XRP. The contours in (e) are 2.2, 2.6, and 3.0×10^6 K; the contours in (f) are 28.7, 28.9, and 29.1. The temperature and emission measure diagnostics were performed only in and around radio source B because that is the only portion of the active region which was mapped in multiple X-ray emission lines: because it was such a weak X-ray emitter, the rest of the active region was mapped only in the emission line of Fe XVII. (g) Brightness temperature map at 20 cm calculated for the free-free emission mechanism using the electron temperature and column emission measure maps in (e) and (f). The contours are 1.7, 1.9, and 2.1×10^6 K. (h) Brightness temperature map at 6 cm calculated for the free-free emission mechanism using the electron temperature and column emission measure maps in (e) and (f). The contours are 0.1, 0.3, and 0.5×10^6 K.

Figure 2. I and V maps at each of the four frequencies in the 20 cm waveband. The I contour levels are 0.53, 0.79, 1.05, 1.31, 1.57, 1.83, 2.09, and 2.35×10^6 K for all frequencies. The V contour levels are 0.29 and 0.38×10^6 K at 1375 MHz; 0.27, 0.36, and 0.46×10^6 K at 1420 MHz; 0.31, 0.41, 0.51, and 0.61×10^6 K at 1550 MHz; and 0.40, 0.53, and 0.66×10^6 K at 1665 MHz. Celestial north is up, and west is to the right. The tick spacing is one minute of arc, and the crosses mark the location of the phase center of the VLA observations.

Figure 3. Sequence of contour maps showing the extrapolated magnetic field strength at heights of (a) 0 km, (b) 5000 km, (c) 10000 km, and (d) 15000 km above the photosphere. Celestial north is up, and west is to the right. The numbers along the axes are distances from solar disk center in units of 104 km in the plane of

the sky. The contour levels in (a) and (b) are 150, 250, 350, 500, and 800 G. The contour levels in (c) and (d) are 150, 200, 250, 350, and 500 G. Crosshairs mark the phase centers of the VLA 6 and 20 cm maps, to assist in coaligning images. A 40" line segment is shown in (d) to assist in scaling and coaligning.

Figure 4. Magnetic field of a model sunspot consisting of a vertically oriented point dipole buried below the photosphere. The depth and dipole moment were calculated from the height variation of the extrapolated maximum sunspot magnetic field strength. Numbers along the x and y axes represent the distance from the point dipole in units of 104 km. The x-axis is in the plane of the photosphere, and the y-axis is perpendicular to the plane of the photosphere. Solid lines are field lines, dashed lines numbered 1 through 5 are contours of constant magnetic field strength, and the dotted horizontal lines represent heights above the photosphere of 5000, 10000, and 15000 km. In (a) the dashed lines are magnetic field contours corresponding to the 1st through 5th harmonics of 1665 MHz: 594, 297, 198, 149, and 119 G. In (b) the dashed lines are magnetic field contours corresponding to the 1st through 5th harmonics of 4900 MHz: 1749, 875, 583, 437, and 350 G.

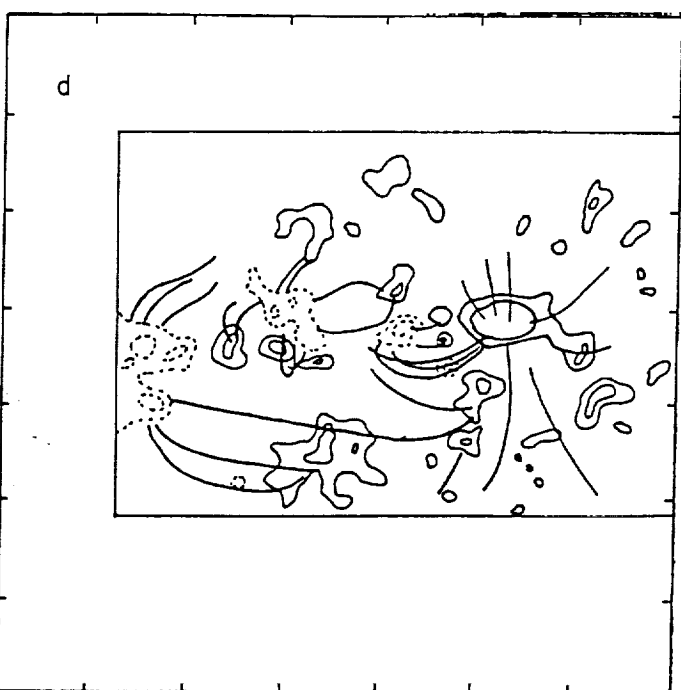
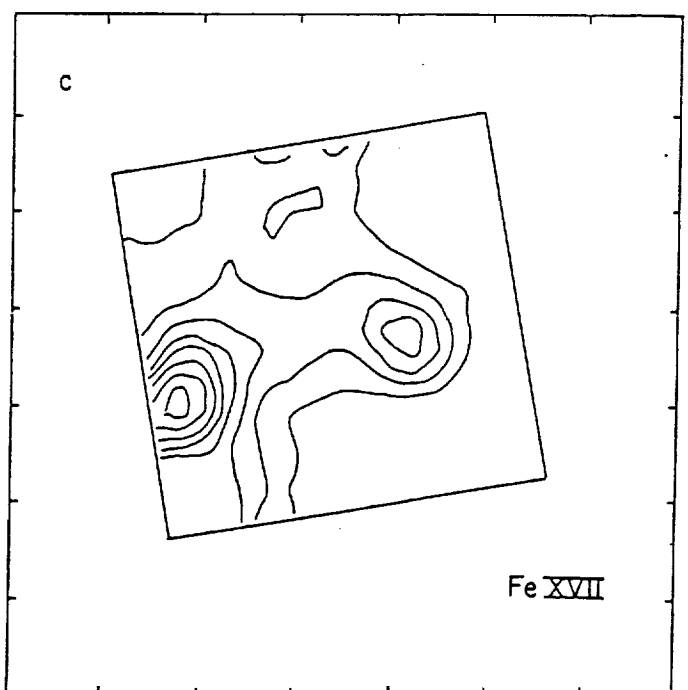
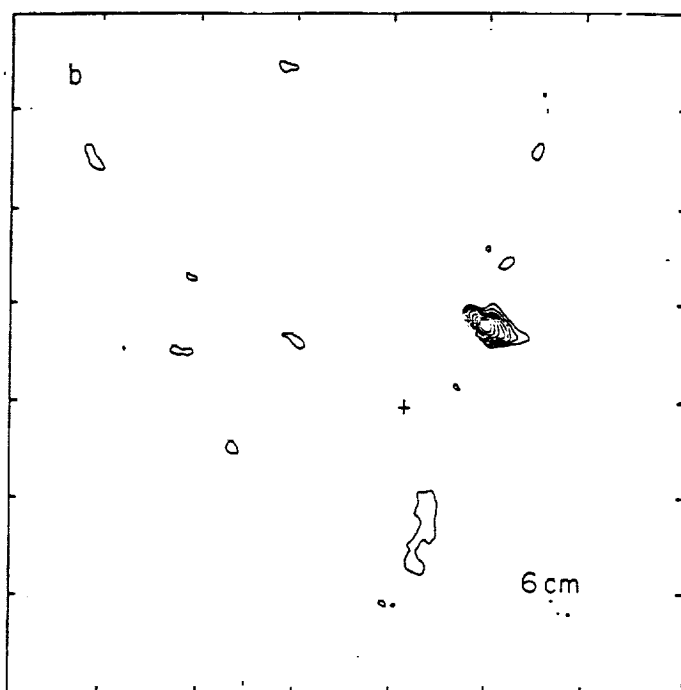
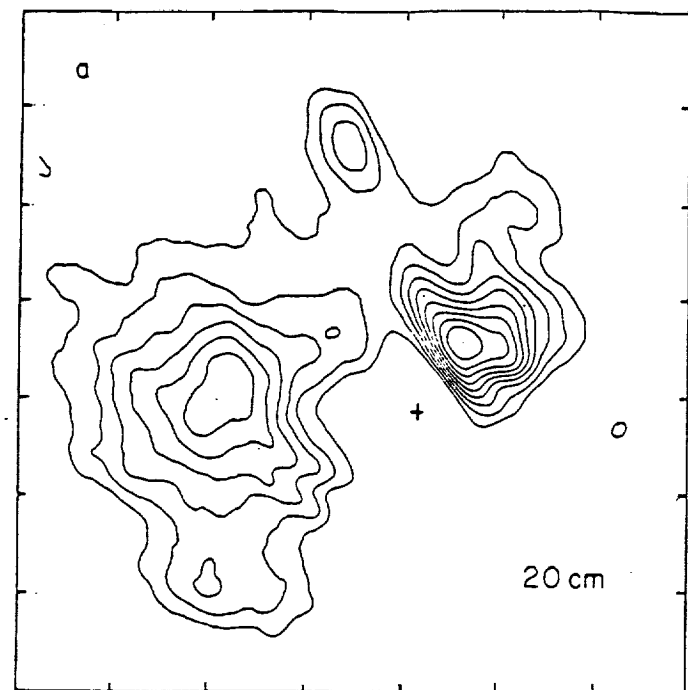
Figure 5. I and V maps calculated for observation frequencies of 1665 MHz and 4900 MHz for the sunspot model whose magnetic field is shown in Figure 4. Numbers along the x and y axes are in units of arcsec, and the crosshairs intersect at the center of the sunspot. Contour line thickness increases with increasing contour value. In (a) the 1665 MHz I contours are 0.84, 1.37, and 1.90×10^6 K, and in (b) the 1665 MHz V contours are 0.27, 0.53, and 0.80×10^6 K. In (c) the 4900 MHz I contours are 0.66, 1.28, and 1.90×10^6 K, and in (d) the 4900 MHz V contours are 0.31, 0.62, and 0.93×10^6 K.

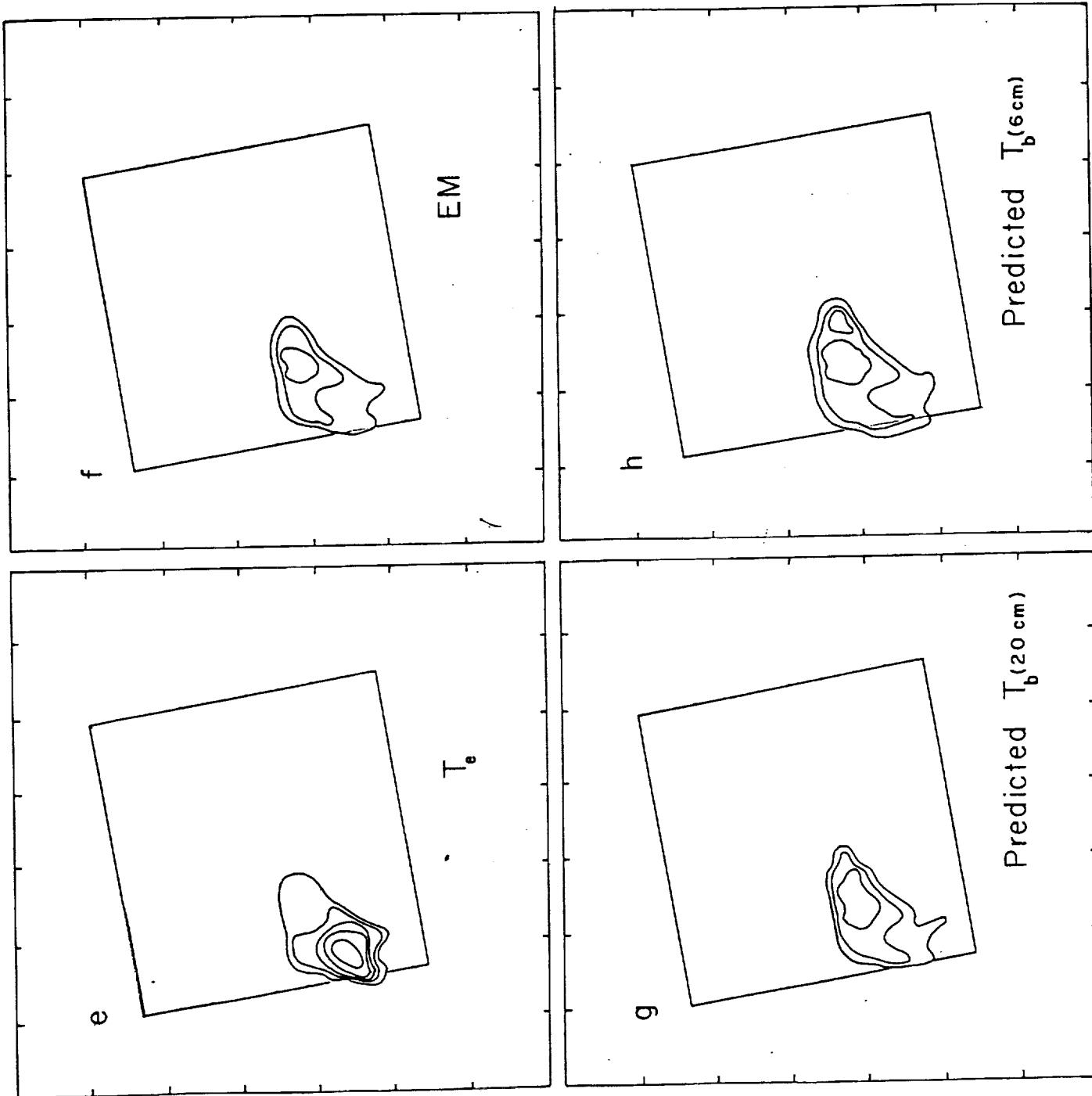
Figure 6. Portion of the magnetogram showing the locations of the 6 and 20 cm emission along the field lines which outline the loop-like structure connecting the sunspot with the nearby region of opposite polarity. Celestial north is toward the top, and west is toward the right. A segment of 10" length is shown for scaling purposes. Shaded areas show where the photospheric longitudinal field exceeds 200 G. The solid magnetic field contours represent outward directed fields of 200 and 500 G, while the short-dashed magnetic field contours represent inward directed fields of 200 and 500 G. The sunspot is the shaded area in the upper right. The long-dashed contour corresponds to an intensity I of 0.79×10^6 K at the representative 20 cm microwave frequency of 1375 MHz. The "+" symbols mark the locations of the peak brightness temperature of each of the four closely-spaced frequencies in the 20 cm waveband. The location of the peak brightness temperature shifts systematically closer to the footpoint inside the sunspot with increasing frequency: the "+" farthest to the left corresponds to the 1375 MHz emission, and the "+" farthest to the right corresponds to the 1665 MHz emission. The dotted contour corresponds to an intensity I of 1.56×10^6 K at 4900 MHz in the 6 cm waveband.

The dot-dash contours correspond to a V of 0.39×10^6 K at 4900 MHz.

Figure 7. Theoretical 4900 MHz I and V maps for the model loop described in the text. The model loop has a constant temperature of 2.5×10^6 K, a density of $1 \times 10^9 \text{ cm}^{-3}$, and a field strength of 583 G (3rd harmonic) in the footpoints at a height of ~ 5000 km above the photosphere. The I contours are 0.52, 1.04, 1.56, and 2.34×10^6 K. The V contours are 0.39, 0.52, 0.64, and 1.00×10^6 K. These model I and V sources reproduce the observed 6 cm I and V sources fairly well.

Figure 8. Illustration of the two models used to explain the observed polarization of the 20 cm microwave emission from the plage. The arrows labeled with an “R” correspond to right hand circular polarization, and the arrows labeled with an “L” correspond to left hand circular polarization. The propagation mode, extraordinary or ordinary, is indicated by an “X” or an “O” in parentheses. The propagation mode is determined by the orientation of the local magnetic field, indicated by arrows labeled B_z . The lengths of the arrows labeled R and L indicate the relative brightness temperatures of the emergent emission in the given mode of polarization. (a) The hot/cool/hot layer model. Emission with high brightness temperature and low polarization ($T_{BX}, O \sim 2 \times 10^6$ K) emerges from the lowest layer. This emission is then absorbed by the overlying cooler layer, from which low brightness temperature emission ($T_{BX}, O < 5 \times 10^5$ K) emerges. Highly polarized emission ($T_{BX} \sim 2 \times 10^6$ K, $T_{BO} \sim 7 \times 10^5$ K) emerges from the highest layer, which is a hot plasma embedded in a magnetic field which is sufficiently strong for at least 3rd harmonic gyroresonance emission. (b) The hot/cool/QT layer model. Emission with high brightness temperature and low polarization ($T_{BX}, O \sim 2 \times 10^6$ K) emerges from the lowest layer. This emission is then attenuated in the overlying cooler layer, in which magnetic fields sufficient for gyroresonance absorption cause the optical depth (and hence the attenuation) to be greater for the X-mode (L) than for the O-mode (R). This results in the emission of O-mode-dominated (R) emission. The polarization is then inverted to its observed (L) value upon traversal of the overlying quasi-transverse (QT) layer in the magnetic field overlying the plage.





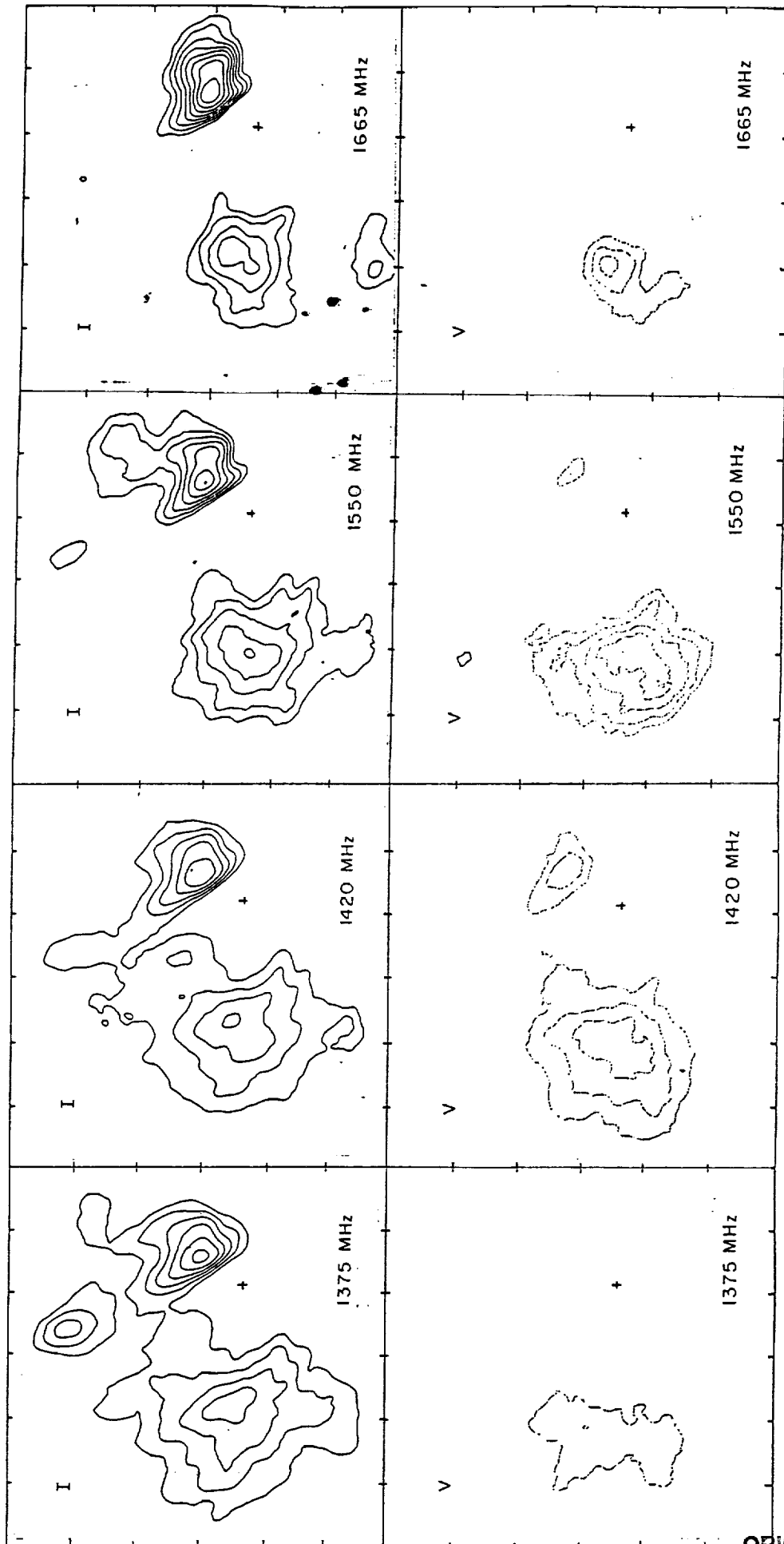


Fig. 2

ORIGINAL PAGE IS OF POOR QUALITY

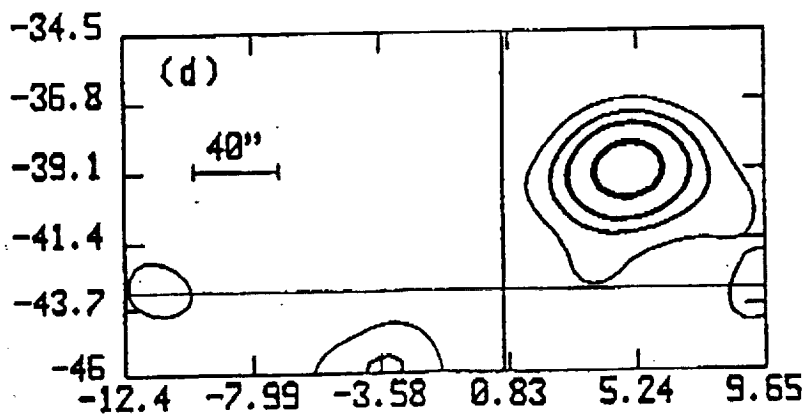
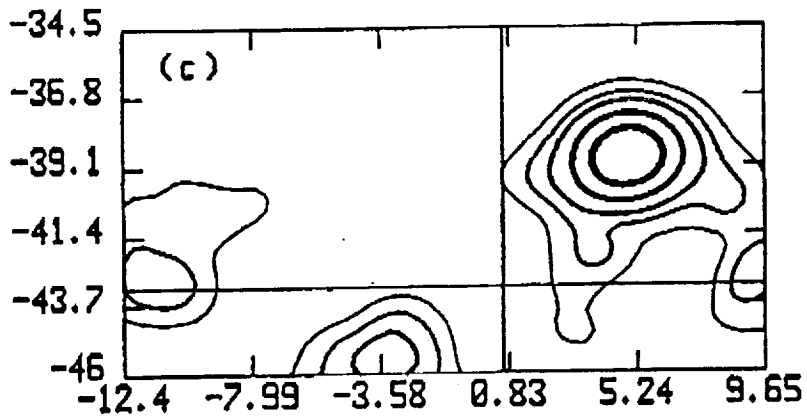
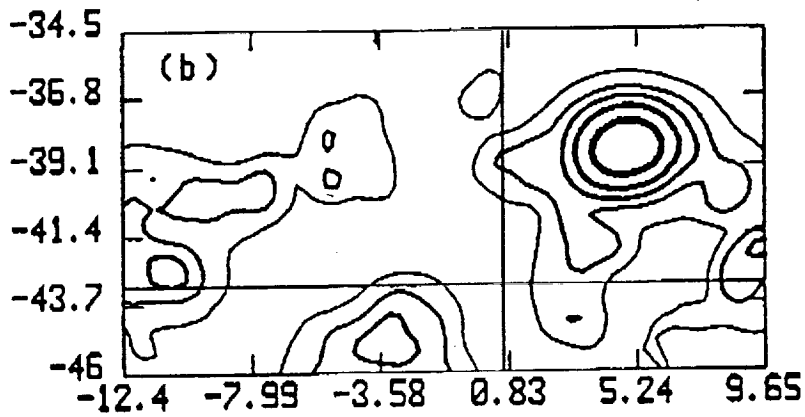
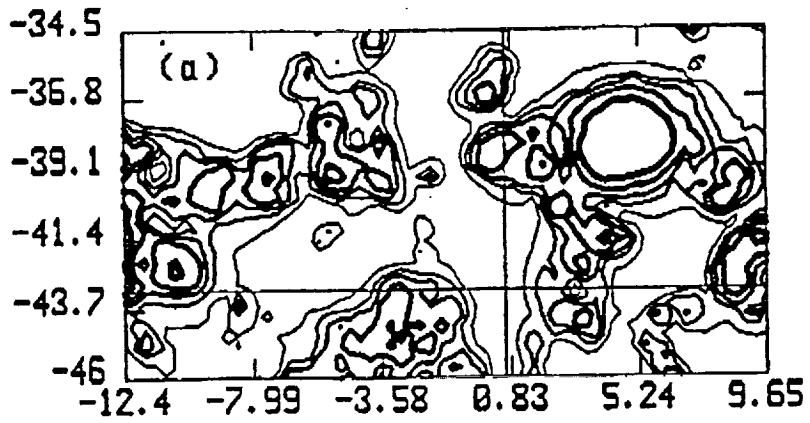


Fig. 3²⁹² C-4

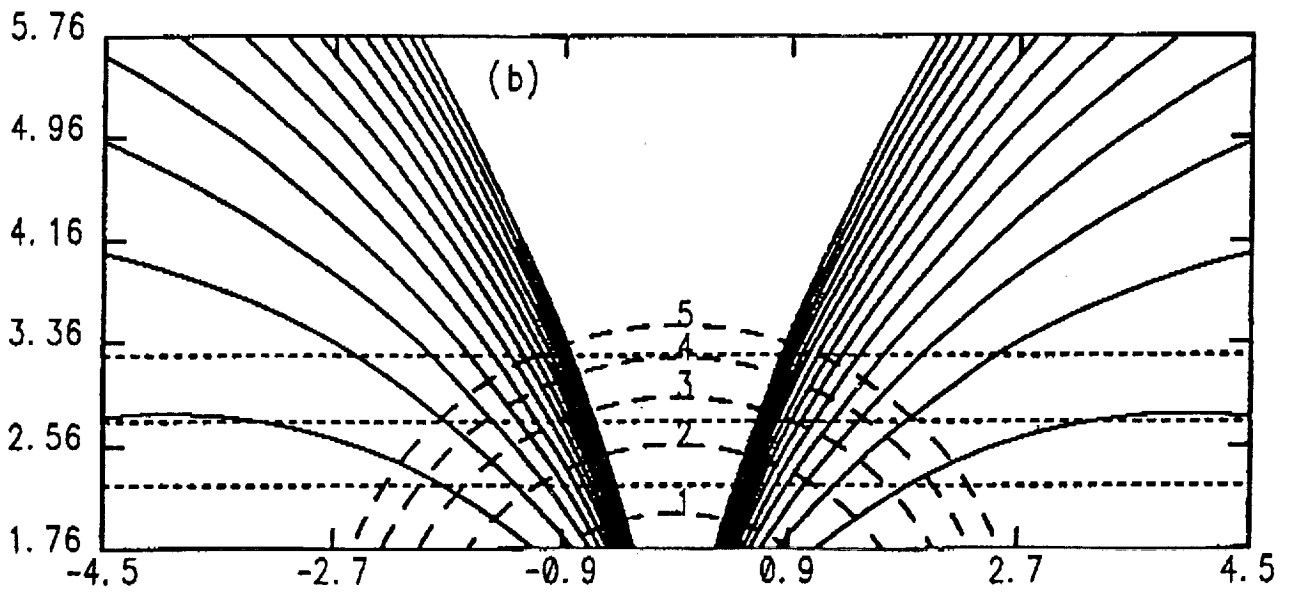
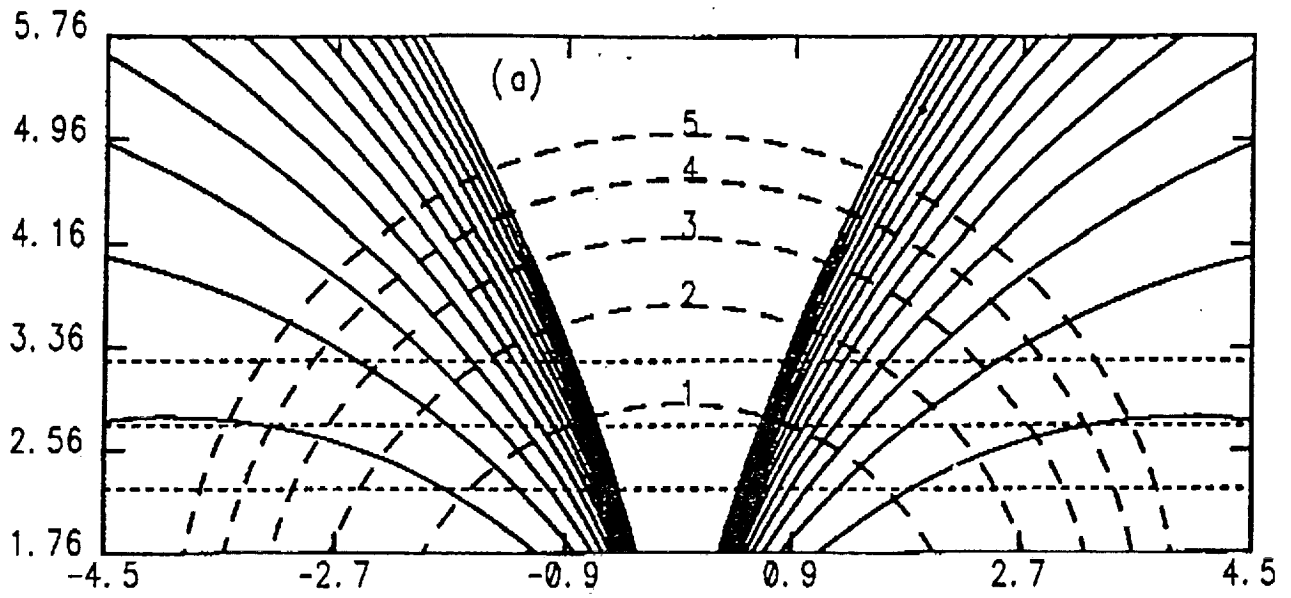


Fig 4.

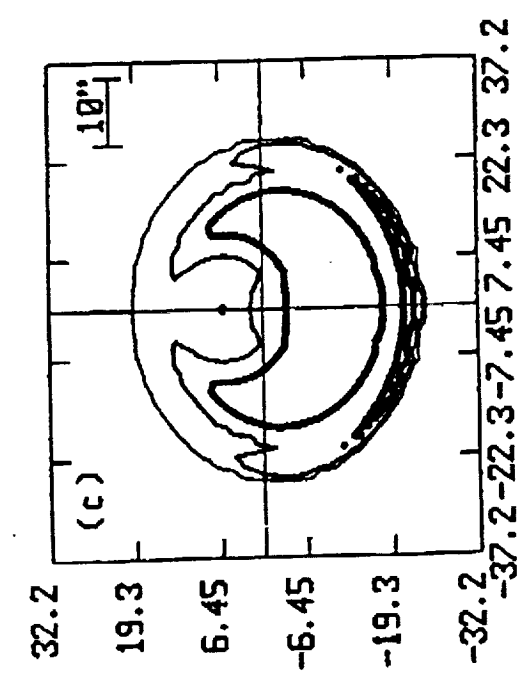
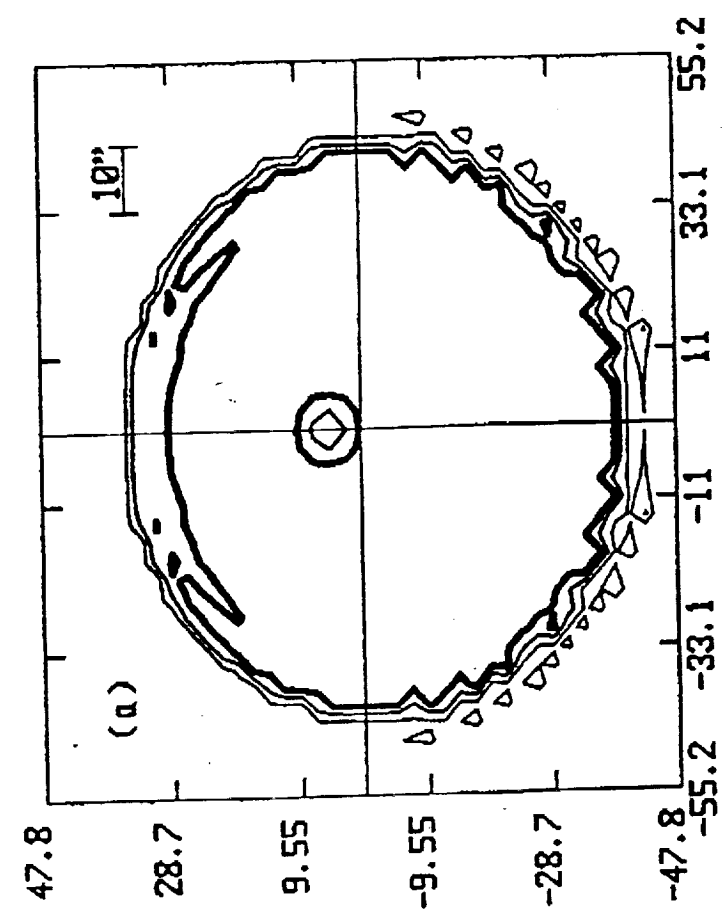
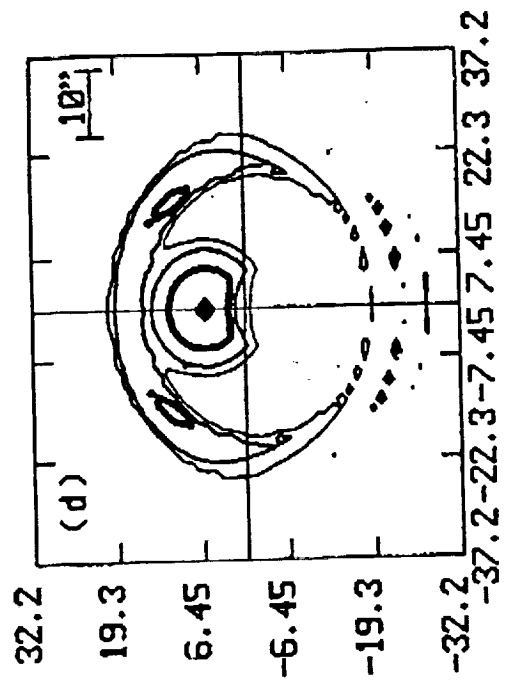
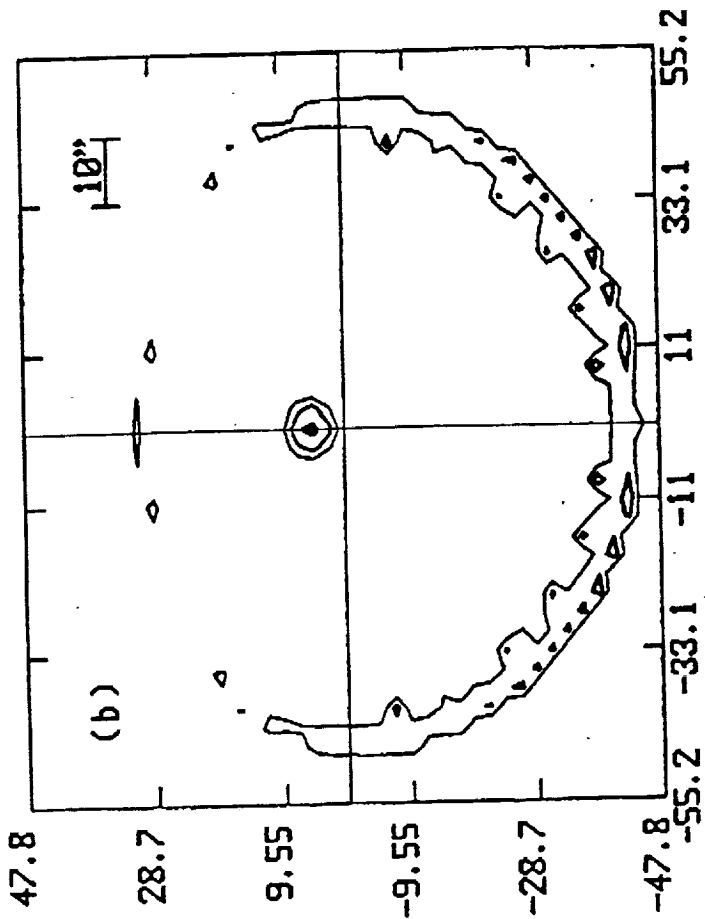


Fig 5

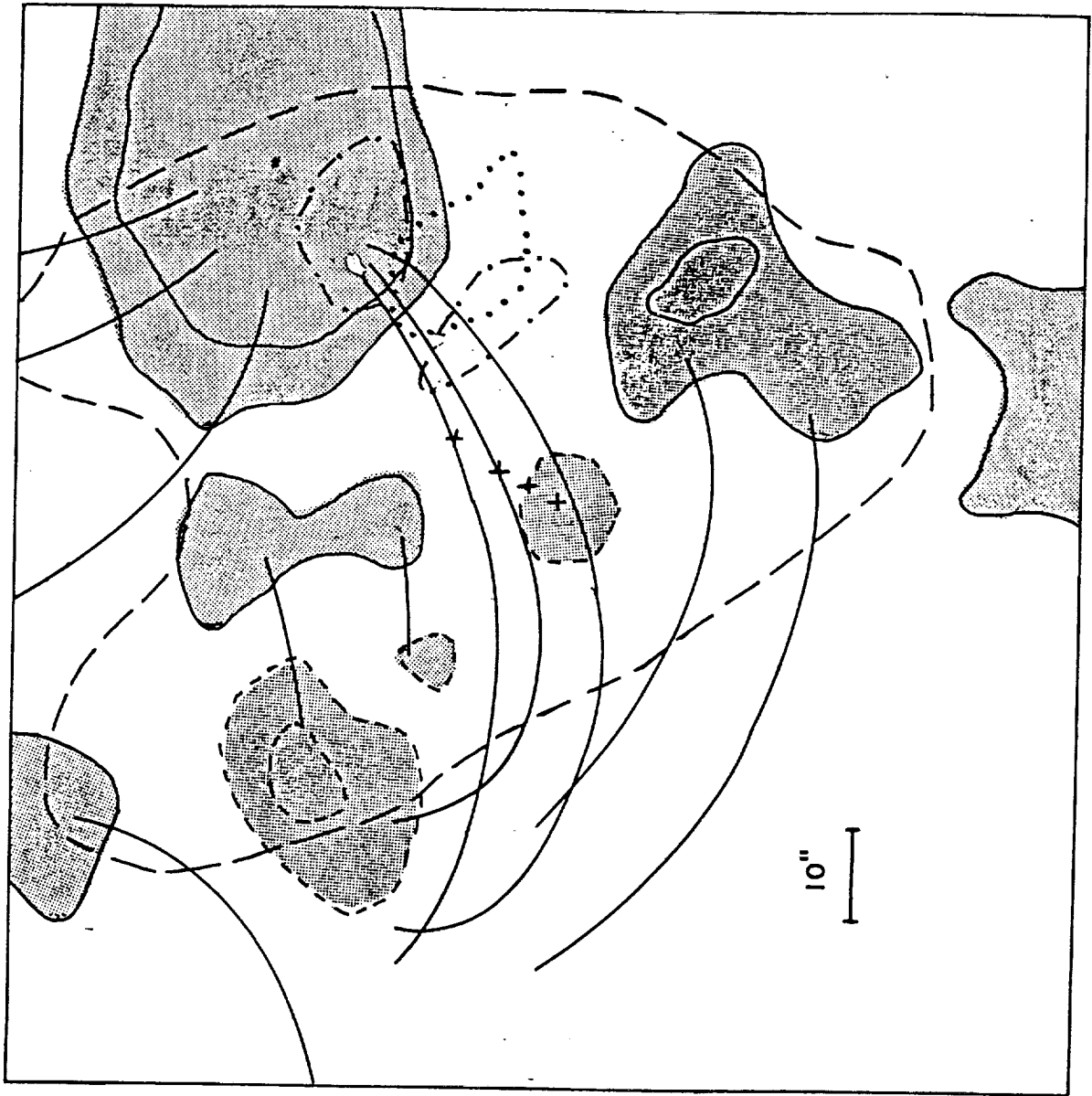


Fig. 6

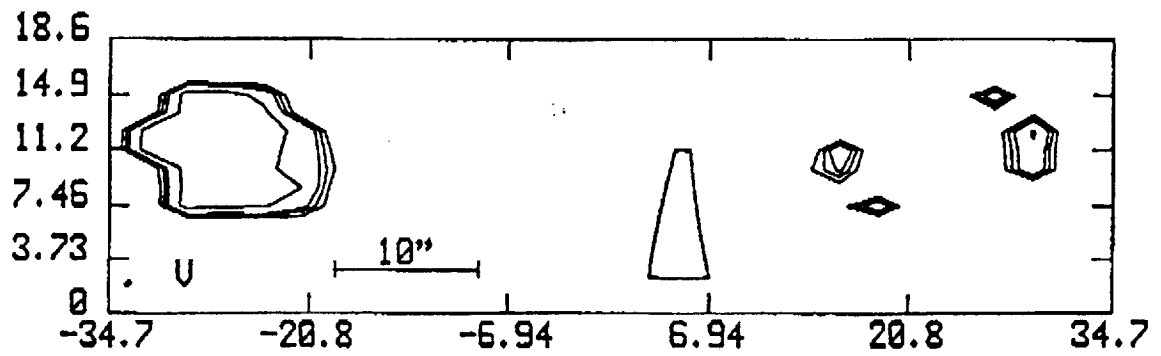
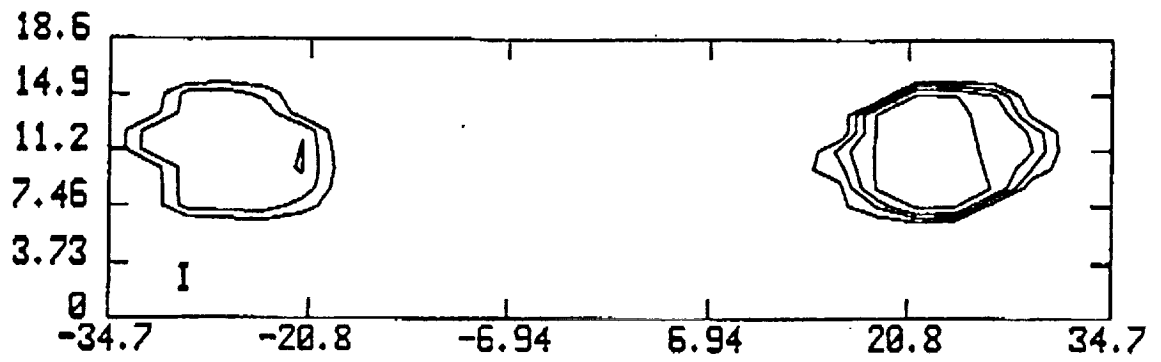


Fig. 7.

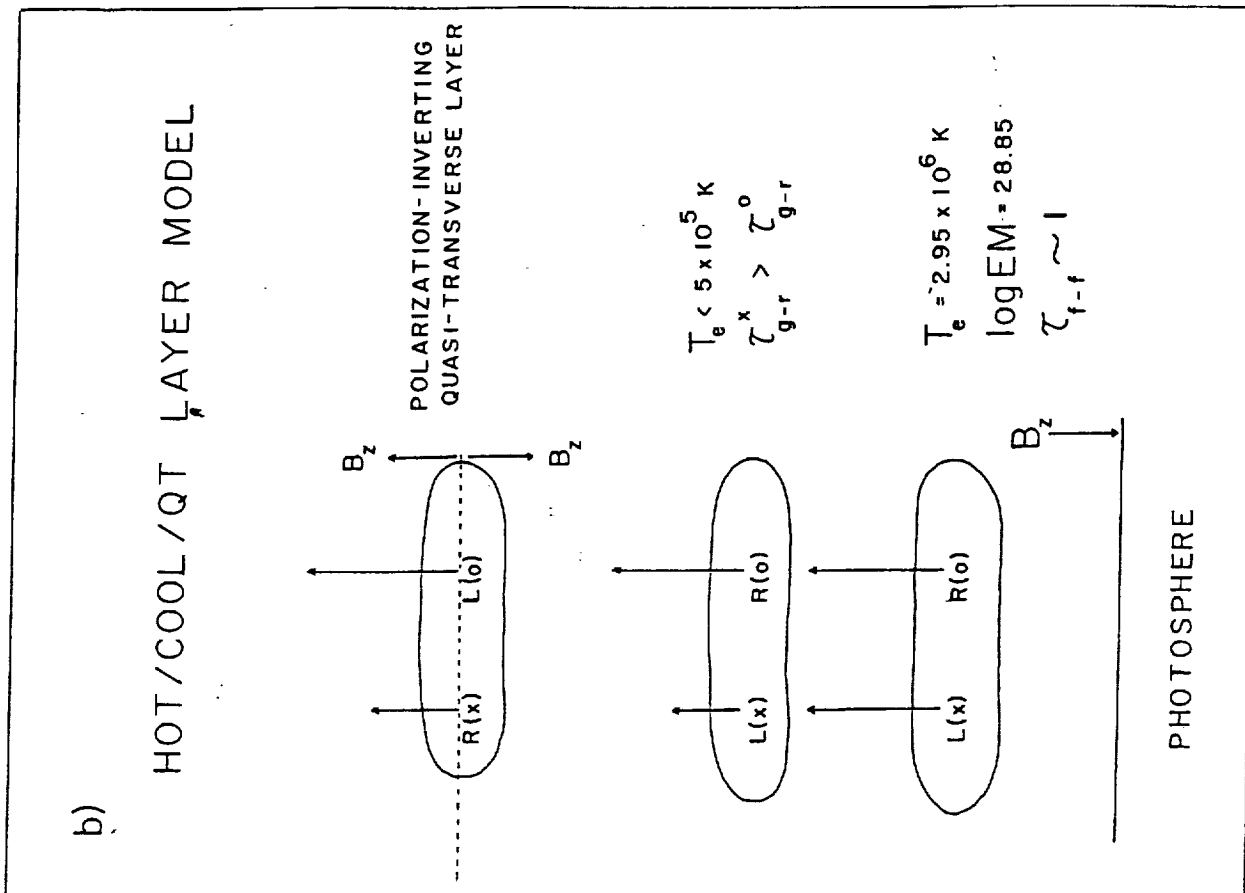
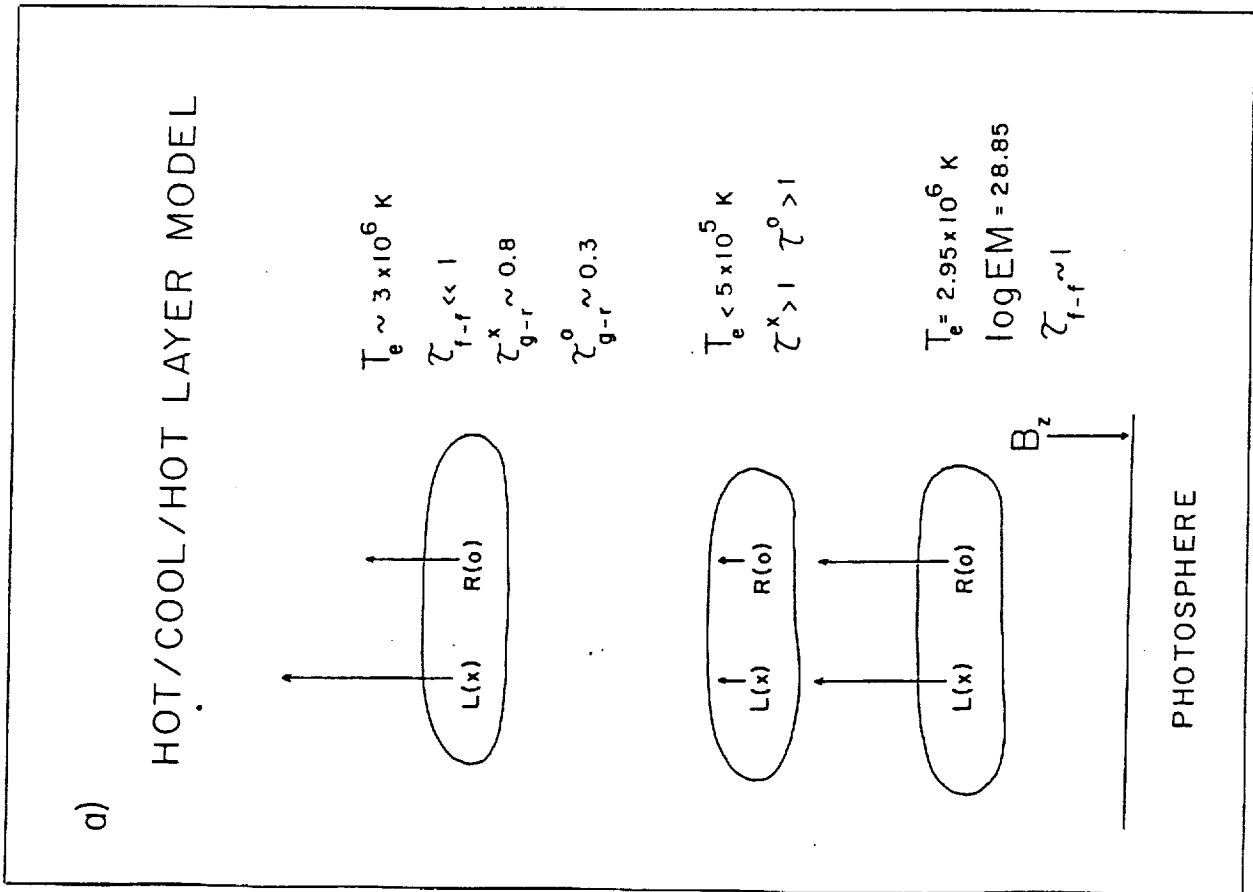


Fig. 8